

**Structural controls on multistage gold mineralisation within the  
Baie Verte Peninsula of Newfoundland, Canada**

Georgian Mănuș

Submitted in accordance with the requirements for the degree of  
Doctor of Philosophy

The University of Leeds  
School of Earth and Environment

September 2023

## **Declaration**

The candidate confirms that the work submitted is his own and that appropriate credit has been given where reference has been made to the work of others.

This copy has been supplied on the understanding that it is copyright material and that no quotation from the thesis may be published without proper acknowledgement.

The right of Georgian Mănuc to be identified as Author of this work has been asserted by Georgian Mănuc in accordance with the Copyright, Designs and Patents Act 1988.

## Acknowledgments

First and foremost, I extend my sincerest thanks to my supervisors, Dr. Taija Torvela and Dr. Rob Chapman. None of this would have been possible without the support, guidance, patience, and encouragements that you have provided me with throughout my PhD journey. Thank you for all the input into my academic training, for all the advice, either professional or personal, and for looking over my well-being through the entire time. Your enthusiasm and kindness combined with the numerous field trips and other fun activities (failed attempts to learn how to brew beer) made the whole experience extremely enjoyable and for this, I am forever grateful.

I would also like to thank Dr. Stephen Piercey from the Memorial University of Newfoundland and Labrador for initiating the project in Newfoundland and for all his guidance and support. Signal Gold, formerly Anaconda Mining, is thanked for accepting me to conduct my PhD on one of their sites, for providing access to all their data, and for providing logistic support during my field campaigns.

Chief geologist David Copeland is gratefully acknowledged for all his contribution. Thank you for sharing with me your enthusiasm and vast experience on the Baie Verte Peninsula. Your guidance during fieldwork in conjunction with all the discussions and insights helped me to better understand the geological framework of the study area. Moreover, thank you for all the enthusiasm that you showed towards the project and for accepting all my ideas.

Carly, Dean, Mike, Lindsay, Matt, Owen, Alisson, and Michelle, thank you for all the support towards my fieldwork, but more importantly, thank you for your kindness and hospitality, for all the fun evenings that we spent together, and for introducing me to the “*Newfy*” culture.

Dr. Simon Tapster and Dr. Nick Roberts from BGS are thanked for their collaboration on the geochronological work. In particular I want to thank Nick for conducting the analysis and for all his training, suggestions, and corrections.

Dr. Mark Cooper from the Geological Survey of Northern Ireland and Dr. Steve Hollis from the University of Edinburgh are greatly appreciated for their invaluable contributions through comparative discussions regarding the geological settings of the Newfoundland Appalachians and of the Irish Caledonides. These significantly enhanced my comprehension on the regional geotectonic setting of the

two areas. Additionally, I extend my gratitude for the enjoyable field trips we had in Ireland, Northern Ireland, and Scotland.

Special thanks are extended to members of staff from the University of Leeds who have played a significant role in my academic development, who advised me on different parts of my project or who have assisted me with various analytical techniques. Here I want to name a few: Dan Morgan, Richard Walshaw, David Banks, John Wyn Williams (in short Harri), Graham McLeod.

I extend my honest thanks to many of my friends and colleagues who have had a great positive input towards my PhD experience at both personal and professional levels. I will start this list with special thanks to Roxana for all her friendship over the last 10+ years and for being a great housemate while in Leeds. I cannot imagine my life in Leeds without you in the frame. I will continue the list with Hugh, Carl, James, Dan, Lucia, Moh, Simon, Charlotte, Sissy, Antonio, Rachel, and Matt – thank you guys for being amazing colleagues and friends, for all the fun memories that we share, and for all your positive encouragements during the less pleasant times of the PhD. Vlad & Andra (now I have to mention you only as a “*package*”), Emma, Mishu, Adriana, Nina, Lili, Gabi – thank you for the endless support that you showed me over the years, and also for the direct input into the thesis, either through proof readings, format editing, or even discussions related to the project. I will end this list with Alin and Alex, two of my oldest friends – thank you for all the moral support and for all the confidence that you inspired me with lately, and for your direct or indirect contributions towards the thesis.

I extend my sincere gratitude to my mother and sister who have supported me during every step of this journey, but most importantly for their unerring support with anything that I choose to do.

Lastly, this project would have not been possible without the financial and logistic support received from: the University of Leeds and the School of Earth and Environment; Natural Environment Research Council; British Geological Survey; Geological Survey of Northern Ireland; Society of Economic Geologists; Institute of Materials, Minerals and Mining; The Geological Society of London.

## Abstract

The Baie Verte Peninsula (BVP) is one of the richest auriferous regions within the Newfoundland Appalachians hosting more than 100 economic and sub-economic gold occurrences. The geological setting of the BVP resulted from the accretion of several micro-terranes of Iapetus origin to the Laurentian margin during the Ordovician Taconic Orogeny. The Baie Verte Line (BVL), a major crustal fault, represents the suture between the Laurentian margin and the accreted island arcs. Subsequent progressive deformation ( $D_2$ ) developed under a sinistral transpressional setting during the Salinic and Acadian orogenic events. Later deformational phases ( $D_3$ - $D_4$ ) resulted in response to complex dextral transcurrent motions localised along the BVL during the Neo-Acadian Orogeny.

The studied gold occurrences, Stog'er Tight, Argyle, Romeo & Juliet, Deer Cove, and Pine Cove lie along splays of the BVL. New structural, mineralogical, and geochronological data has been collected through geological mapping, optical and SEM/CL investigations of mineralized samples, and in-situ LA-ICP-MS U-Th-Pb geochronology of monazite, xenotime, and titanite. Structural data analysis showed that at least three deformational events ( $D_2$ - $D_4$ ) influenced the formation and the present geometry of the gold deposits. Mineralogical and geochronological data revealed complex paragenetic sequences in each deposit and at least two periods of gold precipitation.

The age of the first gold mineralising moment is constrained between ~420 to 410 Ma. The mineralised veins formed during the  $D_2$  progressive deformation, under brittle-ductile conditions, broadly synchronous with the development of E-W striking and south directed thrusts, splays of BVL.

The maximum age of the second gold mineralising event is ~396 Ma, whereas the best estimate age is ~380 Ma. The gold bearing veins formed during the  $D_3$ - $D_4$  deformational events. At this time the entire BVP was under extension-related exhumation processes. Currently, it is unclear whether the later mineralising fluids either augmented the existing gold endowment or remobilized the pre-existing gold.

## **Table of contents**

<b>I. Introduction.....</b>	<b>1</b>
I.1. Project Rationale .....	1
I.2. Study area and project aims .....	6
I.3. Thesis structure .....	8
<b>II. Literature Review .....</b>	<b>10</b>
II.1. Architecture of Newfoundland Island.....	10
II.2. Tectonic evolution of Newfoundland Appalachians .....	13
II.3. Geological Setting of the Baie Verte Peninsula.....	17
II.3.1. Stratigraphy and palaeoenvironment of the Baie Verte Peninsula .....	20
II.3.2. Structural evolution of the Baie Verte Peninsula.....	34
II.4. Gold mineralisation in the BVP.....	39
II.5. Current understandings of the studied gold deposits .....	47
<b>III. Methodology .....</b>	<b>52</b>
III.1. Field work (geological mapping and sample collection) .....	52
III.1.1. Mapping rationale and visited areas .....	53
III.1.2. Data Processing and Visualisation .....	56
III.1.3. Sample collection .....	57
III.2. Sample selection & preparation .....	59
III.2.1. Sample selection.....	59
III.2.2. Sample preparation.....	60
III.3. Geophysical data .....	63
III.3.1. Data enhancement .....	63
III.4. Microstructural analyses.....	65
III.5. Petrographic analyses.....	67
III.5.1. Optical microscopy.....	67
III.5.2. SEM-CL techniques .....	68
III.5.3. EDS and BSE .....	68
III.5.4. Cathodoluminescence (CL).....	70
III.6. SEM & EPMA analysis of gold particles.....	72
III.6.1. Analytical techniques .....	74
III.6.2. Data presentation.....	75
III.7. In-situ LA-ICP-MS U-Th-Pb geochronology .....	78
III.7.1. Analytical techniques and data visualisation.....	79

<b>IV Structural setting of the Point Rouse Complex (Results &amp; Interpretations)</b>	<b>82</b>
IV.1 Structural elements identified within the Point Rouse Complex (field, microstructural and aeromagnetic observations)	82
IV.1.1 Folds	83
IV.1.2 Planar and linear fabrics	99
IV.1.3 Fault systems	110
IV.1.4 Minor structures	129
IV.2 Interpretations	131
IV.2.1 1 <sup>st</sup> deformation phase	131
IV.2.2 2 <sup>nd</sup> deformation phase	135
IV.2.3 3 <sup>rd</sup> deformation phase	143
IV.2.4 4 <sup>th</sup> deformation phase	146
IV.2.5 Syn-to-post D <sub>4</sub> structures	148
IV.2.6 Post–D <sub>4</sub> structures	148
IV.2.7 Structures of uncertain generation	149
IV.3 Summary	150
<b>V. Gold mineralisation in the Point Rouse Complex (Results and Interpretations)</b>	<b>153</b>
V.1. Geological characteristics of the studied gold deposits (field, mineralogical/petrographical and geochemical observations)	154
V.1.1. The Pine Cove deposit	155
V.1.2. The Stog’er Tight deposit	188
V.1.3. The Argyle deposit	219
V.1.4. The Romeo & Juliet prospect	242
V.1.5. The Deer Cove prospect	271
V.1.6. Geochemical signature of gold populations	297
V.2. Interpretations	307
V.2.1. Vein development and relative timing	307
V.2.2. Mineral paragenetic evolution	314
V.2.3. Insights from gold geochemistry	325
V.3. Summary	327
<b>VI. Timing of gold mineralisation in the Point Rouse Complex based on in-situ LA-ICP-MS U-Th-Pb analysis of monazite, xenotime and titanite (Results &amp; Interpretations)</b>	<b>330</b>
VI.1. Description of analysed grains	330
VI.2. Data quality assessment	332

VI.2.1. Excluded monazite and xenotime data points .....	333
VI.2.2. Monazite data (Stog' er Tight and Argyle) .....	338
VI.2.3. Xenotime data (Stog' er Tight, Argyle, and Romeo & Juliet).....	342
VI.2.4. Titanite data (Deer Cove).....	346
VI.3. Interpretations .....	347
VI.3.1. Grain textures and morphologies .....	347
VI.3.2. Reasons for date discordance in the excluded points .....	347
VI.3.3. Age interpretation of monazite data .....	349
VI.3.4. Age interpretation of xenotime data.....	355
VI.3.5. Age interpretation of titanite data.....	358
VI.4. Timing of gold mineralisation.....	359
VI.5. Summary .....	361
<b>VII. Discussions and Synthesis .....</b>	<b>363</b>
VII.1. Implications for the structural evolution of the Baie Verte Peninsula .....	363
VII.1.1. Evolution of the PRC during Salinic & Acadian orogenic cycles .....	367
VII.1.2. Evolution of the PRC during the Neo-Acadian orogeny .....	369
VII.2. A regional genetic framework for gold mineralisation within the Baie Verte Peninsula (BVP).....	371
VII.3. Implications for exploration strategies .....	374
VII.4. Recommendations for future work .....	377
<b>VIII. Conclusions .....</b>	<b>379</b>
<b>Bibliography .....</b>	<b>381</b>
<b>Appendix I.....</b>	<b>404</b>
<b>Appendix II.....</b>	<b>425</b>
<b>Appendix III.....</b>	<b>441</b>
<b>Appendix IV.....</b>	<b>450</b>
<b>Appendix V.....</b>	<b>511</b>



## **List of tables**

<b>Table II.1</b> – Summary descriptions of Precambrian to Early Ordovician continental margin successions .....	22
<b>Table II.2</b> – Summary descriptions of obducted Late Cambrian to Mid Ordovician ophiolitic complexes and cover sequence rocks.....	25
<b>Table II.3</b> – Summary descriptions of Late Ordovician to Mid Silurian continental volcano-sedimentary rocks.....	33
<b>Table II.4</b> – General characteristics of orogenic gold deposits .....	41
<b>Table II.5</b> – Characteristics of epigenetic gold occurrences from the Baie Verte Peininsula after Evans 2004.....	44
<b>Table III.I</b> – Accepted number of gold particles with relevant results, analysed from each of the studied deposit/prospect. ....	62
<b>Table IV.1</b> – Summary description of the main structural elements identified within the Point Rousse Complex .....	85
<b>Table IV.2</b> -Descriptions of minor structural elements identified within the Point Rousse Complex .....	130
<b>Table IV.3</b> – Correlation chart between the structural sequence interpreted within this study and previous works on structural domains from within and outside the Point Rousse Complex (PRC). Pacquet Harbour Group (PHG); Ming’s Bight Group (MBG); Cape Brulé Porphyry (CBP); Cape St. John Group (CJG). Red dashed line = synchronously or progressive deformation.....	133
<b>Table V.1</b> – Descriptions of vein sets identified within the Pine Cove open pit .....	159
<b>Table V.2</b> – Summary characteristics of the alteration minerals identified in the proximal alteration halo and in the ore zone of the Pine Cove deposit.....	168
<b>Table V.3</b> – Summary CL characteristics of the quartz generations observed in samples from the Pine Cove deposit. ....	170
<b>Table V.4</b> – Summary characteristics of the ore minerals from the Pine Cove deposit. ....	187
<b>Table V.5</b> – Descriptions of vein sets identified within the Stog’er Tight and East Zone open pits .....	193
<b>Table V.6</b> – Summary characteristics of the alteration minerals identified in the proximal alteration halo and in the ore zone of the Stog’er Tight deposit. ....	201
<b>Table V.7</b> – Summary CL characteristics of the quartz generations observed in samples from the Stog’er Tight deposit. ....	203
<b>Table V.8</b> – Summary characteristics of the ore minerals from the Stog’er Tight deposit.	217
<b>Table V.9</b> – Summary characteristics of the alteration minerals identified in the proximal alteration halo and in the ore zone of the Argyle deposit.....	224
<b>Table V.10</b> – Summary CL characteristics of the quartz generations observed in samples from the Argyle deposit.....	226
<b>Table V.11</b> – Summary characteristics of the ore minerals from the Argyle deposit.....	241
<b>Table V.12</b> – Descriptions of vein sets identified within and outside the Juliet zone .....	246
<b>Table V.13</b> – Summary characteristics of the alteration minerals identified in the proximal alteration halo associated to the veins from the Juliet South zone of the Romeo & Juliet prospect. ....	254
<b>Table V.14</b> – Summary CL characteristics of the quartz generations observed in samples from the Juliet South zone of the Romeo & Juliet prospect.....	256
<b>Table V.15</b> – Summary characteristics of the ore minerals from the Juliet South zone of the Romeo & Juliet prospect. ....	270

<b>Table V.16</b> – Descriptions of vein sets identified in the Deer Cove area .....	276
<b>Table V.17</b> – Summary characteristics of the alteration minerals identified in the proximal alteration halo of the Deer Cove prospect. ....	282
<b>Table V.18</b> – Summary CL characteristics of the quartz generations observed in samples from the Deer Cove prospect.....	284
<b>Table V.19</b> – Summary characteristics of the ore minerals from the Deer Cove prospect.	297
<b>Table V.20</b> – Characteristics of gold types identified in the studied gold populations .....	305
<b>Table V.21</b> – Mineral inclusion species identified in both the in-situ and liberated gold particles from all the studied localities.....	307
<b>Table VI.1</b> – Summarised descriptions of the analysed grains.....	331
<b>Table VI.2</b> – List of sections, analysed minerals and number of data points .....	333
<b>Table VI.3</b> – Minimum (min) and maximum (max) U-Th-Pb monazite dates .....	340
<b>Table VI.4</b> – Minimum (min) and maximum (max) values for Pb, Th, and U concentrations of the analysed monazite, xenotime and titanite grains.....	341
<b>Table VI.5</b> – Minimum (min) and maximum (max) U-Pb xenotime dates .....	345
<b>Table VI.6</b> – Minimum (min) and maximum (max) U-Pb titanite dates.....	345
<b>Table VI.7</b> – Interpreted ages of gold mineralisation.....	360

## **List of figures**

- **Figure I.1** – General tectonic setting of different types of gold deposits ..... 3
- **Figure I.2** – A – Location of Newfoundland Island on the North American continent. B – Distribution of known gold occurrences across Newfoundland. C – Simplified geological map of the Baie Verte Peninsula ..... 5
- **Figure II.1** – A - Location of Newfoundland Island within the Appalachian–Caledonian belt. B – Simplified geological map of Newfoundland and location of the BVP (red square) ..... 11
- **Figure II.2** – Tectonic evolution of Newfoundland Appalachians during the Late Cambrian to Late Ordovician ..... 14
- **Figure II.3** – Tectonic evolution of Newfoundland Appalachians during the Early Silurian to Early Carboniferous ..... 16
- **Figure II.4** – Simplified map of the Baie Verte Peninsula ..... 18
- **Figure II.5** – Stratigraphic model of the Baie Verte Peninsula ..... 19
- **Figure II.6** – Development and closure of the Humber Sea during Mid Cambrian to Mid Ordovician ..... 23
- **Figure II.7** – Structural evolution model of the Baie Verte Peninsula modified after Waldron et al., 1998. .... 36
- **Figure II.8** - Time correlation chart between the main orogenic events that affected the Baie Verte Peninsula, local magmatic activity, and the formation of the studied orogenic gold occurrences ..... 46
- **Figure II.9** - A - Geological map of the Point Rousse Complex (PRC). B – Representative stratigraphic column of the PRC ..... 48
- **Figure III.1** - Google Earth image of northern part of the Baie Verte Peninsula, Newfoundland, and the location of the observation points from both fieldwork campaigns (2018 - red points and 2019 - green points). .... 55
- **Figure III.2** - Comparison between the poles to the foliation plane measurements collected for this study (red poles, N=241) and the poles to the foliation measurements of Skulski et al., (2017) (black poles, N=103) from the northern part of the Flat Water Point Group and the southern part of the Advocate Complex. .... 57
- **Figure III.3** – Example of an oriented sample annotated while still in place. .... 58
- **Figure III.4** - Example of an oriented sample cut perpendicular to the foliation and parallel to the stretching mineral lineation, note the location of the future section plane marked on the cut surface and the top and the dip marks. .... 61
- **Figure III.5** – Kinematic indicators used in this study: A – asymmetric porphyroclast systems. B – C-S-C' composite fabric. C – Pyrite fringes ..... 67
- **Figure III.6** – Full section image scans of the MPAG1 thin section, section length ~4.5 centimeters. A – microscope scan in transmitted light; B – BSE panoramic image scan; C – CL panoramic image scan ..... 69
- **Figure III.7** – Example of chart where the cumulative percentile vs increasing concentration of Ag are plotted. .... 77
- **Figure IV.1** - A - Geological map of the Point Rousse Complex (PRC).. ..... 89
- **Figure IV.2** – Orientation of  $F_{MR}$  folds within the Point Rousse Area ..... 96
- **Figure IV.3** - Southern-hemisphere, equal-area, stereographic projections of the  $F_{NT}$  fold axes and crenulation lineations (A) and of the poles (black dots) to their fracture cleavages (grey dashed lines) (B). .... 99

- **Figure IV.4** - Southern-hemisphere, equal-area, stereographic projections of the  $S_R/S_{LC}$  foliation plane and mineral stretching lineation measurements from the Point Rouse Complex (PRC)..... 107
- **Figure IV.5** - Tilt Derivative aeromagnetic map of the Baie Verte Peninsula (A); and zoomed in image into the study area (B - black square on image A)..... 112
- **Figure IV.6** – Tilt derivative aeromagnetic map of the central-south part of the Point Rouse Complex..... 120
- **Figure IV.7** – Southern-hemisphere, equal-area, stereographic projections of the reverse, brittle-ductile fault measurements from the Point Rouse Complex..... 121
- **Figure IV.8** - Southern-hemisphere, equal-area, stereographic projections for the brittle-ductile to brittle faults and shear bands identified within the Point Rouse area. .... 127
- **Figure IV.9** - Southern-hemisphere, equal-area, stereographic projections for the late, brittle faults identified within the Point Rouse Complex.. .... 129
- **Figure IV.10** – Cartoons that show the structural evolution of the Point Rouse Complex during the  $D_2$  phase.. .... 139
- **Figure IV.11** – Representative diagrams illustrating inferred and observed outcrop geometries that resulted between the superposition of different structural elements within the PRC. .... 142
- **Figure IV.12** – Cartoons that show the structural evolution of the Point Rouse Complex during both the  $D_3$  phase (A) and the  $D_4$  phase (B)..... 145
- **Figure IV.13** – 3D Sketch diagram illustrating the overall relationships between the four identified fold generations and their associated planar fabrics; the image is most representative for areas located in the proximity of major ductile thrusts, but it can be extrapolated across the region.....152
- **Figure V.1** - A – Simplified geological map of the Pine Cove deposit; B, C, D - Southern-hemisphere, equal-area, stereographic projections of the poles to the foliation planes (B), of the stretching mineral lineation (C), and of the poles to the main mineralised vein sets (D) from the Pine Cove area. .... 158
- **Figure V.2** - A – Simplified geological map of the Stog'er Tight deposit; B - Southern-hemisphere, equal-area, stereographic projections of the poles to the foliation planes and of the stretching mineral lineation; C - The poles to the main mineralised vein sets. .... 189
- **Figure V.3** - A – Simplified geological map of the Argyle deposit; B - Southern-hemisphere, equal-area, stereographic projections of the poles to the foliation planes and of the stretching mineral lineation. .... 220
- **Figure V.4** - A – Simplified geological map of the Romeo & Juliet prospect; B - Southern-hemisphere, equal-area, stereographic projections of the poles to the foliation planes and to the  $D_{2b}$  shear zones, and of the stretching mineral lineation; C - The stereographic projections of the poles to the main mineralised vein sets. .... 244
- **Figure V.5** - A – Simplified geological map of the Deer Cove area. B, C - Southern-hemisphere, equal-area, stereographic projections of the poles to the foliation planes and of the stretching mineral lineation (B), and of the poles to the main mineralised vein sets (C) from the Deer Cove area. .... 273
- **Figure V.6** – Representative plots that show the random distribution of the inclusion, annealed, and free Au on the Ag or Cu profiles in the Pine Cove (A), Romeo & Juliet (B) and Argyle (C, D) deposits/prospects: note the two free Au grains with high Cu content in Argyle (D).....299

- **Figure V.7** – Representative plots that show differences in the Ag and Cu concentrations of the inclusion Au and the free Au from Stog’er Tight..... 301
- **Figure V.8** – Representative plots that show some differences in the Ag and Hg concentrations of the inclusion Au and the free Au from Deer Cove ..... 302
- **Figure V.9** – Plots between the cumulative percentile and the increasing values of Ag (A), Hg (B), and Cu (C) for all the studied deposits..... 304
- **Figure V.10** – Hg vs Ag (A) and Cu vs Ag (B) binary plots for gold particles from all the studied gold populations..... 306
- **Figure V.11** – The relative timing of the vein sets observed in each of the studied gold deposits/prospects..... 308
- **Figure V.12** – 3D sketch diagram illustrating the overall relationships between the F<sub>2b</sub>, F<sub>3</sub>, and F<sub>4</sub> fold generations and some of the vein sets observed in the Pine Cove, Stog’er Tight, Argyle, and Deer Cove areas..... 313
- **Figure V.13** – Mineral paragenetic sequence for the Pine Cove deposit..... 315
- **Figure V.14** – Mineral paragenetic sequence for the Stog’er Tight deposit..... 316
- **Figure V.15** – Mineral paragenetic sequence for the Argyle deposit..... 316
- **Figure V.16** – Mineral paragenetic sequence for the Romeo & Juliet prospect..... 317
- **Figure V.17** – Mineral paragenetic sequence for the Deer Cove prospect..... 317
- **Figure V.18** – Schematic cartoons that show the development of the first and second generations of quartz (Q<sub>1</sub>, Q<sub>2</sub>) with respect to the evolution of the syn-to-post D<sub>2b</sub> veins (A & B) and the formation of the third generation of quartz (Q<sub>3</sub>) during the development of the syn-to-post D<sub>3</sub> veins (C).. ..... 319
- **Figure V.19** – Schematic cartoons that show the development of pyrite (Py) during both the first (A) and second (B) hydrothermal events. .... 323
- **Figure VI.1** - Stog’er Tight monazite data plotted on <sup>208</sup>Pb/<sup>232</sup>Th vs <sup>206</sup>Pb/<sup>238</sup>U (A, B), Tara-Wasserburg (C, D), and Wetherill (E, F) concordia diagrams.....335
- **Figure VI.2** - Argyle monazite data plotted on <sup>208</sup>Pb/<sup>232</sup>Th vs <sup>206</sup>Pb/<sup>238</sup>U (A, B), Tara-Wasserburg (C, D), and Wetherill (E, F) concordia diagrams.....336
- **Figure VI.3** – Xenotime data plotted on Tara-Wasserburg concordia diagram; A, B – Stog’er Tight; C, D – Argyle; E, F – Romeo & Juliet..... 336
- **Figure VI.4** – Th-Pb and U-Pb binary plots for the Stog’er Tight (A, B) and Argyle (C, D) monazites..... 341
- **Figure VI.5** – Binary plots of U vs <sup>206</sup>Pb/<sup>238</sup>U dates (A) and U vs Discordance (between the <sup>208</sup>Pb/<sup>232</sup>Th and the <sup>206</sup>Pb/<sup>238</sup>U dates) (B) for the accepted Stog’er Tight monazites. .... 342
- **Figure VI.6** –Pb-U and Pb-Th binary plots for the Stog’er Tight (A, B) and Argyle (C, D) xenotimes.. ..... 343
- **Figure VI.7** – Binary plots between Pb and U (A), Pb and Th (B), and between U and Th (C) for the Romeo & Juliet xenotimes. .... 344
- **Figure VI.8** – Deer Cove titanite data plotted on Tara-Wasserburg concordia diagram; note the lower intercept age of 380.7 ± 17.4 interpreted as best estimate for titanite crystallisation. .... 346
- **Figure VI.9** – Interpreted weighted mean ages for the accepted Th-Pb dates recorded in the Stog’er Tight monazites. .... 351

- **Figure VI.10** – Interpreted weighted mean ages for the accepted Th-Pb dates recorded in the Argyle monazites..... 352
- **Figure VI.11** – Interpreted weighted mean ages for the accepted concordia dates recorded in the Stog’er Tight xenotimes. .... 356
- **Figure VI.12** – Interpreted weighted mean ages for the accepted concordia dates recorded in the Argyle xenotimes. .... 357
- **Figure VI.13** – Interpreted weighted mean ages for the accepted concordia dates recorded in the Romeo & Juliet xenotimes. .... 358
- **Figure VI.14** – Compilation of geochronological data for the Pine Cove, Stog’er Tight, Argyle, Romeo & Juliet, and Deer Cove gold occurrences; shaded intervals represent the timing of the two gold mineralising events; ages provided in million years (Ma); the length of the bars represent the age uncertainties..... 362
- **Figure VII.1** – Time correlation chart between the main orogenic events that affected the Baie Verte Peninsula, structural setting, local magmatic activity, and gold mineralisation. .... 365
- **Figure VII.2** – Cartoons illustrating the structural evolution of the Baie Verte Peninsula (BVP) during Mid to Late Silurian (A), Early Devonian (B), late Early to Mid-Devonian (C). D<sub>2a</sub>, D<sub>2b</sub>, and D<sub>3</sub> represent the deformation phases described during this study.. .... 366
- **Figure VII.3** – Compilation of geochronological data for orogenic gold occurrences from west and central Newfoundland... .... 376

## **List of plates**

<b>Plate IV.1</b> – Representative field photographs for the intrafolial folds ( $F_i$ , interpreted as $F_{2a}$ ) and for the south verging folds ( $F_{SV}$ , interpreted as $F_{2b}$ ) and of their associated fabrics:.....	91
<b>Plate IV.2</b> – Representative field photographs for the mesoscale recumbent folds ( $F_{MR}$ , interpreted as $F_3$ ) and of their associated fabrics.....	95
<b>Plate IV.3</b> – Representative field photographs for the north trending folds ( $F_{NT}$ , interpreted as $F_4$ ) and of their associated fabrics.....	98
<b>Plate IV.4</b> – Representative field photographs for the $S_R$ and $S_L/S_{LC}$ planar fabrics (interpreted as $S_{2a}$ and $S_{2b}$ , respectively), and for the $L_R$ (interpreted as $D_{2a}$ ) and $L_{MR}$ (interpreted as crenulation lineation related to $F_3$ folds) linear fabrics .....	103
<b>Plate IV.5</b> – Representative photographs of microstructural elements that suggest South directed transport along the $D_{2a}/D_{2b}$ structures and also their reactivation as extensional structures (down-dip sliding).....	104
<b>Plate IV.6</b> – Representative field photographs for the major ductile to brittle-ductile thrusts (interpreted as $D_{2a}$ structures) and for the brittle-ductile reverse faults and shears (interpreted as $D_{2b}$ structures) .....	113
<b>Plate IV.7</b> – Representative photographs of microstructural elements that suggest South directed transport along the $D_{2a}/D_{2b}$ structures and also their reactivation as extensional structures (down-dip sliding).....	118
<b>Plate IV.8</b> – Representative field photographs for both the south dipping faults and steep, NW trending faults (interpreted as syn-to-post $D_4$ ).....	126
<b>Plate IV.9</b> – Representative field photographs for minor and late structures .....	127
<b>Plate V.1</b> – Representative images of the vein sets identified in the Pine Cove pit.	163
<b>Plate V.2</b> – Representative images of different altered intervals observed in the Pine Cove deposit .....	167
<b>Plate V.3</b> – Representative images of different types of quartz generations related to the Pine Cove mineralisation .....	173
<b>Plate V.4</b> – Representative images for different alteration minerals related to the Pine Cove mineralisation .....	179
<b>Plate V.5</b> – Representative images for different alteration and ore minerals related to the Pine Cove mineralisation .....	185
<b>Plate V.6</b> – Representative images of the vein sets identified in the Stog’er Tight and East Zone open pits and of some structures discussed in the text.....	194
<b>Plate V.7</b> – Representative images of different altered intervals observed in the the Stog’er Tight deposit.....	198
<b>Plate V.8</b> – Representative images of different quartz generations related to the Stog’er Tight mineralisation .....	206
<b>Plate V.9</b> – Representative images of different alteration minerals related to the Stog’er Tight mineralisation .....	210
<b>Plate V.10</b> – Representative images of different alteration minerals related to the Stog’er Tight mineralisation .....	214
<b>Plate V.11</b> – Representative images of different ore minerals related to the Stog’er Tight mineralisation.....	218
<b>Plate V.12</b> – Representative images for the mineralised veins and proximal alteration halo of the Argyle deposit.....	221
<b>Plate V.13</b> – Representative images of different quartz generations related to the Argyle mineralisation.....	227

<b>Plate V.14</b> – Representative images of different alteration minerals related to the Argyle mineralisation.....	231
<b>Plate V.15</b> – Representative images of different alteration and ore minerals from the Argyle deposit.....	235
<b>Plate V.16</b> – Representative images for the main structures that affect the Juliet South zone.....	245
<b>Plate V.17</b> – Representative images for the main vein sets identified in the Romeo & Juliet area.....	247
<b>Plate V.18</b> – Representative images for the proximal and the outer alteration halos observed in the Juliet area.....	253
<b>Plate V.19</b> – Representative images of different quartz generations related to the Juliet South mineralisation.....	259
<b>Plate V.20</b> – Representative images of different ore and alteration minerals observed in the Juliet South zone.....	263
<b>Plate V.21</b> – Representative images of different ore and alteration minerals observed in the Juliet South zone.....	268
<b>Plate V.22</b> – Representative images for the main vein sets identified in the Deer Cove area.....	277
<b>Plate V.23</b> – Representative images for the proximal and distal alteration halos observed in the Deer Cove area.....	281
<b>Plate V.24</b> – Representative images of different quartz generations related to the Deer Cove mineralisation.....	288
<b>Plate V.25</b> – Representative images of different alteration and ore minerals observed in the Deer Cove samples.....	293
<b>Plate V.26</b> – Representative images of different alteration and ore minerals observed in the Deer Cove samples.....	296



**List of abbreviations**

<b>Geological domains, formations, and structures</b>	
<b>BVL</b>	Baie Verte Line
<b>BBL</b>	Baie-Verte-Brampton Line
<b>EMPS</b>	East Pond Metamorphic Suite
<b>FLS</b>	Fleur de Lys Supergroup
<b>BC</b>	Birchy Complex
<b>MBG</b>	Ming's Bight Group
<b>BVB</b>	Baie Verte Belt
<b>BVOT</b>	Baie Verte Oceanic Tract
<b>BCC</b>	Betts Cove Complex
<b>SAG</b>	Snooks Arm Group
<b>MMF</b>	Mount Misery Formation
<b>SPF</b>	Scrape Point Formation
<b>BCF</b>	Bobby Cove Formation
<b>VBF</b>	Venam's Bight Formation
<b>BBCF</b>	Balsam Bud Cove Formation
<b>AC</b>	Advocate Complex
<b>PHG</b>	Pacquet Harbour Group
<b>RRF</b>	Round Harbour Formation
<b>PRC</b>	Point Rousse Complex
<b>FWPG</b>	Flatwater Pond Group
<b>BGC</b>	Burlington Granodioritic Complex
<b>BG</b>	Burlington Granodiorite
<b>DG</b>	Dunamagon Granite
<b>CBP</b>	Cape Brulé Porphyry
<b>LIS</b>	La Scie Intrusive Suite
<b>MLG</b>	Micmac Lake Group
<b>KPC</b>	King's Point Complex
<b>CJG</b>	Cape St. John Group
<b>VMS</b>	Volcanic massive sulphide
<b>Analytical techniques, used samples, measure units</b>	
<b>BSE</b>	backscattered electron microscope
<b>EDS</b>	electron dispersive microscopy
<b>CL</b>	cathodoluminescence
<b>LA-ICP-MS</b>	laser-ablation inductively-coupled-plasma
<b>EPMA</b>	electron probe micro analyzer
<b>WDS</b>	wavelength dispersive X-ray spectroscopy
<b>ppm</b>	parts per million
<b>1s %</b>	confidence level of one sigma (68%)
<b>Wt%</b>	Weight percent
<b>nA</b>	nanoampere
<b>kV</b>	kilovolt
<b>LOD</b>	detection limit
<b>LQD</b>	quantification limit
<b>PTS</b>	polished thin section
<b>PTkS</b>	polished thick section
<b>TS</b>	unpolished thin section
<b>OM</b>	optical microscopy (includes both reflected and transmitted light analysis)
<b>MsA</b>	microstructural analysis
<b>g/t</b>	grams / ton
<b>m</b>	meters

<b>cm</b>	centimetres
<b>Minerals, Chemical Elements</b>	
<b>Au</b>	gold
<b>Cpy</b>	chalcopyrite
<b>Aspy</b>	arsenopyrite
<b>Gn</b>	galena
<b>Sph</b>	sphalerite
<b>Tnt</b>	tennantite
<b>AuTe/AuAgTe/AgTe</b>	Undifferentiated Gold/silver tellurides
<b>PbTe</b>	Undifferentiated Lead telluride
<b>BiTe</b>	Undifferentiated Bismuth telluride
<b>Ap</b>	Apatite
<b>Mnz</b>	monazite
<b>Xtm</b>	xenotime
<b>Zr</b>	Zircon
<b>Bdy</b>	Baddeleyite
<b>Tit / Ttn</b>	titanite
<b>Chl</b>	chlorite
<b>Ser</b>	sericite (fine grained muscovite/phengite)
<b>Rt</b>	rutile
<b>Ank</b>	ankerite
<b>Brt</b>	barite
<b>Ms</b>	muscovite
<b>Phen</b>	phengite
<b>Qtz / Q</b>	quartz
<b>Py</b>	pyrite
<b>Cal</b>	calcite
<b>Ank</b>	ankerite
<b>Dolo</b>	dolomite
<b>Ab</b>	albite
<b>Sch</b>	scheelite
<b>Lx</b>	leucoxene (alteration of titanium bearing minerals; in the studied samples occurs mostly as fine-grained rutile or titanite)
<b>Cb</b>	carbonate
<b>Hem</b>	hematite
<b>Ilm</b>	ilmenite
<b>Ab</b>	albite
<b>FeOx</b>	iron oxides
<b>Th</b>	thorium
<b>U</b>	uranium
<b>Pb</b>	lead
<b>Y</b>	yttrium
<b>Sm</b>	samarium
<b>Pd</b>	palladium
<b>S</b>	sulfur
<b>Fe</b>	iron
<b>Cu</b>	copper
<b>Hg</b>	mercury
<b>Ag</b>	silver
<b>Pa</b>	protractium

## **I. Introduction**

### **I.1. Project Rationale**

Gold is one of the most sought-after commodities in the history of mankind, being known and used for more than 5000 years (Boyle, 1979; Frimmel, 2008). Due to its rarity, resistance to corrosion, and malleability, gold was primarily used as currency and for jewellery or exquisite object manufacturing, functions that still persist in present times (Butt and Hough, 2009). Although gold has high heat and electrical conductivity, it is biocompatible, and has both chemical and physical durability, only 12% of the annual gold demand goes in industry, most of it being used for electrical components followed by dentistry and to a lesser degree, in engineering, aerospace, medicine and catalysis (Butt and Hough, 2009). However, considering the current transition of the energy sector towards renewable energy, and the utility of gold in clean energy technologies (e.g. power electronics in electric vehicles, Grandell et al., 2016) the industrial need for gold may increase. Moreover, in 2022, the overall demand for gold showed the highest increase in over a decade and further increase is predicted (World Gold Council, 2022). To keep up with the demand, gold production rate must increase and consequently, the discovery and the development rate of new deposits must also grow. Currently, gold exploration programs are conducted in both brownfield (in the proximity of a known deposit) and greenfield (underexplored) areas (Groves et al., 2020a). The former has the potential to expand the mine life of a deposit for a foreseeable future, whereas the latter is needed to maintain the long-term production by replacing the depleted resources (Groves et al., 2020a). Yet, the mining industry seems to face a decline in new discoveries, especially in green-fields, and a rise in exploration costs (Groves and Santosh, 2015). To overcome this, innovative exploration programs based on mineral system analysis (trigger-source-transport-trap) applied systematically from regional- to local scale and using a multidisciplinary approach must be used (Hageman et al., 2016; Groves et al., 2020a). At a regional scale, understanding the geodynamic evolution with respect to the formation of mineral systems can point towards more prospective districts, whereas at local scale, geochemical and/or geophysical anomalies can be used as vectors to ore (Hageman et al., 2016).

Gold can be found in native form or as metallic minerals in a wide variety of mineralizing systems that differ in geology, geometry, and geodynamic setting

(Boyle, 1979; Frimmel, 2008; Hough et al., 2009; Lipson, 2014). The space and time distribution of gold systems are directly controlled by the Earth's geodynamic evolution, from mantle–plume influenced tectonism in the Archean to modern plate tectonics (Kerrick et al., 2005; Frimmel, 2008). Most of the gold-rich metallogenic provinces are intimately related to active margins, particular with convergent boundaries (*Figure I.1*, Goldfarb 2021; Sillitoe 2020). These complex tectonic environments host various gold systems that can form throughout the entire evolution of an orogenic belt as a result of magmatic, metamorphic, and sedimentary processes (Groves & Bierlein, 2007). The main gold deposits associated with magmatic activity are represented by “Porphyry (Cu-Au) / Epithermal (Au-Ag)” systems and gold-rich “Volcanic Massive Sulphide” deposits (Lipson, 2014; Frimmel, 2008). These are hosted by continental arcs, island arcs and back arcs environments, usually located in the shallow crust (0-5 km depth; *Figure I.1*; Groves et al., 2003; Groves et al., 1998). Another class of gold deposits that shows a close relation with magmatic intrusions are the so called “intrusion-related gold systems” (Lang and Baker, 2001). This type of mineralization is located in the inboard margin of accreted terranes and sometimes it may be unclear whether specific deposits belong to this class or are “Orogenic Gold Deposits” which owe their formation to fluids of metamorphic origin (*Figure I.1*; Hart & Goldfarb, 2005; Goldfarb and Pitcairn, 2023). Orogenic gold deposits are hosted within metamorphosed accreted terranes and accretionary prisms (*Figure I.1*) and usually do not show any spatial or temporal relation with intrusive bodies (Groves et al., 2003).

Commonly, the evolution of an orogenic belt involves a multi-stage accretion of different terranes onto a continental margin (Cawood et al., 2009). Ore deposition can occur during each accretionary event as a result of significant hydrothermal and/or magmatic activity (Sillitoe 2020). Gold deposition usually occurs during the transition from compression to transpression, although gold deposits formed during the main collisional phase or even during post-orogenic extensional stage are also known (Groves, et al., 2018, 2020b and references herein). Moreover, multi-stage gold mineralisation events which are separated in time but overlapped in space are common and result from the spatial-temporal evolution of the structural-hydrothermal system related to the progression of collisional zones (Meffre et al., 2016). These multigenerational processes can increase the gold

endowment of an existent orebody or upgrade distinct sections within it, either by introducing new gold in the system or by remobilising the pre-existent mineralisation (Meffre et al., 2016; Hastie et al., 2020). However, multi-stage gold enrichment phases started to be documented only recently and in a limited number of deposits (Meffre et al., 2016). Thereby, it is possible that many gold deposits across the globe formed as a result of such processes.

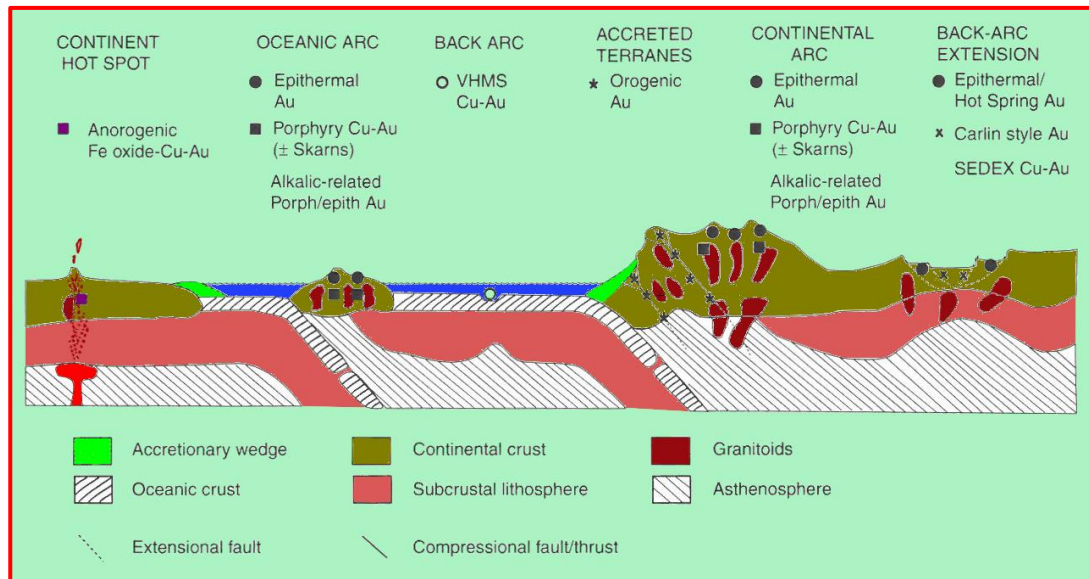


**Figure 1.1** – General tectonic setting of different types of gold deposits (adapted after Groves et al., 1998; Hagemann and Cassidy, 2000).

From an economic point of view, identifying multi-stage mineralising events has significant implications for both exploration and development strategies. At a regional scale, districts where several tectono-metamorphic and magmatic events overlap in space have a higher chance of hosting high grade deposits and so, represent better exploration targets. At district to deposit scale, identifying the richest metalliferous fluid phase(s) and linking them to distinct structural elements permit to plan cost effective exploration programs and mine or pit designs that minimise waste. In turn, this is crucial for a sustainable mine cycle. Beside the economic relevance, the identification of multi-stage mineralising events can give insights into the evolution of the continental lithosphere and the fluid sources and pathways within it. Studies that incorporate deposit-scale investigations into regional context using an integrated structural-geochemical approach are challenging, but particularly valuable in the efforts to gain such holistic understanding.

The island of Newfoundland, Canada, is currently the focus of intense gold exploration being considered the locus of a modern-day “gold rush” (*Figure 1.2-A, B*) Mason, 2023 – press release). Several gold camps emerged in the recent years (e.g. Central Newfoundland gold district, Honsberger, et al., 2020), and large discoveries are expected to enter production (e.g. Valentine Gold Project, Powell et al., 2022). The geological setting of Newfoundland resulted from multiple orogenic events that generated spatially over-lapping thickening-magmatism-exhumation-transcurrent faulting cycles during the Paleozoic eon (Willner et al., 2018). All across the island, and dominantly in the western and central parts, structurally controlled gold occurrences extend over hundreds of kilometres in strike, in the vicinity of long-lived, NE-SW oriented, terrane boundary faults (e.g. the Baie Verte Line, *Figure 1.2*; Honsberger et al., 2020, 2022, Sandeman et al., 2022). The geochronological data compilation of Sandeman et al. (2022) for gold occurrences from western and central Newfoundland suggest that gold precipitated during two distinct hydrothermal events active between ~ 433 to 405 Ma and ~ 390 to 372 Ma. However, across the island, direct geochronological data of gold occurrences is limited. Also, integrated regional to local scale multidisciplinary (structural-geochemical) metallogenic studies are lacking. Thus, the relationships between the formation of gold mineralisation and both the regional and deposit-scale structural-magmatic-metamorphic processes are poorly constrained for most of the known gold districts from Newfoundland.

This PhD project is the first to integrate regional- to deposit scale structural observations with paragenetic associations, gold geochemistry, and in-situ U-Th-Pb geochronology of multiple gold occurrences from the Baie Verte Peninsula of Newfoundland (*Figure 1.2-C*). The study brings new understandings regarding the formation of gold mineralisation with respect to the structural evolution of the entire district and links the timing of gold precipitation to distinct orogenic phases, and therefore, to different tectonic processes. Consequently, the research can be used to inform both local and regional scale exploration strategies in Newfoundland and also in other regions within the Appalachian-Caledonian belt (e.g. Nova Scotia, Northern Ireland, Scotland, etc.).

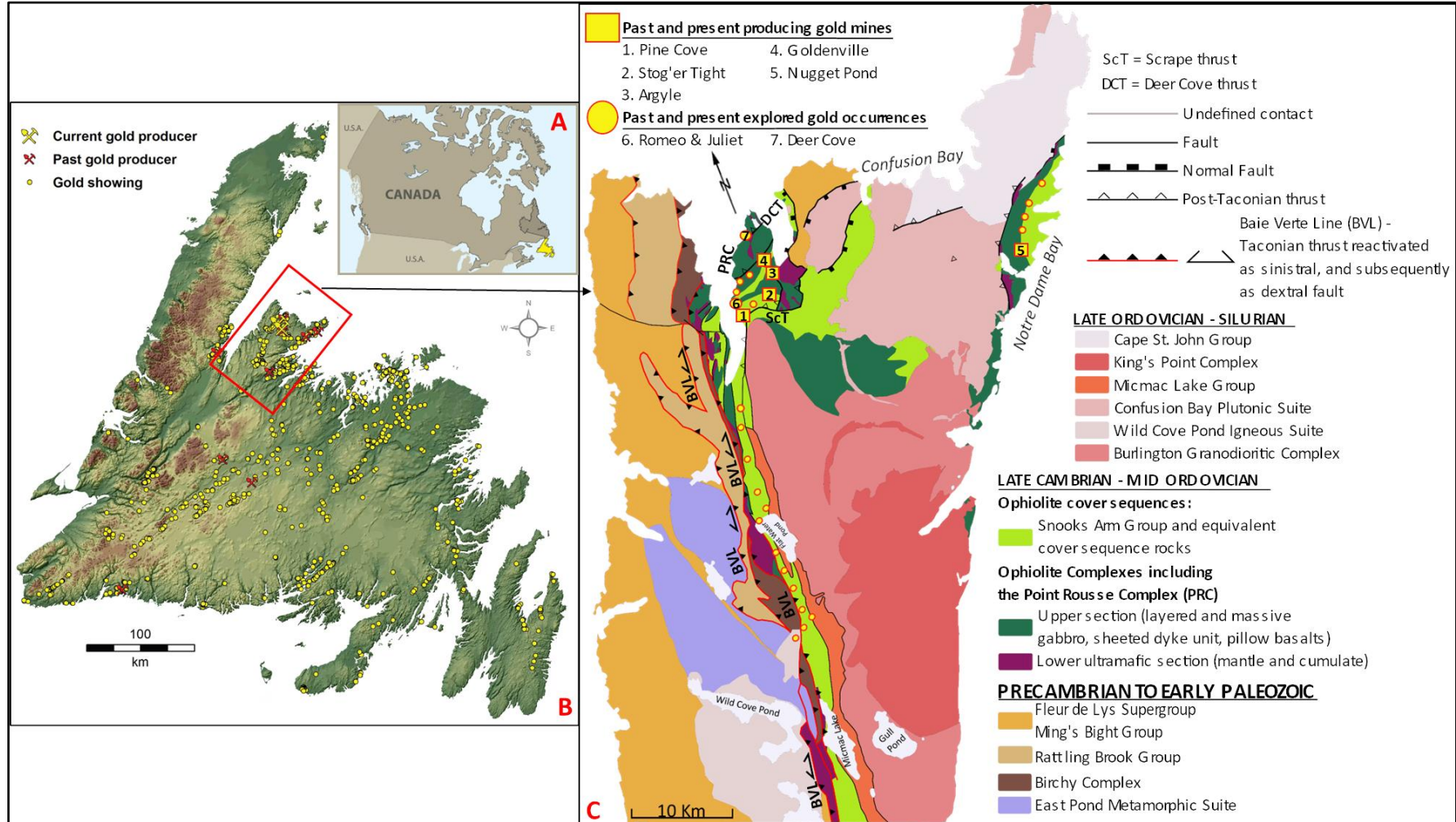


**Figure 1.2** – A – Location of Newfoundland Island on the North American continent. B – Distribution of known gold occurrences across Newfoundland. A & B – from “Gold in Newfoundland” - Newfoundland government pamphlet (2021). C – Simplified geological map of the Baie Verte Peninsula after Skulski et al. (2015 a,b,c) and the location of minor orogenic gold occurrences together with the present and past active mines; 1 – the Romeo & Juliet prospect, 2 – the Argyle deposit.

## **I.2. Study area and project aims**

The Baie Verte Peninsula (BVP) is one of the richest auriferous regions within the Newfoundland Appalachians hosting more than 100 economic and sub-economic, epigenetic, structurally-controlled, gold occurrences (**Figure I.2–C**; Evans, 2004, 1999). In addition, gold also occurs in syn-genetic mineralisation within volcanic massive sulphide deposits (VMS) (Evans, 2004). Currently, brownfield exploration programs are conducted in several parts of the BVP by different mining companies (e.g. Signal Gold Inc.).

The geological setting of the BVP (*detailed descriptions in chapter II*) resulted from the accretion of several micro-terranes of Iapetus origin to the Laurentian margin during the Ordovician Taconic Orogeny (Waldron et al., 1998; van Staal et al., 2007). Subsequent deformation developed under a sinistral transpressional setting during the Silurian Salinic Orogeny, followed by a complex dextral transpressional to transtensional tectonic regime, during the Devonian Acadian and Neo-Acadian orogenic events (Waldron et al., 1998; Anderson et al., 2001; Castonguay et al., 2009, 2014; Skulski et al., 2010, 2015 a, b).

The majority of gold occurrences are located along the Baie Verte Line (BVL, the suture between the Laurentian margin and the accreted island arcs) and along its subsidiary structures (**Figure I.2–C**; Evans, 2004; Pitman et al., 2020). To the present day, economically significant deposits were found only along splays of the BVL, e.g.: the Scrape and the Deer Cove thrusts (**Figure I.2–C**). Direct geochronological ages for gold mineralisation in the BVP are limited to three deposits and suggest two episodes of Au mineralization (Kerr & Selby, 2011; Sangster et al., 2008): one episode at the Silurian-Devonian boundary (420 – 410 Ma) and a younger episode of Middle-Late Devonian age (380 – 370 Ma). Anderson et al. (2001) speculates that in these periods a sinistral transpressional tectonic regime and a dextral transtensional regime respectively, were active in the BVP. However, the exact structural evolution of the BVL in relation to its subsidiary structures and consequently, to the formation and localisation of the gold mineralisation is poorly understood.

The studied gold occurrences, Stog'er Tight, Argyle, Romeo & Juliet, Deer Cove, and Pine Cove, are located in the Point Rousse Complex (PRC) and lie along splays of the BVL (**Figure I.2-C**; Pitman et al., 2020). The PRC was under



exploration and development by Signal Gold Inc. (formerly Anaconda Mining Inc., and henceforward referred to as such) until 2023, when the mining rights were sold to Maritime Resource. The Pine Cove, Stog'er Tight and Argyle deposits were already mined out. The Deer Cove and Romeo & Juliet prospects are currently sub-economic, but the mineralisation is open both in strike and dip (Cullen et al., 2018). Hence, further exploration may lead to the definition of an economic reserve. In addition to these gold deposits/prospects, within the Point Rouse Complex, other gold mineralised areas were identified by Anaconda Mining (more details in chapter II) and therefore, new deposits may be outlined and developed in the future. Currently, there are no published academic studies that focussed on the geological characteristics of multiple deposits in a comparative way and neither their evolution with respect to the structural history of the entire Point Rouse Complex. Except for the collaborative work between the Anaconda Mining and researchers from the Memorial University of Newfoundland, which integrate the results of several mineralogical and geochemical deposit-scale studies of gold occurrences (e.g. Piercey and Copeland, 2017), most of the existing papers describe either the structural controls or the mineralogical and geochemical characteristics of only one deposit at a time (see chapter II).

The main aims of this research project are the following:

- To establish a structural deformational sequence for the PRC with respect to the regional setting of the BVP.
- To characterise the vein generations and their associated alteration and ore mineralogy in each of the study cases in order to generate vein and mineral paragenetic sequences and in turn, to deduce if multiple ore forming stages occurred.
- To highlight any differences or similarities between the evolution of the hydrothermal systems in terms of contributions of various ore phases.
- To constrain the relative timing of each deposit/prospect with respect to the structural setting of the PRC and establish a link between different mineralogical and structural evolution stages within individual deposits.
- To determine the absolute age of the studied gold occurrences.
- To bring a more comprehensive understanding of the relationship between gold mineralisation processes and the regional tectonic evolution of the BVP.

### **I.3. Thesis structure**

This manuscript consists of eight chapters, including the current section.

*Chapter II – Literature Review*, this chapter provides a summarised description regarding the evolution of the Newfoundland Appalachians together with a detailed characterisation of the geologic and metallogenic setting of the BVP. The chapter also includes a review of the current theories related to the formation of the studied gold occurrences.

*Chapter III – Methodology*, describes the workflow and systematics engaged to achieve the thesis objectives. It presents the mapping and sampling rationale together with the concepts and the technical details of the methods used for sample preparation and analysis.

*Chapter IV – Structural setting of the Point Rouse Complex (Results and Interpretations)*, provides a detailed characterisation of all the structural elements identified in the Point Rouse Complex based on new structural observations and data collected during this study. 2D and 3D sketches that display the interaction of various structural features are generated and an updated structural deformation sequence is proposed. The latter is compared to previous models of the region.

*Chapter V – Gold mineralisation in the Point Rouse Complex (Results and Interpretations)*, describes the main geological characteristics (structural setting, vein types, alteration mineral assemblages, ore mineralogy and gold geochemistry) of the studied deposits based on field, mineralogical/petrographic and geochemical observations. Based on this, vein and mineral paragenetic sequences are proposed and the relative timing of each gold occurrence is established with respect to the structural sequence of the PRC.

*Chapter VI - Timing of gold mineralisation in the Point Rouse Complex based on in-situ LA-ICP-MS U-Th-Pb analysis of monazite, xenotime and titanite (Results & Interpretations)*, presents new in-situ LA-ICP-MS U-Th-Pb isotope analysis of monazite, xenotime, and titanite for four of the studied gold occurrences. The data are interpreted with respect to the mineral paragenetic sequences presented in chapter V and maximum and minimum ages are obtained for two gold mineralising events.

*Chapter VII – Discussion and Synthesis*, integrates the observations and interpretations from previous chapters and assesses the formation of the gold

mineralisation with respect to the regional tectonic evolution of the BVP. It presents the local and regional implications for gold exploration in Newfoundland and in other areas along the Appalachian-Caledonian belt and propose topics that should be included in future academic studies. A summary of the main findings of this research is provided in *Chapter VIII – Conclusions*.

## **II. Literature Review**

This chapter provides brief information regarding the geological evolution of Newfoundland Island and a detailed geological characterisation of the Baie Verte Peninsula. It also reviews the current theories related to the formation of the studied gold occurrences and highlights the gaps that this study aims to cover.

### **II.1. Architecture of Newfoundland Island**

The island of Newfoundland occupies the northeastern margin of the North American Appalachian Orogen (*Figure II.1-A*), and its tectonic evolution is largely related to the opening and closure of the Iapetus and Rheic Oceans during Ediacaran to Early Devonian and Devonian to Carboniferous, respectively (Tuach et al., 1988; Swinden et al., 1991; Kerr et al., 2005; van Staal & Barr, 2012; van Staal, 2019). Based on the location of the remnant parts of the Iapetus oceanic crust in the central-northeastern Newfoundland, together with the distribution of Precambrian rocks and Paleozoic shelf sequences on the northwestern and southeastern sides of the island, Williams (1964) divided the area in three tectonic domains. These domains, initially referred as the “western Precambrian rocks and Lower Paleozoic deposits”, the “central Paleozoic mobile belt” and the “eastern Precambrian rocks and Lower Paleozoic deposits” (Williams, 1964), were later revised by Williams (1979) and renamed from west to east as the “Humber”, “Dunnage”, “Gander” and “Avalon” tectonostratigraphic zones (Figure II.1; Williams, 1979; Williams et al., 1988; Dunning & Blackwood, 1990; Swinden et al., 1991; Ramezani, 1992; Anderson, 1998). Within this background, the Newfoundland Appalachians are viewed as a “two-sided symmetrical system” (Williams, 1964) that resulted from the collision of the Laurentian Margin (Humber Zone) with the Iapetus oceanic vestiges (Dunnage Zone) and with domains of Gondwanan origin, Gander, and Avalon zones (Williams, 1964; Williams, 1979; Williams et al., 1988; Dunning & Blackwood, 1990; Swinden et al., 1991; Williams, 1995; Anderson, 1998; Evans, 2004; Kerr et al., 2005).

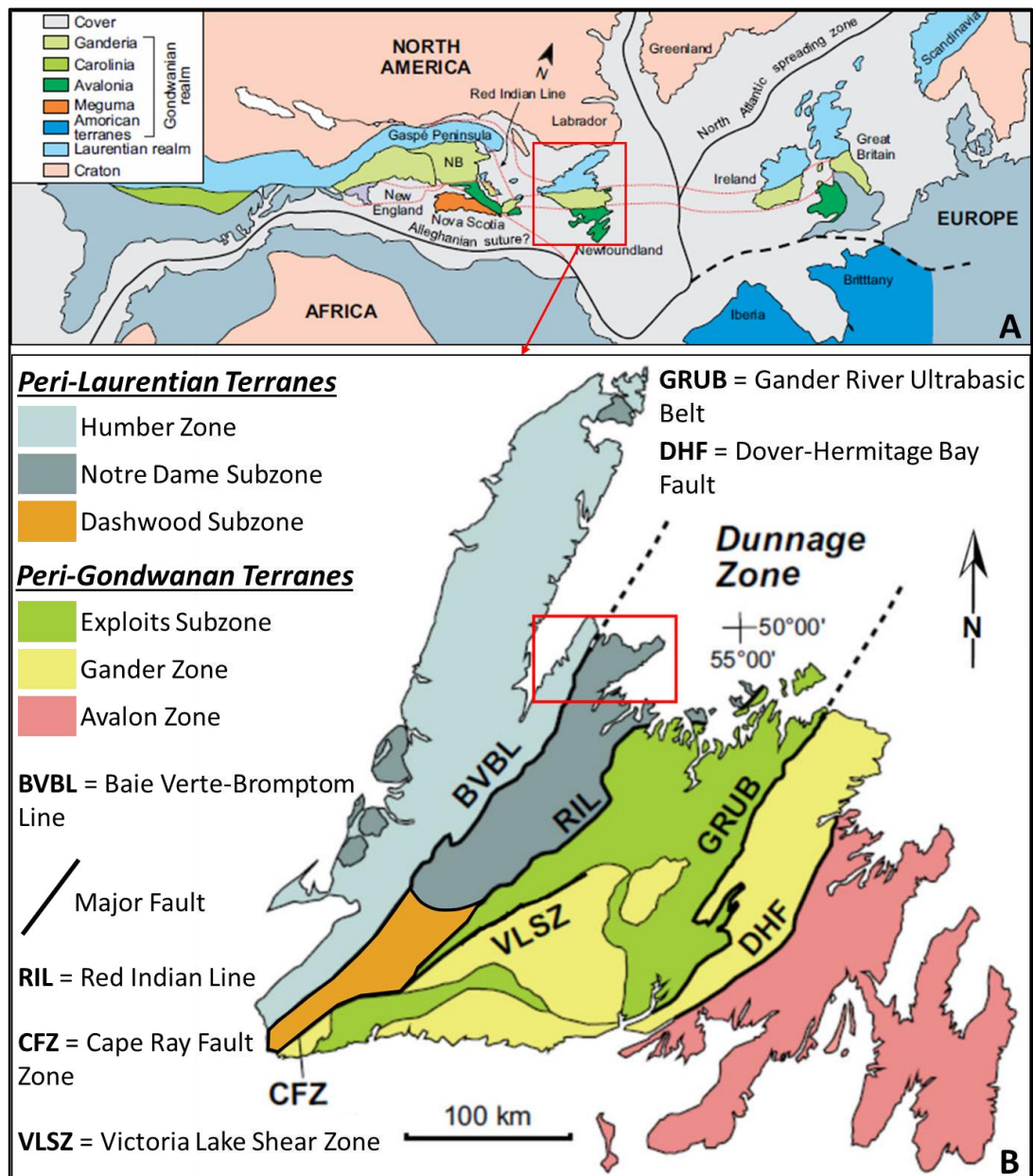


**Figure II.1 – A** - Location of Newfoundland Island within the Appalachian–Caledonian belt, from van Staal & Barr (2012). **B** – Simplified geological map of Newfoundland and location of the BVP (red square), modified from Honsberger et al. (2020).

The Humber Zone is interpreted as the remnant of the North American, Laurentian continental margin (*Figure II.1*; Swinden et al., 1991; Evans 2004; Kerr et al., 2005). It consists of a Precambrian, crystalline “Grenvillian” basement that is unconformably overlain by sedimentary sequences associated with rifting, continental margin and foreland basin domains and by structurally emplaced ophiolitic allochthons of Iapetus affinity (Williams, 1979; Swinden et al., 1991; Williams, 1995; Anderson, 1998; Cawood et al, 2001; Evans, 2004; Kerr et al., 2005). In the western part of the region, the crystalline basement is intruded by mafic dykes

and associated basaltic flows dated at ~600 Ma which are related to the initial rifting of the Iapetus Ocean (Williams 1979; Swinden et al., 1991; Kerr et al., 2005). The mafic rocks are overlain by a Cambro-Ordovician sedimentary cover sequence composed of siliciclastic rocks and a thin carbonate platform unit (Williams 1979, 1995; Swinden et al., 1991; Cawood et al., 2001; Kerr et al., 2005). The eastern side of the Humber Zone consists of metamorphosed equivalents of a deep-water foreland basin and accretionary prism facies developed during the subduction of the Laurentian margin beneath island arcs of Iapetus origin (Williams, 1995; Waldron et al., 1998; Kerr et al., 2005).

The Dunnage Zone occupies the central part of the Newfoundland Appalachians (**Figure II.1**). It is the widest and the most complex tectonostratigraphic zone of Newfoundland (Williams, 1995; Kerr et al., 2005). It comprises remnants of island arcs, back-arcs and foreland basins formed on both Laurentian and Gondwanan margins of the Iapetus Ocean (Williams et al., 1988, 1992; Colman-Sadd et al., 1992; Williams, 1995; Evans 1996; Andreson, 1998; Kerr et al., 2005; Zagorevski et al., 2008; Cutts et al., 2012). Based on structural, geochemical, geochronological, geophysical, stratigraphic, and faunal characteristics, the Dunnage zone was subdivided by Williams et al., (1988) in two other subzones: the “*Notre Dame Subzone*” in the northwest, and the “*Exploits Subzone*” in south and east (**Figure II.1-B**). The two regions are interpreted to be formed separately along the opposing sides of the Iapetus Ocean, the Laurentian margin and Gondwanan margin, respectively (Williams et al., 1988, 1992; Colman-Sadd et al., 1992). These two subzones are separated by the “*Red Indian Line*”, a complex fault system which represents the suture zone along which the Iapetus Ocean has closed (**Figure II.1-B**; Wilner et al., 2018).

A third subzone – the Dashwood Subzone or the Central Gneiss Terrane *sensu* van Berkel and Currie (1988) - was documented in the southwestern part of Newfoundland (**Figure II.1-B**; Williams, 1995). This additional subzone contains geological formations characteristic of both the Humber and Dunnage zones (Williams, 1995). Waldron and van Staal (2001) interpreted this domain as a microcontinent that was rifted from the Laurentian margin during the opening of the Iapetus Ocean and subsequently accreted during the Taconic Orogeny (**Figure II.2-A**).

The Gander Zone extends east of the Dunnage zone, although rocks pertaining to this zone have also been documented in structural windows within the Exploits Subzone (*Figure II.1 – B*; Kerr et al., 2005). The nature of the boundary between Gander and Dunnage zones was interpreted as both tectonic and stratigraphic (Williams, 1995 and references herein). The zone comprises Cambrian to Ordovician clastic metasedimentary rocks that were subject to multiple deformational stages associated to metamorphic conditions that vary from greenschist to upper amphibolite facies (Williams, 1995; Kerr et al., 2005; van Staal et al., 2014).

The Avalon Zone is located in the eastern part of Newfoundland and is separated from the Gander Zone by the Hermitage Bay and Dover Faults (*Figure II.1-B*; Anderson, 1998; Kerr et al., 2005). The zone consists of Upper Precambrian sedimentary and felsic volcanic rocks which are unconformably overlain by Cambrian to Ordovician shales and sandstones (Williams, 1995; Kerr et al., 2005). Compared to the adjacent Gander Zone, rock successions of Avalon Zone show little evidence of deformation and metamorphism (Williams, 1995).

Igneous intrusive rocks occur in all tectonostratigraphic zones of Newfoundland and range in age from Precambrian to Carboniferous (Currie, 1995; Williams, 1995). Precambrian bodies are restricted to the Humber and Avalon zones (Currie, 1995; Williams, 1995). Early Paleozoic plutons (Ordovician to Silurian) are most common in the Notre Dame Subzone of the Dunnage Zone (Currie, 1995; Williams, 1995). Mid Paleozoic magmatic rocks (Silurian and Devonian) are the most abundant, occur throughout Newfoundland from the Humber to the Avalon Zone, but show a higher density in the Exploits subzone and the Gander Zone (Currie, 1995; Williams, 1995; Kerr et al., 2009). A few Early Carboniferous plutonic bodies occur in the Gander zone, whereas post Paleozoic small intrusive bodies are known in both north-central and southeastern parts of Newfoundland (Currie, 1995; Williams, 1995).

## **II.2. Tectonic evolution of Newfoundland Appalachians**

The earliest, major deformation and metamorphic phase recorded in the Humber Zone is represented by the Early to Middle Ordovician, Taconian orogeny that involved the accretion of island arcs, vestiges of the Iapetus Ocean, against rift and carbonate dominated shelf sequences of the Laurentian margin (Williams 1979; Waldron & Milne, 1990; Swinden et al., 1991; Williams, 1995; Kerr et al., 2005; van

Staal, et al., 2007). Although the main stage of the Taconic orogeny is believed to have occurred during the Early to Middle Ordovician, two additional accretionary cycles have been reported preceding and succeeding this main phase and included, by some authors, into the Taconian orogeny (van Staal et al., 2007, van Staal and Barr, 2012). The early stage (*Taconic 1*) consisted of the Late Cambrian obduction of the Lushs Bight oceanic tract onto the Dashwood microcontinent (**Figure II.2–A**). The main phase of deformation and metamorphism, *Taconic 2*, was characterized by the accretion of the Notre Dame and Snooks Arm arcs to Laurentia (**Figure II.2–B**). The Taconic orogeny terminated with an arc-arc collision between the leading edge of Ganderia and Laurentia, in the Late Ordovician (455–450 Ma; *Taconic 3*; **Figure II.2–C**; van Staal et al., 2007, van Staal and Barr, 2012).

The tectonic evolution of the Newfoundland Island during Silurian to Carboniferous is related to three distinct orogenic phases (**Figure II.3**; van Staal et al., 2009; van Staal & Barr, 2012). The Salinic orogeny was correlated with the Late Ordovician – Early Silurian (450 – 423 Ma) sinistral-oblique collision of the composite Laurentia with the Gander margin (**Figure II.3–A**; van Staal et al., 2009; van Staal and Barr, 2012; Wilson et al., 2017). Closing of the Acadian Seaway, located between Avalonia and Ganderia during the Late Silurian – Early Devonian (420–395 Ma), led to the development of the Acadian orogeny (**Figure II.3–B**; Kerr et al., 2005; van Staal and Barr, 2012). This event concluded in the collision and underthrusting of Avalonia underneath Laurentia (Wilson et al., 2017; van Staal et al., 2021). Both the Salinic and the Acadian events inflicted an overall sinistral transpressional regime localised along the NNE to NE oriented terrane boundary faults (Waldron et al., 2022). The Neoacadian orogeny resulted from the dextral-oblique accretion of Meguma to Avalonia in the Maritime Canada during Middle Devonian to Early Carboniferous (**Figure II.3–C**; van Staal et al., 2009, 2021; van Staal and Barr, 2012). In Newfoundland, the far field stresses associated to this event caused the reactivation of the Salinic and the Acadian structures under dextral transcurrent motions (van Staal et al., 2021; Waldron et al., 2022).



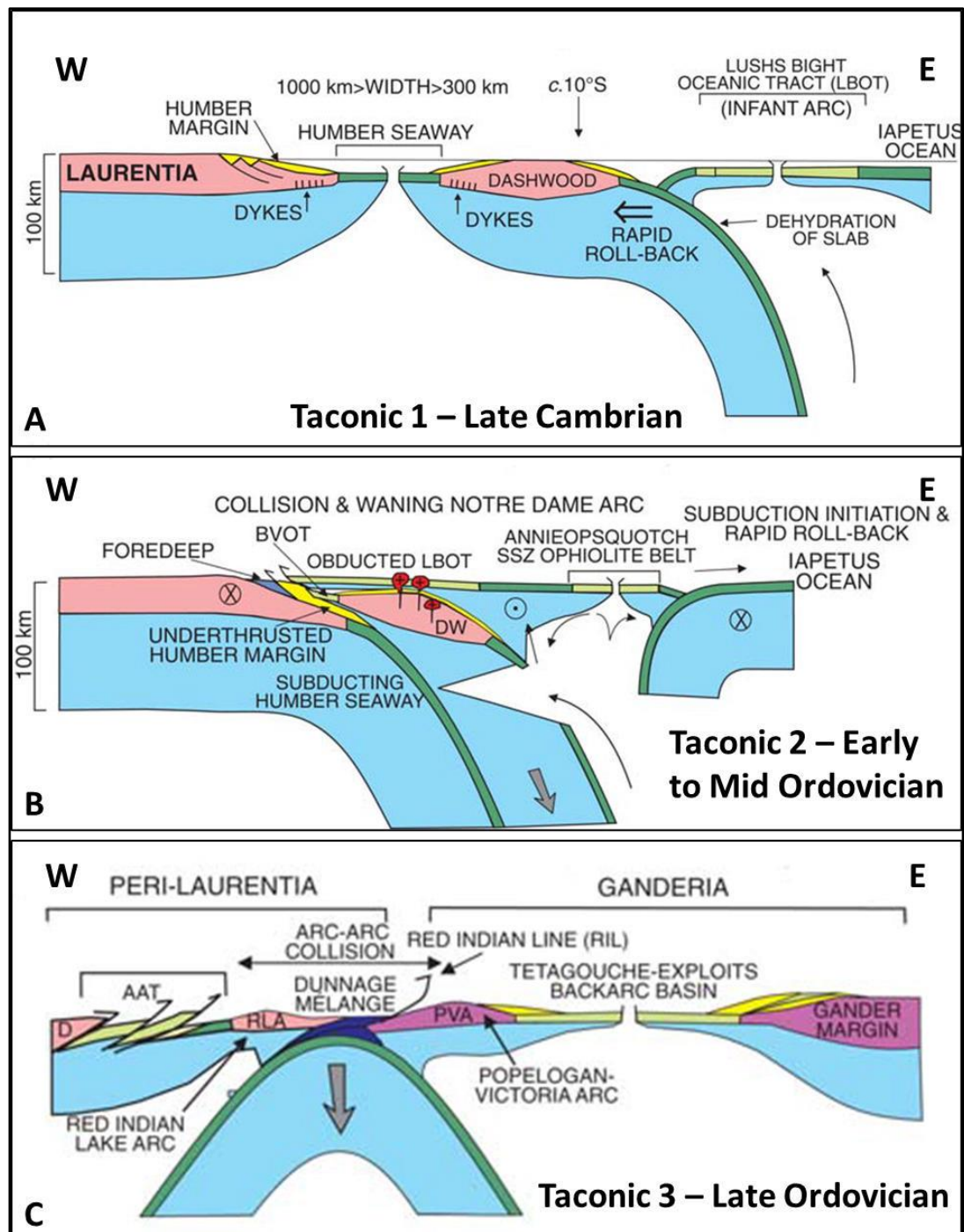


**Figure II.2** – Tectonic evolution of Newfoundland Appalachians during the Late Cambrian to Late Ordovician (modified from figures 4 & 5 of van Staal et al., 2009). **A** – Formation of Lushs Bight oceanic tract as a result of slab roll-back and early obduction. **B** – Closure of the Humber seaway, obduction of the Baie Verte Oceanic Tract (BVOT), arc-continent collision, and development of the supra-subduction zone Annieopsquotch ophiolite belt. **C** – Arc-arc collision between the Red Indian Lake arc and the Popelogan-Victoria arc (marginal part of Ganderia). This marks the closure of the main Iapetus oceanic tract along the Red Indian Line.

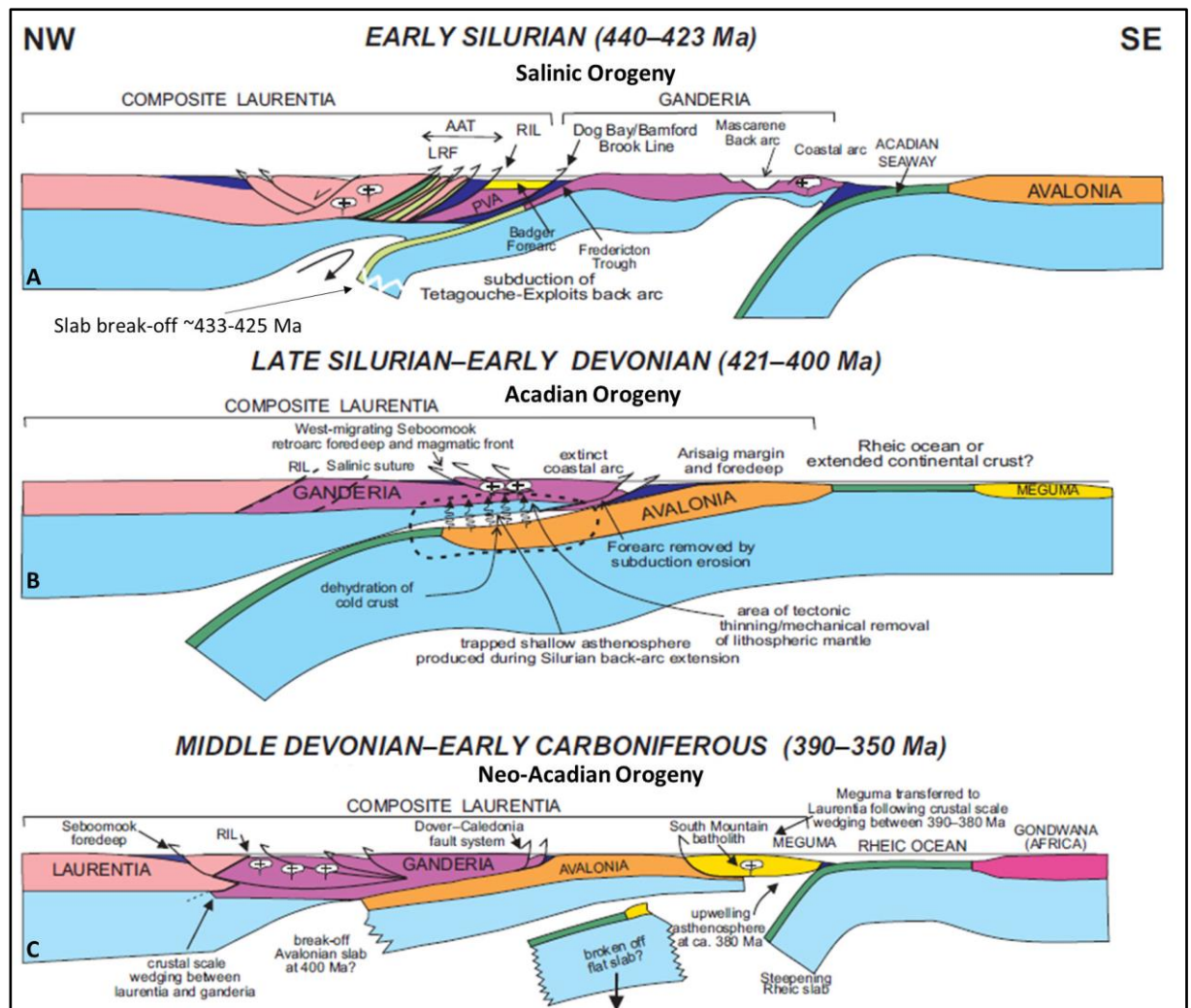


**Figure II.3** – Tectonic evolution of Newfoundland Appalachians during the Early Silurian to Early Carboniferous (modified from figure 16 of van Staal and Barr, 2012). **A** – Closure of the Tetagouche-Exploits back arc basin and collision between composite Laurentia and Ganderia during the Salinic orogenic cycle; break-off of the Gander slab ~ 433-425 after Whalen et al. (2006); start of subduction of the Acadian Sea beneath Ganderia. **B** – Closure of the Acadian Sea and collision between composite Laurentia and Avalonia during the Acadian orogenic cycle. **C** – Docking of Meguma onto Avalonia and closure of the Rheic Ocean during the Neo-Acadian orogeny.

### **II.3. Geological Setting of the Baie Verte Peninsula**

The Baie Verte Peninsula is an important metallogenic area within the Newfoundland Appalachians and has a rich endowment of gold, copper, asbestos, and other commodities (Skulski et al., 2009). The region is the main host for orogenic gold style mineralization (Evans, 2004; Kerr et al., 2005) and has been the focus of numerous, local and regional scale, stratigraphic (Hibbard, 1983; Skulski et al., 2010), structural (Anderson, 1998; Castonguay et al., 2009), geochemical (Bédard, 1999; Patey et al., 1993), geophysical (Spincer, 2010) and metallogenetic (e.g. Dubé et al., 1993; Ramezani et al., 2001; Pilote, 2018; Pawlukiewicz, 2019, etc.) studies that concluded with BSc/MSc/PhD theses, governmental reports, field trip guidebooks, research papers and geological maps.

The Baie Verte Peninsula consists of two contrasting tectono-stratigraphic belts, the Humber Zone to the west, and the Notre Dame subzone (western part of the Dunnage zone) to the east (Williams et al., 1988; Hibbard, 1983; Anderson, 1998; Evans, 2004; Skulski et al., 2009; Skulski et al., 2010). The border between the two zones is marked by a major fault zone named the “*Baie Verte Line*” (BVL) (**Figure II.4 & Figure II.5**) (Hibbard, 1983). The BVL represents the northern termination of the “*Baie – Verte – Brompton Line*” (BBL), which is a major structural zone within the Canadian Appalachians that separates the Laurentian Margin from the vestiges of the Iapetus Ocean (Williams & St. Julien, 1978; Hibbard, 1982). The steeply dipping NNE-SSW striking BVL includes multiple long-lived, brittle-ductile shear zones and contains slivers of ophiolitic sequences along its length (Malo et al., 1992; Anderson, 1998; Skulski et al., 2015; Pawlukiewicz, 2019). In the northern part of the peninsula, the trace of the BVL sharply swings to an almost east – west strike (**Figure II.4**) (Hibbard, 1982; Anderson, 1998). Hibbard (1982) named the eastward deviation of the BVL as the “*Baie Verte Flexure*” and considered that it follows the original geometry of the Laurentian Margin and that it can be traced to the contact between the Ming’s Bight Group (MBG) and the Dunamagon Granite (**Figure II.4**). However, Anderson (1998) argues that the eastward swing of the geological trends, including that of the BVL, was caused by differential strain partitioning during Silurian sinistral transpression, inflicted by the location of the large Burlington Granodiorite in the footwall of the BVL (**Figure II.4**). Moreover, according to the seismic, magnetic, and gravimetric data interpretation of Miller and Wiseman (1994) and to the structural

interpretation of Anderson (1998), the BVL passes through the Point Rouse Ophiolite Complex and not through the Point Harbour Group as previously inferred by Hibbard (1982) (*Figure II.4, Figure II.5*).

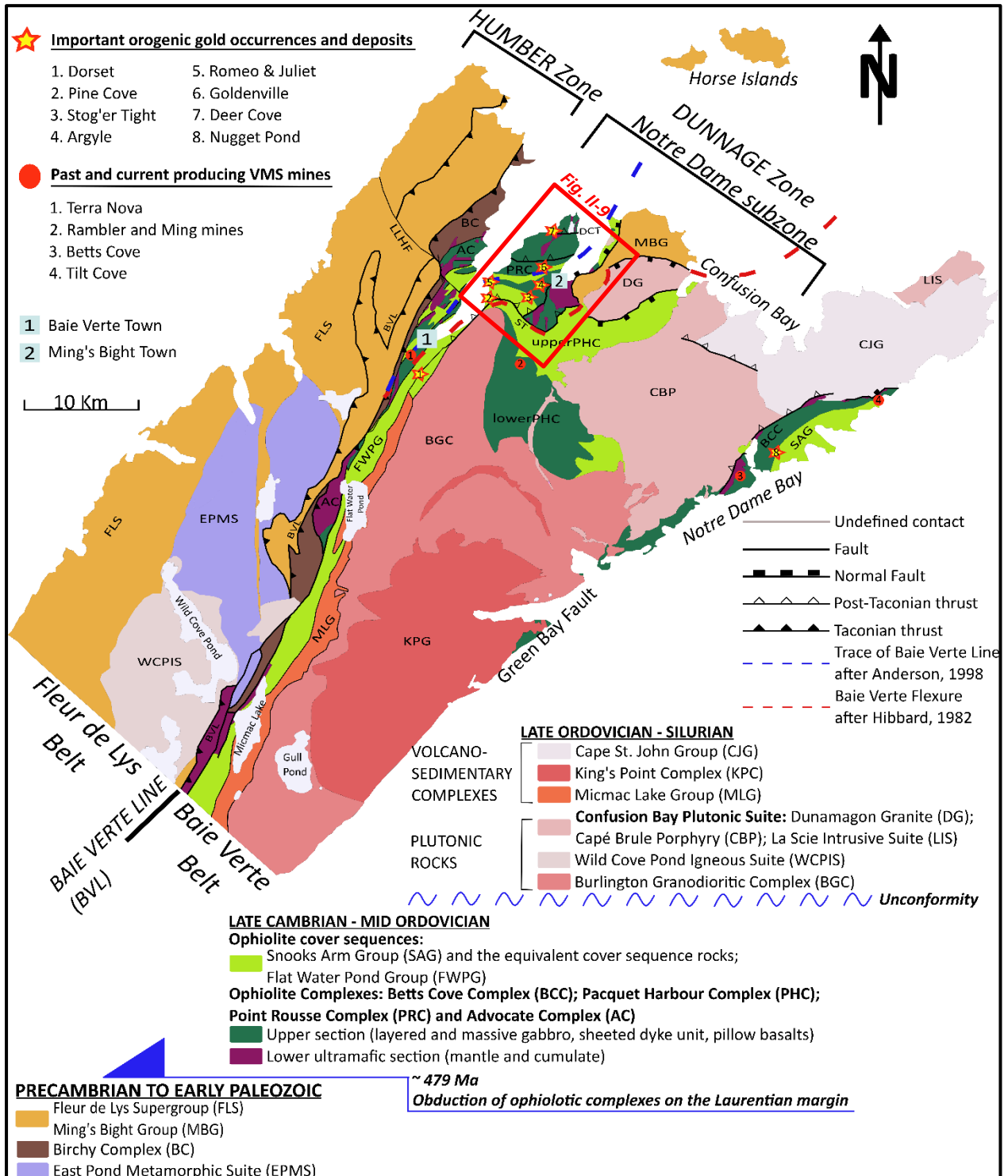


**Figure II.4** – Simplified map of the Baie Verte Peninsula after Anderson (1998), Skulski et al. (2010, 2015) and van Staal et al. (2013); ST = Scrape thrust; DCT = Deer Cove thrust; LLHF = Little Lobster Harbour Fault. Red square – location of *Figure II-9*.

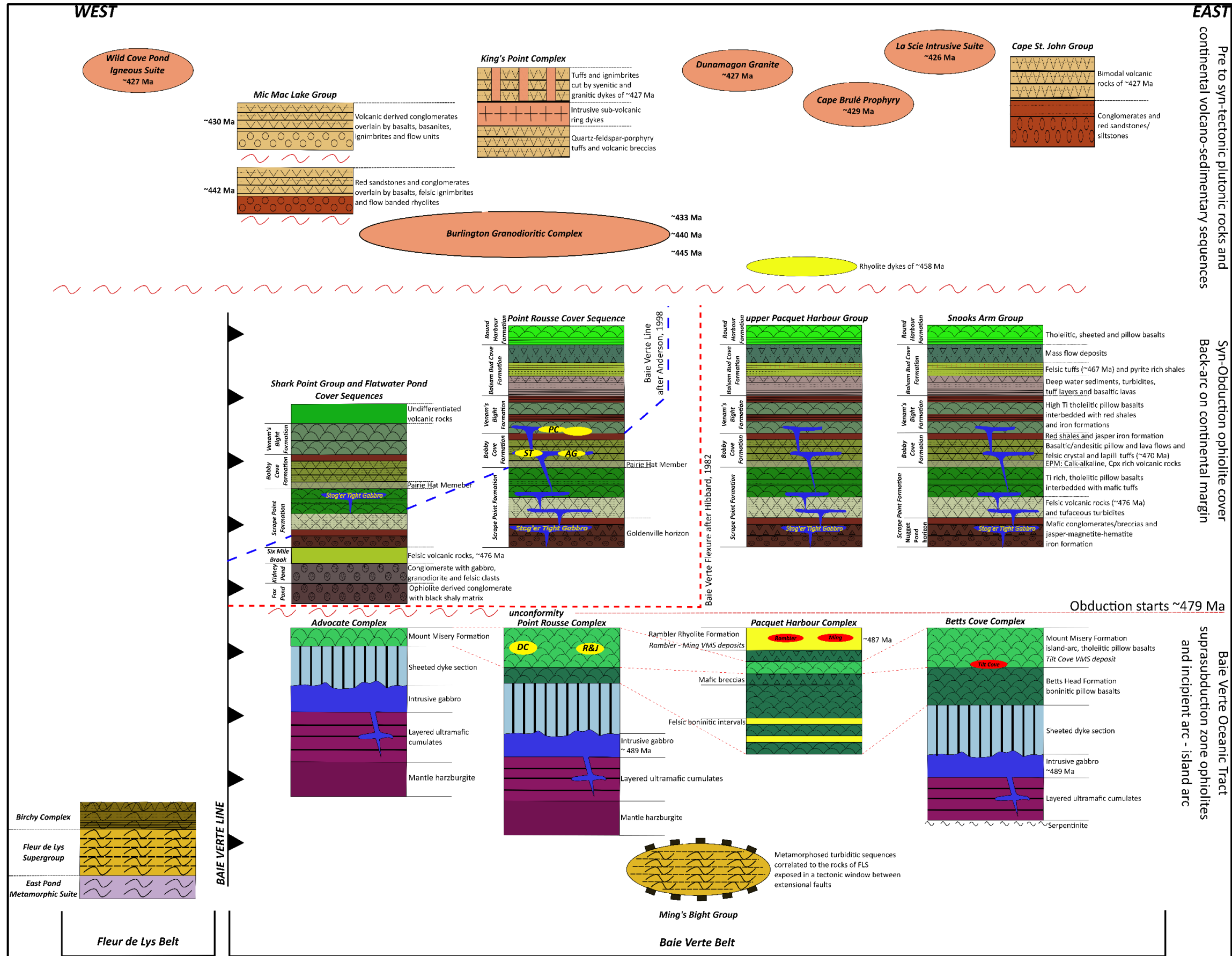


Figure II.5 – Stratigraphic model of the Baie Verte Peninsula modified after Hibbard (1983), Bédard et al. (2000) and Skulski et al. (2009, 2010).

### II.3.1. Stratigraphy and palaeoenvironment of the Baie Verte Peninsula

Within the area of interest, the formation and location of the studied gold deposits are partially controlled by the litho-geochemical properties of the hosting stratigraphic intervals. Therefore, it is appropriate to provide a summary of the characteristics of the main stratigraphic domains from the Baie Verte Peninsula together with the current understanding of their palaeotectonic environment. A detailed characterisation of the geological setting of the entire Baie Verte Peninsula together with a description of the main metalliferous and non-metalliferous deposits located within the region can be found in Hibbard (1983).

Hibbard (1983) divided the Baie Verte Peninsula in two main lithostratigraphical domains: i) the “*Fleur de Lys Belt*”, composed of Precambrian to Early Ordovician rocks with a Laurentian margin affinity that outcrop west of the BVL; and ii) the “*Baie Verte Belt*” which represents the eastern part of the peninsula and consists of Late Cambrian to Mid Ordovician ophiolitic sequences and their cover rocks that were obducted on the Laurentian margin during the Ordovician (**Figure II.4 & Figure II.5**) (Hibbard, 1983; Skulski et al., 2010; Castonguay et al., 2014). Both zones are locally unconformably overlain by late Ordovician to Silurian continental volcano-sedimentary rocks and intruded by synvolcanic plutonic complexes (**Figure II.4 & Figure II.5**) (Hibbard, 1983; Anderson, 1998; Skulski et al., 2009, 2010). For this review the main stratigraphic sequences that outcrop across the Baie Verte Peninsula were grouped based on their ages and crust-type affinity as presented in the legend of **Figure II.4**, and their geological characteristics are summarised in the following subsections.

#### II.3.1.1. Precambrian to Early Ordovician continental margin successions

Four main stratigraphic domains with Laurentian margin affinity were identified in the Baie Verte Peninsula (**Table II.1**). Three of these compose the Fleur de Lys Belt and consist of: a Precambrian Grenvillian basement named the “*East Pond Metamorphic Suite*” (EPMS) that is structurally overlain by a Precambrian to Early Ordovician cover sequence termed the “*Fleur de Lys Supergroup*” (FLS) and a late Precambrian “*ocean-continent transitional zone*” known as the “*Birchy Complex*” (BC) (Hibbard, 1983; Winchester et al., 1992; van Staal et al., 2013) (**Table II.1, Figure II.4 & Figure II.5**). The “*Ming’s Bight Group*” (MBG) represents the fourth

domain that shows a Humber Zone affinity and is located east of the BVL (Hibbard, 1983, Castonguay et al., 2009) (*Table II.1, Figure II.4 & Figure II.5*).

The Birchy Complex (BC) is a steeply dipping, structurally disrupted zone squeezed between the FLS and the Baie Verte Fault Zone (Hibbard, 1983; Winchester et al., 1992; van Staal et al., 2013) (*Figure II.4*). The BC consists of metamorphosed and polydeformed mafic volcano-sedimentary sequences and blocks of serpentinitised ultramafic rocks (Hibbard, 1983; Skulski et al., 2010) and was initially interpreted as a tectonic mélangé zone associated with the Ordovician obduction of ophiolitic blocks on the Laurentian Margin (Bursnall, 1975). However, more recent geochemical and geochronological data revealed a Precambrian age (~565-550 Ma, U-Pb zircon ages from metagabbro and tuffaceous schist) for this unit (V. McNicoll, unpublished data, 2007, presented in Skulski, 2010; van Staal et al., 2013). This led van Staal et al. (2013) to interpret the BC as an “*ocean-continent transition zone*” related to the hyperextension of the Laurentian margin during the opening of the “Humber/Taconian Seaway” between the Laurentian Margin and the Dashwoods microcontinent (a rifted ribbon continental crust of Laurentian affinity) (*Figure II.6 - A*) (Waldron & van Staal 2001; van Staal et al., 2007; Skulski et al., 2010; van Staal et al., 2013).

The Ming’s Bight Group (MBG) is a terrane exposed in a tectonic window within the Baie Verte Belt (*Figure II.4 & Figure II.5*) (Hibbard, 1983, Castonguay et al., 2009). This domain has been interpreted by Hibbard (1982) as part of a continuous Humber Zone promontory that is separated to the south from rocks of Dunnage Zone origin by the Baie Verte Flexure (*Figure II.4*) (Hibbard, 1982). This theory was based on the lithological similarities that the MBG show with respect to the Fleur de Lys Supergroup (FLS) and to the rocks exposed on the Horse Islands, north of BVP (*Figure II.4*) (Hibbard, 1982). The hypothesis was also supported by the geophysical data interpretation of Haworth et al., (1976), who considered that the FLS extends offshore towards the Horse Islands composing a continuous domain. However, Anderson (1998) stated that the MBG was at least stratigraphically, and most likely even geographically separated by the Humber margin during the Taconian orogeny, because prior to Silurian times, the recorded metamorphic facies for the MBG and the FLS were different. Moreover, based on structural field observations, Anderson et al. (2001) interpreted the MBG as a “*symmetrical core complex*” of mid-Devonian age developed in a local transtensional regime and bordered by extensional shear zones (*Figure II.4 & Figure II.5*).

**Table II.1** – Summary descriptions of Precambrian to Early Ordovician continental margin successions

<b>Unit Name</b>	<b>Framework</b>	<b>Age</b>	<b>Rocks</b>	<b>References</b>
East Pond Metamorphic Suite (EPMS)	Basement rocks of the Fleur de Lys Belt ( <i>Fig. II.7</i> )	Precambrian	Migmatites, banded gneisses, metaconglomerates and meta-psammites/pelites exposed in a major anticline located in the central part of the belt	Baird, 1951; deWit, 1980; Hibbard, 1983; Anderson, 1998; Skulski et al., 2010
Fleur de Lys Supergroup (FLS)	Structurally overlies EPMS, covers most of Fleur de Lys Belt ( <i>Fig. II.7</i> )	Precambrian to Early Ordovician	Metamorphosed continental margin sediments and rift – related mafic intrusive rocks	Hibbard, 1983; Anderson 1998; Skulski et al., 2010
Birchy Complex (BC)	Structurally complex zone squeezed between the FLS and the BVL ( <i>Fig. II.7</i> )	Precambrian (~565-550 Ma)	Metamorphosed and polydeformed mafic schists, metabasalts/metagabbros, quartzites, graphitic schists, pelites, jasper units and serpentinised ultramafic rocks	Hibbard, 1983; Winchester et al., 1992; Skulski et al., 2010; van Staal et al., 2013
Ming's Bight Group (MBG)	Tectonic window exposed E of the BVL ( <i>Fig. II.7</i> )	Precambrian to Mid Ordovician	Metamorphosed turbiditic sequences correlated to the rocks of FLS and subordinate greenschists and amphibolitic rocks within shear zones	Hibbard, 1983; Anderson, 1998



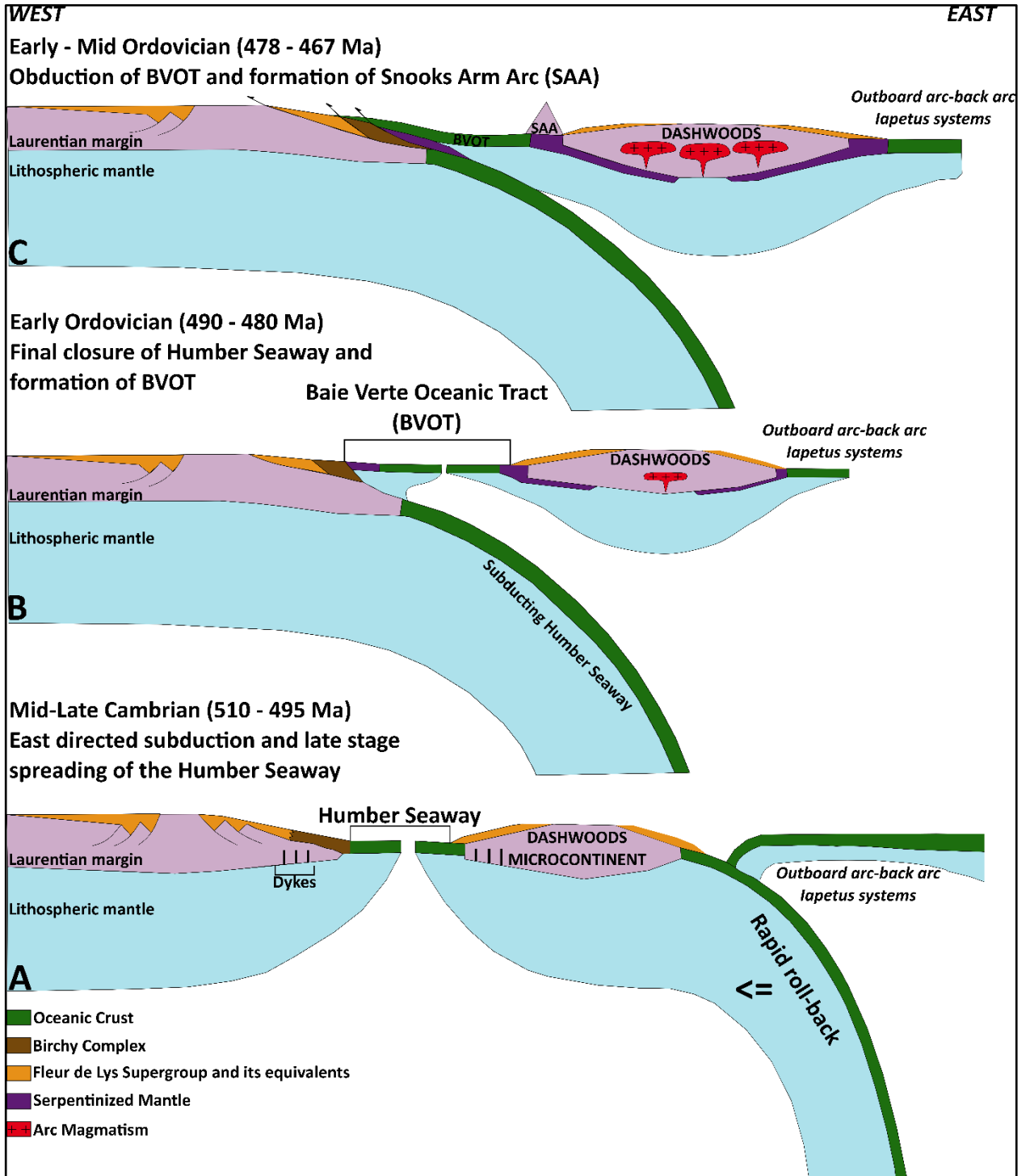


**Figure II.6** – Development and closure of the Humber Sea during Mid Cambrian to Mid Ordovician; A – modified after van Staal et al., 2007; B – modified after Zagorevski and van Staal, 2011; C – modified after Castonguay et al., 2014.

### ***II.3.1.2. Obducted Late Cambrian to Mid Ordovician ophiolitic complexes and cover sequence rocks***

Four, Early Ordovician (~490 Ma, Skulski et al., 2010) boninite ophiolitic complexes compose the infrastructure of the Baie Verte Belt and each of them are unconformably overlain by Early to Mid-Ordovician (~479 to 467 Ma, Skulski et al., 2010) submarine volcano-sedimentary cover sequences (***Figure II.4 & Figure II.5, Table II.2***) (Hibbard, 1983; Skulski et al., 2009, 2010). The ophiolitic complexes (*Betts Cove, Pacquet Harbour, Point Rousse and Advocate*) represent the remnants of the “*Baie Verte Oceanic Tract*” (BVOT) that formed in a fore-arc marginal basin over a subduction zone during the closure of the Humber seaway (***Figure II.6-B***) (Bédard et al., 2000); van Staal et al., 2007; Skulski et al., 2010; van Staal et al., 2013). The cover sequence rocks that overlie the ophiolitic bodies developed during the obduction of the ophiolitic complexes on the Humber zone in an arc-back arc volcanic system (***Figure II.6-C***) (Hibbard, 1983; Skulski et al., 2010; Skulski et al., 2012b; Castonguay et al., 2014).

The four ophiolitic complexes are metamorphosed and either partial deposited or dismembered (Hibbard, 1983). The Betts Cove Complex (BCC) and its cover sequence, the Snooks Arm Group (SAG), outcrop on the eastern shore of the peninsula (***Figure II.4 & Figure II.5, Table II.2***). These two stratigraphic domains are the best exposed and the least deformed representatives of the ophiolitic units and of their cover sequences (Hibbard, 1983; Bédard et al., 2000; Skulski et al., 2009, 2010). Also, the BCC and the SAG form distinct, continuous mappable units in contrast with the other three ophiolitic complexes which are structurally imbricated with their cover sequence rocks (Hibbard, 1983; Bédard et al., 1999, 2000; Skulski et al., 2010). Skulski et al. (2010) identified regional scale marker horizons through consideration of lithogeochemical, geochronological, bedrock mapping, geophysical and remote sensing data. Same authors used the stratigraphic sequence described by Bédard et al. (1999, 2000) for the BCC and for the SAG as a template to anchor correlations and to create a generalized stratigraphic nomenclature that can be applied for the entire Baie Verte Belt (***Fig. II.5***). Detailed stratigraphic and petrographic descriptions of the BCC and SAG can be found in Bédard et al. (1999, 2000) and in Skulski et al., (2009, 2010), whereas summarised descriptions are provided in the following paragraphs, in ***Figure II.5***, and in ***Table II.2***.

**Table II.2** – Summary descriptions of obducted Late Cambrian to Mid Ordovician ophiolitic complexes and cover sequence rocks

Unit Name	Framework	Age	Stratigraphic Fm.	Rocks	References
Snooks Arm Group (SAG)	Represents the volcano-sedimentary sequence of the BCC and its stratigraphic formations are characteristic for the entire peninsula ( <i>Fig. II.5</i> )	Early to Mid Ordovician (~479 - ~467)	Round Harbour Formation (RHF)	Tholeiitic, sheeted and pillow basaltic flows interbedded with chert layers	Kessler & Bédard, 2000; Bédard et al., 2000; Skulski et al., 2009, 2010
			Balsam Bud Cove Formation (BBCF)	Epiclastic, thick-bedded, mafic mass flow deposits	
				Felsic tuffs (~467 Ma, U-Pb zircon age) and sulphidic shale layers	
				Deep water sediments, volcanoclastic turbidites, tuff layers and basaltic lavas	
			Venam's Bight Formation (VBF)	High-Ti (>1.5 %), tholeiitic pillow, amygdaloidal and plagioclase porphyritic basalts interbedded with red, silicified mudstone and iron formations	
			Bobby Cove Formation (BCF)	Thin layers of red shales and jasper iron formation	
				Basaltic to andesitic pillows and lava flows, felsic crystal and lapilli tuffs (~470 Ma, U-Pb zircon age) resedimented volcanic turbiditic layers interbedded with deep water silicious mudstone and thin-bedded felsic tuffs	
				Calc-alkaline clinopyroxene rich volcanoclastic interval	
			Scrape Point Formation (SPF)	Ti rich, tholeiitic, amygdaloidal, and plagioclase-porphyrific pillow basalts interbedded with mafic tuffs	
				Felsic volcanic rocks (~476 Ma, U-Pb zircon age) and grey-green tuffaceous turbiditic layers	
Nugget Pond Horizon: conglomerates and/or breccias with basaltic clasts bound by a matrix of iron oxides and cherty quartz, red siliciclastic rocks and a jasper-magnetite-hematite iron formation					

Betts Cove Complex (BCC)	Well preserved, but incomplete ophiolitic sequence missing the noncumulate ultramafic lower part. Exposed in the eastern part of the Peninsula ( <i>Fig. II.5</i> )	Late Cambrian – Early Ordovician (~489 Ma, U-Pb zircon age)	Mount Misery Formation (MMF)	Olivine and plagioclase-clinopyroxene porphyry basalts with an island-arc tholeiitic chemical signature interbedded with boninitic basaltic lava flows and overlain by breccia and conglomeratic units with mafic and ultramafic clasts	Bédard et al., 1999, 2000; Skulski et al., 2009, 2010, 2015 b
			Betts Head Formation (BHF)	Boninitic olivine-chromite-orthopyroxene pillow basalts and thin felsic flows and associated breccia and hyaloclastite facies	
			Sheeted dyke section	Boninitic microgabbro and olivine-chromite-pyroxene-plagioclase porphyry dykes	
			Layered and massive gabbros	Medium to fine grained gabbro cut by gabbro dykes, overlain by gabbro to gabbronorite massive intrusive bodies and subordinate porphyry diorite and trondhjemite	
			Layered, ultramafic cumulate rocks	Boninitic peridotites and pyroxenites with altered and serpentinised equivalents	

The “*Betts Cove Complex*” (BCC) *sensu* Hibbard (1983), later defined as the “*Betts Cove Ophiolite*” by Bédard et al. (1999, 2000), is a well preserved, but incomplete ophiolitic sequence because its noncumulate ultramafic basal part is not exposed (**Figure II.5**) (Hibbard, 1983; Ramezani, 1992). The BCC comprises basal ultramafic cumulate rocks which are overlain by layered and massive gabbros dated at ~489 Ma (U-Pb zircon age), a sheeted dyke section, and boninitic pillow basalts and thin felsic flows of the “*Betts Head Formation*” (Dunning & Krogh, 1985; Bédard et al., 1999, 2000; Skulski et al., 2009, 2010) (**Figure II.5, Table II.2**). Skulski et al. (2009, 2010) considers the “*Mount Misery Formation*” (MMF) (Bédard, 1999) as the youngest part of the BCC (**Figure II.5**), contrasting with the stratigraphy presented by Bédard et al. (1999, 2000) where the MMF represents the lower section of the overlying Snooks Arm Group. The MMF is the main host for the majority of the known volcanic massive sulphide deposits from the Baie Verte Peninsula and for several orogenic gold occurrences (**Figure II.4 & Figure II.5**) (e.g. the Deer Cove and the Romeo & Juliet gold prospects, case studies for the present thesis) (Skulski et al., 2009, 2010; Pawlukiewicz, 2019). Rock descriptions for the MMF can be found in both **Figure II.5** and **Table II.2**.

The “*Snooks Arm Group*” (SAG) (**Figure II.5** and **Table II.2**) represents the volcano-sedimentary sequence that overlies the BCC and is composed, from base to top, of five lithostratigraphic units: i) the “*Scrape Point Formation*” (SPF) (Bédard et al., 2000; Skulski et al., 2010); ii) the “*Bobby Cove Formation*” (BCF) (Upadhyay, 1973; Hibbard, 1983; Bédard et al., 2000; Skulski et al., 2010); iii) the “*Venam’s Bight Formation*” (VBF) (Upadhyay, 1973; Hibbard, 1983; Bédard et al., 2000; Skulski et al., 2010); iv) the “*Balsam Bud Cove Formation*” (BBCF) (Upadhyay, 1973; Hibbard, 1983; Bédard et al., 2000; Skulski et al., 2010); and v) the “*Round Harbour Formation*” (RHF) (Upadhyay, 1973; Hibbard, 1983; Bédard et al., 2000; Skulski et al., 2010).

The Scrape Point Formation (SPF) (**Figure II.5**) represents the lowest unit of the SAG and is composed of three main intervals described in **Figure II.5** and **Table II.2**. The lower part of the SPF, termed by Skulski et al., (2010) the “*Nugget Pond Horizon*” (NPH), can be found across the entire Baie Verte Belt and thereby was used as a marker interval for stratigraphic correlations. In the eastern part of the Baie Verte Peninsula the NPH hosts the Nugget Pond gold deposit, whereas in the Point Rouse Complex, a banded iron formation that is considered the stratigraphic equivalent to

the NPH, termed “*The Goldenville Horizon*” by Skulski et al. (2010), hosts the Goldenville gold deposit (**Figure II.5**) (Skulski et al., 2009, 2010). The middle interval of the SPF contains felsic rocks that yield a U-Pb zircon age of ~476 Ma (**Figure II.5**) (Skulski et al., 2010).

The Bobby Cove Formation (BCF) overlies the SPF and in its basal section contains a distinctive calc-alkaline clinopyroxene rich volcanoclastic horizon. For the Betts Cove area, this interval was named by Skulski et al. (2010) the “*East Pond Member*” and was correlated by the same author with the “*Pairie Hat Member*” defined by Kidd (1974) within both the Flat Water Pond Group and the Point Rouse Complex (**Figure II.5**) and with a clinopyroxene rich porphyry tuff interval identified by Hibbard (1983) in the Paquet Harbour Group (**Figure II.5**). The age of the BCF was interpreted to be ~470 Ma based on U-Pb zircon age from a felsic volcanoclastic unit that overlies the East Pond member (V. McNicoll, unpublished data, 2007, presented in Skulski et al., 2009, 2010). Within the Point Rouse Complex, in the Pine Cove area (**Figure II.4**), the BCF is overturned and structurally imbricated with the Venam’s Bight Formation and locally represents the host for some mineralised zones of the Pine Cove gold deposit (**Figure II.5**) (study case for the present project) (Ybarra, 2019).

The Venam’s Bight Formation (VBF), the Balsam Bud Cove Formation (BBCF) and the Round Harbour Formation (RHF) represent the middle and the upper parts of the Snooks Arm Group and contain marker horizons that can be correlated across most of the Baie Verte Belt (**Figure II.5; Table II.2**) (Skulski et al., 2009, 2010). Within the Point Rouse Complex, the high-Ti (>1.5 %) tholeiitic pillow basalts of the VBF together with Fe-Ti oxide rich gabbro sills and dykes represent the main host for the Pine Cove deposit (Ybarra, 2019). The felsic volcanic rocks of the BBCF (**Figure II.5; Table II.2**) were dated by V. McNicoll (2007) (unpublished data presented in Skulski et al., 2009, 2010) and yielded a U-Pb zircon age of ~467 Ma that was interpreted as the minimum deposition age for the Snooks Arm Group (Skulski et al., 2010).

In the Point Rouse Complex the cover sequence rocks are intruded by tholeiitic, Fe-Ti-oxides-rich gabbro sills and dykes (**Figure II.5**) (Skulski et al., 2010). These intrusions are referred here as the “*Stog’er Tight Gabbro*” (**Figure II.5**) after Ramezani (1992). Ramezani (1992) dated the gabbro sills through U-Pb geochronological techniques and obtained an imprecise Early Ordovician age of 483

+3/-2 Ma that was interpreted as the gabbro crystallization age. Skulski et al. (2010) considered the age of the Stog'er Tight Gabbro represents an approximate minimum age for the basal part of the cover sequence rocks. However, recent work conducted by the Anaconda Mining geologists and by MSc students from the Memorial University of Newfoundland in the Point Rouse area, showed that the Fe-Ti-oxides-rich gabbro sills can also be found at higher stratigraphic levels, within the Bobby Cove and the Venam's Bight Formations (**Figure II.5**) (Cullen et al., 2018; Ybarra, 2019). Considering that the age of the BCF is  $470 \pm 4$  Ma as proposed by Skulski et al. (2010), it means that the age obtain by Ramezani (1992) for the Stog'er Tight Gabbro sills should be interpreted as a maximum age in a time interval between  $\sim 480$  to  $\sim 470$  Ma and not as an absolute age value. Within the Point Rouse Complex, the Stog'er Tight Gabbro sills serve as the main host for the Stog'er Tight and the Argyle gold deposits, and partially for the Pine Cove gold deposit, all three deposits being study cases for this project (**Figure II.5**) (Ramezani 1992; Pawlukiewicz, 2019; Ybarra, 2019).

The “*Pacquet Harbour Group*” (PHG) initially defined by Church (1969), and further subdivided into the lower and upper PHG by Skulski et al. (2010), outcrops in the central – north part of the Baie Verte Belt (**Figure II.4 & Figure II.5**) (Hibbard, 1983; Skulski et al., 2010, 2015 a, b). According to Skulski et al. (2009, 2010), the lower part of the group represents the upper section of an ophiolite complex and consists of boninitic pillow basalts that can be correlated with the ones from the Bets Head Formation of the Betts Cove Complex (**Figure II.5**). The boninitic successions are overlain by rhyodacitic lavas and felsic tuffs of the “*Rambler Rhyolite formation*” (RRF) (**Figure II.5**) (Skulski et al., 2010). The RRF hosts the Rambler and Ming VMS deposits, has an age of  $\sim 487$  Ma (U-Pb zircon age, unpublished data of V. McNicoll, 2007, presented in Skulski et al., 2009, 2010) and is locally overlain by tholeiitic basalts corresponding to the ones of MMF (**Figure II.55**) (Skulski et al., 2010). The upper part of PHG (**Figure II.5**) is the volcano-sedimentary cover sequence and contains a basal conglomeratic unit like the lower unit of the SPF and a middle and upper section composed of several tholeiitic pillow basalt layers which can be correlated to the Venam's Bight and Round Harbour Formations of the SAG (**Figure II.5**) (Skulski et al., 2009, 2010).

Compared to the Betts Cove Complex, the “*Point Rouse Complex*” (PRC) (Hibbard, 1983) (**Figure II.4 & Figure II.5**) is a complete, but dismembered

ophiolitic sequence, including the lower unit of mantle harzburgite and to a lesser degree serpentinitised dunites and pyroxenites (**Figure II.5**) (Norman & Strong, 1975; Hibbard, 1983; Ramezani, 1992; Castonguay et al., 2009; Skulski et al., 2009, 2010). The age of the PRC was determined at ~489 Ma based on a U-Pb zircon age of a trondhjemite sample collected from the layered gabbro section (**Figure II.5**) (unpublished data, V. McNicoll, 2007, presented in Skulski et al., 2009, 2010). The rocks of the Point Rousse cover sequence outcrop between two ophiolitic blocks, one to the north and one to south-east, and are tectonically imbricated both within themselves and with slivers pertaining to the MMF (**Figure II.4**) (Ramezani, 1992). All the stratigraphic formations described for the SAG (**Table II.2**) are partially to fully found within the Point Rousse cover sequence and, with few exceptions, follow the same terminologies (**Figure II.5**) (Skulski et al. 2009, 2010).

The “*Advocate Complex*” (AC) (Hibbard, 1983) outcrops close to the Baie Verte town as steeply dipping and northeasterly striking tectonic slivers along the BVL and is in tectonic contact with the Birchy Complex to the west (**Figure II.4 & Figure II.5**) (Hibbard, 1983; Skulski et al., 2009, 2010). The unit is highly structurally dismembered, lacking its boninitic pillow basalts section (**Figure II.5**) (Hibbard, 1983; Skulski et al., 2009, 2010). Tholeiitic pillow basalts similar to the ones from the Mount Misery and the Scrape Point Formations, together with other volcanoclastic rocks comparable to those from the upper part of the Snooks Arm Group, outcrop as fault-bounded slices along the Baie Verte Line (Skulski et al., 2010, 2015 a). These rocks compose the cover sequence of the AC (**Figure II.5**) and were termed by Bursnall (1975) the Shark Point Group (Skulski et al., 2010).

In addition to the four volcano-sedimentary cover sequences attributed to the above mentioned ophiolitic complexes, Hibbard (1983) introduced another cover unit, the “*Flatwater Pond Group*” (FWPG), which outcrops along the eastern part of the BVL, between the town of Baie Verte to the north, and the Micmac Lake to the south (**Figure II.4**) (Skulski et al., 2010). The group consists of mafic volcanic and volcanoclastic rocks and to a minor degree, conglomerates (“*Fox Pond and Kidney Pond Formations*”), and felsic volcanic rocks (“*Six Mile Brook Formation*”) (**Figure II.5**) (Hibbard, 1983, Skulski et al., 2009, 2010). Initially, Hibbard (1983) interpreted the age of the FWPG as Silurian, based on granodiorite clasts from the conglomerate interval that showed common properties to the adjacent, Silurian Burlington Granodiorite (**Figure II.4**). However, according to new geochronological data



presented in Skulski et al. (2010), the maximum depositional age for the FWPG is  $\sim 479$  Ma (U-Pb zircon age of granitic clast in conglomerate). Furthermore, based on geochemical data, Skulski et al. (2010) identified in the FWPG tholeiitic pillow basalts identical to the ones from the MMF, and other felsic and mafic rocks that resemble stratigraphic intervals of SAG (**Figure II.5**). It is considered that the FWPG represents the equivalent of the Shark Point Group forming the cover sequence for the Advocate Complex (AC) south of the Baie Verte town (**Figure II.4 & Figure II.5**) (Skulski et al., 2010). This interpretation is based on two aspects: i) ophiolitic lenses of the AC occur as tectonic slices imbricated in both the Flat Water Pond and the Shark Point Groups; and ii) the Fox Pond conglomerate is present in the base of the aforementioned groups (**Figure II.5**) (Skulski et al., 2010).

### ***II.3.1.3. Late Ordovician to Silurian plutonic and continental volcano-sedimentary rocks***

The Baie Verte Peninsula is intruded by large, granodioritic to granitic plutons of Late Ordovician to Silurian age (**Figure II.4 & Figure II.5**) (Hibbard, 1983; Anderson, 1998; Skulski et al., 2009, 2010). The plutons are interpreted to be early to syn-genetic with respect to the Late Ordovician - Silurian continental volcano-sedimentary units that unconformably overlie the Ordovician cover sequence rocks of the ophiolitic complexes (**Figure II.4 & Figure II.5**) (Hibbard, 1983; Anderson, 1998; Skulski et al., 2009, 2010).

All the Late Ordovician to Silurian plutonic rocks are located within the Baie Verte Belt except for the Silurian ( $427 \pm 2$  to  $423 \pm 3$  Ma, U-Pb monazite and titanite age, respectively) dioritic to granitic bodies of the “*Wild Cove Pond Igneous Suite*” (WCPIS) that intrude the Fleur de Lys Belt (**Figure II.4 & Figure II.5**) (Hibbard, 1983; Cawood & Dunning, 1993; Skulski et al., 2010, 2015c). The “*Burlington Granodioritic Complex*” (BGC) (Skulski et al., 2012a) (**Figure II.4 & Figure II.5**) is the largest pluton on the peninsula and is composed of an early ( $445 \pm 4$  Ma, U-Pb zircon age) calc-alkaline, granodioritic phase followed by synvolcanic, intermediate dioritic to granodioritic bodies dated at  $441 \pm 1.2$  Ma based on U-Pb analysis of zircon and titanite, and a late ( $433 \pm 0.8$  Ma, U-Pb zircon & titanite age), ferroan, granodioritic to monzogranitic phase (Skulski et al. 2012a; Skulski et al., 2015a) (**Figure II.5**). Rhyolitic dykes of  $458 \pm 4$  Ma (U-Pb zircon age) intrude the lower Paquet Harbour Group and might represent early phases of the BGC (**Figure II.5**)

(Skulski et al., 2015a). The syn-volcanic, “*Confusion Bay Plutonic Suite*” (Skulski et al., 2015b) outcrop in the northern part of the Baie Verte Belt and comprises several coeval, tholeiitic to alkaline plutons (**Figure II.4 & Figure II.5**): the  $427 \pm 1.4$  Ma “*Dunamagon Granite*” (DG) (U-Pb zircon age; Hibbard, 1983; Skulski et al., 2009, 2010, 2012, 2015 a); the  $429 \pm 4$  Ma “*Cape Brulé Prophyry*” (CBP) (U-Pb zircon age; Hibbard, 1983; Skulski et al., 2009, 2010, 2012, 2015b); and the  $426 \pm 1$  Ma “*La Scie Intrusive Suite*” (LIS) (U-Pb zircon age; Hibbard, 1983; Skulski et al., 2012a, 2015b).

The Late Ordovician to Silurian continental volcano-sedimentary rocks outcrop east of the BVL and unconformably overlie the rocks of the Baie Verte Belt (**Figure II.4 & Figure II.5; Table II.3**) (Skulski et al., 2010). The “*Micmac Lake Group*” (MLG) (**Figure II.4**) is in tectonic contact with the Flat Water Pond Group to the west and unconformably overlies the Burlington Granodioritic Complex to the east (Hibbard, 1983; Skulski et al., 2009, 2010). The MLG consists of two unconformably stacked units described in **Table II.3** (Skulski et al., 2015a, c): the lower unit was dated at  $442 \pm 4$  (Skulski et al., 2015 c), whereas the upper unit yielded an age of  $\sim 430$  Ma (V. McNicoll, unpublished data, 2008, presented in Skulski et al., 2010). The “*King’s Point Complex*” (KPC) outcrop in the south-central part of the Baie Verte Belt (**Figure II.4**) and includes both intrusive and extrusive rock sequences (**Table II.3**). The upper part of the KPC contains syenite dykes dated at  $427 \pm 2$  Ma (**Figure II.5**) (Coyle, 1990; Skulski et al., 2015c). The “*Cape St. John Group*” (CJG) is exposed in the north-eastern part of the peninsula and unconformably overlies the Snooks Arm Group and the Betts Cove Complex (**Figure II.4**). The CJG is composed of continental derived sedimentary sequences and of bimodal volcanic rocks dated at  $\sim 427$  Ma (**Figure II.5, Table II.3**) (Skulski et al., 2009, 2010, 2015b).

**Table II.3** – Summary descriptions of Late Ordovician to Mid Silurian continental volcano-sedimentary rocks

Unit Name	Framework	Age	Rocks	References
Micmac Lake Group (MLG)	Unconformably overlies the BGC to the east; tectonic contact with the FWPG to the west ( <i>Fig. 1</i> )	Late Ordovician to Mid Silurian (442 ± 4, U-Pb zircon age of felsic tuff) to 430 ± 4 Ma, U-Pb zircon age of mafic lapilli tuff)	Upper part: volcanic derived conglomerates overlain by basalts, basanites, ignimbrites, and flow units	Hibbard, 1983; Skulski et al., 2010, 2015a, b, c
			Lower part: red sandstones and conglomerates overlain by basalts, felsic ignimbrites and flow banded rhyolites	
King's Point Volcanic Complex (KPVC)	Outcrop in the south-central part of the peninsula; the ring dykes cut the BGC ( <i>Fig. 1</i> )	Mid Silurian (427 ± 2 Ma)	Upper part: tuffs and ignimbrites cut by syenitic and granitic dykes	Coyle, 1990; Skulski et al., 2010, 2015c
			Middle part: intrusive sub-volcanic ring dykes	
			Lower part: quartz-feldspar-porphyry tuffs and volcanic breccias	
Cape St. John Group (CJG)	Exposed in the north-eastern part of the peninsula and unconformably overlies the SAG and BCC ( <i>Fig. 1</i> )	Mid Silurian (~427 Ma, U-Pb zircon ages of flow banded rhyolite and welded tuff)	Continental derived sedimentary unit, consisting of conglomerates and red sandstones/siltstones and bimodal volcanic rocks: massive and flow basalts, massive and flow banded rhyolites and felsic volcano-clastic rocks	Skulski et al., 2009, 2010, 2015b

### II.3.2. Structural evolution of the Baie Verte Peninsula

The Baie Verte Peninsula shows a complex polyphase deformation history that resulted from prolonged plate interaction between the Humber Zone and the outboard terranes during Palaeozoic times (Castonguay et al., 2009, 2012). The intensity and the structural style of the deformation phases vary across the peninsula which creates difficulties in regional correlations (Hibbard, 1983; Castonguay et al., 2009; Skulski et al., 2010). However, multidisciplinary studies conducted over the last two decades that combine structural, geochronological, litho-geochemical, and geophysical data sets, led to the development of multiple regional and sub-regional structural models for the Baie Verte Peninsula (Anderson 1998; Waldron et al., 1998; Castonguay et al., 2009, 2014; Skulski et al., 2010, 2012, 2015; Willner et al., 2022). All the models consist of at least four deformational events and show a consensus with respect to the broad timing and implications of the main tectonic events that shaped the peninsula (**Figure II.7**) (Waldron et al., 1998; Castonguay et al., 2009, 2014; Skulski et al., 2010, 2012, 2015). Yet, for the post-Ordovician periods there are differences between the classification used by previous authors for each of their deformational events. In turn, this creates uncertainties related to the kinematic movements that occurred along the Baie Verte Line during each deformational sequence, and regarding the ages of some structural elements that resulted from strain partitioning processes. The results of this study are used to cover some of the present uncertainties and to provide an updated structural evolution model for the Baie Verte Peninsula (*see chapter VII*).

The earliest deformation phase that affected the Baie Verte Peninsula is strongly overprinted by younger events and was mostly described in the western part of the peninsula, within the Fleur de Lys and the Birchy Complex (**Figure II.4**) ( $D_1$  of Waldron et al, 1998;  $D_1$  of Castonguay et al., 2009;  $D_1$  of Skulski et al. 2009, 2010, 2015). The  $D_1$  phase is associated with the westward obduction of the ophiolite complexes on the Laurentian margin and arc collision of the Baie Verte Oceanic Tract and of the Snooks Arm Group during the main phase of the Taconic Orogeny (~481 – 461 Ma) (**Figure II.6-B, Figure II.7-A**) (Waldron et al., 1998; van Staal et al., 2007; Castonguay et al, 2009, 2014; Skulski et al., 2010, 2015). The early development of the Baie Verte Line was related to this tectonic event and was interpreted as the obduction “*root zone*” (**Figure II.7-A**) (Hibbard, 1983 and references herein; Anderson, 1998). It is accepted that during the Taconic event, the Fleur de Lys block experienced a burial depth of more than 30 km based on the eclogite metamorphic

facies recorded in the East Pond Metamorphic Suite (**Figure II.4**) (Castonguay et al., 2014).

There is an agreement between previously published studies that the main tectonometamorphic phase that affected the entire Baie Verte Peninsula occurred between Mid Silurian to Late Silurian/Early Devonian time and resulted in the rapid uplift of the Fleur de Lys Belt and the subsidence, folding, and south directed thrusting of the Baie Verte Belt (**Figure II.7-B**) ( $D_1$  of Waldron et al., 1998 east of the BVL;  $D_2/D_{2b}$  of Castonguay et al., 2009; and  $D_2/D_3$  of Skulski et al. 2010, 2015). It is considered that this event developed in a sinistral transpressional regime localised along the BVL during the Silurian Salinic Orogeny (Anderson 1998; Waldron et al., 1998; Castonguay et al., 2009, 2012; Skulski et al., 2009, 2010, 2012 b, 2015). According to Hibbard (1983) and to Bélanger et al. (1996), the steeply dipping, east directed, reverse faults (e.g. the Baie Verte Road Fault system) that overprint the BVL, and imbricate parts of the Advocate Complex with the Flat Water Pond and the Burlington Granodiorite, may represent splays of the BVL that formed syn-to-post Silurian.

The strain intensity and the characteristics of the structural fabrics and of the metamorphic facies associated with this deformation phase vary across the region (Hibbard, 1983; Castonguay et al, 2009; Skulski et al., 2010). West and along the Baie Verte Line (BVL) the structural fabrics are steeply dipping, show an overall NNE - SSW orientation and are associated with greenschist to amphibolite metamorphic facies (**Fig. II.7-B**) (Castonguay et al., 2014; Skulski et al., 2015). Shear zones developed W and NW of the BVL accommodate a NW directed transport, whereas the faults formed along the BVL show evidence of opposing transport direction, towards ESE (Hibbard, 1982; Bélanger et al., 1996; Castonguay et al., 2014).

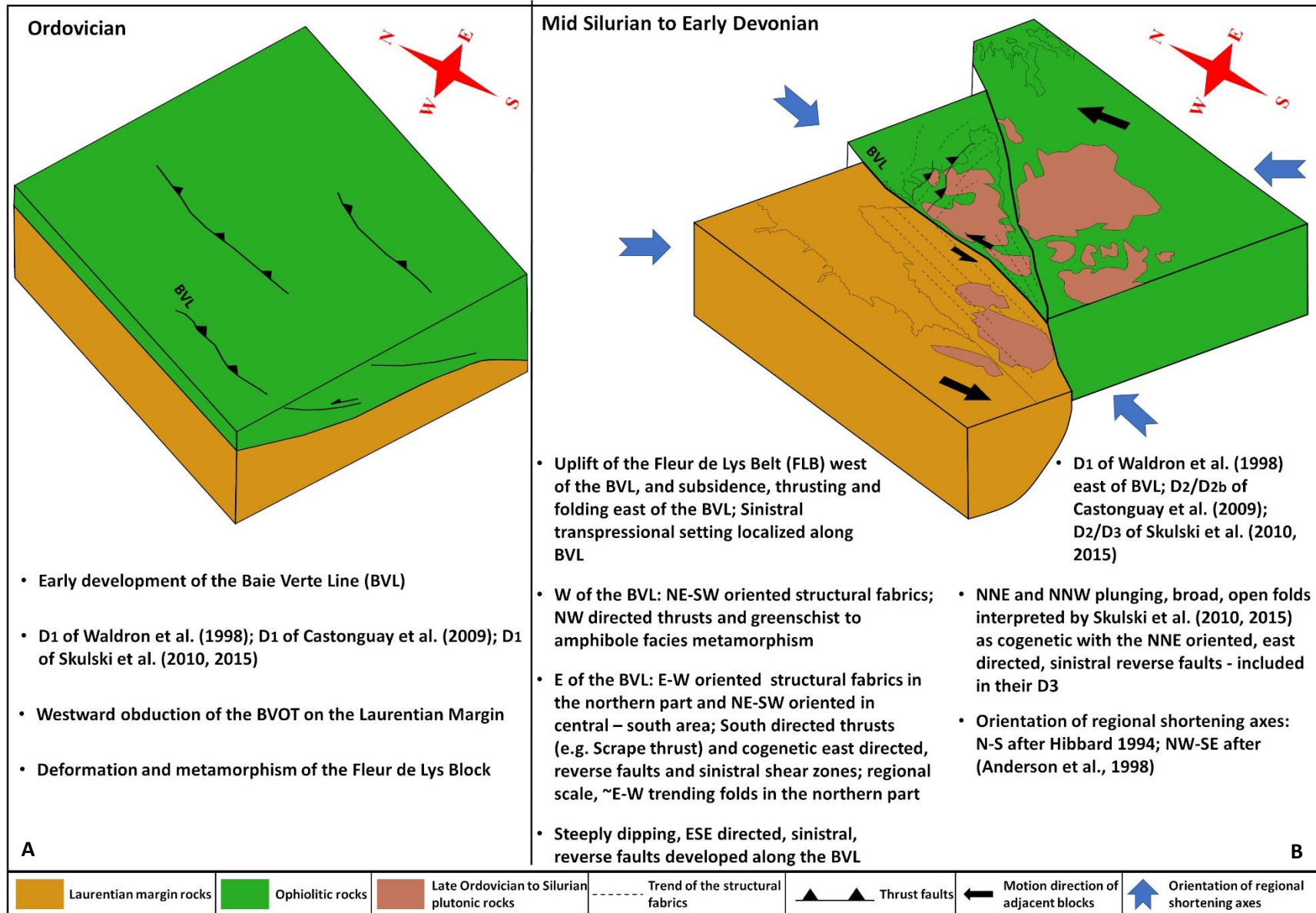
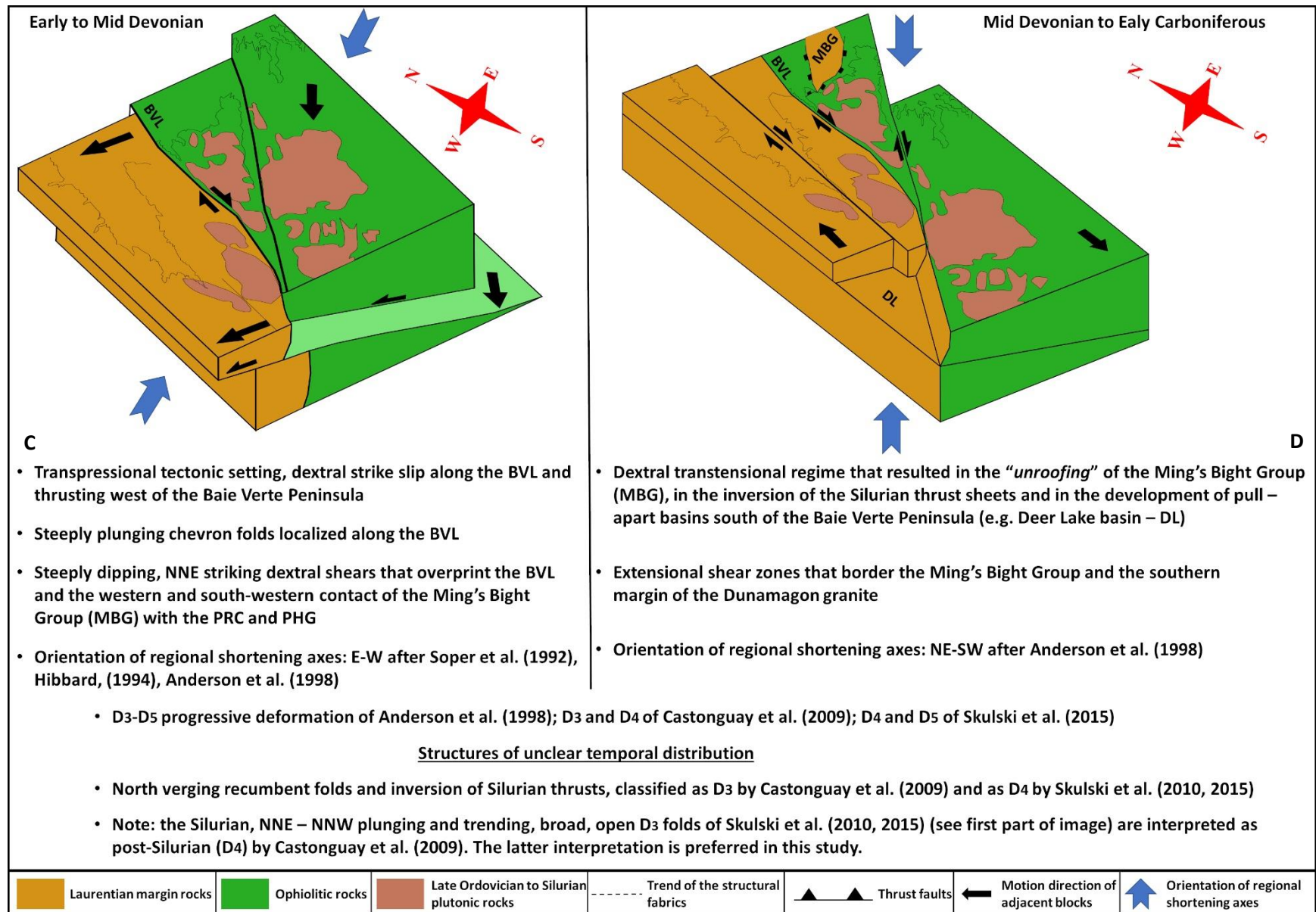


Figure II.7 – Structural evolution model of the Baie Verte Peninsula modified after Waldron et al., 1998.



**Figure II.7 (continuation)** – Structural evolution model of the Baie Verte Peninsula modified after Waldron et al., 1998.

On the central and eastern parts of the peninsula the intensity and the related metamorphic facies of this deformation phase increase from south to north (Castonguay et al., 2009). The spaced to mylonitic foliation fabric dips moderately to steeply, has a general easterly strike in the northern part of the peninsula and an approximately NE-SW strike in the central and southern parts, and is locally characterized by a strong, moderately to steeply dipping stretching and mineral lineation fabric (L>S) (**Figure II.7-B**) (Castonguay et al., 2009; Skulski et al., 2015). The foliation is interpreted to be cogenetic with south verging thrusts and reverse faults (**Figure II.7-B**) (e.g. Scrape and Deer Cove thrusts, **Figure II.4**) and with open to tight, isoclinal to overturned, east trending and south verging folds (Castonguay et al., 2009; Skulski et al., 2010, 2015).

NNE-SSW striking, west dipping, sinistral reverse faults and shear zones are also common east of the BVL (Castonguay et al., 2009). These structures were classified as D<sub>2b</sub> by Castonguay et al. (2009) and as D<sub>3</sub> by Skulski et al. (2010, 2015), and were interpreted as tear faults or lateral ramps that developed synchronously with the south directed thrusts due to strain partitioning processes under a sinistral progressive deformation. Moreover, Skulski et al. (2010, 2015) reported open to upright NNE to NNW trending and plunging folds in the Paquet Harbour and Cape St. John Groups which were formed during the same Silurian sinistral deformation phase. However, these folds were interpreted by Anderson (1998) and Castonguay et al. (2009) as being post Silurian in age and developed in an overall dextral transpressional / transtensional tectonic regime (see below). The results of this study support the latter hypothesis, see **chapters IV and VII**.

The youngest deformational events that shaped the Baie Verte Peninsula took place in the time span of Early Devonian to Early Carboniferous (**Figure II.7-C, D**) and correspond to D<sub>3</sub>-D<sub>5</sub> of Anderson (1998), to D<sub>3</sub>-D<sub>4</sub> of Castonguay et al. (2009) and to D<sub>4</sub>-D<sub>5</sub> of (Skulski et al., 2010, 2015). The structural features associated with these late deformational phases are heterogeneously distributed across the area and consist of variable structural elements (Anderson, 1998; Castonguay et al., 2009; Skulski et al., 2010, 2015a): i) steeply plunging chevron folds along the BVL; ii) north verging recumbent folds associated with the inversion of the thrust sheets in the Paquet Harbour Group (PHG); iii) extensional kink bands that reactivate the south directed thrusts from the Point Rousse Complex (PRC) with a north side-down motion; iv) NNE to NNW plunging and trending folds that refold earlier structures



within the Paquet Harbour and Cape St. John groups; v) steeply dipping, NNE striking, dextral shears that overprint the BVL and the western and south-western contact of the Ming's Bight Group (MBG) with the PRC and PHG; and vi) extensional shear zones that border the Ming's Bight Group and the southern margin of the Dunamagon granite. The current understanding is that these structures formed under a dextral transpressional setting localised along the BVL during the Early Devonian followed by a dextral transtensional regime that resulted with the “*unroofing*” of the MBG and with the inversion of the Silurian thrust sheets between Mid Devonian to Early Carboniferous (**Figure II.7–C, D**) (Waldron et al., 1998; Skulski et al., 2010, 2015). However, regional correlations between these structures are difficult, and their association to a transpressional or a transtensional tectonic regime is debatable. Thereby, interpretations regarding the evolution of these structural elements and their inferred chronological order within the deformational sequences presented by different authors usually varies - e.g. the recumbent, north verging folds are assigned to a D<sub>3</sub> event by Castonguay et al. (2009), but to a D<sub>4</sub> event by Skulski et al. (2010), whereas the NNE – NNW plunging and trending folds are considered post-Silurian by Castonguay et al. (2009), but syn-Silurian by Skulski et al. (2010, 2015), (**Figure II.7**).

Within the following chapters, some of the above-mentioned uncertainties and debates related to the structural evolution of the Baie Verte Peninsula are reconciled based on new structural observations and geochronological data gathered for this study. An updated structural model for the Baie Verte Peninsula is presented in **chapter VII**.

#### **II.4. Gold mineralisation in the BVP**

The Baie Verte Peninsula has a long history of gold exploration that goes back for more than 150 years (Evans, 1999, 2004; Skulski et al., 2009). Initially, the gold was extracted as by-product from volcanic massive sulphide deposits (VMS) (Evans, 2004). The opening of the Terra Nova mine (**Figure II.4**) in 1860's, a VMS deposit operated for both base-metals and gold, marks the starting of the modern mining times within the region (Evans, 1999, 2004; Kerr et al., 2005; Skulski et al., 2009). Gold bearing veins were first discovered in 1867 in the Ming's Bight area, but their exploitation was unsuccessful (Evans, 1999, 2004; Kerr et al., 2005). The first

economic gold deposit, the Goldenville site (*Figure II.4*), was discovered in 1903, and its production started in 1904 (Evans, 2004; Copeland et al., 2015). No other significant gold deposits were discovered until 1986, when the Norada Mining Company identified the Deer Cove deposit (*Figure II.4*) (Evans, 2004). This finding led to the development of intensive exploration programs that resulted with the discovery of more than 100 epigenetic gold occurrences over the last 3 decades (Evans, 1999, 2004). The gold occurs in syn-genetic mineralisation within Ordovician volcanic massive sulphide deposits (VMS) and as epigenetic mineralisation within structurally controlled quartz-carbonate veins and disseminated within altered rocks (Evans, 1999, 2004). The most comprehensive review of the epigenetic gold occurrences from the Baie Verte Peninsula can be found in Evans (1999, 2004) and provides the names, location, exploration history and geological characteristics for over 100 gold occurrences. According to the mentioned author, the bulk characteristics of these gold occurrences fall within the orogenic gold style mineralisation (summarised characteristics provided in *Table II.4*). The deposits that represent the case-studies for this thesis were also included in this category (Evans 1999, 2004; Pitman et al., 2020). Thus, short description of the overall geological attributes of structurally controlled epigenetic gold occurrences from the BVP is provided below. The gold mineralization associated with the VMS deposits is not considered further. Yet, geological assessments of gold bearing VMS deposits from the Baie Verte Peninsula can be found within the following studies: Gale (1971); Upadhyay, 1973; Tuach & Kennedy, 1978; Hibbard (1983); Swinden et al. (1991); Cook & Cochrane, 2006; Piercey and Hickey (2012); Pilote (2018).

*Table II.4. – General characteristics of orogenic gold deposits*

<b>Feature</b>	<b>Description</b>	<b>References</b>
Tectonic setting/regime	Compressive or transpressive stresses associated with subduction or collisional processes. Hosted by deformed and metamorphosed accreted terranes, accretionary prisms, fore-arc and back-arc frameworks.	Cox et al., 2001; Groves et al., 2003; Phillips and Powell, 2010; Goldfarb and Groves 2015; Groves et al., 2018, 2020; Nassif et al., 2022; Goldfarb and Pitcairn, 2023
Structural controls	Strongly structurally controlled, being hosted by ductile to brittle low-order structural features associated with crustal-scale shear zones or major thrust faults.	
Deposition environment	Hypozonal to epizonal; vary from ~200 °C up to 650 °C, respectively from 0.5 Kbars to 5 Kbars. Most commonly form in the brittle-ductile seismic zone ~12-6 Km.	
Mineralisation	Most common - gold bearing quartz veins with associated Fe-sulphides and carbonates; less common - Pb-Zn-Cu sulphides, sulfosalts and even tellurides.	
Alteration	Mineral assemblages vary according to the host rock lithology and consist mostly of carbonates (calcite, dolomite, ankerite and siderite), sulphides (pyrite, pyrrhotite and arsenopyrite), sericite, and subordinate chlorite (especially in mafic wall-rocks).	
Fluid sources	Metamorphic fluids sourced from devolatilization of crustal rocks during the transition from greenschist to amphibolite facies conditions or from the devolatilization of subcontinental lithospheric mantle.	
Fluid chemistry	Aqueous-carbonic mixtures, up to 20 mol% CO <sub>2</sub> characterized by low to moderate salinities (~3.7 wt% NaCl equivalent), near - neutral PH (~5.5) and considerable contents of CH <sub>4</sub> and N <sub>2</sub> .	
Fluid transport mechanism	Fluid migration along fracture networks driven by fault-valving events.	
Gold transport mechanism	As gold-sulphide complexes and colloids (nanoparticles in solution).	

More than 90% of the epigenetic gold occurrences from the Baie Verte Peninsula are located along, and east of the Baie Verte Line, within rocks of the Baie Verte Belt (*Figure II.4*) (Evans 1999; Evans, 2004). Almost all these occurrences show a strong structural control being frequently located in the hanging wall compartments of major fault zones and hosted by small scale shear zones that represent splays of the main faults (Evans, 2004). Evans (1999, 2004) separated the gold occurrences in two major classes, each of which with their own subdivisions, based on the geological characteristics of each mineralised zone. The main characteristics of each epigenetic gold class and of their sub-classes are provided in *Table II.5*.

Most of the epigenetic gold deposits from the BVP were interpreted as orogenic gold type occurrences (Evans, 2004; Pitman et al. 2020), but uncertainties exist regarding both the fluid and metal sources involved in their formation. Deposit scale studies consisting of a combination of geochemical techniques (fluid inclusion, trace element, and/or oxygen/carbon/sulphur isotopic analyses) point to variable metal reservoirs (volcano-sedimentary units with an island-arc affinity, ultramafic ophiolitic rocks and/or Grenvillian basement rocks) and to fluids resulted from magmatic and/or metamorphic processes (Patey & Wilton, 1993; Ramezani et al., 2001; Evans 2004 and references herein). The magmatic source of the mineralising fluids is less favoured within the more recent studies (e.g. Kerr & Shelby, 2012) because the geochronological ages available for the plutonic/volcanic intrusive complexes and for the gold deposits suggest that the mineralisation is younger than the regional magmatic activity, with the exception of a very discrete overlapping between the far end spectrum of their associated analytical errors (*Figure II.8*). However, the timing of the gold mineralisation from the Baie Verte Peninsula is poorly constrained (*Figure II.8*) (Kerr & Shelby, 2012). Existing interpretations based on structural analysis favour a relative age of Mid to Late Silurian for the formation of most of the gold occurrences and subsequent deformation of the deposits during Devonian and/or Carboniferous (Bélanger et al., 1996; Castonguay et al., 2009; Skulski et al., 2009, 2010). Yet, the few existing geochronological ages,  $420 \pm 5$  Ma &  $411 \pm 7$  Ma (the Stog'er Tight deposit),  $420 \pm 7$  Ma (the Pine Cove deposit) and  $374 \pm 8$  Ma (the Nugget Pond deposit), suggest a larger mineralisation window from Mid Silurian to Late Devonian, or two distinct events of Late Silurian / Early Devonian and Late Devonian, respectively (*Figure II.8*) (Ramezani, 1992; Sangster et al. 2008; Kerr &

Shelby, 2012). These time intervals overlap with both the Salinic and the Acadian orogenic events (*Figure II.8*) (Evans, 2004) and hinder exact correlations between the formation of the gold mineralisation and the regional geodynamic setting active at the time of the gold deposition. Still, the current assumption is that the Late Silurian/Early Devonian period represents the main phase of gold mineralisation and is correlated with the waning stages of the Silurian, Salinic orogenic event, whereas the Late Devonian ages may reflect a local remobilisation due to subsequent deformation of the deposits during the Acadian and/or the Neo-Acadian orogeneses (*Figure II.8*) (Ramezani et al. 2001; Evans, 2004; Kerr & Shelby, 2012).

This study brings new understandings regarding the timing of gold mineralisation within the BVP based on U-Th-Pb dating of monazite, xenotime, and titanite from four gold occurrences (Stog'er Tight, Argyle, Romeo & Juliet, and Deer Cove; *Chapter VI*). The ages are combined with structural observations to establish connections between the formation of gold mineralization and specific tectonic events (*Chapter VII*). Moreover, mineralogical, and geochemical analysis of mineralised veins and gold grains, respectively, are used to make deductions regarding fluid sources and depositional conditions (*Chapters V & VII*).

**Table II.5** – Characteristics of epigenetic gold occurrences from the Baie Verte Peininsula after Evans 2004

Major Class	Sub-class	Charateristics		
		Mineralisation & Vein Type	Alteration	Host Lithology
<b>Gold bearing veins</b>	<i>“quartz gold veins”</i>	Visible, free gold occurs within laminated and sheared veins composed of multiple quartz generations; Low sulphide content	Iron carbonate and silica alteration hallos	Occur in all types of rocks: Pre-Cambrian basement rocks, Cambro-Ordovician ophiolitic rocks; Ordovician cover sequence rocks; and Silurian, felsic volcanic and intrusive rocks
	<i>“quartz- pyrite veins”</i>	The gold appears both free and within the pyrite crystals; High gold values are directly associated with increase of pyrite content; Breccia type and tension-gash veins	Fe-carbonate alteration of mafic rocks, sericitization and silicification of felsic rocks; disseminated pyrite within the altered host rock is common	Occur in all types of rocks: Pre-Cambrian basement rocks, Cambro-Ordovician ophiolitic rocks; Ordovician cover sequence rocks; and Silurian, felsic volcanic and intrusive rocks
	<i>“base-metal rich quartz veins”</i>	Coarse gold grains and patches occur in shear and tension-gash veins; The sulphides (galena, chalcopyrite and to a lesser degree sphalerite) appear as patches and stringers; High silver values are common	Overall, weak alteration, but when developed is represented by silica and sericite hallos	Restricted to Ordovician volcano-sedimentary cover rocks
	<i>“carbonate-quartz-pyrite”</i>	Gold occurs as inclusions in pyrite crystals or free within fractured pyrite crystals and aggregates; Tension gash, breccia, and shear type quartz-carbonate veins; Mineralisation and alteration confined within shear zones	Distal hallo consisting of chlorite-carbonate and strong Fe-carbonate alteration hallo with distinctive orange-rusty colour proximal to mineralisation	Mafic volcanic rocks and gabbro sill/dykes of both the ophiolitic rocks and of the cover sequences
		The gold mineralisation occurs in quartz veins and disseminated throughout the	The main alteration types are sericitization and silification, but in ultramafic rocks hematitization is also a	Occur in all types of rocks: Pre-Cambrian basement rocks, Cambro-Ordovician ophiolitic rocks; Ordovician cover

<b>Disseminated gold in altered wall rock</b>	<i>“sericite-quartz-pyrite”</i>	altered wall rock; shear type and tension gash veins	common feature giving a jasper like aspect; disseminated Py is common in the alteration hallos	sequence rocks, and Silurian, felsic volcanic and intrusive rocks
	<i>“talc-magnesite-magnetite”</i>	The gold occurs in talc-magnesite-dolomite stockwork zones and tension-gash veins restricted to narrow sheared areas	Strong talc-magnesite alteration mineral assemblage close to the veins	Serpentinised ultramafic rocks of the Point Rousse Complex
	<i>“red albite-ankerite-pyrite”</i>	The gold occurs mostly as inclusions and on fractures within the pyrite crystals and to a lesser degree, free within the veins or disseminated in the altered rock; the mineralised zones are within or in the proximity of shear zones; Quartz tension gash veins are usually barren and postdate the mineralization; shear-parallel quartz-albite-ankerite veins are abundant in both the proximal alteration zone and in the ore zone	Strong alteration proximal and within the ore zone composed of red albite and pyrite	Most common, Fe-oxides rich Gabbro sills

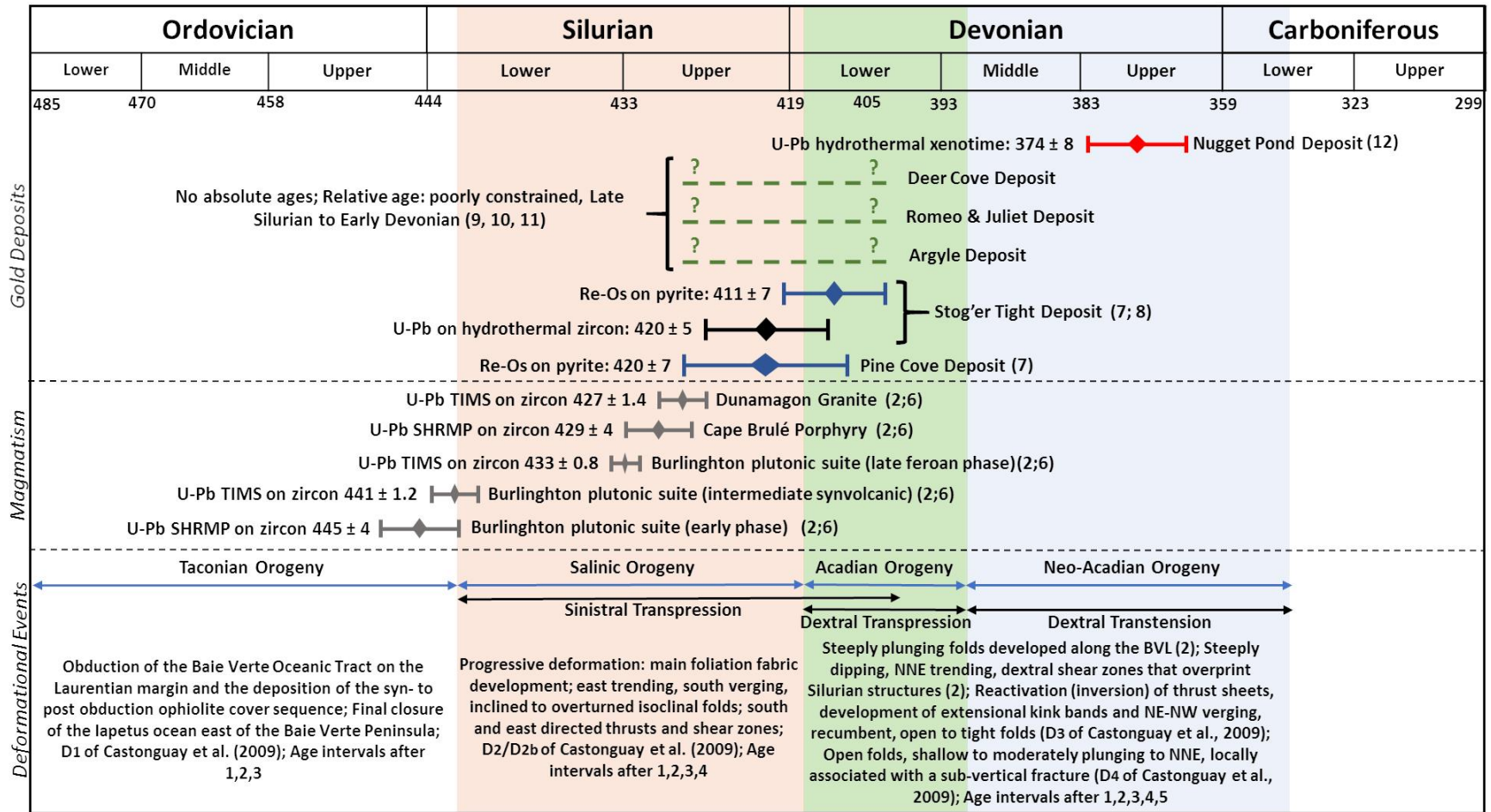


**Figure II.8** - Time correlation chart between the main orogenic events that affected the Baie Verte Peninsula, local magmatic activity, and the formation of the studied orogenic gold occurrences (Pine Cove, Stog'er Tight, Argyle, Romeo & Juliet & Deer Cove). The Nugget Pond deposit is included to highlight a potential younger mineralizing event within the area. 1 – van Staal & Barr (2012); 2 – Skulski et al. (2015); 3 – Willner et al. (2018); 4 – Anderson (1998); 5 – Waldron et al. (1998); 6 – Skulski et al. (2012); 7 – Kerr & Shelby (2012); 8 – Ramezani et al. (2001); 9 – Patey & Wilton (1993); 10 - Pitman et al. (2020); 11 - Evans (2004); 12 - Sangster et al. (2008).



## **II.5. Current understandings of the studied gold deposits**

For this study, the geological characteristics of five gold prospects/deposits were assessed in order to bring new understandings regarding the timing and the structural controls of gold mineralisation in the Baie Verte Peninsula (BVP). All study cases, the Pine Cove, the Stog'er Tight, the Argyle, the Romeo & Juliet, and the Deer Cove deposits/prospects, are located in the northern part of the BVP, within the Point Rouse Complex (PRC), approximately 6 km north-east from the Baie Verte town (**Figure II.4, Figure II.9**) (Pitman et al., 2020). The entire area covers approximately 58 square kilometres, and as of December 2017 has an indicated mineral resource of 1,610,600 tonnes with 2.3 g/t Au for 119.570 ounces combined from the Pine Cove, Stog'er Tight and Argyle deposits (Pitman et al., 2020). Reviews regarding previous ownership, exploration and exploitation history, and past resource and reserve data of gold occurrences from the PRC can be found in Evans (2004) and in most of the Anaconda Mining's technical reports (e.g. Copeland et al., 2015; Cullen et al., 2018; Pitman et al., 2020).

Within the area of interest, there are three developed deposits and multiple prospects distributed along three prospective gold trends: the Scrape trend, the Goldenville trend and the Deer Cove trend (**Figure II.9-A**) (Pitman et al., 2020). The Pine Cove, the Stog'er Tight and the Argyle deposits together with the Romeo & Juliet prospect are distributed along the Scrape Trend, whereas the Deer Cove prospect is located within the Deer Cove trend (**Figure II.9-A**) (Pitman et al., 2020). The Pine Cove, Stog'er Tight and Argyle deposits were already mined out, but near-mine exploration is still active aiming for potential extensions. The Deer Cove and Romeo & Juliet prospects are currently sub-economic, but the mineralisation is open both in strike and dip (Cullen et al., 2018). A compilation of the results and conclusions from previous studies conducted on each of these five gold occurrences is provided in **Appendix I**.

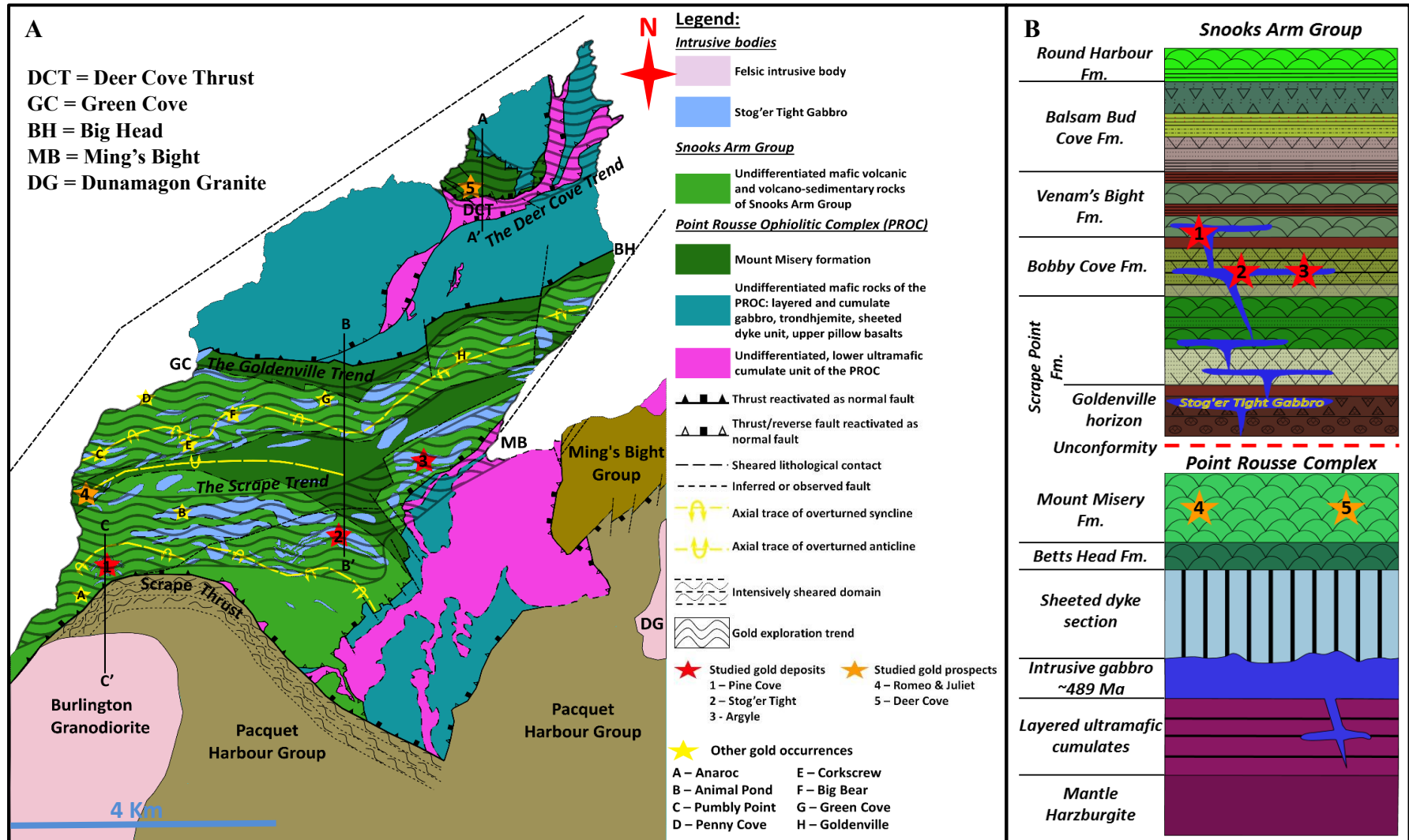
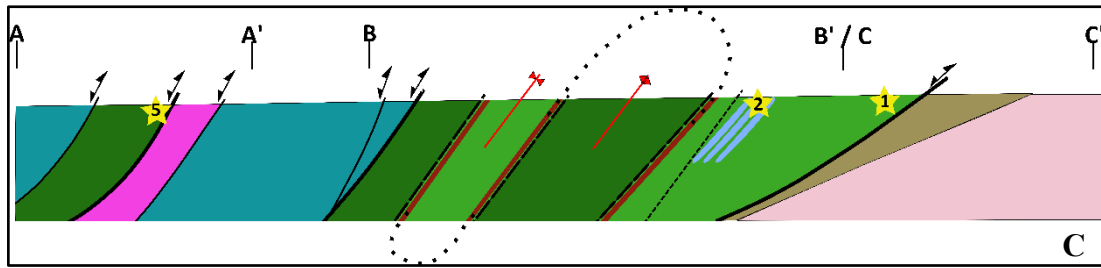


**Figure II.9.** *A* - Geological map of the Point Rouse Complex (PRC) after Anderson et al. (2001), Skulski et al. (2015) and after the unpublished geological map of Anaconda Mining (2018). *B* – Representative stratigraphic column of the PRC modified after Hibbard (1983), Bédard et al. (2000) and Skulski et al. (2009, 2010) and the location of the study deposits/prospects within it. *C* (page below) - Regional geological cross section sketch modified after Kidd (1974) and Kirkwood & Dubé (1992).



According to the revised tectonostratigraphy of the Baie Verte Peninsula (Skulski, 2010) the studied gold occurrences are hosted by gabbros and pillow basalts of the upper part of a boninitic ophiolitic sequence, the Mt. Missery Formation, and by its volcano-sedimentary cover sequence (**Figure II.9**). The general geometry of the Point Rouse Complex (PRC) was initially described as a tight, roughly E-W oriented, mega scale synclinal overturned to SE and segmented by south directed thrust sheets and reverse faults (Norman and Strong 1975; Kidd et al., 1978; Hibbard, 1983; Anderson, 1998; Castonguay et al., 2009). More recent mapping conducted by Skulski et al. (2015), divided the cover sequence rocks of the PRC in multiple large scale, overturned synforms and antiforms. The latest work conducted by the Anaconda Mining geologists together with deposit-scale studies carried out by students from the Memorial University of Newfoundland (Pitman et al., 2020; Ybarra, 2019) confirmed the overturned nature of the stratigraphy, but revealed that at least locally, the stratigraphic succession differs from the one presented by Skulski et al. (2015). Litho-geochemical and stratigraphical collaborative studies between the Anaconda Mining and the Memorial University of Newfoundland are currently ongoing and aim to define the exact architecture of the Point Rouse Complex stratigraphic stack.

The structural evolution of the Point Rouse area involves at least four deformational events as proposed by Castonguay et al. (2009): i) the  $D_1$  phase is poorly preserved in the Point Rouse Complex, is associated to the Ordovician obduction of ophiolitic bodies on the Laurentian Margin, and where visible, is represented by a pervasive  $S_1$  foliation, isoclinal folds and locally developed shear zones; ii) the  $D_2$  deformation stage generated E-W oriented regional scale folds, north dipping south directed thrust panels (e.g. the Scrape and the Deer Cove thrusts) and the main  $S_2$  foliation fabric associated with a well-developed down dip stretching mineral  $L_2$  lineation; NNE trending WNW dipping sinistral shear zones and reverse faults classified as  $D_{2b}$ , transect the  $D_2$  thrusts and were interpreted as tear faults or lateral ramps that formed synchronously with the south directed thrusts in a progressive

deformation framework; iii) the D<sub>3</sub> event is characterised by asymmetric north verging recumbent folds associated with an S<sub>3</sub> crenulation fabric and with shear zones that dip gently to moderately to south, and by extensional kink bands that reactivate the D<sub>2</sub> thrusts with a north side-down motion; and iv) the youngest deformational phase, D<sub>4</sub>, affects all the previously described structures and consist of broad, local to large scale, NNE plunging and trending F<sub>4</sub> open folds associated with a NNE oriented and steeply dipping fracture cleavage. The F<sub>3</sub> and F<sub>4</sub> folds of Castonguay et al. (2009) were initially observed and described only in the Paquet Harbour Complex but were later recognised by the Anaconda Mining geologists also in the Point Rouse Complex (Copeland et al., 2015; Callon et al., 2017; Pitman et al., 2020).

All the gold occurrences are located in the hanging wall of the D<sub>2</sub> south directed Scrape and Deer Cove thrusts, eastern splays of the BVL (**Figure II.4 & Figure II.9**) (Castonguay et al., 2009; Pitman et al., 2020). The Scrape thrust represents the principal structural feature within the area, marks the contact between the greenschist-facies rocks of the Point Rouse Complex in the hanging wall and the amphibolite-facies rocks of the Pacquet Harbour Group in the footwall, dips 30°-35° to north and show an arcuate geometry striking from SW to SE (Dimmell & Hartley, 1991; Castonguay et al., 2009; Ybarra, 2019; Pitman et al., 2020). The Deer Cove fault was initially described as a “*sole thrust*” by Gower et al. (1988) and redefined as a “*high angle reverse fault*” by Dubé et al. (1993). The fault zone is a few meters wide, strikes approximately E-NE and dip 50-70° to N-NW (Dubé et al., 1993; Pitman et al., 2020). According to Gower et al. (1988), the Deer Cove fault juxtapose pillow basalts from the upper part of an overturned ophiolitic sequence in the hanging wall, over the lower ultramafic section of another ophiolitic sequence in the foot wall. Castonguay et al. (2009) and Skulski et al. (2010) attested that the thrusts formed during a sinistral tranpressional regime localised along the BVL during Silurian time but inverted as normal faults during Devonian and Carboniferous periods when a transtensional setting is assumed to be characteristic for the entire region (**Figure II.7; Figure II.9**). In most cases the mineralised zones show a spatial association with small-scale branches of the main thrusts (Pitman et al., 2020). The development of the splays with respect to the temporal activity of the thrusts and to the timing of gold deposition is poorly defined. This topic is covered in **chapters V & VI**.

The relative timing of the mineralised veins was interpreted by the Anaconda Mining geologists as pre-to syn D<sub>2</sub> because the hosting structures are affected by both

the D<sub>3</sub> and D<sub>4</sub> structures (Copeland et al., 2015; Callon et al., 2017; Pitman et al., 2020). However, the existing direct ages from the Pine Cove and the Stog'er Tight deposits show a wider mineralisation time span that lasted until early Devonian (**Figure II.8**). Furthermore, metallogenic deposit scale studies revealed that all the mineralised sites have their own geological complexities: i) multiple gold bearing vein generations associated with different structural fabrics (e.g. the Pine Cove deposit, Calon & Weick, 1990); ii) late chlorite-carbonate veinlets that locally remobilise the gold (e.g. the Argyle deposit, Pawlukiewicz, 2019); and/or iii) overprinting alteration hallos (e.g. Deer Cove deposit, Dearin, 2009). Thereby, it may be possible that at least some of the mineralisation post-dates the development of the D<sub>2</sub> thrusts. This topic is addressed in *chapters V and VI*.

### **III. Methodology**

This chapter provides information regarding the workflow and systematics engaged to achieve the thesis objectives. It presents the mapping and sampling rationale together with the concepts and the technical details of the methods used for sample preparation and analysis.

During this project, new observations and data sets were obtained and generated through field and laboratory work. These consist of: i) field observations and structural measurements collected through classic geological mapping techniques; ii) microstructural observations from oriented thin sections; iii) petrographic characterisation of vein material, ore and alteration minerals based on classic optical microscopy and Scanning Electron Microscope techniques (backscattered electron microscopy (BSE), energy dispersive X-ray spectroscopy (EDS), cathodoluminescence (CL)); iv) Electron Probe Microanalyzer (EPMA) analysis of hypogene gold grains; and v) in-situ Laser Ablation Inductively Coupled Plasma Mass Spectrometry (LA-ICP-MS) U-Th-Pb analysis of hydrothermal monazite, xenotime and titanite.

Open-source regional-scale geological and geophysical data from the Baie Verte Peninsula (Skulski et al., 2017) together with sub-regional and deposit-scale geological and geophysical data, courtesy of the Anaconda Mining INC., were also used.

#### **III.1. Field work (geological mapping and sample collection)**

The fieldwork stage represented one of the most important parts of the project providing the necessary geological context for achieving all the aims of this study. Two field work campaigns, each of approximately 6 weeks, were carried out in the summers of 2018 and 2019 in the Baie Verte Peninsula of Newfoundland. Most part of the time was used for structural data collection through classical geological mapping techniques at both regional and deposit-scale, and for sample collection. A few days were also used to log and sample drill core sections from mineralised intervals from all the studied deposits and drill holes that intersect the Scrape and Deer Cove faults.

The “regional scale” terminology is used herein for large areas (tens to hundred square kilometres) that cover at least one geological domain from the Baie

Verte Peninsula, e.g. the Point Rousse Complex (PRC). The “deposit-scale” nomenclature refers to restricted mineralised regions (a few square kilometres) that are subject to exploration and development, for example the Stog’er Tight area.

### III.1.1. Mapping rationale and visited areas

As previously mentioned, all the studied deposits are hosted within the Point Rousse Complex (PRC), and thereby, most of the mapping was conducted within this area (*Figure II.4; Figure III.1*). Outside the PRC, geological mapping was also conducted in the following areas: i) along the western terminations of the Baie Verte Line, within the northern part of the Flatwater Pond Group (FWPG) and the southern part of the Advocate Complex (AC); and ii) in the northern and north-eastern parts of the Pacquet Harbour Group (PHG), along the La Scie Highway and along the south-western contact between the Dunamagon Granite and the PHG (*Figure II.4; Figure III.1*).

Regional scale mapping within the PRC involved structural data collection along profiles oriented both perpendicular and parallel (~N-S / ~ E-W) to the major lithological/tectonic contacts (e.g. the Scrape Thrust, *Figure II.4*). This phase had two main goals: i) to decipher the structural evolution of the main fault zones and of their associated splays by analysing the overprinting nature of kinematic indicators related to different fault reactivation events; and ii) to identify and characterise different folding stages and their affiliated structural products that occur at a regional scale (e.g. cleavage).

Deposit-scale mapping consisted of structural data collection, alteration, and vein mapping from open pits at the Pine Cove and Stog’er Tight deposits, and from mineralised outcrops at Romeo & Juliet and Deer Cove prospects. The main objective was to record the relationships between different structural features and the observed veins and mineralised intervals in each location. Description of both barren and mineralised veins and characterisation of their alteration halos were equally important.

The costal exposures provided continuous kilometre-scale profiles that revealed the structural complexity of the large-scale, NNE to NE oriented fault zones that represent the western and the eastern borders of the PRC (*Figure II.4; Figure III.1*). The evaluation of the Stog’er Tight and the Pine Cove open pits,

where continuous horizontal and vertical exposures exist, permitted a 3D evaluation of most of the structural features present in the PRC, whereas mapping transects between the studied deposits were used to support correlations from one deposit to another.

Mapping outside the Point Rouse Complex (*Figure III.1*) was conducted to better understand the regional setting of the Baie Verte Peninsula. Overall, the field mapping together with subsequent data processing and microstructural analysis (see below) permitted the assessment of the existing structural models for the Baie Verte Peninsula (Anderson, 1998; Waldron et al., 1998; Castonguay et al., 2009, 2014; Skulski et al. 2010, 2015 a) and the generation of an updated deformation sequence for the PRC. Descriptions of structural features identified in the PRC and interpretations regarding the structural evolution of the PRC constitute the content of *chapter IV*. The proposed deformation sequence of the PRC is discussed with respect to the regional structural evolution of the Baie Verte Peninsula in *chapter VII*. The deposit-scale observations and the microstructural analysis (see below) represented the main tools for evaluating the local structural controls and the relative timing of the mineralisation in each of the studied deposits/prospects. This part is presented in *chapter V*.



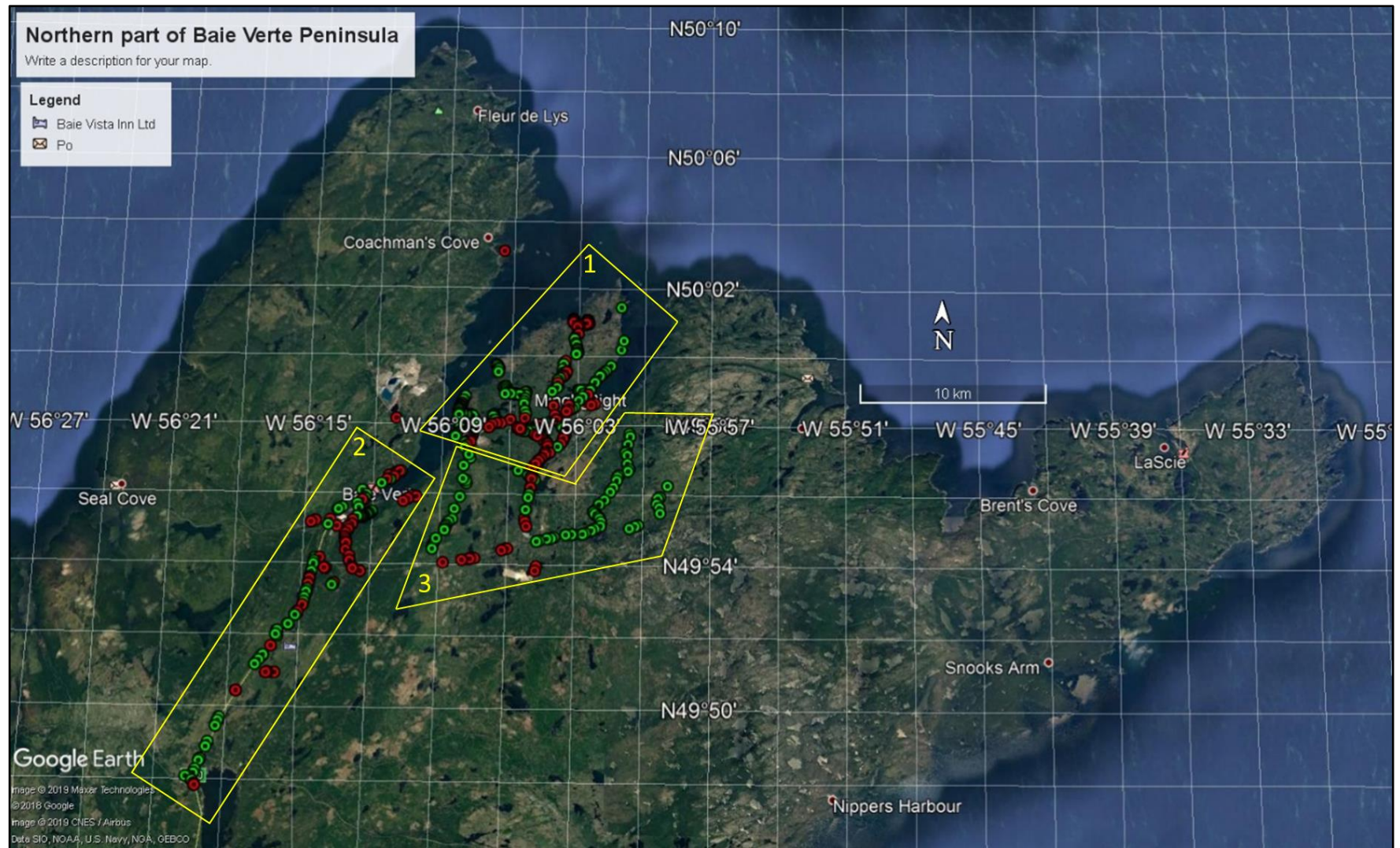


**Figure III.1** - Google Earth image of northern part of the Baie Verte Peninsula, Newfoundland, and the location of the observation points from both fieldwork campaigns (2018 - red points and 2019 - green points). The yellow shapes represent the contour trace of the three mapped areas: 1 = the Point Rouse Complex; 2 = the northern part of the Flat Water Pond Group and the southern part of the Advocate Complex; 3 = the northern part of the Paquet Harbour Group.

### III.1.2. Data Processing and Visualisation

All the field observations and structural measurements collected during the two field work campaigns were introduced into excel data-files. The open-source program, Google Earth Pro, was used for the geographic visualization of observation points. The observation points were also introduced into a GIS database and plotted on topographic and regional bedrock maps (1:50.000 scale) of the Baie Verte Peninsula (Skulski et al., 2015a, b, c) and on the unpublished geological map of the Point Rouse Complex made by the Anaconda Mining Company (2018). Alteration of these maps were made in ArcMAP software (license provided through the University of Leeds) according to the new geological information gained during this study. Final edits of the geological maps and cross-sections presented in this thesis were made using the open-source GIMP and Inkscape image manipulation programs and with Power Point Office suite.

For rapid manipulation and visualization of the structural data, the structural measurements were plotted using the open-source program “*Stereonet*”, version 10. Descriptions of the algorithms used by this program can be found in Allmendinger et al. (2013) and in Cardozo and Allmendinger (2013). The open-source structural data available for the entire Baie Verte Peninsula (Skulski et al., 2017) was also assessed using “*Stereonet*” and compared with the data collected for this study. The compatibility of the two data sets was evaluated for two reasons: i) as a control factor to see if any errors occurred during data collection; and ii) to assess the regional structural models presented by previous authors (Castonguay et al., 2009; Skulski et al., 2015a). Overall, the two data sets are similar (example **Figure III.2**), with an approximate error of  $\pm 10^\circ$  between measurements collected from the same outcrop. This is acceptable considering that measurements were made by different people and using different acquisition techniques. The structural data collected by the survey was recorded using the “*UK right hand rule*” for planar elements and the “*trend and plunge*” for linear elements, whereas for this study, the dip direction and the dip was recorded for the planar structures and the trend and plunge, or the rake/pitch, was measured for the linear elements. Descriptions for these acquisition methods can be found in Fossen (2016). The same programs mentioned in the above paragraph were used for image editing.

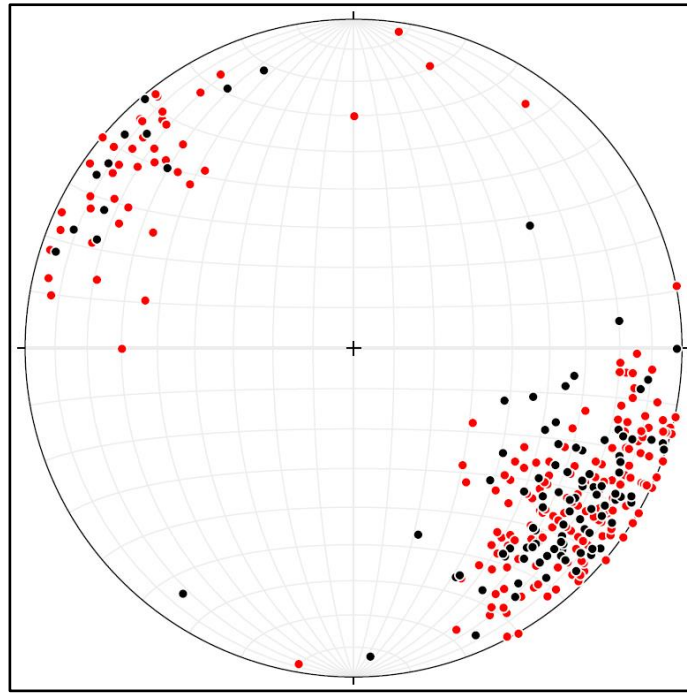


**Figure III.2** - Comparison between the poles to the foliation plane measurements collected for this study (red poles, N=241) and the poles to the foliation measurements of Skulski et al., (2017) (black poles, N=103) from the northern part of the Flat Water Point Group and the southern part of the Advocate Complex (shape 1 on **Figure III.1**).

### III.1.3. Sample collection

Throughout the field work campaign, multiple types of samples were collected and used for different purposes: a) outcrop samples; b) float samples; c) core samples; and d) crushed and milled ore material.

a) Two types of outcrop samples were collected from all the visited areas (PRC, FWPG, PHG): oriented samples which were used for microstructural analysis and unoriented samples used for mineralogical and geochemical analysis. In general, the size of the collected specimens was at least 10 x 5 x 5 centimetres (length x width x thickness).

The oriented samples were mostly collected from fault zones and from their nearby proximity (a few meters both within the footwall and hanging wall), and where possible, from altered and mineralised zones from the studied deposits/prospects. For each sample, the dip and the dip direction of the local schistosity and the trend and plunge of the stretching mineral lineation were recorded. A strike arrow and a short perpendicular line for the dip, together with a

circled “plus” or “minus” were marked on the specimen while still in place (*Figure III.3*). The “plus” was marked on samples collected from the upper foliation surface equivalent to the top, whereas the “minus” was put on samples collected from below the foliation (bottom). The values of the strike and dip were also marked on the specimen.



*Figure III.3* – Example of an oriented sample annotated while still in place.

The unoriented outcrop samples consist of both barren and mineralised vein material and of altered and mineralised wall rock. These types of samples were collected from each of the studied deposits/prospects and from other veined, mineralised and altered zones from both within and outside the PRC regardless of their economic potential.

b) The float samples represent ore material collected from the visited open pits or from the ore stockpiles of different deposits/prospects. The samples either contain visible gold, show intense mineralisation and alteration, or display important crosscutting relationships between different vein generations. These samples were collected for petrographic and geochemical analysis.

c) The core samples were collected from veined, altered, and mineralised intervals from all the studied deposits/prospects, and from gauge material from both the Stog'er and the Deer Cove fault zones. The Point Rousse area has been under exploration for over 30 years and thereby, the studied deposits benefit from a wealth of drill core material. All the logging and assay reports for both historic (early 80s until 2010) and recent (2010-2018) drill holes were provided by the Anaconda

Mining Inc. and informed the selection of the investigated drill holes and sampled intervals. The samples were used for petrographic and geochemical analysis.

d) Crushed and milled ore material was collected from four of the studied deposits/prospects: approximately 30 kg of milled ore material with average gold grades of ~2 g/t was collected from the Pine Cove deposit; approximately half a kilogram of low to medium gold grade material (2 to 7 g/t) from blast reject samples and around 5 kg of crushed material (ore from an ore stock-pile with gold grades  $\geq 2$  g/t) was collected from the Stog'er Tight deposit; ~30-40 kg of crushed material from each of the studied prospects (Deer Cove and Romeo & Juliet - ore from old ore stock-piles with average gold grades  $\geq 2$  g/t). The milling was conducted at the Pine Cove mill during the exploitation stage of the Pine Cove and Stog'er Tight deposits. The crushing was carried out by the author during the second fieldwork campaign using the industrial jaw crusher of the Anaconda Mining Company. From both the milled and crushed ore material gold particles were extracted and analysed by SEM and EPMA techniques.

## **III.2. Sample selection & preparation**

### **III.2.1. Sample selection**

A total of 131 samples (outcrop, float, and core) were collected during the two field work campaigns. From these, polished and unpolished, thin (50-30  $\mu\text{m}$ ) and thick (150-100  $\mu\text{m}$ ) sections had to be made for the microstructural, petrographic, and geochemical analysis. All samples were first cleaned, cut, and macroscopically described to select the most appropriate samples for further processing into sections. A total of 45 polished and unpolished thin/thick sections were made from the selected samples. A characterisation of these samples together with the micro-analytical techniques that were applied on each thin/thick section are listed in *Appendix II*. The criteria based on which the samples were selected for further preparation are the following:

i) For petrographic and geochemical analysis, samples with high potential of hosting gold were preferred in order to conduct detailed petrographic and geochemical analysis on gold grains (e.g. EPMA analysis) or on minerals for which the spatio-temporal relationship with the gold had to be well described (e.g. in-situ LA-ICP-MS U-Th-Pb geochronology of dateable accessory phases). Therefore, the

core samples collected from medium to high gold grade zones and float samples with visible gold from blasted ore zones were selected. The drawback of these samples is that most of them host a multitude of veins with complicated crosscutting relationships and this hinders correlations with vein types identified in the field (*see chapter V*). All the sections used for both petrographic and geochemical analysis are polished.

ii) The oriented samples that were selected for thin section preparation and used for the microstructural analysis come from the following zones: from the lowermost/uppermost part of the hanging-wall/footwall of the Scrape and Deer Cove faults; from altered and mineralised shear zones; from intense folded mineralised zones; and from ore hosting structures. These samples were considered the most suitable to provide information regarding a) the kinematic evolution of the major structures and of their mineralised splays; and b) the structural controls on the formation and further deformation of the mineralised veins and of their associated alteration halos.

### **III.2.2. Sample preparation**

#### ***III.2.2.1. Thin section preparation***

All the sections were crafted in the thin section preparation laboratory at the University of Leeds, School of Earth, and Environment. The preparation process involved the following steps.

i) All samples were cut in multiple slabs to identify the best region that would end up on the section slide. The samples used for mineralogical/geochemical analysis were cut such that they would provide the most exposure for the mineralised parts, or perpendicular to the investigated veins to better characterise their internal textures and relationships with the altered wall rock material. The oriented samples were cut parallel to the stretching mineral lineation and perpendicular to the foliation plane (*Figure III.4*). This observation plane provides the most reliable kinematic indicators because in shear zones the trend of the stretching mineral lineation indicates the movement/shear direction, whereas the foliation plane represents the plane along which movement occurs (Jackson, 1992; Blenkinsop, 2002; Fossen, 2016). A few exceptions from this rule were reported in nature (Blenkinsop, 2002) but do not apply to the selected samples.

ii) The location of the section plane was marked on the sample slab with a permanent marker. Each sample had an associated label with the corresponding section code and other indications. For the oriented samples, the top and the dip direction of the foliation was also indicated on the slab (*Figure III.4*).

iii) In the marked regions, the samples were further cut down to blocks of approximately 5x3x3 (length x width x thickness) centimetres. One face of the blocks was flattened on rotating diamond-impregnated grinding disks of 40 and 10  $\mu\text{m}$ , and then glued on a glass slide using epoxy resin. The blocks were further cut down to 1 mm in thickness and from here, grinded, and polished until the required thickness of the section was reached (50-30  $\mu\text{m}$  for thin sections and 150-100  $\mu\text{m}$  for thick sections). A few sections used only for microstructural analysis were left unpolished.



*Figure III.4* - Example of an oriented sample cut perpendicular to the foliation and parallel to the stretching mineral lineation, **note** the location of the future section plane marked on the cut surface and the top and the dip marks.

### III.2.2.2. Gold grain extraction and preparation of gold particle mounts

As previously mentioned, the milled and crushed ore material was collected to extract gold grains used for SEM & EPMA investigations (see below). The material was first screened at 4 mm mesh diameter. All material finer than 4 mm was further passed through a portable sluice for a fast separation between the heavy and light weight minerals. From the sluiced material, the gold particles were isolated and extracted by hand panning processes. The terms gold “grain” and “particle” are used henceforth after Chapman et al., (2021): one gold grain represents a zone defined by one continuous crystal, whereas gold particle is assigned for a physical body that can contain several gold grains.

The recovery of gold particles by hand panning is influenced by the gold particle size and the density of matrix. The lower size limit for recovery is typically ~60  $\mu\text{m}$  (Chapman et al., 2022), although significantly smaller particles may be collected. Within the Stog’er Tight and Pine Cove deposits the gold particle size is small and mostly hosted in pyrite, whereas in the Romeo & Juliet and the Deer Cove prospects the gold is coarser and occurs both free in quartz veins and as inclusions in pyrite. Therefore, different recovery rates between deposits were inevitable (**Table III.I– liberated Au**).

The mounting process was conducted within the preparation facilities of the University of Leeds. The gold particles were dried, separated in groups based on their relative size, and arranged in rows of 5 on an adhesive double-sided tape fixed on perspex that formed the base of a polished block. The blocks were ground and polished until the internal part of the gold particles was exposed.

**Table III.I** – Accepted number of gold particles with relevant results, analysed from each of the studied deposit/prospect.

<b>Deposit</b>	<b>In-situ gold particles (section labels)</b>	<b>Liberated gold particles</b>	<b>Total</b>
Pine Cove	42 (section PC100)	31	73
Stog’er Tight	26 (sections SOZ2 & BN215)	4	30
Argyle	46 (sections AG3 & MPAG1)	0 (no samples)	46
Romeo & Juliet	7 (section RJ4)	97	104
Deer Cove	17 (sections DCD1 & DC2)	91	108



### **III.3. Geophysical data**

As presented in *chapter II*, the eastern side of the Baie Verte Peninsula hosts several structurally bonded ophiolitic sequences and their associated volcano-sedimentary cover sequence rocks (*Fig. II.1*). These geological units have high magnetic susceptibility which produce elevated magnetic signals compared to the surrounding rocks (Spicer, 2010). A thorough characterisation of the geophysical setting of the Baie Verte Peninsula, which includes parts of the Point Rouse Complex can be found in Spicer (2010). In this study, magnetic anomaly maps are also used to map structures/contacts that border lithological blocks with different magnetic response. Although further geophysical characterisation of the Point Rouse Complex is beyond the purpose of this study, geophysical data has been used to indicate potential unexposed, or large to regional-scale structural features that were not observed during the mapping campaign. In addition, where possible, magnetic responses have been correlated with some of the structural features identified in the field.

The tilt derivatives maps (TDR) of the reduced to pole magnetic maps (RTP) of the Baie Verte Peninsula and of the south-central part of the Point Rouse Complex are presented in *chapter IV* (*Fig. IV.2 & IV.3*) and display local and regional-scale, onshore and offshore structures that border and crosscut the Point Rouse Complex. Two types of aeromagnetic data sets were available for this study: i) a regional survey data acquired by the Geological Survey of Canada in 2007 for the northern and central parts of the Baie Verte Peninsula; and ii) a local scale survey conducted by the Anaconda Mining company in 2013 that covers almost the entire Point Rouse Complex except for the northern part of the territory. Information related to the acquisition process and to the primary filtering and data processing can be found in Skulski et al., (2017) and in Kilfoil (2009) for the regional aeromagnetic survey, and in Evans (2013) for the local-scale airborne survey.

#### **III.3.1. Data enhancement**

The raw data was introduced into Oasis Montaj software, MAGMAP extension, (license provided by the University of Leeds) where it was filtered and

prepared for interpretation (several transformations and derivatives were computed). The following steps were applied to generate the final maps which were exported as raster images.

The reduced to pole transformation was applied on the residual magnetic field (RTF) maps. The total residual field (RTF) was obtained by subtracting from the levelled total field (total magnetic intensity, TMI) the Earth's magnetic field, known as the International Geomagnetic Reference Field (IGRF) (Isles and Rankin, 2013; Skulski et al., 2017). The IGRF is subtracted to obtain the local magnetic anomalies without the effect of the earth's magnetic field (Isles and Rankin, 2013; Ibraheem et al., 2019).

The reduction to the pole transformation (RTP) is used in magnetic data interpretation to eliminate the distortion of the TMI anomalies caused by the obliquity of the magnetic field (Baranov et al., 1957; Isles and Rankin, 2013). By applying this transformation, the magnetic anomalies better define the geometry (shape, dip, and plunges) of the investigated rocks (Isles and Rankin, 2013). The mathematical algorithms for the RTP transformation can be found in Baranov (1957) and in Baranov and Naudy (1964). To calculate the RTP, the magnetic declination ( $-18.75^\circ$ ) and inclination ( $69.33^\circ$ ) of the Baie Verte Peninsula at the time of data processing (June – November 2020) have been used. These values were taken from the online declination calculator - <https://www.magnetic-declination.com>. An upward continuation of 25 meters filter was applied to reduce the effect of the short wave-lengths anomalies that may have a non-geological input (acquisition artefacts: e.g., along-line noise).

The TDR is preferred as a final representation product because it has the potential to sharpen anomalies and to better define the shape and the edges of the source bodies (Verduzco et al., 2014). The amplitude of the TDR is negative outside a magnetic source, zero along and near its edges/contact, and positive over the source (Verduzco et al., 2014). For insights into the mathematical algorithms necessary to compute the TDR the reader is referred to Miller & Singh (1994) and to Verduzco et al. (2014).

### **III.4. Microstructural analyses**

Microstructural analyses were conducted in this study as a complementary support tool for the field observations. The objective of this stage was to identify shear sense indicators that would reveal the kinematic history of the main fault zones and of their associated splays.

The thin sections were studied under transmitted and reflected light using petrographic microscopes available at the University of Leeds. It is common for some microscopes to alter the orientation of the image at the objective end, either by a rotation of 180° or by a right-lateral translation. These factors can hinder the correct interpretation of the asymmetry of the shear sense indicators and thus, must be corrected. Therefore, all the oriented sections were first scanned with a desktop manual petrographic slide scanner in both plane and crossed polarised light. Full section images with the right orientation were generated and used as reference to correct any rotation/translation produced by the microscope.

In this study, three main asymmetrical structures were used to determine the sense of movement (**Figure III.5**): i) asymmetric porphyroclast systems; ii) C-S-C' fabric; and iii) pyrite fringes.

i) Relict, eye-shaped mega-crystals preserved within a fine-grained, foliated matrix, known as porphyroclasts, are a common feature in shear zones (Jackson, 1992; Zhang & Fossen, 2019). The porphyroclasts are usually composed of rigid minerals such as quartz or feldspar and exhibit external mantle or elongated tails composed of recrystallised material (Passchier & Simpson, 1986; Jackson, 1992; Blenkinsop, 2002). Based on the tail geometry, four main groups of porphyroclasts are known: three of them have the shape of the Greek letters  $\sigma$ ,  $\delta$ , and  $\Phi$ , and so are named accordingly, whereas the fourth shows a more complex geometry having multiple tail generations on each side (**Figure III.5– A**; Passchier & Simpson, 1986; Blenkinsop, 2002; Fossen, 2016). The  $\sigma$  and the  $\delta$  porphyroclasts have a monoclinical symmetry relative to a central reference plane and can be used as reliable shear sense indicators (**Figure III.5 – A**; Passchier & Simpson, 1986; Jackson, 1992). The sense of shear is given by the configuration of the tails relative to the reference plane (Passchier & Simpson, 1986; Jackson, 1992). However, as presented by Zhang & Fossen (2019), there is no clear difference between  $\sigma$  porphyroclasts formed through

back-ward or forward rotation, and so, a third-party shear sense indicator should be used to avoid misinterpretations.

ii) C-S-C' composite fabrics are frequently found within shear zones formed under intense non-coaxial deformation and can be used as kinematic indicators to determine the shear direction (**Figure III.5-B**; Lister & Snoke, 1984; Jackson, 1992; Fossen, 2016). The “S” plane represents the foliation planes (“*shistosité*” in French), whereas the “C” surfaces (“*cisaillement*” for shear in French) correspond to small-scale planar shears that are subparallel to the main shear zone, and which affect the foliation (Berthé et al., 1979; Lister & Snoke, 1984; Jackson, 1992; Blenkinsop, 2002; Fossen, 2016). The “C” planes occur later in the deformation history, are oblique to the shear planes and antithetic to the foliation (Jackson, 1992). The sense of shear is given by the rotation sense of the S planes relative to the C planes (**Figure III.5-B**; Blenkinsop, 2002; Fossen, 2016).

iii) Pyrite fringes are strain shadows usually represented by fibrous soluble minerals (e.g. quartz, calcite) that grow subparallel to the instantaneous stretching axes in low minimum stress ( $\sigma_3$ ) domains around pyrite crystals (Aerden, 1996; Blenkinsop, 2002; Bons et al., 2012). In simple cases involving undeformed fringes, the sense of shear can be determined from the acute rotation angle between the fringe and the shear plane (**Figure III.5-C**; Blenkinsop, 2002). However, the geometry of the pyrite fringes can be quite complex and may result either during polyphase deformation (e.g. Aerden, 1996; Aerden & Sayab, 2017) or under progressive non-coaxial deformation (Koehn et al., 2000, 2003). In this case the whole shape of the pyrite fringe, defined by its median line or by the enveloping surface, form an “S” or a “Z” shape and indicate a dextral or a sinistral shear sense, respectively (**Figure III.5-C**; Blenkinsop, 2002). Exceptions of this “rule” may occur because the fringes can rotate together with the pyrite inclusion during a later deformation stage and so, it may indicate an incorrect shear sense (Blenkinsop, 2002).

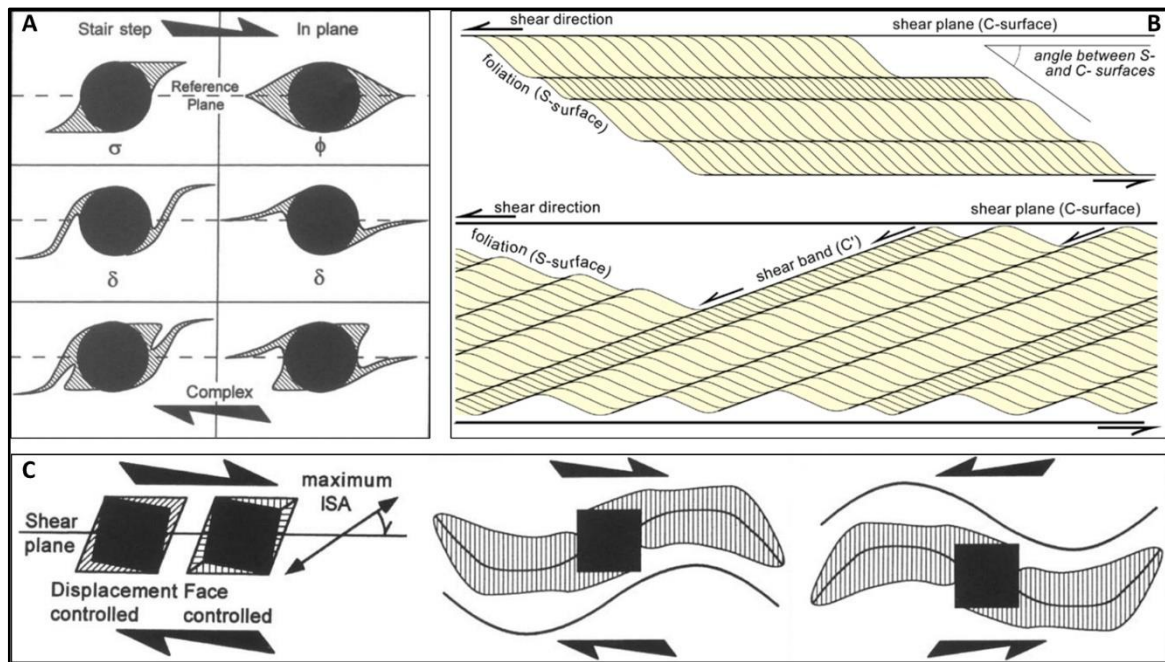


**Figure III.5** – Kinematic indicators used in this study: A – asymmetric porphyroclast systems, image source – Blenkinsop (2002); B – C-S-C’ composite fabric, image source – Burg, 2018; C – Pyrite fringes, image source – Blenkinsop (2002).

### **III.5. Petrographic analyses**

Detailed petrographic characterisation of vein textures and of ore and gangue minerals have been conducted for this study and in each case the observations have been used to generate mineral paragenetic sequences, to speculate on ore forming conditions, and to link different mineralogical and structural evolution stages within and between localities. The analytical techniques engaged in this part of the study are listed and briefly described below, whereas the related results and interpretations are presented in *chapter V*.

#### **III.5.1. Optical microscopy**

All the thin/thick sections were first studied under transmitted and reflected light to record the main mineral phases, to gain preliminary textural information, and to highlight features that would benefit from further SEM investigations. For this, petrographic microscopes with attached digital cameras available at the University of Leeds have been used, and millimetre-scale images were acquired for representative sites. Full section image scans were also acquired in both plane and crossed polarised light using a desktop manual petrographic slide scanner (**Figure III.6-A**). The scans provided a wider scale petrographic context compared to the

restricted views of microscope objectives. These were also used as reference maps for further SEM work (see below).

### **III.5.2. SEM-CL techniques**

Most of the detailed petrographic work was conducted using the Tescan VEGA3 XM Scanning Electron Microscope (SEM) available at the University of Leeds Electron Microscopy and Spectroscopy Centre. The SEM machine is equipped with Oxford Instruments X-max 150 energy dispersive X-ray spectroscopy (EDS) detector associated with Aztec 3.3 energy software, with a TESCAN colour cathodoluminescence (CL) imaging system, and with the Alicona MEX 3D software for 3D imaging and evaluation of surface roughness.

### **III.5.3. EDS and BSE**

The energy dispersive X-ray spectroscopy (EDS) detector of the SEM was used routinely to obtain semi-quantitative element data based on which all the present mineral phases were accurately identified. The backscattered electron (BSE) imaging system was used for detailed characterisation of mineral grain morphologies, to assess the spatial distribution and proportions of the present minerals, and to record the crosscutting and the overprinting relationships between different minerals.

High resolution BSE scans were first made for all the investigated sections. Each scan is composed of multiple images stitched together into a panoramic image saved at a resolution of 1024x1024 pixels (*Figure III.6-B*). The individual images have view fields between 1500x1500 and 2700x2700 microns depending on the resolution at which a particular section was scanned. The panoramic images provided section-scale overviews of the textural features. These were also used as navigation maps on which to identify and mark the location of sites suitable for detailed characterisation.

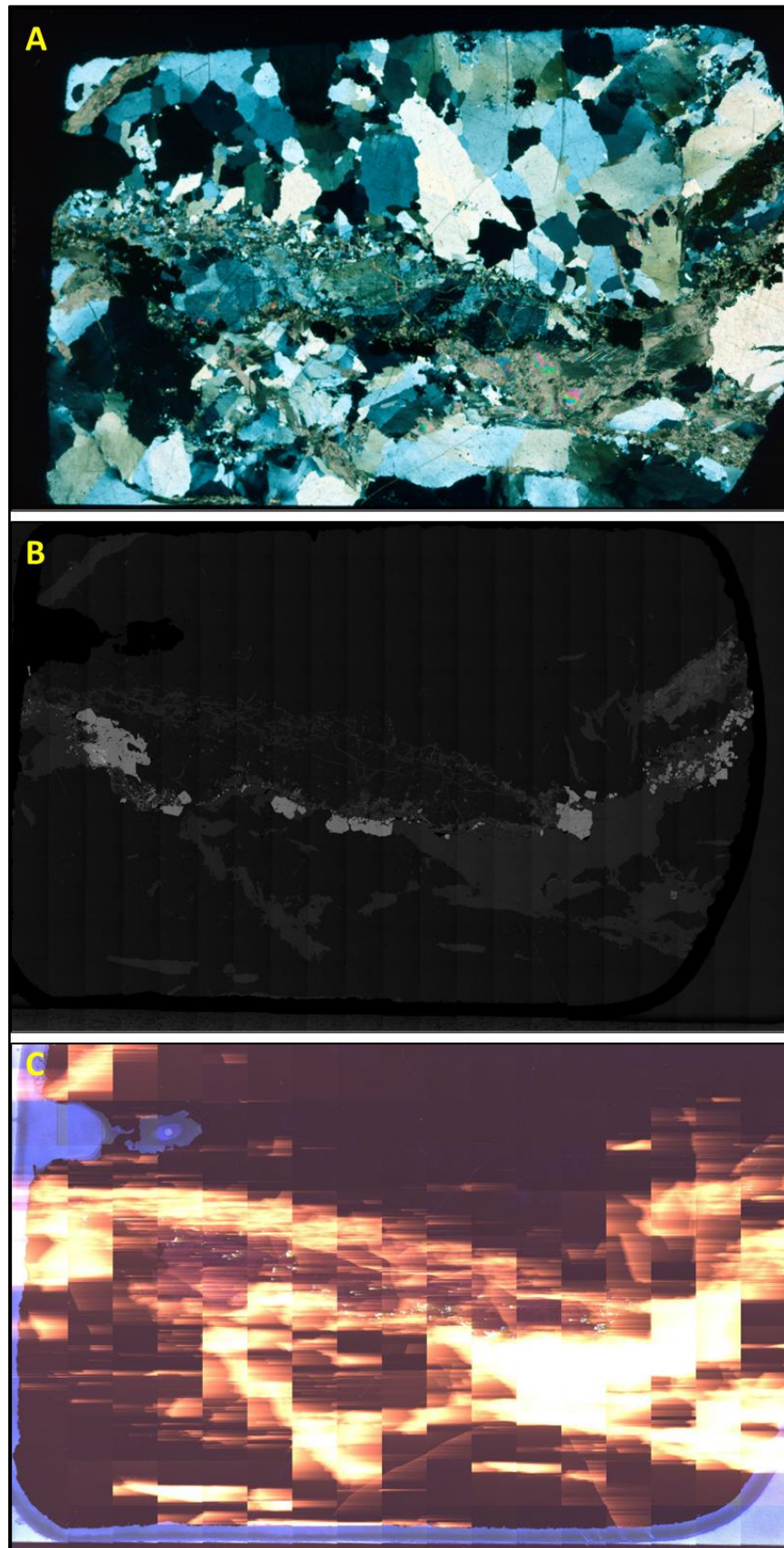


**Figure III.6** – Full section image scans of the MPAG1 thin section, section length ~4.5 centimeters. A – microscope scan in transmitted light; B – BSE panoramic image scan; C – CL panoramic image scan, note the high interference of the calcite (bright red domains and associated streaks).

Each site comprises EDS spot analysis corresponding to all the mineral phases present within the investigated site, and an associated high resolution BSE image with view fields smaller than 500x500 microns, which shows the textures and the mineral grain morphologies. The number of studied sites vary from one section to another depending on the textural complexity and mineral heterogeneity. The sections with less variable mineralogy and uniform textural features contain 10 to 20 sites. The sections with highly variable mineralogy and complicated textures or with mineral grains that required detailed morphological characterisation prior to any other geochemical analysis (e.g. gold, monazite, xenotime, and titanite grains, see below) contain up to 60 investigation sites. For the BSE-EDS analysis the SEM machine had the following settings: an acceleration voltage of 20 KV, a working distance of ~14 millimeters, and a beam intensity between 14 to 17 (usually set at 15). A list of all the samples analysed by BSE and EDS techniques is provided in *Appendix II*.

#### **III.5.4. Cathodoluminescence (CL)**

The SEM-CL imaging of quartz can reveal internal textures (e.g. growth zones, laminae, etc.) otherwise undetectable when studied in transmitted light or in backscattered electron emission (Frelinger et al., 2015). The CL response of quartz is given by the internal structural defects in the crystal lattice (e.g. site vacancies) and/or by the presence of trace elements within quartz (e.g. Al, Ti), and hence, can provide information on the environmental forming conditions and on its evolution (Götze et al., 2021; Rusk 2012; Frelinger et al., 2015; Shah et al., 2022). In this study, CL imaging of quartz was undertaken to differentiate between different quartz generations. This was a key part of the study and had the following implications: i) it helped to thoroughly characterise quartz from the main mineralised veins, which in turn, permitted comparison between veins from both the same deposit and from different deposits; ii) the relationships between a distinct quartz generation and specific ore and alteration minerals revealed the presence of multiple mineralisation stages in all the studied deposits/prospects; and iii) the association of different quartz generations with a particular vein type, and consequently to a specific structural feature, permitted the determination of the relative timing of different mineralisation events.



Other mineral phases, such as phosphates, carbonates, and feldspars also luminescence under CL (Götze 2002). Thereby, these were also subject to CL investigations during this study.

CL imaging of apatite, monazite, and xenotime was conducted to characterise their zonation pattern. This contributed to the paragenetic studies and informed the interpretations of the geochronological data gained from the in-situ LA-ICP-MS U-Th-Pb isotope analysis of monazite and xenotime (methodology described below).

CL studies of carbonates were not successful. The calcite has a very high intensity under CL making differentiation between generations impossible. It also generated bright stripes that blurred all the adjacent mineral phases covering the textural relationships. Separation between ankerite and calcite was however possible because the ankerite does not have any CL response.

The CL response of albite was evaluated in the samples where multiple generations of albite were prior identified either macroscopically or microscopically. The aim was to see if any extra textural information can be obtained and used for the paragenetic studies. The CL characteristics of the different albite phases is very similar and so, no reliable results were obtained.

Both full section CL scans and high-resolution CL images of representative sites were acquired. Compared to the BSE section scans which required a low acquisition time (~15 minutes), a full CL section scan with a good image quality needed an acquisition time between 7 to 12 hours, depending on the machine settings. Thus, only a limited number of full CL scans were made (*see Appendix II*). The prioritizing criteria were the following: i) the sections used for further geochronological studies were scanned to assess the overall setting of the monazite/xenotime/titanite within the paragenetic sequence of the studied deposit; and ii) the sections with multiple quartz veinlets and related mineralisation were also scanned to observe the relationships between different quartz generations and ore minerals. All the full section scans were acquired under colour CL (red-green-blue filters are applied; *Figure III.6 - C*). Calcite fluorescence is maximum under the red CL filter. Thereby, for the sections where calcite was abundant, full CL scans were avoided, and the high-resolution site images were acquired under monochrome CL (colour spectrum between black and white) to reduce the streaking effect generated by calcite.

The running settings for the SEM machine during the CL imaging sessions were the following: an acceleration voltage of 20 KV, beam intensity of 20, a low scanning speed of 5 or 6 to produce good quality images, and a working distance of ~14 millimeters. The high-resolution site images have view fields <500x500 microns. The CL section scans are composed of multiple images stitched together with an overlap of 20% and saved as a panoramic image with a resolution of 1024x1024 pixels. The images that compose the CL scans have view fields between 1300x1300 and 2700x2700 microns (most common set at 2000x2000 microns), depending on the resolution at which a particular section was scanned.

### **III.6. SEM & EPMA analysis of gold particles**

Native gold occurs mostly as a solid solution with silver, and can also incorporate minor amounts of other elements (e.g. Hg, Cu, Pd, etc.) (Chapman et al., 2021). Gammons and Williams-Jones (1995) demonstrated that the Au/Ag ratio is a complex function of temperature, pressure, and fluid chemistry (i.e. pH, Eh,  $fS_2$ , Au/Ag<sub>aq</sub>). Thereby, based on a detailed characterisation of populations of gold particles (henceforward “sample populations”) it can be inferred whether the mineralising system was stable (constant Au/Ag alloy) during the entire time of the gold precipitation or if any parameters have changed leading to variations in the Au/Ag alloy in an evolving hydrothermal system.

Gold particles can also contain inclusions of other mineral species (Chapman et al., 2021). These inclusions are considered cogenetic with the gold, and hence, can inform on the overall mineral assemblage of the auriferous mineralising stage (Leake et al., 1997; Chapman et al., 2000a, b). Compositional data sets based on mineral inclusion species were described as the best method to infer the type of deposit from which the gold is generated (Chapman et al., 2021; 2022), however this approach is sometimes constrained by the number of inclusions observed.

The analysis of the abovementioned chemical and physical variations in the internal composition of natural gold have been used over the years in many ore deposit studies to characterise either hypogene or placer gold particles for various aims: i) to establish the link between placer gold occurrences and their hypogene sources (Knight et al., 1999; Chapman et al., 2010, Chapman & Mortensen, 2016); ii) to indicate the type of deposit from which detrital gold is originated or to infer the

local forming conditions of its mineralising source (Morrison et al., 1991; Townley et al., 2003; Chapman et al., 2009; Chapman et al., 2017, 2018); and iii) to investigate genetic relationships between gold from different parts of the same mineralising system or from different deposits/occurrences in order to understand the local and regional metallogenic settings (Chapman et al., 2000a, b; Grimshaw 2018; Spence-Jones 2021; Chapman et al., 2023). The main approach engaged in these types of studies is to generate a “microchemical signature” for the sample populations based on their mineral inclusions and alloy compositions (Chapman et al., 2000a, b; Chapman et al., 2021). For detailed systematics of the methodology that should be conducted when dealing with gold particle studies the reader is referred to Chapman et al. (2021).

For this study, a similar approach was engaged to characterize the gold form each of the studied gold deposits and prospects. The results and the associated interpretations are presented in *chapter V*. The sample populations analyzed herein are both from thin sections created from samples collected from high gold grade intervals (*Appendix II*) and from crushed/milled ore material (see previous methodology sections). The gold observed within thin sections will be further referred to as “in-situ”, whereas that from crushed/milled material will be described as “liberated” (*Table III.I*). The geochemical characterization of gold contributes to the study in two ways:

- i) To establish whether there is any compositional difference between the gold that occurs as inclusions in the pyrite and the gold that is free (either along fractures within and between pyrite crystals or in the altered ground mass – see chapter V for descriptions). In turn, this is used to speculate if the P-T-X conditions remained stable or if these have changed during the temporal evolution of each of the studied deposits.
- ii) To permit comparison of the compositional characteristics of sample populations from the five mineralized localities. In turn, this facilitates speculation on the degree of commonality between the different hydrothermal systems.

Similar deposit and district-scale studies have been conducted on other gold occurrences around the world. For example, Spence-Jones (2021) has shown that the Ag concentration within the gold alloy from the Cononish deposit, Scotland, increases in the later paragenetic stages. Based on this and on sulfur isotope data, the

author inferred that the gold was precipitated through multiple pulses of fluid flow of different origins, and that the early stages were responsible for the bulk gold endowment of the deposit. Chapman et al. (2010) conducted comparison studies between gold alloy compositions and mineral inclusion suites of both placer and hypogene gold populations collected from multiple locations from the northern part of the Klondike mining district, Canada, and concluded that the studied gold occurrences have been generated by a single hydrothermal system that shows both spatial and temporal variation in the depositional environment.

### III.6.1. Analytical techniques

The backscattered electron (BSE) imaging system of the SEM was used to assess the alloy heterogeneity, whereas the energy dispersive spectroscopy (EDS) system was used to gain semi-quantitative element data from which the mineral inclusion species hosted by the gold particles could be determined. Geochemical analyses using an electron probe microanalyser (EPMA) were conducted to quantify the Au, Ag, Hg, Cu, and Pd contents of each gold particle.

The analyses were conducted at the analytical facilities of the University of Leeds and followed the systematics described by Chapman et al., (2021). For the SEM analysis two types of machines were used: for the in-situ gold, the Tescan VEGA3 XM machine described in the previous section of this chapter was utilised, whereas the liberated gold particles were analysed using a FEI Quanta 650 SEM machine equipped with Oxford Instruments INCA 350 EDX system/80mm X-Max SDD detector, EBSD and KE Centaurus EBSD system, and Aztec 3.3 energy software. The EPMA analyses were conducted using a Jeol 8230 automated electron microprobe with 5 spectrometers and EDS capabilities. The following settings for the EPMA were used for all the analysed particles: accelerating voltage of 20 kV, a beam current of 50 nA, and 1-minute analytical time for each particle (combined on- and off-peak counting time of 60 seconds per element). The machine was calibrated before each analytical session using a gold-silver alloy of 81.5% Au and 18.5% Ag for Au and Ag, pure metal standards for Cu and Pd, and a cinnabar standard for Hg. All the results for the EPMA analysis are provided in *Appendix III*. The detection limits (LOD) are defined at  $3\sigma$  and are slightly variable from one analytical session to another according to the functioning conditions of the machine during the daily

runs (*Appendix III*). The average detection limits for each element are the following: 0.09% for Au; 0.07% for Ag; 0.1% for Hg; 0.02% for Cu; and 0.09% for Pd. The iron and sulfur content were also measured for some of the in-situ particles and the LOD for these elements is 0.02% and 0.15%, respectively (*Appendix III*). In the session when these elements were measured, a chalcopyrite standard was used to calibrate the machine for Fe, S and Cu also. The analysed gold particles are homogenous under BSE and thus one EPMA analysis per particle was conducted. The results were accepted if the total sum of the analysed elements was between 98% and 102% for the liberated particles and between 97% and 103% for the in-situ particles (*Appendix III*). The slightly lower/higher total values for the in-situ gold are accepted because these particles are significantly smaller compared to the liberated gold particles, and are hosted within other minerals, hence, small interferences from the surrounding ground mass can occur. *Table III.1* shows the number of particles with relevant analysis for each deposit and their provenance (in-situ or liberated).

### III.6.2. Data presentation

The analysed gold particles are grouped in populations. The term population is used herein after Leake et al. (1997) and Chapman et al. (2000a, b) and refers to all the gold particles collected from a specific location. In this study, the in-situ and the liberated gold particles from one particular deposit/prospect are combined and compose a population. However, before the compositional data of the in-situ and the liberated gold particles were combined, these were first compared to assess if any gold signatures are present in only one of the two data sets. In turn, these informed interpretations related to the paragenetic setting of gold with different chemical signatures (*see chapter V*).

Two types of graphics are used to evaluate the alloy compositional data for each population: i) plots between the cumulative percentile vs the increasing values of Ag, Hg and Cu (*Figure III.7*); and ii) binary plots between different elements (e.g. Ag vs Hg) (*e.g. Fig. V.10*). The first type of plots permits direct comparison between multiple populations regardless of the number of particles present in each population, whereas the second type can highlight different compositional fields (Chapman et al., 2000a, b; Chapman et al., 2010; Chapman et al., 2023). Both

Microsoft Office Excel and ioGAS programs were used to generate the plots. Logarithmic scales were used where appropriate. The data containing minor alloying elements is here described as in (Chapman et al., 2023), according to what proportion of the gold particles contain the interest element above the detection limit (LOD) or above the quantification limit ( $LQD = 3 \times LOD$ ). The shape of the alloy profiles is used here to compare the gold populations in terms of “same or different” and to speculate on the stability of the mineralising system over the time of gold deposition. For example, a horizontal or shallowly inclined profile of the Ag alloy may indicate gold precipitation under stable mineralising conditions; clear steps in the profile can correspond to multiple gold generations or different fluid sources that contributed to the mineralisation; and a profile with a high gradient curve defined by a wide range of values could suggest changes of the mineralising conditions over time or multiple fluid pulses associated with gold precipitation (*Figure III.7*) (Chapman et al., 2000a, b; 2010; Grimshaw 2018).

The Hg and Cu contents in the Au/Ag alloy were in many cases  $>LOQ$  and have also been used to support interpretations (*Appendix III*). The Pd values are below LOD and are not considered further.

The number of particles containing mineral inclusions was insufficient to support a comparative quantitative characterization. Also, the identified mineral inclusions are roughly the same in all populations and so no graphic representation was implemented. The inclusion suites are listed in *chapter V* and used for interpretations related to the paragenetic sequences.

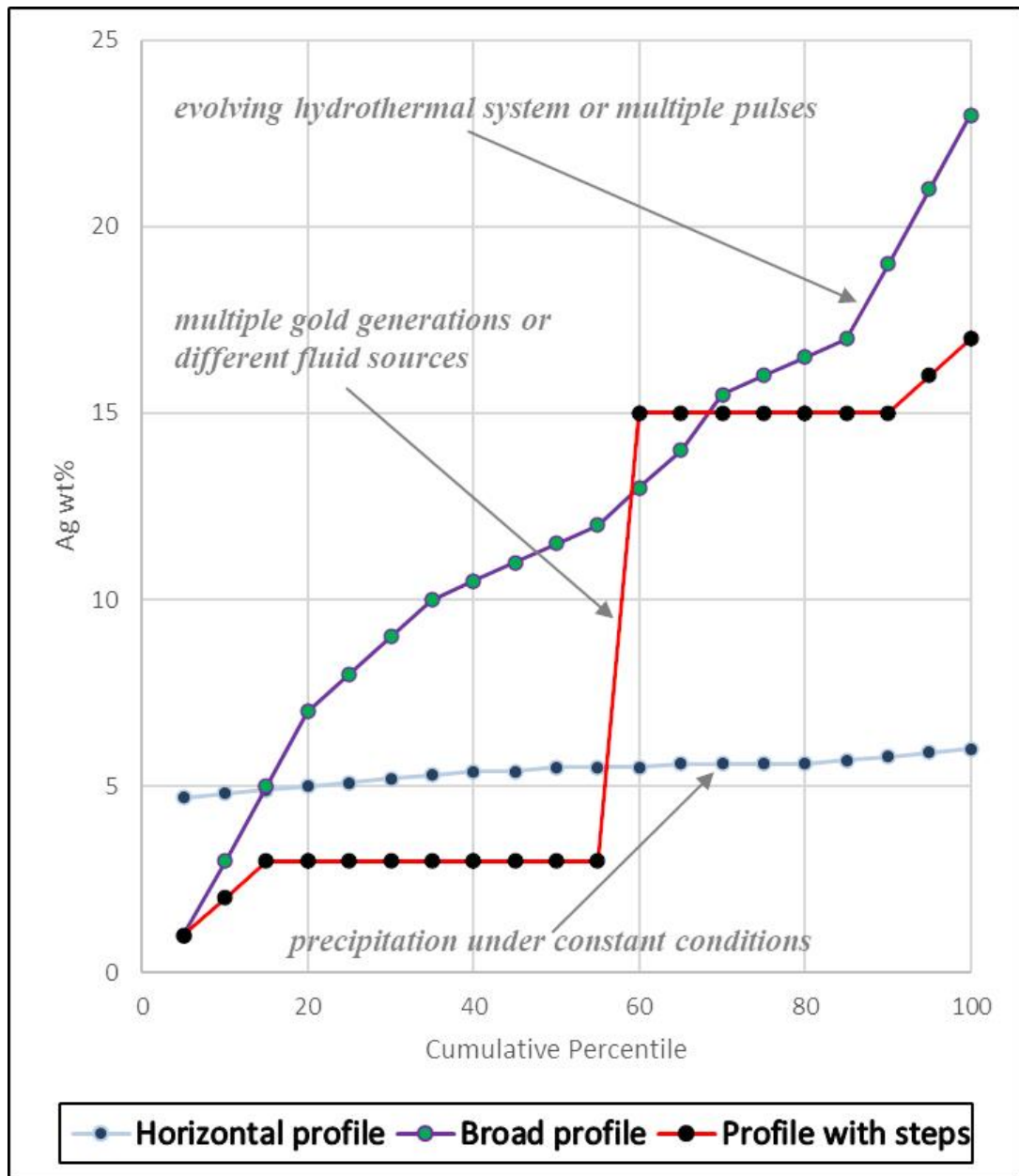


**Figure III.7** – Example of chart where the cumulative percentile vs increasing concentration of Ag are plotted, note the different types of shapes for the Ag profiles, see text for discussions, plot created based on synthetic data.

### **III.7. In-situ LA-ICP-MS U-Th-Pb geochronology**

Several accessory minerals such as zircon, monazite, xenotime, apatite, rutile, titanite, and others, have the capacity to incorporate U and/or Th into their crystal lattice during their formation (Harrison et al., 2002; White 2015; Zack & Kooijman, 2017). These minerals occur in a variety of geological settings and have been used over the years as U-Th-Pb geochronometers to resolve the timing of various geological processes such as: volcanic eruptions and/or plutonic emplacement (e.g. Li et al., 2013; Ene, 2021), metamorphic events (e.g. Martin et al., 2007; Picazo et al., 2019; Barnes et al., 2021;), formation of ore deposits (e.g. Vielreicher et al., 2015; Pi et al., 2017; Fielding et al., 2017; Molnár et al., 2018; Mohammadi et al., 2019; Feng et al., 2020; Zhang et al., 2022), provenance and deposition of sedimentary/volcano-sedimentary successions (e.g. Rasmussen et al., 2020; Suzuki & Kurihara, 2021), etc.. In this study, U-Th-Pb dating of hydrothermal monazite, xenotime, and titanite is used to determine the time span in which the studied deposits/prospects have formed.

In orogenic gold deposits, hydrothermal monazite and xenotime are common accessory phases intergrown with alteration and ore related minerals (Vielreicher et al., 2003). Hence, these minerals are frequently used as geochronometers to obtain direct ages for orogenic gold style mineralisation (e.g. Vielreicher et al., 2015; Fielding et al., 2017; Molnár et al., 2018; Herzog et al., 2023; etc.). Both monazite and xenotime are excellent geochronometers because they contain negligible amounts of initial Pb (non-radiogenic), are stable over a wide range of geological conditions, have high blocking temperatures ( $> 600^{\circ}\text{C}$ ) for diffusive Pb loss, and are resilient to auto-irradiation damage, propriety that prevents the escape of parent and daughter minerals from their structures (Harrison et al., 2002; Vielreicher et al., 2003). However, these minerals are prone to alteration and partial or total recrystallisation through fluid-aided dissolution-precipitation processes which can affect the initial U-Th-Pb isotopic system (Harrison et al., 2002; Hetherington et al., 2010; Seydoux-Guillaume et al., 2012; Grand'Homme et al., 2016; Engi, 2017; Budzyń & Sláma, 2019; Budzyń et al., 2021). In turn, the obtained dates could be partially reset leading to geologically meaningless ages, or completely reset indicating a younger geological event in which the monazite/xenotime recrystallised (Li et al., 2021).



Titanite has also been used as a geochronometer to determine the age of orogenic gold deposits (e.g. F. Zhang et al., 2022). It has a high closing temperature (up to 850° C) for diffusive Pb loss but can incorporate significant quantities of common Pb (non-radiogenic) during crystallisation which may cause problems for age determinations (Kirkland et al., 2018; Holder et al., 2019; Walters et al., 2022). Furthermore, similar to monazite and xenotime, titanite is also susceptible to alteration and recrystallisation through fluid mediated dissolution-precipitation processes or during plastic deformation, and so, partial and/or total resetting of U-Pb dates can occur (Holder & Hacker, 2018; Gordon et al., 2021).

Zoned crystals, intra-grain dislocations, porous crystal textures, and the presence of polycrystalline aggregates can indicate that the monazite/xenotime/titanite have been affected by alteration and/or recrystallisation processes (Townsend et al., 2000; Hetherington et al., 2010; Engi 2017; Holder & Hacker, 2018; Gordon et al., 2021). Therefore, in order to obtain geologically relevant ages of mineralising events, it is crucial that the physio-chemical structure of titanite, monazite, and xenotime to be characterised in detailed and their paragenetic relationships with the ore related minerals to be well-established prior to any U-Th-Pb geochronological studies.

### **III.7.1. Analytical techniques and data visualisation**

There are several analytical techniques used for U-Th-Pb dating (e.g. thermal ionisation mass spectrometry (TIMS) and secondary ion mass spectrometry (SIMS; etc.; Reiners et al., 2018). Some of these techniques can be performed directly on a section slide (“*in-situ*”), without destroying the sample nor the analysed mineral, whereas others require sample crushing and extraction of the selected mineral (Reiners et al., 2018). For this study, laser ablation inductive coupled plasma mass spectrometry (LA-ICP-MS) analysis of U-Th-Pb isotopes on monazite, xenotime, and titanite grains have been conducted *in-situ*. This was considered the most suitable method for this project because it permitted the observation of the spatial relationships between the analysed minerals and gold particles, and the identification and analysis of different zoned or growth domains within the selected mineral.

Maximum and/or minimum ages have been obtained for four of the studied deposits. For the Stog’er Tight and the Argyle deposits both monazite and xenotime

ages were determined, whereas for the Romeo & Juliet and the Deer Cove prospects the ages were obtained using xenotime and on titanite, respectively. Within the Pine Cove deposit, both monazite and xenotime are present, but the particle size was too small (<10 microns), to permit analysis.

All the mineral particles selected for analysis were first described in terms of their morphology. High-resolution CL and BSE imaging was conducted to evaluate both the internal (growth and/or sector zoning, inclusions) and the external (size and shape) textures of each grain (*Appendix IV*). Moreover, EPMA X-ray intensity maps were generated for five monazite grains with sizes bigger than 50x30 microns from the Stog'er Tight deposit to assess their internal distribution of Th, Y, and Sm. Compositional zonation of these elements and/or any CL/BSE zoning can correlate with different age domains which give insights into the mineral evolution. Only a limited number of X-ray scans were conducted because each scan takes several hours. Also, the target particle must be sufficiently large to contain compositionally heterogeneous zones that are individually suitable for analysis ( $\geq 10 \times 10 \mu\text{m}$ , the smallest size of the laser beam). The spatial relationships of each analysed particle with the rest of the ore and alteration minerals were also assessed to establish their place within the paragenetic sequences (*see chapters V and VI*). In turn, these relationships informed the age interpretation process (*see chapter VI*). The grain characterisation stage was conducted at the University of Leeds using the Tescan VEGA3 XM SEM-CL machine and the Jeol 8230 automated electron microprobe described in the previous sections of this chapter.

The LA-ICP-MS U-Th-Pb isotope analyses were carried out at the British Geological Survey (BGS) isotope facilities, in Keyworth, UK, by research scientist and laboratory manager Dr. Nick Roberts. Descriptions of the used machinery and data acquisition procedure are provided in *Appendix V*. The data assessment and filtering process together with the related results and interpretations comprise the content of *chapter VI*. The raw data for all the particles analysed during this study is provided in *Appendix IV*.

Two main terms are used when dealing with geochronological data sets, "date" and "age". The term "date" is used here to refer to the number obtained for each analysed spot from the isotope ratio between the measured daughter and parent isotopes and the decay constant using the following formula:  $t = 1/\lambda * \ln*(D/P + 1)$ , where "t" is the relative age to the starting point of the decay chain, "D" is the

daughter isotope, “*P*” the parent isotope, and “ $\lambda$ ” is the decay constant ( $t_{1/2} = \ln 2 / \lambda$ ) (White, 2015). The word “age” is used for one date or multiple averaged dates that are interpreted and are geologically relevant for the present study.

Four dates can be computed and used for age determination based on U-Th-Pb isotopes, three of which are for the uranium decay chain ( $^{206}\text{Pb}/^{238}\text{U}$ ,  $^{207}\text{Pb}/^{235}\text{U}$ , and  $^{207}\text{Pb}/^{206}\text{Pb}$ ), and one for the thorium decay series ( $^{208}\text{Pb}/^{232}\text{Th}$ ) (Spencer et al., 2016). For descriptions related to the theoretical principles of the U and Th decay chains and to the mathematical approach of the decay and dating equations the reader is referred to White (2015) and to Reiners et al. (2018).

The data are plotted and evaluated in U-Pb concordia space, using the Wetherill diagram (Wetherill, 1956) and the Tera-Wasserburg diagram (Tera & Wasserburg, 1972a, b) and in U-Th-Pb concordia space, using the  $^{208}\text{Pb}/^{232}\text{Th}$  vs  $^{206}\text{Pb}/^{238}\text{U}$  diagram of Vermeesch (2020). The construction of U-Pb and U-Th-Pb concordia plots and weighted mean age calculations were generated using the free, online program “*IsoplotR*” of Vermeesch (2018). The default settings of the program for the decay constants and the  $^{238}\text{U}/^{235}\text{U}$  ratio were kept. Details regarding the software architecture and the mathematical equations and computational algorithms used by the software to generate the plots used in this thesis can be found in Vermeesch (2018) and Vermeesch (2020). All ages are provided with a  $2\sigma$  or a 95% confidence level.

## **IV Structural setting of the Point Rouse Complex (Results & Interpretations)**

Currently, there are no academic studies that provide a detailed description of the structural setting of the Point Rouse Complex (PRC). In previous works, structural information from the PRC is limited and presented as a support for regional correlations, which in turn are used for the assessment of the structural evolution of the entire Baie Verte Peninsula (BVP) (e.g. Castonguay et al., 2009; Skulski et al., 2010; 2015a). Some thorough descriptions exist for the coastal areas or for the south and south-eastern borders of the PRC, but do not include structural information from the central parts of the complex (e.g. Anderson, 1998; Anderson et al., 2001). Therefore, this chapter is the first to provide a detailed description of all structural elements from the entire PRC using new structural data gathered during this study. A new structural deformation sequence for the PRC is proposed and compared to the pre-existent ones (e.g. Castonguay et al., 2009). A simplified 3D geometrical model that can be used to display the relationships between different fold generations is also recommended.

Descriptions of magnetic lineaments observed on the aeromagnetic maps of the BVP and of the PRC are used herein to highlight regional-scale features that could be linked with local-scale structures mapped during the field campaigns. Information regarding mapping rationale, sample collection process, and location of field observations can be found in the *Methodology* chapter. Summarised descriptions of the samples used for microstructural analysis are provided in *Appendix II*.

### **IV.1 Structural elements identified within the Point Rouse Complex (field, microstructural and aeromagnetic observations)**

A summarised description of the main structural elements from the Point Rouse Complex (PRC), listed in order of their interpreted relative age, can be found in *Table IV.1* whereas detailed information regarding all the identified structures is provided below. Although this section is designed to describe the observed structures, a few interpretations are also included to give a meaning to some of the

observed geometries and to highlight the relationships between different structural elements.

#### **IV.1.1 Folds**

Four different fold types were identified within the study area (*Table IV.1 – i; v; viii; xi*). These are presented below in the order of their interpreted relative age (old to young).

##### ***IV.1.1.1 Intrafolial folds (Fi)***

Small-scale (amplitude of a few centimetres) intrafolial folds (*Fi*) can be observed in both outcrops and drill cores (*Table IV.1–i*). These are tight to isoclinal, overturned to recumbent, rootless and dismembered (*Plate IV.1–A, B, C, D*). Throughout the area, the *Fi* folds are poorly preserved and strongly overprinted by subsequent folding and faulting. The *Fi* folds are segmented and transported by south directed brittle-ductile shears or refolded by at least one of the other fold generations (*Plate IV.1–A, B, C, D*).

##### ***IV.1.1.2 South verging folds (F<sub>SV</sub>)***

Mesoscale, south to south-west verging folds (*F<sub>SV</sub>*) were observed in multiple locations scattered across the entire area (*Table IV.1–v*). These folds affect the regional foliation fabric, refold the *Fi* folds, and are best developed in the proximity of both the major thrust sheets and of the brittle-ductile faults (*Figure IV.1–B; Plate IV.1 –A, C, D–box 1, E, F, G*). Most commonly, these folds plunge gently to moderately to west-northwest and usually occur in fold trains. However, the *F<sub>SV</sub>* folds show variable orientations across the region. This variation is interpreted to be caused by fold superposition processes (see section *IV.2*. for further details). The geometry of the *F<sub>SV</sub>* folds range from open and upright in the competent rocks, to tight asymmetric to overturned folds in the volcano-sedimentary units (*Plate IV.1–E, F*). Kink to chevron type folds are also common in the strongly foliated rocks. Locally, especially in the most competent rocks, the *F<sub>SV</sub>* folds lack of an associated axial cleavage and show a more brittle nature. The majority of the observed *F<sub>SV</sub>* folds show amplitudes from a few centimetres to decimetres. Nevertheless, asymmetric to overturned folds with amplitudes of tens of meters that

verge from SW to WSW were recorded in the Pine Cove pit (*Plate IV.1-G*). Here, the folds were seen in the core of a large scale, open, north trending and plunging  $F_{NT}$  fold (*Table IV.1–xi*). Thus, it is interpreted that the initial orientation of the  $F_{SV}$  folds was affected by the superposition of the  $F_{NT}$  fold.

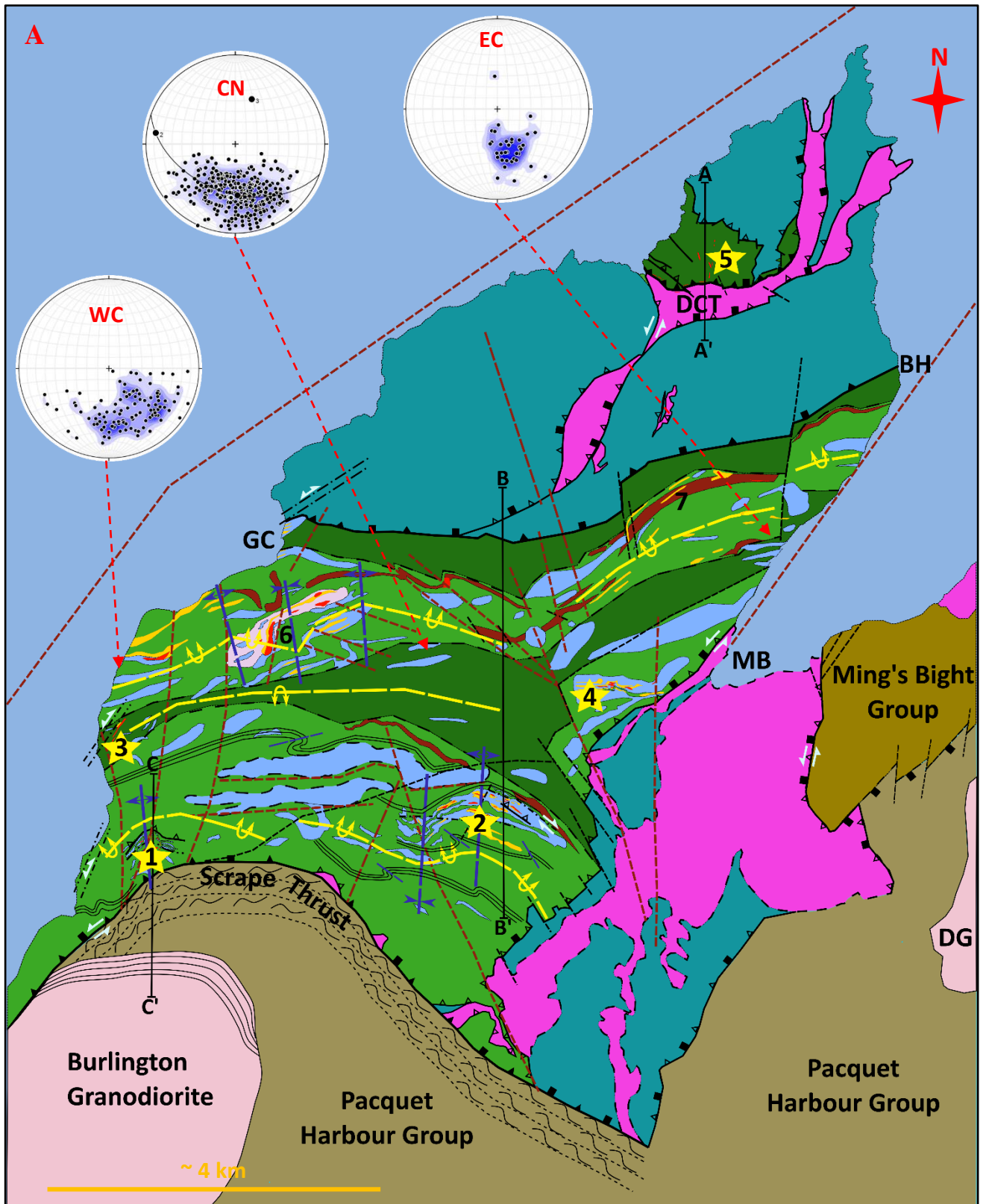
*Table IV.1 – Summary description of the main structural elements identified within the Point Rouse Complex*

No.	Structures	Abbreviation	Distribution	Characteristics	Associated structures	Relationship with other structures	Relative age
<b>i</b>	Intrafolial folds	Fi / F <sub>2a</sub>	Preserved in the volcano-sedimentary units	Small scale (cm – dm in amplitude); tight to isoclinal, overturned to recumbent folds, rootless or dismembered and refolded ( <i>Plate IV.1– A, B, C, D</i> )	Genetically linked to the S <sub>R</sub> foliation	Refolded by the rest of the presented folds	D <sub>2a</sub>
<b>ii</b>	Regional developed foliation fabric	S <sub>R</sub> / S <sub>2a</sub>	Regional - affects all rocks	Parallel with bedding/layer; Vary from a weak spaced cleavage to a strong schistosity ( <i>Plate IV.4– A, B</i> ); Dips moderately to steeply from NW to NE ( <i>Figure IV.4 – A, B, C, E, G, I</i> )	Axial planar cleavage for the Fi folds	Affected by all the structures described below	D <sub>2a</sub>
<b>iii</b>	Regional developed stretching mineral lineation	L <sub>R</sub> / L <sub>2a</sub>	Regional - affects all rocks	Well defined, down-dip to oblique plunging; Defined by stretched chlorite, amphibole, and plagioclase crystals ( <i>Plate IV.4- F, G Fig. IV.4 – D, F, H, J</i> )	Developed on the S <sub>R</sub> plane	Affected by all the structures described below (except Fi)	D <sub>2a</sub>
<b>iv</b>	Major thrust sheets	Not applicable	Regional - divide the area in multiple lithostratigraphic domains	North dipping, E-W trending, ductile to brittle-ductile south directed thrust sheets: e.g. the Scrape and the Deer Cove thrusts ( <i>Figure IV.1; Plate IV.4– D &amp; Plate IV.6- A</i> )	S <sub>LC</sub> fabric developed close and within the fault zones	Subparallel to the S <sub>R</sub> fabric; Folded and reactivated by both the F <sub>MR</sub> and the F <sub>NT</sub> folds	D <sub>2a</sub>
<b>v</b>	South verging folds	F <sub>SV</sub> / F <sub>2b</sub>	Regional to domianal (best developed close to brittle-ductile faults and major thrust zones)	Open to isoclinal, asymmetric to overturned, S to SW verging folds; Plunge gently to moderately from W to NW; Show variable scale with amplitudes from a few centimeters to a couple of meters ( <i>Plate IV.1– A, C, D, E, F, G</i> )	Associated with the formation of S <sub>L</sub> fabric	Affect the S <sub>R</sub> fabric and the Fi folds; refolded by both the F <sub>MR</sub> and the F <sub>NT</sub> folds	D <sub>2b</sub>
<b>vi</b>	Locally developed planar fabrics	S <sub>L</sub> / S <sub>LC</sub> / S <sub>2b</sub>	Regional to domianal (well developed in the proximity of major thrust sheets)	Occur as: i) a crenulation cleavage; ii) a strain slip cleavage (usually “C” planes in a “S-C” fabric configuration) ( <i>Plate IV.4– E</i> ); and iii) axial planar cleavage for the F <sub>SV</sub> folds ( <i>Plate IV.1– F</i> ); Close and within the fault zones the S <sub>R</sub> is fully transposed into parallelism with the S <sub>L</sub> and a composite mylonitic foliation (S <sub>LC</sub> ) is developed ( <i>Plate IV.4– C</i> ); Overall is steeper and it forms at a slightly oblique angle with respect to the S <sub>R</sub> fabric		S <sub>L</sub> cuts through the S <sub>R</sub> fabric; Affected by the F <sub>MR</sub> and the F <sub>NT</sub> folds	D <sub>2b</sub>

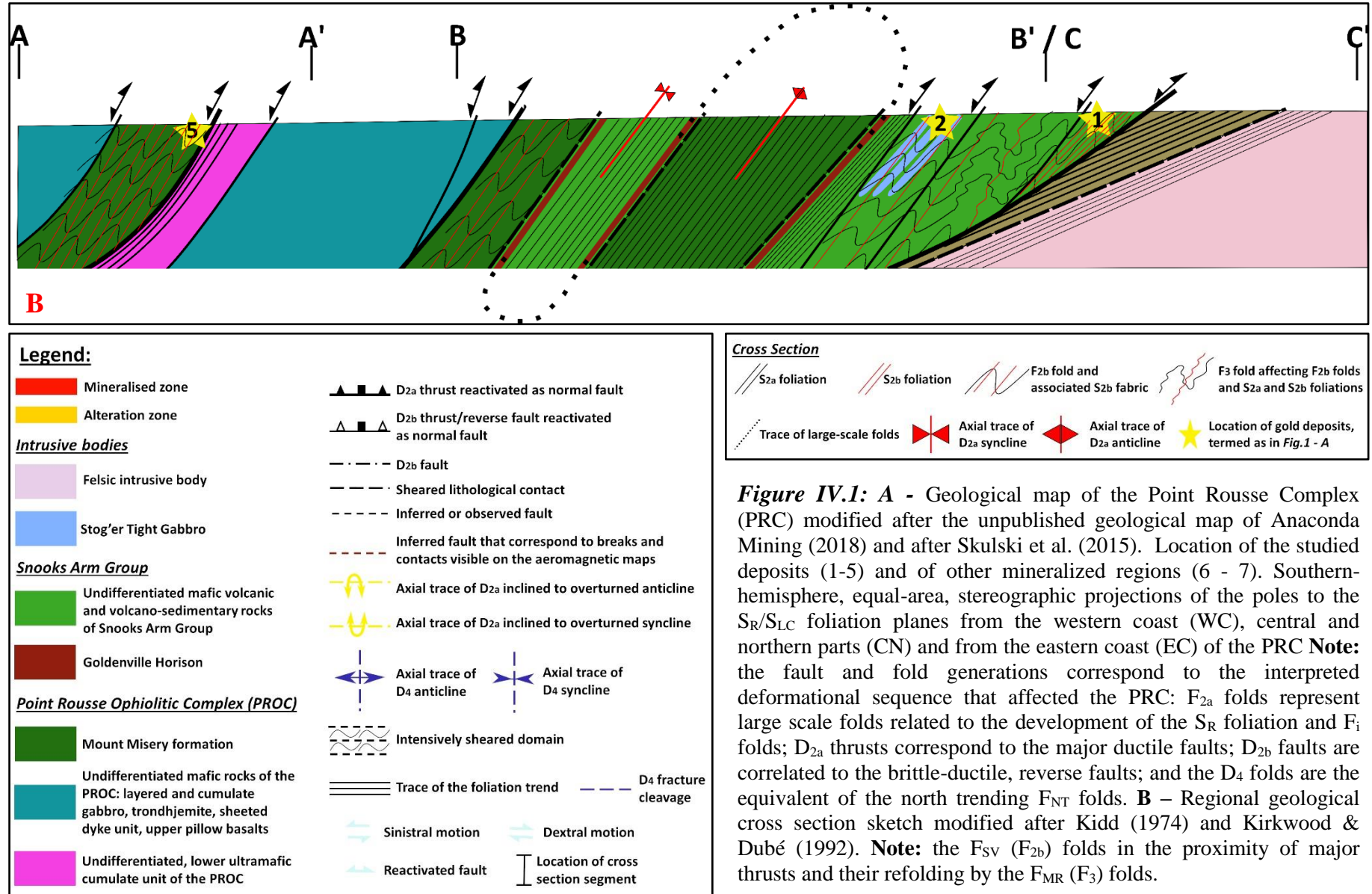
vii	Brittle-ductile reverse faults	Not applicable	Regional to domanial (best developed in the proximity of major thrust sheets)	Occur as four main fault systems that accommodate a N over S transport direction: i) N dipping, E-W striking thrusts and reverse faults ( <b>Figure IV.7- A; Plate IV.1- E</b> ); ii) Moderately to steeply dipping to NE-ENE, reverse faults and dextral shear zones ( <b>Figure IV.7- B; Plate IV.6- F</b> ); iii) N to NNE trending, E directed reverse faults and steeply dipping sinistral shear zones ( <b>Figure IV.7- C; Plate IV.6- H</b> ); and iv) Moderately to steeply dipping to WNW-NW faults and shear zones with ambiguous kinematics ( <b>Figure IV.7- D; Plate IV.1- G</b> )	Subparallel to the $S_L$ ; Locally generate an overall “fault propagation fold” geometry with the $F_{SV}$ folds	Affect the $S_R$ fabric; the N-NNE and the NNW-NW oriented faults cut through the major thrust sheets; Are folded and reactivated by both the $F_{MR}$ and the $F_{NT}$ folds	$D_{2b}$
viii	Mesoscale recumbent folds	$F_{MR} / F_3$	Regional - affect all rocks	Shallow plunging, open to tight, asymmetric, recumbent folds; Variable verging direction, geometry, and size (amplitudes from a few cm to a couple of meters) ( <b>Figure IV.2; Plate IV.2</b> )	Related to the $S_{MR}$ and $L_{MR}$ fabrics	Affect all previous structures; Are folded by the $F_{NT}$ folds	$D_3$
ix	Horizontal planar fabrics	$S_{MR} / S_3$	Regional to domanial (in the high strain $D_3$ zones)	Most common - a roughly horizontal, spaced crenulation cleavage; in high strain domains a strong, penetrative foliation ( <b>Plate IV.2- B, C</b> )	Axial planar cleavage for the $F_{MR}$ folds	Affect all the $D_2$ structures; Are folded by the $F_{NT}$ folds	$D_3$
x	Horizontal crenulation lineation	$L_{MR}$	Regional to domanial	Sub-horizontal crenulation lineation, weakly to strongly developed on $S_R$ and $S_L / S_{LC}$ ( <b>Plate IV.4- I</b> )	Related to the $F_{MR}$ folds	Affect all the $D_2$ structures; Affected by the $F_{NT}$ folds	$D_3$
xi	North trending folds	$F_{NT} / F_4$	Regional - affect all rocks	Gently to steeply plunging, open to tight, upright to asymmetric, NW to NE trending folds ( <b>Plate IV.3- A - E; Figure IV.3</b> ); Variable scale, from folds with amplitudes of a few cm to local and regional synforms and antiforms (a few meters to hundreds of meters)	Associated with a weak, steeply dipping, NNW to NE trending axial fracture cleavage and to the $L_{NT}$	Affect all the afore-mentioned structures and are cut by the steeply dipping NW trending faults	$D_4$



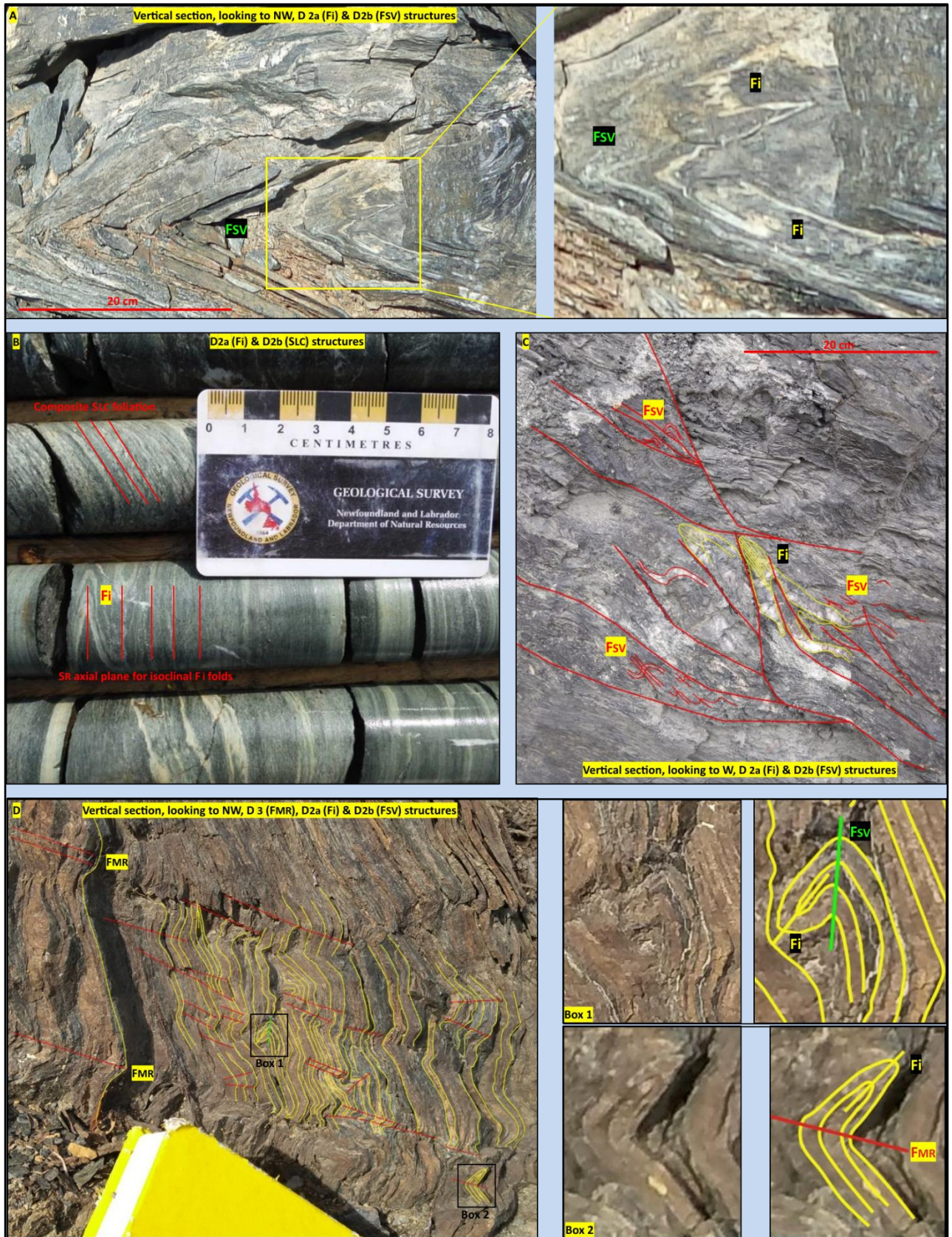
<b>xii</b>	NW to NE trending crenulation lineation	L <sub>NT</sub>	Regional to domianial	Crenulation lineation that plunges gently to steeply from NW to NE; weakly to strongly developed on the S <sub>R</sub> and the S <sub>L</sub> /S <sub>LC</sub> ( <b>Plate IV.3 – F</b> )	Related to the F <sub>NT</sub> folds	Affect both the D <sub>2</sub> and D <sub>3</sub> structures	D <sub>4</sub>
<b>xiii</b>	South dipping faults	Not applicable	Regional to domianial (best developed in strongly foliated rocks)	The faults dip moderately to steeply towards south and accommodate a normal to oblique movement to S - SE ( <b>Figure IV.8– A; Plate IV.1-E; Plate IV.4-D; Plate IV.8– A, B, C</b> )	Partial Riedel system with the steep, NW trending faults	Affect both the D <sub>2</sub> and D <sub>3</sub> structures and possibly also the D <sub>4</sub>	Syn-to-post-D <sub>4</sub>
<b>xiv</b>	Steep, NW trending faults	Not applicable	Regional to domianial (well-developed close to the N-NE oriented large-scale contacts)	In map view show an apparent sinistral, right stepping geometry ( <b>Figure IV.1- A; Figure IV.8- B</b> ); Display ambiguous kinematic in the field, but locally foliation drags indicate sinistral movement combined with a down-dip component ( <b>Plate IV.8– D</b> ); Where closely spaced, generate a local fracture cleavage	Partial Riedel system with the south dipping faults	Affect the D <sub>2</sub> , D <sub>3</sub> and D <sub>4</sub> structures	Syn-to-post-D <sub>4</sub>
<b>xv</b>	Late brittle faults	Not applicable	Regional	Steeply dipping to vertical, E-W and N-S striking, brittle faults and associated joints ( <b>Figure IV.9</b> ); Unclear kinematics for the N-S oriented faults; The E-W oriented faults show a down-dip throw of approximately 2 meters ( <b>Plate IV.9– F</b> )	Not applicable	Affect all the previous described structures	Post-D <sub>4</sub>



Studied deposits/prospects: 1 = Pine Cove, 2 = Strog'er Tight, 3 = Rome & Juliet, 4 = Argyle, 5 = Deer Cove; Other gold occurrences: 6 = Corkscrew, 7 = Goldenville; Abbreviations: DCT = Deer Cove Thrust; GC = Green Cove; BH = Big Head; MB = Ming's Bight; DG = Dunamagon Granite



**Figure IV.1: A** - Geological map of the Point Rouse Complex (PRC) modified after the unpublished geological map of Anaconda Mining (2018) and after Skulski et al. (2015). Location of the studied deposits (1-5) and of other mineralized regions (6 - 7). Southern-hemisphere, equal-area, stereographic projections of the poles to the S<sub>R</sub>/S<sub>LC</sub> foliation planes from the western coast (WC), central and northern parts (CN) and from the eastern coast (EC) of the PRC **Note:** the fault and fold generations correspond to the interpreted deformational sequence that affected the PRC: F<sub>2a</sub> folds represent large scale folds related to the development of the S<sub>R</sub> foliation and F<sub>i</sub> folds; D<sub>2a</sub> thrusts correspond to the major ductile faults; D<sub>2b</sub> faults are correlated to the brittle-ductile, reverse faults; and the D<sub>4</sub> folds are the equivalent of the north trending F<sub>NT</sub> folds. **B** – Regional geological cross section sketch modified after Kidd (1974) and Kirkwood & Dubé (1992). **Note:** the F<sub>SV</sub> (F<sub>2b</sub>) folds in the proximity of major thrusts and their refolding by the F<sub>MR</sub> (F<sub>3</sub>) folds.



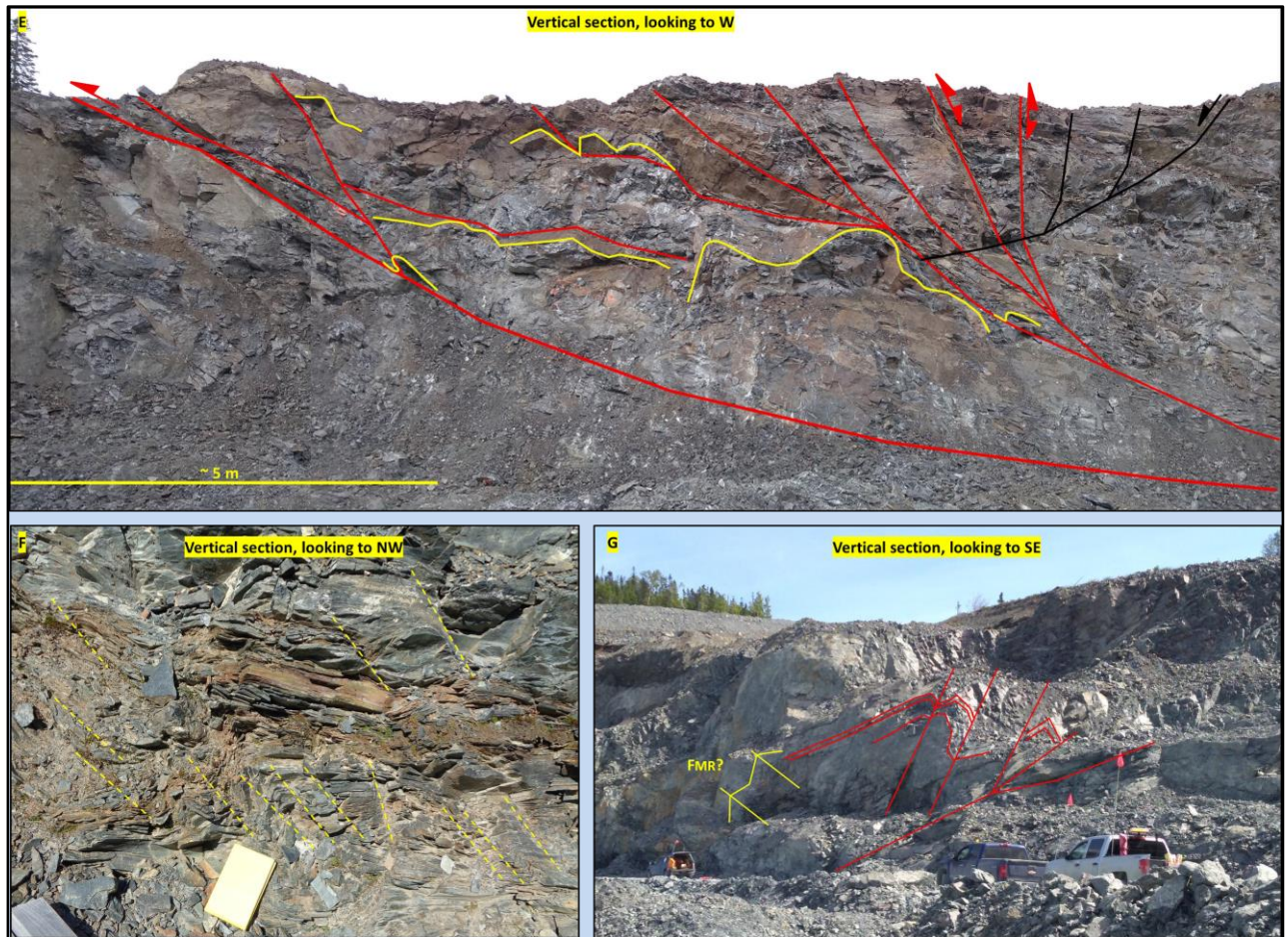


**Plate IV.1** – Representative field photographs for the intrafolial folds ( $F_i$ , interpreted as  $F_{2a}$ ) and for the south verging folds ( $F_{SV}$ , interpreted as  $F_{2b}$ ) and of their associated fabrics: **A** - Recumbent  $F_i$  folds affecting a compositional layering in the footwall of the Scrape Thrust, Pine Cove area; **Note** the location of the  $F_i$  folds within the core of a larger  $F_{SV}$  fold. **B** – Isoclinal  $F_i/F_{2a}$  folds and associated  $S_R/S_{2a}$  axial cleavage (continuous red lines) observed in drill core from the Stog'er Tight area; image source – courtesy of Anaconda Mining geologists. **C** – Refolded  $F_i$  folds (yellow) transported along small-scale brittle-ductile shears (red), Pine Cove area; the shears are sub-parallel to the axial cleavage of the  $F_{SV}$  folds (red). **D** – Refolded  $F_i$  folds by both  $F_{SV}$  and  $F_{MR}$  folds, approximately 1 km west from the Stog'er Tight deposit along the mining road; yellow lines represent the trace of the  $S_R/S_{2a}$  foliation; green line represents the trace of the  $F_{SV}$  axial plane; red lines represent the trace of the  $F_{MR}/F_3$  axial planes and associated shear bands. **E** – South directed, E-W oriented, brittle-ductile thrust imbricates (red lines) and associated open to tight  $F_{SV}$  folds (yellow lines) in the western extension of the Pine Cove deposit; black lines represent the trace of south dipping extensional shear bands (see text for further information). **F** – SW verging, asymmetric to overturned  $F_{SV}/F_{2b}$  folds in the footwall of the Scrape Thrust, ~ 400 m south from the Pine Cove deposit; yellow dashed lines represent the trace of the  $F_{SV}$  axial cleavage ( $S_L/S_{2b}$ ). **G** – SW verging, large scale  $F_{SV}$  fold and associated faults (red lines) observed in the southern wall of the Pine Cove pit; **Note**: the fold is located in the core of a large scale  $F_{NT}/F_4$  anticline; yellow lines represent the trace of either  $F_{MR}/F_3$  folds or, of  $F_{SV}$  folds related to back thrusting (see interpretations).

#### ***IV.1.1.3 Mesoscale recumbent folds ( $F_{MR}$ )***

Open to tight, asymmetric to recumbent, mesoscale folds ( $F_{MR}$ ) with a long upper limb and an overturned short lower limb were recorded in most parts of the PRC (**Table IV.1– viii; Figure IV.1 - B; Plate IV.2-A**). These folds affect the previously described  $F_i$  and the  $F_{SV}$  folds and display a broad range of geometries, scales, and orientations. The  $F_{MR}$  folds verge from E to W and have shallow plunge angles between 0°- 20° towards four general trends (E-W; N-S; NW-SE and NE-SW) (**Figure IV.2– B, C**). Overall, the dominant verging direction is northwards. The  $F_{MR}$  folds show wavelengths from a few centimetres to a couple of meters and are associated with flat lying to steeply dipping axial planes that show dipping directions to both north and south (**Plate IV.2– C, D, E; Figure IV.2- A**). In low to medium strain zones, the  $F_{MR}$  folds are asymmetric, open to tight, with flat lying to moderately dipping axial planes (**Plate IV.2– A, B, D, G**), whereas in high strain domains, the  $F_{MR}$  folds occur as box folds and recumbent chevron-type folds associated with gently to moderately dipping shear bands that accommodate a north side-down motion (**Plate IV.2– C, F, G**). It is interpreted that the geometrical variations that the  $F_{MR}$  folds display in the field are caused by the differences in the strain intensity and rock rheology and anisotropy, whereas the broad spectrum of orientations is given by the strike of the pre-existent structures on which they formed, and by the overprint of the  $F_{NT}$  folds (**Figure IV.2- C**).

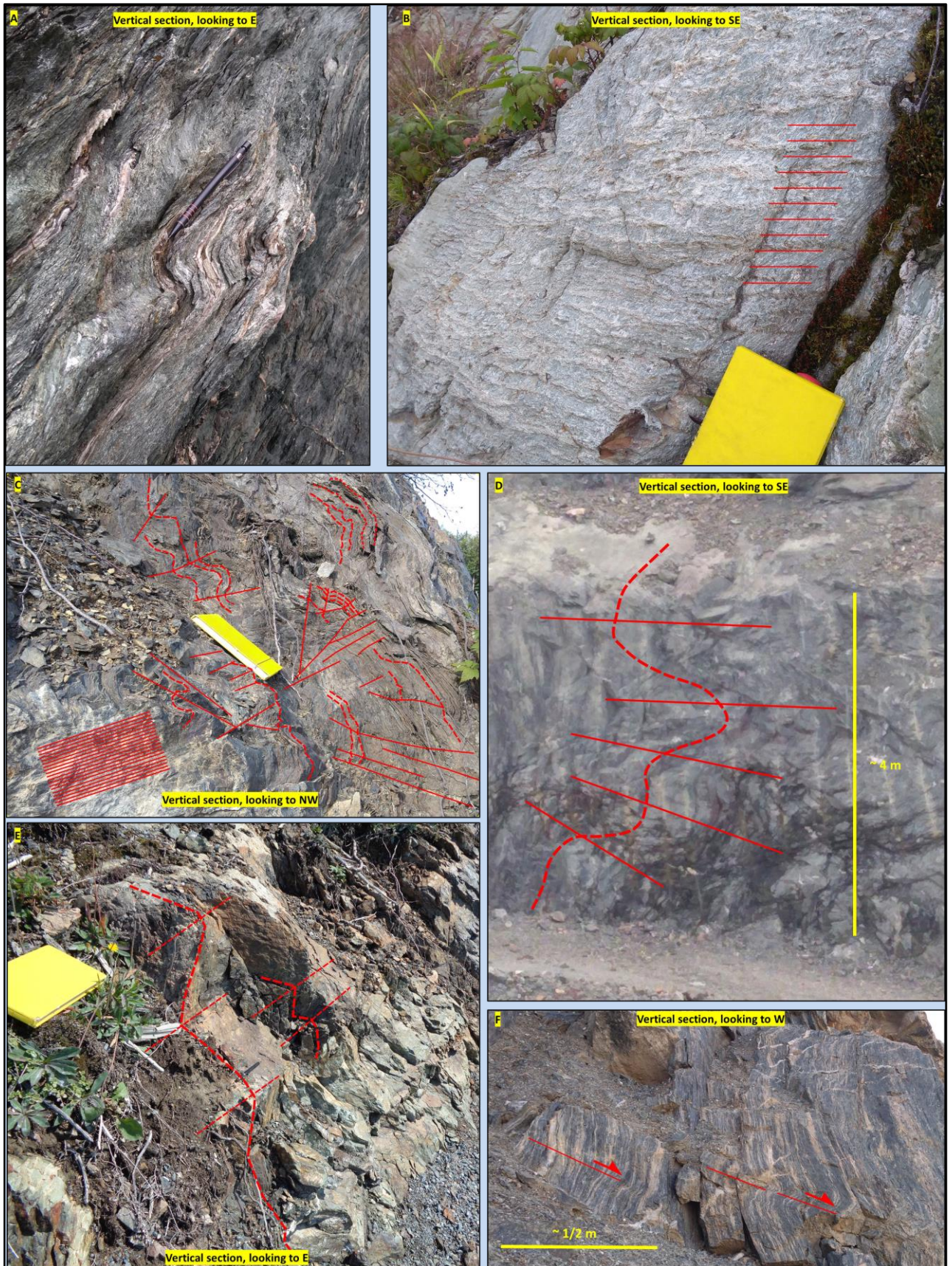
#### ***IV.1.1.4 North trending folds ( $F_{NT}$ )***

NW to NE trending folds ( $F_{NT}$ ) affect the entire PRC (**Table IV.1– xi; Figure IV.1 - A**). The  $F_{NT}$  folds show a wide variety of geometries: gentle to open folds within the competent rocks (e.g. gabbros, quartz veins), and open to tight, asymmetric, kink and box folds associated with conjugate kink bands within strongly anisotropic rocks (**Plate IV.3– A, B, C**). The scale of the folds varies from small parasitic “Z-M-S” type folds (Fossen, 2016) to local and regional scale synforms and antiforms (wavelengths from a few meters to hundreds of meters) (**Figure IV.1- A; Plate IV.3– D, E**). The folds plunge gently to steeply from NW to NE and in general are devoid of a visible axial plane. Where the axial plane of the  $F_{NT}$  folds is observed, it resembles a steeply dipping fracture cleavage that trends from NNW to NE (**Figure IV.3- A, B**).

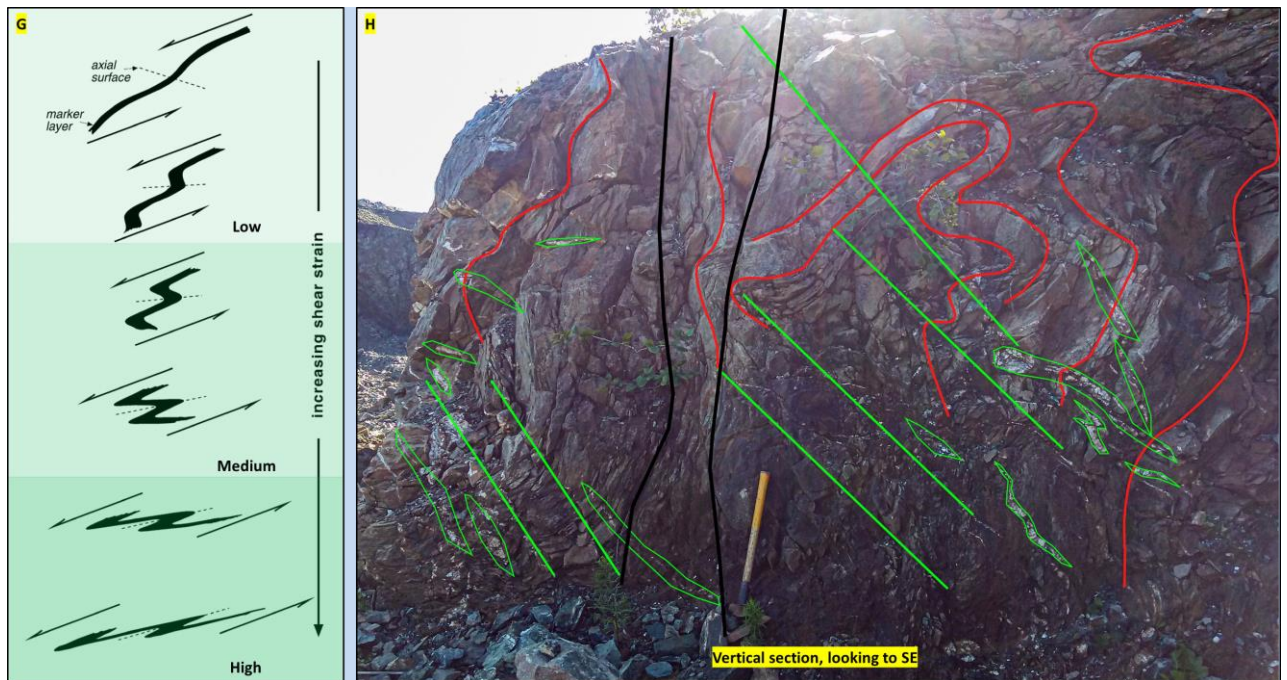
Where large scale  $F_{NT}$  folds (more than 3 meters in amplitude) affect competent rocks (e.g. pillow basalts), horizontal to oblique stretching mineral lineation, slickenfibres and associated steps were locally observed on the limbs of the folds (*Plate IV.3– I*). Fragments of pre-existent folds that are transported and rotated on the limbs of the  $F_{NT}$  folds were also observed (*Plate IV.3– E*). Drag folds are common within the strong anisotropic rocks at the contact between incompetent and competent layers and are interpreted to form in response to shearing between rocks with contrasting strengths during the development of the  $F_{NT}$  folds (*Plate IV.3 – B*).

The planar fabrics associated to the  $F_{SV}$  and the  $F_{MR}$  folds are crenulated by small scale, north plunging folds. The latter are interpreted here as parasitic  $F_{NT}$  folds (*Plate IV.3- G*). It was also noticed that in the volcano-sedimentary units, where the strain is usually high, a mutual cross-cutting relationship occurs between the axial planar cleavages of the  $F_{MR}$  and of the  $F_{NT}$  folds (*Plate IV.3- H*).

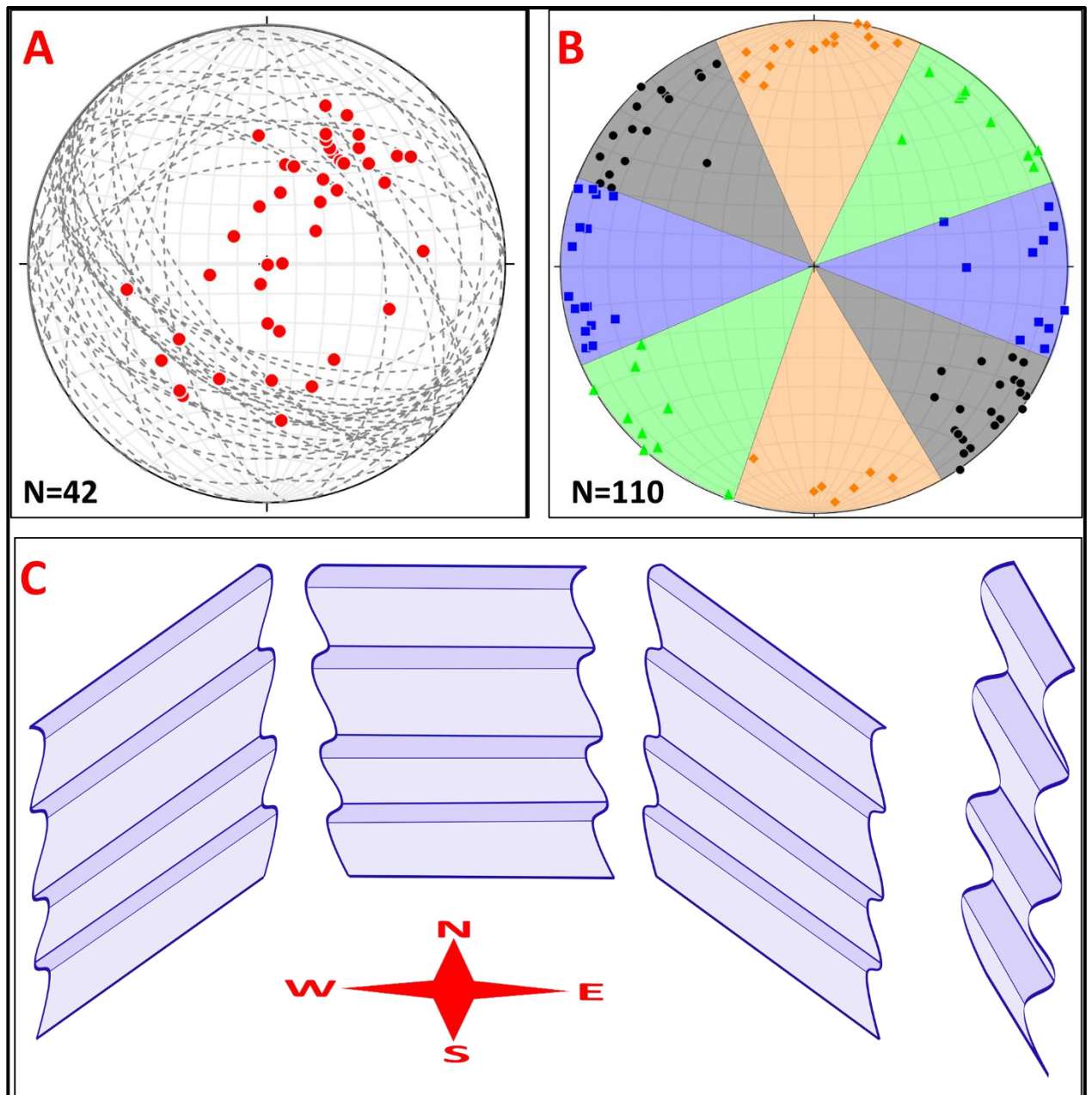
The meter scale  $F_{NT}$  folds usually show wavy hinge lines, whereas the decimetre scale, asymmetric  $F_{NT}$  folds from the strong anisotropic rocks have a double plunging nature. These aspects suggest that these are non-cylindrical folds. In contrast to the  $F_{NT}$  folds, the cylindricity of the  $F_i$ ,  $F_{SV}$ , and of the  $F_{MR}$  folds cannot be properly assessed due to intense structural superposition which affected their initial geometries.



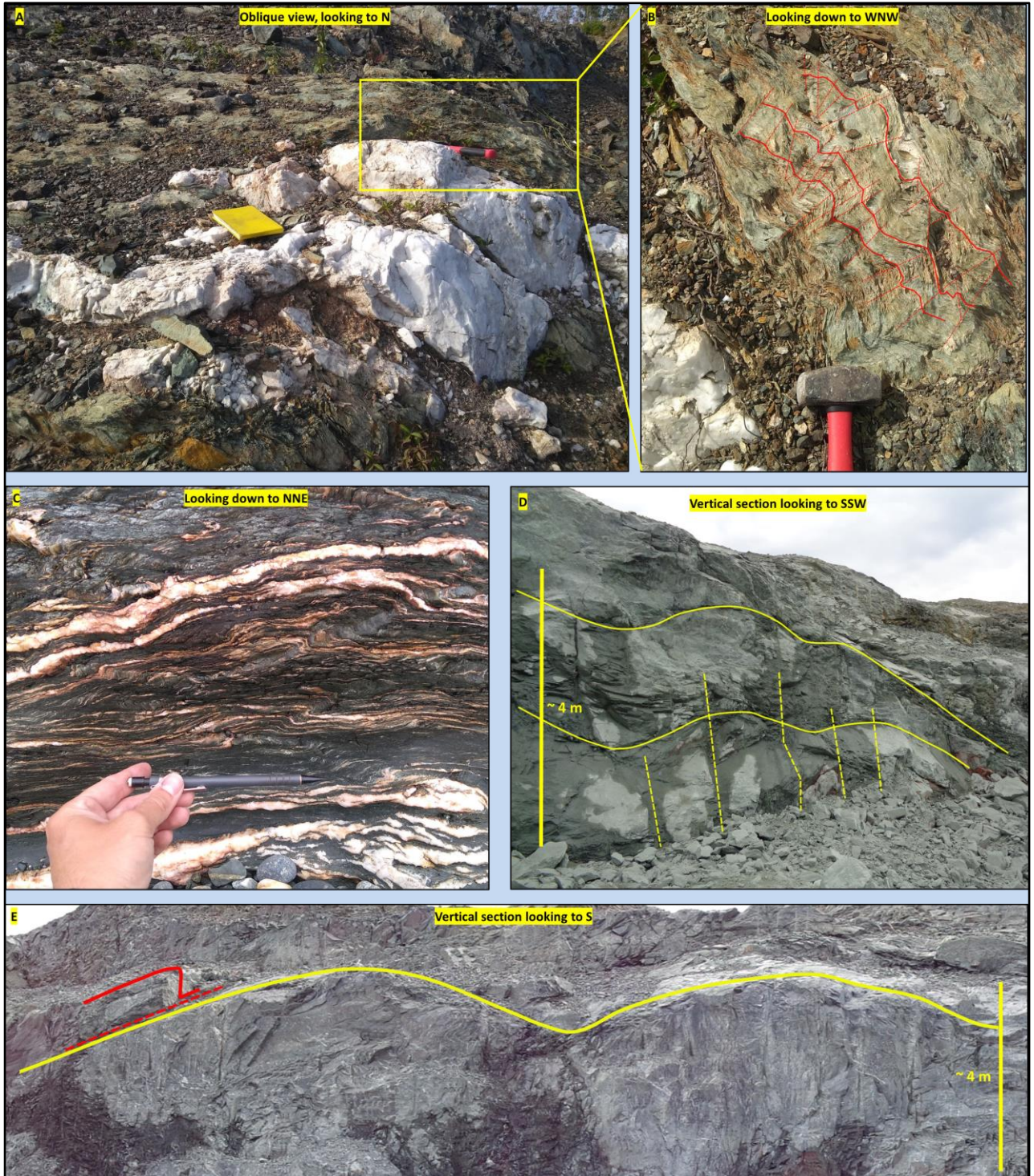




**Plate IV.2** – Representative field photographs for the mesoscale recumbent folds ( $F_{MR}$ , interpreted as  $F_3$ ) and of their associated fabrics: **A** – Most representative geometry of the  $F_{MR}$  folds; Pine Cove coast. **B** – Flat lying, spaced crenulation cleavage (red lines) associated with  $F_{MR}$  folds developed in medium strain domains. **C** –  $F_{MR}$  folds developed in high strain domains; composite foliation (continuous, closely spaced red lines) associated with the development of  $F_{MR}$  folds; N dipping axial planes and shear bands together with box fold geometries are common in high strain domains (continuous red lines represent the trace of the axial planes and shear bands, whereas the red dashed lines illustrate the folded layers); same location as for **Plate IV.1** – **D**. **D** – Large scale, NE verging  $F_{MR}$  folds observed in the southern wall of the Stog’er Tight pit; red dashed lines = trace of folded layers; continuous red lines = trace of  $F_{MR}$  axial planes. **E** – Rotated  $F_{MR}$  folds in high strain domains resulting with a change in the fold asymmetry from N to S; 1 km south from the Stog’er Tight area along the mining road. **F** – shear bands that dip shallowly to N developed along the axial planes of the  $F_{MR}$  folds accommodating N side-down motion; eastern Stog’er Tight pit. **G** – Representative sketch of different  $F_{MR}$  fold geometries developed with respect to the increase in strain intensity; image modified after Fig.10 of Harris et al. (2002). **H** – Geometry characteristic of Type III fold interference pattern between the  $F_{MR}$  folds and the  $F_{SV}$  folds; continuous red lines represent the trace of the folded layers; green lines correspond to fractures developed along the  $F_{MR}$  axial planes and the green contours highlight the presence of quartz-carbonate veins along the  $F_{MR}$  fold axial planes; black lines = late brittle faults; eastern Stog’er Tight Pit.



**Figure IV.2** – Orientation of  $F_{MR}$  folds (interpreted as  $F_3$  folds) within the Point Rouse Area. **A** - Southern-hemisphere, equal-area, stereographic projections of the poles (red dots) to the  $F_{MR}$  axial planes (grey dashed lines). **B** - Southern-hemisphere, equal-area, stereographic projections of the  $F_{MR}$  fold hinges and their classification in 4 broad trend categories: blue = E-W; black = NW-SE; orange = N-S; and green = NE-SW. **C** – Sketch diagram illustrating the geometries and the orientations of the  $F_{MR}$  folds with respect to their location on pre-existing structures; **Note**: the NW and NE trends are influenced by both the strike of the pre-existing brittle-ductile faults and by the presence of the  $F_{NT}/F_4$  folds that amplifies the sinusoidal geometry of younger structures – see text for further information.



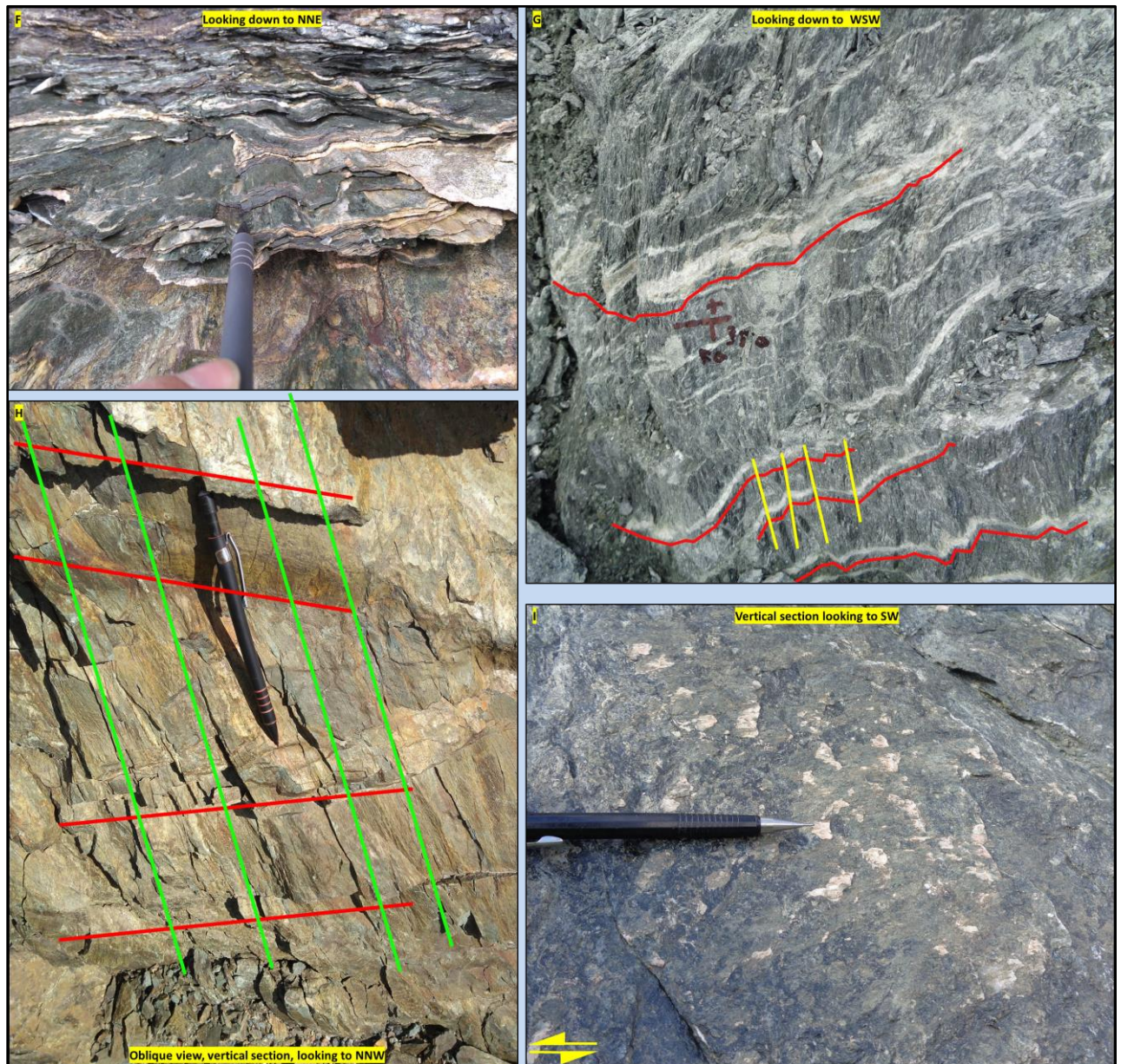


**Plate IV.3** – Representative field photographs for the north trending folds ( $F_{NT}$ , interpreted as  $F_4$ ) and of their associated fabrics: **A** – Open, NNE plunging  $F_{NT}$  fold affecting a quartz vein; Stog’er Tight area; the yellow rectangle shows the location of image **B**. **B** - Kink and drag-type  $F_{NT}$  folds formed in highly anisotropic rocks at the contact between competent and incompetent rocks; continuous red lines represent the trace of the folded layers, whereas the dashed lines are the  $F_{NT}$  fold axial planes. **C** –  $F_{NT}$  folds associated to conjugate kink bands in strongly foliated rocks; Deer Cove area. **D & E** – medium scale, gentle to open  $F_{NT}$  folds (yellow line = trace of folded layers) and associated  $F_{NT}$  axial fracture cleavage (yellow dashed lines); **Note** the rootles, potential  $F_{SV}$  fold (red contour line) from image **E** transported along the limb of the  $F_{NT}$  fold; Stog’er Tight W pit. **F** – crenulation lineation ( $L_{NT}$ ) generated by the  $F_{NT}$  folds subparallel with the  $L_R$  stretching mineral lineation; Deer Cove area. **G** – Quartz-carbonate veins formed along the axial planes of the  $F_{MR}$  folds crenulated by  $F_{NT}$  folds; red lines represent the trace of the folded veins, whereas the yellow lines represent the trace of the  $F_{NT}$  axial planes; Stog’er Tight W pit. **H** –  $F_{MR}$  and  $F_{NT}$  fracture axial cleavages (red lines – trace of  $F_{MR}/F_3$  axial cleavage; green lines – trace of the  $F_{NT}$  axial cleavage) intersected at high angles, showing mutual cross-cutting relationships; 1 km south from the Stog’er Tight area along the mining road. **I** – Horizontal steps and slicken-fibers indicating sinistral movement along a NE dipping limb of a large scale  $F_{NT}$  fold; Pine Cove pit.

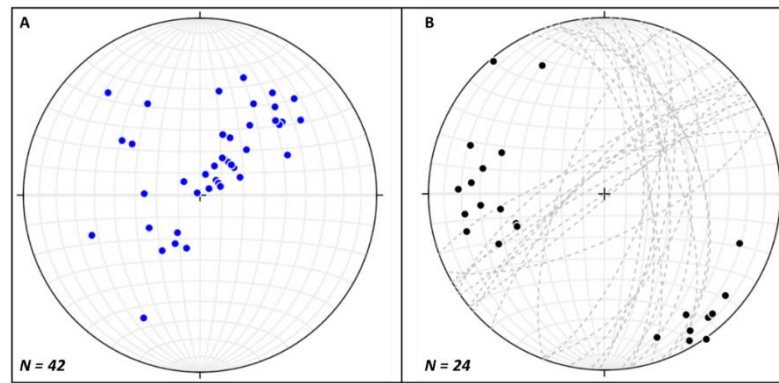


**Figure IV.3** - Southern-hemisphere, equal-area, stereographic projections of the  $F_{NT}$  (interpreted as  $F_4$ ) fold axes and crenulation lineations (**A**) and of the poles (black dots) to their fracture cleavages (grey dashed lines) (**B**).

#### IV.1.2 Planar and linear fabrics

Multiple planar and linear fabrics were observed within the Point Rouse Complex. These are listed below with respect to their style, orientation, and crosscutting relationships.

##### IV.1.2.1 Regional foliation fabric ( $S_R$ )

Throughout the Point Rouse area, a regional developed foliation fabric, noted here as  $S_R$ , is represented by a layer/bedding parallel cleavage that is best preserved in low strain domains or in the hinges of the south verging folds (**Table IV.1 - ii**). The  $S_R$  is interpreted to correspond to the axial planar cleavage of the intrafolial folds ( $F_i$ ). It varies in intensity from a weak spaced cleavage in the more competent rocks (e.g. gabbro, pillow and massive basalts, greywackes), to a phyllitic cleavage and a strong schistosity in the volcano-sedimentary units (**Plate IV.4- A, B**). The  $S_R$  is defined by the alignment of different minerals that varies with respect to the rock type: i) chlorite-albite-quartz  $\pm$  epidote - actinolite – sericite - calcite in the mafic volcanic rocks; ii) sericite – quartz – chlorite in the metasedimentary rocks; and iii) serpentine group minerals + talc and to a lesser degree tremolite, actinolite and carbonates in the ultramafic rocks.

##### IV.1.2.2 Local foliation fabric ( $S_L/S_{LC}$ )

A locally developed foliation fabric that crosscuts the  $S_R$  foliation was also observed in multiple parts of the PRC. This fabric named here as  $S_L$  (**Table IV.1- vi**), occurs as a crenulation cleavage (as defined in Fossen, 2016) generated by the  $F_{SV}$  microfolds, a penetrative axial planar cleavage associated with mesoscale south

verging folds ( $F_{SV}$ ), and as a shear related cleavage in the proximity, and within major ductile to brittle-ductile thrust sheets (*Plate IV.1- F, Plate IV.4- E*). The  $S_L$  is mostly defined by chlorite  $\pm$  muscovite, phengite and fuchsite.

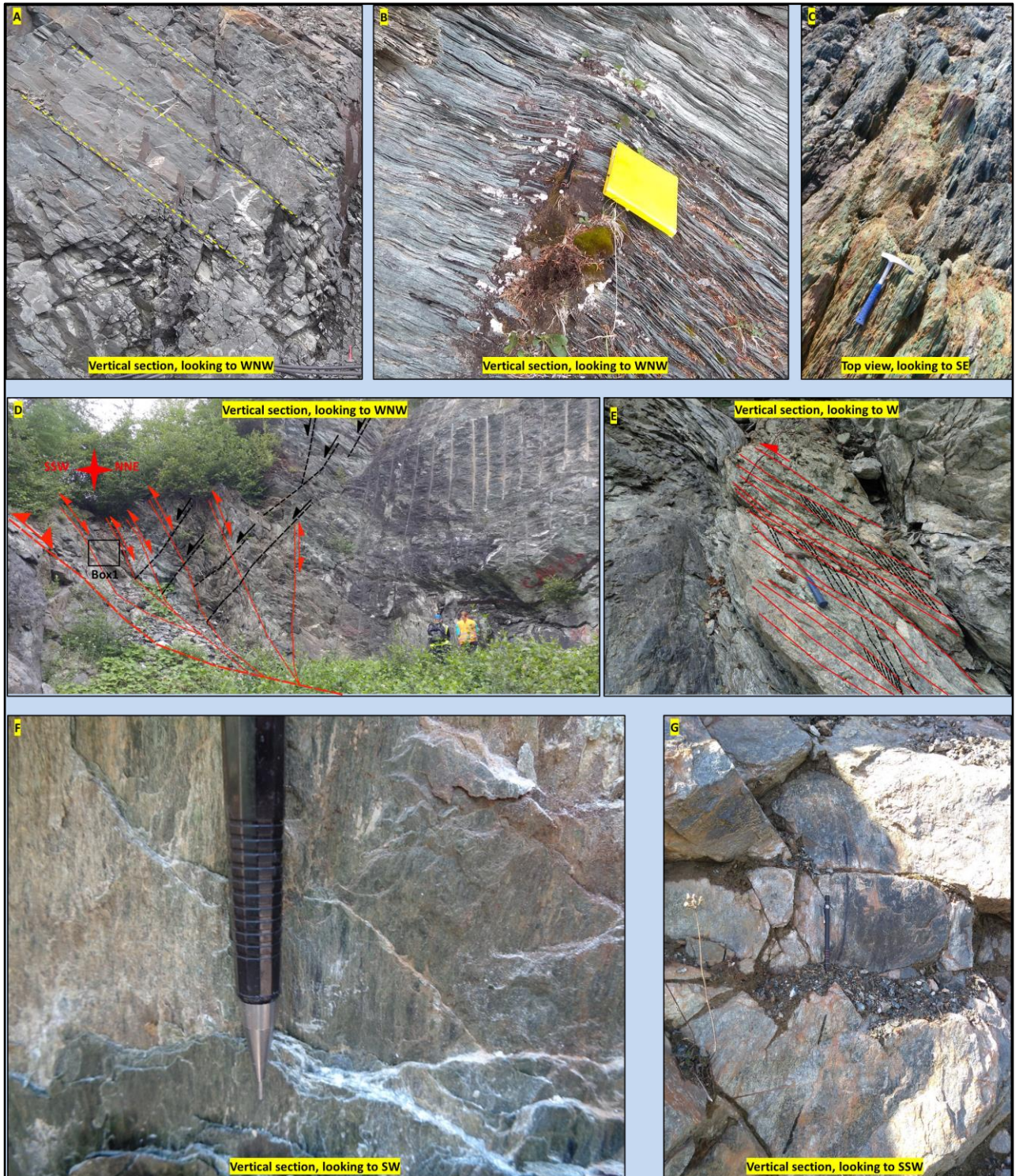
The exact geometrical relationships between the  $S_R$  and the  $S_L$  fabrics are not easily observable in the field because of subsequent superposition of younger fabrics. However, based on a couple outcrops where the early structures are better preserved, some common characteristics were noticed: i) the  $S_L$  cleavage is in general steeper than the  $S_R$  foliation with the exception when the  $S_L$  represents the axial planar cleavage of overturned south verging folds, case in which the  $S_L$  is less inclined than the  $S_R$  on the overturned limb of the  $F_{SV}$  folds (*Plate IV.1- F*); ii) overall, the  $S_L$  fabric is slightly oblique to the  $S_R$  foliation yet, in areas where the  $F_i$  and the  $F_{SV}$  fold axes are coaxial, the  $S_L$  and the  $S_R$  fabrics have the same orientation (*Plate IV.1- C*); and iii) where the  $S_L$  is a shear slip cleavage associated with brittle-ductile faults, a “S-C” style geometry is frequently formed between the  $S_R$  and the  $S_L$  fabrics – in this situation the  $S_L$  fabric is interpreted as the “C” shear plane, whereas the pre-existing  $S_R$  foliation is associated to the “S” planes (*Plate IV.4- E*).

In the central part of the Point Rousse Complex the  $S_R$  fabric represents the dominant foliation, but in the proximity of high-strain fault zones (e.g. the Scrape and the Deer Cove thrusts, *Figure IV.1*) the  $S_R$  is transposed into parallelism with the  $S_L$  fabric and forms a local mylonitic composite foliation referred to as  $S_{LC}$  (*Table IV.1 - vi*). A  $S_{LC}$  foliation is also characteristic for the brittle-ductile shear zones that accommodate a N over S transport direction (*Table IV.1- vii; Plate IV.4- C*). Oriented thin sections generated from mylonite samples collected from the brittle-ductile faults were studied under the microscope and a faint fabric defined by recrystallised quartz, feldspar, and micas or by inclusion trails in feldspar porphyroclasts was observed between the  $S_L$  fabric planes (*Plate IV.5- A, B, C*). This fabric is interpreted herein as the transposed  $S_R$  foliation.

Overall, the  $S_R$  and the composite  $S_{LC}$  dip moderately to steeply ( $\sim 35^\circ$ -  $80^\circ$ ) from NW to NE and the variation is interpreted to be caused by the presence of the  $F_{NT}$  folds (*Figure IV.4- A, B*). The poles to the foliation planes plotted on an equal area stereonet align on a statistical best-fit great circle (*Figure IV.4- B*). It is considered that the alignment of the poles reflects the rough geometry of the  $F_{NT}$  profile plane, whereas the “ $\beta$ ” pole represents the trend and plunge of the fold axis.

Locally, the  $S_R$  and the  $S_{LC}$  fabrics also dip shallowly to steeply towards SW or SE (*Figure IV.4- A, C*). It is interpreted herein that this variation is dependent on the geometries of both the  $F_{SV}$  and of the  $F_{MR}$  folds. *Figure IV.4 - C*, illustrates the plotted poles to the foliation planes measured on the limbs of the north verging, recumbent  $F_{MR}$  folds. The data align on a “best-fit” griddle circle that is associated to the  $F_{MR}$  fold profile plane, while the “ $\beta$ ” pole is interpreted as the approximate trend and plunge of the fold hinge line.

The foliation plane measurements collected from the western and the eastern coastlines, together with the ones from the south-eastern contact between the Point Rousse Complex and Pacquet Harbour Group (PHG), are presented separately in *Figure IV.4- E, G, I*. Along the W coast, the  $S_R$  and the composite  $S_{LC}$  foliation dip moderately to steeply from W to N (*Figure IV.4 - E*), whereas along the E coast, the foliation fabric dips to NNW (*Figure IV.4- G*). On the south-eastern contact, the dominant fabric is the composite  $S_{LC}$  foliation with the  $S_R$  fabric being visible only in very few locations. Here, the orientation of the foliation is quite variable, but a dip direction to W-NW is the most characteristic (*Figure IV.4- I*). Compared to the central part of the complex, these areas are intensively deformed and show a multitude of overprinting structures. These regions are associated herein with the NNE to NE trending lineaments that border the PRC, as observed on the Tilt Derivative aeromagnetic map of the Baie Verte Peninsula (*Figure IV.5*). These lineaments represent the edges of lithological blocks with different magnetic response and, together with the field observations, are interpreted here as large-scale fault zones.





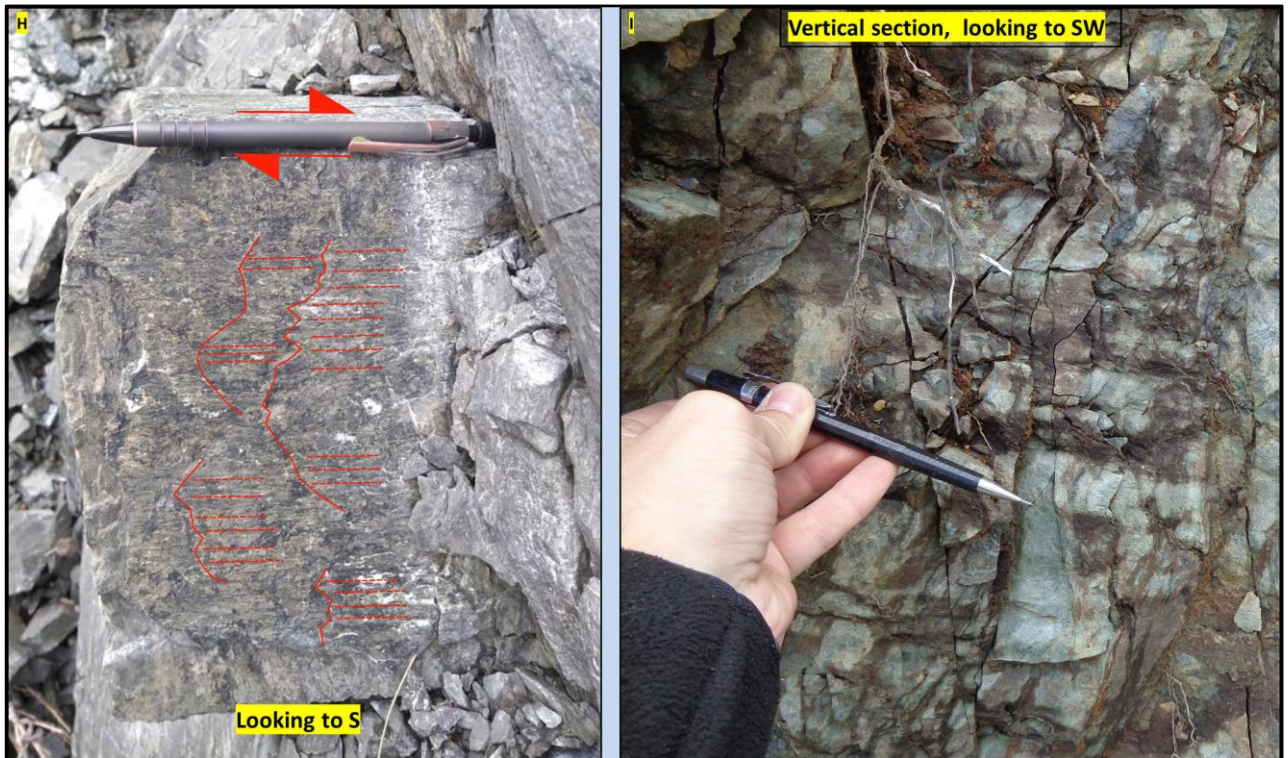


**Plate IV.4** – Representative field photographs for the  $S_R$  and  $S_L/S_{LC}$  planar fabrics (interpreted as  $S_{2a}$  and  $S_{2b}$ , respectively), and for the  $L_R$  (interpreted as  $D_{2a}$ ) and  $L_{MR}$  (interpreted as crenulation lineation related to  $F_3$  folds) linear fabrics: **A** – Spaced  $S_R$  bedding-parallel cleavage within the greywackes of the Bobby Cove Formation, Pine Cove area (yellow dashed lines – trace of  $S_R$  cleavage); **note** hammer for scale, bottom right corner. **B** - Strong  $S_R$  phyllitic cleavage within the volcano-sedimentary rocks of the Mount Misery Formation, close to Big Head area. **C** – Mylonitic  $S_{LC}$  foliation within a strongly altered (Fuchsite-Pyrite-Iron Oxides) brittle-ductile shear zone, west cost - Deer Cove area. **D** - Approximately N-S oriented section of the Deer Cove Thrust, red lines represent the trace of the thrust and associated shears; black lines represent south dipping extensional shear bands (see text for further information); **Box 1** – shows the location of image **E** - “S-C” fabric indicating N over S motion within the Deer Cove Thrust; the black lines represent the “S” planes, whereas the red lines correspond to the “C” shears; the “C” planes are interpreted here as the  $S_L$  slip cleavage related to thrusting, and the “S” planes as the  $S_R$  foliation. **F** – Well-developed, down-dip plunging stretching mineral lineation ( $L_R$ ) on the foliation plane, Deer Cove area. **G** – Deflection of the stretching mineral lineation ( $L_R$ ) within the hinge of a  $F_{MR}$  fold (note the black line), Stog’er Tight area. **H** - Horizontal slickenfibres and stretching mineral lineation observed in the Pine Cove area. Steps and fibers indicate dextral motion. **I** - Almost horizontal  $L_{MR}$  crenulation lineation associated with  $F_{MR}$  microfolds.

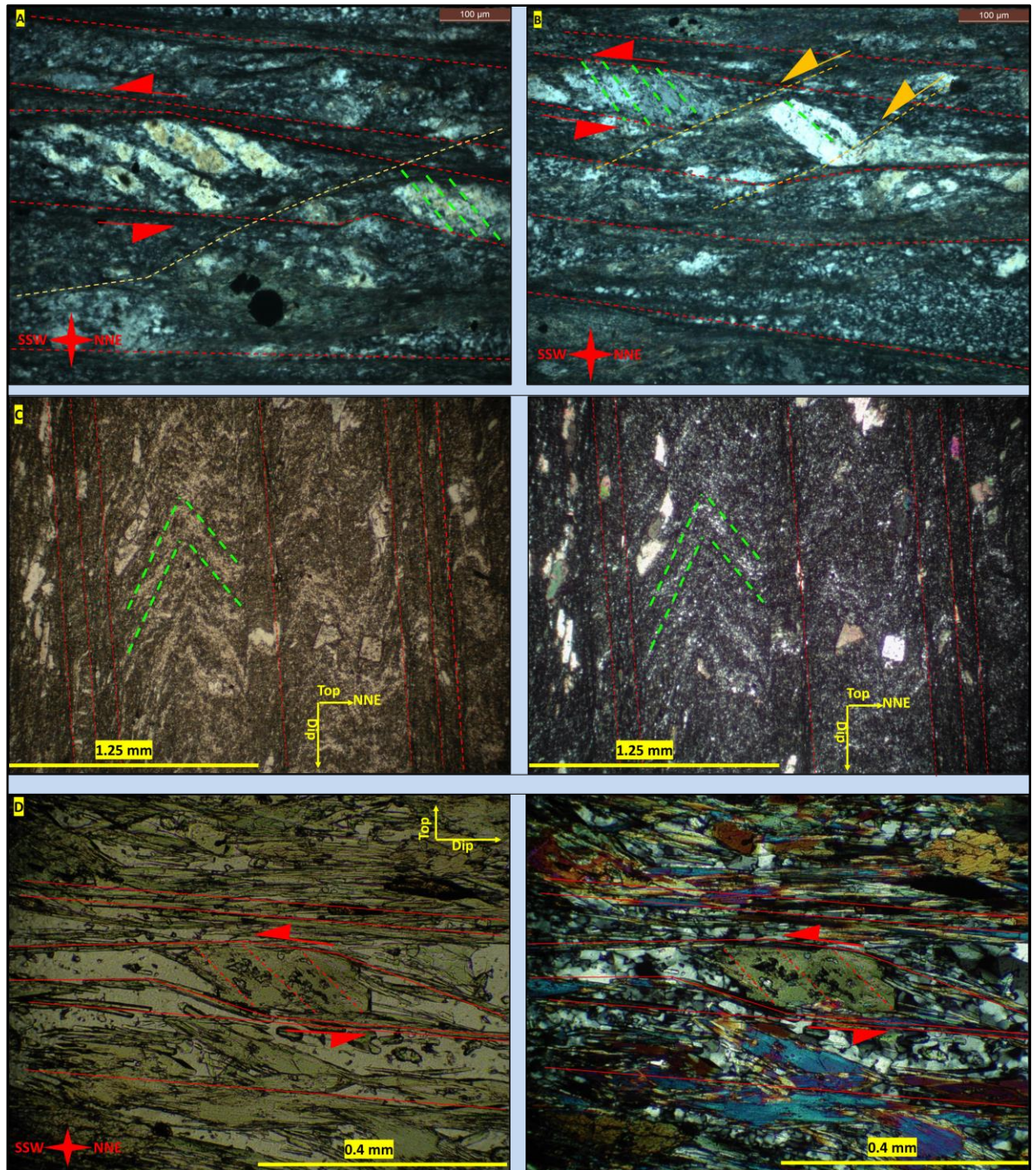


**Plate IV.5** – Representative photographs of microstructural elements that suggest South directed transport along the  $D_{2a}/D_{2b}$  structures and also their reactivation as extensional structures (down-dip sliding): **A (XPL)** - Fragmentation and rotation of feldspar porphyroclasts indicating up-dip motion towards south. **B (XPL)** - inclusion trails preserved in quartz porphyroclasts representing a relic fabric (green dashed lines,  $S_R$ ) that forms a “S-C” configuration with the main foliation planes (red dashed lines,  $S_{LC}$ ) indicating top the S movement; **note** the presence of the extensional shears (orange dashed lines) that affect the pre-existing fabrics. **C (left-PPL, right-XPL)** - Preservation of folded  $S_R$  foliation (green dashed lines) between  $S_L$  planes (red dashed lines) in the hanging wall of the Deer Cove thrust; **note** in this case the  $S_L$  represents the axial planar cleavage for  $F_{SV}$  folds. **D (left-PPL, right-XPL)** - “ $\sigma$ -type” amphibole porphyroclast that indicate top-to-SSW motion in an oriented sample collected from the footwall of the NNE dipping segment of the Scrape thrust; **note** the S-C fabric configuration between the inclusion trails from the amphibole porphyroclast (red dashed lines) and the main foliation fabric (red continuous lines). Plate continuation on the next two pages.

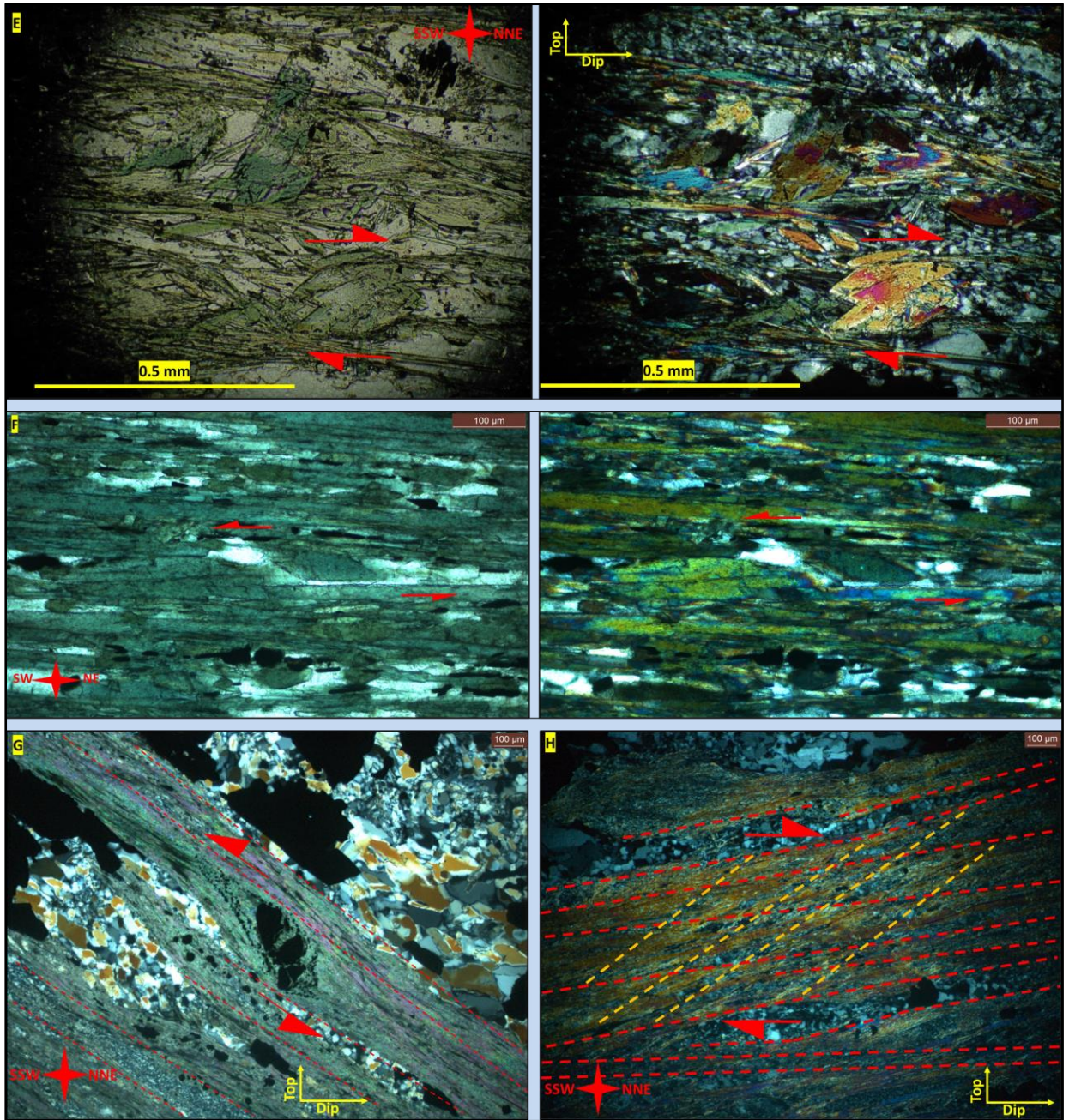


**Plate IV.5 (continuation)** – *E* (left-PPL, right-XPL) – Amphibole porphyroblasts that overgrows the main foliation and indicate a down-dip motion towards N; sample collected from the from the footwall of the NNE dipping segment of the Scrape thrust. *F* (left-PPL, right-XPL) – Photograph of a “ $\sigma$ -type” amphibole porphyroclast within a mylonitic foliation indicating sinistral movement towards SW; the thin section was cut perpendicular to the foliation and parallel to a gently plunging NE-ENE stretching mineral lineation; sample collected from a strongly sheared interval within the footwall of the Scrape Thrust, ~ 400 m south from the Pine Cove deposit. *J* (XPL) – Fragmentation of chromite porphyroclast, indicating up-dip motion towards SSW within a NW striking brittle-ductile fault ( $D_{2b}$ ) from the Deer Cove area. *H* (XPL) – potential “S-C” fabric geometry created between the main foliation fabric (red dashed lines) and a crenulation cleavage (orange dashed lines) indicating down-dip motion towards north (see text for interpretations). Plate continuation on next page.

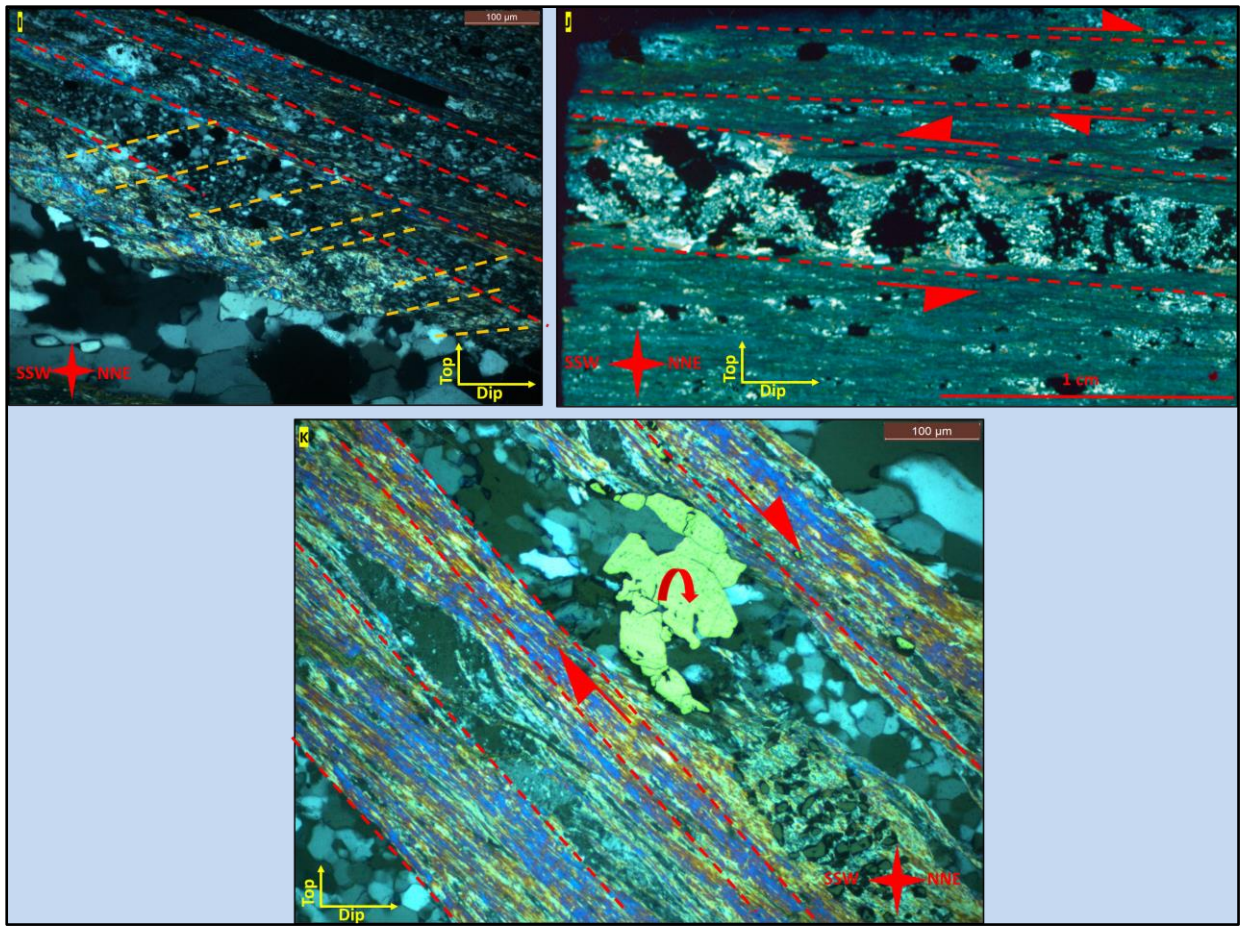


**Plate IV.5 (continuation) – I (XPL)** – Crenulation generated by extensional shears (orange dashed lines) that affect pre-existing foliation (red dashed lines). **J (XPL)** – Full thin section scan illustrating rotated pyrite porphyroclasts that indicate two motion directions: top to south and down-dip to north. **K (XPL)** – Pyrite porphyroclast recrystallised and rotated towards N between the main foliation planes (red dashed lines). All images are from samples collected from a NW striking brittle-ductile fault ( $D_{2b}$ ) from the Deer Cove area.

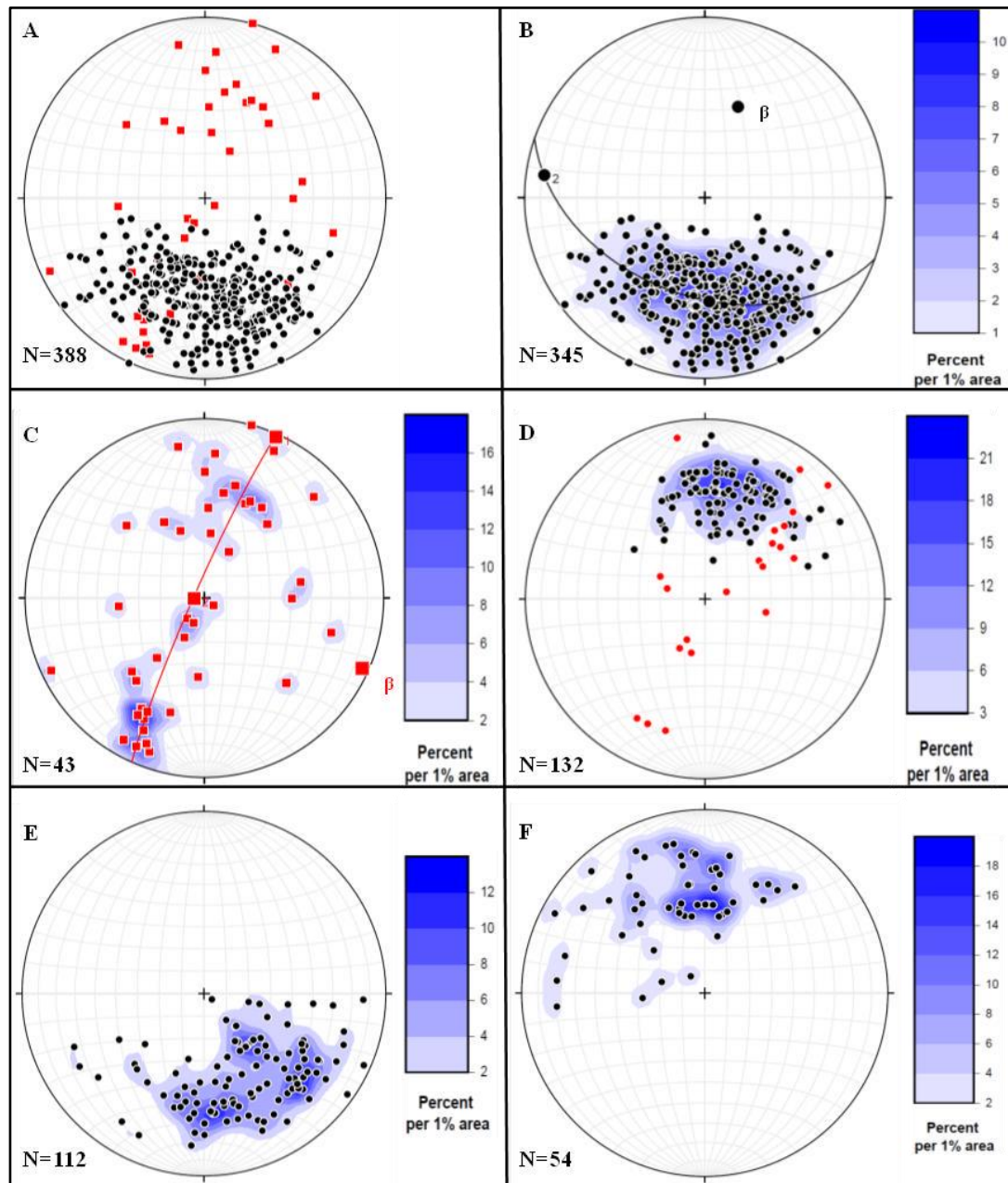


**Figure IV.4** - Southern-hemisphere, equal-area, stereographic projections of the  $S_R/S_{LC}$  foliation plane (interpreted as  $S_{2a}/S_{2b}$ ) and mineral stretching lineation measurements from the Point Rouse Complex (PRC). **A, B, C** - Poles to the  $S_R/S_{LC}$  foliation planes measured in the southern, central, and northern parts of the Point Rouse Complex: **A** - all data; red squares represent measurements collected on the limbs of  $F_{MR}$  folds. **B** - “1% area” contoured plot of poles to foliation planes unaffected by  $F_{MR}$  folds, note the statistical best fit gridle which corresponds to the profile plane of the  $F_{NT}$  folds, whereas pole “ $\beta$ ” represents the  $F_{NT}$  fold axis. **C** - “1% area” contoured plot of poles to foliation planes measured on the limbs of  $F_{MR}$  folds, note the statistical best fit gridle which corresponds to the profile plane of the  $F_{MR}$  folds, whereas pole “ $\beta$ ” represents the  $F_{MR}$  fold axis. **D** - stretching mineral lineation measurements from the southern, central, and northern parts of the Point Rouse Complex - red dots represent measurements collected on the limbs of  $F_{MR}$  folds, whereas the “1% area” contoured plot is for stretching mineral lineation measurements in areas unaffected by  $F_{MR}$  folds (black dots). **E** - “1% area” contoured plot of poles to the  $S_R/S_{LC}$  foliation planes measured along the west coast; **F** - “1% area” contoured plot of stretching mineral lineation measurements from the western coastline.

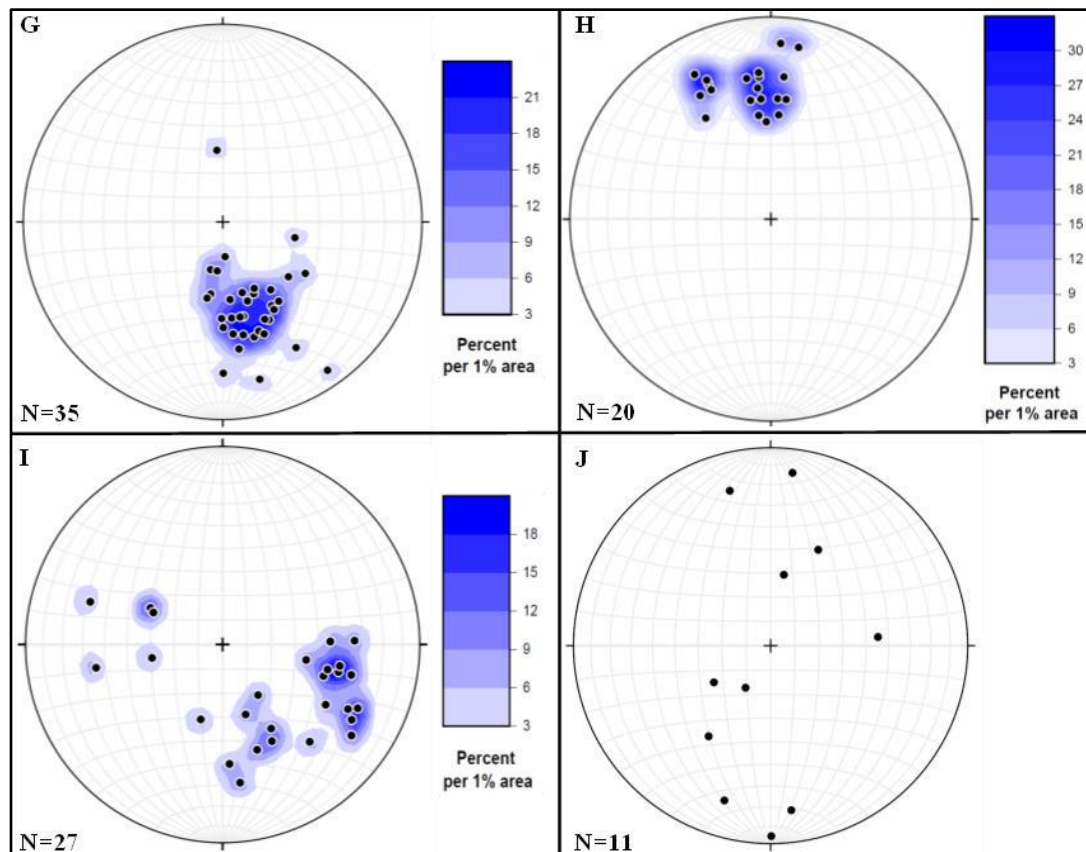


**Figure IV.4 (continuation)** - **G** - “1% area” contoured plot of poles to the  $S_R/S_{LC}$  foliation planes measured along the east coast. **H** – “1% area” contoured plot of stretching mineral lineation measurements from the eastern coastline. **I** - “1% area” contoured plot of poles to the  $S_R/S_{LC}$  foliation planes measured along the south-eastern contact of the PRC. **J** – stretching mineral lineation and slicken fibers measurements collected along the south-eastern contact of the PRC.

#### IV.1.2.3 Horizontal crenulation cleavage ( $S_{MR}$ )

Across the area, a horizontal crenulation cleavage affects the  $S_R$  and the  $S_L$  fabrics. This cleavage is interpreted here as the axial plane of small-scale  $F_{MR}$  folds. Locally, the crenulation cleavage becomes a penetrative foliation within highly anisotropic rocks where the  $F_{MR}$  are usually tight to isoclinal (*Plate IV.2 – B, C*). These planar fabrics are named here  $S_{MR}$  (*Table IV.1- ix*).

#### IV.1.2.4 Regional stretching mineral lineation ( $L_R$ )

A prominent, regional developed, down-dip to oblique plunging stretching mineral lineation, termed here as  $L_R$ , defined by chlorite, amphibole and plagioclase crystals is well developed on the  $S_R$  foliation planes (*Table IV.1– iii; Plate IV.4- F*). Even though the overall plunging trend of the  $L_R$  stretching mineral lineation is towards N in most of the PRC (*Figure IV.4– D, F, H*), its orientation is influenced

by all the folds that affect the  $S_R$  fabric (*Table IV.1– v; viii; xi*). Where the  $F_i$  folds are coplanar with the  $F_{SV}$  folds, the  $L_R$  stretching mineral lineation is interpreted to be steepened and/or amplified due to continuous layer flattening. However, when the  $F_{SV}$  folds form at an oblique angle to the  $S_R$  fabric, the  $L_R$  is re-oriented towards NE and ENE. It was observed that on the overturned limb of the north verging recumbent folds ( $F_{MR}$ ), the  $L_R$  plunges southward (*Figure IV.4- D*), whereas in the  $F_{MR}$  hinge zone the  $L_R$  is deflected towards east or west depending on the exact orientation of the  $F_{MR}$  folds (*Plate IV.4- G*). Where the main fabric is represented by the mylonitic  $S_{LC}$  foliation, a strong mineral stretching lineation that shows a similar trend and plunge as the  $L_R$  lineation is developed within the foliation plane. This aspect hinders a proper separation between the regional developed stretching mineral lineation and the local stretching mineral lineation associated with the  $S_{LC}$  fabric.

Horizontal slicken fibres and steps that indicate dextral motion and a well-developed associated stretching mineral lineation that overprint the regional  $L_R$  stretching mineral lineation were observed locally in the Pine Cove area between E-W oriented layers (*Plate IV.4- H*). Given the local distribution of this lineation fabric, the relationship between it and the rest of the structures observed in the field is not clear. A possible interpretation would be that this fabric developed during the formation of the  $F_{NT}$  folds as a result of layer-parallel shearing.

#### ***IV.1.2.E. Crenulation lineations ( $L_{MR}/L_{NT}$ )***

Two crenulation lineations that affect the  $S_R/S_{LC}$  fabrics were recorded in multiple locations within the PRC. One of these crenulations is sub-horizontal, whereas the other one is plunging gently to steeply from NW to NE and are termed here as the  $L_{MR}$  and the  $L_{NT}$ , respectively (*Table IV.1– x, xii; Plate IV.4- I and Plate IV.3– F*). The relationship between the two crenulation lineations is not very clear but based on very few outcrops where these intersect, it seems that the  $L_{NT}$  disturbs the  $L_{MR}$ . It is interpreted herein that the sub-horizontal crenulation formed in association with the  $F_{MR}$  folds, whereas the NW-NE plunging one is related to the  $F_{NT}$  folds.

### IV.1.3 Fault systems

Within the Point Rouse area multiple fault systems were observed. These are presented below with respect to their deformation style, type, scale, and orientation.

#### IV.1.3.1 Major ductile to brittle-ductile thrusts (Table IV.1 – iv)

Major thrust sheets with an approximate E-W trend that dip moderately to steeply towards north divide the area in multiple lithostratigraphic domains (**Figure IV.1**) (Norman and Strong, 1975; Kidd et al., 1978; Kirkwood & Dubé, 1992; Castonguay et al., 2009, Skulski et al., 2010, 2015). These regional developed faults show a ductile to brittle–ductile behaviour and are parallel to sub-parallel to the main lithological contacts and to the  $S_R$  foliation fabric (**Figure IV.1**). Two of these thrust sheets, the Scrape and the Deer Cove thrusts, are of great importance for the present study due to their spatial and genetic association to the investigated gold deposits.

The Scrape thrust is the most significant feature within the study area. It overthrusts the greenschist-grade metamorphic rocks of the Point Rouse Complex to the north, over the amphibolitic rocks of the Pacquet Harbour Group (PHG) to the south (**Figure IV.1**) (Castonguay et al., 2009). The fault zone shows a sinuous trace and consists of segments that dip gently to moderately ( $25 - 45^\circ$ ) towards NW, N and NE (**Figure IV.1; Figure IV.5**). Along its outcrop trace, lenses of intensively altered ultramafic rocks occur (**Figure IV.1; Plate IV.6- A**). A mylonitic composite foliation fabric ( $S_{LC}$ ) is characteristic within and in the proximity of the thrust zone.

In the Pine Cove area, the fault zone, and the basal part of the hanging wall are characterised by intense sheared, folded, and brecciated zones. The brecciated intervals contain a high amount of quartz-carbonate vein fragments surrounded by a chlorite-carbonate  $\pm$  sericite altered matrix, whereas the intense sheared and folded zones display intensively folded foliation-parallel quartz-carbonate veins which are subsequently brecciated (**Plate IV.6- B**). Rounded structures forming “eye” shaped patterns were also observed close and within the fault zone and are interpreted herein as either intrafolial sheath type folds or a result of fold superposition between at least two fold generations (**Plate IV.6– D**). The uppermost part of the footwall unit (first 200m) consists of intensively sheared rocks that display on the foliation plane a strong down-dip stretching mineral lineation generating geometries

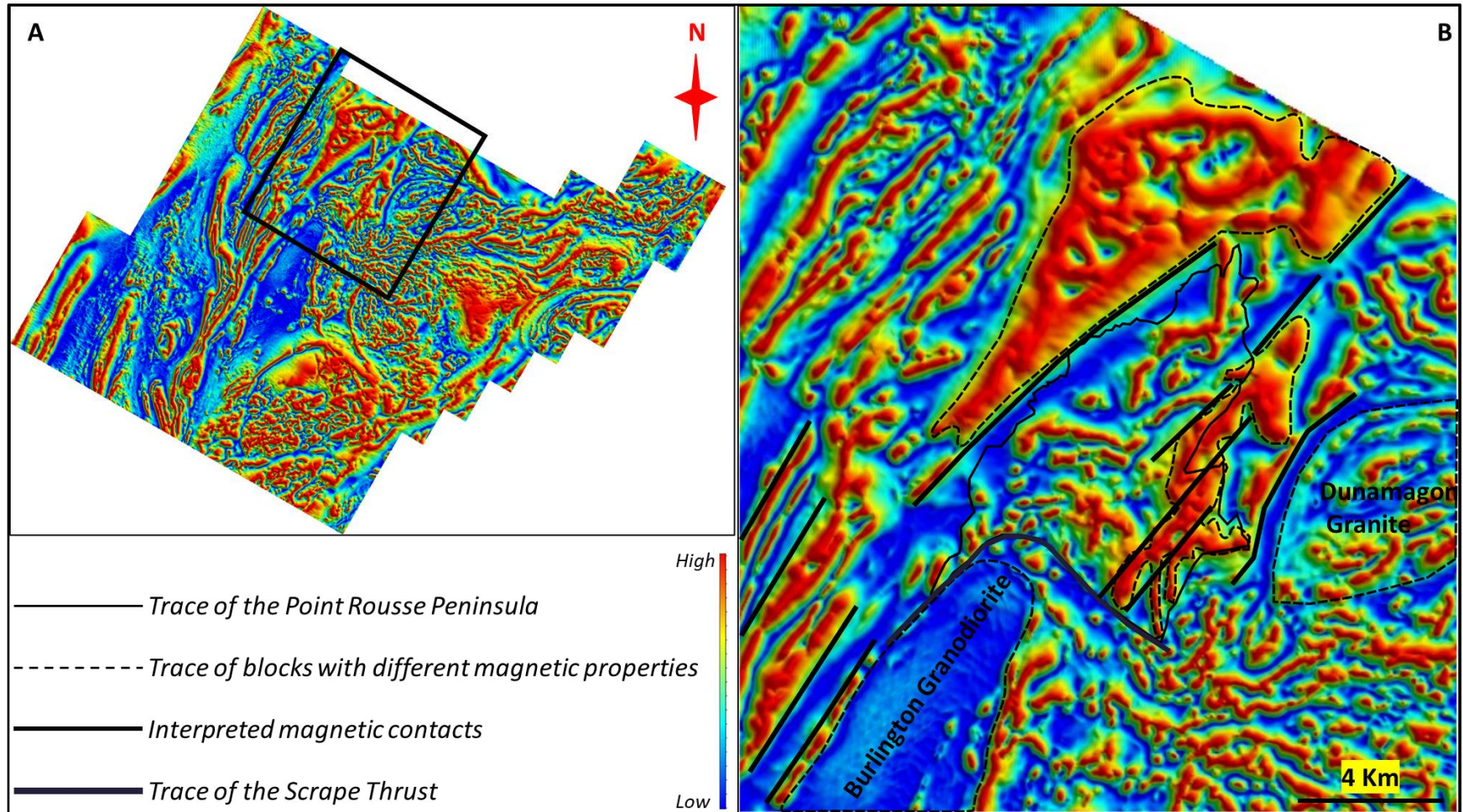


characteristic of “LS” to even “L” type tectonites (*Plate IV.6- E*). In the northern tip of the Burlington Granodiorite, ~700m south from the trace of the Scrape Thrust, a few meters wide, strongly foliated domains, ESE striking and moderately dipping to N were also observed (*Figure IV.1; Plate IV.6 - C*). A well-developed down-dip stretching mineral lineation defined by feldspar and amphiboles occurs in these intervals. These sheared intervals are associated herein with the development of the Scrape thrust based on their orientation and deformation style.

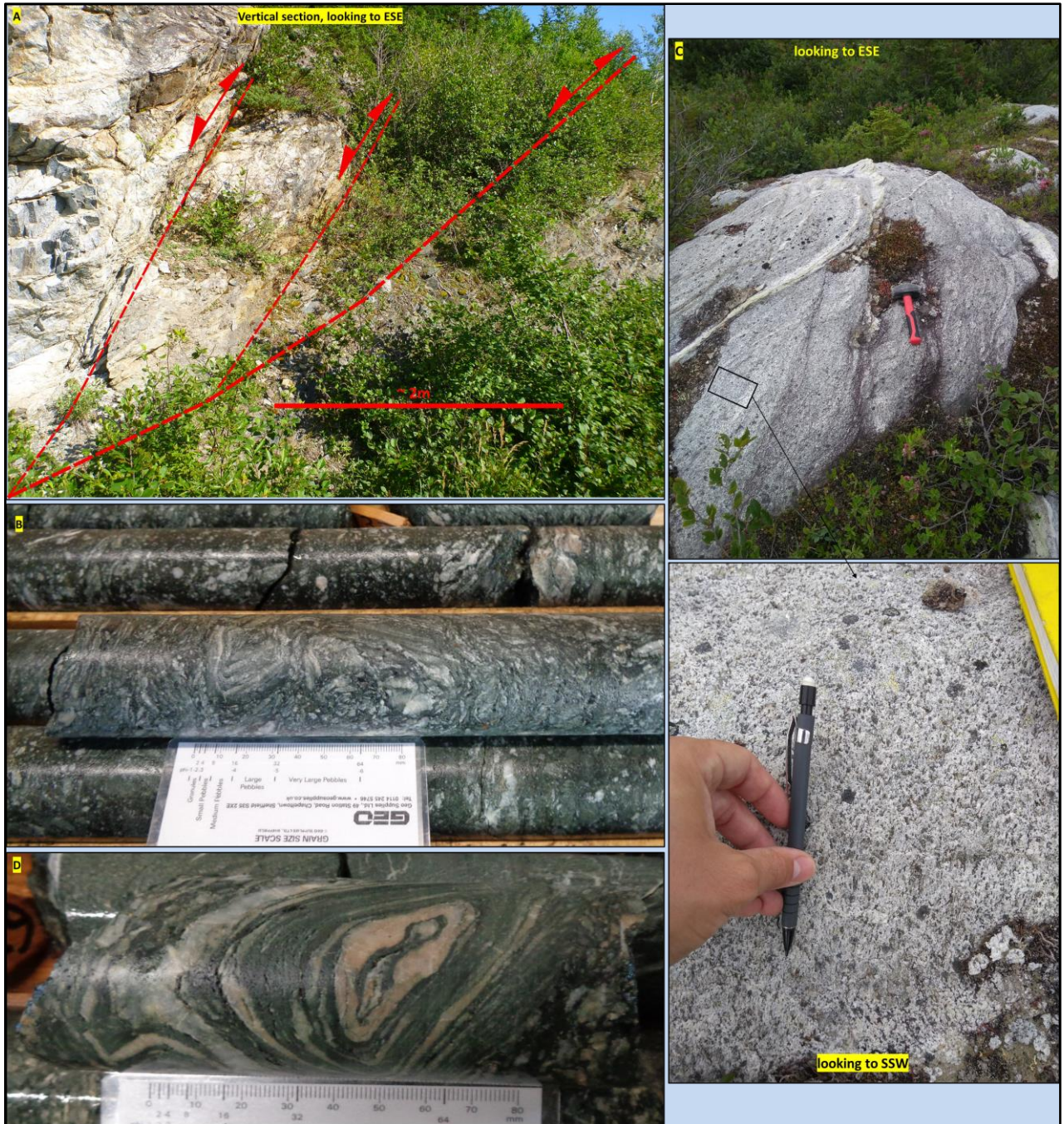
Microscopical analysis of an oriented sample collected from the NNE-NE dipping segment of the Scrape fault, revealed “ $\sigma$ -type” (Zhang & Fossen, 2020) amphibole porphyroclasts that indicate a reverse, top-to-SSW motion (*Plate IV.5– D*). However, amphibole porphyroblasts that overprint the mylonitic foliation and pre-existent porphyroclasts also exist, and their orientation indicate a down-dip motion towards N (*Plate IV.5– E*).

Along the NW dipping segment of the Scrape thrust, a stretching mineral lineation that plunge gently to moderately towards NE-ESE was locally observed within one of the footwall shears. “ $\sigma$ -type” amphibole porphyroclasts observed within a thin section that was cut perpendicular to the foliation and parallel to the ENE plunging lineation indicate an oblique, top-to-SW motion (*Plate IV.5- F*). Furthermore, asymmetric folds that verge to SW are well developed in this area and accommodate a SW directed transport (*Plate IV.1– F*).

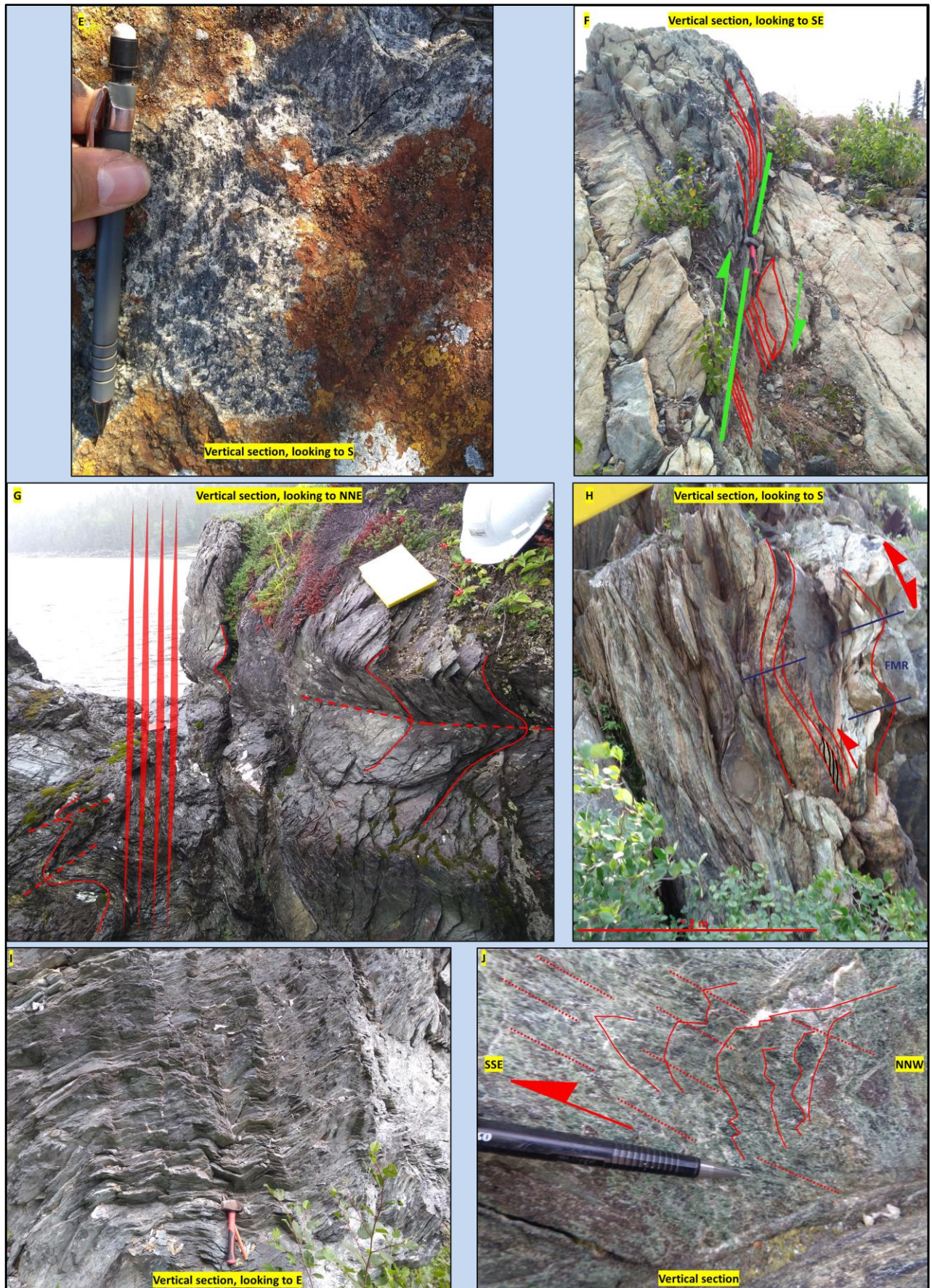
Both the eastern and the western terminations of the Scrape fault are structurally complex. To the west, the Scrape thrust wraps around the northern tip of the Burlington Granodiorite and changes its orientation towards SW (*Figure IV.1, Figure IV.5*). It is not clear if it links with the east directed NE-SW striking thrusts that cut through the Flat Water Pond Group (*Figure. II.4*), or if it stops against these structures. The eastern termination of the fault is masked by moderately to steeply dipping, NNW to NNE trending shear zones that correspond to the contact between the ultramafic ophiolitic rocks of the PRC to the west, the Pacquet Harbour Group to E and SE and the Ming’s Bight Group to NE (*Figure IV.1, Figure IV.5*).

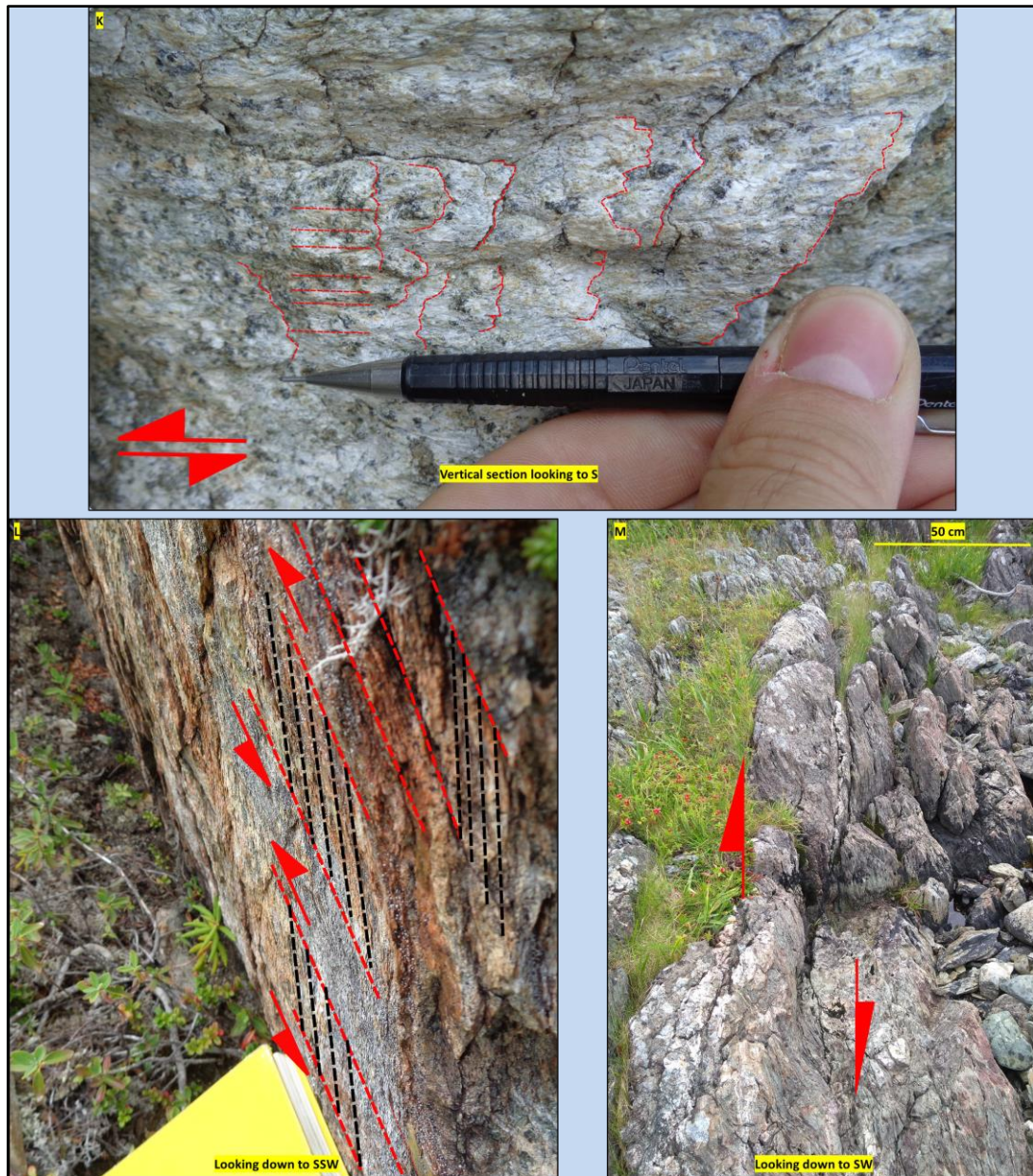


**Figure IV.5** - Tilt Derivative aeromagnetic map of the Baie Verte Peninsula (A); and zoomed in image into the study area (B - black square on image A). **Note** the NNE to NE oriented magnetic lineaments that border the Point Rouse Complex.



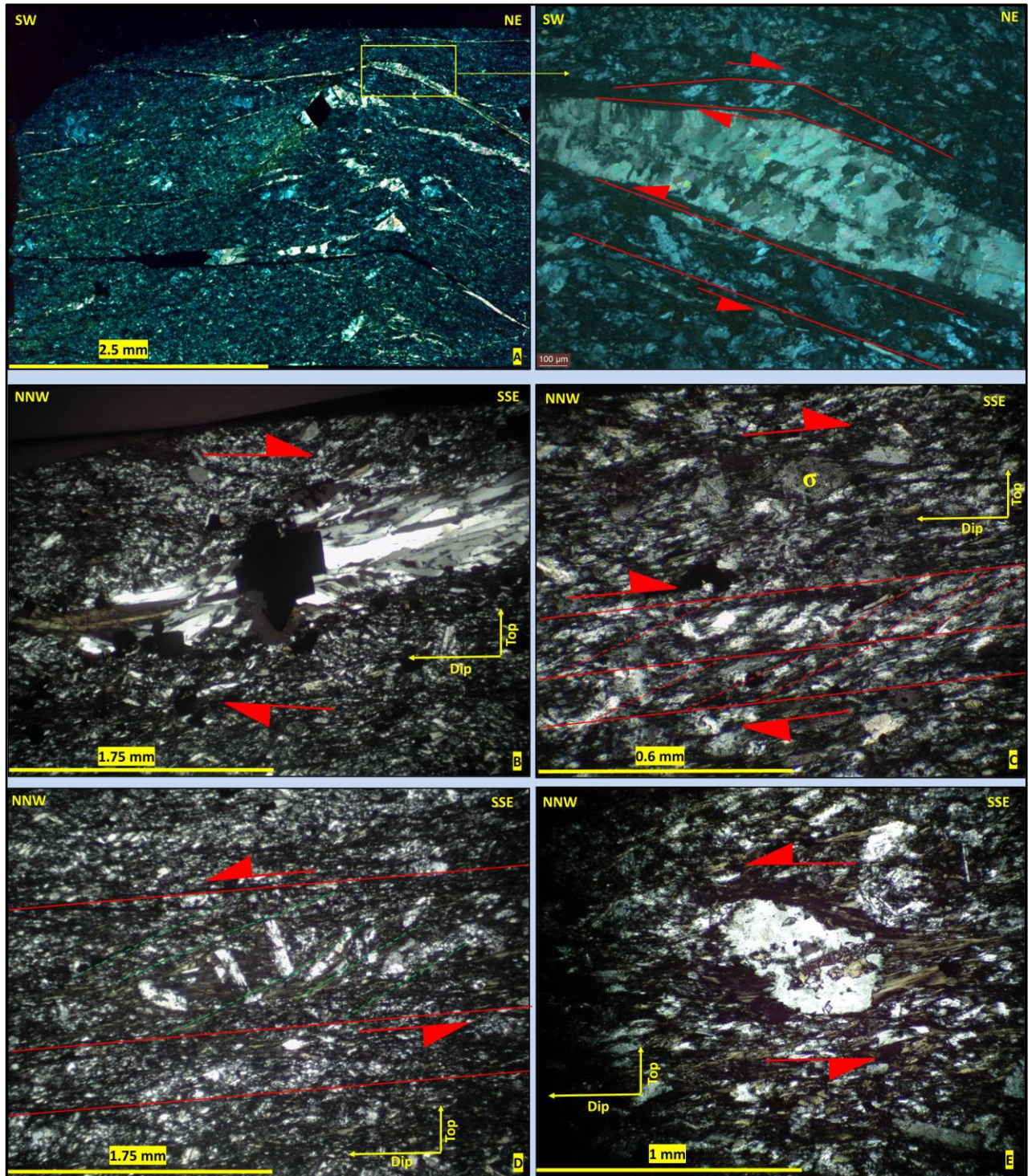
**Plate IV.6** – Representative field photographs for the major ductile to brittle-ductile thrusts (interpreted as  $D_{2a}$  structures) and for the brittle-ductile reverse faults and shears (interpreted as  $D_{2b}$  structures): **A** - Approximately N-S oriented section of the Scrape thrust exposed along the Ming’s Bight Road (NL418); intensively altered (talc-serpentinite) ophiolitic lens of the Point Rouse Complex in the hanging-wall, overthrust on the amphibolitic rocks of the Pacquet Harbour Group in the footwall; red lines represent the trace of the Scrape Thrust and associated shears. **B** - Folded, foliation-parallel quartz-carbonate veins (middle core) and fragments of brecciated quartz-carbonate veins in a chloritic ground mass (upper core) observed in the lower-most part of the hanging wall of the Scrape Thrust; drill core PC-92-112. **C** - Sheared interval in the northern part of the Burlington Granodiorite, **note** the strong, down-dip plunging stretching mineral lineation developed in the sheared interval (zoomed in image). **D** - “Cat eye” structure observed in a strongly deformed interval few meters above the Scrape Thrust, Pine Cove area, drill core PC-92-112. Plate continuation on next two pages.





**Plate IV.6 (Continuation)** – *E* - Strong developed stretching mineral lineation ( $L \geq S$ ) defined by stretched, almost “rod-like” amphibole and plagioclase crystals on the foliation plane within an intense sheared interval in the footwall of the Scrape Thrust, ~ 1 km south from the Pine Cove deposit. *F* - SSE directed, NW-SE striking, reverse brittle-ductile fault (green line) with a dextral component; red lines represent the trace of the foliation drags; Stog’er Tight area. *G* - NNE striking brittle-ductile shear zone affected by  $F_{MR}$  folds; red planes represent the trace of the fault zone, whereas the red lines the contour of the  $F_{MR}$  folds and of the trace of their axial planes; Pine Cove coast. *H* - East directed, reverse brittle-ductile fault, folded and reactivated as normal fault during  $F_{MR}$  folding; red lines represent the trace of the SL foliation and shears; Note the relic “S-C” fabric configuration that indicate reverse movement; blue lines show the trace of the  $F_{MR}$  axial planes; Ming’s Bight area. *I* - Steeply dipping to south, E-W oriented kink bands generating south verging folds above the steeply dipping hanging wall segment of the Deer Cove thrust. *J* - Steps and associated oblique stretching mineral lineation on a NE dipping shear zone indicating reverse motion towards SSE; same fault as the one presented in **Plate IV.4– C**. *K* - Horizontal slicken-fibres that indicate sinistral motion on a brittle-ductile, N trending fault in the Ming’s Bight area. *L* - “S-C” fabric geometry indicating sinistral, S directed motion along the NNE oriented segments of the Deer Cove Thrust; red dashed lines correspond to the “C” planes, whereas the black dashed lines to the “S” planes. *M* - Steeply dipping, NE-SW oriented shear zone observed along the Pine Cove coast; foliation drags indicate NW side-down motion combined with a dextral component.

The Deer Cove thrust outcrops in the northern part of the region and overlaps pillow basalts from the upper part of an overturned ophiolitic sequence in the hanging wall, over the lower ultramafic section of another ophiolitic sequence in the foot wall (**Figure IV.1; Plate IV.4- D**) (Gower et al., 1991; Patey and Wilton, 1993). The Deer Cove fault shows an undulating shape being composed of segments that trend to NW, N and NE (**Figure IV.1**). During the mapping campaign only the central and western segments of this fault were examined. Along these portions the Deer Cove fault dips moderately to steeply (40°- 65°) to both north and north-east. Both within the fault zone and in the hanging wall, “S-C” fabric configuration, as defined by Lister & Snoke, (1984), is locally developed and record a reverse, north over south transport direction (**Plate IV.4 - E**). A mylonitic composite foliation and a strong down-dip to slightly oblique plunging stretching mineral lineation is characteristic for the fault zone and for both the hanging and footwall rocks. Locally, a NE to ENE moderately plunging stretching mineral lineation was also observed within the fault zone. Microscopical analysis of an oriented thin section that was cut parallel to the NE-ENE plunging stretching mineral lineation and perpendicular to the foliation revealed micro-folds that verge to SW (**Plate IV.7- A**). Within the same section, internal deformation of a carbonate vein, together with adjacent “S-C” fabric formed between inclusions trails in feldspar porphyroclasts (interpreted as the “S” plane) and a chlorite foliation fabric (interpreted as the “C” plane) show contradictory movement directions: reverse, top-to-SW and down-dip motion, towards NE (**Plate IV.7- A**). In drill core, the fault is defined by a narrow zone (~1 – 2 m) of gouge material followed by a strongly folded and sheared interval of approximately 4 meters length. The footwall rocks show an intense talc-carbonate alteration.



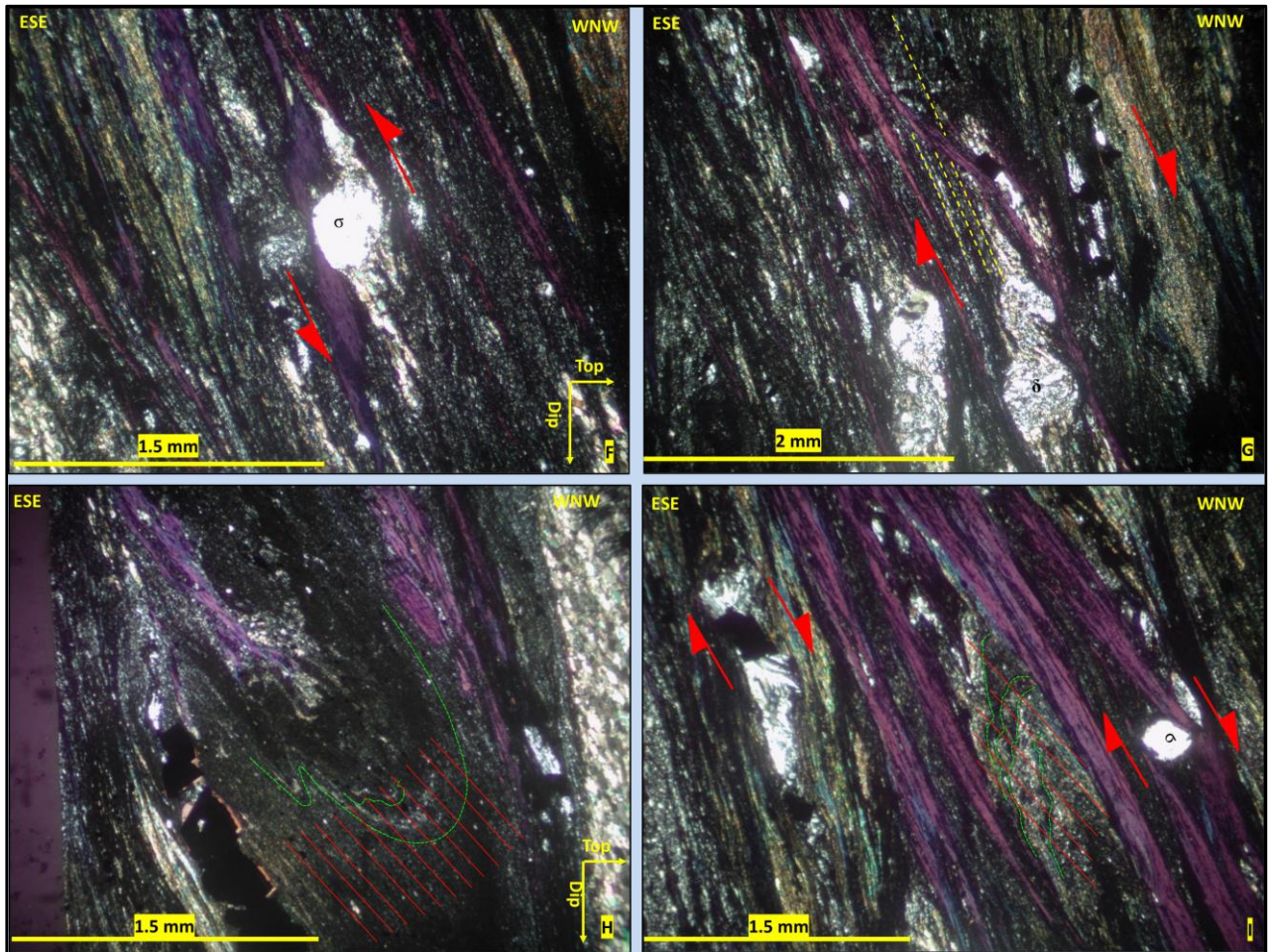


**Plate IV.7** – Representative photographs of microstructural elements that suggest South directed transport along the  $D_{2a}/D_{2b}$  structures and also their reactivation as extensional structures (down-dip sliding): **A (XPL)** – full section scan of an oriented thin section that was cut parallel to the NE-ESE plunging stretching mineral lineation observed locally in the hanging wall of the Deer Cove thrust; **note** the SW verging microfold and the and the contradictory movement direction indicated by feldspar porphyroclasts and the local foliation fabric (red continuous lines) defined by chlorite in the zoomed-in area; **B (XPL)** - quartz chlorite pyrite fringes indicating reverse, top to SSE motion. **C (XPL)** – C-S fabric formed between the main foliation (red continuous lines) and a pre-existent fabric defined by fine grained recrystallised quartz feldspar chlorite (red dashed lines) indicating reverse motion to SSE; **note** the  $\sigma$  type porphyroclast from the upper part of the section that suggest the same movement direction. **D (XPL)** - Rotated feldspar porphyroclasts between chlorite shear bands (green lines) forming at a low angle to the main foliation (red lines) indicating down-dip motion towards north. **E (XPL)** -  $\sigma$  type porphyroclast partially replaced by chlorite, indicating down-dip movement towards north. **B to E** images are from a sample collected from a brittle-ductile, ENE striking shear zone (interpreted as  $D_{2b}$ ) from the Big Head area. **F (XPL)** -  $\sigma$ -type feldspar porphyroclast indicating up-dip motion, top-to-ESE. **G (XPL)** -  $\delta$ -type feldspar porphyroclast and quartz pyrite fringes indicating down-dip motion towards WNW; **note** the crosscutting relationship between the pre-existent foliation fabric (yellow, dashed line) and the late fabric defined by chlorite (anomalous purple color). **H & I (XPL)** - relic  $S_R$  foliation fabric (green dashed lines) preserved in the hinge zones of ESE verging microfolds (**H** – part of synform, **I** – part of antiform) and  $S_L$  axial planar cleavage of the folds (red lines) overgrown by a later fabric defined by chlorite (blue – purple anomalous colour); **note** the low intersection angle between the late fabric and  $S_L$ , and the  $\sigma$ -type quartz porphyroclast and pyrite fringes that indicate down-dip motion in **I**. **F to I** images are from a sample collected from a brittle-ductile WNW dipping shear zone observed in the Green Cove area interpreted as a reactivated  $D_{2b}$  fault.

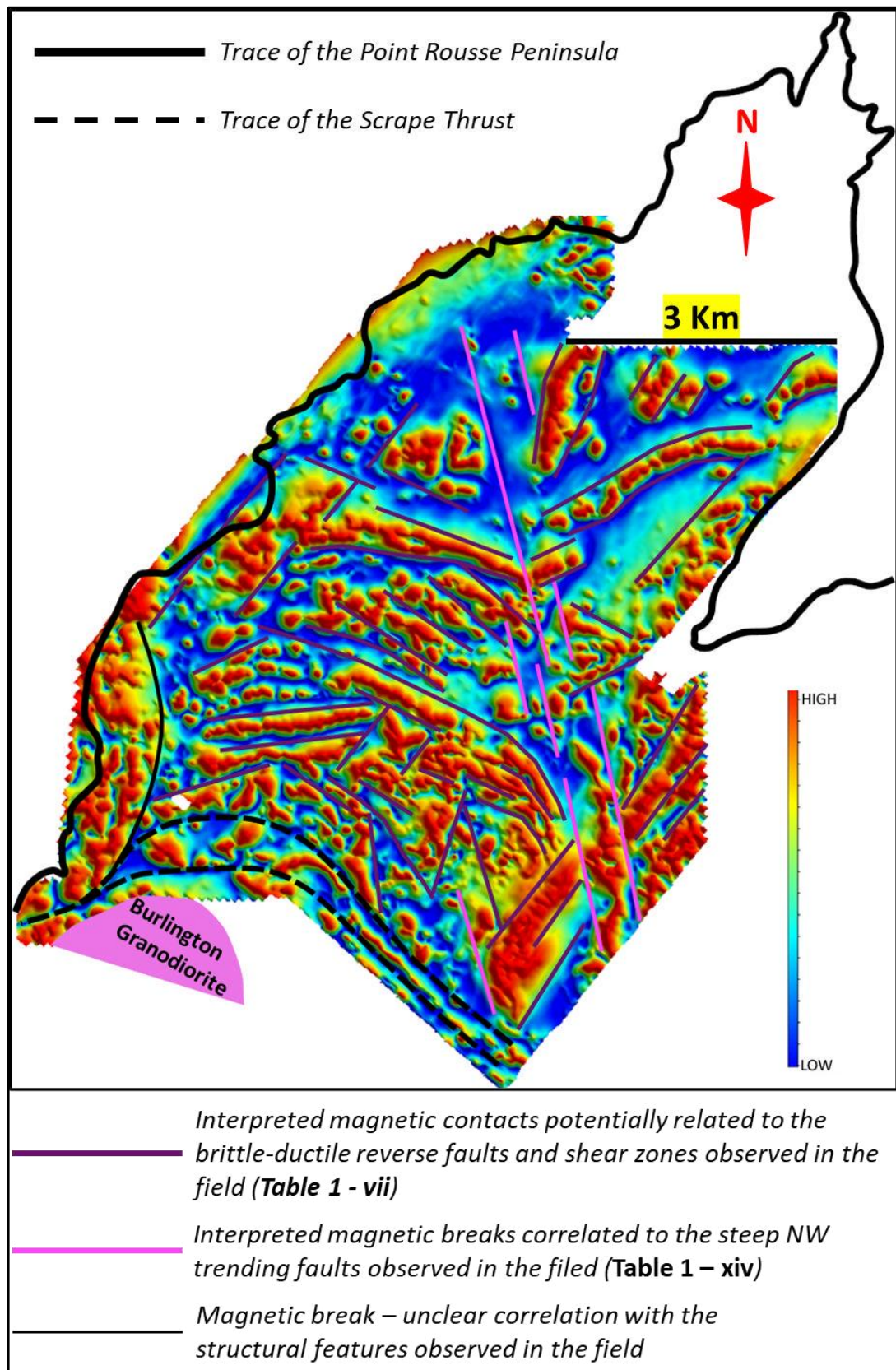


**IV.1.3.B. Brittle-ductile, reverse faults and associated shears (Table IV.1– vii)**

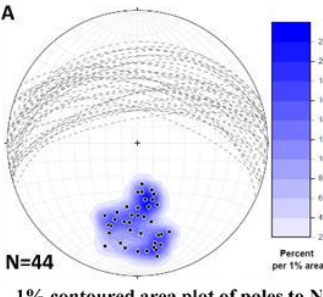
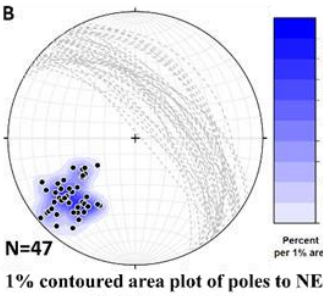
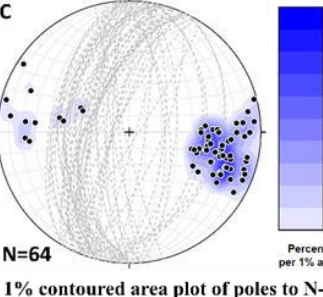
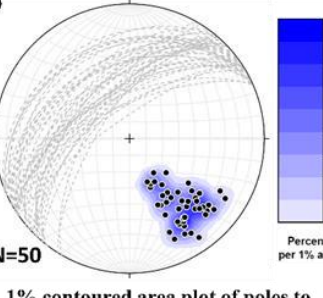
Four main brittle-ductile fault systems that affect both the  $S_R$  foliation and the  $F_i$  folds were recognised within the Point Rouse Complex (**Figure IV.1; Figure IV.7**): **a)** N dipping, E-W striking thrusts and reverse faults (**Plate IV.1 – E; Figure IV.7 - A**); **b)** NE to ENE moderately to steeply dipping, NW to NNW oriented, reverse faults and dextral shear zones (**Figure IV.1; Plate IV.6– F; Figure IV.7- B**); **c)** N-S and NNE trending, E directed reverse faults and steeply dipping sinistral shear zones (**Figure IV.1; Plate IV.6– H; Figure IV.7- C**); and **d)** reverse faults and shear zones with ambiguous kinematics that dip moderately to steeply to WNW - NW (**Figure IV.1; Plate IV.2– G; Figure IV.7– D**). On the Tilt Derivative aeromagnetic map of the central-south part of the Point Rouse Complex, lineaments with similar orientations separate lithological bodies with different magnetic properties. It is interpreted herein that at least a part of these lineaments are related to the four brittle-ductile fault systems observed in the field during the mapping campaign (**Figure IV.6**).

**a)** The approximately E-W trending thrusts and reverse faults accommodate a N over S transport direction and affect the entire PRC. These structures are best developed in the hanging-wall of the Scrape thrust where they occur as fault imbricates connected by low angle thrusts (**Plate IV.1- E**). Similar architectures were observed to a lesser extent in the hanging wall of the Deer Cove thrust. The faults show a spatial association with the  $F_{SV}$  folds being sub-parallel to their axial planar cleavage and cutting through their forelimbs generating an overall geometry characteristic of “*fault propagation folds*” (Suppe and Medwedeff, 1990).

Microstructural analysis on a thin section cut parallel to the down-dip plunging stretching mineral lineation of an oriented sample collected from an ENE striking shear zone from the Big Head area (**Figure IV.1**) confirmed the reverse nature of the E-W oriented faults because *S-C* fabric configuration,  $\sigma$ -type feldspar porphyroclasts and quartz-chlorite pyrite fringes that indicate a reverse, up-dip motion towards south were observed (**Plate IV.7- B, C**). However, fragmented, and rotated feldspar porphyroclasts between chloritic shear bands formed at a low angle to the main foliation fabric, together with  $\sigma$ -type feldspar porphyroclasts partial replaced by chlorite, indicate a down-dip movement towards north which is associated here with a later reactivation of the faults (**Plate IV.7– C, D**).



**Figure IV.6** – Tilt derivative aeromagnetic map of the central-south part of the Point Rouse Complex.

Structure	Characteristics	Location
<p><b>A</b></p>  <p>N=44 1% contoured area plot of poles to N dipping faults</p>	<p>Moderately to steeply dipping, E-W trending, south directed thrusts and reverse faults; Spatially and genetically associated with the <math>F_{SV}</math> folds.</p>	<p>Common in the entire PRC, but best developed in the Pine Cove area, in the hanging wall of the Scrape Thrust.</p>
<p><b>B</b></p>  <p>N=47 1% contoured area plot of poles to NE-ENE dipping faults</p>	<p>Moderately to steeply dipping, NW to NNW trending faults; Show brittle-ductile to brittle characteristics; Accommodate N over S transport direction, locally combined with dextral motion component; Reactivated as sinistral faults during younger deformational stages.</p>	<p>Common in the entire PRC, but best developed in the Deer Cove and Stog'er Tight areas.</p>
<p><b>C</b></p>  <p>N=64 1% contoured area plot of poles to N-NNE trending faults</p>	<p>~N-S trending faults that dip moderately to steeply to W-WNW or, locally, to E-ESE; Mostly sinistral faults and E directed reverse faults. Locally reactivated showing W to NW down-dip motion and dextral kinematics.</p>	<p>Well-developed in high strain domains; Mark the SE contact between the PRC and PHG; define the trace of the lower ultramafic ophiolitic unit in the Deer Cove area.</p>
<p><b>D</b></p>  <p>N=50 1% contoured area plot of poles to WNW-NW dipping faults</p>	<p>Moderately to steeply dipping, NNE to NE oriented faults with contradictory, both sinistral and dextral kinematics; Locally the dextral component it is associated with oblique, dip-slip motion to NW.</p>	<p>Well-developed along the SE contact between the PRC and PHG and along the W coast; Show a spatial association with the N to NNE trending faults.</p>

**Figure IV.7** – Southern-hemisphere, equal-area, stereographic projections of the reverse, brittle-ductile fault measurements from the Point Rouse Complex.

*b*) Faults and shear zones that dip steeply ( $50^{\circ}$ - $80^{\circ}$ ) to NE-ENE occur in the entire Point Rousse Complex. In the Deer Cove area this fault system shows brittle-ductile characteristics and displays both oblique and dip slip kinematic indicators which suggest a reverse, top-to-south motion (*Plate IV.6– J*). Gently plunging to horizontal steps and slickenfibres are locally developed on the fault planes and reveal a dextral horizontal motion component. Along the Deer Cove coast, these shears contain a  $S_{LC}$  mylonitic foliation, are approximately 5 m in width and show an intense alteration composed of fuchsite and iron oxides (*Plate IV.4– C*). Oriented samples were collected from these shear zones and used for microstructural analysis. Fragmentation and rotation of feldspar and chromite porphyroclasts and their associated strain shadows support the macroscopic observations indicating a reverse, top-to-south directed movement (*Plate IV.5– A, G*). Moreover, a relic fabric which is preserved as inclusion trails in fragmented quartz and feldspar porphyroclasts creates a “*S-C*” fabric geometry with the  $S_L$  foliation planes and suggest the same south directed motion (*Plate IV.5– A, B*). Calcite fibre steps that locally overgrow the slickenfibres/slickensides associated to the south directed motion are present on some of these faults and indicate a down-dip motion towards north. Under the microscope, rotation and recrystallisation of pyrite porphyroclasts together with related strain fringes suggest opposing movement directions: up-dip movement to the south and down-dip motion to the north (*Plate IV.6– K, J*). A crenulation fabric that affect the  $S_R$  and the  $S_L$  foliations is also visible under the microscope (*Plate IV.5– B, H, I*). This can be interpreted as either a  $C'$  plane formed in a *C-S-C'* configuration during the top-to-S motion, or as a shear band formed in response to the later down-dip motion accommodated by the main foliation planes.

In the Stog'er area, NE to ENE dipping faults that affect the main foliation fabric show a more brittle nature and are usually associated with centimetre-wide zones of chloritic gouge that forms along their outcrop trace. Foliation drags around the faults indicate top-to-SSE movement (*Plate IV.6– F*). The faults are affected by both the recumbent, north verging  $F_{MR}$  folds and by the north trending  $F_{NT}$  folds and show evidence of later reactivation. A similar fault set which dips steeply to NE-ENE and which forms a “*S-C*” type geometry with the  $S_R$  foliation suggesting a horizontal dextral motion (hanging wall-to-SE) was also observed in the Corkscrew

area (*Figure IV.1*). In this case, the faults were observed in top view so no indicators regarding their dip slip component were noticed.

In the Pine Cove area, the NE dipping thrusts, and reverse faults are common on the NE dipping limb of a large, open, north plunging anticline delineated by the Anaconda Mining geologists (*Figure IV.1*) (Pitman et al., 2020). Likewise, NW dipping thrusts and reverse faults occur on the NW dipping limb of the north plunging anticline.

c) The entire Point Rouse Complex is affected by N to NNE striking faults that cut the  $S_R$  foliation and the E-W oriented thrusts with a sinistral motion. This fault system marks the south-eastern contact between the Point Rouse Complex, Pacquet Harbour Group and Ming's Bight Group (*Figure IV.1*). The faults dip moderately to steeply to W – WNW and occur both on the western and eastern sides of the ophiolitic body and within it. Anderson (1998) and Castonguay et al. (2009) described these faults as sinistral shear zones combined with a reverse component directed towards east. Anderson (1998) recorded a shallowly south plunging mineral lineation and slickenfibres on both the foliation and on the fault planes. However, during this study, stretching mineral lineations that plunge gently to steeply to both north and south were observed, as well as horizontal to gently plunging talc-serpentinite slickenfibres that suggest both sinistral and dextral motions (*Figure IV.4– J; Plate IV.6– K*). Furthermore, the reverse component described by the above-mentioned authors is less clear because the faults are affected by recumbent folds that overprint the kinematic indicators associated to the up-dip movement (*Plate IV.6- H*).

In the north-central part of the PRC, both north and south from the Deer Cove thrust, N and NNE striking faults that dip moderately to steeply towards W-WNW define the map trace of the lower ultramafic unit of the ophiolitic sequence (*Figure IV.1*). “S-C” fabric geometry together with talc and serpentinite horizontal and oblique slicken fibres indicate a sinistral sense of motion combined with both reverse and normal dip-slip components (*Plate IV.6- L*).

d) NW dipping, NE-SW striking faults occur in association with the N-NE trending shears along the south-eastern boundary of the Point Rouse Complex and along the western coastline (*Figure IV.1*). The kinematic indicators associated to these faults show contradictory motion directions: sinistral and dextral horizontal

movement and both up-dip and down-dip slip components. The kinematic indicators that suggest a dextral motion usually overprint the indicators related to sinistral movement. These faults affect the  $S_R$  fabric and are locally folded by the recumbent  $F_{MR}$  folds (*Plate IV.6- G*).

A prominent shear zone composed from multiple segments that dip moderately to steeply to W and NW outcrop sporadically along the western coastline all the way from Pine Cove to Green Cove (*Figure IV.1*). Along the Pine Cove coast, the shear zone has a N to NNE trend, but further north swings gradually towards NE. Within the shear zone a mylonitic foliation with a down dip plunging stretching mineral lineation is characteristic. The kinematic indicators associated to this large-scale fault zone are ambiguous, but locally foliation drags indicate a W to NW side-down motion combined with a dextral horizontal component (*Plate IV.6– M*). As well as the NE-SW striking shears, this fault zone cuts through the main foliation and is affected by the  $F_{MR}$  folds (*Table IV.1- viii*). Microstructural analysis on an oriented sample collected from a WNW dipping shear zone observed in the Green Cove area and associated here to this large-scale NNE to NE striking fault, revealed both up-dip and down-dip kinematic indicators (*Plate IV.7- F, G*). The fabric associated with the down-dip motion forms at a very low angle and overgrows two pre-existent foliations related to ESE oriented microfolds (*Plate IV.7– H, I*). These observations suggest that initially the fault accommodated reverse, ESE directed motion, but was later reactivated as a normal fault. The folded fabric is interpreted as the  $S_R$ , whereas the axial cleavage of the microfolds as the  $S_L$ .

#### ***IV.1.3.2 South dipping faults (Table IV.1– xiii)***

A system of extensional, moderately to steeply, roughly E-W oriented, south dipping faults and kink bands affect the entire PRC and are best developed in strongly foliated lithologies (*Plate IV.8 – A, B, C; Figure IV.8- A*). In many areas, the kink bands form on, or at a low angle to the axial planes of both the  $F_{SV}$  and the  $F_{MR}$  folds (*Plate IV.8- A*). Foliation drags indicate that the structures accommodate a normal to oblique movement to S-SE (*Plate IV.8 – B*). Where the shears are closely spaced, the layers are rotated between adjacent shears forming small scale drag-folds (*Plate IV.8– C*). No cross-cutting relationships were observed between these faults and the  $F_{NT}$  folds, but along the Deer Cove coast and in the Big Head area, the kink-bands cut all the pre-existing structures. Along the Deer Cove coast, the faults

correspond to the orientation of the late crenulation fabric described under the microscope in *Plate IV.5– B, H, I*, and may be related. Moreover, in the hanging wall of the Deer Cove and the Scrape Thrusts, these faults together with the N dipping faults show a geometry characteristic of extensional “*synthetic and antithetic*” fault configuration (*Plate IV.1 – E, IV.4 - D*).

#### ***IV.1.3.3 Steep, NW trending faults (Table IV.1 - xiv)***

Steeply to vertical (70°-90°), NW-SE oriented faults and an associated joint set affect the entire PRC (*Figure IV.8 – B; Plate IV.8 - D*). Along the SE margin of the PRC, between the cover sequence rocks and the Point Rouse ophiolitic unit, these faults show an apparent sinistral, right stepping geometry observed in map view (*Figure IV.1*). However, the NW trending faults observed in the field around the SE contact display ambiguous kinematics. Along the western coastline, in the Pine Cove area, a closely spaced joint set that dips steeply to both NE and SW was recorded during the field campaign. Foliation drags between these joints indicate sinistral motion combined with a down-dip component (*Plate IV.8- D*). In the Stog'er area, NW striking faults that dip steeply to SW cut through both the  $F_{MR}$  and the  $F_{NT}$  folds.

A pronounced NW trending break in the magnetic anomalies is also visible on the partial Tilt Derivative aeromagnetic map of the Point Rouse Complex, in the south-eastern and north-central parts of the region (*Figure IV.6*). This kilometre-scale break is associated here with the NW trending fault system identified in the field because it affects the N-NE and the E-W oriented magnetic lineaments related to the brittle-ductile reverse faults and shear zones (*Table IV.1 - vii*).

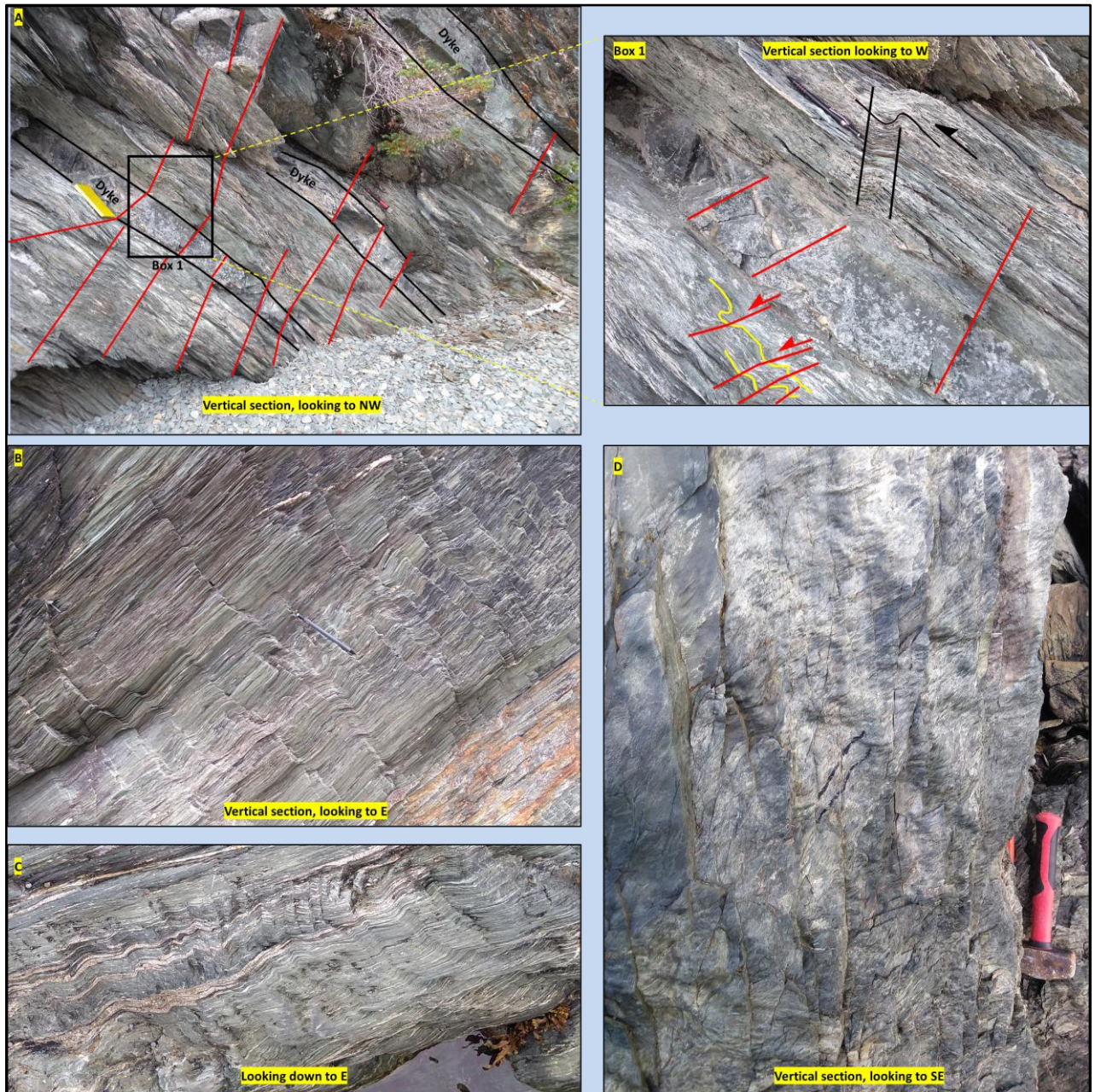


**Plate IV.8** – Representative field photographs for both the south dipping faults and steep, NW trending faults (interpreted as syn-to-post  $D_4$ ): **A** – South dipping extensional kink bands (red lines) overprinting both the E-W oriented, kink band and associated south verging fold (black lines – box 1), and the north verging folds (yellow lines represent the trace of the folded foliation); eastern coastline, ~ 200 m south from the Big Head area. **B** – South dipping faults and kink bands exposed along the Deer Cove coast. **C** – Microfolds resulting from layer rotation between closely spaced south dipping shear bands, Deer Cove coast. **D** - Steeply to vertical, NW-SE oriented, closely spaced joints exposed on the western coastline in the Pine Cove area; **note** the foliation drags between the joints (black lines) indicating normal movement combined with a sinistral component.



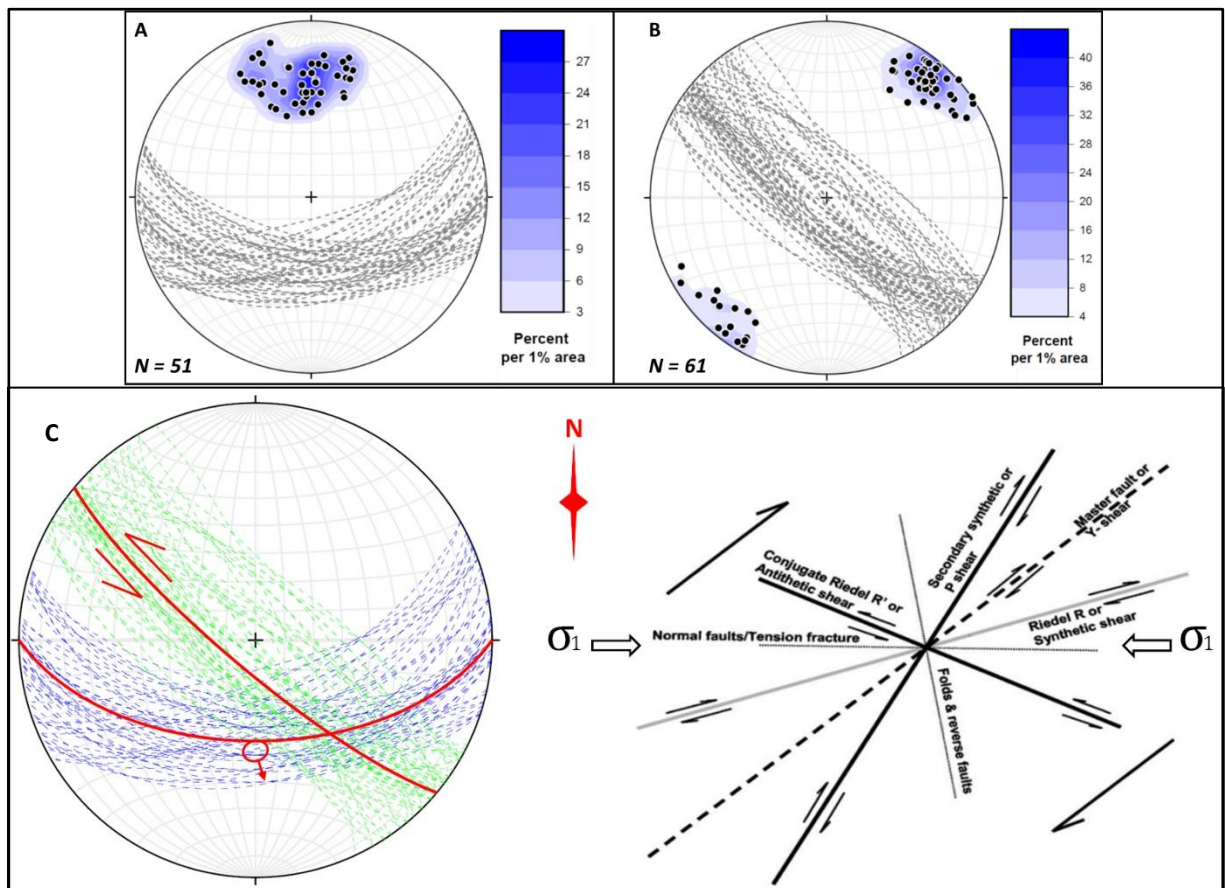
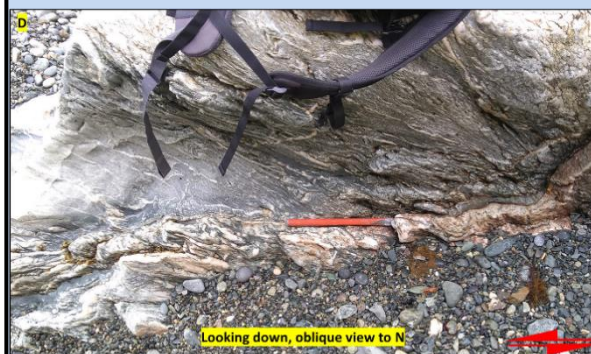
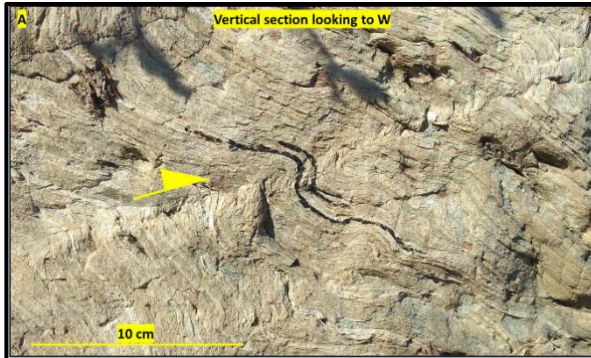


**Figure IV.8** - Southern-hemisphere, equal-area, stereographic projections for the brittle-ductile to brittle faults and shear bands identified within the Point Rouse area; **A** – contoured plot of the poles to the E-W trending, south dipping, extensional faults, and kink-bands. **B** - contoured plot of the poles to the NW-SE trending, steeply to vertical faults that accommodate a sinistral motion combined with a down-dip component. **C** – Combined plot of both fault systems: green dashed lines represent the NW-SE trending faults, the blue dashed lines the south dipping faults and the red continuous lines show the average attitude for the two fault sets. Red arrows represent the fault kinematics, whereas the red circle and arrow the slip vector. Right side of **C** shows an idealized right-lateral simple shear system developed under E-W oriented compression, modified after Tavakoli et al., 2020.

**Plate IV.9 (next two pages)** – Representative field photographs for minor and late structures: **A** – South dipping, reverse shear band associated with asymmetric, north verging fold; Pine Cove area. **B, C** – ESE to SE, steeply plunging folds observed in the Stog’er Tight (**B**) and in the Deer Cove (**C**) areas. **B** – black lines represent the trace of the folded foliation. **C** – green lines represent the trace of the folded pre-existent foliation, the black dashed lines the trace of the fold axial planes/shear bands, and the red lines mark the folding and normal displacement of layers in oblique view. **D, E** – West verging, steeply plunging shear folds, indicating sinistral motion towards W observed in the Deer Cove (**D**) and Pine Cove (**E**) areas. **F** – Late, brittle, E-W striking normal fault affecting all the pre-existent structures within the Pine Cove pit; yellow line represents the trace of the marker horizon (the rusty/oxidized layer). **G** - Shear zone developed at the contact between the Stog’er Tight gabbro and volcano-sedimentary sequences observed in the central part of the PRC.





#### IV.1.3.4 Late, brittle faults (Table IV.1 – xv)

Steeply dipping to vertical, E-W and N-S striking, brittle faults and associated joints occur in the entire PRC and cut through all the above-mentioned structures (*Figure IV.9 – A, B*). The kinematics of the N-S oriented faults are not clear, but the E-W oriented faults show a down-dip throw of approximately 2 meters (*Plate IV.9- F*).

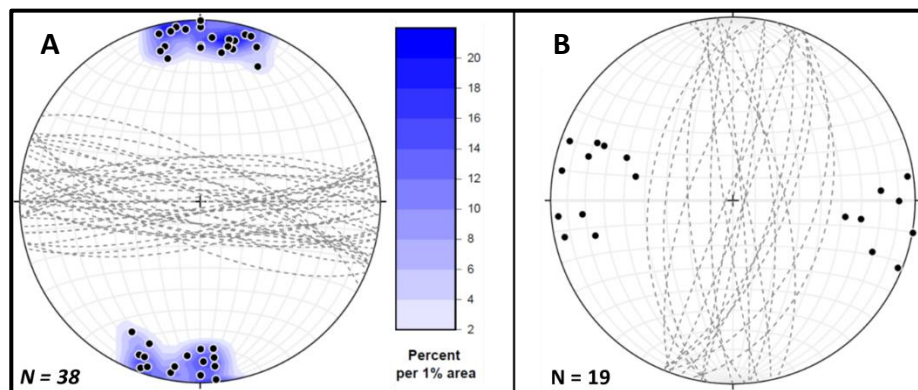


*Figure IV.9* - Southern-hemisphere, equal-area, stereographic projections for the late, brittle faults identified within the Point Rousse Complex. **A** – contoured plot of the poles to the E-W trending, steeply to vertical faults and joints. **B** – poles to the N-S trending faults and joints.

#### IV.1.4 Minor structures

Compared to the rest of the elements described above which are distributed regionally to sub-regionally, there were a couple of small-scale structural elements observed only locally. These structures are described in *Table IV.2* and their correlation with the rest of the structures is presented in the interpretation section.

*Table IV.2 -Descriptions of minor structural elements identified within the Point Rouse Complex*

No.	Structures	Distribution	Characteristics & Relationships with other structures	Relative age
<b>i</b>	Ductile to brittle-ductile shears	Observed in the central part of the PRC and around the Stog'er Tight deposit	A few meters wide, ductile to brittle-ductile shear zones that are subparallel to the $S_R$ foliation and to the lithological contacts were observed in the field. Best preserved at the contact between gabbro sills and the volcanoclastic sequences ( <b>Plate IV.9-G</b> ). The shears are usually folded by at least the $F_{NT}$ folds, and their present geometries and characteristics reflect a long-lived activity.	Syn-to-post- $D_{2a}$
<b>ii</b>	E-W oriented kink bands	Recorded in the hanging-wall of the E-W trending thrusts and reverse faults, within strongly foliated rocks	E-W oriented kink bands that dip steeply to both north and south; Kink to chevron type folds that plunge shallowly to west and/or to east occur in association with these kink bands and their vergence usually indicate a south directed transport ( <b>Plate IV.6-I</b> ).	$D_{2b}$ , but reactivated during later events
<b>iii</b>	Reverse faults and shears bands	Pine Cove area	The faults are subparallel to the axial planar cleavage of north verging folds. The folds show variable amplitudes, from few centimetres to a couple of meters and have a slightly different geometry comparing to the north verging, recumbent $F_{MR}$ folds ( <b>Plate IV.1-G; Plate IV.9-A</b> ).	$D_{2b}$ or $D_3$
<b>iv</b>	ESE to SE steeply plunging folds	Stog'er and Deer Cove areas	ESE to SE steeply plunging folds, associated with steeply dipping NE axial planes occur in narrow domains bordered by NE dipping, brittle-ductile faults, and affect a strong pre-existent foliation oriented at a relative high angle to their axial planes. The folds were observed from top to slightly oblique view and thus their full geometry and kinematics cannot be properly evaluated ( <b>Plate IV.9-B, C</b> ).	$D_{2b}$ or syn-to-post- $D_4$
<b>v</b>	West verging, shear type folds	Observed along the the Deer Cove and Pine Cove coastlines	West verging, shear type folds, were recorded within lithological blocks with an E-W oriented pre-existent foliation ( <b>Plate IV.9-D, E</b> ). The folds plunge steeply from NNE to E and are associated with a closely spaced crenulation cleavage that dips moderately to steeply from NE to E. The folds indicate a sinistral sense of motion towards W and affect a strong pre-existing schistosity.	Syn-to-post- $D_4$ (?)

## **IV.2 Interpretations**

The following section provides interpretations regarding the structural evolution of the Point Rousse Complex based on the observed geometries, cross-cutting relationships, and on the kinematics of the structures identified in the field. The deformation sequence presented below is compared with the ones of other authors that worked in the area in order to create a consistent deformational model that reconciles the differences in the interpreted deformational events of both deposit and regional-scale studies. Interpretations regarding the overall geometries that resulted from fold superposition processes are also presented.

### **IV.2.1 1<sup>st</sup> deformation phase**

The first deformation phase recorded in the Baie Verte Peninsula is associated by other authors with the WNW-NW directed obduction of the Baie Verte Oceanic Tract (BVOT) on the Laurentian margin during the Taconian Orogeny ( $D_E$  and partially  $D_M$  of Hibbard, 1983;  $D_1$  of Castonguay et al., 2009;  $D_1$  of Skulski et al., 2010, 2015a) (*Table IV.3*). The event was documented from outcrops located in the western and northwestern parts of the peninsula where structural fabrics associated to this phase are best preserved in the Birchy Complex (*Fig. II.4*; Kidd, 1974; Hibbard, 1983, Skulski et al., 2015a). According to different authors, east of the Baie Verte Line (BVL), the Taconic related fabrics are non-existent (Anderson, 1998; Anderson et al., 2001) or poorly preserved (Castonguay et al., 2009, 2014; Skulski et al., 2010, 2015; Willner et al., 2022).

Anderson (1998) considered that the upper part of the ophiolitic bodies and of their cover sequence rocks occupied a higher stratigraphic level within the Taconian thrust stack which prevented them from being subject to intense deformation and metamorphism during the Ordovician. At that time, his theory was supported by the lack of regionally developed, medium to high temperature metamorphism east of the BVL prior to Mid Silurian times and by the fact that the Late Ordovician - Mid Silurian Burlington Granodiorite and the Mid Silurian Dunamagon granite were affected by his interpreted  $D_1$  structures (Anderson, 1998 and references herein). Furthermore, the updated model for the evolution of the Baie Verte Peninsula proposed by Skulski et al. (2010; 2015) in which the Snook's Arm cover sequence rocks formed during the obduction of the BVOT on the Laurentian

margin (*Figure. II.6-C*) also imply that the cover sequence of the Point Rouse Complex (PRC) occupied the highest stratigraphic level during the main stage of the Taconian orogeny. However, new geothermobarometric analyses of rocks from both west and east of the BVL (Willner et al., 2022) suggest that at least partially, the ophiolitic units and the lower section of their cover sequence rocks, including portions of the PRC, have been metamorphosed and deformed in the mid to late stages of the Taconic orogeny, but the structural and geochronological evidence of this event were strongly overprinted or even erased by younger deformational phases.

During this study, structural elements indicative of a WNW or a NW directed transport, specific to the Taconian orogeny, have not been observed in the Point Rouse Complex. Even if such structural elements existed, because of intense subsequent deformation their initial orientations and geometries could have been overprinted and totally transposed into parallelism with younger structures, becoming indistinguishable. Moreover, the early foliation and lineation fabrics ( $S_R$ ,  $L_R$ ) identified in the PRC have the same orientations as the planar and linear fabrics observed in the tip of the ~445 – 433 Ma Burlington Granodioritic Complex (BGC). Hence, these fabrics are interpreted as synchronous, developed syn-to-post emplacement of the BGC. Consequently, all the structures identified within the PRC are interpreted herein in agreement with Anderson (1998) as post Ordovician in age and unrelated to the Taconian deformation event. Nevertheless, for a better correlation between the deformation sequence presented in this section and the deformational events proposed by previous authors, a  $D_1$  terminology related to the Taconic orogeny is included in the deformation record used for this study (*Table IV.3*).

**Table IV.3** – Correlation chart between the structural sequence interpreted within this study and previous works on structural domains from within and outside the Point Rouse Complex (PRC). Pacquet Harbour Group (PHG); Ming’s Bight Group (MBG); Cape Brulé Porphyry (CBP); Cape St. John Group (CJG). Red dashed line = synchronously or progressive deformation.

This Study Point Rouse Complex (PRC)	Hibbard (1983) Paratectonic block (descriptions for PRC)	Callon and Weick (1990) Pine Cove area	Kirkwood & Dubé (1992) Stog’er Tight area	Anderson (1998) Ming’s Bight Area	Castonguay et al. (2009) Point Rouse Complex	Skulski et al. (2010; 2015a) Fleur de Lys Belt (descriptions for PRC)
<b>Post-D<sub>4</sub></b> : Steeply dipping to vertical, E-W and N-S striking, brittle faults	<b>D<sub>1</sub></b> : Steeply and shallowly dipping SL crenulation fabric; minor, moderately to steeply plunging FL folds; NW dipping faults that affect the main foliation	<b>Structures not observed</b>	<b>Structures not observed</b>	<b>Structures not observed</b>	<b>Structures not observed</b>	<b>Structures not observed</b>
<b>Syn-to-post-D<sub>4</sub></b> : *Steeply dipping to vertical, NW-SE striking faults. **Extensional faults and kink bands that dip steeply to moderately to south		<b>Structures not observed</b>	<b>Structures not observed</b>	<b>D<sub>5</sub></b> : Observed on the western side of MBG and eastern coast of PRC; Dextral-normal oblique-slip, south dipping shear zones	<b>Structures not observed</b>	<b>W from PRC</b> , NW-SE oriented faults that accommodate an apparent, NE directed normal motion combined with a sinistral component (e.g. Little Lobster Harbour and Advocate Faults)
<b>D<sub>4</sub></b> : Open to tight, local to regional scale, NW to NE moderately to steeply plunging folds associated with a NNW to NE axial fracture cleavage; Regional developed crenulation lineation; Re-orientation of older folds and reactivation of pre-existing faults and shear zones		<b>D<sub>4</sub></b> : Gently to steeply N-NE plunging, open folds associated with a N striking axial cleavage; Complex fold interference pattern between F4 and pre-existent structures	<b>D<sub>3</sub></b> : Broad N-NE trending anticlines and synclines	<b>D<sub>4</sub></b> : Southeastern margin of PRC, common in the MBG; Dextral, ductile to brittle ductile shear zones (e.g. Grand Toss Cove Shear Zone); Mylonitic S4 foliation, shallowly dipping to S; Open to isoclinal, reclined F4 that verge north and plunge shallowly to W; S-C mylonites common	<b>D<sub>4</sub>: Structures not observed in the PRC</b> ; N-NE trending, upright, open folds associated with a fracture and crenulation cleavage; Recorded in the PHG, CBP and CJG	<b>D<sub>4</sub>-D<sub>5</sub></b> : Dextral transpressional to transtensional shear zones and dextral, steeply plunging chevron folds, identified <b>mostly outside the PRC</b>  <b>D<sub>3</sub></b> : NE trending and plunging cross folds <b>recorded outside the PRC</b>
<b>D<sub>3</sub></b> : Asymmetric recumbent folds with an overall north vergence associated with shears and crenulation cleavage that dip gently to moderately towards south; Moderately north dipping axial planes and shear bands that accommodate north side-down motion are common in high strain domains		<b>Structures not observed</b>	<b>No recumbent folds mentioned</b>  Near horizontal south dipping kink bands – included in their D <sub>2</sub> , but potentially misinterpreted	<b>D<sub>3</sub>: Observed outside the PRC</b> , most common in the north-central part of PHG; Shallowly dipping from SW to SE, S3 crenulation cleavage; Open, recumbent F3 folds, shallowly plunging to N and S, locally reclined; Shallowly south-dipping shear zones	<b>D<sub>3</sub></b> : Moderately to steeply north dipping S3 crenulation cleavage; Kink bands and asymmetric folds indicating N side-down motion; Extensional shear bands associated with the reactivation of the D <sub>2</sub> thrusts as extensional faults; Recumbent folds associated with flat-lying axial planes <b>were observed outside the PRC</b>	<b>D<sub>4</sub></b> : Crenulation fabric that dips steeply to N, extensional kink-bands and shear bands associated with the reactivation of D <sub>2</sub> thrusts as normal faults; Recumbent folds with a gently dipping to SE axial plane <b>catalogued east of PRC</b>

Table continuation on next page

This Study Point Rouse Complex (PRC)	Hibbard (1983) Paratectonic block (descriptions for PRC)	Callon and Weick (1990) Pine Cove area	Kirkwood & Dubé (1992) Stog'er Tight area	Anderson (1998) Ming's Bight Area	Castonguay et al. (2009) Point Rouse Complex	Skulski et al. (2010; 2015a) Fleur de Lys Belt (descriptions for PRC)
<p><b>D<sub>2b</sub>:</b> Development of N dipping, S<sub>2b</sub> crenulation and strain slip cleavage to a mylonitic, composite S<sub>2a/2b</sub> foliation in high strain domains; Dextral, SE striking and sinistral N-NE trending faults with a reverse component; Southerly verging, gently to moderately plunging, open to tight, asymmetric to overturned folds associated with south directed, steep reverse faults</p> <hr style="border-top: 1px dashed red;"/> <p><b>D<sub>2a</sub>:</b> Major south directed thrusts (e.g. Scrape and Deer Cove) associated to large-scale folds overturned southwards; Rare, refolded, tight to isoclinal, small-scale F<sub>2a</sub> folds; Regional developed, bedding parallel, spaced cleavage to penetrative S<sub>2a</sub> foliation that dips from NW to NE and associated with a prominent down-dip stretching mineral lineation</p>	<p><b>D<sub>M</sub>:</b> Bedding parallel to sub-parallel S<sub>M</sub> slaty cleavage; S<sub>M</sub> crosscuts the bedding in the western part of the block; Minor, easterly plunging, upright F<sub>M</sub> folds that are best preserved in Bobby Cove Formation; Major, east trending F<sub>M</sub> syncline, slightly overturned to SE affects most part of PRC; Thrusts that dip steeply to NW are considered coeval with fabric development; Thrusting of the PRC on the PHG along the Scrape thrust</p> <p>Deformation affecting rocks of pre-Ordovician and Ordovician ages may be related to the Taconian Obduction</p>	<p><b>D<sub>3</sub>:</b> South directed thrusts; tens of meter scale, E and S verging, asymmetric to overturned folds; Development of the Scrape Thrust and an associated “<i>fault and thrust belt</i>”</p> <hr style="border-top: 1px dashed red;"/> <p><b>D<sub>1</sub>&amp;D<sub>2</sub>:</b> Two generations of folds associated to the development of regional penetrative cleavage and mineral elongation lineation; Transposition of bedding into parallelism to cleavage</p>	<p><b>D<sub>2</sub>:</b> South verging, asymmetric kink folds; E-SE trending, brittle-ductile shears and kink bands that record N over S movement</p> <hr style="border-top: 1px dashed red;"/> <p><b>D<sub>1</sub>:</b> Regional scale folding; Regional, penetrative, moderately N dipping S<sub>1</sub> foliation with a down-dip stretching lineation; Subparallel to S<sub>1</sub>, meter scale, D<sub>1</sub> shear zones</p>	<p><b>D<sub>2</sub>:</b> Observed in the PHG and MBG, but not in the PRC; Steeply, west dipping S<sub>2</sub> foliation; Locally developed, shallowly plunging to south, L<sub>2</sub> mineral lineation; Sinistral strike-slip motion parallel to S<sub>2</sub>; Symmetric and asymmetric, open to isoclinal, shallowly to steeply south plunging F<sub>2</sub> folds at various scales</p> <hr style="border-top: 1px dashed red;"/> <p><b>D<sub>1</sub>:</b> Regional developed spaced cleavage to a mylonitic S<sub>1</sub> foliation within D<sub>1</sub> shear zones (e.g. Scrape Thrust), variable orientations because of younger deformation events; Prominent N-NE plunging stretching lineation within the foliation plane; Reclined, shallowly north plunging, tight to isoclinal F<sub>1</sub> folds; D<sub>1</sub> structures resulted from the south directed thrusting of the PRC over the PHG</p>	<p><b>D<sub>2b</sub>:</b> S-SE to S trending, transverse shear zones interpreted as tear faults and lateral ramps associated to the S directed thrusts; E directed, sinistral transpressional shears (e.g. the SE contact between the PRC, MBG and PHG)</p> <hr style="border-top: 1px dashed red;"/> <p><b>D<sub>2</sub>:</b> moderately north dipping, spaced cleavage to penetrative S<sub>2</sub> foliation usually containing a down-dip stretching lineation; Tight mesoscopic folds; N dipping, south directed shear zones (e.g. Scrape Thrust)</p>	<p><b>D<sub>3</sub>:</b> S-SW striking, S<sub>3</sub> foliation fabric associated with sinistral, E directed transpressional fault zones</p> <hr style="border-top: 1px dashed red;"/> <p><b>D<sub>2</sub>:</b> SW to NW dipping S<sub>2</sub> foliation; prominent L<sub>2</sub> mineral lineation with locally, L-S developed fabric; Megascopic, E trending, open to tight F<sub>2</sub> folds; South directed thrusts and shear zones (e.g. Scrape Thrust)</p>
<p><b>D<sub>1</sub>:</b> W-NW directed obduction of BVOT on the Laurentian Margin: <i>Not observed in the study area</i></p>	<p>Obduction</p>	<p>Potentially part of D<sub>1</sub></p> <p><b>Structures not observed</b></p>	<p><b>Structures not observed</b></p>	<p>All deformation is considered post-Early Silurian age - no structures associated to Taconian obduction</p>	<p><b>D<sub>1</sub>:</b> Poorly preserved, local, relic S<sub>1</sub> associated to ophiolite obduction and composite S<sub>1</sub>-S<sub>2</sub> foliation fabrics</p>	<p><b>D<sub>1</sub>:</b> S<sub>1</sub> fabric developed locally in the ophiolitic rocks, associated to the obduction event</p>



### IV.2.2 2<sup>nd</sup> deformation phase

The dominant tectonometamorphic phase observed in the Point Rousse Complex (PRC) is related here to a D<sub>2</sub> event. This deformation phase was separated into an early and a late D<sub>2</sub>, noted as D<sub>2a</sub> and D<sub>2b</sub>, respectively. The division is needed to better characterise the progressive evolution of this event, and to record the relative timing of the gold formation with respect to the development of the D<sub>2</sub> structures (see following chapters).

The regional foliation fabric (S<sub>R</sub>), the stretching mineral lineation (L<sub>R</sub>), the intrafolial folds (Fi) and the major ductile to brittle-ductile south directed thrusts presented above are affected by all the rest of the structural elements identified in the field. Thereby, these are interpreted as the oldest structural features formed within the PRC and are ascribed to a **D<sub>2a</sub> phase (PRC)** (*Table IV.1 i-iv & Table IV.3*). These structures can be correlated with some of the structural elements from the D<sub>M</sub> of Hibbard (1983), D<sub>1</sub> of Kirkwood & Dubé (1992) and of Anderson (1998), D<sub>1</sub>-D<sub>2</sub> progressive deformation of Callon & Weick (1990) and from the D<sub>2</sub> phase of Castonguay et al (2009) and of Skulski et al. (2015a) (*Table IV.3*). These structures are thought to be formed in a framework dominated by ductile shearing (Fossen, 2016) based on the strong penetrative to even mylonitic nature of the foliation, the well-developed stretching mineral lineation, and the characteristics of the intrafolial folds (mostly recumbent and rootless).

The mesoscale south verging F<sub>SV</sub> folds, the brittle-ductile reverse faults and shear zones, together with their associated planar fabrics (S<sub>L</sub>/S<sub>LC</sub>) are here assigned to a **D<sub>2b</sub> deformation event** (*Table IV.1v-vii & Table IV.3*). The D<sub>2b</sub> phase can be associated to D<sub>M</sub> of Hibbard (1983); D<sub>3</sub> of Callon & Weick (1990); D<sub>2</sub> of Kirkwood & Dubé (1992) and of Anderson (1998); D<sub>2b</sub> of Castonguay et al (2009) and D<sub>3</sub> of Skulski et al. (2010, 2015a) (*Table IV.3*).

It is interpreted that the D<sub>2b</sub> structures formed after the development of the D<sub>2a</sub> structures, but during the same protracted deformation phase (D<sub>2</sub>) that resulted in response to a N over S transport direction. This interpretation is supported by the following arguments: **a)** the D<sub>2b</sub> structures usually fold and crosscut the D<sub>2a</sub> fabrics and are more brittle in nature compared to the latter; **b)** the straight to slightly rotated nature of the S<sub>R</sub> fabric preserved as inclusion trails in feldspar and amphibole porphyroblasts indicate that the D<sub>2b</sub> deformation occurred post, or in the late stages of the crystal growth (*Plate IV.5 - A, B, C*) (Fossen, 2016); **c)** both the major ductile

to brittle-ductile  $D_{2a}$  thrusts (*Table IV.1- iv*) and the  $D_{2b}$  brittle-ductile fault systems (*Table IV.1 - vii*) observed throughout the PRC accommodate an overall reverse, top-to-S movement; **d**) the stretching mineral lineation, which is interpreted to lie parallel to the transport direction, has a plunging direction towards N-NE on both the regional  $S_R$  foliation and on the local mylonitic composite  $S_{LC}$  foliation from the proximity of the  $D_{2b}$  brittle-ductile reverse faults which suggest that the instantaneous stretching axes remained fairly constant during the entire deformation; **e**) both the regional  $S_R$  foliation and the local developed planar fabrics ( $S_L/S_{LC}$ ) show a general dipping direction towards north; **f**) the mineral associations that define both the  $S_R$  foliation and the later  $S_L/S_{LC}$  fabrics suggest similar metamorphic conditions typical of greenschist facies metamorphism; and **g**) any initial variability in the orientation of the  $D_{2b}$  structures with respect to the  $D_{2a}$  structures, prior to their deformation by later folding events, can be easily explained as a result of strain intensity variations, rheological differences, and strain partitioning phenomena, rather than through reorientation of the maximum principal stress at a regional scale (e.g. Fossen et al., 2019).

#### ***IV.2.2.1 Evolution of $D_{2a}$ and $D_{2b}$ structures***

The ductile nature and the ubiquitous presence of the  $D_{2a}$  fabrics throughout the PRC indicate that their development is related to regional scale folding. Furthermore, the geometry of the intrafolial folds combined with the constant parallelism between the regional foliation and bedding and with their shallow to steeply N dipping attitude, suggest that the regional scale folds are tight to isoclinal and inclined to recumbent. The overturned nature of the stratigraphy towards south, as proposed by Skulski et al. (2015) and by Pitman et al. (2020), is associated herein with the  $D_{2a}$  folding event because none of the following fold generations have neither the scale nor the geometries required to accommodate kilometre scale stratigraphic reversal (*Figure IV.1- B*). However, the initial orientation of the  $F_i(F_{2a})$  folds cannot be restored with high accuracy because each of the later folding events would have, at least locally, reoriented and reshaped them. Also, the formation and the original geometry of the  $F_i$  folds may have been very complex from the start: e.g. the folds could have formed at a high angle to the shearing direction but subsequently rotated towards the flow direction (in this case towards south) and/or they could have developed directly as sheath type folds similar to the

models proposed by Alsop (1992) and Alsop & Holdsworth (1999) for the formation of the early “ $D_2$ ” folds from the Irish and Scottish Caledonides.

The major ductile to brittle–ductile thrusts from the PRC (e.g. Deer Cove and Scrape thrusts, **Figure IV.1; Table IV.1 - iv**) are interpreted as long-lived structures that accommodated strain during multiple deformational events. The early development of the faults is interpreted as syn-to-post  $D_{2a}$  regional scale folding. This is supported by: **a**) the thrusts are parallel to sub-parallel to the main lithological contacts and to the regional foliation fabric (**Figure IV.1- B**); **b**) overall, the orientation of the stretching mineral lineation remains constant across the entire area, plunging moderately to steeply towards north both within and outside the fault zones; **c**) most of the structures that affect the  $D_{2a}$  fabrics also reactivate or fold the major thrusts; and **d**) the brittle textures observed within the fault zones are usually superimposed on the ductile fabrics and so are interpreted to be related to later reactivations rather than to the early development of the faults.

The exact relationships between the development of the thrust sheets and of the large-scale  $D_{2a}$  folds cannot be restored with certainty based only on the observations presented above. It is not clear if the major thrust panels represent branches of a main sole thrust that culminates with the Scrape fault or which goes even further into Point Harbour Group, or if they are related to separate subparallel low-angle detachment zones located at different levels in the stratigraphic stack. Regardless, it can be inferred that the Scrape fault represents one of the lower-most detachment zones within the PRC based on its location at the boundary between greenschist facies and amphibolite facies domains and on the higher strain rates recorded in its proximity compared to the rest of the thrusts that occur within the area. Considering the overturned nature of the stratigraphy towards south, the top-to-south transport direction accommodated by the thrusts, and the north plunging transport-parallel stretching mineral lineation, it is possible that the main sole thrust acted initially as the “*root zone*” for the large scale recumbent folds and evolved with splays that cut through the overturned limb of the folds in response of continuous shortening and fold lock-up, similarly to other models proposed for the formation of “*fold/thrust nappes*” (**Figure IV.10- A**) (Twiss & Moores, 1992; Alsop et al. 2010; Poblet & Lisle, 2011; Bastida et al., 2014 and references herein). The existence of the Burlington Granodiorite Complex (BGC) prior to folding and

faulting may have facilitated the fold lock-up by acting as a “buttress” that hindered the normal propagation of the thrust nappes. It is inferred herein that after the initial development of the  $D_{2a}$  large-scale recumbent folds and thrust zones, continuous shortening against the BGC led to steepening of the early fabrics, to internal imbrication and folding of the thrust blocks and to the reactivation of the major thrust sheets during the  $D_{2b}$  event (*Fig. IV.10 - B*).

Previous authors interpreted the NW and the NE dipping segments of the Deer Cove and Scrape thrusts as oblique ramps, whereas the N dipping parts as frontal thrust ramps (Calon & Weick, 1990; Dubé et al., 1993; Anderson, 1998). The field observations presented in this study support this interpretation. Furthermore, the presence of the oblique to shallow plunging stretching mineral lineation that overprint an early down-dip plunging stretching mineral lineation, together with the composite nature of the foliation fabric within the different segments of the faults indicate a  $D_{2b}$  evolution for the thrust ramp geometry. The NW, NE and N dipping, south directed, reverse faults and shear zones (*Table IV.1vii; Figure IV.7*) identified in the central parts of the PRC and in the hanging wall of the major thrust panels are interpreted herein as brittle-ductile splays that formed in response to the development of the oblique-frontal-oblique ramp framework (*Figure IV.10- C*). The “*fault-propagation-fold*” geometries observed between the south directed reverse faults and the  $F_{SV}$  folds suggest that the  $D_{2b}$  shortening was accommodated by synchronous faulting and folding (Mitra, 1990; Suppe & Medwedeff 1990; Poblet & Lisle, 2011). The contradictory dip-slip and horizontal motion indicators recorded on some of the  $D_{2b}$  faults reflect fault reactivation during different deformational events (see below).

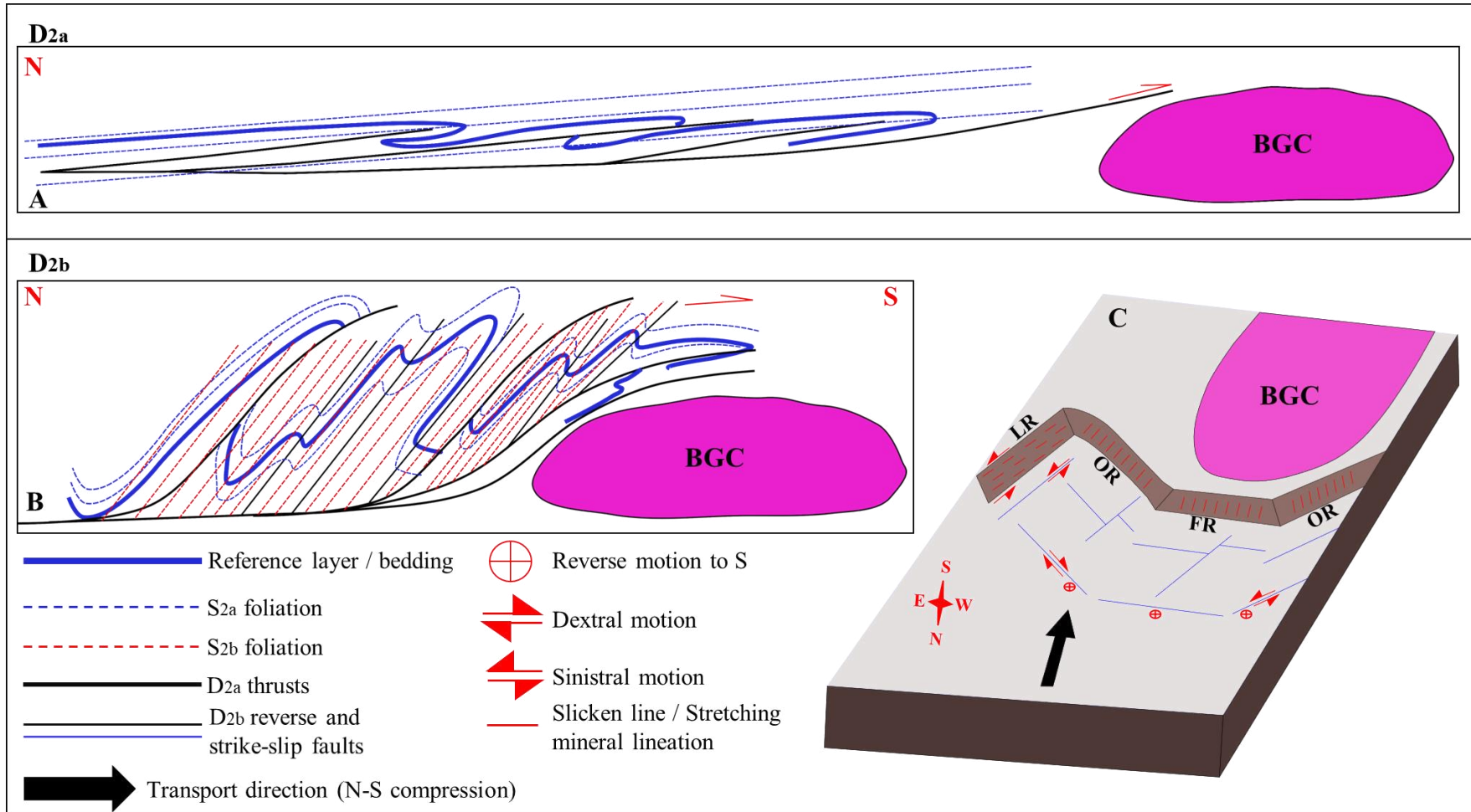


**Figure IV.10** – Cartoons that show the structural evolution of the Point Rouse Complex during the D<sub>2</sub> phase. **A** – Formation of regional-scale recumbent folds and associated thrusts during the early D<sub>2</sub> phase (D<sub>2a</sub>); **B** – Steepening and internal refolding and faulting of the D<sub>2a</sub> structures in response to further shortening against the Burlington Granodioritic Complex (BGC) during late D<sub>2</sub> (D<sub>2b</sub>). **C** – Illustration of the Scrape Thrust ramp geometry and development of D<sub>2b</sub> reverse faults and shear zones with similar orientations. LR = lateral ramp; OR = oblique ramp; FR = frontal ramp.

The brittle-ductile N to NNE trending faults (*Table IV.1 vii; Figure IV.1, Figure IV.5, Figure IV.10-C*) from the PRC were interpreted by previous workers as “tear faults” or “lateral ramps” that formed synchronous with the south verging thrusts and reverse faults (Castonguay et al., 2009; Dubé et al., 1993; Gower et al., 1991 and Kidd et al., 1978). This interpretation is supported by the field observations listed above. The relative age of this fault system is considered here as  $D_{2b}$  because in most places these faults cut through the  $S_R(S_{2a})$  foliation forming composite fabrics that indicate a sinistral motion (hanging wall motion towards south) (*Plate IV.6-L; Figure IV.10-C*). In the Deer Cove area, their evolution seems to be at least partially influenced by the heterogeneous nature of the local stratigraphic stack, because the faults are well developed at boundaries between lithological units with different rheological properties (e.g. the intensively altered part of the lower ophiolitic unit and the more massive gabbroic ophiolitic unit – *Figure IV.1*).

As previously mentioned, the south-eastern border of the PRC (*Figure IV.1*) is also defined by N to NNE oriented faults. These were interpreted by Anderson (1998) as being part of sinistral transpressional shear zone system through which the PRC, PHG and MBG were imbricated. Moreover, the same author described this contact as a lateral ramp of the Scrape thrust formed as a response of large-scale strain partitioning. These interpretations are consistent with the field investigations of this study, and it is inferred that the shear system that represents the south-eastern contact of the PRC has developed synchronously with the frontal and oblique ramp sections of the Scrape Thrust during the  $D_{2b}$  event (*Figure IV.10-C*). As all the other ramp segments, the N to NNE fault system is affected by the  $F_{MR}$  folds and show multiple kinematic indicators that suggest opposing movement directions which are interpreted to be the result of fault reactivation during later deformational events (see below).

#### ***IV.2.2.2 Fold interference patterns between $F_i(F_{2a})$ and $F_{sv}(F_{2b})$ folds***

The superposition between the  $F_{2b}$  and the  $F_{2a}$  folds was observed in the field in several locations and resembles Ramsay's (1967) type III fold interference pattern (***Plate IV.1–A, C, D – box 1***) (***Figure IV.11-A***). The idealised end member of this refolding pattern results from the superposition of two generation of folds with parallel hinges, but with a high angle between their axial planes - e.g. one fold is recumbent, whereas the second fold is upright (***Figure IV.11-A***) (Ramsay, 1967; Rowland et al, 2007). As presented above, the geometry and the orientation of the  $F_{2b}$  folds are variable and their axial planes are steep or inclined. It is possible that at least in some locations, where the  $F_{2b}$  hinges are at a low angle to the transport direction (e.g. in the proximity of the N-S oriented  $D_{2b}$  tear faults), these could have formed as syn-shearing flow perturbation folds similar to the  $F_3$  folds presented by Holdsworth (1990) and by Alsop & Holdsworth (2002) in the Moine Thrust of Sutherland, Scotland. If this is the case, the  $F_{2b}$  fold hinges would have been oriented at high angle to the  $F_{2a}$  folds. Also, the  $F_{2a}$  are recumbent, but the initial orientation of their fold axis may have been variable across the area. This leads to the conclusion that at the time of the fold formation, the hinge lines of the  $F_{2a}$  and of the  $F_{2b}$  folds were not parallel, and neither the angle between their axial planes was not high throughout the region. Thus, it should be expected that at a regional scale, depending on the observation point, the superposition of the  $F_{2b}$  folds on the  $F_{2a}$  folds can show a range of fold interference patterns transitional between, at least, the type II and the type III patterns of Ramsay (1967) (***Figure IV.11-A***). The three end-member fold interference patterns (type I to type III of Ramsay, 1967) that can occur from the superposition of two generations of folds are described in ***Figure IV.11***. Type 0 of Ramsay (1967) is not included here because it usually ends with a tight fold that does not show any noticeable pattern in the field (Rowland et al., 2007; Fossen, 2016).

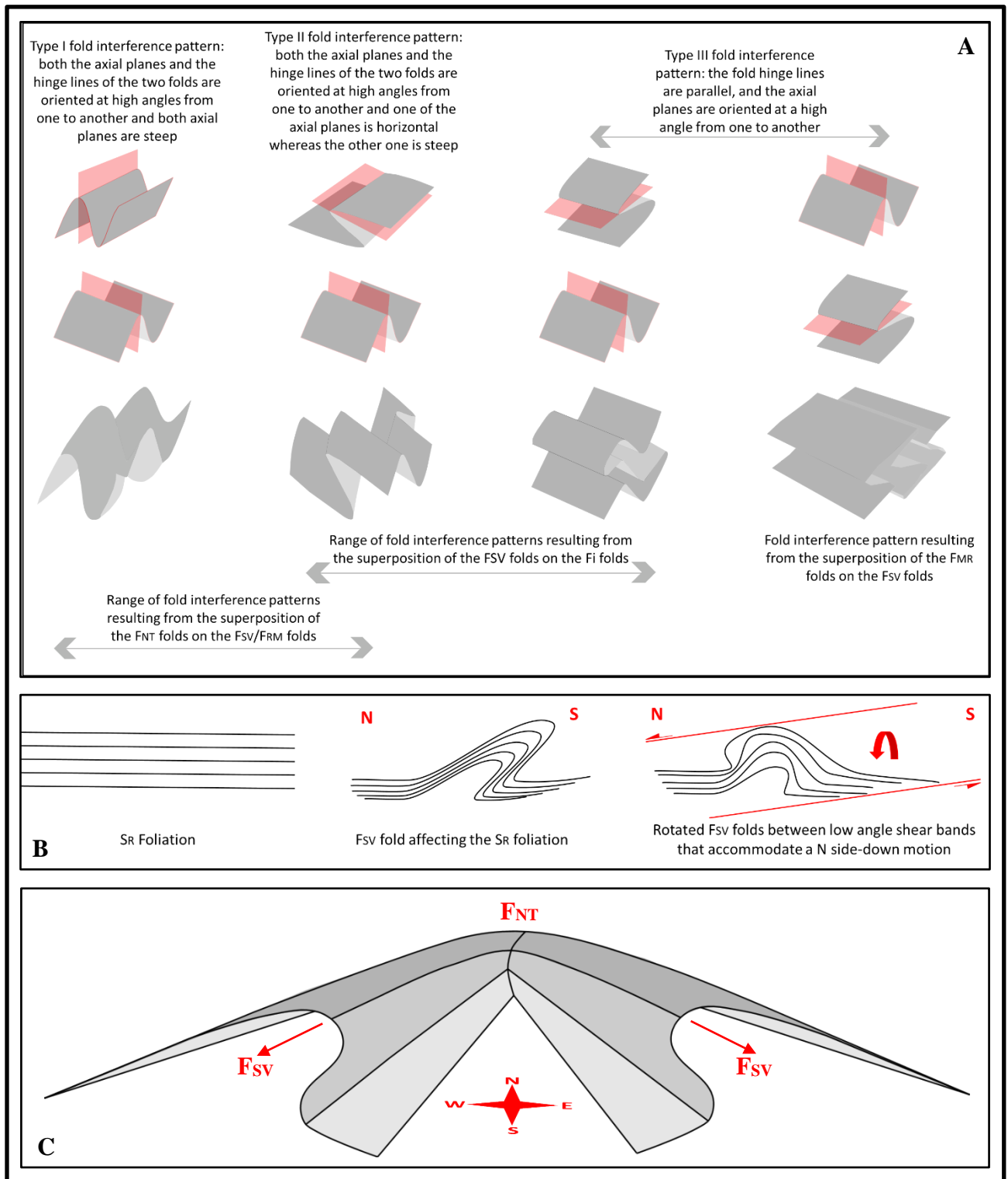


**Figure IV.11** – Representative diagrams illustrating inferred and observed outcrop geometries that resulted between the superposition of different structural elements within the PRC. **A** – Spectrum of fold interference patterns that can result from the interaction of the Fi/F<sub>SV</sub>/F<sub>MR</sub>/F<sub>NT</sub> folds; the end members represent the type I to type III fold interference patterns of Ramsay 1967; diagram modified after Fossen (2016), Rowland et al. (2007) and Grasemann et al. (2004). **B** – Rotation of F<sub>SV</sub> folds between low angle, N directed shear bands; **Note:** the shear bands form in association with the F<sub>MR</sub> folds. **C** – Sketch diagrams illustrating the folding of a F<sub>SV</sub> fold by a F<sub>NT</sub> fold and the change in the vergence of the F<sub>SV</sub> folds.



### IV.2.3 3<sup>rd</sup> deformation phase

The mesoscale, north verging, recumbent  $F_{MR}$  folds and their associated flat lying to moderately dipping foliation fabric ( $S_{MR}$ ) and extensional shear bands affect all the  $D_2$  structures and are in turn folded by the  $F_{NT}$  folds (**Table IV.1 – viii - x**). Furthermore, the geometry and the opposing vergence of the  $F_{MR}$  folds compared to the  $F_2$  folds (**Figure IV.1-B**) suggest that the former, formed under different kinematic conditions. These structures are here associated with a later deformational phase noted as  $D_3$ . Correlative structural features to the  $D_3$  ones presented herein, were recorded by previous workers mostly outside the Point Rouse Complex, within the Paquet Harbour Group, Ming's Bight Group and within the Cape St. Johns Group:  $D_3$  and partially  $D_4$  of Anderson (1998),  $D_3$  of Castonguay et al. (2009) and  $D_4$  of Skulski et al. (2010, 2015a) (**Table IV.3**). Some of the  $D_2$ , flat lying, and steeply dipping kink bands described by Kirkwood & Dubé (1992) in the Stog'er Tight area, feature the same characteristics as the  $D_3$  structures described in this study and thus, are also correlated (**Table IV.3**).

Previous workers recorded an overall inversion of the  $D_2$  thrusts that resulted with a down-side motion towards north and west (Kidd et al., 1978; Anderson et al., 2001; Castonguay et al., 2009; Skulski et al., 2010, 2015a). As presented in the description section, both the  $D_{2a}$  major thrusts and the  $D_{2b}$  brittle-ductile reverse faults do show evidence of a down-dip motion that overprint the earlier reverse component (**Plate IV.5–E, J, K; Plate IV.7–C, D, E, G, I**) and are affected by the  $F_{MR}(F_3)$  folds. It is interpreted that the inversion of the  $D_2$  faults was synchronous with the formation of the  $F_3$  folds and occurred during the  $D_3$  event (**Figure IV.12-A**). This interpretation is based on the following consideration: regardless of the orientation of the  $D_2$  faults, the asymmetry and the vergence of the  $F_3$  folds indicate a transport direction consistent with a down-dip, normal motion along the faults. Also, the association between the fault inversion and fold geometries, combined with the flat lying to moderately dipping  $S_{MR}(S_3)$  foliation and extensional shear bands related to the  $F_3$  folds, suggest that the  $D_3$  structures formed under vertical shortening in an extensional framework (**Figure IV.12-A**). Overall, these interpretations agree with the work of Anderson (1998), Castonguay et al. (2009) and Skulski et al. (2010, 2015a).

Structural features that mirror the characteristics of the  $D_3$  structures described in this study were recorded elsewhere in the Appalachian – Caledonian trend (e.g. Holdsworth, 1989; Fossen, 2016; Wiest et al., 2020), and in other orogenic belts (e.g. Froitzheim, 1992 – Swiss Alps; Carmignani and Kligfield, 1990), and were interpreted to have formed during post-orogenic collapse or gravity driven backsliding of thrust wedges. Similar processes can be inferred for the development of the  $D_3$  structures, although the exact geodynamic conditions cannot be assessed based only on the observations presented above. This topic will be further addressed in *chapter VII – discussions and synthesis*.

#### ***IV.2.3.1 Fold interference patterns between the $F_{MR}(F_3)$ and the $F_2$ folds***

The fold interference pattern resulted from the superposition of the  $F_3$  folds on the  $F_{2a}$  folds was observed in the field in only one location and was interpreted as a partial Type III fold interference pattern (*Plate IV.1–D–box 2; Figure IV.11-A*). Considering that the  $F_{2a}$  folds are scarce and refolded at least once before the formation of the  $F_3$ , the observed geometry should not be taken as a template for the entire area.

The superposition between the  $F_3$  folds on the  $F_{2b}$  folds was observed in the field in several outcrops. Out of these, the most frequent catalogued geometries reflect a convergent-divergent configuration interpreted as the Type III fold interference pattern (*Figure IV.1-B; Plate IV.2–H; Figure IV.11 – A, B*). A less common architecture was recorded in strongly foliated rocks where low angle shear bands that accommodate a N side-down motion, interpreted herein as the  $F_3$  fold axial planes, affect the enveloping surface of the  $F_{2b}$  folds making their upper layers to slide and to rotate towards north, and their core to get into an upright position (*Figure IV.11–B*).

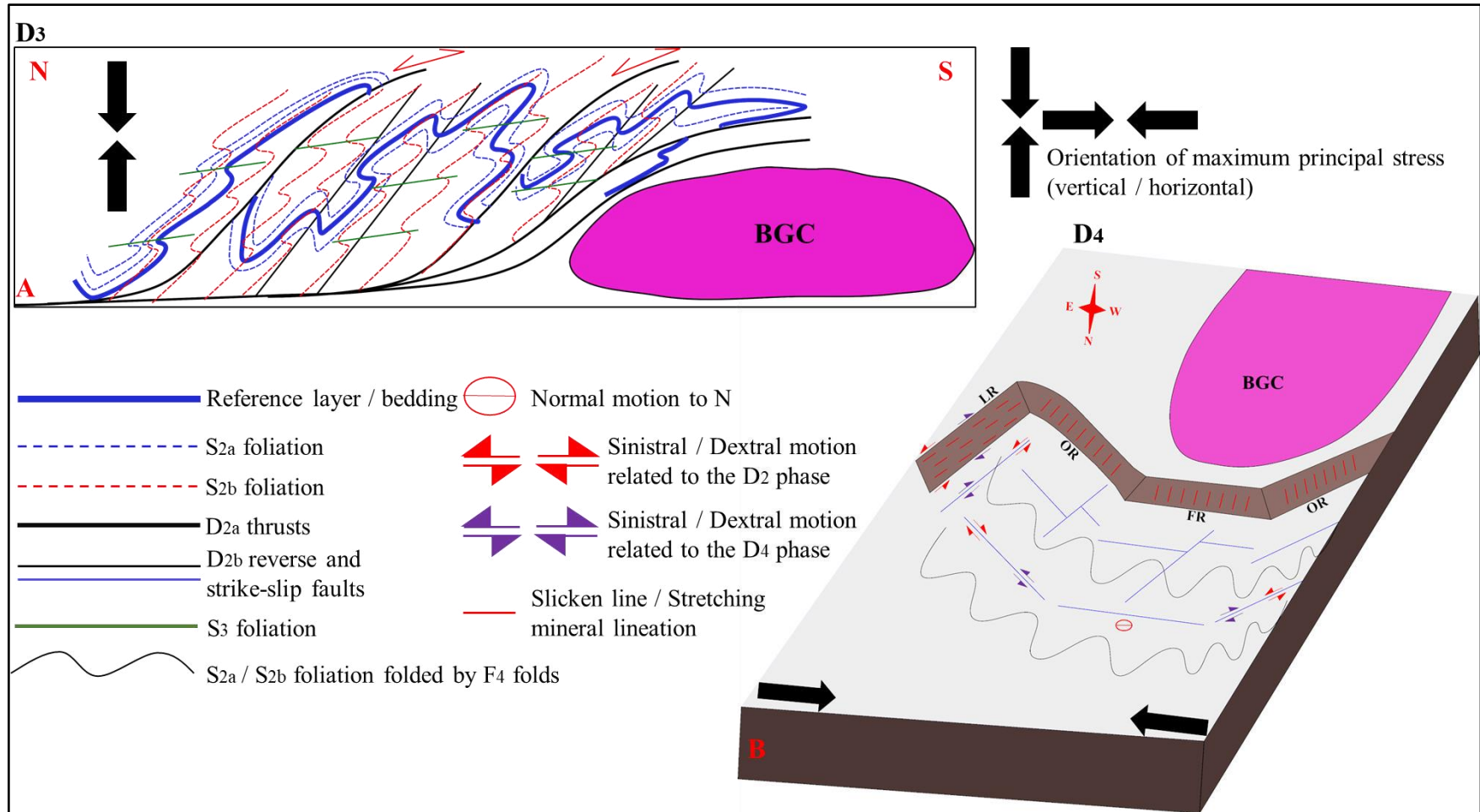


**Figure IV.12** – Cartoons that show the structural evolution of the Point Rouse Complex during both the D<sub>3</sub> phase (**A**) and the D<sub>4</sub> phase (**B**). **A** – Reactivation of D<sub>2</sub> thrusts and reverse faults as normal faults, and development of the north verging recumbent F<sub>MR</sub>/F<sub>3</sub> folds. **B** – Development of meso- to regional-scale, open, north trending F<sub>NT</sub>/F<sub>4</sub> folds, and reactivation of the D<sub>2b</sub> brittle-ductile faults with opposing horizontal motion directions compared to their initial ones.

#### IV.2.4 4<sup>th</sup> deformation phase

The north trending and plunging  $F_{NT}$  folds affect both the  $D_2$  and  $D_3$  structures. Hence, these are assigned to a separate deformational event, termed here as  $D_4$ . In literature, these folds are described as shallowly to moderately plunging, N to NE trending, broad open folds (Kirkwood & Dubé, 1992; Castonguay et al., 2009). However, in this study, this deformation phase is considered more complex than previously mapped, comprising different fold types that show significant variation in their scale, geometry, and orientation (*Table IV.1xi; Plate IV.3-A-D*). These variations are interpreted to be influenced by the rheological characteristics of the affected rock units and by strain partitioning in response to the orientation of the pre-existent structures. The structural features pertaining herein to the  $D_4$  deformation stage can be correlated to structures from one or even more deformational sequences presented by previous authors:  $D_L$  of Hibbard (1983),  $D_3$  of Kirkwood & Dubé (1992),  $D_4$  of Callon & Weick (1990),  $D_4$  of Anderson (1998),  $D_4$  of Castonguay et al (2009) and  $D_3$ ,  $D_4$  and  $D_5$  of Skulski et al., (2010, 2015a) (*Table IV.3*).

Skulski et al. (2010, 2015) attested that the N to NE trending folds that affect the eastern part of the Baie Verte Peninsula formed during the progressive deformation phase that resulted with the juxtaposition between the Point Rouse Complex and the Paquet Harbour Group, the  $D_2$  phase presented in this study. According to these authors, the folds developed in response to strain partitioning between the E-W and N-NE oriented faults, in an overall sinistral transpressional regime localised along the Baie Verte Line. However, as presented in this study, the  $F_{NT}$  folds affect all the  $D_2$  structures, and more importantly, also the  $D_3$  structures which clearly formed during a distinct deformational phase that post-date the  $D_2$  one. Therefore, a fourth deformation phase that succeeded both the  $D_2$  and  $D_3$  events is considered more appropriate to explain the evolution of the  $F_{NT}(F_4)$  folds.

Based on the observations collected within the Point Rouse Complex, it can be inferred that the  $D_4$  event occurred under an overall E-W oriented shortening based on the orientations of the  $F_{NT}$  folds (*Figure IV.12-B*). However, if taking into consideration the regional tectonic setting and the structural architecture of the Baie Verte peninsula these folds could also have formed under a transtensional regime. This topic is further addressed in *chapter VII – Discussions and Synthesis*.

Regardless the structural setting in which these folds formed, the presence of younger fold fragments along the limbs of the  $F_{NT}$  folds, together with the intra-layer horizontal to oblique slicken fibres and stretching mineral lineation and the drag folds that occur at the contact between rocks with contrary rheological properties, suggest that the limbs of the  $F_{NT}$  folds acted as shear zones and that both flexural slip and flow processes occurred during folding (Fossen, 2016) (*Plate IV.3–B, E, I*).

#### ***IV.2.4.1 Fold interference patterns and geometrical relationships between the $F_{NT}(F_4)$ and earlier structures***

Based on the observed relationships between the  $F_{NT}$  folds and the pre-existent structures affected by these folds, it is interpreted that: **a)** the  $F_{NT}$  folds are responsible for the broad, NW to NE variation in the trend of the main foliation fabric, and up to a certain degree for the sigmoidal shape of the Scrape and Deer Cove thrusts and of the E-W oriented brittle-ductile reverse faults (*Figure IV.1, Figure IV.4 – B*); **b)** the  $F_{NT}$  folds inflict a double-plunging nature on the previously formed  $F_{SV}$  and  $F_{MR}$  folds and a change in their vergence: from SW to SE for the  $F_{SV}$  folds and from NW to NE for the  $F_{MR}$  folds (*Figure IV.11-C, Figure IV.2-C*); **c)** in the volcano-sedimentary units, where both the  $D_3$  and the  $D_4$  strains are high, the  $F_{MR}$  axial shear bands are reactivated as strike-slip shears during the  $F_{NT}$  folding (*Plate IV.3–H*); and **d)** the reactivation of the  $D_{2b}$  brittle-ductile faults with opposing horizontal motion directions compared to their initial ones (e.g. the N-NE striking sinistral faults become dextral; *Figure IV.12 - B*) can be explained under an E-W oriented shortening – hence, is considered synchronous with the formation of the  $F_{NT}$  folds during the  $D_4$  event.

The exact 3D geometry that results from the superposition of the  $F_{NT}$  folds on the previously described folds cannot be easily decipher because it involves four different planar surfaces that were initially oriented at variable angles from one to another. However, a range of fold interference patterns between the Type I (“dome and basin”) and the Type II (“mushroom/boomerang”) end members of Ramsay’ (1967) are expected to result from the superposition of the  $F_{NT}$  folds on the  $F_{SV}$  and on the  $F_{MR}$  folds (*Figure IV.11-A*). This is based on the following field observations: **a)** the hinge lines and the axial planes of the  $F_{SV}$  and of the  $F_{MR}$  folds are oriented at a high angle to both the hinge and the axial plane of the  $F_{NT}$  folds

(*Plate IV.3-H*); **b**) the overall dip of the  $F_{NT}$  fold axial plane is steep, whereas the axial planes of the  $F_{SV}$  and of the  $F_{MR}$  folds vary from shallow to steep with respect to the resultant geometry of their previous Type III superposition pattern (*Figure IV.11-A*). Moreover, the outcrop pattern of the Stog'er gabbro in both the Stog'er and the Pine Cove areas reflect a rather boomerang shaped geometry (*Fig. IV.1*).

#### **IV.2.5 Syn-to-post D<sub>4</sub> structures**

The relative timing for the formation of the south dipping faults and the steep, NW striking faults (*Table IV.1– xiii, xiv, Table IV.3, Figure IV.8*) is interpreted herein as syn-to-post D<sub>4</sub>, based on the cross-cutting relationships observed in the field. Furthermore, due to their orientation and kinematics it can be inferred that these faults formed as a partial “*Riedel*” system (Riedel, 1929; Fossen, 2016) associated to the reactivation of the D<sub>2</sub> N-NE trending faults as dextral shears during the D<sub>4</sub> event (*Figure IV.8-C*). Under this configuration, the south dipping faults would represent a tension fault system oriented parallel to the maximum principal stress, whereas the NW striking faults would serve as antithetic Riedel (*R'*) shears to a N-NE oriented master fault (*Figure IV.8- C*). In this setting, it is also expected that the N dipping D<sub>2</sub> thrusts and reverse faults to be reactivated and to accommodate normal to oblique motion.

In the north-western part of the Ming's Bight Group (*Figure IV.1*), Anderson (1998) described D<sub>5</sub>, north and south dipping extensional shear zones, up to 15 meters in width. The south dipping shears of Anderson (1998) show similar characteristics to the south dipping faults presented in this study and thus, it is inferred that the faults are genetically related (*Table IV.3*).

In the north-western part of the Baie Verte Peninsula (*Fig. II.4*), Skulski et al. (2015a) mentioned two NW striking fault systems, the Little Lobster Harbour Fault and the Advocate Fault, which show a normal motion to NE combined with a sinistral component. The orientation and the kinematics of these faults match with the nature of the syn-to-post D<sub>4</sub>, NW oriented faults from the Point Rouse Complex. Based on the latter statement, these fault systems may be analogous (*Table IV.3*).

#### **IV.2.6 Post–D4 structures**

The late, E-W and N-S oriented, brittle faults that affect the entire PRC (*Table IV.1–xv; Figure IV.9*) crosscut through all the above-mentioned structures. Therefore, their relative age is inferred as post-D<sub>4</sub>. Unfortunately, based on the available data, no other constraints can be stated with respect to the age of these fault systems.

#### **IV.2.7 Structures of uncertain generation**

The small scale, ductile to brittle-ductile, shear zones identified within the central part of the PRC (*Table IV.2–i; Plate IV.9–G*) are affected by most of the above presented structures. Based on their characteristics these faults are classified here as syn-to-post-D<sub>2a</sub>. The observed shear zones can be correlated with the D<sub>1</sub> small-scale, reverse, ductile shear zones of Kirkwood and Dubé (1992) and in agreement with their interpretation, may represent subordinate ductile structures that accommodated layer-parallel shortening at the contact between competent and incompetent layers during the early development of the major thrust zones.

The E-W oriented kink bands and chevron type folds (*Table IV.2–ii, Plate IV.6–I*) from the hanging wall of the E-W brittle-ductile reverse faults were associated by different authors to either the compressional phase that resulted in the juxtaposing of the PRC over the PHG (Kirkwood & Dubé, 1992; Dubé and Poulsen, 1993), or to an extensional event that reactivated the pre-existent thrusts as normal faults (Anderson, 1998; Castonguay et al., 2009). However, a dual origin of these structures cannot be excluded because kink bands and kink type folds with similar geometries can occur in association with both thrusts and normal listric faults (Twiss & Moore, 1992). Based on the field observations presented above, it is considered that some of these structures formed in response to layer-parallel shortening above fault ramps during D<sub>2b</sub> thrusting and folding in a “*fault-bend/fault-propagation fold*” architecture (Suppe, 1983; Suppe & Medwedeff, 1990), but overprinted by south dipping shears and reactivated during the inversion of the D<sub>2</sub> faults (*Plate IV.4–D*).

The reverse faults and shear bands and their associated north verging folds from the Pine Cove area (*Table IV.2–iii; Plate IV.1–G; Plate IV.9–A*) can be attributed to either the D<sub>2b</sub> or to the D<sub>3</sub> events. The reverse faults could have formed as back-thrusts synchronously with the D<sub>2b</sub> reverse faults, or as reverse shear bands

during down-dip sliding of moderately dipping layers during the D<sub>3</sub> event. However, considering the vast geometries that the F<sub>MR</sub> folds display across the area, together with their constant association with a south dipping fracture cleavage, a D<sub>3</sub> evolution for these structures is favoured.

The ESE to SE steeply plunging folds observed in the Stog'er and Deer Cove areas (*Table IV.2–iv; Plate IV.9–B, C*) can be interpreted as F<sub>2b</sub> folds exposed in low D<sub>2b</sub> strain domains, or as drag folds associated with normal movement along closely spaced shear zones. At least for the Deer Cove area, the latter option is preferred because in the oblique view, it can be noticed that some of the layers are displaced with a normal component towards NE between the fold axial planes (*Plate IV.9-C*). If the folds are related to normal movement along the NE dipping shears, then a relative timing of syn- to post D<sub>4</sub> for the formation of the folds can be inferred.

The formation of the west verging, shear type folds, observed along the Deer Cove and Pine Cove coastlines (*Table IV.2–v; Plate IV.9–D, E*) is not well constrained with respect to the above-mentioned deformational events. Based on their orientation and kinematics, their genesis can be linked to the sinistral motion that occurred on the Scrape and Deer Cove thrusts during the D<sub>2b</sub> event. Yet, the folds were assessed from a top to oblique perspective which prevented the identification of any down-dip motion indicators along their axial planes and thus, a late extensional nature for these folds and an association with the syn-to-post D<sub>4</sub>, steeply to vertical NE dipping faults presented above cannot be ruled out.

### **IV.3 Summary**

The Point Rousse Complex (PRC) shows a complex structural setting characterised by the presence of multiple structural elements and different styles of deformation that account for a complex strain partitioning between different structural domains. The actual geometry of the area resulted from the superposition of at least four generations of folds (*Table IV.1, Figure IV.13*). Each folding event generated their own regional or local scale planar and linear fabrics. Most of the folding stages developed in association with one or more fault systems or have reactivated some of the pre-existent faults. Fold superposition resulted in multiple



overprinting patterns such as refolded folds, composite foliation fabrics, and reactivated structures.

The most pronounced foliation fabrics, the  $S_R$  and the  $S_L$ , represent the axial planar cleavages of small scale, intrafolial  $F_i$  folds and of mesoscale, asymmetric, south verging  $F_{SV}$  folds, respectively (**Figure IV.13**). A composite, mylonitic  $S_{LC}$  foliation, is the dominant fabric close and within the ductile and brittle-ductile faults, whereas the  $S_R$  represents the main foliation in the low strain domains. A strong, steeply plunging, north to north-east trending, stretching mineral  $L_R$  lineation is developed on the  $S_R$  fabric. Major ductile to brittle-ductile, south directed thrusts divide the PRC in multiple fault-bounded blocks. Brittle-ductile reverse faults that dip moderately to steeply to N are well developed in the hanging wall of the major thrust sheets. The faults accommodate a N over S transport direction and are subparallel to the axial planar cleavage of the  $F_{SV}$  folds (**Figure IV.13**). These structures were ascribed here to a  $D_2$  progressive deformation phase which formed in response to regional scale, north over south transport direction (**Figure IV.13**). The early  $D_{2a}$  stage developed under ductile conditions and resulted with the formation of large-scale recumbent folds and major ductile to brittle-ductile thrust sheets (*e.g. the Scrape thrust*) (**Figure IV.10-A**). The late  $D_{2b}$  stage accounts for further internal folding and imbrication of the  $D_{2a}$  thrust sheets, under brittle-ductile conditions, as a consequence of prolonged horizontal shortening against the Burlington Granodioritic Complex (**Figure IV.10-B**).

Recumbent, mostly north verging  $F_{MR}$  folds affect the  $F_i$  and the  $F_{SV}$  folds and their associated planar fabrics, as well as the major thrusts and the brittle-ductile faults (**Figure IV.13**). These folds are associated to the inversion of the  $D_2$  thrusts and reverse faults as normal faults, under vertical shortening during a later,  $D_3$  deformational event (**Figure IV.12-A**).

Both the  $D_2$  and  $D_3$  structures are in turn folded by open, gently to steeply plunging, north trending  $F_{NT}$  folds (**Figure IV.13**). The  $F_{NT}$  folds were assigned here to a  $D_4$  deformational event developed with respect to an E-W oriented shortening (**Figure IV.12-B**). The  $D_4$  folding contributed to the overall undulous shape of the major thrust faults, to the NW to NE variation in the trend of the main foliation fabric, and to the reactivation of all the pre-existent faults. It is inferred that a partial Riedel fault system composed of normal, south dipping faults and NW trending,

sinistral faults combined with a down-dip component, formed with respect to the reactivation of the N-NE oriented  $D_{2b}$  faults as dextral shears during-to-post- $D_4$  (*Figure IV.8 - C*).

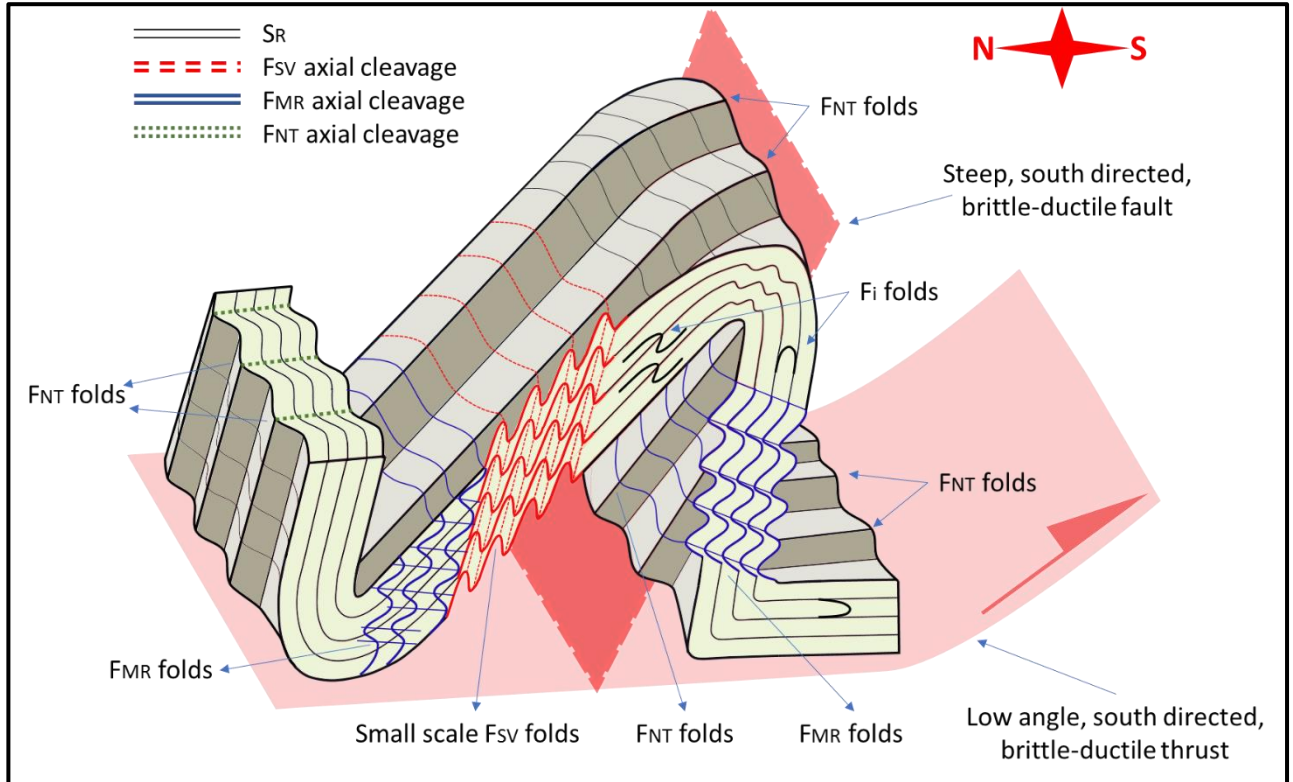


**Figure IV.13** – 3D Sketch diagram illustrating the overall relationships between the four identified fold generations and their associated planar fabrics; the image is most representative for areas located in the proximity of major ductile thrusts, but it can be extrapolated across the region; a  $F_{SV}$  fold is taken as reference in order to show its relationship with the ductile thrusts and with brittle-ductile reverse faults as well as for emphasizing their refolding by the  $F_{MR}$  and  $F_{NT}$  folds. **Note** the opposing vergence of  $F_{SV}$  and of the  $F_{MR}$  folds and the folding of the  $F_{SV}$  and of the  $F_{MR}$  cleavages by  $F_{NT}$ .  $F_1 = F_{2a}$ ;  $F_{SV} = F_{2b}$ ;  $F_{MR} = F_3$ ;  $F_{NT} = F_4$ ;  $S_R = S_{2a}$

## **V. Gold mineralisation in the Point Rouse Complex (Results and Interpretations)**

As presented in *chapter II*, the Point Rouse Complex (PRC) hosts several gold occurrences, some of which have proven economically valuable and were already extracted (GoldenVlle, Pine Cove, Stog'er Tight and Argyle), whereas others are still under exploration (e.g. Romeo & Juliet, Deer Cove, Anaroc, etc.) (Pitman et al., 2020). In addition to the already known occurrences, areas that show potential for gold mineralisation represent new drilling targets (e.g. Penny Cove, *Figure. II.9*) (press release January 2022-[www.anacondamining.com](http://www.anacondamining.com)), and thus, other gold showings may yet to be discovered. Given this prolific metallogenic setting, the current chapter compares and contrasts the geological characteristics (e.g. structure, alteration, mineralisation) of five gold occurrences: three mined deposits (Pine Cove, Stog'er Tight and Argyle) and two exploration prospects (Romeo & Juliet and Deer Cove) (*Figure. II.9*).

A literature review that presents the main geological characteristics and the current understandings regarding the genesis of each of the studied deposits/prospects can be found in *chapter II, section II.5 and in Appendix I*. A re-evaluation of the structural and mineral paragenetic characteristics of the deposits is provided in this chapter based on the new structural, mineralogical, and geochemical data gathered during this study.

The main goal of this chapter is to bring a more comprehensive understanding regarding the gold mineralisation processes that occurred at the scale of the entire district. To achieve this, the local structural setting of each deposit together with their mineral paragenetic sequence are evaluated with respect to the structural deformation sequence of the entire PRC (*see chapter IV*). Through this approach, the relative timing of the deposits is constrained, and a link between different mineralogical and structural evolution stages within individual deposits is inferred. In addition, EPMA analysis on gold grains from each of the studied deposits are used to characterise the geochemical signature of gold. This informs if there are any differences or similarities between the fluids that led to the formation of the gold deposits within each location.

### **V.1. Geological characteristics of the studied gold deposits (field, mineralogical/petrographical and geochemical observations)**

This section describes the main geological characteristics (structural setting, vein types, alteration mineral assemblages, ore mineralogy and gold geochemistry) of the studied deposits based on field, mineralogical/petrographical and geochemical observations. Where field exposure did not permit at least a partial evaluation of the ore zones (e.g. at the Argyle deposit), field observations gathered by the Anaconda Mining geologists were used to inform the relationships between the local structural setting and the mineralised veins.

The mapping and sampling rationale together with the analytical techniques that were used for this section are presented in the *Methodology* chapter, and a summarised characterisation of the analysed samples is provided in *Appendix II*. The terminologies used for the structural elements identified at a deposit-scale correspond to their interpreted deformational stage (e.g. *F<sub>3</sub> folds* instead of *mesoscale, north verging, recumbent folds* ( $F_{MR}$ )). This approach is preferred to avoid repetitive descriptions between different chapters and to aid correlations between the local structural elements that host/affect the mineralisation and the deformational phases that affected the entire PRC. Some interpretations regarding the textures and the cross-cutting relationships of different gangue and ore minerals are also provided in this section to highlight the presence of multiple generations of a mineral species, and to give insights regarding the evolution of the mineral system in time.

### V.1.1. The Pine Cove deposit

The structural data and field observations presented below were gathered from the Pine Cove open pit and from the outcrops located in its near vicinity (*Figure V.1*). Detailed characterisations of all the lithological units present in the Pine Cove area can be found in Duncan and Graves (1992), Ybarra (2019) and Pitman et al. (2020), whereas summarised descriptions extracted from the work of the afore-mentioned authors are provided in *Appendix I*.

#### V.1.1.1. Structural setting

Structural elements pertaining to all the interpreted deformational events that affected the entire PRC are very well developed in the Pine Cove area (*Table IV.1 & IV.2*). The gold bearing mineralised zones are hosted in the hanging wall of the D<sub>2a</sub>, major ductile to brittle-ductile Scrape thrust (*Figure V.1-A*). The mineralisation extends from the thrust towards north, over a strike length of approximately 500 meters (*Figure V.1-A*). Across this distance, it was observed that the host lithologies show a rapid increase in strain intensity from north to south.

In the northern most part of the area, in the hanging-wall of the D<sub>2b</sub> Paster Pond thrust, the bedding-parallel S<sub>2a</sub> foliation represents the dominant fabric, whereas south from the Paster Pond thrust the S<sub>2a</sub> foliation is gradually transposed into parallelism with the S<sub>2b</sub> crenulation and shear related cleavages, becoming a strong composite S<sub>2a/2b</sub> foliation ~200 meters away from the Scrape thrust. The S<sub>2a</sub> and the composite S<sub>2a/2b</sub> foliation fabrics dip moderately to steeply (30° to 60°) from NW to NE and locally towards ESE, SE, and S (*Figure V.1-B*). The variation in the orientation of the foliation fabrics from the Pine Cove area is like the one observed in the entire PRC, and it is interpreted to be caused by the presence of the F<sub>3</sub> and F<sub>4</sub> folds (*Figure. IV.4–A, B, C*). On both the S<sub>2a</sub> and on the S<sub>2a/2b</sub> fabrics a strong L<sub>2</sub> stretching mineral lineation that plunges moderately from N to NE was observed (*Fig. V.1-C*).

The D<sub>2b</sub> thrusts and reverse faults together with their associated F<sub>2b</sub> folds occur with a high density in the hanging wall of the Scrape thrust and locally affect parts of the mineralisation (*Plate V.1-H*). The F<sub>2b</sub> folds vary in size showing amplitudes from of a few centimetres to a few meters (*Plate V.1–H; IV.1–C, G, F*). The D<sub>2b</sub> fault sets strike from NE to NW, with the E-W oriented ones being the most common.

The F<sub>3</sub> and the F<sub>4</sub> folds cover a broad spectrum of sizes, having amplitudes from a couple of centimetres up to a few of meters. On the geological map, the outcrop

trace of the lithologies define a large-scale (wavelength of a couple hundred meters) NNW plunging F<sub>4</sub> fold (**Figure V.1-A**). Both the F<sub>3</sub> and the F<sub>4</sub> folds affect the mineralised zones (**Plate V.1-I, J, R**). The syn-to-post D<sub>4</sub>, south dipping, extensional faults (**Table IV.1-xiii**) and the late, steeply dipping, E-W oriented, brittle normal faults (**Table IV.1-xv**) were also observed in the Pine Cove pit and crosscut the mineralisation.

#### **V.1.1.2. Vein sets observed in the Pine Cove pit**

Six different vein sets, termed here from VS<sub>1</sub> to VS<sub>6</sub>, were identified in the walls of the Pine Cove Pit. Descriptions for each vein set are provided in **Table V.1**, and their associated images can be found in **Plate V.1**. A “vein set” is here referred to as an association of veins with similar textures, mineralogy, and orientations. For consistency, this terminology will be used throughout this chapter.

Vein sets VS<sub>1</sub> and VS<sub>6</sub> are barren, and in general devoid of any alteration halos (**Table V.1; Plate V.1-A, O**), whereas VS<sub>2</sub> to VS<sub>5</sub> occur in association with different alteration mineral assemblages and with disseminated auriferous pyrite (**Table V.1; Figure V.1-D; Plate V.1**). The crosscutting relationships between different veins and the structural characteristics of each vein set are presented in **Table V.1**. The vein sets are listed from oldest to youngest based on their mutual crosscutting relationship and on their relationship with the local structural elements.

Two other vein types associated to mineralisation, but with uncertain affiliation with respect to the afore-mentioned veins were also observed in the field: i) flat-lying laminated and sheared quartz lenses/pods (**Plate V.1-P, Q**); and ii) small-scale (few centimetres in length and width) quartz-carbonate-chlorite ± hematite veins (**Plate V.1-C, T**).

i) A flat-lying, milky-white quartz-carbonate lens of approximately 1 m in length and 20-30 cm in thickness was observed in the eastern part of the Pine Cove pit (**Plate V.1-P, Q**). The vein crosscuts the S<sub>2a</sub> foliation, has sheared margins and displays internal layering composed of mm to cm scale, milky-white quartz-carbonate layers separated by thin slivers (mm to cm in thickness) of sheared and chloritized wall-rock material. Fine grained pyrite occurs mostly at the contact between the quartz-carbonate layers and the wall-rock material, but also disseminated around the vein in the host rock. This type of vein was observed only in one location and no

relationships with the rest of the vein sets was noticed. Assumptions regarding the formations of this vein and its relationships with the other veins sets are provided in the interpretation section of this chapter.

ii) Small-scale (few centimetres in length and width) quartz-calcite-chlorite ± hematite veins were observed in the mineralised zones (*Plate V.1–C, T*). In outcrop the chlorite shows a distinct dark green to black colour, whereas under the microscope, it displays anomalous blueish grey to dark-blue and purple birefringence colours (*Plate V.1–T; Plate V.4–F, G, H*). The veins occur at high angle to the  $S_{2a}$  and to the  $S_{2a/2b}$  foliation and as infills between the foliation planes. The foliation parallel part of the veins shows syntaxial morphologies with elongate blocky quartz-carbonate crystals, whereas the sections that crosscut the foliation have a more massive texture (*Plate V.1–T*). These veins crosscut the  $VS_2$  and the  $VS_3$  vein sets (*Plate V.1–C*). Direct relationships with the rest of the described vein sets were not observed, but their mineralogy, texture and partially their orientation (steeply to moderately dipping to south), indicate a genetic relationship with  $VS_5$  (*Table V.1*).

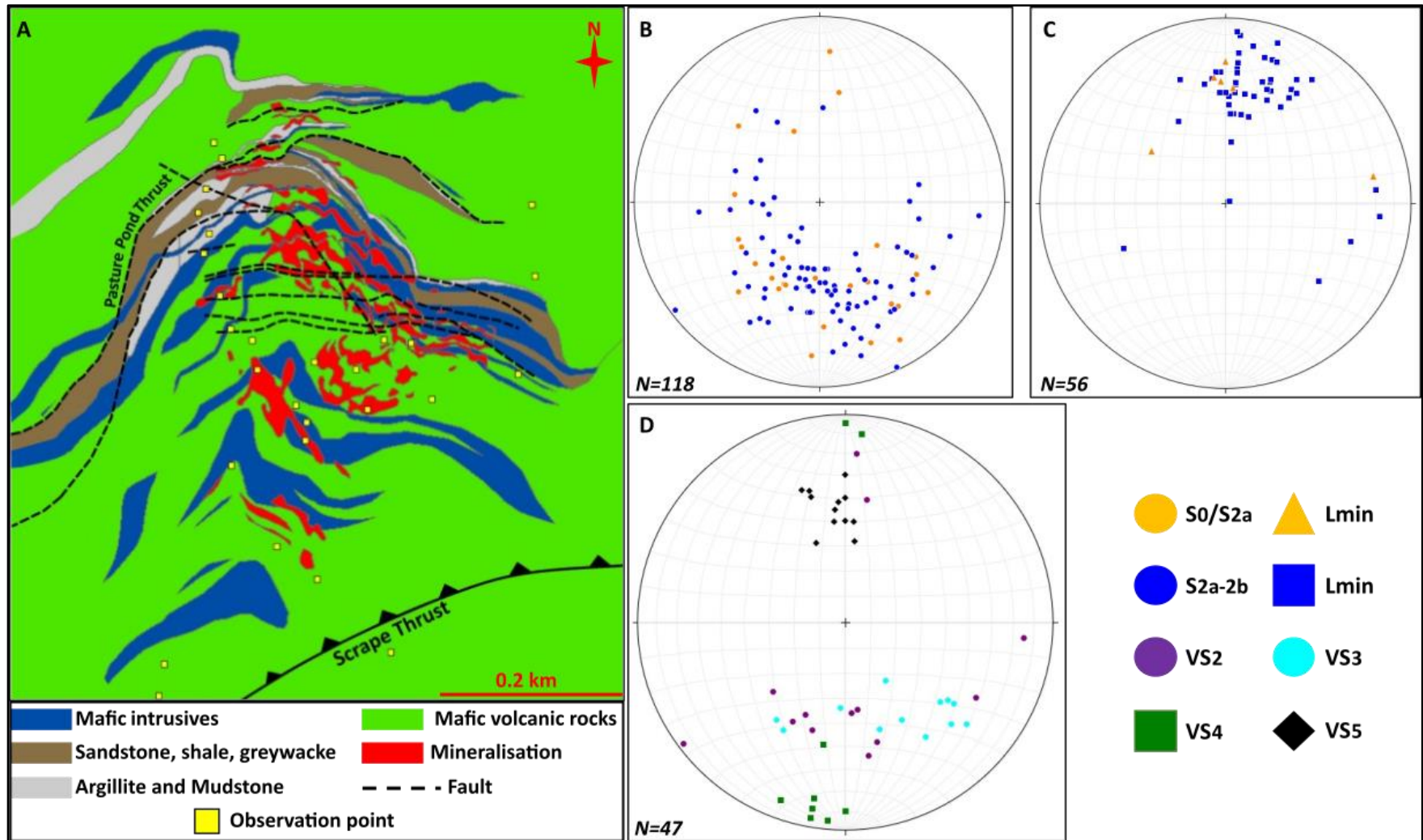


**Figure V.1:** *A* – Simplified geological map of the Pine Cove deposit after the unpublished geological map of Anaconda Mining (2018) and Pitman et al. (2020); *B*, *C*, *D* - Southern-hemisphere, equal-area, stereographic projections of the poles to the foliation planes (*B*), of the stretching mineral lineation (*C*), and of the poles to the main mineralised vein sets (*D*) from the Pine Cove area.

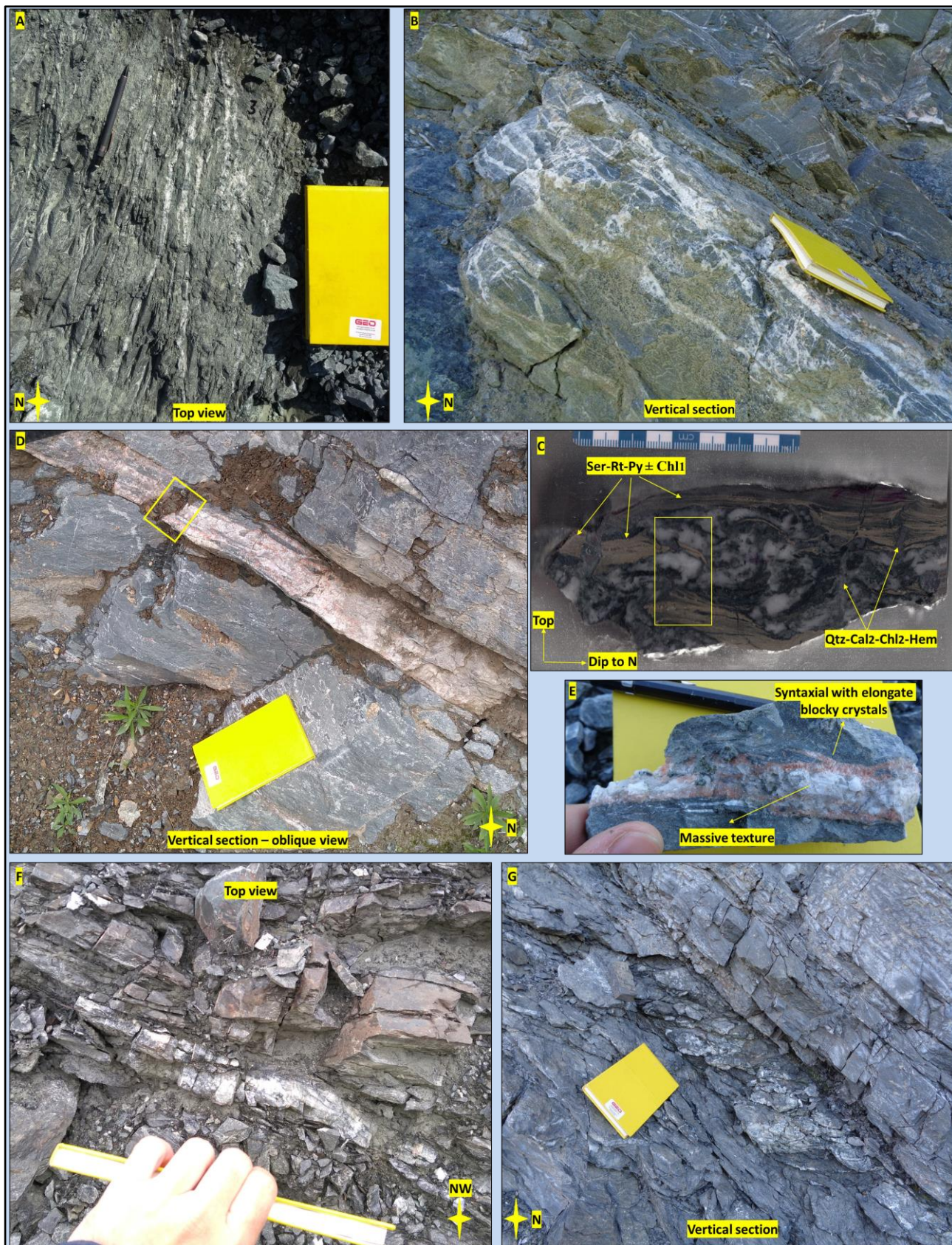


**Table V.1. – Descriptions of vein sets identified within the Pine Cove open pit.**

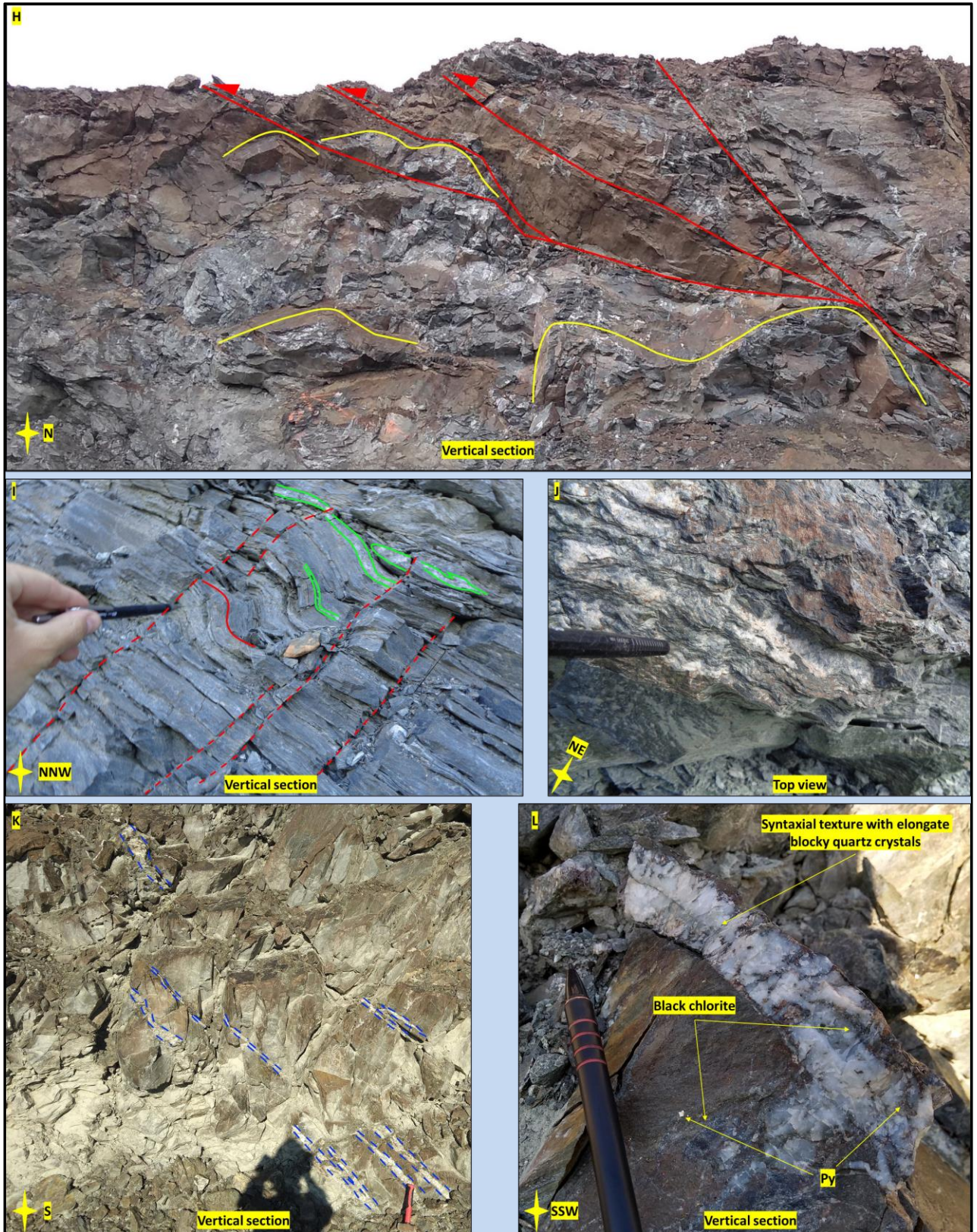
Terminologies regarding vein and crystal morphologies are used according to Bons (2000) and Bons et al. (2012)

<b>Vein set</b>	<b>Characteristics</b>	<b>Alteration / Mineralisation</b>	<b>Crosscutting relationships</b>	<b>Structural constrains</b>
<b>VS<sub>1</sub></b> <i>Plate V.1 - A</i>	Thin, barren veins, with massive internal texture, composed of both translucent and milky white quartz. More common in the northern part of the pit, within the sedimentary units.	Lacks mineralisation and alteration halo.	Relationships with the rest of the vein sets are not clear because of intense transposition.	The veins are discontinuous, folded and boudinaged, transposed into parallelism to the S <sub>2a</sub> and to the S <sub>2a/2b</sub> foliations. The veins are affected by most of the observed structures (D <sub>2b</sub> to syn-to-post D <sub>4</sub> structures).
<b>VS<sub>2</sub></b> <i>Fig. V.1-D Plate V.1 – B, C, H; R</i>	Breccia type veins composed of parallel, syntaxial and ataxial, milky white, quartz - albite veins with elongate blocky and stretched crystals, separated by zones of intense brecciation. In the brecciated zones the veins show random orientations, and the wall-rock clasts have a jigsaw texture. Internal recrystallisation with fine grained blocky crystals are common. Occur preponderately in hard rocks with very low anisotropy (pillow basalts and greywackes).	Disseminated auriferous py in the surrounding alteration halo composed of ser-rt-ab-chl-cal mineral assemblages, and to a lesser degree within veins.	Sub-parallel to VS <sub>3</sub> . Crosscut by VS <sub>5</sub> and VS <sub>6</sub> . Unknown relationship with VS <sub>4</sub> .	Overall, the veins are subparallel or cut at a low angle the bedding parallel S <sub>2a</sub> foliation. When the veins occur along, or/and in between D <sub>2b</sub> shears and reverse faults these are intensively sheared. In high strain zones the veins are transposed into parallelism to the S <sub>2a/2b</sub> foliation. The veins are folded by the F <sub>2b</sub> , F <sub>3</sub> and F <sub>4</sub> folds and cut by the syn-to-post D <sub>4</sub> south dipping faults.
<b>VS<sub>3</sub></b> <i>Fig. V.1-D Plate V.1 – D, E, F, G, I, J</i>	Laminated and sheared quartz-albite ± carbonate veins with translucent and milky-white quartz, pink albite and white–orange carbonates. Composite vein morphology with multiple domains: syntaxial, massive, stretched. Observed in rocks with a well-developed fabric (volcano-sedimentary units).	Auriferous py along suture zones within veins (margins between different growth zones are usually defined by slivers of altered wall rock) and in the alteration halo	Sub-parallel to VS <sub>2</sub> . Crosscut by VS <sub>5</sub> and VS <sub>6</sub> . Unknown relationship with VS <sub>4</sub> .	The veins are parallel to the S <sub>2a</sub> foliation and in high strain domains to the S <sub>2a/2b</sub> also. Sheared and brecciated when hosted by D <sub>2b</sub> faults. The veins are folded by the F <sub>2b</sub> , F <sub>3</sub> and F <sub>4</sub> folds and cut by the syn-to-post D <sub>4</sub> south dipping faults.

		which consist of ab-ser-rt-cal-chl-hem.		
<b>VS<sub>4</sub></b> <i>Plate V.1 – M, N, S; Fig. V.1-D</i>	Steeply dipping, E-W oriented, tension gashes composed of milky-white quartz ± calcite with syntaxial textures, locally brecciated in the thick parts.	Disseminated py in the wall-rock associated with a chl-ser-rt-cal ± hem-ab alteration halo.	Unknown relationships with the rest of the vein sets.	Cuts the S <sub>2a/2b</sub> foliation fabric and shows internal shearing and folding. The observed exposures did not permit an exact evaluation between the veins and the local structures, but locally these look folded by F <sub>3</sub> folds.
<b>VS<sub>5</sub></b> <i>Fig. V.1-D Plate V.1 – K, L, R</i>	South dipping, E-W oriented quartz – calcite ± chlorite - hematite veins with translucent and milky white, elongate blocky quartz crystals. The veins show multiple opening domains that vary between syntaxial and ataxial/stretched. When chlorite occurs within or around the veins it displays a distinct black color.	The veins are mineralised (py within the veins and in the wall-rock) in areas where they crosscut other veins (especially VS <sub>2</sub> and VS <sub>3</sub> ), but barren otherwise.	Crosscuts the VS <sub>2</sub> and the VS <sub>3</sub> vein sets. Unknown relationships with the rest of the vein sets.	Cuts through the S <sub>2a/2b</sub> foliation. Occurs along the axial plane of the F <sub>3</sub> folds. As mentioned in <i>chapter IV</i> , the syn-to-post D <sub>4</sub> south dipping faults form along, or at a low-angle to the F <sub>3</sub> axial planes. The veins are also folded by F <sub>4</sub> .
<b>VS<sub>6</sub></b> <i>Plate V.1 – O</i>	Thin, quartz-carbonate veins with orange-rusty color. Display syntaxial growth morphologies and elongate blocky to fibrous crystals.	Barren, weak carbonisation around them.	Crosscuts the VS <sub>2</sub> and VS <sub>3</sub> . Unknown relationships with the rest of the vein sets.	Cuts the S <sub>2a/2b</sub> foliation. Late features, cut most of the observed structures, but are affected by the late, brittle, steeply dipping, E-W oriented normal faults.



**Plate V.1(A to G see above)** – Representative images of the vein sets identified in the Pine Cove pit. **A** – Thin quartz veins pertaining to VS<sub>1</sub>, transposed into parallelism with S<sub>2a/2b</sub>, notebook for scale, see descriptions in **Table V.1.** **B** – Hydraulic breccia vein (VS<sub>2</sub>) within massive basalts, notebook for scale. **C** – Cut and polished oriented sample collected from a breccia type vein (VS<sub>2</sub>), note the orange-brown and dark green colour of the altered wall rock fragments (given by ser-rt-ab ± chl<sub>1</sub> alteration minerals) and the qtz-cal-chl<sub>2</sub> ± hem veins that crosscut everything; the yellow square shows the location of the thin section presented in **Plate V.3.**–**A**, ruler for scale. **D** – Laminated vein (VS<sub>3</sub>), parallel to S<sub>0/S2a</sub> within greywackes, notebook for scale, yellow rectangle shows the location of image **E** – fragment from laminated vein (**D**) showing different internal textures, note the pink layers consisting of pink albite and iron rich carbonates. **F** – Laminated and sheared vein (VS<sub>3</sub>) parallel to S<sub>0/S2a</sub> within greywackes, notebook for scale, note the dark-green, intensively altered (chl-py) slivers that define the internal suture zones and the contact with the wall rocks. **G** – Strongly sheared and brecciated vein (VS<sub>3</sub>) along a reactivated D<sub>2b</sub> fault, notebook for scale. (**H to L see on next page**) **H** – Breccia type veins (VS<sub>2</sub>) folded and imbricated by F<sub>2b</sub> folds (yellow line show the fold profile) and D<sub>2b</sub> reverse faults (red lines); **I** – Sheared veins (VS<sub>3</sub> - traced by green line) parallel to S<sub>2a/2b</sub> folded by F<sub>3</sub> (red continuous line) and crosscut by south dipping fractures (red dashed line) formed along the F<sub>3</sub> axial plane, pencil for scale; **J** – F<sub>4</sub> microfolds affecting foliation parallel, sheared type veins (VS<sub>3</sub>), pencil for scale; **K** – South dipping veins (VS<sub>5</sub>) subparallel to the axial plane of F<sub>3</sub> folds, blue dashed line – trace of veins, hammer for scale; **L** – Part of a south dipping vein (VS<sub>5</sub>), note the syntaxial texture of the vein, its multiple suture zones that suggest a couple of opening stages and the associated black chlorite (Chl<sub>2</sub>), pencil for scale.



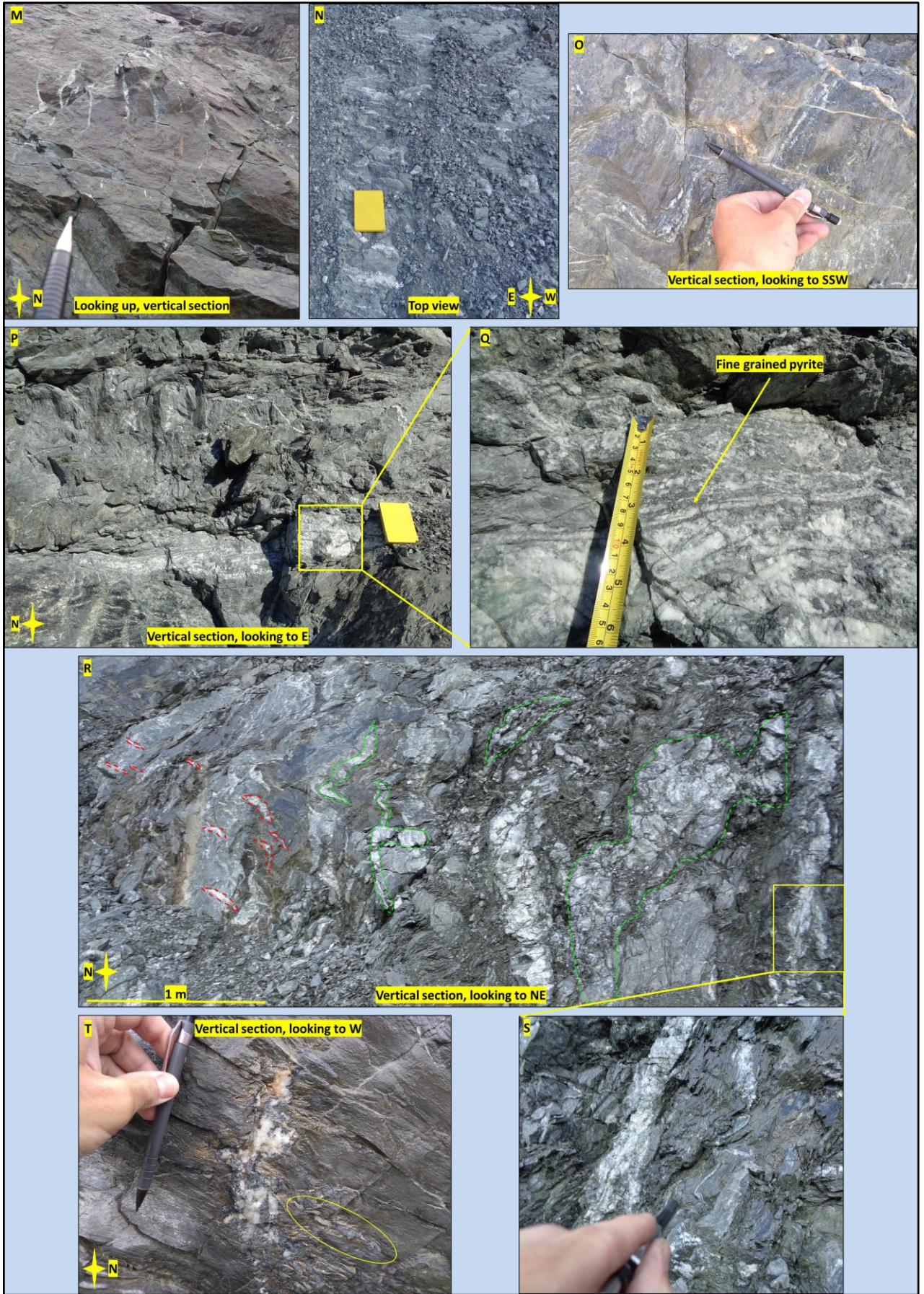


**Plate V.1 (M to S see above)** – Representative images of the vein sets identified in the Pine Cove pit. **M & N** – Arrays of steeply dipping, E-W oriented tension gashes characteristic of VS<sub>4</sub>, pencil and notebook for scale; **O** – Barren qtz-cb vein (VS<sub>6</sub>) crosscutting VS<sub>3</sub>, pencil for scale; **P & Q** – Flat lying, sheared and laminated quartz lens, notebook and ruler for scale, **note** the dark, thin layers of fine grained pyrite between the qtz-cb domains; **R** – Breccia type veins (VS<sub>2</sub>, green, dashed lines) folded by F<sub>3</sub> folds and quartz lenses that dip moderately to south (VS<sub>5</sub>, red, dashed lines) along the F<sub>3</sub> axial plane; **S** – zoomed in image of steeply dipping, E-W oriented veins that crosscut the composite S<sub>2a-2b</sub> foliation and which are affected by F<sub>3</sub> folds, the veins may be part of VS<sub>4</sub>; **T** - Qtz-cal-chl (black) ± hem vein that crosscuts an intense altered zone (ser-rt-ab-py), pencil for scale, the vein is steeply dipping, but is also parallel to the foliation (yellow circle).

### V.1.1.3. Alteration

As presented in *chapter II* and in *Appendix I*, the mineralised lenses from the Pine Cove area are predominantly hosted within Fe-Ti oxide rich pillow basalts and dolerites of Venam's Bight Formation (Ybarra, 2019; Pitman et al., 2020). Unaltered, these rocks show a dark grey-green colour, are fine to medium grained, massive to weakly foliated, moderately magnetic, and composed of feldspar, pyroxene, and titanomagnetite (*Plate V.2-E*).

Ybarra (2019) attested that three main alteration zones can be delineated within the Pine Cove deposit according to their relative distance to the mineralisation (*see Table A1.1*). These alteration types were also observed during this study in the Pine Cove pit and in the investigated drill core sections. A very deformed and intense altered (sericite-rutile-chlorite ± calcite) interval was also observed in drill core, in the footwall of the deposit, just above the Scrape Thrust (*Plate V.2-A*). This interval is associated herein with the “*phylionite*” unit of Ybarra (2019).

Except for macroscopical investigations, during this study there were no detailed petrographic analysis conducted on the distal and the intermediate alteration halos of the Pine Cove deposit and neither on the phylionite interval (*see chapter III – Methodology for rationale and sample collection process*). Thereby, for complete descriptions of these alteration types, the reader is directed to Ybarra (2019). Detailed characteristics of the gangue and ore minerals that compose the proximal alteration halo and the ore horizon are provided below.

Petrographic analyses of samples from medium to high gold grade zones (*Appendix II*) revealed that quartz-sericite-rutile-albite-chlorite-calcite-pyrite ± ankerite-hematite represent the main hydrothermal alteration minerals associated with

gold mineralisation at the Pine Cove deposit. Summarised descriptions for these minerals are provided in *Table V.2*, whereas detailed descriptions are listed below. A significant amount of phosphates (apatite, monazite, and xenotime) are also common in the mineralised zones. Their descriptions can also be found in *Table V.2*.

Within the ore zone, the mineral assemblages related to the initial composition of the host lithologies and to the metamorphism are fully replaced by the alteration minerals. The pre-existent volcanic textures have been obliterated, and the rocks display alternating areas of white-green (calcite-chlorite), pink to orange-brown (albite-sericite-rutile) and dark green (black chlorite) hues (*Plate V.1-C; V.2-B, C, D*).



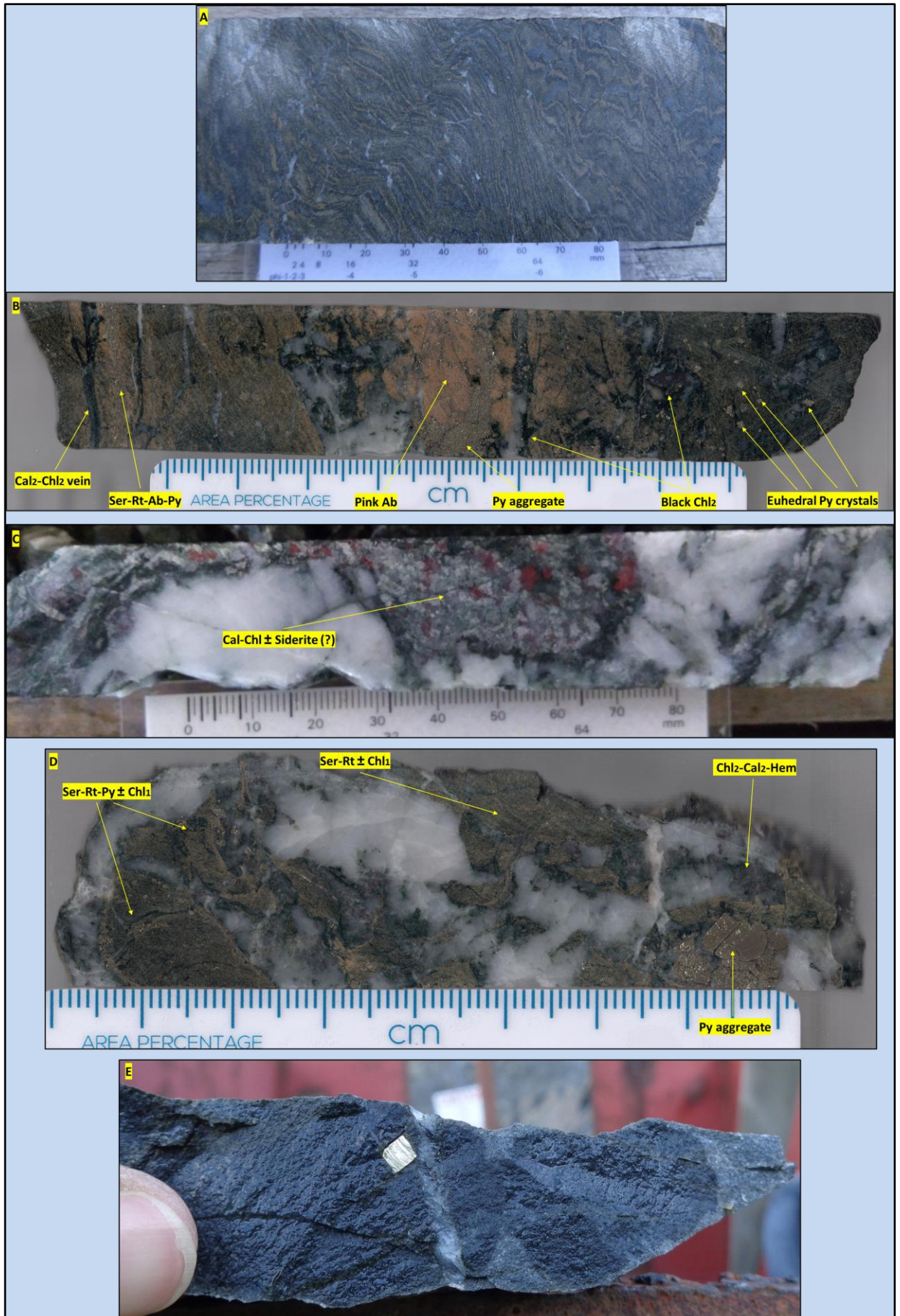


**Plate V.2 (page above)** – Representative images of different altered intervals observed in the the Pine Cove deposit: **A** – Strongly deformed and altered (ser-rt-chl ± cal) interval (“phylionite”) located between the ore zones and the Scrape Thrust; note the qtz-cal infills in the hinges of microfolds (F<sub>2b</sub> and/or F<sub>3</sub>); **B** - Intense ser-rt-ab-py ± ank-chl<sub>1</sub> alteration overprinted by cal<sub>2</sub>-chl<sub>2</sub> veinlets and patches within a high gold grade interval (19.8 g/t); **C** – Intense carbonitisation of host rocks between qtz-cal veins in low gold grade interval (~ 1 g/t); **D** – Intense altered (ser-rt-py ± chl<sub>1</sub>) wall rock fragments incorporated in breccia type veins and cal<sub>2</sub>-chl<sub>2</sub>-hem patches within a high gold grade interval (18.6 g/t). **E** – Hand specimen of unaltered to weakly altered basalt from Venam’s Bight Formation.

**Table V.2** – Summary characteristics of the alteration minerals identified in the proximal alteration halo and in the ore zone of the Pine Cove deposit.

Mineral	Occurrence	Texture	Spatial association with other alteration minerals	Overprinting relationships
<b>Qtz</b>	As vein material in all the described vein sets; rarely, within the altered wall rock in silicified zones	Multiple generations (Q <sub>1</sub> , Q <sub>2</sub> , Q <sub>3A</sub> and Q <sub>3B</sub> ), see <i>Table V.3</i>	See <i>Table V.3</i>	See <i>Table V.3</i>
<b>Ser</b>	Pervasive in the altered wall rock around VS <sub>2</sub> and VS <sub>3</sub> , and as stringers and patches within qtz veins		Q <sub>2</sub> -rt-ab-py-ank-chl <sub>1</sub> ± cal <sub>1</sub>	Replaces ab; replaced and crosscut by Q <sub>3</sub> -cal <sub>2</sub> -chl <sub>2</sub>
<b>Rt</b>	Mostly in the altered wall rock around VS <sub>2</sub> and VS <sub>3</sub> ; less common within the veins	Aggregates composed of fine grained, irregular to prismatic crystals	Q <sub>2</sub> -ser-ab-py-ank-chl <sub>1</sub> ± cal <sub>1</sub>	Overgrown by py; fragmented and recrystallised within chl <sub>2</sub> veins/patches
<b>Ab</b>	Within VS <sub>2</sub> and VS <sub>3</sub> and in the associated alteration selvages	Coarse grained within the veins; irregular to subrounded crystals within intense sericitized zones	Q <sub>2</sub> -ser-rt-py-ank-chl <sub>1</sub> ± cal <sub>1</sub>	Locally replaced by ser; crosscut and overprinted by Q <sub>3</sub> -cal <sub>2</sub> -chl <sub>2</sub> veinlets/patches
<b>Chl</b>	Two generations: chl <sub>1</sub> within the alteration halos that surround VS <sub>2</sub> and VS <sub>3</sub> ; chl <sub>2</sub> within both VS <sub>5</sub> and in the associated alteration halo	Chl <sub>1</sub> – fine grained intergrown with sericite; Chl <sub>2</sub> – coarse and fine-grained in veins, coarse as py fringes and fine-grained in chl <sub>2</sub> -cal <sub>2</sub> patches	Chl <sub>1</sub> : Q <sub>2</sub> -ab-ser-rt-py-ank ± cal <sub>1</sub>  Chl <sub>2</sub> : Q <sub>3</sub> -cal <sub>2</sub> -py-hem	Chl <sub>2</sub> overprints the rest of the alteration minerals including chl <sub>1</sub> , and shows mutual crosscutting relationships with Q <sub>3</sub> and cal <sub>2</sub>

<b>Cal</b>	Within veins (VS <sub>3</sub> , VS <sub>4</sub> , VS <sub>5</sub> , VS <sub>6</sub> ) and in the altered wall rocks; Two generations termed Cal <sub>1</sub> & Cal <sub>2</sub>	Mostly as veins and patches composed of crystals with variable sizes and textures: fine-grained irregular crystals, fine to medium grained patches of blocky to coarse-grained elongate blocky to fibrous crystals	Cal <sub>1</sub> : Q <sub>2</sub> -ab-ser-rt-py-ank-chl <sub>1</sub>  Cal <sub>2</sub> : Q <sub>3</sub> -chl <sub>2</sub> -py-hem (most common)	Cal <sub>2</sub> shows mutual crosscutting relationships with Q <sub>3</sub> -chl <sub>2</sub> -hem and overprints the rest of the alteration minerals including cal <sub>1</sub>
<b>Py</b>	Within the altered wall rock or at the contact between veins and host rocks; within the veins, but lower amounts compared to the host rocks	Fine to very coarse grained anhedral to euhedral crystals, either with inclusion rich cores and inclusion free rims or without inclusions; patches (up to cm <sup>2</sup> in size) of brecciated or annealed polycrystalline aggregates	All the other alteration minerals	Brecciated by Q <sub>3</sub> -chl <sub>2</sub> -cal <sub>2</sub> veins but further annealed and recrystallised; all the alteration minerals (including Q <sub>3</sub> -chl <sub>2</sub> -cal <sub>2</sub> ) were observed as inclusions in py
<b>Ank</b>	Within the altered wall rock	Fine-grained, relict, irregular to anhedral crystals preserved mostly as inclusions in py	Q <sub>2</sub> -ab-ser-rt-py-chl <sub>1</sub> ± cal <sub>1</sub>	Replaced by Q <sub>3</sub> -chl <sub>2</sub> -cal <sub>2</sub> -py-hem
<b>Hem</b>	In both altered wall rock and veins (mostly within VS <sub>5</sub> ); supergene along open fractures and outcrop faces	Staining or thin films on py crystals and irregular to prismatic crystals in cal <sub>2</sub> patches	Chl <sub>2</sub> -cal <sub>2</sub> -py	Staining on py but also overgrown by py
<b>Ap</b>	Within the altered wall rock; rarely within veins	Irregular to sub-rounded, fine-grained to coarse grained (a few microns to 1-2 mm) crystals	Q <sub>2</sub> -Ab-ser-rt-py-chl <sub>1</sub> ± cal <sub>1</sub> / Q <sub>3</sub> -chl <sub>2</sub> -cal <sub>2</sub> -py	Brecciated by Q <sub>3</sub> -cal <sub>2</sub> -chl <sub>2</sub> and further recrystallised incorporating py; brecciated and overgrown by Py
<b>Mnz</b>	Within the altered wall rock; rarely within veins	Disseminated, very fine-grained (~10µm in average), sub-rounded to rounded crystals	Q <sub>2</sub> -ab-ser-rt-py-chl <sub>1</sub> ± cal <sub>1</sub> / Q <sub>3</sub> -chl <sub>2</sub> -cal <sub>2</sub>	Brecciated by Q <sub>3</sub> -chl <sub>2</sub> -cal <sub>2</sub> but also hosted by them

<b>Xtm</b>	Within the altered wall rock; rarely within veins	Disseminated, very fine-grained (~10µm in average), sub-rounded to rounded crystals	Q <sub>2</sub> -ab-ser-rt-py-chl <sub>1</sub> ± cal <sub>1</sub> / Q <sub>3</sub> -chl <sub>2</sub> -cal <sub>2</sub>	Brecciated by Q <sub>3</sub> -chl <sub>2</sub> -cal <sub>2</sub> but also hosted by them
------------	---	---	---	--

**Table V.3** – Summary CL characteristics of the quartz generations observed in samples from the Pine Cove deposit. The texture terminologies are used according to Rusk et al. (2004) and Rusk (2012).

Quartz (Q) generation	Optical properties	CL colour and intensity	CL texture	Crosscutting relationships	Association with other alteration minerals	Related vein set	
Q <sub>1</sub>	Undistinguishable from Q <sub>2</sub>	Blue-purple (medium intensity when compared to Q <sub>2</sub> )	Occurs as relict fragments of Q crystals with massive texture	Brecciated and enclosed in Q <sub>2</sub>	N/A	Both Q <sub>1</sub> & Q <sub>2</sub> were observed in VS <sub>2</sub> & VS <sub>3</sub> , unclear relationships with VS <sub>4</sub> & VS <sub>6</sub> (due to the nature of samples)	
Q <sub>2</sub>	Large areas of coarse blocky to elongate blocky crystals that give an overall massive texture, and zones of recrystallised, very fine-grained crystals	Regardless the granulometry, dark purple (low intensity)	Homogenous/massive to mottled due to the presence of the Q <sub>1</sub> fragments	Is crosscut by Q <sub>3</sub> -Cal <sub>2</sub> -Chl <sub>2</sub> ± hem veins	Ab-ser-rt-py ± ank-cal <sub>1</sub> -chl <sub>1</sub>		
Q <sub>3</sub>	Q <sub>3A</sub>	Occurs as thin veinlets (a few microns to millimetres); the thicker veins are brecciated	Bright blue (high intensity compared to Q <sub>2</sub> )	Thin veinlets that create cobweb textures; laminated – growth zones with oscillating CL intensities; folded, and brecciated by Q <sub>3B</sub>	Affects both Q <sub>1</sub> and Q <sub>2</sub> ; mutual crosscutting relationships between Q <sub>3A</sub> -Q <sub>3B</sub> -Cal <sub>2</sub> -Chl <sub>2</sub>	Cal <sub>2</sub> -chl <sub>2</sub> ± py-hem	Observed in VS <sub>5</sub> , unclear relationships with VS <sub>4</sub> & VS <sub>6</sub> (due to the nature of samples)
	Q <sub>3B</sub>	Undistinguishable from Q <sub>3A</sub>	Dark blue to black (very low intensity, lower than Q <sub>2</sub> )	Occurs as thin veinlets with homogenous internal texture		Cal <sub>2</sub> -chl <sub>2</sub> ± py-hem	

The quartz occurs mostly as vein material, and to a lesser degree in silicified areas within the altered wall rock (*Table V.2*). Under the microscope, the quartz displays the common undulatory extinction and a variety of textures and sizes, with the most common being the following: i) coarse, blocky to elongate blocky crystals with euhedral growth zones, and ii) recrystallised, fine grained, anhedral and subhedral crystals (*Plate V.3-A*).

SEM-CL investigations showed that at least 3 main generations of quartz are present in the ore related veins from the Pine Cove deposit. These are termed and presented based on their crosscutting relationships and their interpreted relative timing, Q<sub>1</sub> being the earliest and Q<sub>3</sub> the latest. Summary descriptions of their CL characteristics are provided in *Table V.3*.

The 1<sup>st</sup> quartz generation (Q<sub>1</sub>) has a moderate CL response showing a blue-purple colour when imaged by coloured CL (red-green-blue filters are applied) and a grey colour when monochrome CL is used (colour spectrum between black and white). Q<sub>1</sub> occurs as relict, irregular, and subrounded to rounded fragments of quartz crystals with homogenous internal texture, brecciated and enclosed in the second quartz generation (Q<sub>2</sub>) (*Plate V.3-C, D*).

Q<sub>2</sub> is characteristic for VS<sub>2</sub> and VS<sub>3</sub> comprising most of their volume. Usually, the Q<sub>2</sub> crystals are coarse grained, elongated, and display undulatory extinction in cross polarised light. The grain boundaries are lobate or serrated and the biggest crystals terminate with domains of recrystallised sub-grains (*Plate V.4-E*). The Q<sub>2</sub> shows a homogenous/massive to mottled internal texture and has a low CL response. When imaged by colour CL the Q<sub>2</sub> displays a dark purple/blue colour, whereas under monochrome CL it has a dark grey colour (*Plate V.3-B, C, D*). Commonly, it is spatially associated with sericite-rutile-albite-pyrite ± ankerite alteration selvages.

In the studied samples, a third quartz generation (Q<sub>3</sub>) occurs within mono or poly mineral (qtz and/or chl and/or cal) thin veinlets (a few microns to millimetres) that crosscut both Q<sub>1</sub> and Q<sub>2</sub> (*Plate V.3-A*). Within the veins, Q<sub>3</sub> is fine-grained and brecciated. Under CL it was observed that Q<sub>3</sub> is composed of two sub-generations of quartz, Q<sub>3A</sub> and Q<sub>3B</sub> which show different CL characteristics. The Q<sub>3A</sub> has a medium to high CL response displaying a moderately to bright blue colour under coloured CL (*Plate V.3-B, E, F, H, I, G*) and bright grey colour in monochrome CL (*Plate V.3-D*). It usually occurs in networks of thin veinlets (a few microns to a few millimetres

in thickness) brecciating Q<sub>2</sub>, locally generating cobweb textures (*Plate V.3-E*). The Q<sub>3A</sub> shows a banded/laminar texture defined by growth zones with alternating low and high CL intensities within the thicker veins, or when it infills open spaces within or between Q<sub>2</sub> (*Plate V.3-D, box 2*). Internal micro-folding is also common in thicker and laminated Q<sub>3A</sub> veins. The Q<sub>3A</sub> is crosscut and brecciated by thin quartz veinlets (Q<sub>3b</sub>) that have a very low CL response, displaying a dark blue/grey to black colours (*Plate V.3-D box 2, H, I*). A reverse relationship, where the Q<sub>3A</sub> crosscuts Q<sub>3B</sub> veinlets was also observed. However, most times, the Q<sub>3A</sub> and Q<sub>3B</sub> are found together within patches or veins. Furthermore, both Q<sub>3A</sub> and Q<sub>3B</sub> show a close relationship with cal<sub>2</sub>-chl<sub>2</sub> veinlets (see below and in *Table V.2*), either forming as tension gashes between them (*Plate V.3-F*) or being opened and re-used by them, generating composite quartz-calcite-chlorite veins (*Plate V.3-D, I*). As presented above, the black chlorite (Chl<sub>2</sub>) and calcite (Cal<sub>2</sub>) are common minerals within the VS<sub>5</sub> veins, and thereby, Q<sub>3</sub> is also interpreted to be associated with this vein set.

As presented in *Appendix II*, the only mineralised sample collected from outcrop is PC04. The sample is oriented and contains both the VS<sub>2</sub> and VS<sub>5</sub> veins (*Plate V.3-A*). The studied core and float samples contain VS<sub>2</sub> and VS<sub>3</sub> veins that are crosscut by a multitude of thinner veins. Some of these thin veins can be associated with VS<sub>5</sub> based on their mineralogy (presence of the black chlorite), but the VS<sub>4</sub> and VS<sub>6</sub> veins cannot be distinguished in the core samples. Thereby, it is unknown if any of the identified quartz generations from VS<sub>2</sub>, VS<sub>3</sub> and VS<sub>5</sub> are also found in the VS<sub>4</sub> and VS<sub>6</sub> vein sets (*Table V.3*).

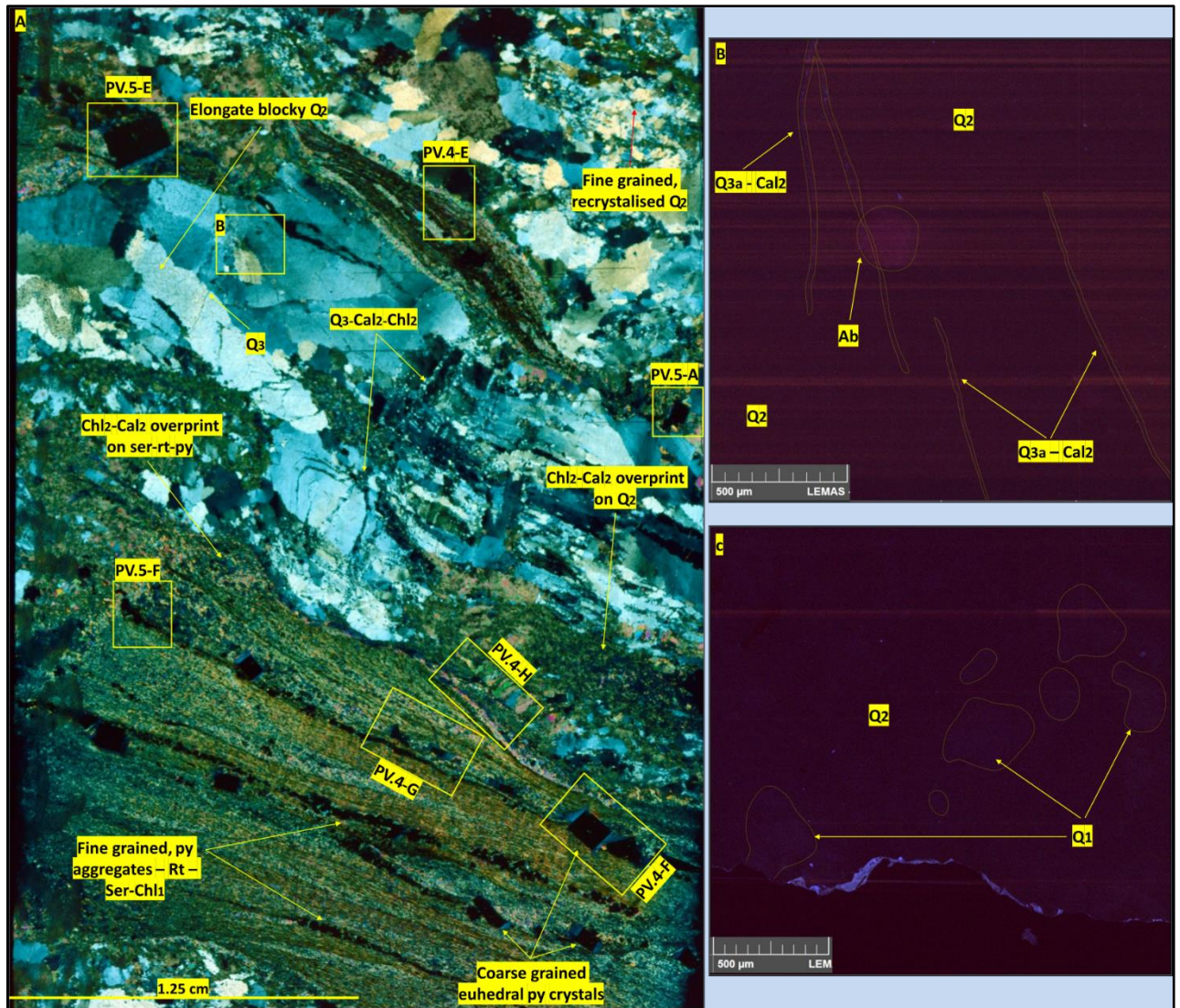


**Plate V.3** – Representative images of different types of quartz generations related to the Pine Cove mineralisation. **A** – Microscope scan (cross – polarized light) of an oriented thin section (PC-04) made through a breccia type vein (VS<sub>2</sub>) and its associated alteration halo (hand specimen presented in **Plate V.1–C**), note the different textures of quartz crystals, the different sizes and morphologies of the pyrite crystals and aggregates and the cal<sub>2</sub>-chl<sub>2</sub> overprint; the yellow rectangle **B** shows the location of image **B** on the section, the yellow rectangles **PV-4E** to **PV-4H** and **PV-5A, E, F** show the location of images **E, F, G, H** from **Plate V-4** and the location of images **A, E, F** from **Plate V-5**, respectively (see below). **B** – Colored CL image of Q<sub>2</sub>, note the low CL response and its dark purple/blue colour; the red stripes are caused by the high fluorescence of calcite which disturb the CL image; **C** – Colored CL image of Q<sub>1</sub> and Q<sub>2</sub> generations, note the relict Q<sub>1</sub> crystals and their better CL response (brighter blue) within the homogenous Q<sub>2</sub> (dark purple/blue mass), sample PC-167. **Note**, for images **B** and **C** the contrast was increased to better highlight the differences between different quartz generations.

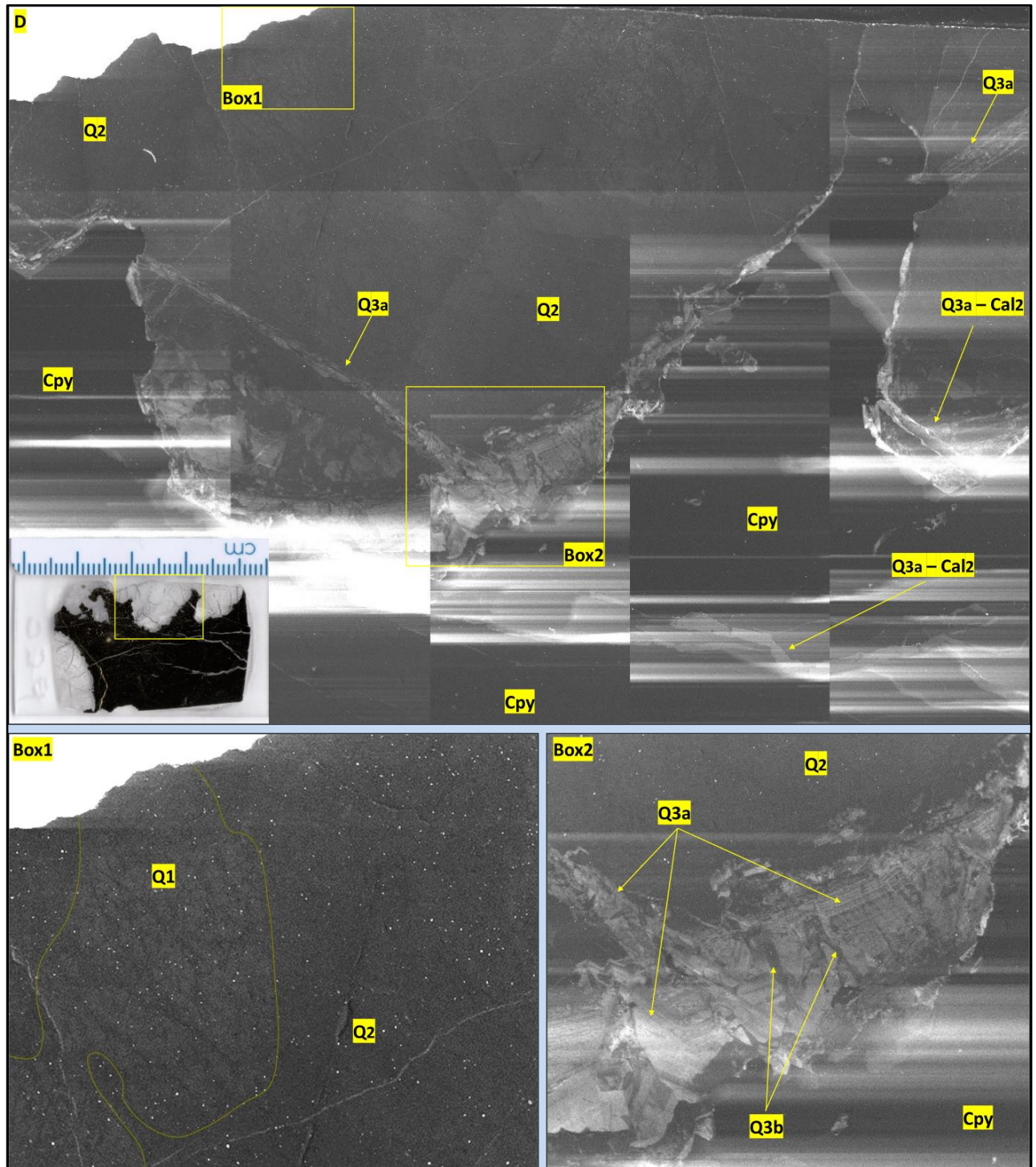


**Plate V.3.** – Representative images of different types of quartz generations related to the Pine Cove mineralisation. **D** – Monochrome CL scan showing relationships between Q<sub>1</sub>, Q<sub>2</sub>, Q<sub>3A</sub> and Q<sub>3B</sub> quartz generations (the scan location on the PCC section is shown in the small image from the lower left corner), **note** the calcite overprint in the large image, the relationships between Q<sub>1</sub> and Q<sub>2</sub> in **Box 1**, and the laminated and folded nature of Q<sub>3A</sub> and its brecciation by Q<sub>3B</sub> in **Box 2**, sample PCC. **Note**, the contrast of Box1 was increased to highlight the differences between Q<sub>1</sub> and Q<sub>2</sub>. **Continuation below.**



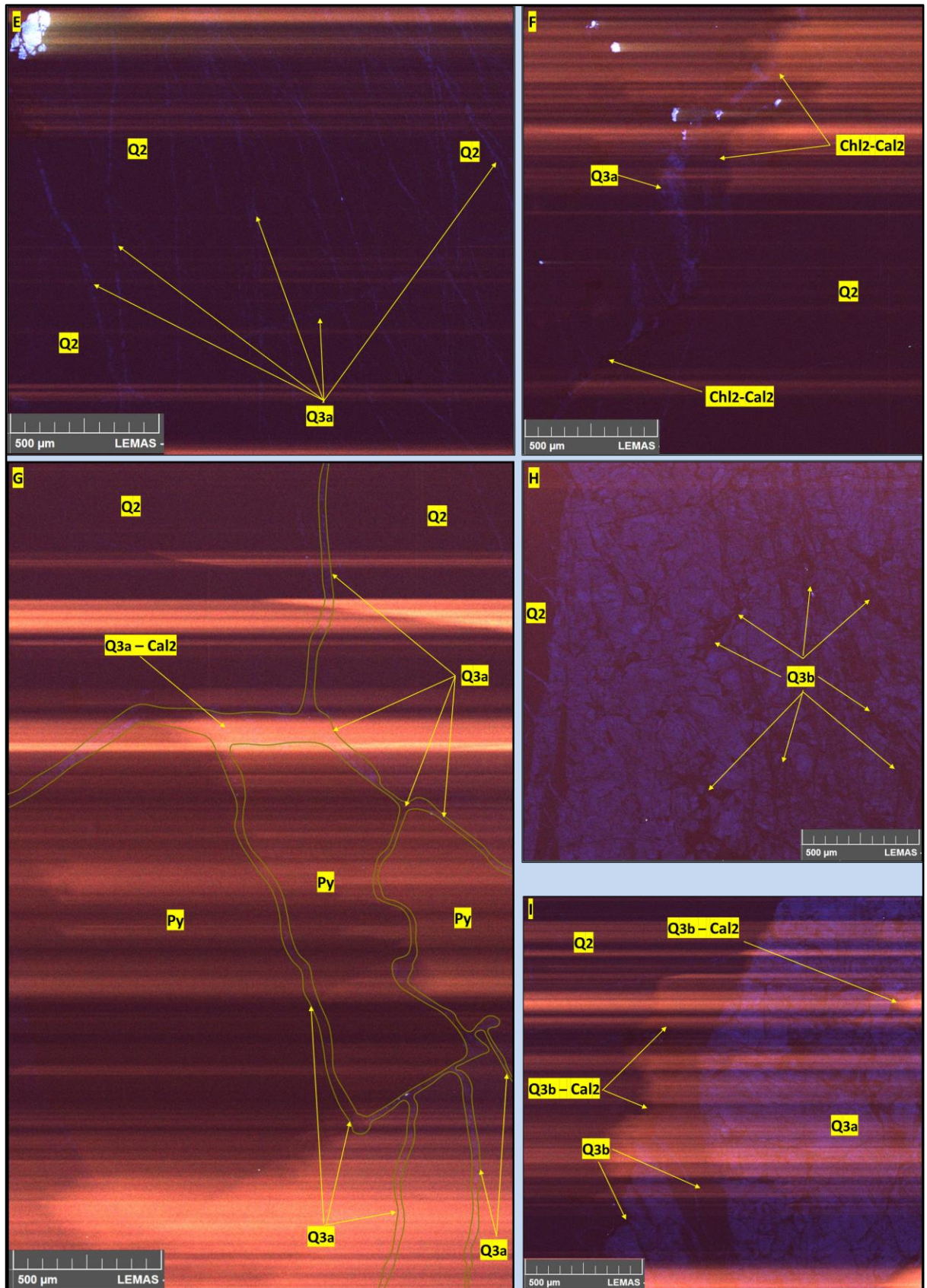


**Plate V.3 (E to I, see above)** – Representative images of different types of quartz generations related to the Pine Cove mineralisation. **E** – Colored CL image showing cobweb texture of  $Q_{3A}$  overprinting homogenous  $Q_2$ , sample PCHG; **F** – Colored CL image showing a  $Q_{3A}$  tension gash forming in association with  $Cal_2$ - $Chl_2$  veinlets, the red stripes are caused by the presence of calcite, sample PCHG; **G** – Colored CL image showing the brecciation of an euhedral pyrite crystal (black in CL) by  $Q_{3A}$  and  $Cal_2$ , sample PCHG; **H & I** – Colored CL image showing a brecciated  $Q_{3A}$  vein by  $Q_{3B}$  and  $Cal_2$  veinlets, sample PCHG. **Note**, for images **E-I** the contrast was increased to better highlight the differences between different quartz generations.

The sericite and rutile show an intimate spatial relationship and provide the orange-brown colour to the host rocks (**Plate V.1-C; V.2-B, D; V.3-A**). The sericite-rutile masses form alteration envelopes around the 2<sup>nd</sup> quartz generation ( $Q_2$ ) and are affected by  $F_3$  folds and related structures (**Plate V.1-C; V.3-A; V.4-E**). The sericite is composed of muscovite and minor phengite (differentiation made based on EDS data). It occurs oriented along the foliation planes within the wall rock and as stringers and patches between quartz and albite crystals within the veins. A coarser grained muscovite was also observed as shadow pressures around euhedral pyrite crystals and within micro-folded, foliation-parallel veinlets (**Plate V.4-E**). The rutile appears as aggregates of very fine grained, irregular to prismatic crystals within the sericite mass or as inclusions in pyrite crystals and aggregates (**Plate V.4-A, B; V.5-A, B, D**). Relict crystal fragments of ilmenite were locally observed within the rutile aggregates, and as inclusions in the pyrite crystals.

The albite has a white to a distinct pink-orange colour and occurs as vein component within  $VS_2$  and  $VS_3$ , and within the altered wall rock material in association with sericite, rutile, chlorite<sub>1</sub> and pyrite (**Plate V.1-B**). In the veins, the albite has straight or recrystallised crystal boundaries with  $Q_2$  and is crosscut by  $Q_3$ . When imaged by CL, the albite, regardless of its macroscopic colour, shows a particular magenta colour that varies in intensity from pale to bright (**Plate V.4-C, D**). In areas of intense sericitization the albite is preserved only as irregular crystal fragments enclosed in the sericite mass (**Plate V.4-A, B**).

At least two types of chlorite can be differentiated within the alteration halos of the Pine Cove deposit with respect to their optical and geochemical properties. These are termed here as chlorite<sub>1</sub> ( $Chl_1$ ) and chlorite<sub>2</sub> ( $Chl_2$ ) based on their crosscutting relationships, association with other alteration minerals and on their

interpreted relative timing. Chl<sub>1</sub> is interpreted as an early phase, whereas Chl<sub>2</sub> as a later phase.

Chl<sub>1</sub> is very fine-grained, either intergrown with albite, sericite, and rutile, or as patches with calcite (*Plate V.3–A, V.4–B, V.5–D*). In plane polarised light, chl<sub>1</sub> is medium pleochroic and has a green colour, whereas in crossed polarised light it shows dark to brown birefringence colours.

Chl<sub>2</sub> has a distinct dark green to black colour in outcrop and overgrows most of the other alteration minerals (*Plate V.5. –C, L, T; V.2–B, D*). In plane polarised light, chl<sub>2</sub> displays a strong pleochroism with colours varying from yellow green to intense green, and distinct, blueish grey to intense blue and purple anomalous birefringence colours in crossed polarised light (*Plate V.4–F, G, H*). Chl<sub>2</sub> occurs in both mono-mineral and poli-mineral (with Cal<sub>2</sub> and Q<sub>3</sub>) veins formed both at a high angle and parallel to the foliation planes (*Plate V.3–F; V.4–G, H*). It also forms pyrite fringes for euhedral pyrite crystals bordered by extensional shear bands that are sub-parallel to the axial planes of F<sub>3</sub> microfolds (*Plate V.4–F*). Large patches of Chl<sub>2</sub>-Cal<sub>2</sub> are also common and overprint the rest of the alteration minerals.

EDS analysis of different particles of Chl<sub>1</sub> show similar Mg and Al contents, with ranges of 7 to 11%, and Fe between 16 to 23%. In contrast, Chl<sub>2</sub> shows compositional ranges: Fe (21 – 29%), Al (7 – 13%) and Mg (4 to 8 %). When compared, Chl<sub>1</sub> has high Mg and low Fe contents, whereas Chl<sub>2</sub> has low Mg, moderate to high Al and high Fe contents (*Plate V.4–I, J*).

Siderite was macroscopically observed in core sections from low gold grade intervals within intense carbonatized zones (*Plate V.2–C*), but no microscopical nor geochemical analysis were conducted. Hence, the relationship between the siderite and the rest of the alteration minerals is unknown.

Within the studied samples, two types of carbonates were identified based on their Fe, Mg and Ca contents (EDS analysis): calcite and ankerite. The calcite is the dominant phase, occurs in most of the identified vein sets and shows a variety of textures (*Table V.2*). Two types of calcites were separated based on the association with other alteration minerals and on overprinting relationships (*Table V.2*). Cal<sub>1</sub> develops together with Chl<sub>1</sub> as patches within the albite-sericite-rutile masses. Cal<sub>2</sub> forms late, mono and poli-mineral (Q<sub>3</sub>-Cal<sub>2</sub>-Chl<sub>2</sub> ± Hem) veins and large patches that infill open spaces in Q<sub>2</sub> and overprint the albite-sericite-rutile association (*Plate V.3–*

A, D; V.4-C, D, H; V.5-B, C). Thin, veins of Cal<sub>2</sub> crosscut Q<sub>3A</sub> and show mutual crosscutting relationships with both Chl<sub>2</sub> and Q<sub>3b</sub> veins.

The ankerite was observed only within the altered host rocks, in association with sericite, albite, rutile and pyrite. It mostly occurs as inclusions or as relict crystal fragments inside and between pyrite crystals and aggregates, and to a lesser degree as large grains within the altered ground mass (*Table V.2; Plate V.5-D*).

Hematite was observed in association with Cal<sub>2</sub>-Chl<sub>2</sub> within VS<sub>5</sub> (*Plate V.1-C; V.2-D*). It presents itself as small aggregates of irregular to prismatic crystals within calcite patches (*Plate V.5-A*), or as stringers crosscutting all the alteration minerals. Hematite also occurs as staining related to supergene alteration on outcrop faces and along open fractures.

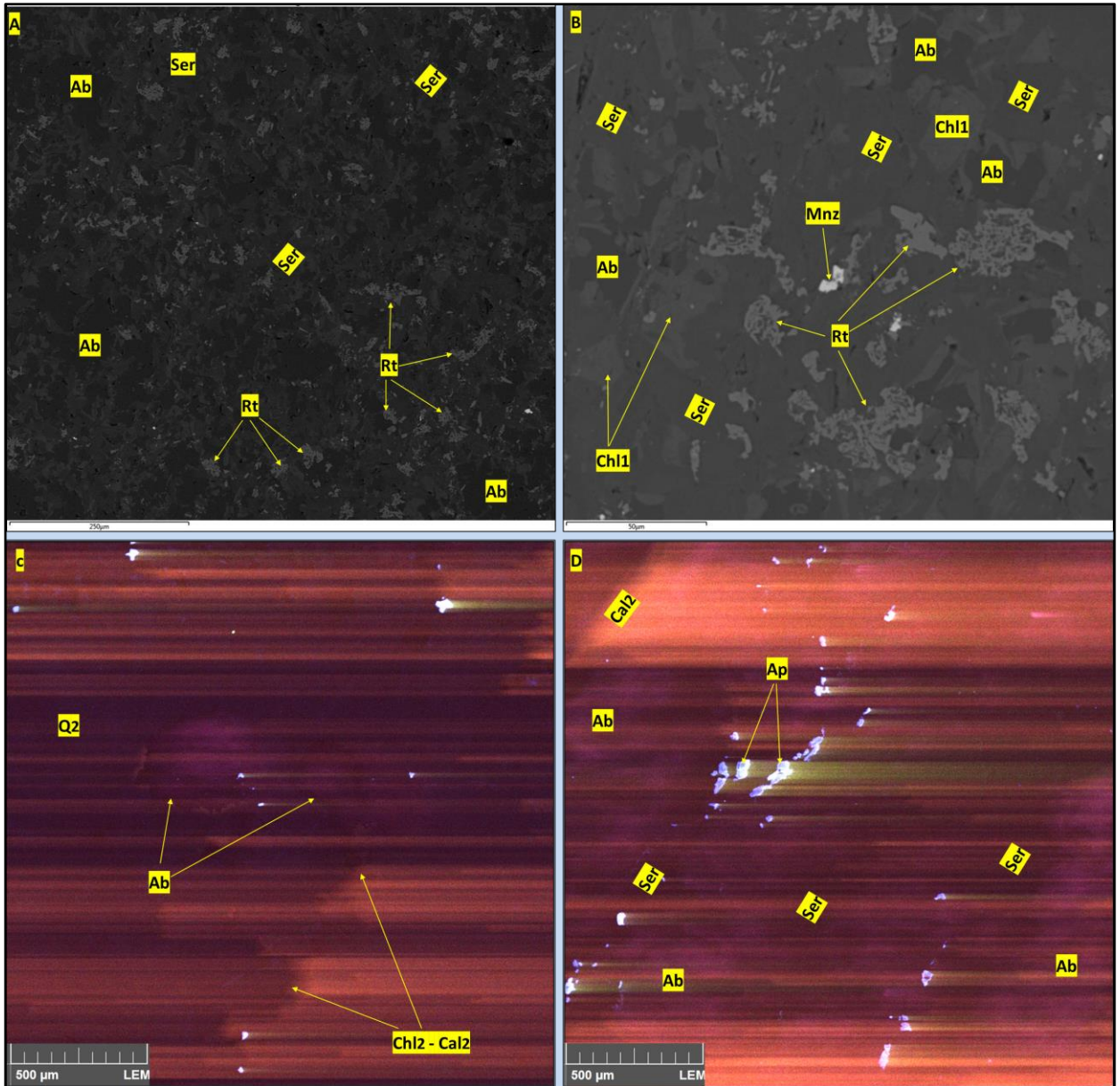


**Plate V.4.** – Representative images for different alteration minerals related to the Pine Cove mineralisation. **A, B** – BSE images of Ser – Rt – Ab – Ch<sub>1</sub> domains, note the irregular and embedded nature of the Ab and Rt crystals within the sericite mass; **C** – Colored CL image showing Q<sub>2</sub> intergrown with Ab (note the distinct magenta colour) and their brecciation by Ch<sub>1</sub>–Ch<sub>2</sub> veinlets; **D** – Colored CL image showing Ab (magenta color) – Ser (black) – Ap (bright blue) domains overprinted by Calcite (bright red and associated red interference stripes EDS spectra for the two types of chlorite generations: Ch<sub>1</sub> and Ch<sub>2</sub>, respectively, note the high Mg and low Fe content of Ch<sub>1</sub> vs low Mg and high Fe content of Ch<sub>2</sub>). Images **A to D** from sample PC-167. **Note**, for images **C & D** the contrast was increased to better highlight the differences between the minerals of interest. Plate continuation on next page.

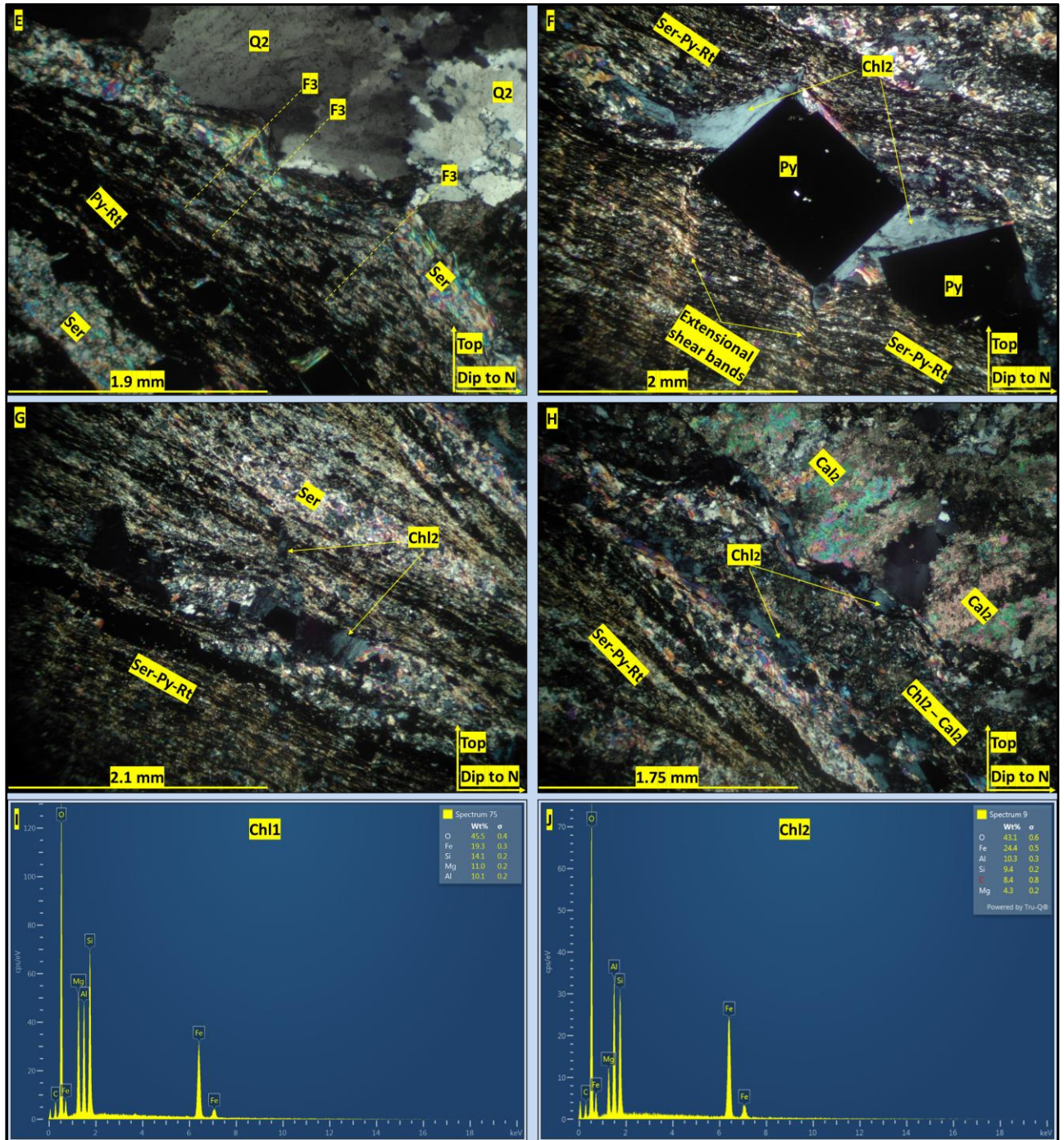


**Plate V.4.**—**E** – Microscope image (cross polarized light) of Ser-Py-Rt foliation-parallel alteration affected by F<sub>3</sub> microfolds, note the coarser sericite flakes; **F** – Microscope image (cross polarized light) showing rotated euhedral pyrite crystals between extensional shear bands related to F<sub>3</sub> folding, note the chlorite pyrite fringes and the distinct blueish-grey birefringence colour of Chl<sub>2</sub>; **G** – Microscope image (cross polarized light) showing a Chl<sub>2</sub> veinlet crosscutting at a high angle the foliation-parallel Ser-Rt-Py alteration; **H** – Cal<sub>2</sub> patches and foliation-parallel Chl<sub>2</sub> veinlets overprinting Ser-Rt-Py alteration; **I & J** – Representative EDS spectra for the two types of chlorite generations: Chl<sub>1</sub> and Chl<sub>2</sub>, respectively, **note** the high Mg and low Fe content of Chl<sub>1</sub> vs low Mg and high Fe content of Chl<sub>2</sub>. Images **E** to **H** from sample PC-04, **I** from sample PC-167 and **J** from sample PC-04.

Pyrite is the most abundant sulphide within the Pine Cove deposit. It occurs disseminated within the alteration selvages that surround the vein sets VS<sub>2</sub>, VS<sub>3</sub>, VS<sub>4</sub> and VS<sub>5</sub>, in the altered wall rock fragments incorporated into the veins, and at the contact between the veins and the host rocks (*Plate V.1-L, Q; V.2-B, D; V.3-A*). Pyrite hosted directly in the veins was also observed. The pyrite crystals vary in size from a few tens of microns to a few millimetres and show anhedral to euhedral shapes. Two types of pyrite crystals were differentiated based on their textural characteristics: i) simple zoned crystals with inclusion rich core, mantled by inclusion free euhedral rims (*Plate V.5-A, B*); and ii) neat crystals, un-zoned, without or with very few inclusions (*Plate V.5-C*). Within the coarse-grained euhedral crystals, multiple inclusion rich domains separated by inclusion free areas were also observed suggesting a complex growth history (*Plate V.5-D*). All the alteration minerals presented in *Table V.2* plus relict fragments of ilmenite and epidote occur as inclusions within the pyrite crystals. A distribution pattern for the mineral inclusions found within the pyrite crystals was observed: the ser-rt-ab-ank-chl<sub>1</sub>-cal<sub>1</sub> are usually found in the inclusion rich domains (*Plate V.5-A, B, D, E*) whereas the cal<sub>2</sub> and chl<sub>2</sub> were observed mostly in the rims oriented parallel to the crystal faces or aligned along healed fractures and at the crystal boundary interface in aggregates (*Plate V.5-E*).

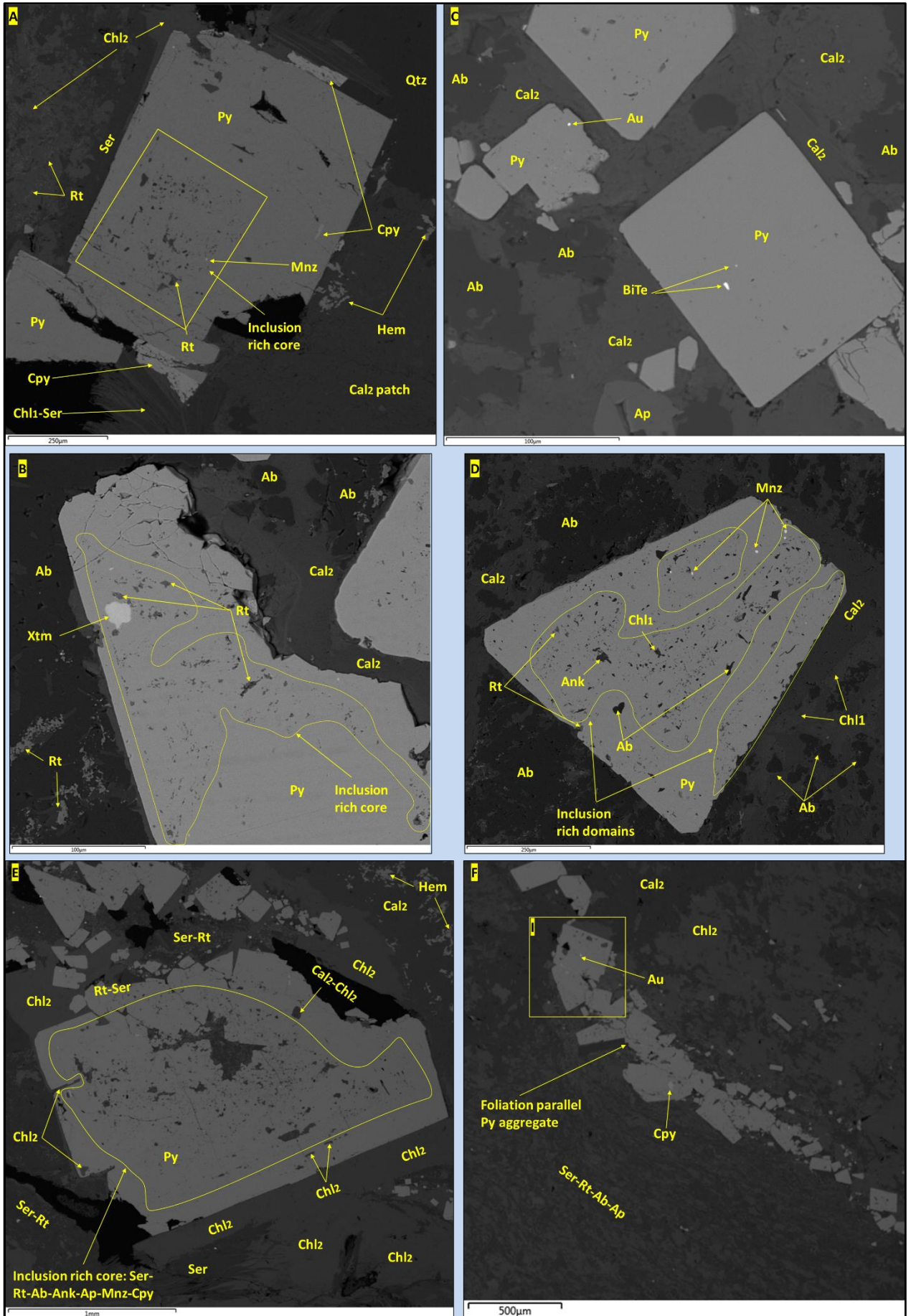
In the studied samples (*Appendix 2*) the pyrite occurs mostly as patches (up to square centimetres in size) of brecciated or annealed polycrystalline aggregates (*Plate V.2-B, D*). Commonly, fine grained stand-alone pyrite crystals and polycrystalline aggregates with visible crystal boundaries are aligned along the foliation planes together with rutile, sericite, and albite, whereas the coarser crystals and aggregates overgrow the foliation fabric and the rest of the alteration minerals (*Plate V.2-D; V.3-A; V.4-F, G; V.5-F*). The largest patches of pyrite aggregates are in general clean, with few inclusions, and show variable degrees of brecciation caused by mono or poly mineral veinlets composed of Chl<sub>2</sub> and/or Cal<sub>2</sub> and/or Q<sub>3</sub> (*Plate V.5-G*). However, irregular patches and wires of pyrite that overprint and brecciate other alteration minerals were also observed within Cal<sub>2</sub>-Chl<sub>2</sub> patches and veins (*Plate V.5-H*). These textures together with the presence of Cal<sub>2</sub>-Chl<sub>2</sub> inclusions within the large pyrite crystals and aggregates suggest that annealing and recrystallisation of pyrite occurred in association with the Q<sub>3</sub>-Chl<sub>2</sub>-Cal<sub>2</sub> veins. Further, interpretations regarding the

growth history of the pyrite with respect to the evolution of the mineral system are provided in the interpretation section of this chapter.

Three types of phosphates were observed in the studied samples: apatite, monazite, and xenotime. The apatite is the most abundant and show variable sizes, from a few microns up to 1-2 millimetres. It occurs disseminated along the foliation planes together with sericite-rutile-albite and pyrite, as inclusions within pyrite crystals, or as large patches at the interface of quartz and/or calcite and/or pyrite crystals (*Plate V.5-I*). The large apatite crystals contain inclusions of rutile, albite, sericite, pyrite, monazite, and xenotime and are usually brecciated by the calcite<sub>2</sub>-chlorite<sub>2</sub> ± pyrite veinlets (*Plate V.5-H*).

The monazite and xenotime occur as small inclusions (~10 µm in size) in pyrite and in apatite and free between the pyrite crystals (*Plate V.5-B, D*). Small, disseminated, subrounded to rounded grains of monazite/xenotime are also common within the albite-sericite-rutile ground mass. Both the monazites and the xenotimes are brecciated by the chl<sub>2</sub>-cal<sub>2</sub> veinlets. Some monazite and xenotime grains were also observed along the chlorite<sub>2</sub>-calcite<sub>2</sub> veins, but it is not clear if these were incorporated within the veins from the wall rock, or if they formed within the veins.





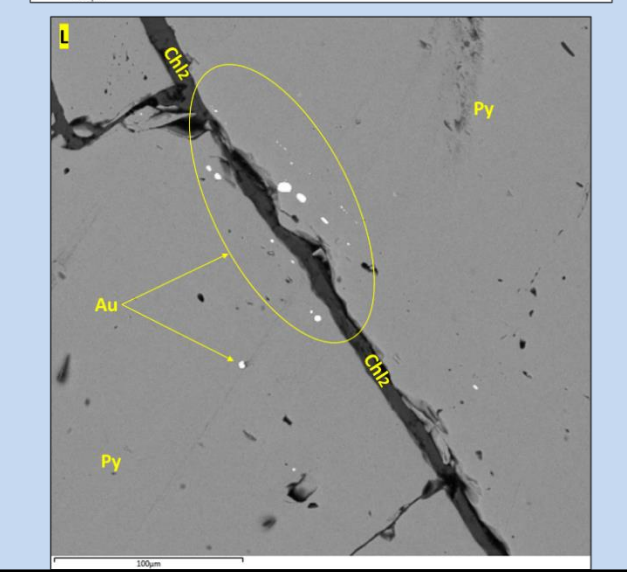
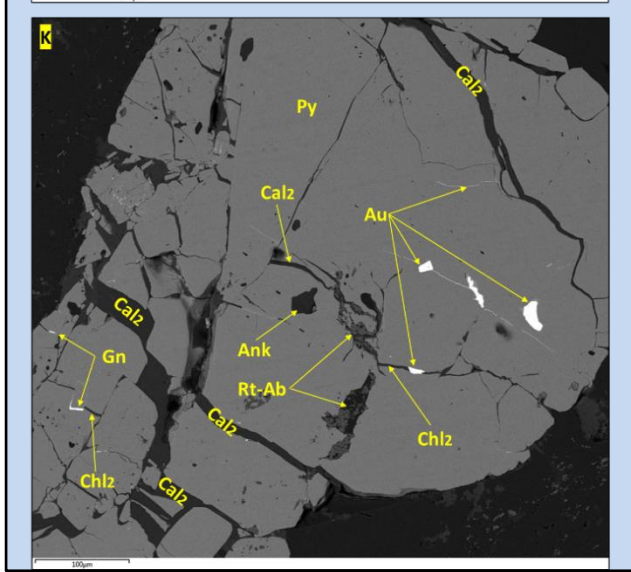
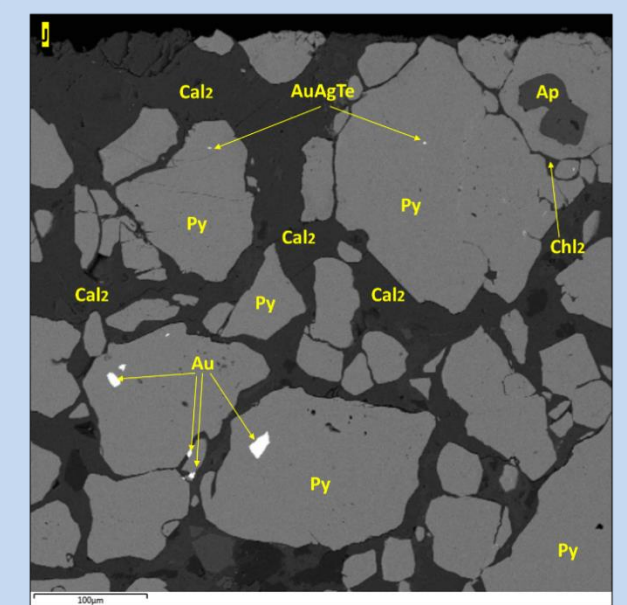
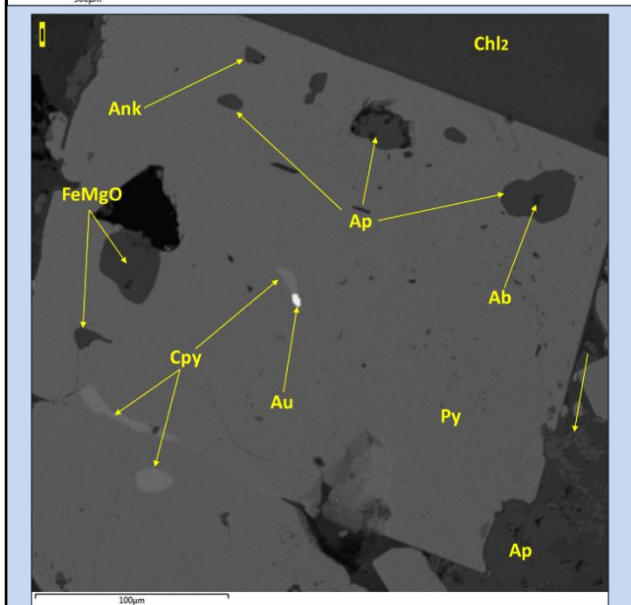
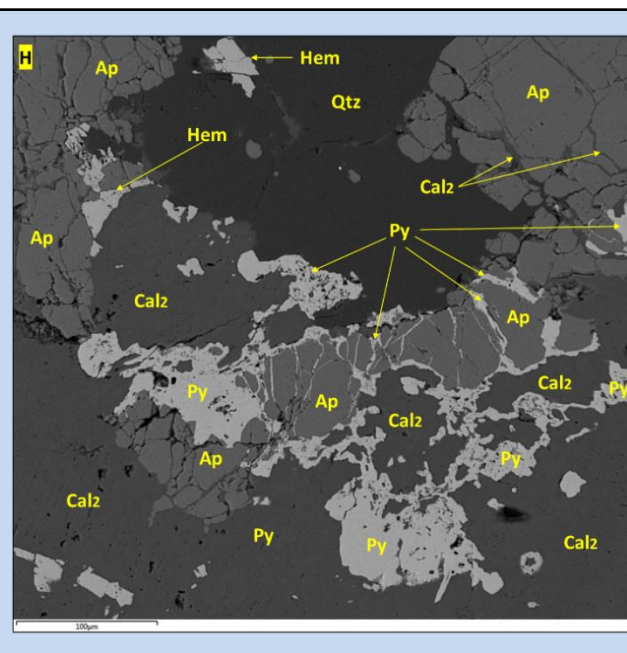
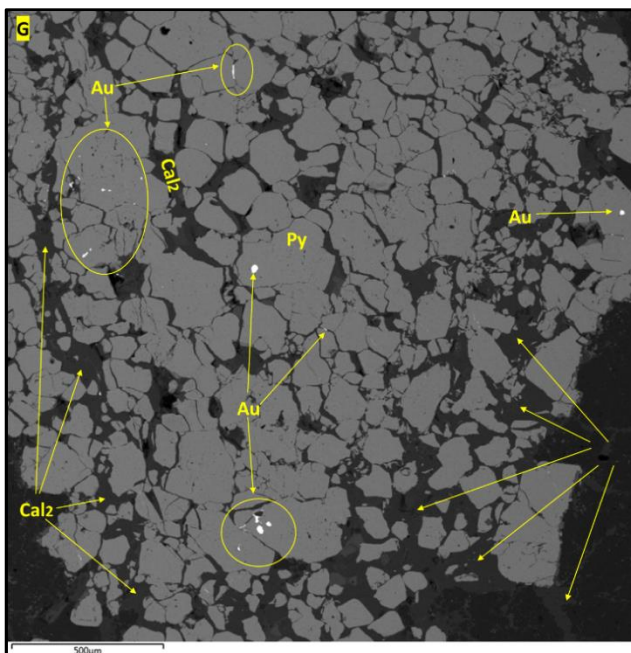


**Plate V.5.** – Representative images for different alteration and ore minerals related to the Pine Cove mineralisation. **A, B** – BSE images of coarse-grained pyrite crystals with inclusion rich cores and neat, outer domains and rims, note the mnz, rt, cpy and xtm inclusions in the py crystals. **C** – BSE image of neat, almost inclusion free pyrite crystals, note the Au and BiTe inclusions within the py crystals. **D** – BSE image of coarse-grained pyrite crystal with multiple inclusion rich domains separated by inclusion free zones, note the presence of mnz, ank, rt, ab and chl<sub>1</sub> inclusions within the py. **E** – BSE image of coarse-grained pyrite crystal/aggregate (small py crystals that compose the large one are still visible in the middle and on the margins) with inclusion rich core (rt-ab-ank-ap-mnz-cpy) with neat rims, note the presence of chl<sub>2</sub>-cal<sub>2</sub> inclusions within the rims, aligned parallel to the crystal faces. **F** – BSE image of fine-grained pyrite aggregate aligned parallel to the foliation planes along with ser-rt-ab-ap, note the still visible crystal boundaries within the pyrite aggregate and the cal<sub>2</sub>-chl<sub>2</sub> overprint. **G** – BSE image of a large, neat (almost inclusion free) patch of pyrite aggregate brecciated by cal<sub>2</sub> veinlets, note the high amount of Au grains and their irregular to rounded shapes. **H** – BSE image of pyrite patches and wires in association with cal<sub>2</sub>, note the brecciation of apatite by the cal<sub>2</sub>-py veinlets. **I** – BSE image of gold and cpy inclusions in pyrite crystals, note the Au-cpy intergrown, the cpy at the interface of py crystals and the ap, ank, ab and iron-magnesium-oxides (FeMgO) inclusions. **J** – BSE image of gold and AuAgTe inclusions within pyrite crystals, note the intense brecciation of py by cal<sub>2</sub>-chl<sub>2</sub> veinlets and the presence of Au between py crystals along the veinlets. **K** – BSE image of brecciated pyrite patch by cal<sub>2</sub>-chl<sub>2</sub> veinlets, note the Au wires that connect the irregular Au inclusions from the py, the Au grain located along the chl<sub>2</sub> veinlet, and the Gn wires located along the cal<sub>2</sub> veinlets that brecciate the py. **L** – BSE image of rounded Au inclusions in pyrite aligned parallel to a chl<sub>2</sub> veinlet that crosscut the py crystal. Images **A, E, F, I** from section PC04, image **B** from section PC167, images **C, G, J, K** from section PC100, image **H** from section PC102 and image **L** from section PCHG.

#### **V.1.1.4. Mineralisation**

The ore mineralogy of the Pine Cove deposit is composed of native gold, undifferentiated gold-silver and bismuth tellurides, chalcopyrite, galena, and trace amounts molybdenite, barite and undifferentiated cadmium and cadmium-lead bearing sulphides. Summarised descriptions regarding the occurrence and morphologies of these minerals are provided below and in **Table V.4**, whereas representative images in **Plate V.5**.

The gold shows an intimate relationship with the pyrite crystals. Most of the gold grains were found as irregular to rounded inclusions fully enclosed in the pyrite crystals or free, as wires, rounded blebs, and irregular crystals along mono or poly mineral veinlets composed of Chl<sub>2</sub>-Cal<sub>2</sub>-Q<sub>3</sub>, that brecciate the pyrite crystals and aggregates (**Plate V.5–C, I, G, K**). The gold inclusions within the pyrite crystals were observed both within the inclusion rich domains and in the neat, recrystallised parts of

the crystals. It was also observed that within the neat, large, and brecciated pyrite patches the gold grains are more abundant and coarser compared to the gold found in the finer grained, inclusion rich crystals and aggregates (*Plate V.5-F, G*). Trails of gold inclusions within pyrite crystals that are aligned parallel to Chl<sub>2</sub> or Cal<sub>2</sub>-Chl<sub>2</sub> veinlets that crosscut the pyrite are also common (*Plate V.5-L*).

The chalcopyrite is the second most abundant sulphide phase after the pyrite and was observed as inclusions in the pyrite crystals and free in the altered groundmass or along Chl<sub>2</sub>-Cal<sub>2</sub>-Q<sub>3</sub> veinlets that brecciate the pyrite (*Plate V.5-A, I*). Large patches to almost massive chalcopyrite masses (cubic centimetres) were observed as infills in Q<sub>2</sub> in association to Q<sub>3</sub> (*Plate V.3-D*). These massive zones of chalcopyrite are crosscut by Cal<sub>2</sub>-Q<sub>3</sub> veinlets. Chalcopyrite intergrown with gold was commonly observed when both minerals occur as inclusions within pyrite (*Plate V.5-I*).

Two undifferentiated telluride phases were observed within the study samples: gold-silver telluride and bismuth telluride (*Plate V.5-C, J*). The exact mineral species (eg. Sylvanite vs Petzite) for the gold-silver and bismuth tellurides were not established during this study. This applies for all the studied deposits. Both the gold-silver / bismuth tellurides occur as inclusions within the pyrite crystals or free along Q<sub>3</sub>-Cal<sub>2</sub>-Chl<sub>2</sub> veinlets and at the interface between pyrite crystals (*Plate V.5-C, J*). Gold intergrown with gold-silver tellurides is common when the two phases occur as inclusions in pyrite.

**Table V.4** – Summary characteristics of the ore minerals from the Pine Cove deposit.

Mineral	Occurrence, Morphology
Au	Irregular to rounded inclusions in py; free as wires and irregular to rounded grains along cal <sub>2</sub> -chl <sub>2</sub> -Q <sub>3</sub> fractures that brecciate the py or at the interface of py crystals; less common free in ab, qtz <sub>2</sub> , ser, cal <sub>1</sub> ; variable sizes from 1 µm to up to 100 µm
Undifferentiated Au-Ag telluride	Irregular to rounded inclusions in py; free as wires and irregular to rounded grains along cal <sub>2</sub> -chl <sub>2</sub> -Q <sub>3</sub> fractures that brecciate the py or at the interface of py crystals; small sizes 1 - 20 µm
Cpy	Inclusions in the py crystals; free in the altered groundmass (qtz <sub>2</sub> -ab-ser-rt) or along chl <sub>2</sub> -cal <sub>2</sub> -Q <sub>3</sub> veinlets that brecciate the pyrite; large patches to almost massive chalcopyrite masses (cm <sup>2</sup> )
Gn	Small inclusions (1-20 µm) in the py crystals; free as wires or irregular grains along chl <sub>2</sub> -cal <sub>2</sub> -Q <sub>3</sub> veinlets that brecciate the py
Undifferentiated Bi telluride	Trace* amounts, small (1-10 µm) inclusions within and at the interface of py crystals; free as irregular grains and wires along cal <sub>2</sub> -chl <sub>2</sub> -Q <sub>3</sub> fractures that brecciate the py
Moly	Trace* amounts, small (1-10 µm) inclusions within py crystals; free in the altered ground mass (qtz <sub>2</sub> -ab-ser-rt)
Barite	Trace* amounts, inclusions of ~ 20 µm sizes within py crystals
Undifferentiated Cd and Cd-Pb sulphides	Trace* amounts, very small grains (1-2 µm) within py crystals and free in the altered ground mass

\*trace = none, or very few grains / studied thin section

### V.1.2. The Stog'er Tight deposit

The field observations and structural data presented in this section were collected from the “*Stog'er Tight*” and “*East Zone*” open pits, the two developed zones of the Stog'er Tight deposit, and from other nearby outcrops (**Figure V.2**). The mineralisation is strata-bound, most of it being hosted by the Stog'er Tight gabbro (**Figure. A1.3**). A detailed description of the Stog'er Tight gabbro and of other lithologies that occur in the Stog'er Tight area can be found in Ramezani (1992), whereas summarised descriptions extracted from the work of the afore-mentioned author are provided in **Appendix I**.

#### V.1.2.1. Structural setting

All the structural elements observed at the scale of the entire Point Rousse Complex (**Tables IV.1 & IV.2**) were also observed in the Stog'er Tight area. The Stog'er Tight deposit is located approximately 2 km to the north from the NE dipping segment of the D<sub>2a</sub> Scrape Thrust and roughly 1 km W from the NNE striking section of the same fault (**Figure. IV.1**). Compared to the Pine Cove area, the Stog'er Tight region shows a lower strain intensity with only minor transposition between the S<sub>2a</sub> and the S<sub>2b</sub> fabrics. Across the area, the S<sub>2a</sub> is the main foliation fabric, whereas the S<sub>2b</sub> and the composite S<sub>2a/2b</sub> foliations are common within and in the proximity of D<sub>2b</sub> faults. On both the S<sub>2a</sub> and on the S<sub>2a/2b</sub> foliation fabrics a well-developed, down dip to oblique, stretching mineral lineation (L<sub>2</sub>) was observed (**Figure V.2-B**).

The S<sub>2a</sub> foliation dip shallowly to steeply to NW - NE and locally to S and SW (**Figure V.2-B**). The variable orientation of the S<sub>2a</sub> fabric in the Stog'er Tight area is comparable to the orientation of the S<sub>2a</sub> foliation observed at the scale of the entire PRC (**Figure V.2-A, B, C**), and therefore, it is interpreted to be the result of the F<sub>3</sub> and the F<sub>4</sub> folding events.

The S<sub>2b</sub> and the composite S<sub>2a/2b</sub> fabrics are steep (45° to 80°) and dip preponderantly to NE (**Figure V.2-B**). Most of the structural measurements for the S<sub>2b</sub>/S<sub>2a/2b</sub> fabrics were collected from the NE dipping limb of a large scale F<sub>4</sub> antiform (**Figure V.2-A**). Hence, the constant strike of the S<sub>2b</sub> and of the composite S<sub>2a/2b</sub> fabrics may be only a reflection of the data distribution, rather than a representative template for the entire area.

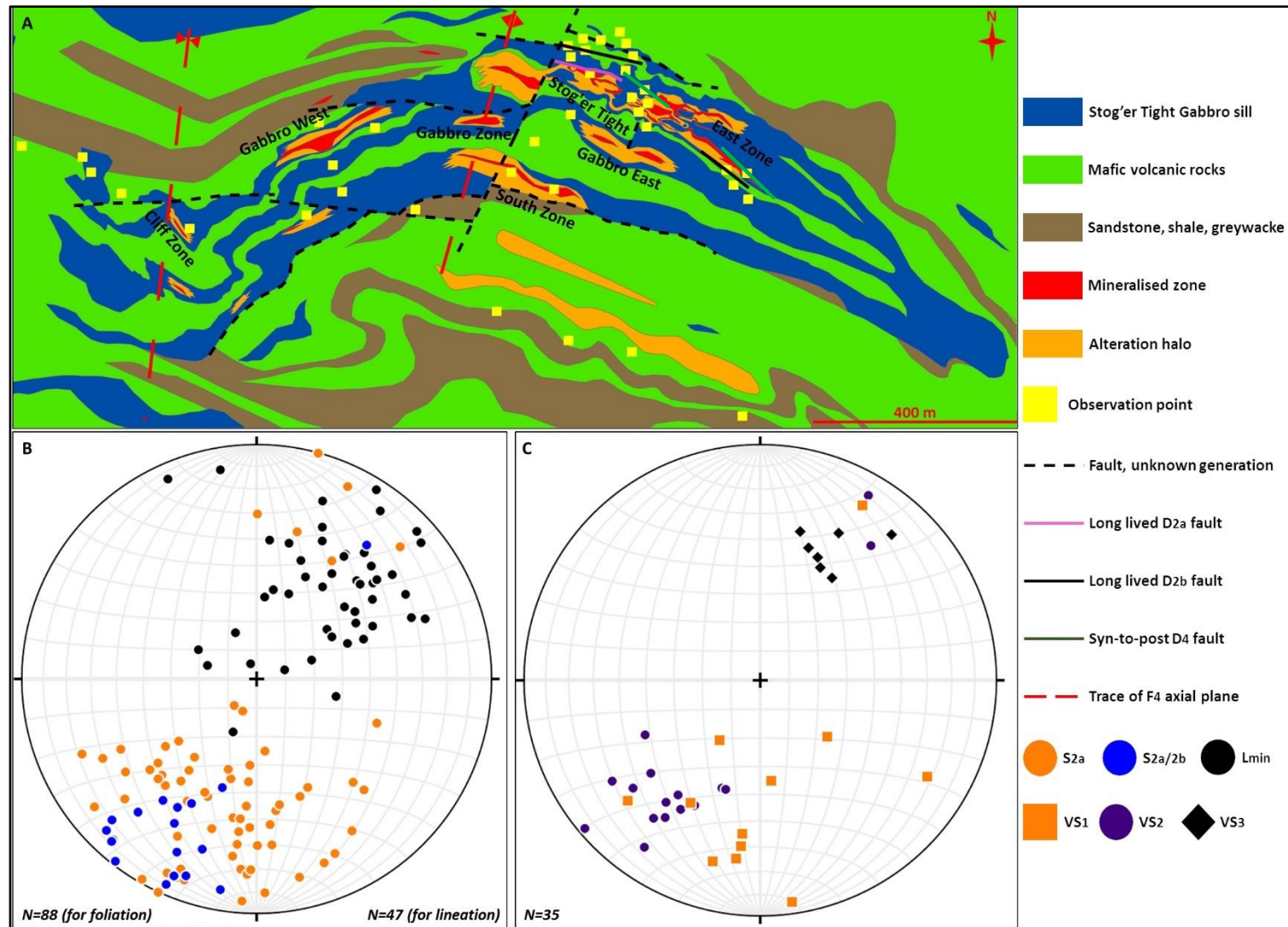


**Figure V.2:** **A** – Simplified geological map of the Stog'er Tight deposit after Copeland et al. (2015) and after the unpublished geological map of Anaconda Mining (2018); **B** - Southern-hemisphere, equal-area, stereographic projections of the poles to the foliation planes and of the stretching mineral lineation; **C** - The poles to the main mineralised vein sets.

D<sub>2a</sub> foliation-parallel ductile shear zones occur within the Stog'er Tight gabbro sills, and at the contact between the sills and the volcanoclastic units. The shears are usually narrow, from a couple of tens of centimetres up to 2-3 meters in width and are characterised by a strong mylonitic fabric associated with a well-developed down-dip stretching mineral lineation. Locally, the D<sub>2a</sub> shears border the mineralisation within the gabbroic bodies (*Figure V.2-A*), are crosscut and altered by quartz-carbonate veins, but do not host any mineralisation.

The D<sub>2b</sub> faults and shear zones observed in the Stog'er Tight area strike from E to SE, dip steeply (45° to 80°) to N – NE and accommodate oblique hanging wall motions to S – SE (*Plate IV.6-F*). The faults vary in width from one to approximately ten meters, but dense fracture sets associated to the faults are well developed for another few meters in both the foot wall and hanging wall. The D<sub>2b</sub> faults and fractures cut the mineralised and altered zones, but also host quartz-carbonate ± chlorite-pyrite veins (VS<sub>2</sub> - see below) (*Figure V.5-A*). Furthermore, narrow (tens of centimetres to a couple of meters in width), fine-grained, mafic dykes that are sub-parallel to the D<sub>2b</sub> faults also cut the mineralised areas. The dykes show mutual crosscutting relationships with the quartz-carbonate ± chlorite-pyrite veins, display a weak, spaced foliation cleavage that is sub-parallel to the S<sub>2b</sub> cleavage, and are folded by the F<sub>3</sub> folds (*Plate V.6-B, C*). These dykes are interpreted herein to be emplaced during D<sub>2b</sub> to early D<sub>3</sub>. The relevance of these dykes for the present study is discussed in *chapter VII - Discussions and synthesis*.

In the central part of the Stog'er Tight pit, a D<sub>2b</sub> brittle-ductile fault of approximately 5 meters in width was observed (*Figure V.2-A, Plate V.6-D*). The fault dip steeply to N and marks the northern contact between the Stog'er Tight gabbro and the surrounding volcanoclastic units. Within the fault a strong foliation fabric associated with a well-developed down-dip stretching mineral lineation is characteristic (*Plate V.6-E*). Brecciated and sheared mineralised lenses and fragmented quartz-albite and quartz-carbonate veins are common within the fault zone. The fault is affected by F<sub>3</sub> folds. Kinematic indicators suggest that the fault was reactivated during younger deformational events and accommodated different motion directions: foliation drags around the fault margins suggest north side-down motion, whereas late horizontal slicken-fibres that overprint the down-dip stretching mineral lineation indicate sinistral motion (*Plate V.6-F*).



The  $F_{2b}$  folds occur predominantly in the strongly foliated rocks and to a lesser degree in the more massive parts of the gabbro and affect some of the mineralised veins. Generally, the strongly foliated rocks accommodate high  $D_3$  strains leading to intense superposition between  $F_3$  and  $F_{2b}$  folds. In these cases, the presence of the  $F_{2b}$  folds can only be deduced from the type III fold interference pattern resulted from the superposition of the two-fold generations (*Plate V.3-H; V.6-G-box 1*).

The  $F_3$  folds are very well developed within the entire area and have wavelengths from a few centimetres up to 1-2 meters (*Plate IV.2-B, D, H*). Extensional shear bands that dip shallowly to moderately ( $5^\circ$ - $30^\circ$ ) to both north and south which are associated to the formation of the  $F_3$  folds are also common (*Plate IV.2-F & V.6-B, G*). The  $F_3$  folds and their associated structures affect the mineralised zones (*Plates IV.2-F & V.6-G*).

The  $F_4$  folds affect all the observed vein sets (see below) and fold and reactivate all the above-mentioned structures. The  $F_4$  folds vary from small parasitic “Z-M-S” type folds (Fossen, 2016) to local and regional scale synforms and antiforms (wavelengths from a few meters to hundreds of meters) (*Plate IV.3-A, D, E*). On the geological map, the outcrop trace of the Stog’er Tight gabbro defines a large  $F_4$  antiform with a wavelength of approximately 1 km (*Figure V.2-A*).

The syn-to-post  $D_4$ , NW striking faults (*Table IV.1-xiv*) truncate the mineralised zones (*Plate V.6-G*). A few mineralised lenses are bordered by these faults (*Figure V.2-A*), but the exact amount of displacement along the faults is unclear.

#### ***V.1.2.2. Vein Sets identified in the Stog’er Tight area***

Three main vein sets were observed in the Stog’er tight area. These are termed here as  $VS_1$ ,  $VS_2$  and  $VS_3$  in order of their relative order of formation. Descriptions for each vein set are provided in *Table V.6*, and representative images can be found in *Plate V.6*. *Figure V.2-D* shows the orientation of each vein set.

Two other vein types, except of the ones listed in *Table V.5*, were observed only locally in mineralised areas affected by intense superposition between  $F_3$  and  $F_{2b}$  folds (high strain  $D_3$  domains). Both vein types are composed of translucent to milky-white quartz and white-cream carbonates, show multiple opening domains with variable textures (massive, sheared, syntaxial), but have different orientations: i)

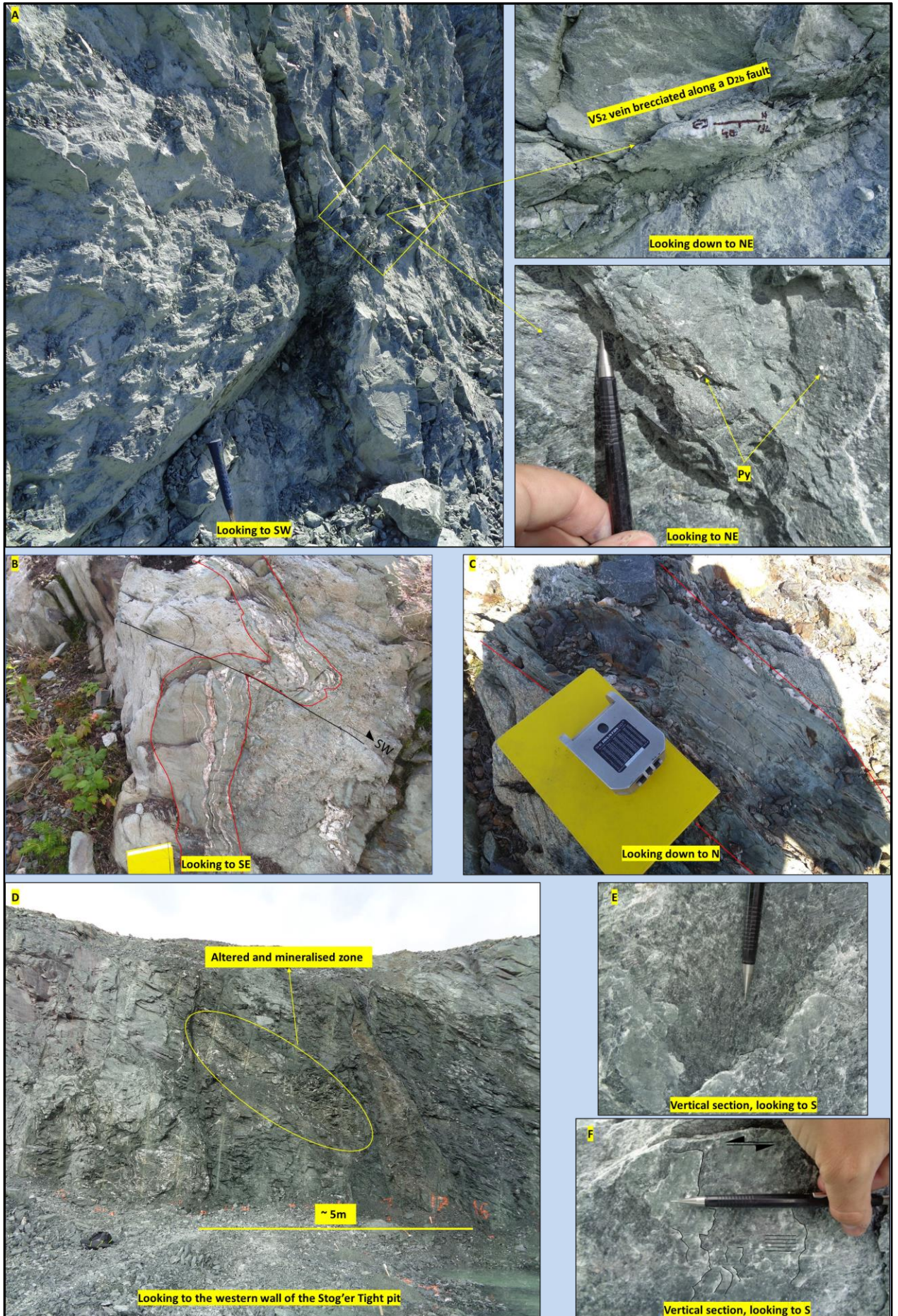
steeply dipping ( $70^{\circ}$ - $80^{\circ}$ ) to both north and south (*Plate V.6-G-box 1*); and ii) flat-lying and shallowly to moderately dipping to north and south (*Plate V.6-G-box 1*).

The steep veins crosscut the foliation at a low angle. These veins are folded by  $F_3$  folds and in areas where the  $F_3$  folds are tight, the veins are partially transposed into parallelism with the foliation (*Plate V.6-G-box 1*). The flat-lying veins crosscut the foliation and the steep veins and occur along or subparallel to the axial planes of the  $F_3$  folds and to the extensional  $D_3$  shears (*Plate V.6-G-box 1*). Both vein types crosscut and overprint  $VS_1$  (*Plate V.6-G*). Based on their orientations, mineralogy, and relationships with the  $D_3$  structures, the flat lying veins are interpreted to be part of  $VS_3$ , whereas the steep veins are either related to  $VS_2$  or a separate vein set characteristic only to high strain  $D_3$  domains. Interpretations related to the vein formation processes and their relative timing are provided in the interpretation section of this chapter.

**Table V.5. – Descriptions of vein sets identified within the Stog’er Tight and East Zone open pits**

*Terminologies regarding vein and crystal morphologies are used according to Bons (2000) and Bons et al. (2012)*

<b>Vein set</b>	<b>Characteristics</b>	<b>Alteration / Mineralisation</b>	<b>Crosscutting relationships</b>	<b>Structural constrains</b>
<b>VS<sub>1</sub></b> <i>Fig. V.2 – D; Plate V.6 G, H</i>	Quartz-albite-ankerite veins that vary in width from a few centimeters up to a couple of meters. The veins are white-cream-pink in color and show a variety of textures: massive with fine grained, “sugary” crystals in the thin veins; sheared, laminated and massive with coarse, blocky, and elongate blocky crystals in the wider veins; in the more massive and coarse-grained to pegmatitic parts of the Stog’er Tight gabbro these veins form stock-work networks that lead to total replacement or “flooded zones” of quartz and pink albite.	Alteration halo composed of ab-ank-ser-rt and disseminated auriferous py. Auriferous py also occur as polycrystalline aggregates in the replacement/flooded zones.	Crosscut by all the other vein sets	The veins are parallel to sub-parallel to the foliation. Are boudinaged, folded and faulted by all the syn-to-post D <sub>2b</sub> structures.
<b>VS<sub>2</sub></b> <i>Fig. V.2 – D; Plate V.6 – A, I</i>	Massive veins composed of coarse-grained, milky-white quartz and white-cream carbonates. Composite vein morphology with multiple opening domains: massive (dominant), sheared and stretched. Vary in thickness from a few centimeters up to 1-2 m. Sometimes occur as tension gash arrays.	Alteration halo composed of green chl (pervasive and as fault gauge on the veins’ border) and disseminated euhedral py. Trace of py and cpy in the veins as well.	Crosscuts VS <sub>1</sub> and are transected by VS <sub>3</sub>	Occur along or subparallel to the D <sub>2b</sub> faults but are usually brecciated and segmented by the faults, probably during reactivation. Are folded by both F <sub>3</sub> and F <sub>4</sub> folds.
<b>VS<sub>3</sub></b> <i>Fig. V.2 – D; Plate V.6 – G, J</i>	Quartz – carbonate ± chlorite (black) veins that dip moderately to steeply to S - SW. The veins show multiple opening domains with variable morphologies: massive, sheared, syntaxial and stretched. The quartz is milky-white and coarse grained – blocky to elongate blocky crystals. When chlorite occurs within or around the veins it displays a distinct black color.	Both barren and mineralised. The veins are usually mineralised in areas where they crosscut VS <sub>1</sub> , but barren outside the deposit. Alteration halo composed of cb-chl and intense supergene oxidation.	Crosscuts both VS <sub>1</sub> and VS <sub>2</sub>	Crosscuts both the S <sub>2a</sub> and the S <sub>2a/2b</sub> foliation fabrics. Occur along or subparallel to the F <sub>3</sub> axial planes and their associated shears and are folded by F <sub>4</sub> .



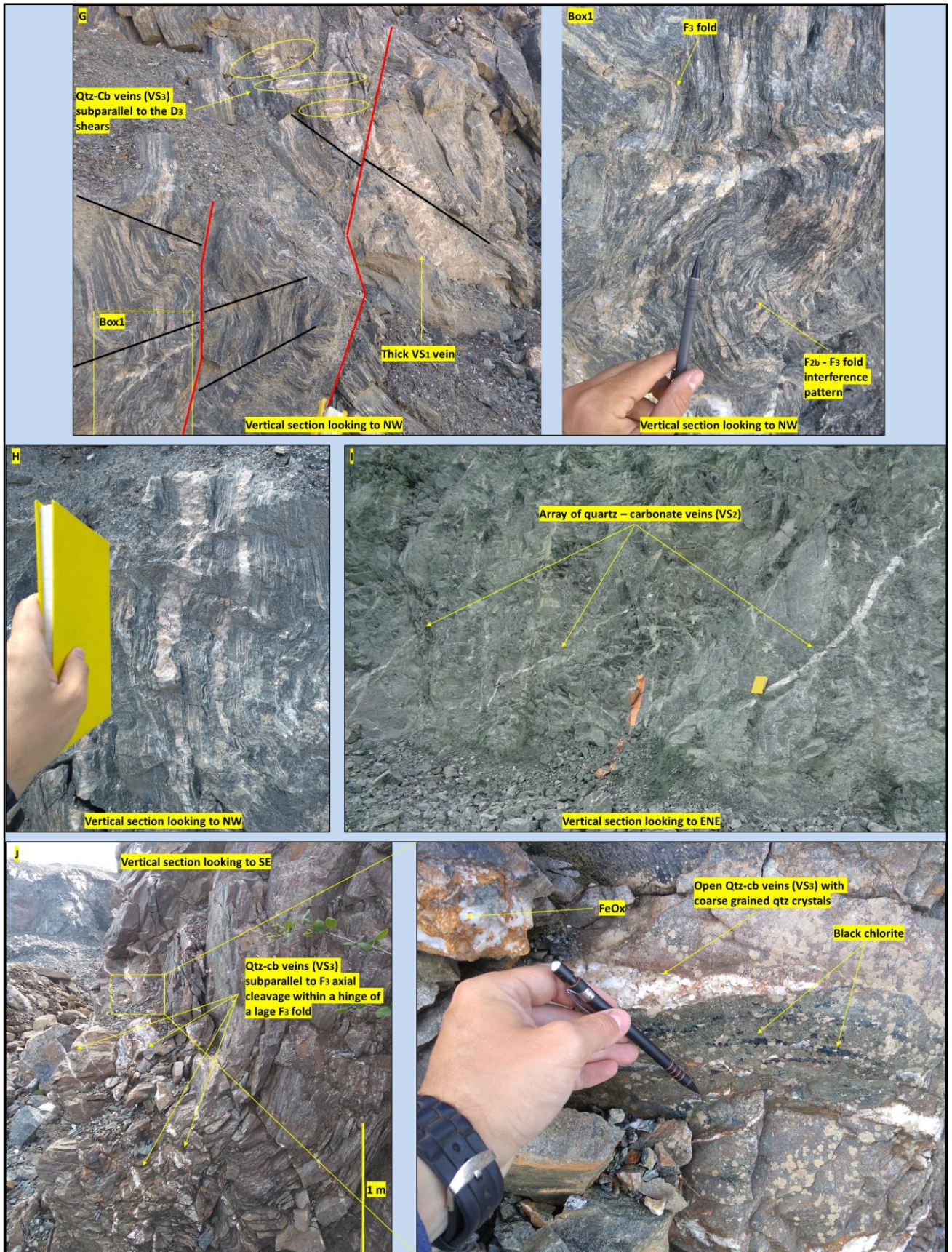


**Plate V.6.** – Representative images of the vein sets identified in the Stog’er Tight and East Zone open pits and of some structures discussed in the text. **A** – Moderately to steeply dipping  $D_{2b}$  fault, note the brecciated qtz-cb vein ( $VS_2$ ) along the fault and the chl-py (disseminated) alteration associated with it; hammer for scale; Stog’er Tight pit; **B** – Fine-grained mafic dyke affected by  $F_3$  folds and associated extensional shear bands, note that the dyke is veined and both the veins and the dyke are affected by  $F_3$  folds and  $D_3$  shears; notebook for scale; East Zone pit; **C** – Fine-grained mafic dyke (same as in image B) subparallel to  $D_{2b}$  fault, note the weak, spaced cleavage parallel to the contact zones interpreted as  $S_{2b}$ ; notebook for scale; East Zone pit; **D** – ~5m wide fault that dip steeply to N which affect the mineralisation and mark the contact between the Stog’er Tight gabbro and the volcanoclastic units, note the altered and mineralised zone within the fault; **E, F** – Down-dip stretching mineral lineation define by elongate chlorite crystals (**E**) and horizontal, steps and slicken-lines define by calcite which indicate sinistral motion (**F**) within the fault zone from image **D**; pencil as scale; **G** – Ore zone within a high strain  $D_3$  domain, note the foliation-parallel  $VS_1$  veins (quartz-albite-ankerite) affected by  $F_{2b}$ - $F_3$  fold interference pattern, the shallow-dipping qtz-cb  $VS_3$  veins subparallel to the  $F_3$  axial planes and  $D_3$  shear zones (black lines), and the steeply dipping qtz-cb vein that crosscut the foliation at a very low angle but is folded by  $F_3$  folds (box 1), the red lines show fractures associated to the syn-to-post  $D_4$ , NW-SE striking, steeply dipping faults; pencil as scale; East Zone pit; **H** – Foliation-parallel qtz-alb-ank veins ( $VS_1$ ); notebook as scale; East Zone pit; **I** – Qtz-cb vein array ( $VS_2$ ) subparallel to  $D_{2b}$  fractures; notebook as scale; Stog’er Tight pit; **J** – Qtz-Cb vein array ( $VS_3$ ) formed along the  $F_3$  axial planes within the hinge of a large  $F_3$  fold, note the open nature of the veins and the coarse grained qtz crystals within it and the black chlorite and the intense rusty-red FeOx alteration associated with the veins, East Zone pit.

### V.1.2.3. Alteration

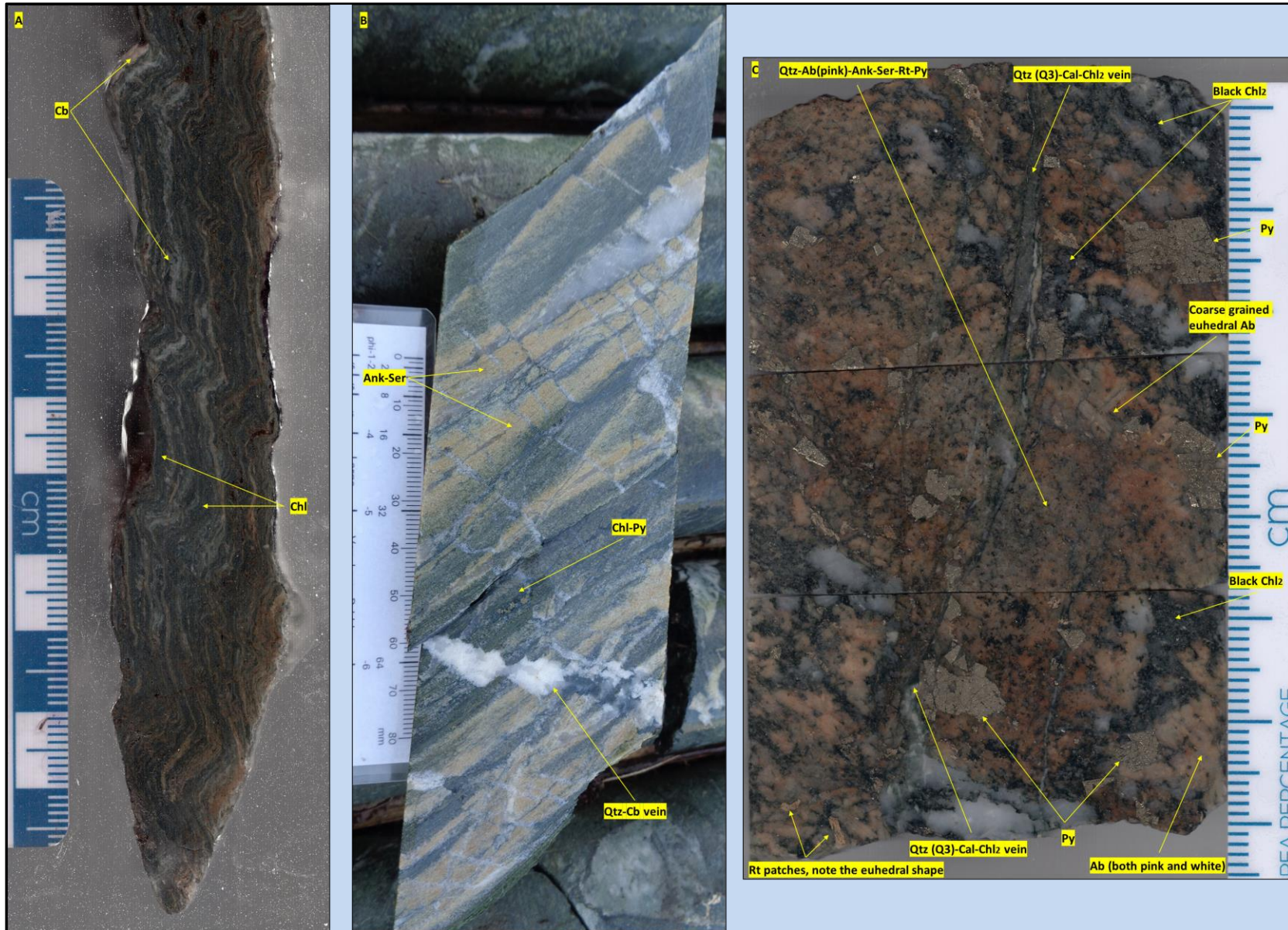
Unaltered exposures of the Stog’er Tight gabbro were observed in several locations with the Point Rousse Complex and were macroscopically described (**Plate V.7–G, H**). However, no further microscopical investigations were conducted. Therefore, the description of fresh sections is provided here based on literature data. The Stog’er Tight gabbros show significant variation in their grain-size which range from fine-grained to almost pegmatitic and display the following mineral composition: plagioclase (60-45%); amphibole (30-45%); titanomagnetite (7-20%); and epidote ( $\leq 5\%$ ) (Kirkwood & Dubé, 1992; Ramezani 1992; Pitman et al., 2020).

In the studied outcrops and core sections multiple alteration halos were observed. From distal to proximal (ore zone) these alteration halos are composed of: chlorite-carbonate (**Plate V.7-A**); ankerite-sericite  $\pm$  albite-chlorite (**Plate V.7-B**); and pink albite-pyrite  $\pm$  ankerite-sericite-rutile overprinted by black chlorite  $\pm$  quartz-calcite-magnetite (**Plate V.7-C**). These are comparable to the alteration zones previously identified by Ramezani (1992) (*see Table II.5; Figure A1.3-D*). Except for macroscopical and microscopical investigations, during this study, detailed

petrographic and geochemical analysis (BSE-CL, EDS, EPMA) were conducted only on samples collected from the ore zone (for rationale see *chapter III – Methodology and for sample descriptions Appendix 2*). Therefore, for complete descriptions of the distal and intermediate alteration halos the reader is referred to Ramezani (1992) & Ramezani et al. (2001).

Petrographic analyses of samples from medium to high gold grade zones (*Appendix 2*) showed that quartz–albite–ankerite–sericite–rutile–chlorite–calcite–pyrite ± dolomite–hematite represent the main hydrothermal alteration minerals associated with gold mineralisation at the Stog’er Tight deposit. Apatite, monazite, xenotime, and zircon are also abundant. Summarised descriptions for these alteration minerals are presented in *Table V.6*. With some exceptions listed below, the optical and geochemical properties, the morphology, the mineral associations, and the overprinting relationships of the alteration minerals from the Stog’er Tight deposit are like the ones of the alteration minerals from the Pine Cove deposit (see below).

The mineralised intervals are characterised by a high density of multiple generations of poly mineral veins with multiple opening domains and complicated overprinting relationships (*Plate V.7-D*). The mineral assemblages related to the initial magmatic composition of the Stog’er Tight gabbro and to the greenschist facies metamorphism are almost fully replaced by the alteration minerals. Relict ilmenite, and epidote are still observable within the pyrite crystals and in the altered ground mass. Total replacement zones composed of quartz, pink albite and pyrite is the most common feature of the ore zones at Stog’er Tight. In these zones the rocks display alternating areas of spotted pink/white to fully pink colour (*Plate V.7-E*). Pink to orange-brown colours are characteristic when ankerite-sericite-rutile are present (*Plate V.7-C*) and dark green to black hues occur in zones of black chlorite overprint (*Plate V.7-C, F*).





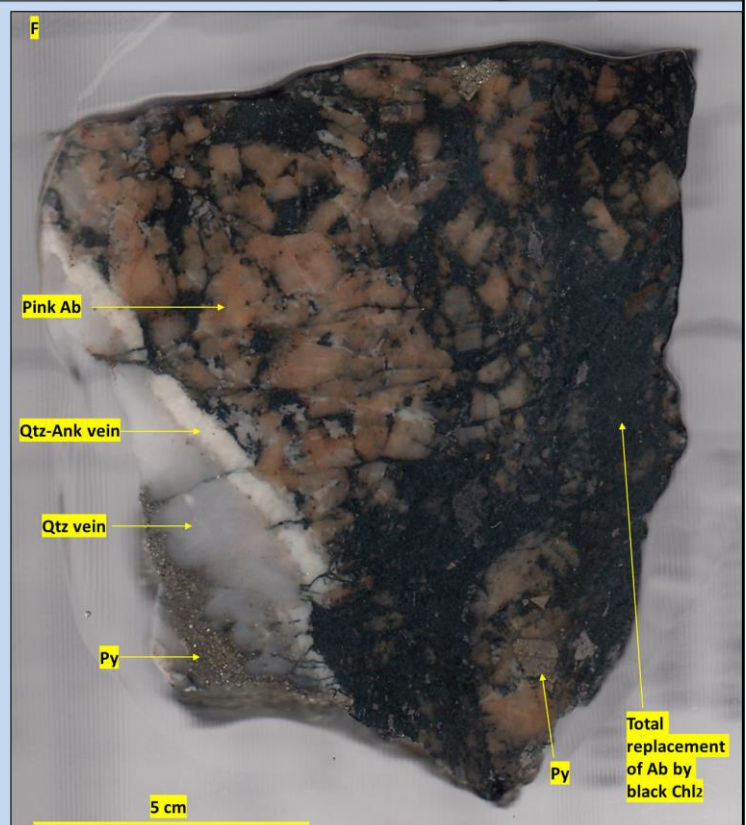
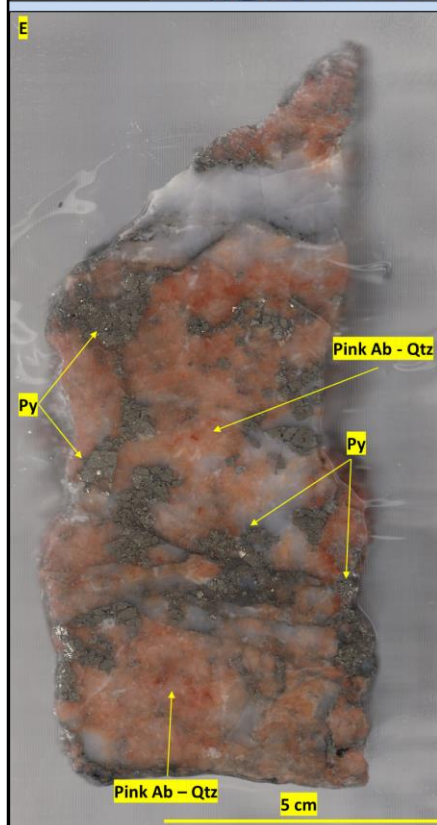
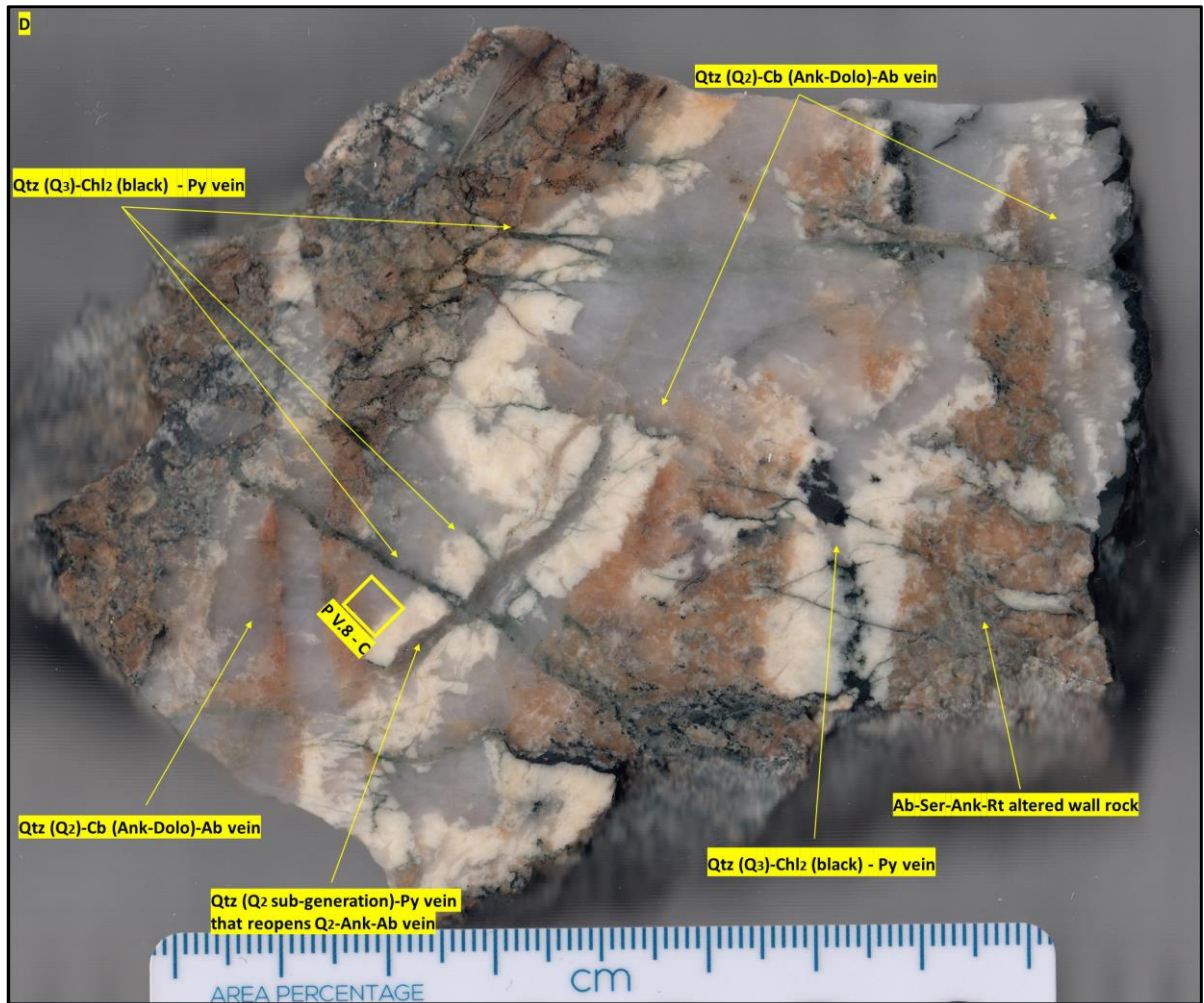




**Plate V.7 (above).** – Representative images of different altered and unaltered intervals observed in the Stog'er Tight area: **A** – Chlorite-carbonate altered rock from the distal alteration zone, **note** the folding ( $F_3$ ) pattern. **B** – Ankerite-sericite  $\pm$  albite-chlorite altered rock from the intermediate alteration zone, **note** the black  $\text{Chl}_2$ -Py overprint and the Qtz-Cb veins that crosscut the alteration. **C** – Albite-ankerite-sericite-rutile-pyrite proximal alteration and black  $\text{Chl}_2$  overprint, **note** the white, coarse-grained Ab crystals, the euhedral Rt patches, and the Qtz ( $Q_3$ )-Cal- $\text{Chl}_2$  vein that crosscut the albite-ankerite-sericite-rutile-pyrite alteration. **D** – Intensively veined sample with complicated crosscutting relationships: 1<sup>st</sup> vein – translucent Qtz( $Q_2$ ) – Cb (cream-white ank-dolo) – Ab (pink) cut by 2<sup>nd</sup> vein – translucent Qtz( $Q_2$  sub-generation, fine grained) - Py (fine grained, euhedral Py crystals), 1<sup>st</sup> and 2<sup>nd</sup> veins are cut at a high angle by a 3<sup>rd</sup> vein composed of Qtz( $Q_3$ )- $\text{Chl}_2$ (black)-Cal veinlets, see below for description of qtz generations, the yellow rectangle PV.8-C shows the location of image **C** from **Plate V.8**. **E** – Typic proximal alteration / ore zone of the Stog'er Tight deposit - Qtz-Ab(pink)-Py (auriferous); **F** – Ore interval characterised by Qtz-Ab(pink)-Py alteration intensively brecciated by black  $\text{Chl}_2$  veins, **note** the zones where the initial alteration is fully replaced by  $\text{Chl}_2$ ; **G, H** – Hand specimens from unaltered Stog'er Tight gabbros.

**Table V.6** – Summary characteristics of the alteration minerals identified in the proximal alteration halo and in the ore zone of the Stog'er Tight deposit.

<b>Mineral</b>	<b>Occurrence</b>	<b>Texture</b>	<b>Spatial association with other alteration minerals</b>	<b>Overprinting relationships</b>
<b>Qtz</b>	As vein material in all the described vein sets & within the altered wall rock in the Qtz-ab-py replacement zones	Multiple generations (Q <sub>1</sub> , Q <sub>2</sub> , Q <sub>3A</sub> and Q <sub>3B</sub> ), see <b>Table V.7</b>	See <b>Table V.7</b>	See <b>Table V.7</b>
<b>Ser</b>	Mostly in the altered wall rock around VS <sub>1</sub> and to a lesser degree within the vein	Patches or fine-grained, disseminated at the interface of ab-Qtz-ank crystals	Q <sub>2</sub> -ab-ank-rt-py ± dolo	Replaces ab; replaced and crosscut by cal-chl <sub>2</sub> veins/patches
<b>Rt</b>	Mostly in the altered wall rock around VS <sub>1</sub> and to a lesser degree within the VS <sub>3</sub> veins	Clusters of both fine and coarse grained, irregular to euhedral crystals; bands oriented parallel and at an angle to one another	All the other alteration minerals	Overgrown by py; brecciated by cal-chl <sub>2</sub> veins but also hosted by them
<b>Ab</b>	Within VS <sub>1</sub> and in the associated alteration selvages	Coarse grained within both veins and altered ground mass	Q <sub>2</sub> -ank-ser-rt-py ± dolo	Locally replaced by ser-ank; crosscut and overprinted by cal-chl <sub>2</sub> veinlets/patches
<b>Chl<sub>2</sub></b>	Occurs within both VS <sub>3</sub> and in the associated alteration halo	Coarse and fine-grained in veins and patches	Q <sub>3</sub> -Cal ± py-hem-rt	Shows mutual crosscutting relationships with Q <sub>3</sub> and cal and overprints the rest of the alteration minerals
<b>Epi</b>	Occurs as a relict phase in the altered wall rock	Consumed by calcite and chlorite	N/A	Overprinted by the rest of the alteration minerals
<b>Cal</b>	Within vein set VS <sub>3</sub> and in the associated alteration halo	Mostly as veins and to a lesser degree as patches composed of both fine and coarse-grained crystals	Q <sub>3</sub> -Chl <sub>2</sub> ± py-hem	Shows mutual crosscutting relationships with Q <sub>3</sub> and chl <sub>2</sub> and overprints the rest of the alteration minerals
<b>Py</b>	Within the altered wall rock or at the contact between	Fine to very coarse grained anhedral to euhedral crystals,		Brecciated by some of the Q <sub>2</sub> sub-generations and by

	veins and host rocks; within the veins, but lower amounts compared to the host rocks	either with inclusion rich cores and inclusion free rims or without inclusions; patches (up to cm <sup>2</sup> in size) of brecciated or annealed polycrystalline aggregates	All the other alteration minerals	the Q <sub>3</sub> -chl <sub>2</sub> -cal veins but further annealed and recrystallised; all the other alteration minerals were observed as inclusions in it
<b>Ank</b>	Both within the altered wall rock and in the veins (VS <sub>1</sub> & VS <sub>2</sub> )	As veins and patches with both fine and coarse-grained crystals	Q <sub>2</sub> -ab-ser-rt-py ± dolo	Replaced and brecciated by Q <sub>3</sub> -cal-chl <sub>2</sub> veins
<b>Dolo</b>	Minor component within the ankerite veins	Fine-grained, intergrown with ank	Ank ± Q <sub>2</sub> -ab-ser-rt-py	Replaced and brecciated by cal-chl <sub>2</sub> veins
<b>Hem</b>	Within VS <sub>3</sub> veins and in the associated alteration halo; supergene on outcrop fractures and along open fractures; rarely in the alteration halo of VS <sub>1</sub>	Staining or thin films on py and other Fe bearing minerals; small grains disseminated between other alteration minerals	All the other alteration minerals	N/A
<b>Ap</b>	Within the altered wall rock; rarely within veins	Anhedral to euhedral, fine-grained to coarse grained (a few microns to 1-2 mm) crystals with spongy core (sieve like) and homogenous rims	Q <sub>2</sub> -ab-ank-ser-rt-py ± dolo	The spongy core is overgrown by ab-ser-ank-rt, but the homogenous rims incorporate the latter minerals; both core and rim are brecciated by Q <sub>3</sub> -cal-chl <sub>2</sub> veins
<b>Mnz</b>	Within the altered wall rock; rarely within veins	Fine to coarse grained (1 µm up to 100 µm), irregular to rounded shapes	All the other alteration minerals	Brecciated by Q <sub>3</sub> -cal-chl <sub>2</sub> veins but also hosted by them
<b>Xtm</b>	Within the altered wall rock; rarely within veins	Fine to coarse grained (1 µm up to 50 µm), irregular to rounded shapes	All the other alteration minerals	Brecciated by Q <sub>3</sub> -cal-chl <sub>2</sub> veins but also hosted by them

<b>Zr</b>	Within the altered wall rock; rarely within veins	Fine to coarse grained (10 µm up to 100 µm), irregular to anhedral shapes	Q <sub>2</sub> -ab-ank-ser-rt-py ± dolo	Brecciates and replaces baddeleyite and is brecciated by Q <sub>3</sub> -cal-chl <sub>2</sub> veins
-----------	---	---	---	---

**Table V.7.** – Summary CL characteristics of the quartz generations observed in samples from the Stog’er Tight deposit. The texture terminologies are used according to Rusk et al. (2004) and Rusk (2012).

Quartz (Q) generation	Optical properties	CL colour and intensity	CL texture	Crosscutting relationships	Association with other alteration minerals	Related vein set
<b>Q<sub>1</sub></b>	Undistinguishable from Q <sub>2</sub>	Blue (medium to high intensity when compared to Q <sub>2</sub> )	Occurs as relict fragments of Q crystals that show euhedral growth zones with oscillating CL response	Brecciated and enclosed in Q <sub>2</sub> ; brecciated by Q <sub>3</sub>	N/A	Observed in VS <sub>1</sub> , and in the associated replacement zones; unclear relationship with VS <sub>2</sub>
<b>Q<sub>2</sub></b>	Shows multiple sub-generations: coarse-grained crystals in thick veins and brecciated, fine-grained crystals on thin veins that crosscut and re-open the thicker veins	All sub-generations are dark purple (low intensity)	Homogenous/massive with mottled aspect due to the presence of Q <sub>1</sub> fragments	The fine-grained sub-generations crosscut the ab and ank; It is crosscut by Q <sub>3</sub> -Chl <sub>2</sub> -Cal ± hem veinlets	Ab-ank-ser-rt-py	
<b>Q<sub>3</sub></b>	<b>Q<sub>3A</sub></b>	Occurs as thin veinlets (a few microns to millimetres); the thicker veins are brecciated	Medium to bright blue (moderate to high intensity, higher CL response than Q <sub>2</sub> )	Dense networks of thin veinlets with multiple orientations; laminated – growth zones of oscillating CL intensities; brecciated by Q <sub>3B</sub>	Crosscuts both Q <sub>1</sub> and Q <sub>2</sub> ; mutual crosscutting relationships between Q <sub>3A</sub> -Q <sub>3B</sub> -Cal-Chl <sub>2</sub>	Observed in VS <sub>3</sub>
	<b>Q<sub>3B</sub></b>	Undistinguishable from Q <sub>3A</sub>	Dark purple/blue to black (very low intensity, < Q <sub>2</sub> )	Occurs as thin veinlets with homogenous internal texture		

The quartz occurs as vein material in all the described vein sets and within the altered wall rock in the qtz-ab-py replacement zones (*Table V.6, Table V.7-E*). Under the microscope, the quartz displays the common undulatory extinction and a variety of textures and sizes, with the most common being the following: i) coarse-grained crystals with straight to lobate and serrated grain boundaries, mostly blocky which gives the massive texture to the veins; and ii) brecciated and recrystallised, fine-grained, anhedral and subhedral crystals (*Plate V.8-A*).

SEM-CL investigations showed that similarly to the Pine Cove deposit, at least 3 main generations of quartz are present in the mineralised veins from the Stog'er Tight deposit (*Table V.7*). These are termed and presented based on their crosscutting relationships and their interpreted relative timing, Q<sub>1</sub> being the earliest and Q<sub>3</sub> the latest.

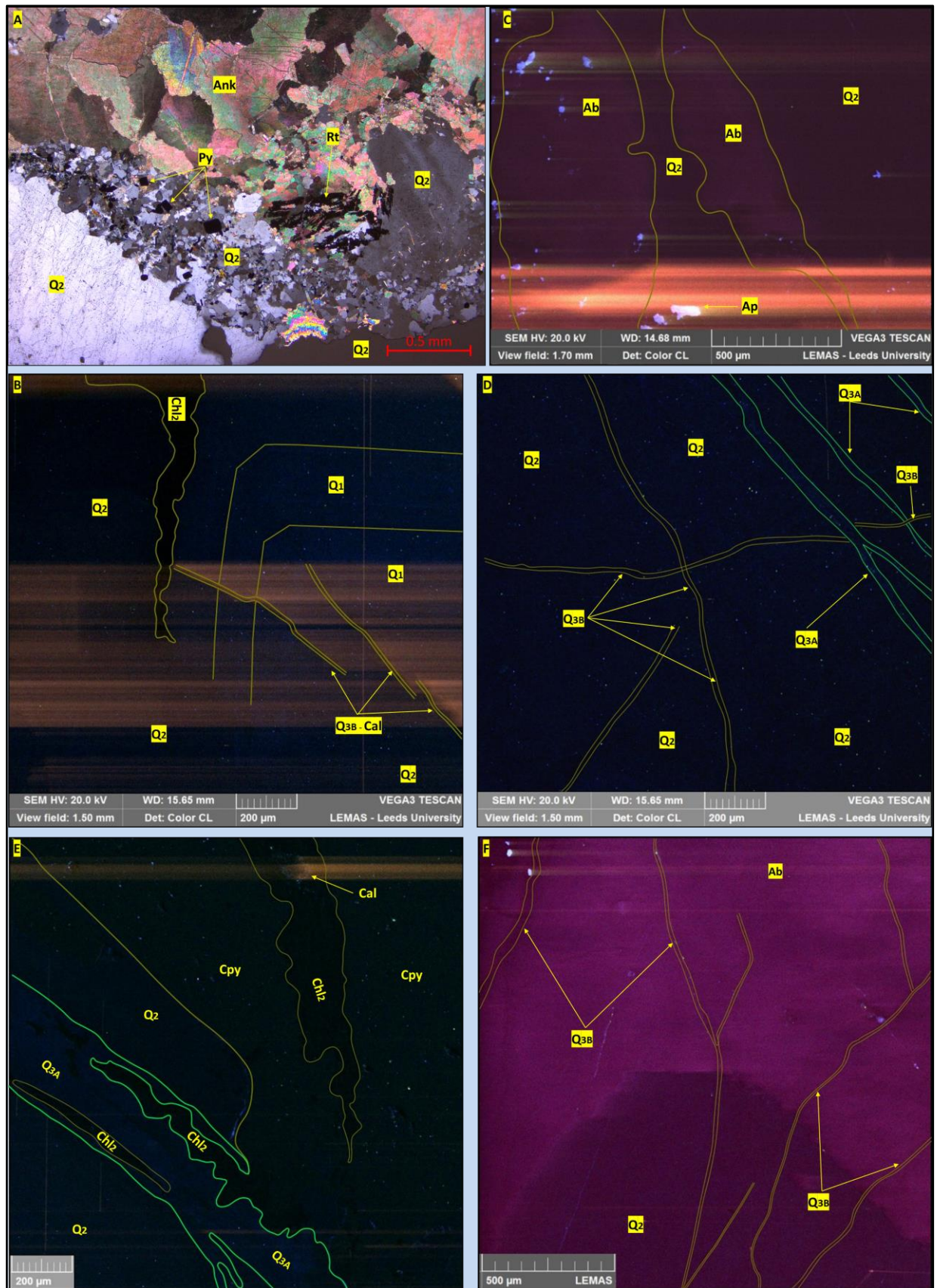
The 1<sup>st</sup> quartz generation (Q<sub>1</sub>) has a moderate to high CL response showing a blue colour when imaged by coloured CL. The Q<sub>1</sub> occurs as relict fragments of quartz crystals with euhedral growth zones defined by oscillating CL intensities, brecciated, and enclosed by/in the second quartz generation (Q<sub>2</sub>) (*Plate V.8-B*).

A second quartz generation (Q<sub>2</sub>) was observed within the VS<sub>1</sub> and the associated replacement zones. Compared to the Pine Cove deposit, it is inferred that Q<sub>2</sub> from the Stog'er Tight is composed of multiple quartz sub-generations based on its optical properties and occurrence: the Q<sub>2</sub> crystals are coarse grained within replacement zones and in the thick qtz-ab-ank veins, and fine-grained within thin veinlets that either crosscut the thicker veins or re-open and infill them along internal pre-existent suture zones or at the interface of different mineral phases (e.g. between ankerite and quartz) (*Plate V.7-D, Plate V.8-A*). However, under CL, regardless the textures and vein generation, the Q<sub>2</sub> has a low CL response, displays a dark purple/blue colour, and has a homogenous/massive internal texture (*Plate V.8-C*). Thereby, no separate terminology was attributed for the different Q<sub>2</sub> sub-generations. The relationship between Q<sub>2</sub> and the second vein set (VS<sub>2</sub>) observed in the field (*Table V.7*) is uncertain, because in the studied samples it is not clear if any of the quartz-carbonate veins that crosscut VS<sub>1</sub> are related to VS<sub>2</sub> or with other veins unrecorded in the field.

In the studied samples, a third quartz generation (Q<sub>3</sub>) was observed within mono or poly mineral (qtz and/or chl (black) and/or cal) thin veinlets (a few microns

to millimetres) that crosscut both Q<sub>1</sub> and Q<sub>2</sub> (*Plate V.8-B, D, E*). Within the veins, Q<sub>3</sub> is fine-grained and brecciated. Under CL it was observed that Q<sub>3</sub> shows the same characteristics as in the Pine Cove deposit, being composed of two sub-generations of quartz (Q<sub>3A</sub> and Q<sub>3B</sub>) that have different CL response. The Q<sub>3A</sub> has a medium to high CL response in comparison to Q<sub>2</sub>, it displays a moderately to bright blue colour, and occurs in networks of thin veinlets with various orientations that brecciate Q<sub>2</sub> (*Plate V.8-D*). In thicker veins, the Q<sub>3A</sub> shows a banded/laminar texture defined by zones of alternating CL intensities (*Plate V.8-E*). The Q<sub>3A</sub> is crosscut and brecciated by thin quartz veinlets (Q<sub>3B</sub>) that have a very low CL response (lower than Q<sub>2</sub>), displaying a very dark blue to black colours (*Plate V.8-B, D*). Rarely, a reverse relationship where the Q<sub>3A</sub> crosscuts the Q<sub>3B</sub> veinlets was also observed (*Plate V.8-D*). As in the Pine Cove deposit, both the Q<sub>3A</sub> and Q<sub>3B</sub> show a close relationship with cal-chl<sub>2</sub> (black) veinlets (see below and in *Table V.6 & Table V.7*), opening and re-using them, and vice-versa (*Plate V.8-B, D*). Q<sub>3</sub> is interpreted to be associated with the VS<sub>3</sub> veins because the black chlorite (Chl<sub>2</sub>) and calcite (Cal) are common minerals within these veins (*Plate V.6-J*).

*Plate V.8 (next page)* – Representative images of different quartz generations related to the Stog'er Tight mineralisation: **A** – Microscope image (cross polarized light) of fine-grained quartz (vein) at the interface of ankerite and coarse-grained quartz, **note** the presence of fine grained Py crystals in the fine grained quartz, sample ST-Ore-Chl; **B** – Large fragment of an euhedral Q<sub>1</sub> crystal (**note** the growth zones define by oscillating CL intensities) within a homogenous Q<sub>2</sub> mass; **C** – CL image of an Ab (magenta colour) - Q<sub>2</sub> (dark purple) groundmass crosscut by a Q<sub>2</sub> sub generation with the same CL properties as the main one, sample ST07-Ore, image location on *Plate V.7 - D*; **D** – Q<sub>3A</sub> and Q<sub>3B</sub> brecciating Q<sub>2</sub>, **note** the mutual crosscutting relationships between the two Q<sub>3</sub> generations; **E** – Q<sub>3A</sub> – Chl<sub>2</sub> vein that crosscut Q<sub>2</sub>, note the laminated texture of Q<sub>3</sub> define by oscillating CL intensities and the brecciation of chalcopyrite by Chl<sub>2</sub>; images **B, D, E** sample BN215; **F** – Q<sub>3B</sub> veinlets crosscutting both Q<sub>2</sub> and albite, **note** the variation in the CL intensity for the albite (bright and darker magenta colour), sample SOZ2; all the CL images have the brightness and the contrast slightly enhanced compared to the original image in order to highlight the different Q generations.





The pink albite is the most distinctive feature of the proximal alteration halo/ore zone at Stog'er Tight and is significantly more abundant than in the Pine Cove deposit. It occurs as vein component within VS<sub>1</sub> and within the altered wall rock material in association with quartz<sub>2</sub>, ankerite, sericite, rutile, pyrite, and dolomite (*Plate V.7–C, D, E, F*). The albite has straight or recrystallised crystal boundaries with the coarse grained quartz<sub>2</sub> and is crosscut by the fine grained quartz<sub>2</sub> veinlets and by Q<sub>3</sub>-Chl<sub>2</sub>-Cal veins (*Plate V.8–C, F*). Within large patches of sericite-ankerite (see below) the albite seems to be consumed being preserved only as irregular crystal fragments enclosed in the ankerite mass (*Plate V.9-A*). Coarse grained (up to a few millimetres), prismatic, white albite crystals are also present in the alteration halo, especially when the mineralisation is hosted in the coarse-grained parts of the Stog'er Tight gabbro (*Plate V.7–C*). BSE imaging showed that the pink albite has a heterogenous internal texture defined by zones with spongy and homogenous aspect (*Plate V.9–A, B*). Under CL the albite shows a patchy/mottled zonation defined by areas with pale and bright magenta colour (*Plate V.8–C, F*). It is unclear if the variation of the CL intensity is related to either the co-existence of the pink and white albite phases, or to the textural zoning.

Within the studied samples, three types of carbonates were identified based on their Fe, Mg and Ca contents (EDS analysis): ankerite, calcite and dolomite (*Table V.6*). Compared to the Pine Cove deposit, at Stog'er the ankerite is more abundant and occurs as both vein material (in VS<sub>1</sub>) and as patches together with sericite and rutile in the alteration halo (*Plate V.9–A, B*). It is fine to coarse-grained and is either zoned (patchy and/or euhedral growth zoning) or homogenous under BSE. In CL it shows no response and occurs as a black material. Trace amount of dolomite was also identified intergrown with ankerite in some of the veins. The calcite occurs along poly-mineral veins composed of Q<sub>3</sub> and black chlorite<sub>2</sub>, and as mono-mineral veinlets that crosscut the albite-ankerite-sericite-rutile assemblage and which show mutual crosscutting relationships with Q<sub>3</sub>-chl<sub>2</sub> veins (*Plate V.8–B; V.9–B*). Where the calcite veinlets intersect the ankerite patches or veins, the calcite infiltrates into the ankerite along its cleavage faces and between crystal boundaries and creates an overall patchy zonation pattern defined by light and dark grey hues in BSE (*Plate V.9–C*).

Microstructural observations of oriented thin sections created from samples collected from the distal to intermediate alteration zones (*Appendix 2*) showed that in

areas affected by  $D_3$  folding, the carbonates (undifferentiated, no EDS data) overgrow the  $S_{2a/2b}$  foliation occurring as elongated patches that are subparallel to the foliation, as veins that are either subparallel to the foliation or formed at a high angle to it along the  $F_3$  axial cleavage, and as infills within the  $F_3$  hinge zones (*Plate V.9-D*). It was also observed that thin carbonate veinlets and lenses that are subparallel to the  $S_{2a/2b}$  foliation crosscut and displace thin quartz veinlets which are oriented at a high angle to the foliation, with a down-dip motion to the north (*Plate V.9-E*).

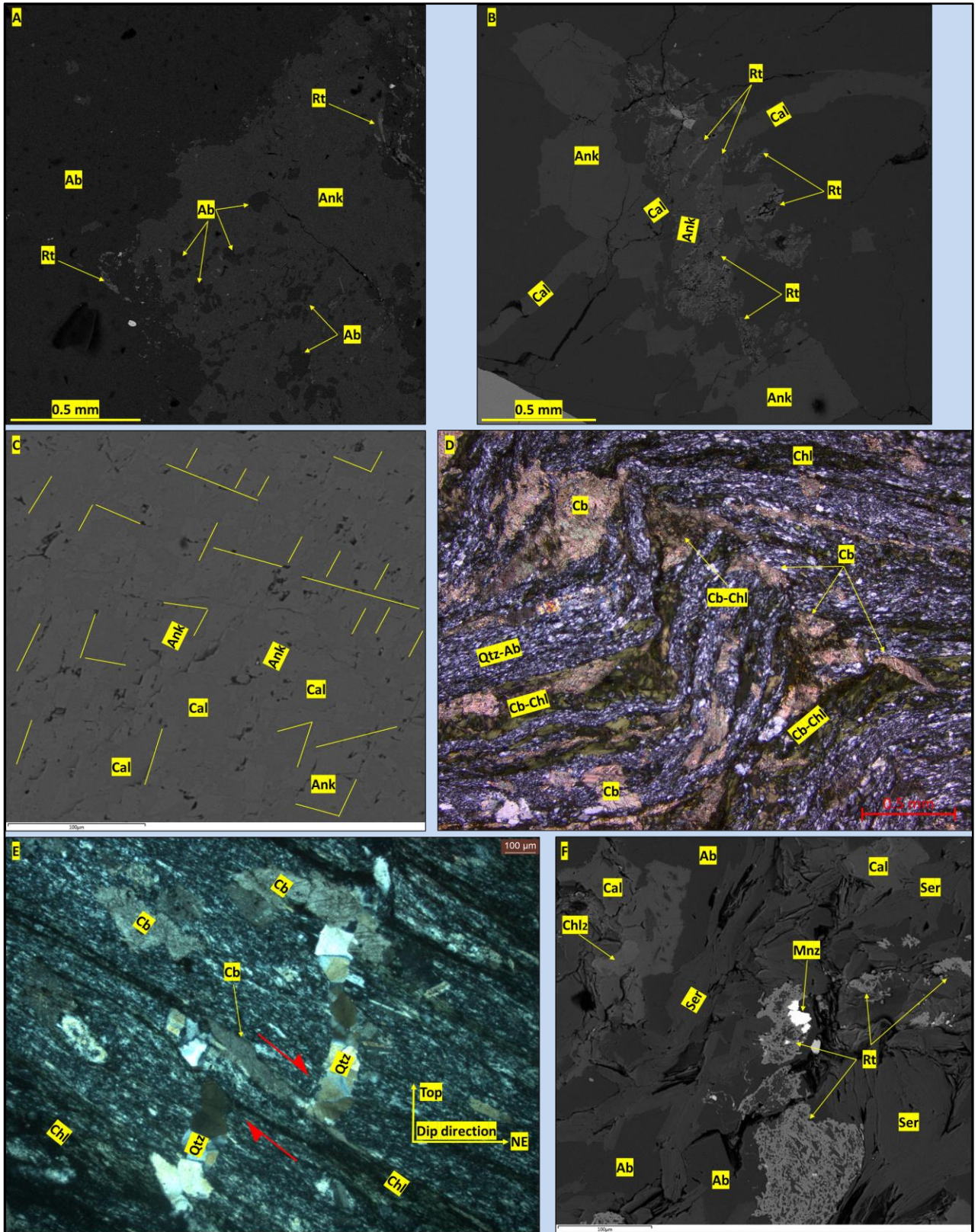
The sericite is less abundant than in the Pine Cove deposit and occurs as thin stringers at the interface of quartz<sub>2</sub>, albite and ankerite crystals, and as patches, with or without ankerite and rutile, replacing albite (*Plate V.9-E*). The sericite is mostly represented by muscovite, but few flakes of phengite were also recorded (differentiation made based on EDS data).

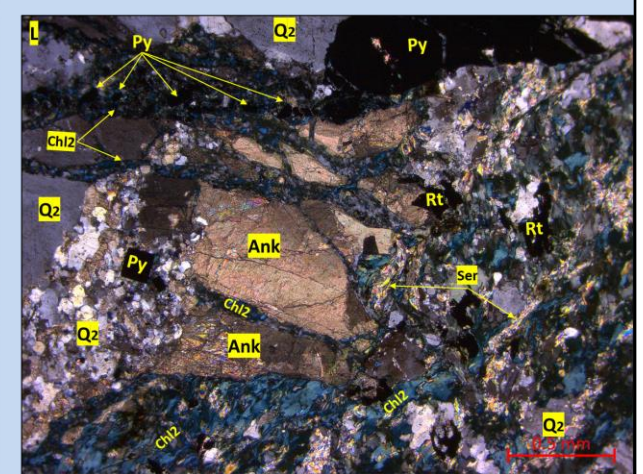
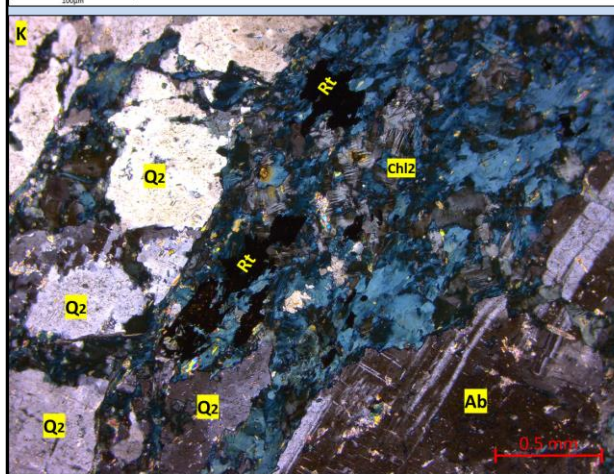
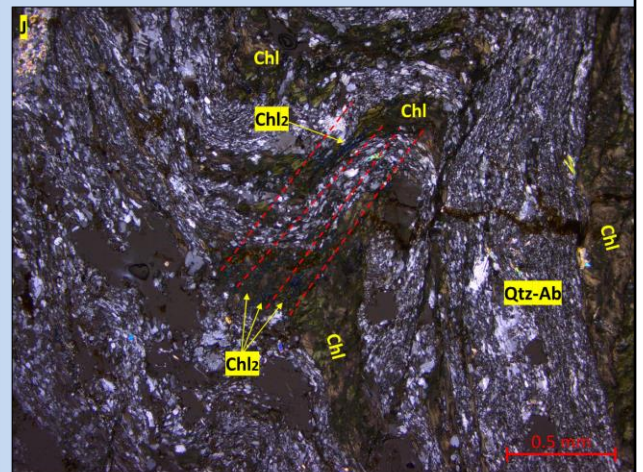
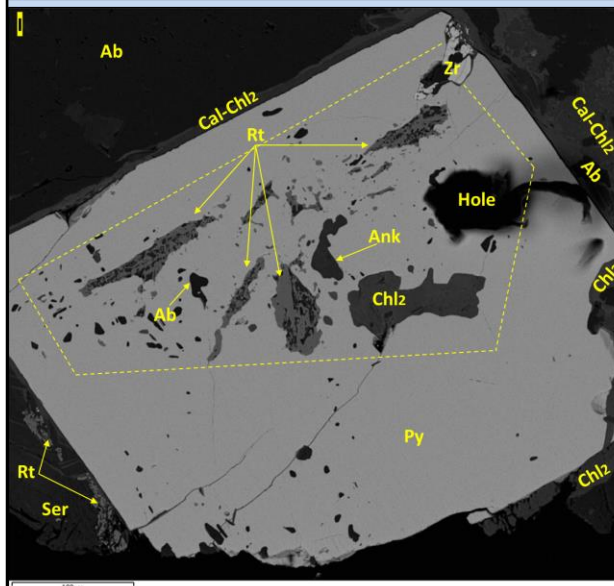
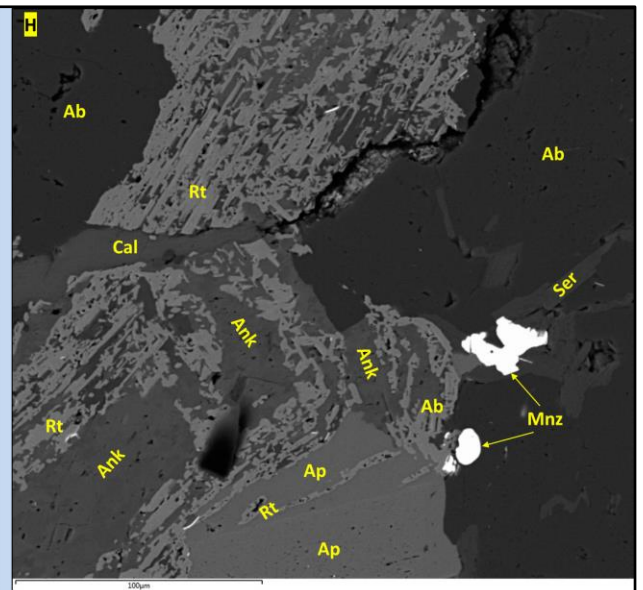
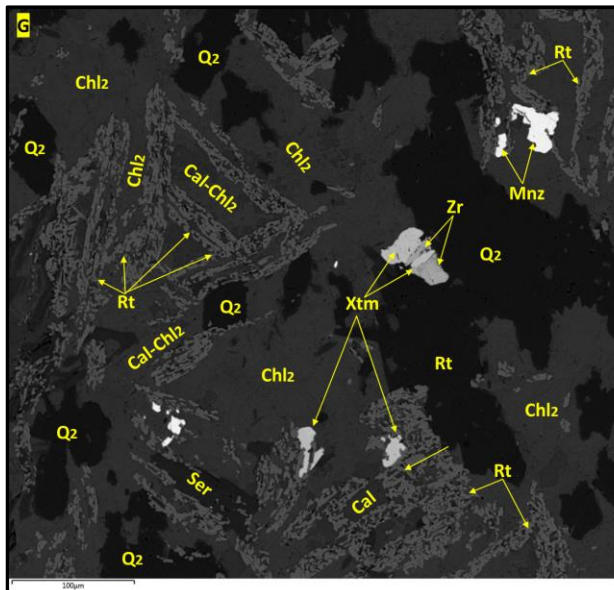
The rutile occurs as cream-beige lumps and patches of variable sizes (a few microns to millimetres) (*Plate V.7-C*). Generally, the rutile crystals are fine grained, irregular to acicular/bladed and aligned in bands that are oriented both parallel and at an angle to one another (*Plate V.9-G*). Coarser grained rutile crystals (a few hundred microns in length), both anhedral and euhedral (prismatic) were also observed within and outside the bands. Between the rutile bands the sericite and ankerite are the most common minerals, and to a lesser degree albite, chlorite<sub>2</sub> and calcite (*Plate V.9-G, H*). These minerals show mutual overgrowing relationships with the rutile. The rutile also shows an intimate spatial relationship with pyrite by which is commonly overgrown (*Plate V.9-I*). Under BSE the rutile shows lighter zones given by high vanadium and some tungsten. The calcite veinlets crosscut the rutile crystals and bands (*Plate V.9-H*).

One type of chlorite was observed within the proximal alteration/ore zone of the Stog'er Tight deposit. It shows the same optical and geochemical characteristics as the chlorite<sub>2</sub> from the Pine Cove deposit: dark green to black in outcrop and in hand specimen (*Plate V.6-J; V.7-C, D, F*); strong pleochroic in plane polarised light; blueish grey to intense blue and purple anomalous birefringence colours in crossed polarised light (*Plate V.9-K, L*); contains (21 – 29%) Fe, (7 – 13%) Al, and (4 to 8%) Mg; occurs in both mono and poly (with quartz<sub>3</sub> and/or calcite) mineral veins and patches that crosscut/overprint all the other mineral phases (*Plate V.8-E; V.9-G, K, L*). In the intense brecciated zones, the chlorite<sub>2</sub> replaces almost entirely the rest of

the alteration minerals (*Plate V.7–F*). This chlorite phase will be referred to as chlorite<sub>2</sub> because in the distal-intermediate alteration zones it was observed that another chlorite with different optical properties also occur (pale green and weak pleochroic in plane polarised light and with black to brown anomalous interference colours in cross polarised light) (*Plate V.9–D, E*). This chlorite phase defines the foliation planes in the studied samples, whereas chl<sub>2</sub> is either aligned subparallel to the axial cleavage of the F<sub>3</sub> folds or occurs together with carbonates as infills in the hinge zone of F<sub>3</sub> folds (*Plate V.9–J*).

*Plate V.9 (next two pages)* – Representative images of different alteration minerals related to the Stog'er Tight mineralisation: **A** – BSE image of albite and a large patch of ankerite, **note** the albite crystal fragments enclosed in the ankerite patch, sample SOZ1; **B** – BSE image of a patch of Ab-Rt in Ab groundmass everything crosscut by a calcite veinlet, sample SOZ1; **C** – BSE image showing calcite (grey) replacement of ankerite (lighter grey) along preferred crystallographic planes, sample ST07-ORE; **D** – Microscope image (cross polarized light) showing carbonate infill in the hinge of F<sub>3</sub> folds; **note** the overgrow of the Cb over the foliation (defined by recrystallised Qtz-ab and chlorite with dark to brown birefringence colour) and the alignment of Cb subparallel to the F<sub>3</sub> axial planes, sample ST07-19; **E** – Microscope image (cross polarized light) showing Cb patches oriented subparallel to the foliation, **note** the crosscutting of the quartz vein with a down dip motion to NE, sample ST07V; **F** - BSE image of stringers and patches of sericite replacing albite, sample SOZ2; **G** – BSE image showing rutile bands composed of fine grained Rt separated by Chl<sub>2</sub> and Chl<sub>2</sub>-Cal; **note** the orientation of the Rt bands at an angle to one another, sample BN215; **H** – BSE image showing Rt and Ank bands, note the Rt thin band from the homogenous part of the Ap and the Cal veinlet that crosscut both the Rt and the Ank, sample SOZ2; **I** – BSE image showing an euhedral Py crystal with inclusion rich core (marked by yellow dashed line) and inclusion free exterior, **note** the Rt inclusions in Py, sample BN215; **J** – Microscope image (cross polarised light) of aligned Chl<sub>2</sub> (blue) subparallel to the F<sub>3</sub> axial cleavage (traced by red dashed lines), note the difference in the birefringence colours of the two chl phases, sample ST07-19; **K** - Microscope image (cross polarised light) showing a large patch of Chl<sub>2</sub> that overgrows Q<sub>2</sub> and Ab; **L** - Microscope image (cross polarised light) showing Chl<sub>2</sub> veinlets that crosscut Q<sub>2</sub> (both coarse and fine grained), Ank and Py, **note** the infiltration of Chl<sub>2</sub> between the Q<sub>2</sub> and Ser crystals in the right hand side of the image, the presence of fine grained fragments of Py crystals in the Chl<sub>2</sub> veinlets and the brecciation of the Py aggregates by the Chl<sub>2</sub> veins; both **K & L** from sample ST-Ore-Chl.





The pyrite is the most abundant sulphide within the Stogér Tight deposit and occurs disseminated in the alteration selvages that surround all vein sets, in altered wall rock fragments incorporated into the veins, and directly within the veins (*Plate V.7-C, D, E, F; V.8-A*). The pyrite crystals vary in size from a few tens of microns to a few millimetres, show anhedral to euhedral shapes and are either simple zoned with inclusion rich core, mantled by inclusion free euhedral rims or un-zoned, without or with very few inclusions (*Plate V.9-I; Plate V.10-A*). Within the coarse-grained euhedral crystals, multiple inclusion rich domains separated by inclusion free areas were also observed suggesting a complex growth history (*Plate V.10-B*). The coarse-grained crystals were mostly seen within the altered wall rock domains in association with albite-ankerite-quartz<sub>2</sub>(coarse)-sericite-rutile, whereas the finer crystals were observed in the fine-grained sub-generations of quartz<sub>2</sub> and within the chlorite<sub>2</sub>-calcite-quartz<sub>3</sub> veins (*Plate V.8-A, Plate V.9-L, Plate V.10-A*). All the alteration minerals presented in *Table V.6*, plus relict fragments of ilmenite and epidote occur as inclusions within the pyrite crystals. Most commonly the pyrite occurs as large (up to square centimetres in size) brecciated or annealed polycrystalline aggregates, instead as stand-alone disseminated crystals. The pyrite aggregates are in general clean, with few inclusion-rich domains, and show variable degrees of brecciation caused by mono or poly mineral veinlets composed of chlorite<sub>2</sub> and/or calcite and/or quartz<sub>3</sub> (*Plate V.9-L, Plate V.10-C*). Grinding and grain size reduction are common in the intense brecciated areas (*Plate V.10-C*). However, quartz<sub>3</sub>, calcite and chlorite<sub>2</sub> were observed as inclusions in both pyrite crystals and aggregates, and as for the Pine Cove deposit, it means that annealing and recrystallisation of pyrite occurred in association with the quartz<sub>3</sub>-chlorite<sub>2</sub>-calcite veins. Further, interpretations regarding the growth history of the pyrite with respect to the evolution of the mineral system are provided in the interpretation section of this chapter.

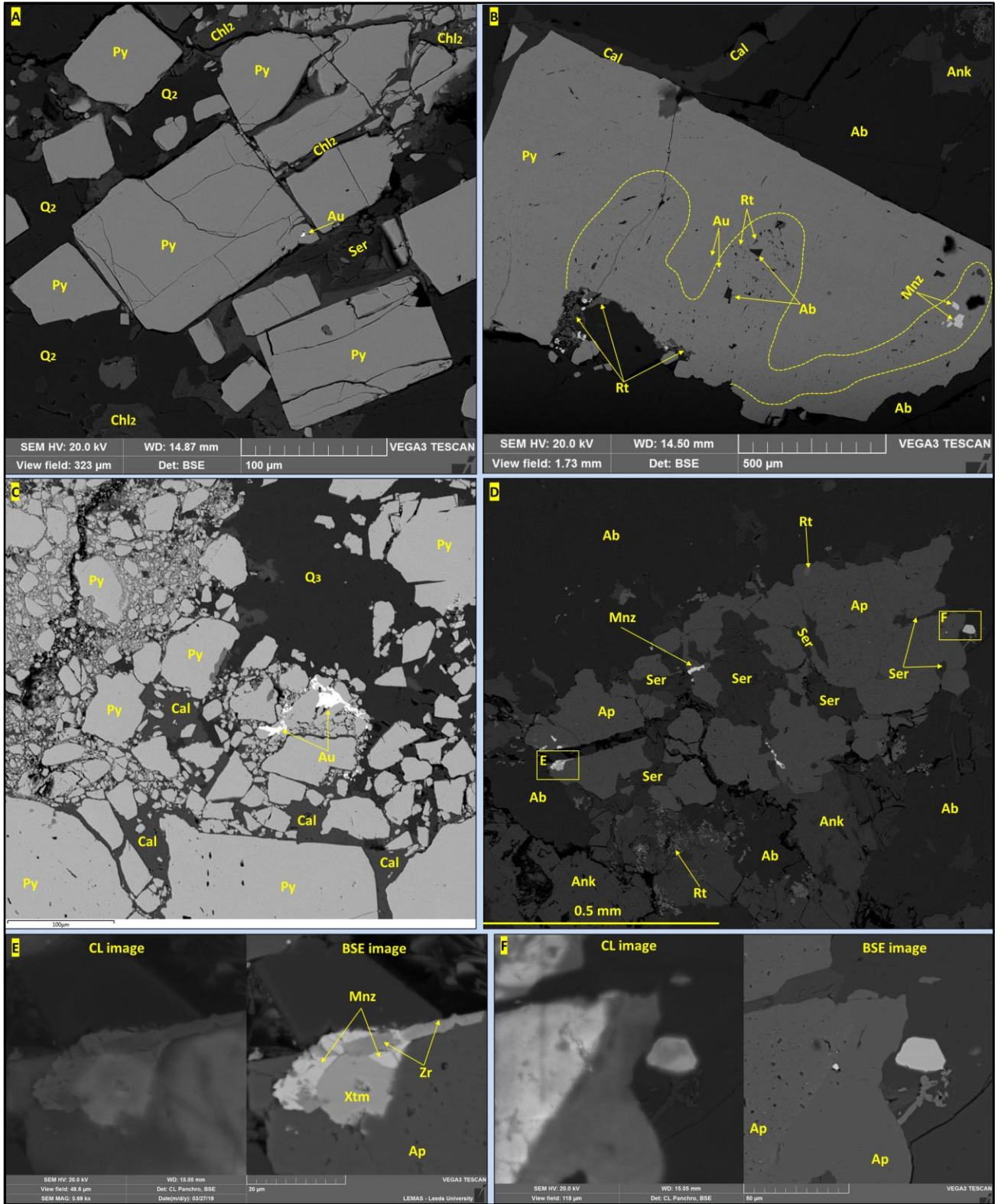
The hematite was observed macroscopically in the alteration halo of VS<sub>3</sub> and to a lesser degree within the veins (*Plate V.6-J*). A few inclusions of hematite were also identified as inclusions in pyrite and in monazite and free between rutile and ankerite (*Plate V.11-C*). Hematite staining related to supergene alteration was also observed on outcrop faces and opened fractures.

The apatite is the most abundant phosphate phase from the Stogér Tight deposit and shows irregular to anhedral shapes and variable sizes, from a few microns

up to 1-2 millimetres. It occurs within the albite-ankerite-sericite-rutile alteration and under BSE it displays a strong zonation given by a spongy core characterised by holes and small monazite and xenotime inclusions, and external rims that are clean and homogenous (*Plate V.10-D, E, F*). In CL the core shows a high intensity, whereas the rims have a lower response (*Plate V.10-E, F*). The core of the apatite is overgrown by albite, ankerite, sericite and rutile, whereas its rims incorporate the mentioned minerals or show straight boundaries with them suggesting simultaneous growth (*Plate V.9-H, Plate V.10-D*). Inclusions of apatite in pyrite are common. It was also observed that both the core and the rims of the apatite are crosscut by the quartz<sub>3</sub>-calcite<sub>2</sub>-chlorite<sub>2</sub> veinlets.

The monazite and xenotime occur as small inclusions (<10 µm in size) in the spongy cores of the apatite and as free grains in association with albite-ankerite-sericite-rutile-pyrite and zircon. The monazite grains are bigger (10 up to ~100 µm in size) and more abundant than the xenotime (10 up to ~50 µm in size). Within larger monazite grains inclusions of zircon, rutile, ankerite, pyrite and even xenotime were observed, whereas in the xenotime only zircon and rutile (*Plate V.10-G, H*). Monazite and xenotime grains of up to 30 µm in size were also observed as inclusions in pyrite (*Plate V.10-B*). Both the monazite and the xenotime are brecciated by the chlorite<sub>2</sub>-calcite-quartz<sub>3</sub> veins (*Plate V.10-I*), and sometimes occur fully enclosed within these veins and in their associated patches. For the latter case, it is not clear if the monazite/xenotime grains were incorporated within the veins from the surrounding material, or if they formed within the veins.

Zircon grains were observed disseminated within the albite-ankerite-sericite-rutile-pyrite alteration halo. The zircon shows irregular to anhedral shapes and variable sizes (from a few microns up to 100 µm). It was observed that the zircon brecciates and replaces baddeleyite (*Plate V.10-J*) which is interpreted as a relict oxide phase from the initial mineral composition of the Stog'er Tight gabbro. As most of the other alteration minerals, the zircon is also brecciated by the chlorite<sub>2</sub>-calcite-quartz<sub>3</sub> veins.





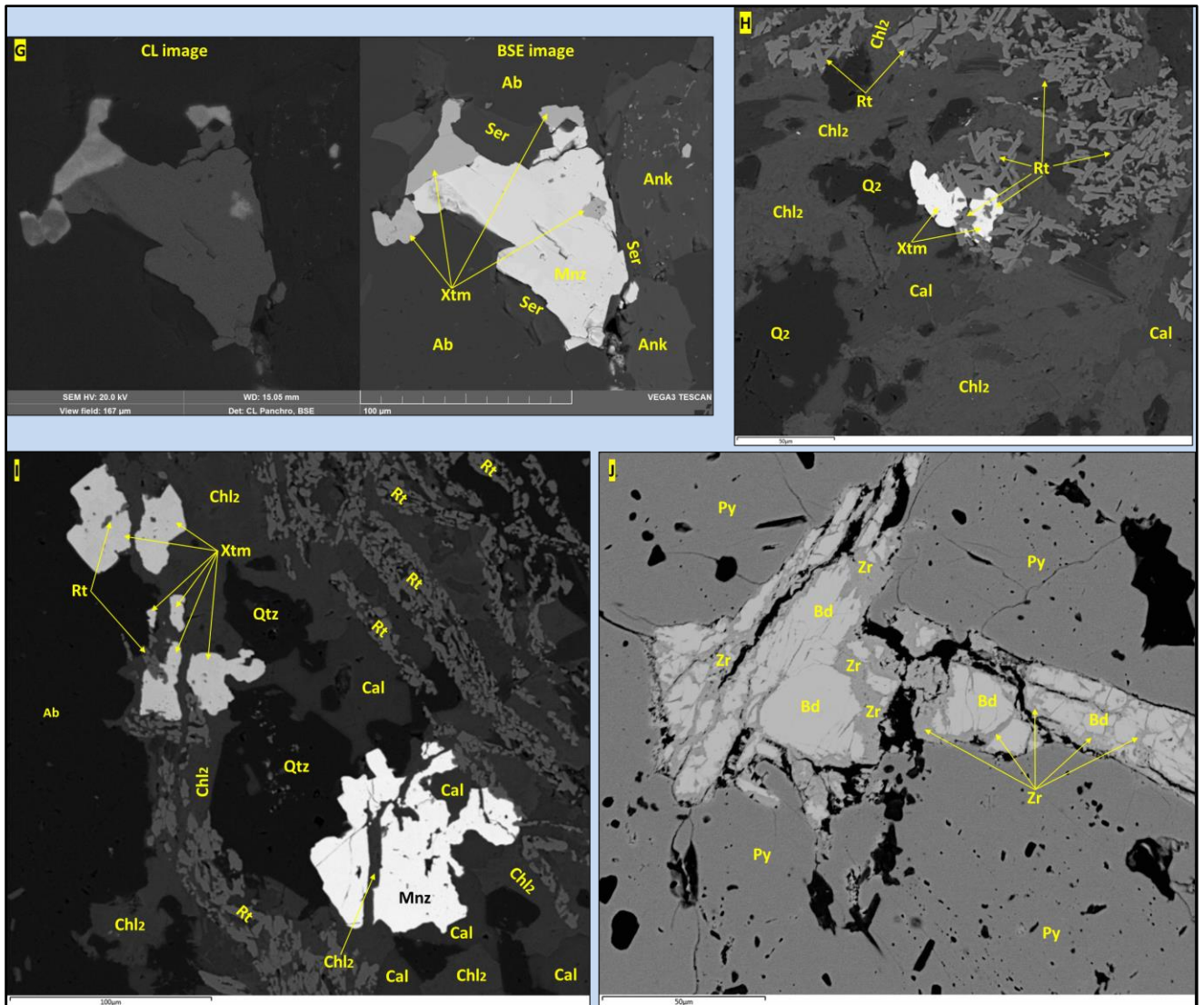


**Plate V.10** – Representative images of different alteration minerals related to the Stog'er Tight mineralisation: **A** – BSE image showing fine grained Py crystals brecciated by Chl<sub>2</sub> veinlets, **note** the small Au inclusion in Py, sample ST-ORE-Chl; **B** – BSE image of a large euhedral Py crystal with multiple inclusion rich zones (marked by the yellow dashed line) and inclusion-free zones, **note** the presence of small inclusions of Au and monazite in the inclusion rich zones, sample SZO1; **C** – BSE image showing strongly brecciated Py aggregate by Cal veinlets, **note** the clear aspect of the Py crystals (few inclusions), the “pulverization” of Py and the coarse, irregular Au grains in the brecciated zones, sample SOZ2; **D** – BSE image showing a large apatite crystal with spongy core and homogenous rims, **note** the infill of sericite within the apatite core and the inclusions of Rt and Ser within the apatite rim, rectangles E and F show the location of the zoomed in images **E & F** – **note** the apatite zonation in both BSE and CL, sample SOZ1; **G** - BSE/CL image of large monazite grain with Xtm inclusion, **note** the size difference between Mnz and Xtm and the homogenous aspect of the Mnz and the zonation pattern of Xtm in CL, sample SOZ1; **H** – BSE image showing Xtm and Rt within a Cal-Chl<sub>2</sub> patch, note the Rt inclusion within the Xtm, sample BN215; **I** – BSE image showing both Mnz and Xtm brecciated by Chl<sub>2</sub> veins, sample BN2015; **J** – BSE image of baddeleyite brecciated and replaced by zircon, both minerals are included in Py, sample SOZ1.

#### ***V.1.2.4. Mineralisation***

The ore mineralogy of the Stog'er Tight deposit is composed of native gold, chalcopyrite, and trace amounts of galena, molybdenite and barite. Detailed descriptions for gold and chalcopyrite are listed below, whereas summarised descriptions for all these minerals are provided in **Table V.8**. In contrast to the Pine Cove deposit, no tellurides phases were identified within the Stog'er Tight ore.

As in the Pine Cove deposit, the gold from the Stog'er deposit shows an intimate relationship with the pyrite crystals. Most of the gold grains occur as irregular to rounded inclusions fully enclosed in the pyrite crystals or free, as wires, rounded blebs, and irregular crystals along mono or poly mineral veinlets composed of chlorite<sub>2</sub> and/or calcite and/or quartz<sub>3</sub> that brecciate the pyrite crystals and aggregates (**Plate V.10-A, B, C; Plate V.11-A, B**). Within the pyrite, the gold was seen both in the inclusion rich domains and in the neat, recrystallised parts of the crystals. It was also observed that the gold is coarser and more abundant within the large and intensively brecciated pyrite patches than the gold found in the fine-grained crystals and aggregates (**Plate V.10-A, C, Plate V.11-A**). The gold was also observed between the rutile crystals within the rutile bands and at the interface of rutile and pyrite crystals, when both the rutile and gold are hosted by pyrite (**Plate V.11-C**).

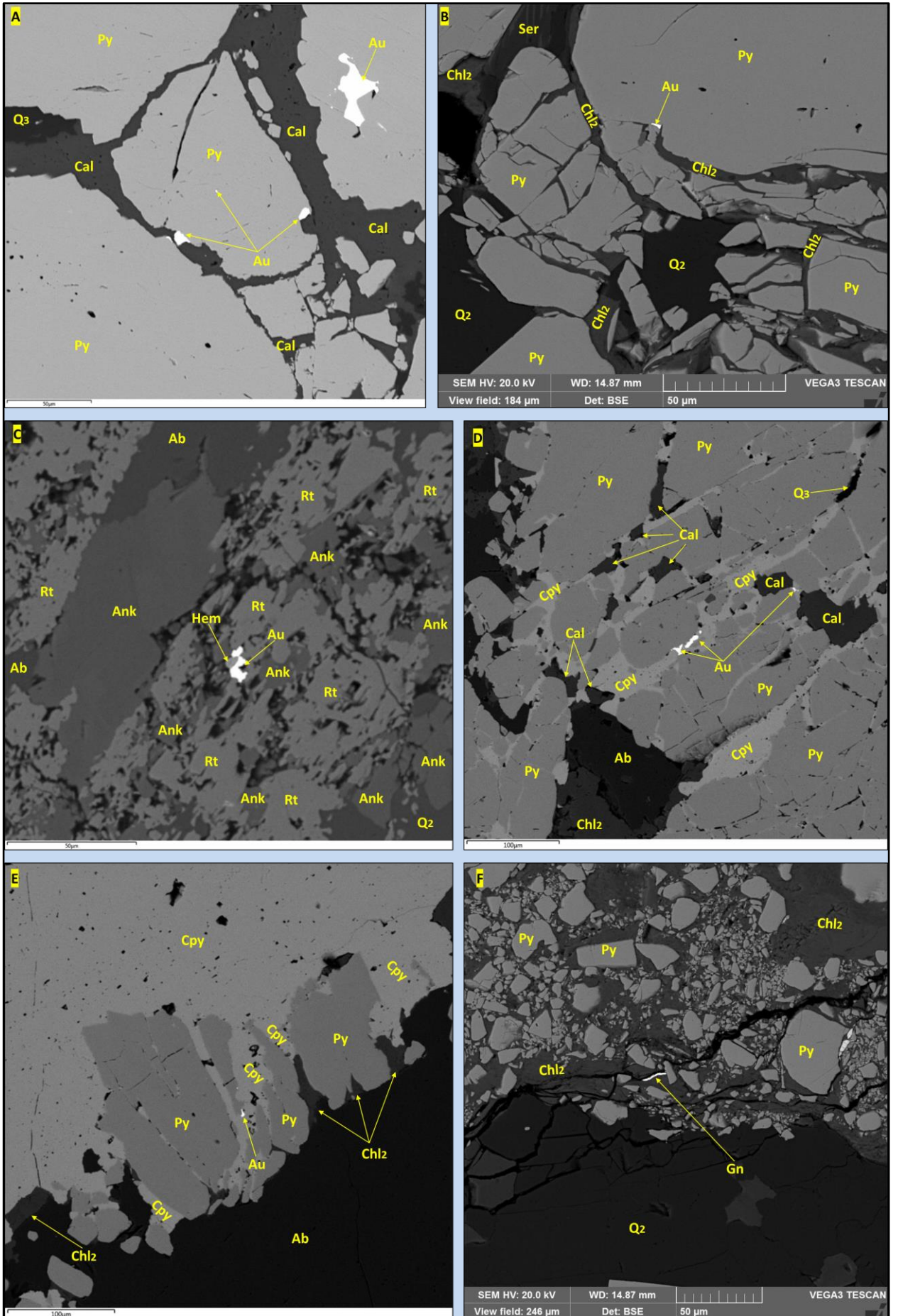
The chalcopyrite is the second most abundant sulphide phase after the pyrite and was observed as wires and irregular to rounded inclusions in the pyrite crystals, free in the albite-ankerite-sericite alteration phases, and along quartz<sub>3</sub>-chlorite<sub>2</sub>-calcite veinlets that brecciate the pyrite (**Plate V.11-D**). Chalcopyrite stringers that brecciate and infill open spaces in the pyrite aggregates or which fully replace pyrite were also seen in association to the quartz<sub>3</sub>-chlorite<sub>2</sub>-calcite veins (**Plate V.11-E**). Gold grains are common along the chalcopyrite stringers or at the interface between chalcopyrite and pyrite crystals (**Plate V.11-D, E**).

**Table V.8.** – Summary characteristics of the ore minerals from the Stog'er Tight deposit.

Mineral	Occurrence, Morphology
Au	Irregular to rounded inclusions in py; free as wires and irregular to rounded grains along cpy stringers and cal-chl <sub>2</sub> -Q <sub>3</sub> veins that brecciate the py or at the interface of py crystals; free in the rutile bands, rarely in ankerite/albite/sericite; variable sizes from 1 µm and up to 100 µm
Cpy	Inclusions in the py crystals; free in the altered groundmass (alb-ser-ank-rt) or along chl <sub>2</sub> -cal-Q <sub>3</sub> veinlets that brecciate the pyrite; large patches formed as infills within open spaces in pyrite aggregates or as replacement zones on pyrite
Gn	Trace* amounts, small grains (<10 µm) in cracks and along chl <sub>2</sub> -cal-Q <sub>3</sub> veinlets ( <b>Plate V.11 – E</b> )
Moly	Trace* amounts, small grains (<10 µm) free in the altered ground mass (ab-ser-ank-rt)
BaSO <sub>4</sub>	Trace* amounts, small grains (<10 µm) free in the altered ground mass (ab-ser-ank-rt)

\*trace = none, or very few grains / studied thin section

**Plate V.11 (next page)** – Representative images of different ore minerals related to the Stog'er Tight mineralisation: **A** – BSE image showing coarse grained Au (both free and as inclusion) in Py aggregate brecciated by Cal veinlets, sample SOZ2; **B** – BSE image showing a gold grain along Chl<sub>2</sub> vein that brecciate Py, sample ST-Ore-Chl; **C** – BSE image of free Au grain at the interface of Rt-Ank-Hem, sample ST07-Ore; **D** – BSE image showing Cpy stringers in association with Cal-Q<sub>3</sub> brecciating Py, note the Au grains along the Cpy stringers, sample BN215; **E** - BSE image showing a large patch of Cpy that incorporates (replace) Py, note the presence of Au at the interface of Py/Cpy, sample BN215; **F** – BSE image showing Gn wire along Chl<sub>2</sub> veins that brecciate Py, sample ST-Ore-Chl.



### V.1.3. The Argyle deposit

When the Argyle area was visited the deposit was not in development and all the exploration trenches were covered. Moreover, in the proximity of the deposit the outcrop exposure is poor. Thereby, the closest visited outcrops are located a few hundred meters to E-NE from the proved economic mineralisation and consist of fine to coarse grained sections of the Stog'er Tight gabbro (**Figure V.3**). A brief description of the Stog'er Tight gabbro sills from the Argyle area is provided in **Appendix I** based on existing literature, whereas a detailed characterisation can be found in Pawlukiewicz (2019).

#### V.1.3.1. Structural setting and vein sets

The visited outcrops are weakly deformed. These show a cryptic to weak  $S_{2a}$  foliation fabric that dip moderately to steeply from N to NW and a weak stretching mineral lineation that plunges shallowly to moderately to N (**Figure V.3-B**). The observed outcrops are not mineralised but are weakly to moderately altered: either silicified or characterised by a pervasive alteration composed of chlorite-carbonate-epidote.

The structural information presented below come from the exploration data provided by the Anaconda Mining Company and from informal communications with the Anaconda geologists. The mineralised zones are located approximately 300 meters N from the NE striking segment of the  $D_{2a}$  Scrape thrust, dip to N, and are restricted to the gabbro sills (strata-bound) (**Figure V.3-A**). The deposit shows the same structural characteristics as the Pine Cove and Stog'er Tight deposits being affected by all the syn-to-post  $D_{2b}$  structures. At least two main vein sets are related to the mineralisation (**Plate V.12-A**): i) foliation-parallel veins that are folded by  $F_3$  folds; and ii) veins that are sub-parallel to the  $F_3$  axial planes.

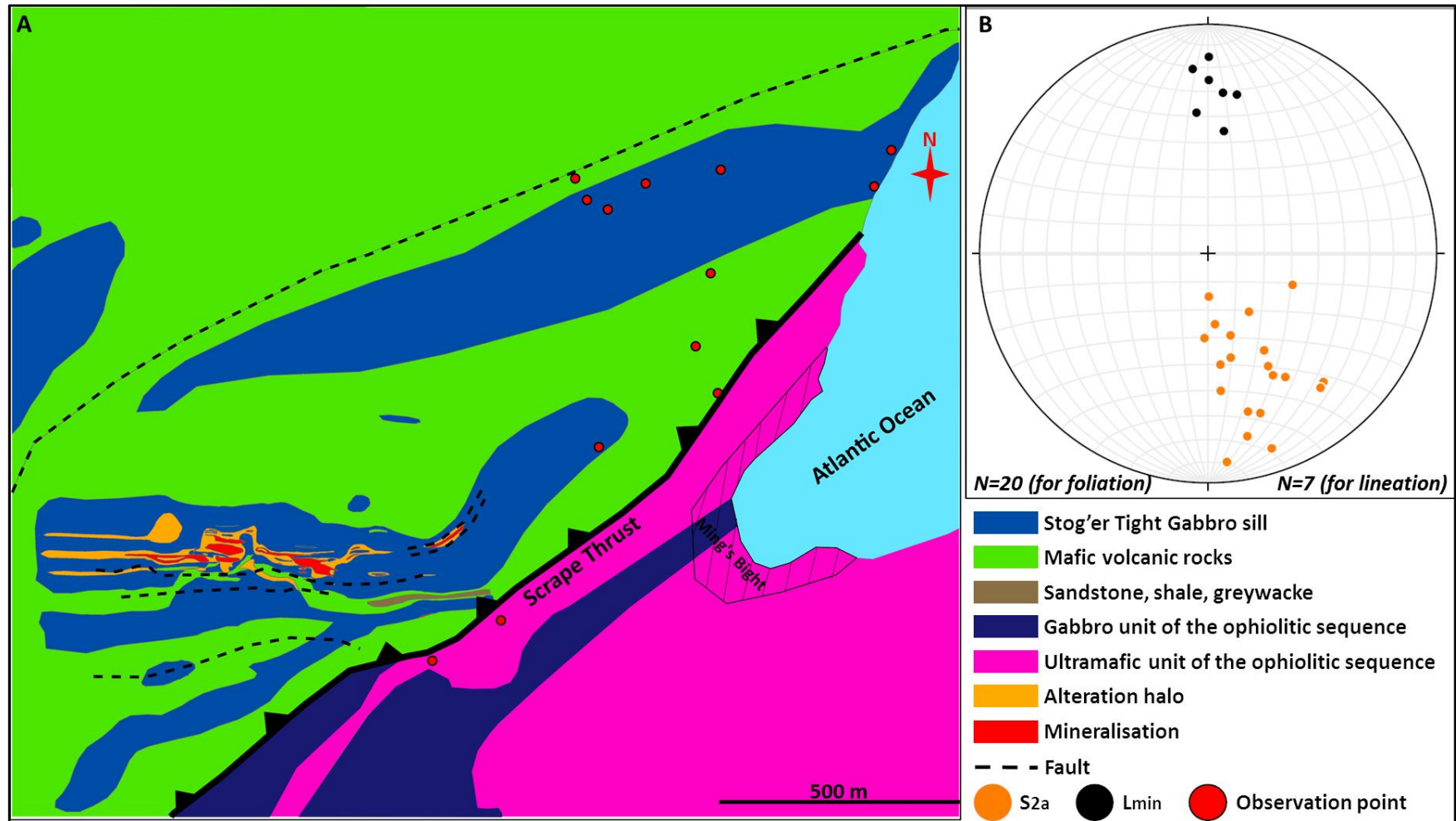


*Figure V.3 . A – Simplified geological map of the Argyle deposit after the unpublished geological map of Anaconda Mining (2018) and Cullen et al. (2018); B - Southern-hemisphere, equal-area, stereographic projections of the poles to the foliation planes and of the stretching mineral lineation.*

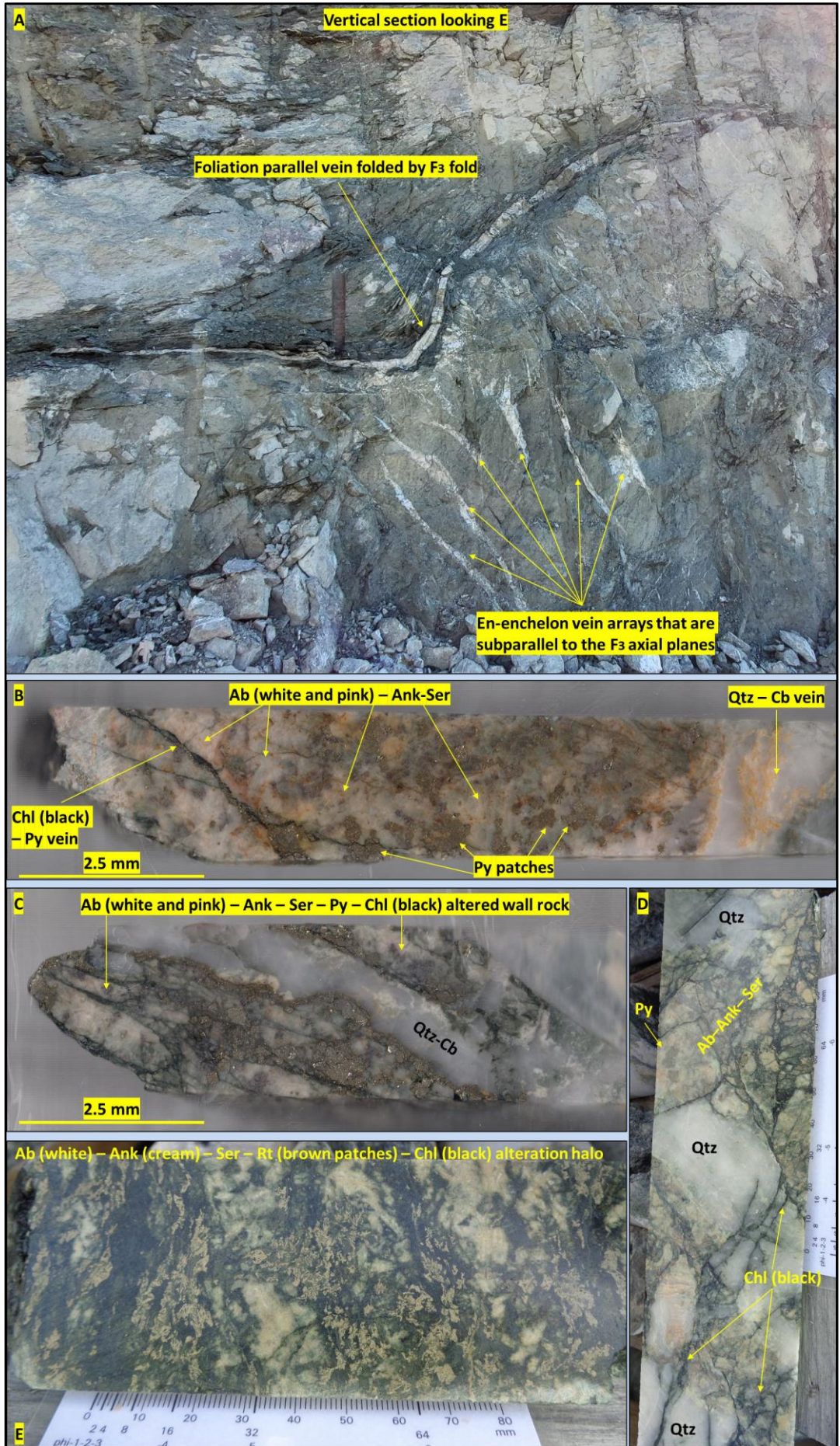


**Plate V.12. (above)** - Representative images for the mineralised veins and proximal alteration halo of the Argyle deposit: **A** – Foliation parallel veins folded by  $F_3$  folds and en-echelon veins arrays emplaced subparallel to the  $F_3$  axial planes, Argyle open pit, image received from David Copeland, chief geologist of Anaconda Mining; **B** - quartz–carbonate vein associated with an intense, white to cream-beige alteration halo composed mainly of albite and large patches of pyrite, and small patches of ser-ank, everything crosscut by late chlorite (black) – pyrite (fine grained) vein; **C** - quartz–carbonate vein associated with an intense, white to cream alteration halo composed mainly of albite and pyrite plus small patches of ser-ank-rt, everything is cross-cut by late chlorite (black) veins; for both **B & C** **note** the lack of Py within the veins and its distribution in the altered wall rock and at the vein margins; **D** – breccia zone composed of quartz vein fragments and intense brecciated pink-beige altered wall rock (alb-ank-ser), everything crosscut by chlorite (black) veins; **E** – Alb-Ank-Ser altered wall rock (white-cream zones) strongly overprinted by chlorite (black) – rutile (brown) veins and patches.

### **V.1.3.2. Alteration**

As presented above and in *Appendix I*, in the Argyle area, the mineralisation is hosted within the Stog' er Tight gabbro. Therefore, the descriptions presented for the unaltered sections of the Stog' er Tight gabbro in *subchapter V.1.2.3* are also applicable herein. Moreover, for the Argyle deposit only core sections from the proximal alteration and the ore zone were investigated. Thereby, for information related to the distal and intermediate alteration halos of the deposit, the reader is referred to Pawlukiewicz (2019). Summarised descriptions from the afore-mentioned author can be found in *section II.4* of this thesis.

Petrographic analyses of samples from medium to high gold grade zones (*Appendix 2*) showed that quartz–ankerite–albite–sericite–rutile–chlorite–calcite pyrite ± titanite–hematite represent the main hydrothermal alteration minerals associated with gold mineralisation in the Argyle deposit. Apatite, monazite, xenotime, and zircon are also abundant. Descriptions for all these alteration minerals are presented in *Table V.9*.

The investigated mineralised sections show a high density of quartz–carbonate (mostly ankerite) veins associated with an intense altered wall rock in which the initial magmatic composition of the gabbro and the mineral assemblages related to the greenschist facies metamorphism have been replaced by the alteration minerals. The alteration halo shows pink to beige–brown hues given by albite–ankerite–sericite–



rutile-pyrite, and dark green to black colours where chlorite veins and patches occur (*Plate V.12–B, C, D, E*).

The quartz from the Argyle deposit shows similar optical properties as the quartz from both Pine Cove and Stog' er Tight deposits (*Table V.10*): occurs only as vein material, it displays the common undulatory extinction, appears as blocky to elongate blocky, coarse-grained crystals with straight to lobate and serrated grain boundaries, and as brecciated and recrystallised, fine grained, anhedral to subhedral crystals (*Plate V.13–A*). Three main quartz generations ( $Q_1$  to  $Q_3$ ) were also identified in the mineralisation related veins from Argyle based on SEM-CL analysis (*Table V.10*). Compared to Pine Cove and Stog' er Tight,  $Q_1$  is more abundant in the Argyle samples, shows moderate blue and yellow-green oscillating CL colours, and has the same morphology occurring as irregular to anhedral crystal fragments brecciated and enclosed within  $Q_2$  (*Plate V.13-B*). The second quartz generation ( $Q_2$ ) shows the same characteristics (optical/CL properties, multiple sub-generations, crosscutting relationship with the rest of the alteration minerals - *Table V.10; Plate V.13*) as  $Q_2$  from the Stog' er Tight deposit (see descriptions above). The third quartz generation ( $Q_3$ ) was observed in very thin (< 1 mm in thickness) veinlets that crosscut both  $Q_1$  and  $Q_2$ , and most of the other alteration minerals (*Table V.10, Plate V.13–C to I*). Under CL it was observed that  $Q_3$  is composed of two sub-generations of quartz ( $Q_{3A}$  and  $Q_{3B}$ ) with different CL characteristics. The  $Q_{3A}$  has a moderate to bright blue CL colour like  $Q_{3A}$  from the previously described deposits, whereas  $Q_{3B}$  has a distinct moderate yellow-green colour (*Plate V.13–C to I*). Most commonly  $Q_{3A}$  and  $Q_{3B}$  occur within the same veinlets and rarely within separate structures. Zones with dense networks of interconnecting  $Q_{3A}$  and  $Q_{3B}$  veinlets that strongly brecciate and replace  $Q_2$ , and other alteration minerals are common (*Plate V.13–F, G*). Within the veins, different relationships were observed between the two  $Q_3$  phases:  $Q_{3A}$  and  $Q_{3B}$  are randomly distributed along the veins (*Plate V.13–D, F, G*);  $Q_{3A}$  and  $Q_{3B}$  occupy different parts of the same vein (*Plate V.13–E*); and  $Q_{3B}$  occupies the central part of the vein, whereas  $Q_{3A}$  is preserved along the margins (*Plate V.13–H*). The relevance of these textures will be discussed in the interpretation section of this chapter. As in Pine Cove and in the Stog' er Tight deposits, poly mineral veins where  $Q_{3A}$  and  $Q_{3B}$  occur together with calcite and chlorite were also observed in the Argyle samples (*Plate V.13–H, I*).

**Table V.9**– Summary characteristics of the alteration minerals identified in the proximal alteration halo and in the ore zone of the Argyle deposit.

<b>Mineral</b>	<b>Occurrence</b>	<b>Texture</b>	<b>Spatial association with other alteration minerals</b>	<b>Overprinting relationships</b>
<b>Qtz</b>	As vein material	Multiple generations (Q <sub>1</sub> , Q <sub>2</sub> , Q <sub>3A</sub> and Q <sub>3B</sub> ), see <b>Table V.10</b>	See <b>Table V.10</b>	See <b>Table V.10</b>
<b>Ser</b>	Mostly in the altered wall rock and to a lesser degree within the veins	Patches and stringers	Q <sub>2</sub> -ab-ank-rt-py	Replaces ab; replaced and crosscut by cal-chl veins/patches
<b>Rt</b>	Mostly in the altered wall rock associated with qtz-ank veins and in the chl (black) patches and veins	Patches of very fine-grained crystals; thin, long bands oriented parallel and at an angle to one another, creating rhombohedral patterns; large, irregular to bladed crystals	All the other alteration minerals	Overgrown by py; crosscut by cal-chl veins but also hosted by them
<b>Ab</b>	Within alteration selvages	Moderate to coarse grained with recrystallised boundaries	Q <sub>2</sub> -ank-ser-rt-py	Locally replaced by ser-ank; crosscut and overprinted by cal-chl veinlets/patches
<b>Chl</b>	As veins and patches	Fine-grained crystals within veins, coarser within patches	Q <sub>3</sub> -cal-py ± tit-rt-hem	Shows mutual crosscutting relationships with Q <sub>3</sub> and cal and overprints the rest of the alteration minerals
<b>Epi</b>	Occurs as a relict phase in the altered wall rock	Consumed by calcite and chlorite	N/A	Overprinted by the rest of the alteration minerals
<b>Cal</b>	As veins and patches	Coarse-grained showing three types of twinning: thin, thick, and curved; fine grained recrystallised crystals that overprint the coarse-grained crystals	Q <sub>3</sub> -chl-py ± tit-rt-hem	Shows mutual crosscutting relationships with Q <sub>3</sub> and chl and overprints the rest of the alteration minerals
<b>Py</b>	Within the altered wall rock or at the contact between	Fine and coarse grained anhedral to euhedral crystals, either with	All the other alteration minerals	Brecciated by the Q <sub>3</sub> -chl-cal veins but further annealed and

	veins and host rocks; within the veins, but lower amounts compared to the host rocks	inclusion rich cores and inclusion free rims or clean - without inclusions; patches (up to cm <sup>2</sup> in size) of brecciated or annealed polycrystalline aggregates		recrystallised; all the other alteration minerals were observed as inclusions in it
<b>Ank</b>	Both within the altered wall rock and in the veins	As veins and patches with both fine and coarse-grained crystals	Q <sub>2</sub> -ab-ser-rt-py	Replaced and brecciated by Q <sub>3</sub> -cal-chl veins
<b>Hem</b>	Within the Cal-chl veins and patches	Staining or thin films on py and other Fe bearing minerals; pseudomorphs on fine grained pyrite crystals	Cal-chl ± tit-rt	N/A
<b>Ap</b>	Within the altered wall rock	Anhedral to euhedral, fine-grained to coarse grained (a few microns to 1-2 mm) crystals with spongy core (sieve like) and homogenous rims	Q <sub>2</sub> -ab-ank-ser-rt-py	The spongy core is overgrown by ab-ser-ank-rt, but the homogenous rims incorporate the latter minerals; both core and rim are overgrown by coarse pyrite crystals and aggregates and brecciated by Q <sub>3</sub> -cal-chl veins
<b>Mnz</b>	Within the altered wall rock and along the Chl-cal veinlets	Fine to coarse grained (1 µm up to 150 µm), irregular to rounded shapes	All the other alteration minerals	Brecciated by Q <sub>3</sub> -cal-chl veins but also hosted by them
<b>Xtm</b>	Within the altered wall rock; rarely within veins	Fine to coarse grained (1 µm up to 200 µm), irregular to rounded shapes	All the other alteration minerals	Brecciated by Q <sub>3</sub> -cal-chl veins but also hosted by them
<b>Zr</b>	Within the altered wall rock	Fine to coarse grained (10 µm up to 100 µm), irregular to anhedral shapes	Q <sub>2</sub> -ab-ank-ser-rt-py	Brecciates and replaces baddeleyite and is brecciated by Q <sub>3</sub> -cal-chl veins
<b>Tit</b>	Within Chl-cal veinlets and patches; inclusions in Py	Fine to coarse grained (up to 500 µm) irregular to anhedral crystals; small inclusions in Py	Cal-chl ± rt-hem	Overgrows Rt and ilmenite and brecciates Py; hosted by, but also brecciated by chl-cal veins

**Table V.10.** – Summary CL characteristics of the quartz generations observed in samples from the Argyle deposit. The texture terminologies are used according to Rusk et al. (2004) and Rusk (2012).

Quartz (Q) generation	Optical properties	CL colour and intensity	CL texture	Crosscutting relationships	Association with other alteration minerals	Related vein set
Q <sub>1</sub>	Undistinguishable from Q <sub>2</sub>	Blue/yellow (medium to high intensity when compared to Q <sub>2</sub> )	Occurs as relict fragments of Q crystals that show euhedral growth zones with alternating yellow-blue CL response	Brecciated and enclosed in Q <sub>2</sub> ; brecciated by Q <sub>3</sub>	N/A	N/A no vein sets defined in the field
Q <sub>2</sub>	Shows multiple sub-generations: coarse-grained crystals in thick veins and brecciated, fine-grained crystals on thin veins that crosscut and re-open the thicker veins	All sub-generations are dark purple (low intensity)	Homogenous/massive with mottled aspect due to the presence of Q <sub>1</sub> fragments	The fine-grained sub-generations crosscut the ab and ank; It is crosscut by Q <sub>3</sub> -chl-cal ± hem veinlets	Ab-ank-ser-rt-py	
Q <sub>3</sub>	Q <sub>3A</sub>	Occurs as thin veinlets of a few microns with no visible crystals or as inclusion trails	Medium to bright blue (moderate to high intensity, higher CL response than Q <sub>2</sub> )	Dense networks of thin veinlets with multiple orientations	Crosscuts both Q <sub>1</sub> and Q <sub>2</sub> ; Q <sub>3A</sub> & Q <sub>3B</sub> were observed mostly within the same veins, and rarely on separate structures; mutual crosscutting relationships between Q <sub>3A</sub> -Q <sub>3B</sub> -Cal-Chl	Cal-chl ± py
	Q <sub>3B</sub>	Undistinguishable from Q <sub>3A</sub>	Medium CL intensity, fluorescent in yellow-green colours	Dense networks of thin veinlets with multiple orientations		Cal-chl ± py

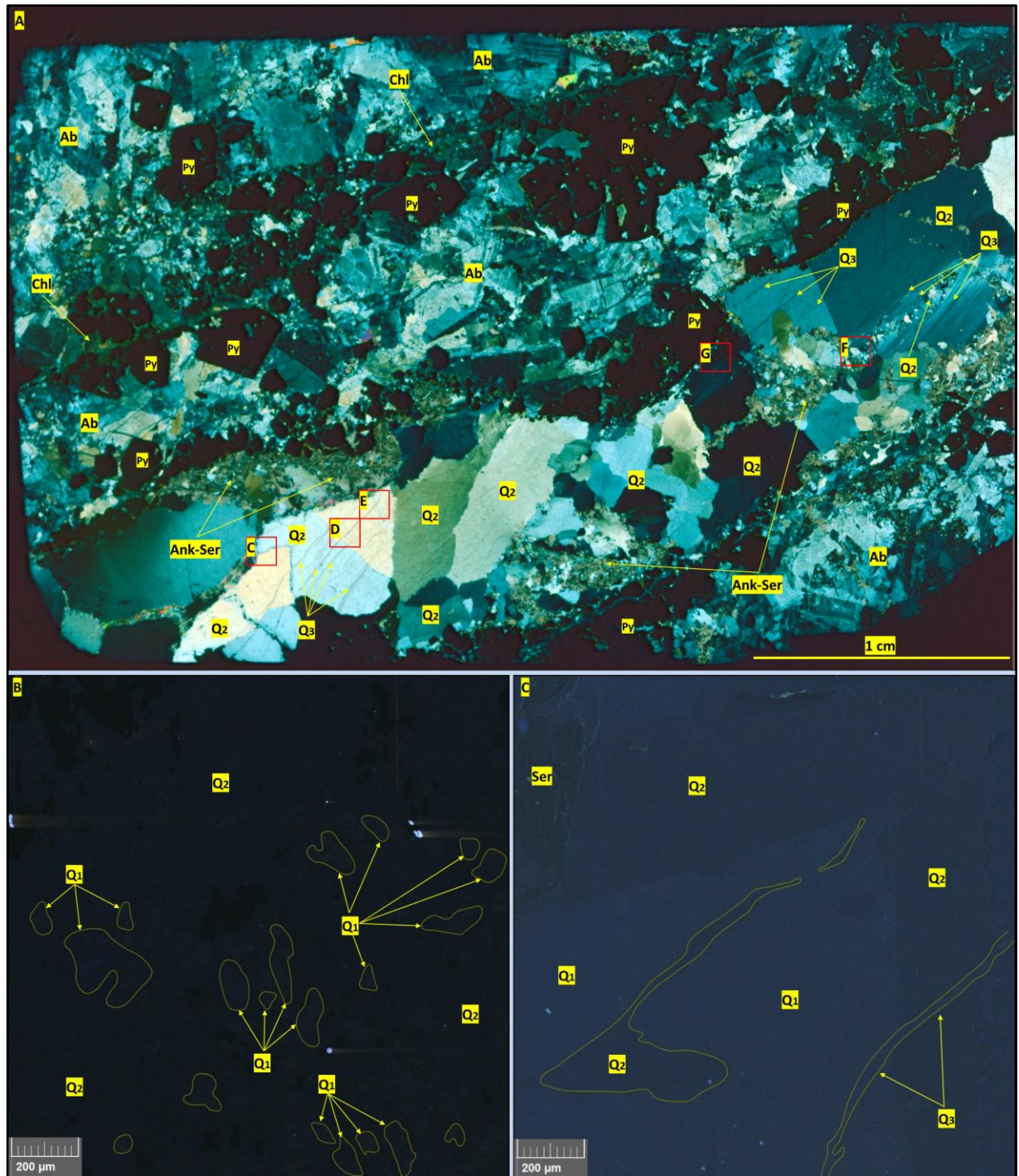


**Plate V.13**– Representative images of different quartz generations related to the Argyle mineralisation: **A** – Microscope image scan (cross polarized light) of section AG3 (section made from the core section illustrated in **Plate V.12 – C**), **note** the coarse-grained blocky to elongate blocky Q<sub>2</sub> crystals and the fine-grained Q<sub>2</sub> crystals (right side of section), the Q<sub>3</sub> thin veinlets, the ankerite-sericite patches, and the distribution of py crystals and patches at the margin of the vein and within the altered wall rock and not in the vein, the red squares **C** to **G** show the location of CL images **C**, **D**, **E**, **F**, **G**. **B** – CL image showing fine-grained Q<sub>1</sub> crystal fragments within a homogenous Q<sub>2</sub> mass, section AG1. **C** – CL image showing a large fragment of an euhedral Q<sub>1</sub> crystal within a homogenous Q<sub>2</sub> mass, and both crosscut by Q<sub>3</sub> veinlet.

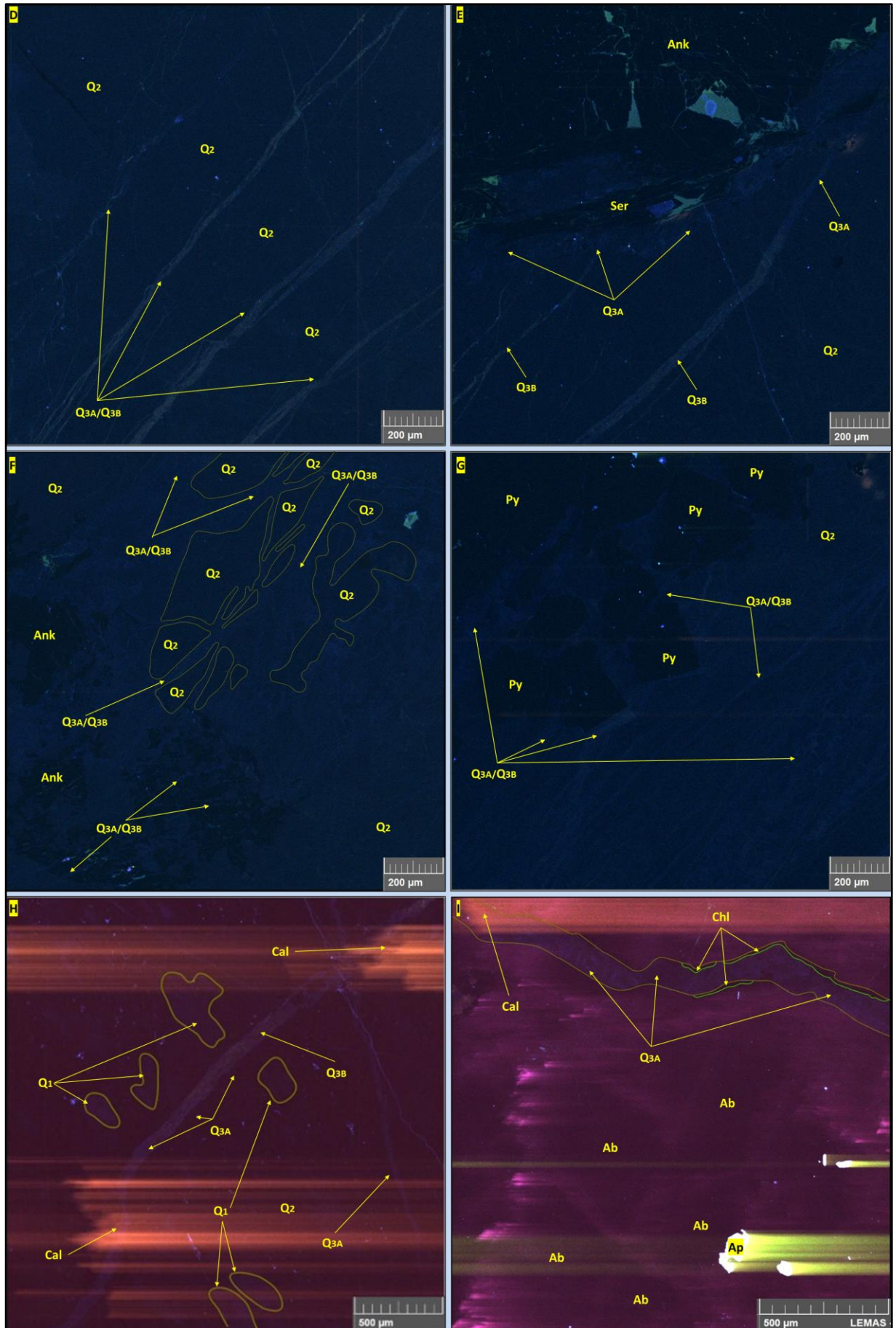


**Plate V.13 (continuation)** –*D* – CL image showing subparallel Q<sub>3</sub> veinlets crosscutting Q<sub>2</sub> homogenous mass, **note** the random coexistence of both Q<sub>3A</sub> and Q<sub>3B</sub> along the Q<sub>3</sub> veins. *E* – CL image showing subparallel Q<sub>3</sub> veinlets crosscutting Q<sub>2</sub> and sericite stringers, **note** the presence of Q<sub>3A</sub> and Q<sub>3B</sub> along different parts of the same veins. *F*, *G* - CL images showing dense networks of interconnecting Q<sub>3</sub> veinlets brecciating Q<sub>2</sub>, ankerite patches and pyrite crystals and aggregates, **note** the presence of Q<sub>3A</sub> and Q<sub>3B</sub> along different parts of the same veins. *H* - CL image showing Q<sub>3</sub> veinlets that intersect one another at approximately 60° and with no displacement typical of conjugate structures, **note** the distribution of Q<sub>3B</sub> within the middle part of the thicker vein and the Q<sub>3A</sub> along the vein walls, and the presence of calcite along the same vein, sample MPAG1. *I* - CL image showing Q<sub>3</sub>-Chl veinlet crosscutting albite, **note** the high Cl intensity along the albite cleavage planes and crystal boundaries, sample AG<sub>4</sub>. **Note**, all the CL images have the brightness and the contrast slightly enhanced compared to the original image to highlight the different Q generations.

Both white and pink albite coexist in approximately equal proportions in the Argyle samples. The albite was observed mostly within the altered wall rock material and rarely within the veins (**Plate V.12-B-E; Plate V.13-A**). The albite crystals vary in size from tens of microns to a few millimetres and display straight, diffuse, lobated and serrated boundaries between themselves and with the coarse grained quartz<sub>2</sub> crystals. Quartz<sub>2</sub>(fine grained)-ankerite-sericite veins and patches crosscut and overprint the albite (**Plate V.14-A**). Internal micro-fracturing is common in the large crystals (**Plate V.14-B**). When imaged by CL, the albite shows both low and high CL intensities defined by dark and moderate to very bright magenta colours. The bright zones correspond to crystal boundaries, crystallographic planes, and twinning faces (**Plate V.13-I**).

Ankerite and calcite (**Table V.9**) are the only carbonate phases identified in the Argyle samples based on EDS analysis. As in the Stog'er Tight deposit, the ankerite occurs as vein material together with fine-grained quartz<sub>2</sub>, and as large patches in association with sericite and rutile (**Plate V.13-A, F; Plate V.14-A**). Calcite occurs as mono or poly (with Q<sub>3</sub> and/or chl) mineral veins and patches that crosscut and overprint the rest of the alteration minerals (**Plate V.13-H, I; Plate V.14-C, D**). Within patches, the calcite shows three types of twinning named here after Burkhard (1993): thin, thick-tabular, and thick curved twins (**Plate V.14-C, D**). Fine grained recrystallised calcite that overprints areas of intense twinning were also seen (**Plate V.14-D**).

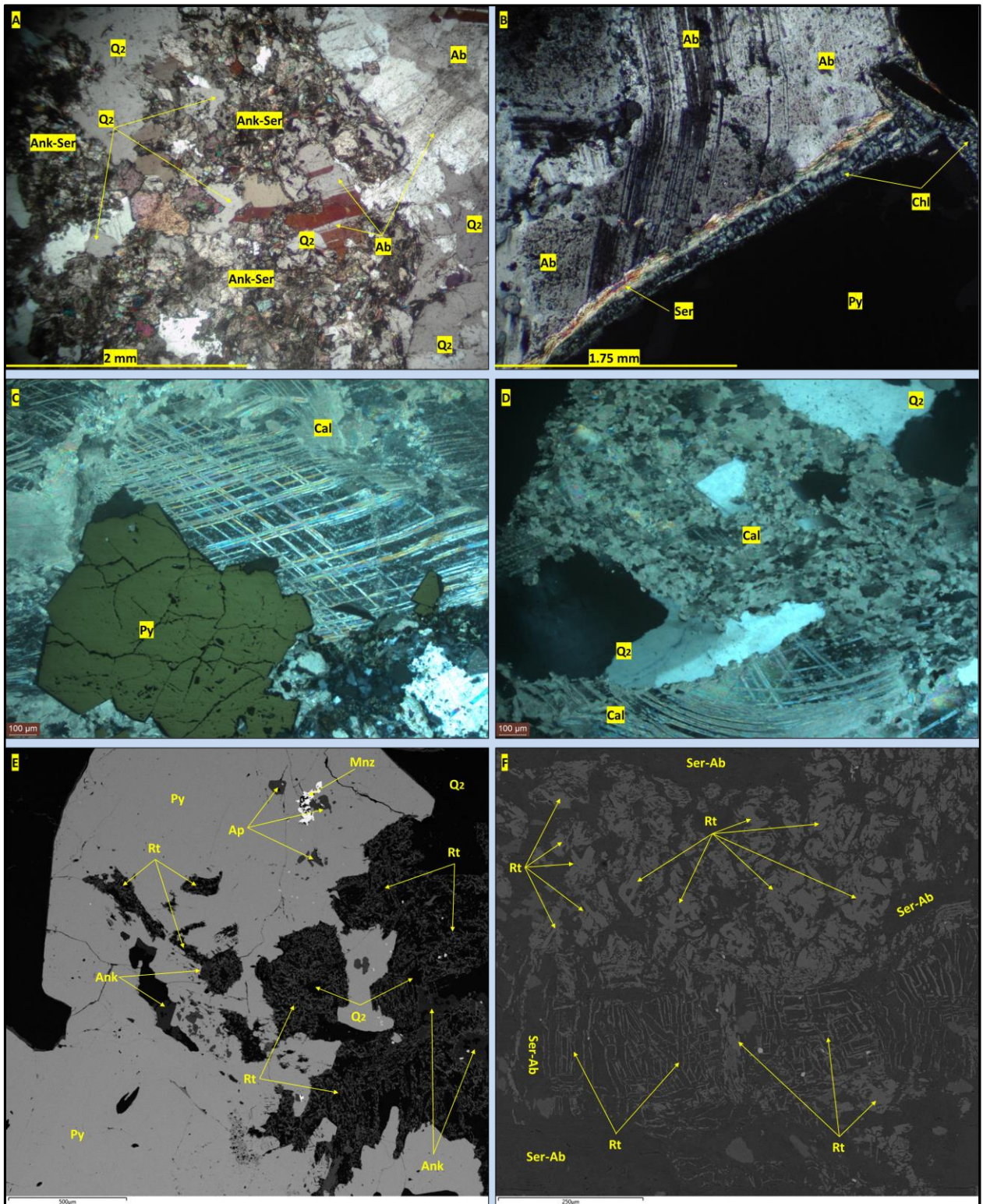
The sericite observed in the Argyle samples is represented by muscovite (determination made based on EDS analysis) and as in the Stog'er Tight deposit, it occurs as stringers and patches that overgrows the albite (*Plate V.14–A, B*). Flakes of coarse-grained muscovite are also common within intense sericitized zones.

Compared to Pine Cove and Stog'er Tight deposits, the rutile is more abundant at Argyle and occurs as cream-beige lumps and patches that can reach a few centimetres (*Plate V.12–E*). The rutile crystals vary significantly in both shape and size: clusters of very fine-grained crystals (*Plate V.14–E*); thin long bands oriented parallel and at an angle to one another, creating rhombohedral patterns (*Plate V.14–F*); and coarse-grained irregular to bladed crystals (*Plate V.14–F, G*). Most commonly, sericite and ankerite are found between, and around the rutile bands and crystals, and rarely albite and chlorite. In the intense sericitized areas, the large rutile crystals seem to be crosscut and overgrown by sericite (*Plate V.14–G*). Chlorite and calcite were also observed to crosscut rutile (*Plate V.14–G*). The rutile also shows an intimate spatial relationship with pyrite, being either intergrown with it or more commonly overgrown by it (*Plate V.14–E, H*).

One chlorite phase was observed in the Argyle samples (*Table V.9*). This has the same optical (black in hand specimen; strong pleochroic in plane polarised light; blueish grey to intense blue and purple birefringence colours) and geochemical properties (low magnesium (4-8%) and high iron (21-30%) as the chlorite<sub>2</sub> from the Pine Cove and Stog'er Tight deposits (see descriptions above) (*Plate V.14–B, I*). As in the other two deposits, the chlorite crosscuts most of the other alteration minerals and is spatially associated with Q<sub>3</sub> and calcite, either occurring together along the same veins or showing mutual crosscutting relationships (*Plate V.14–G, I, J*).

**Plate V.14 (next two pages)** – Representative images of different alteration minerals related to the Argyle mineralisation: **A** – Microscope image (transmitted light, XPL) showing Ank-Ser patches overgrowing albite and Q<sub>2</sub>, sample AG<sub>2</sub>. **B** – Microscope image (transmitted light, XPL) showing a fractured albite crystal, **note** the sericite overgrowing Ab, and the chlorite shadow pressure around the big euhedral Py crystal, sample AG<sub>3</sub>. **C, D** - Microscope images (reflected and transmitted light, XPL) showing large patches of calcite, **note** the thick tabular and curved twinning (both images) and the recrystallised Cal overgrowing the twinned Cal (in D), sample MPAG<sub>1</sub>. **E** – BSE image showing a large patch of fine-grained rutile crystals partially overgrown by Py, sample AG<sub>4</sub>. **F** – BSE image showing large patch of coarse-grained, anhedral to bladed rutile crystals and thin Rt bands within a Ser-Ab groundmass, **note** the distribution of the Rt bands locally creating rhombohedral patterns, sample AG<sub>1</sub>.





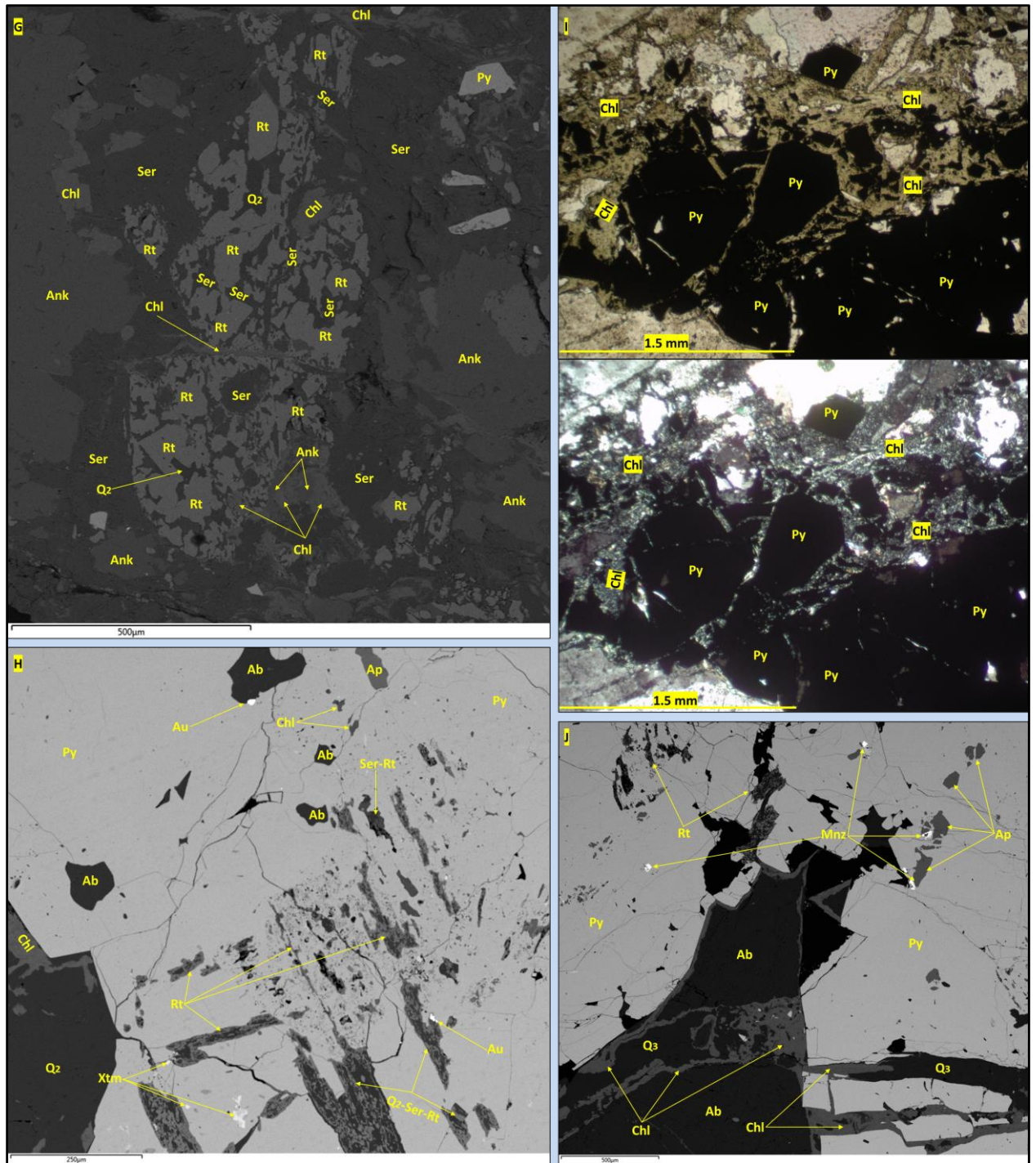


**Plate V.14 (continuation)** –*G* – BSE image showing a large patch of coarse grained rutile in a sericite groundmass, **note** the Rt seems consumed by sericite, and both Ser and Rt are crosscut by Chl veinlet, sample AG1; *H* - BSE image showing Rt bands and crystals enclosed (overgrown) by Py, **note** the gold grains, especially the one next to Rt, and the Xtm grains, sample AG3; *I* - Microscope image (transmitted light, PPL & XPL, up & down respectively) showing the brecciation of a Py aggregate by Chl, sample AG3; *J* – BSE image showing Chl-Q<sub>3</sub> veinlets crosscutting Py and Ab, note the Mnz and Ap inclusions in Py.

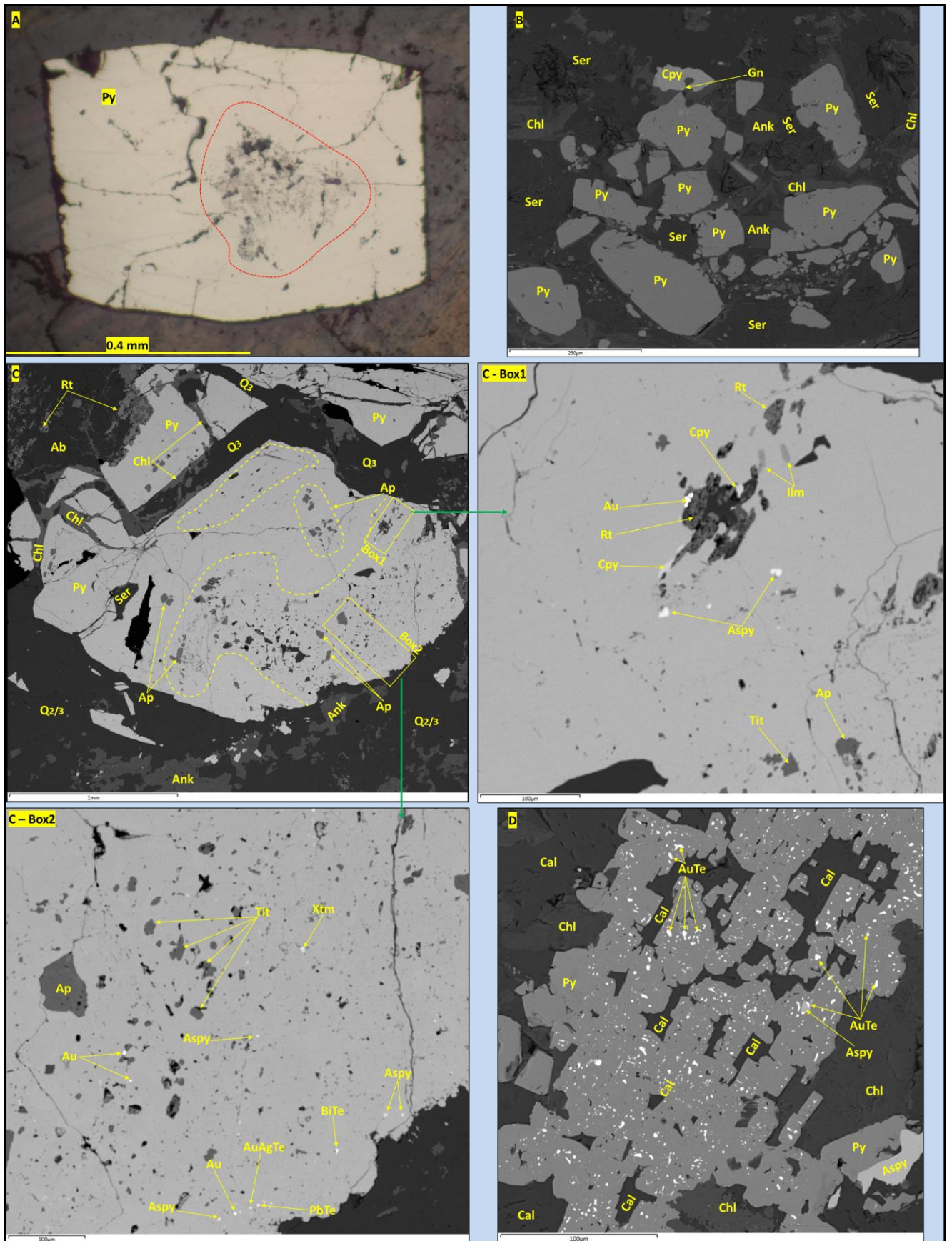
The pyrite is the main sulphide associated with the gold mineralisation at Argyle (*Table V.9*). It occurs disseminated in the alteration halo of the quartz-carbonate veins and rarely directly in the veins, and within the chlorite-calcite veins and patches (*Plate V.12-B, C; Plate V.13-A*). The pyrite crystals/aggregates observed in the Argyle samples show the same textures as the pyrite from the Pine Cove and Stog'er Tight deposits: anhedral to euhedral crystals with sizes from a few tens of microns to a few millimetres; simple zoned crystals with inclusion rich core, mantled by inclusion free euhedral rims (*Plate V.15-A*); coarse-grained euhedral crystals with multiple inclusion rich domains separated by inclusion free areas; un-zoned crystals without or with very few inclusions (*Plate V.15-B*); large, polycrystalline aggregates, with both inclusion-rich and inclusion-free domains (*Plate V.15-C*). The coarse-grained crystals and aggregates were observed mostly within the altered wall rock domains in association with albite-ankerite-quartz<sub>2</sub>(coarse)-sericite-rutile, whereas the fine-grained crystals and aggregates are common within the chlorite-calcite veins and patches (*Plate V.15-D*). Both the coarse-grained crystals and aggregates show variable degrees of brecciation caused by mono or poly mineral veinlets composed of chlorite/calcite/quartz<sub>3</sub> (*Plate V.14-I, J; Plate V.15-C, J*). All the alteration minerals, including quartz<sub>3</sub>, calcite and chlorite<sub>2</sub> were observed as inclusions in both pyrite crystals and aggregates. Relict crystals of ilmenite are also common in the inclusion rich domains (*Plate V.15-C-box1, H*). The aggregates observed within the calcite-chlorite patches are formed from very fine-grained pyrite crystals that show visible crystal boundaries oriented at 90° to one another. Within these aggregates, calcite and chlorite are present as infills between the pyrite crystals (*Plate V.15-D*). Interpretations regarding the afore-mentioned pyrite textures are provided in the interpretation section of this chapter.

In contrast to the previously described deposits, titanite was also observed in the Argyle samples (*Table V.9*). The titanite occurs either as small inclusions in the inclusion-rich domains of pyrite aggregates or in association with the calcite-chlorite veins and patches brecciating and overgrowing the rims of coarse-grained pyrite crystals and aggregates (*Plate V.15-C-box2, E-box1*). However, it was also seen intergrown or partially overgrown with/by the fine-grained pyrite crystals from the calcite-chlorite patches (*Plate V.15-F*). Large crystals of titanite that overgrow

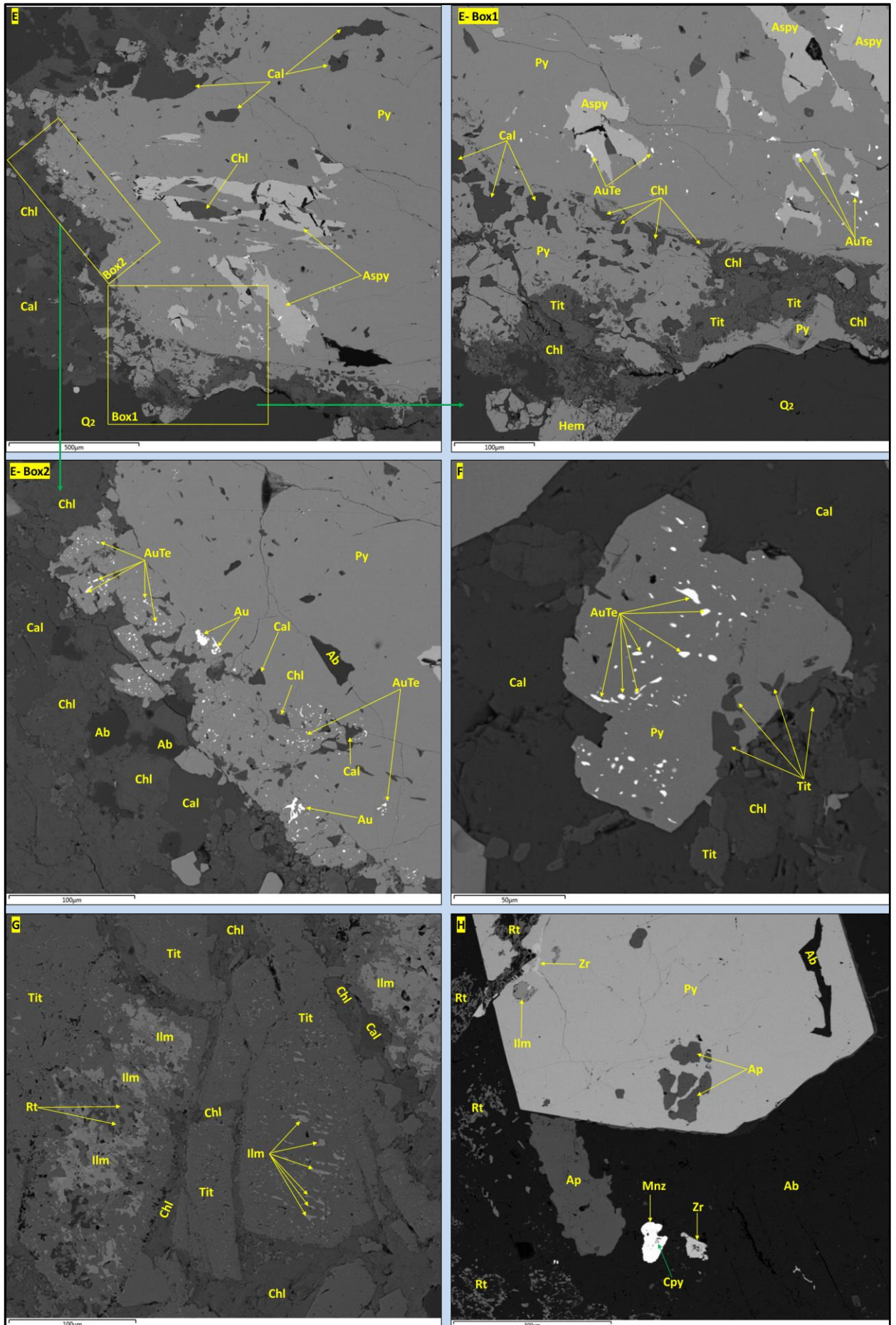
ilmenite and rutile crystals, and which are crosscut by chlorite were also observed (*Plate V.15–G*).

Hematite was observed as staining on pyrite rims and as pseudomorphs on the fine-grained pyrite crystals when is spatially associated with the chlorite-calcite patches (*Plate V.15–E-box1*). It was also observed as small inclusions in pyrite together with the rest of the alteration minerals.

The apatite, monazite, xenotime, and the zircon observed in the Argyle samples show the similar characteristics (size, shape, internal texture, crosscutting relationship with other minerals) as the phosphates and the zircon from the Stog' er Tight deposit (see above). The only exceptions are that both the monazite and the xenotime reach large sizes (up to 200  $\mu\text{m}$ ), and that chalcopyrite inclusions were also observed in monazite grains. Summarised descriptions and representative images can be found in *Table V.9* and (*Plate V.14–H, J; V.1 –C, H, I*).



**Plate V.15 (A-D above)** – Representative images of different alteration and ore minerals from the Argyle deposit: **A** – Microscope image (reflected light) showing an euhedral pyrite crystal with an inclusion-rich core and inclusion-free rims, sample AG<sub>2</sub>; **B** – BSE image showing inclusion-free pyrite crystals within sericitized ground mass, **note** the free chalcopyrite grain and the small galena bleb, sample AG<sub>1</sub>; **C** – BSE image showing a coarse-grained, brecciated (by Q<sub>3</sub>-chl veins) pyrite aggregate with inclusion-rich and inclusion-free domains, **note** the Au-Rt association and the Cpy, Aspy, Ilm, Tit and Ap inclusions from **box1**, and the very fine-grained Au, Aspy, undifferentiated gold, gold-silver, bismuth, and lead tellurides and the Tit, Xtm and Ap inclusions from **box2**, sample AG<sub>3</sub>; **D** – BSE image showing a pyrite aggregate composed of very fine-grained pyrite crystals that show visible crystal boundaries oriented at 90° to one another, **note** the calcite and chlorite infills within the aggregate between the pyrite crystals and the abundance of undifferentiated gold tellurides and the few aspy inclusions within the pyrite, sample MPAG<sub>1</sub>. (**E-H page below**) **E** – BSE image showing a large pyrite aggregate with coarse-grained, anhedral arsenopyrite within it, **note** the lower rim which is brecciated and overgrown by chlorite-calcite-titanite, the hematite staining on Py rim and the spatial association between Aspy and the undifferentiated gold tellurides (**box1**), and the coarse-grained gold in the pyrite rim together with fine-grained undifferentiated gold tellurides (**box2**), sample MPAG<sub>1</sub>; **F** – BSE image showing titanite intergrown / partially overgrown by fine-grained, gold telluride rich Py crystal within a calcite groundmass, sample MPAG<sub>1</sub>; **G** – BSE image showing coarse-grained titanite crystals overgrowing ilmenite and rutile, **note** the titanite is crosscut by chlorite veinlets, sample MPAG<sub>1</sub>; **H** – BSE image showing apatite crystals overgrown by pyrite and coarse-grained monazite with chalcopyrite inclusions, zircon both free and as inclusion in pyrite and ilmenite inclusion in pyrite, sample AG<sub>4</sub>; **I** – BSE image showing a large apatite crystal brecciated by sericite, **note** the free xenotime crystals within sericite, sample AG<sub>1</sub>; **Continuation of legend (I-O) at the end of the plate.**



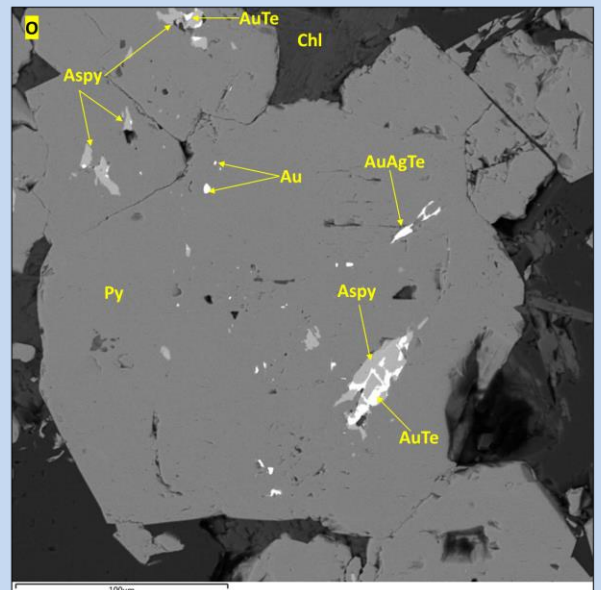
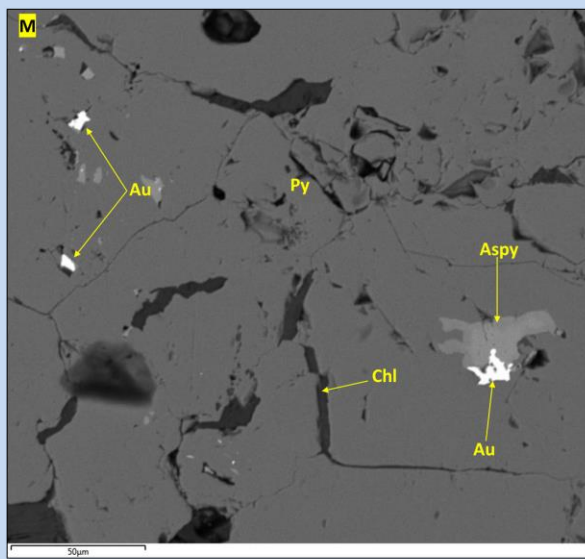
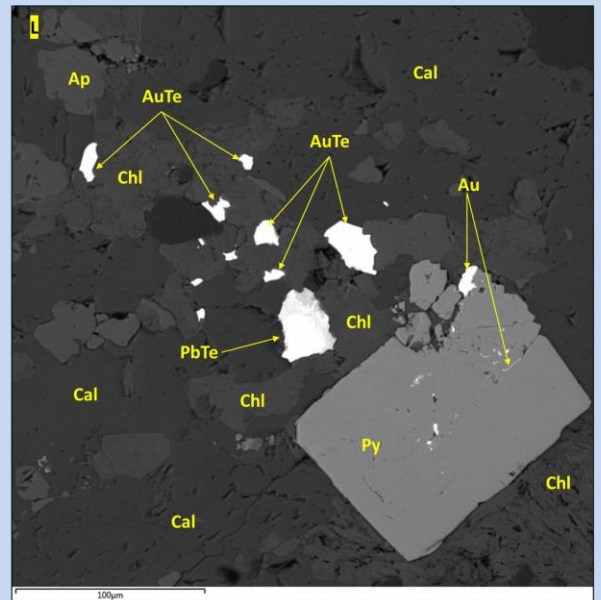
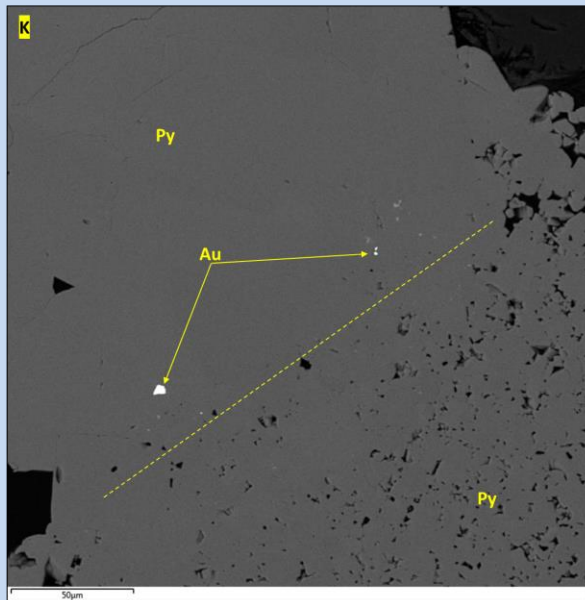
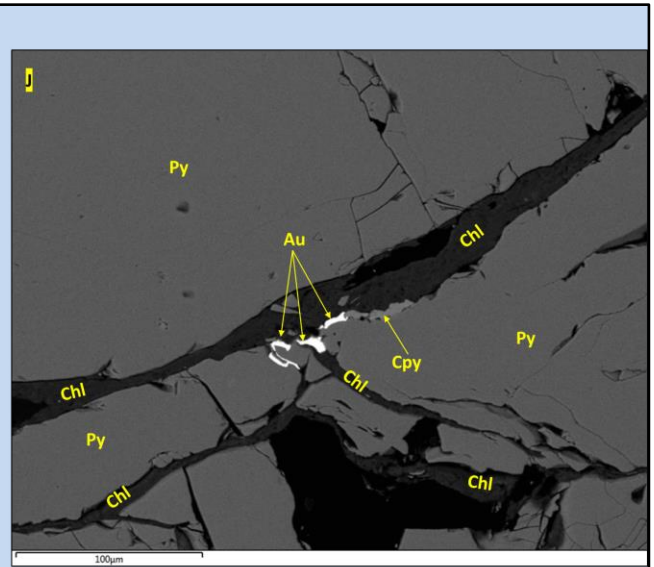
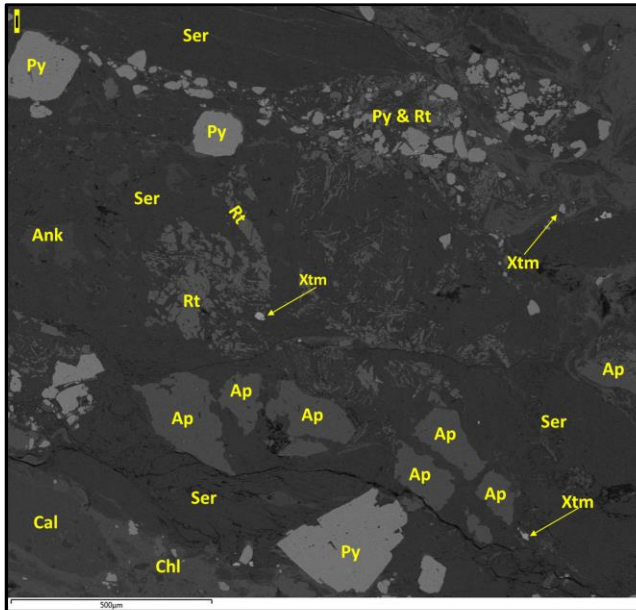




**Plate V.15 (continuation) – I** – BSE image showing a large apatite crystal brecciated by sericite, **note** the free xenotime crystals within sericite, sample AG1. **J** – BSE image showing irregular gold grains and wires free along chlorite veinlets that brecciate a pyrite aggregate, **note** the presence of chalcopyrite along the Chl veinlet. **K** - BSE image showing gold grains within the inclusion free domain of a pyrite aggregate, the yellow dashed line marks the boundary between inclusion-free and inclusion-rich domains, sample AG3. **L** - BSE image showing coarse-grained undifferentiated gold and lead tellurides in calcite-chlorite mass and gold within and on the border of a pyrite crystal, sample MPAG1. **M, O** – BSE images showing arsenopyrite crystals intergrown with gold (**M**) and with gold telluride (**O**), note the presence of the gold-silver telluride from **O**, sample MPAG1.

### V.1.3.3. Mineralisation

In contrast to the previously described deposits, the ore mineralogy at Argyle is more diverse being composed of native gold, undifferentiated gold tellurides, chalcopyrite, arsenopyrite and traces of undifferentiated gold-silver, bismuth, lead and bismuth-lead tellurides, sphalerite, galena and tenantite. Summarised descriptions for all these minerals are provided in *Table V.11*, whereas a more detailed characterisation for gold, gold tellurides, chalcopyrite and arsenopyrite can be found below.

The gold observed in the Argyle samples shows similar morphologies and distribution as the gold from the Stog'er Tight deposit: it occurs as irregular to rounded inclusions fully enclosed in the pyrite crystals or free, as wires, rounded blebs, and irregular crystals along mono or poly mineral chlorite-calcite-quartz<sub>3</sub> veinlets that brecciate the pyrite crystals and aggregates (*Plate V.15–C, E, J, K*); the gold occurs in both the inclusion rich domains and in the neat, recrystallised parts of the pyrite crystals where is usually coarser than in the inclusion-rich areas (*Plate V.15–E, K*); the gold is more abundant and coarser within the large and intensively brecciated pyrite patches and in the telluride rich areas (see below) (*Plate V.15–E, K, L, M*); rarely, the gold was seen as sub-rounded to rounded grains, free in the quartz<sub>2</sub>-albite-ankerite-sericite alteration halo. The gold was also observed in a close spatial association with the rutile crystals and bands enclosed within pyrite crystals (*Plate V.14–H; Plate V.15–C-box1*).

Undifferentiated gold tellurides are abundant within the Argyle samples. These occur mostly as small, irregular to rounded inclusions within the fine-grained pyrite crystals and aggregates from the calcite-chlorite veins/patches or within the rims of large pyrite aggregates that are brecciated and overgrown by calcite-chlorite

veins (*Plate V.15–D, E, F*). Free, coarse-grained gold tellurides were also seen in the calcite-chlorite patches (*Plate V.15–L*). Undifferentiated gold-silver tellurides were also observed as small irregular to rounded inclusions within pyrite, but only in minor/trace amounts (*Plate V.15–C-box2, O*).

Chalcopyrite was observed mostly as small inclusions in pyrite in both the inclusion-rich and inclusion-free domains and along chlorite-calcite-quartz<sub>3</sub> veinlets together with gold (*Plate V.15–C-box1, L*). Less common it also occurs free in the sericite-ankerite patches, and along/within chlorite veins and patches (*Plate V.15–B*).

In contrast to the previously described deposits, arsenopyrite was also identified in the Argyle samples. It occurs as small irregular to rounded inclusions in both the inclusion-rich/free domains of the pyrite crystals and aggregates, and as large irregular to anhedral inclusions in the coarse-grained pyrite aggregates (*Plate V.15–C, D, E*). Arsenopyrite intergrown with native gold and with gold tellurides was observed (*Plate V.15–M, O*).

*Table V.11. – Summary characteristics of the ore minerals from the Argyle deposit.*

<b>Mineral</b>	<b>Occurrence, Morphology</b>
Au	Irregular to rounded inclusions in py; free as wires and irregular to rounded grains along cal-chl-Q <sub>3</sub> veins that brecciate the py or at the interface of py crystals; free in the rutile bands, rarely in ankerite/albite/sericite; observed intergrown with aspy; variable sizes from 1 µm and up to 100 µm
Undifferentiated Au telluride	Mostly small (<1 µm up to 100 µm) irregular to rounded inclusions within the fine-grained pyrite crystals aggregates from the calcite-chlorite veins/patches or within the rims of large pyrite aggregates that are brecciated and overgrown by calcite-chlorite veins. Free, coarse grains were also seen in the calcite-chlorite patches
Cpy	Inclusions in the py crystals (1-2 µm up to a few tens of µm); free in the altered groundmass (alb-ser-ank-rt) or along chl-cal-Q <sub>3</sub> veinlets that brecciate the pyrite
Aspy	Small to coarse grained (<1 µm to a few hundred µm), sub-rounded to rounded, irregular to anhedral inclusions in both the inclusion-rich and inclusion-free domains of the pyrite crystals and aggregates; rarely, free in the calcite-chlorite patches and veins; observed intergrown with native gold and with gold tellurides
Undifferentiated Au-Ag, Pb, Bi & Pb-Bi telluride	Trace* amounts, in general small grains (<1 µm up to 20 µm) that occur as inclusion in pyrite, and rarely free; a coarse grained of Pb telluride of ~100 µm was seen
Gn	Trace* amounts, small grains (<10 µm) inclusions in pyrite and free in the altered ground mass
Sph	Trace* amounts, patches of (up to 150 µm in size) composed of fine-grained crystals within calcite
Tnt	Trace* amounts, small grains (<10 µm) inclusions in pyrite

\*trace = none, or very few grains / studied thin section

#### V.1.4. The Romeo & Juliet prospect

From the Romeo & Juliet prospect (RJ), only the Juliet zone was observed in the field because the exposure in the Connecting and Romeo zones is poor (*Figure V.4-A*). Thereby, this section provides a detailed geological characterisation for the Juliet zone only. Summarised descriptions related to the Connecting and Romeo zones are provided from existing literature in *Appendix I*. Other field observations presented in this chapter were gathered from outcrops exposed along the coastline, approximately 200 meters W from the RJ veins, and from outcrops located on the exploration road that links the Pine Cove mill and the RJ prospect (*Figure V.4-A*). Descriptions for the host rocks of RJ veins can be found in Duncan (1994), Meade et al. (1998) and Pitman et al. (2020), whereas summarised characteristics are provided in *Table A1.1* of this thesis.

##### V.1.4.1. Structural setting

In the Romeo & Juliet area the  $S_{2a}$  foliation dip steeply (mean  $55^\circ$ ) from WNW to NNW. A well-developed,  $L_2$  stretching mineral lineation that plunge steeply to N – NW is observable on the  $S_{2a}$  foliation plane (*Figure V.4-B*).

The entire area is affected by a dense set of  $D_{2b}$  shear zones that are subparallel to the  $S_{2a}$  foliation, but slightly steeper (*Figure V.4-A, B*). These shear zones are associated with a large-scale, WNW to NW dipping and NNE to NE striking fault that outcrop sporadically all the way from Pine Cove to Green Cove (*Figure V.1*). As presented in *chapter V*, this fault is interpreted as a long-lived  $D_{2b}$  shear zone reactivated during younger deformational events. The RJ veins are parallel to this fault zone, but dip in the opposite direction.  $D_{2b}$  shears that transect the mineralised veins and their associated alteration halos were observed (see below). The  $F_{2b}$  folds were not observed in the field, but microscopic-scale  $F_{2b}$  folds are present within the  $D_{2b}$  shears (*Plate IV.7-H*). Within, and in the proximity (a couple of meters) of the  $D_{2b}$  faults a composite  $S_{2a/2b}$  foliation is characteristic. A later fabric associated to the reactivation of the  $D_{2b}$  faults with a down-dip to oblique slip of the hanging wall to WNW-NW, overprint the  $S_{2a/2b}$  foliation (*Plate IV.7-G, H, I*). This fabric is defined by a chlorite that shows the same optical properties as the chlorite<sub>2</sub> from the Pine Cove and Stog'er Tight deposits and the chlorite from the Argyle deposit (see descriptions above).

The relationships between the D<sub>3</sub> and D<sub>4</sub> structures and the RJ veins are unclear because neither the F<sub>3</sub> nor the F<sub>4</sub> folds were observed around the veins. Both the NW striking and the south dipping, syn-to-post D<sub>4</sub> faults (*Table IV–xiii, xiv*) occur throughout the area, especially along the coastline. Fracture and joint sets associated to these structures are common and affect the main Juliet vein (see further descriptions). Joint sets related to the late, brittle E-W and N-S striking faults (*Table IV–xv*) were also observed in the entire area and usually crosscut all types of veins and any alteration halos.

#### ***V.1.4.2. Veins observed within and outside the Juliet zone***

The Juliet zone consists of two mineralised parts, termed in literature as the Juliet north and Juliet south (Meade et al., 1998; Pitman et al., 2020). These two mineralised areas are composed of veins with widths from a few centimetres up to two meters, and lengths of a few meters to tens of meters (*Figure V.4–A*) (Meade et al., 1998; Pitman et al., 2020).

In the norther part of the Juliet north zone, a WNW dipping D<sub>2b</sub> fault that juxtapose unaltered basalts against intensively altered rocks (sericitized and oxidised basalts) was observed (*Plate V.16–A*). Slicken-fibres from the contact zone suggest oblique hanging wall motion to SSE (*Plate V.16–B*). The relationships between this fault and the one that separates the Connecting zone from the Juliet zone are unclear because of poor exposure.

The contact between the Juliet north and Juliet south zones is defined by a fault that dips steeply (70°) to NNW. The fault is strongly overprinted by a dense set of syn-to-post D<sub>4</sub>, south dipping fractures (*Plate V.16–C*). Thereby, the contact is interpreted to pre-date the latter structures and based on its orientation and style is probably a D<sub>2b</sub> structure.

Three main vein sets termed here from VS<sub>1</sub> to VS<sub>3</sub>, according to their relative timing of formation (old to young), were observed in the investigated outcrops from the Juliet zone. The characteristics of these veins are presented in *Table V.12*, whereas representative images can be found in *Plate V.17*.

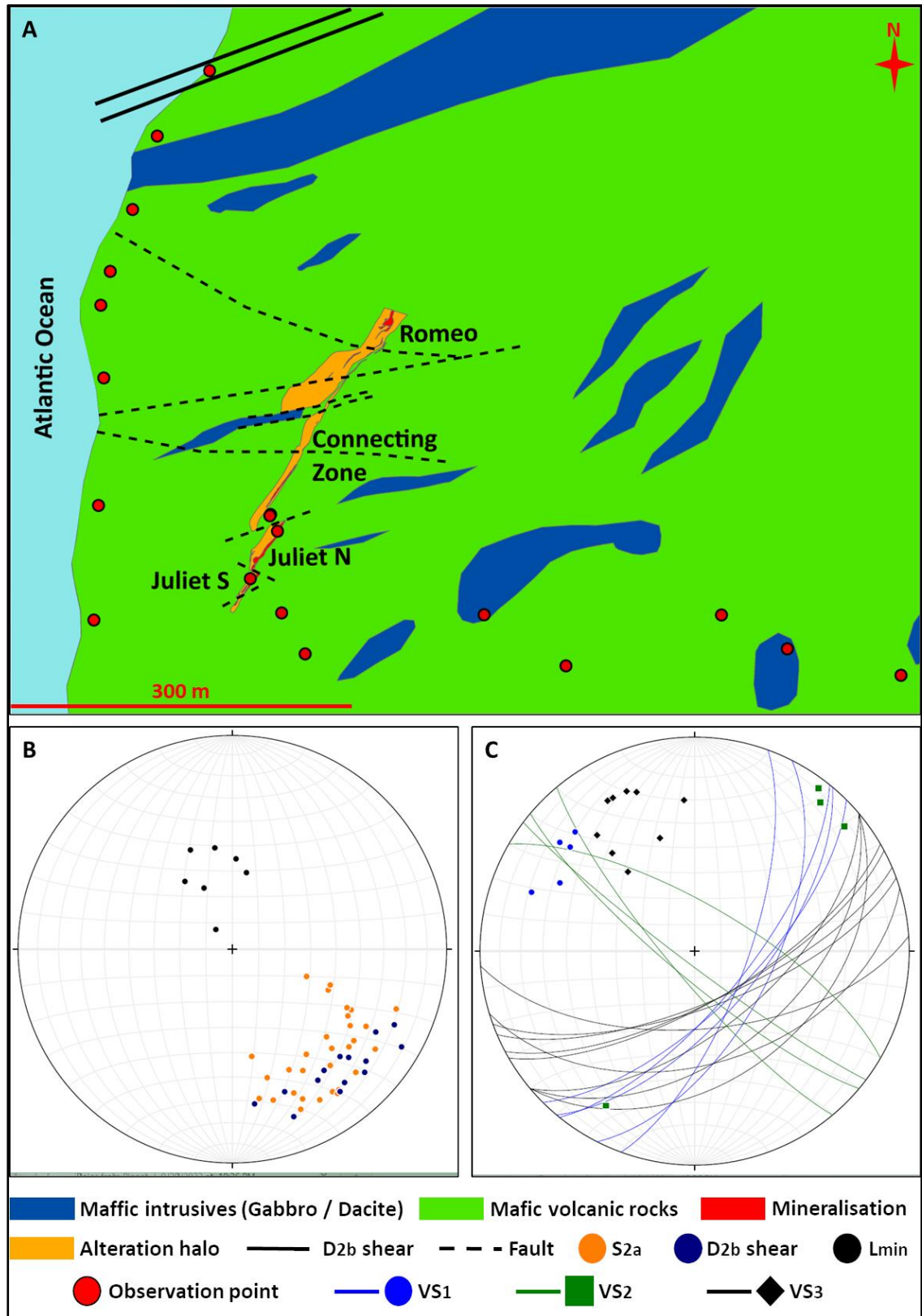


**Figure V.4:** *A* – Simplified geological map of the Romeo & Juliet prospect after Duncan (1994) and after the unpublished geological map of Anaconda Mining (2018); *B* - Southern-hemisphere, equal-area, stereographic projections of the poles to the foliation planes and to the D<sub>2b</sub> shear zones, and of the stretching mineral lineation; *C* - The stereographic projections of the poles to the main mineralised vein sets.



**Plate V.16** – Representative images for the main structures that affect the Juliet South zone: **A** – Contact (traced by the yellow dashed line) between unaltered basalts and intensively altered basalts in the northern part of the Juliet North zone, **note** the contact corresponds to a  $D_{2b}$  fault that accommodates a hanging-wall (top) motion to SSE (**B**); **C** - Contact (traced by the yellow dashed line) between intensively altered basalts and unaltered basalts in the southern part of the Juliet North zone, **note** the syn-to-post  $D_4$  south dipping faults (black dashed lines) that overprint the contact (probably a  $D_{2b}$  structure).

**Table V.12.** – Descriptions of vein sets identified within and outside the Juliet zone  
Terminologies regarding vein and crystal morphologies are used according to Bons (2000) and Bons et al. (2012)

Vein set		Characteristics	Alteration / Mineralisation	Crosscutting relationships	Structural constrains
<b>Juliet zone</b>	<b>VS<sub>1</sub></b> <i>Plate V.17</i> – A, B, C	Main vein: strike from NE to NNE and dip steeply (~65°) to SE/SSE; has a massive to laminated texture and is composed of milky-white quartz; the lower part of the vein is thicker (~ 1.5 m in width), whereas the upper part is narrower (40-50 cm in width)	Free Au in the veins and weathered auriferous Py within the vein and in the alteration halo (ser-FeOx ± cb)	Crosscut by VS <sub>2</sub> ; no direct crosscutting relationship was observed with VS <sub>3</sub>	Crosscuts S <sub>2a</sub> foliation; truncated by D <sub>2b</sub> faults; crosscut by syn-to-post D <sub>4</sub> faults/fractures
	<b>VS<sub>2</sub></b> <i>Plate V.17</i> – D, E	NW striking, steeply dipping to SW and NE, narrow quartz veins (5-10 cm in width) with massive, laminated, and sheared morphologies	Associated with sericite-FeOx alteration in the Juliet zone; barren and devoid of alteration further away from Juliet zone	Crosscuts VS <sub>1</sub> ; outside the Juliet zone shows mutual crosscutting relationships with VS <sub>3</sub>	Crosscuts the S <sub>2a</sub> foliation; occurs along or subparallel to the NW striking syn-to-post D <sub>4</sub> faults/fractures
	<b>VS<sub>3</sub></b> <i>Plate V.17</i> – E, F, G	Steeply dipping to S-SE quartz veins; widths of 5 to 20 cm; both opened and closed veins with syntaxial and/or stretched textures and coarse – grained, blocky to elongate blocky quartz crystals; host dyke like material composed of sugary, coarse-grained quartz-feldspar-amphibole	Associated with sericite-FeOx alteration in the Juliet zone; barren and devoid of alteration outside the mineralised area	No direct crosscutting relationship was observed with VS <sub>1</sub> ; outside the Juliet zone shows mutual crosscutting relationships with VS <sub>2</sub>	Crosscuts the S <sub>2a</sub> foliation; occurs along or subparallel to the south dipping, syn-to-post D <sub>4</sub> faults/fractures





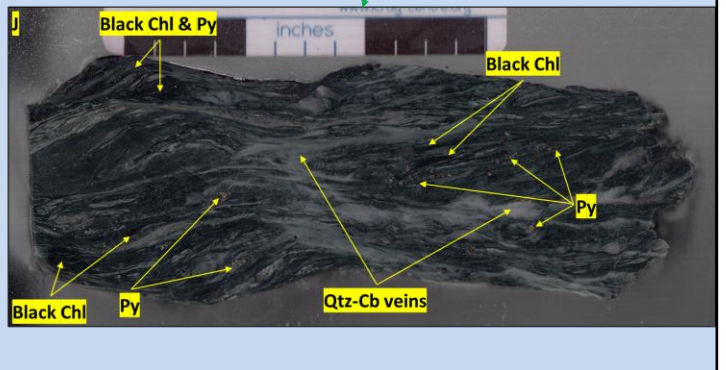
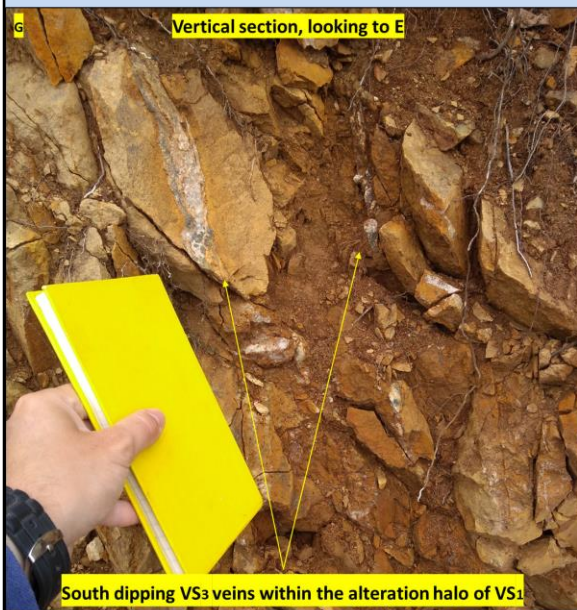


**Plate V.17** – Representative images for the main vein sets identified in the Romeo & Juliet area: **A** – Partial exposure of the southern part of the Juliet North vein, **note** the two fracture systems that affect the vein, yellow square **D** shows the location of image **D**; **B** – Northern part of the Juliet North vein, **note** the thickness difference between the northern and southern parts (images **A**, **C**) of the vein; **C** – Closely spaced fracture cleavage that dips steeply to S affecting the southern part of the Juliet North vein, **note** the south dipping faults (green dashed lines) that overprint the contact (red dashed line) between altered (orange-brown) and unaltered zones; **D** – NW striking and steeply dipping vein pertaining to VS<sub>2</sub> within the Juliet North vein (VS<sub>1</sub>); **E** – Veins from both VS<sub>2</sub> and VS<sub>3</sub> observed a few hundred of meters away from the Juliet zone, **note** the lack of alteration around the veins and the vein textures (VS<sub>2</sub> - massive and sheared, VS<sub>3</sub> – open with coarse-grained, elongate to fibrous quartz crystals); **F** – Dense network of south dipping veins (VS<sub>3</sub>) within the Juliet South zone; **G** - South dipping veins (VS<sub>3</sub>) within the alteration halo of the Juliet North vein; **H** – Loose fragment from a VS<sub>3</sub> vein composed of sugary, coarse-grained quartz (Qtz), amphibole (Amph) and feldspar (Fld); **I**, **J** – Sheared veins within a NNE to NE oriented D<sub>2b</sub> fault (**I**) associated with an intense chlorite-carbonate-pyrite alteration (**J**), **note** the distinct black chlorite.

In the Juliet north zone, a main vein, termed as VS<sub>1</sub>, that strike from NNE to NE and which dips steeply (~ 65°) to ESE-SE was observed (**Figure V.4–B**; **Plate V.17–A, B, C**; **Table V.12**). The vein crosscuts the S<sub>2a</sub> foliation, has a massive texture and is composed of milky-white quartz. The lower part of the vein is thicker (~ 1.5 m in width, **Plate V.17–C**), whereas the upper part is narrower (40-50 cm in width, **Plate V.17–B**). On the thicker part of the vein, steps and slicken-fibres indicate multiple movement directions of the hanging wall: i) oblique, motion combined with either a reverse component to SW or a normal component to NE; and ii) horizontal movements to both NE and to SW. The steps and slicken-lines related to the horizontal motions overprint the ones that indicate oblique movement. No clear overprinting order have been observed between the kinematic indicators related to the two horizontal motions.

The southern-most part of the VS<sub>1</sub> is affected by a strong fracture cleavage that dips steeply to south (**Plate V.17–C**). This fracture cleavage is interpreted to be related to the syn-to-post D<sub>4</sub> south dipping faults that overprint the contact between the two Juliet zones (**Plate V.16–C**; **Plate V.17–C**). Further to the north, VS<sub>1</sub> is crosscut by two other fracture sets (**Plate V.17–A**): i) a steeply dipping and NW striking set, related to the syn-to-post D<sub>4</sub> faults (**Table IV–xiv**); and ii) a fracture set that strike to NNE and dip moderately to WNW. The second fracture set crosscuts the first one. It was observed that both within the VS<sub>1</sub> and further away (tens to hundred meters) from the Juliet zone, the NW striking fractures host narrow (a few centimetres in width) quartz veins termed here as VS<sub>2</sub> (**Table V.12**, **Plate V.17–D, E**).

In the Juliet South zone, a dense network of subparallel SE to S dipping quartz veins, referred to as VS<sub>3</sub>, were observed (*Table V.12; Plate V.17–F*). The VS<sub>3</sub> crosscut the S<sub>2a</sub> foliation and occur along or subparallel to the south dipping, syn-to-post D<sub>4</sub> faults and fractures. This vein set was also observed in the alteration halo of the VS<sub>1</sub> but no direct crosscutting relationship between VS<sub>1</sub> and VS<sub>3</sub> was observed (*Plate V.17–G*). Most veins pertaining to VS<sub>3</sub> are composed only of quartz. However, within loose vein fragments it was observed that sugary and coarse-grained quartz, amphibole, and feldspar also occur (*Plate V.17–H*). When this is the case, the veins look like thin granitic/granodioritic dykes. Within the R&J area there are no known felsic/intermediate intrusive bodies, but Meade et al. (1998) did report a granite boulder in the Romeo zone. Also ~1 km NNE from the RJ, in the Corkscrew area (*Figure V.1*), there is a granodioritic body that host mineralised quartz veins (Pitman et al., 2020).

It was observed that VS<sub>2</sub> and VS<sub>3</sub> show mutual crosscutting relationships. Also, outside the Juliet zone (radius of tens to hundreds of meters), these vein sets are barren and devoid of any alteration selvages (*Plate V.17–E*).

Except for the vein sets presented above, shear type quartz-carbonate veins were observed within a D<sub>2b</sub> shear zone exposed approximately 200 meters NW from the RJ veins (*Figure V.4–A; Plate V.17–I*). This shear zone is considered a segment of the large-scale, WNW to NW dipping and NNE to NE striking D<sub>2b</sub> fault that outcrop sporadically all the way from Pine Cove to Green Cove (*Figure V.1*). Within and around the shear zone there is an intense chlorite-carbonite-pyrite alteration halo (*Plate V.17–J*). An oriented sample was collected from this shear zone (*Appendix 2*). No gold was observed in the sample, but abundant chalcopyrite is present. Microstructural investigations showed that a chlorite with the same optical properties as the chlorite<sub>2</sub>/chlorite related to gold mineralisation in the Pine Cove, Stog'er Tight and Argyle deposits (black in hand specimen; intense pleochroic in plane polarised light and with blueish grey to intense blue and purple anomalous birefringence colours), defines a foliation fabric that overprints the S<sub>2a-2b</sub> foliation and is related to the reactivation of the D<sub>2b</sub> fault with a down-dip to oblique motion of the hanging wall to WNW-NW (*Plate V.17–J; Plate IV.7–F, G, H, I*).

### ***V.1.4.3. Alteration***

The gold bearing quartz veins from the Romeo & Juliet area are hosted by dark grey-green coloured, massive, fine grained, locally vesicular pillow basalts. Examples of the least altered basalts observed in the field are presented in ***Plate V.18 – F, G***. There is not much information in literature regarding the alteration halos of the Romeo and Juliet veins. A summary of what exists is provided in ***Appendix I***. For this study, the samples used for the analysis of the ore and alteration minerals from the RJ prospect come from core sections that intersect medium to high gold grade intervals of the Juliet South zone (*see Appendix 2 for descriptions*). Thereby, a detailed characterisation based on classic petrographic and SEM-CL techniques is provided only for the veins occurring in the afore-mentioned zone and of their proximal alteration halo. Some descriptions are also provided for the outer alteration halo based on macroscopical observations of the examined outcrops and core sections.

It is interpreted that samples RJ<sub>2</sub> & RJ<sub>3</sub> (***Appendix 2***) come from veins pertaining to VS<sub>1</sub> based on their texture, thickness, composition, and depth interval, whereas sample RJ<sub>1</sub> (*see Appendix 2*) has an unclear relationship with the three vein sets observed in the field. Samples RJ<sub>4</sub> and RJ<sub>5</sub> (***Appendix 2***) represent mineralised and altered wall rock material associated to VS<sub>1</sub> (RJ<sub>4</sub>) and to the vein material from sample RJ<sub>3</sub>.

The studied mineralised veins have massive and laminated textures, are composed of fine to coarse grained quartz and low amounts of carbonates and are crosscut by dark-grey, sericite-pyrite stringers (***Appendix 2***). Fragments of altered wall rock material are common within the veins. The veins are surrounded by a strong proximal alteration halo that extends for a few meters (maximum 10m), composed of sericite, disseminated subhedral to euhedral auriferous pyrite, hematite, rutile, chlorite, carbonates and minor titanite and albite. Apatite, monazite, and xenotime are also present but to a lesser extent compared to the previously described deposits. Descriptions of all these alteration minerals and of the vein material are provided in ***Table V.13 & Table V.14***.

Macroscopically, the proximal alteration halo is defined by very fine-grained rocks with an intense, orange-brown colour (***Plate V.17– F, G; V.18 - A***). Streaked domains characterised by orange-brown, grey-cream, and black hues were also seen where black chlorite veins occur (***Plate V.18– B, C***). The pre-existent volcanic

textures have been obliterated and the mineral assemblages related to the initial composition of the host lithologies and to the metamorphism were fully replaced by the alteration minerals.

A well-developed outer alteration halo (intermediate to distal), that extends for ~30-40 meters, composed of epidote-chlorite-carbonate  $\pm$  FeOx-pyrite was observed. The rocks have a yellowish green to green hues and are either pervasively altered or brecciated by epidote  $\pm$  quartz-carbonate veins (*Plate V.18– D, E*). Low amounts of fine to coarse-grained disseminated pyrite is present around the veins. Iron oxide staining is common on most veins and fracture surfaces.



*Plate V.18 (above and next page)* – Representative images for the proximal and the outer alteration halos observed in the Juliet area: **A** – Intense, orange-brown alteration halo composed of sericite, iron oxides (FeOx), and to a lesser degree carbonates, drill hole RJ-00-06; **B** - Intense, orange-brown alteration halo composed of Ser-FeOx  $\pm$  Cb, crosscut by chlorite (black) veinlets; **C** – Grey-cream alteration composed of Ser-Cb crosscut by Qtz-Chl and Chl (black) veins; **D, E** – Outer alteration halo characterized by epidote  $\pm$  quartz-carbonate veins associated with yellowish green (epidote-chlorite) pervasively altered basalts; **F, G** – Hand specimens of least altered basalts from the Juliet South zone - massive, fine grained, weakly silicified basalt (**F**) and fine grained, locally variolitic, weakly epidote altered basalt (**G**); **C, B, D, E** – drill hole RJ-00-08.

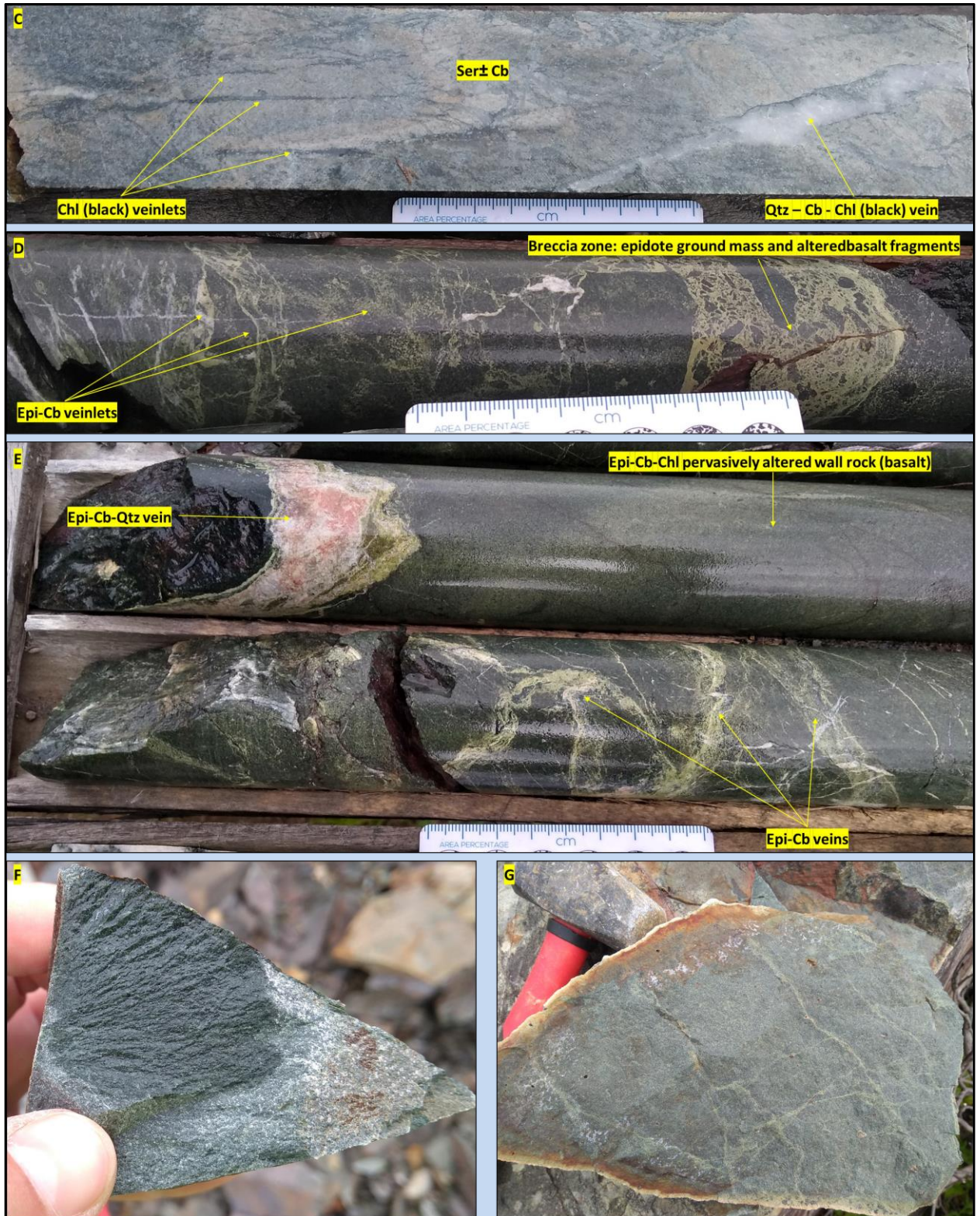


**Table V.13**– Summary characteristics of the alteration minerals identified in the proximal alteration halo associated to the veins from the Juliet South zone of the Romeo & Juliet prospect.

<b>Mineral</b>	<b>Occurrence</b>	<b>Texture</b>	<b>Spatial association with other alteration minerals</b>	<b>Overprinting relationships</b>
<b>Qtz</b>	As vein material and in the altered wall rock in association with sericite	Multiple generations (Q <sub>1</sub> , Q <sub>2</sub> , Q <sub>3</sub> ), see <i>Table V.14</i>	See <i>Table V.14</i>	See <i>Table V.14</i>
<b>Ser</b>	Main alteration mineral in the altered wall rock and as stringers within the quartz veins; at least two generations (Ser <sub>1</sub> & Ser <sub>2</sub> )	Ser <sub>1</sub> fine grained and pervasive; Ser <sub>2</sub> is coarser than Ser <sub>1</sub> and occurs as stringers and patches	Ser <sub>1</sub> : Q <sub>2</sub> -ank-rt-py Ser <sub>2</sub> : Q <sub>3</sub> -Chl-Cal	Ser <sub>1</sub> replaces ab; Ser <sub>2</sub> crosscut Q <sub>1</sub> , Q <sub>2</sub> and Ser <sub>1</sub> and show mutual crosscutting relationships with Chl and Cal
<b>Py</b>	Within the altered wall rock, in the sericite stringers that crosscut the qtz veins and less often within the qtz veins	Fine and coarse grained anhedral to euhedral crystals; crystals with inclusion rich cores and inclusion free rims; clean, inclusion-poor crystals and crystals with both inclusion rich/poor domains	With all the other alteration minerals	Overgrows Q <sub>1</sub> ; brecciated by Chl and/or Cal veins but further annealed and recrystallised; all the other alteration minerals were observed as inclusions in it
<b>Hem</b>	Along the sericite stringers that crosscut the qtz veins and in the alteration halo	Very thin wires within the sericite stringers; as partial or full replacement of pyrite (hematite pseudomorphs on pyrite are common); as veinlets that brecciate both pyrite and chalcopryrite; inclusions in Py	Ser <sub>2</sub> -Chl	Replaces pyrite crystals
<b>Rt</b>	In the quartz veins and in their alteration halos	Patches of fine-grained irregular to acicular crystals; coarse-grained, anhedral to euhedral (bladed/prismatic) crystals	All the other alteration minerals	The coarse grained crystals are crosscut by Q <sub>3</sub> and/or Chl and/or Cal veins, but the fine grained crystals occur in association with Chl crosscutting the rest of the alteration minerals



<b>Chl</b>	Within the alteration halo as veins and patches	Fine to coarse grained in patches	Q <sub>3</sub> -Cal-Ser <sub>2</sub> -Rt-Py	Shows mutual crosscutting relationships with Ser <sub>2</sub> ; occurs along the same veins with Cal, but it is also crosscut and replaced by Cal
<b>Epi</b>	Occurs as a relict phase in the altered wall rock	Consumed by calcite and chlorite	N/A	Overprinted by the rest of the alteration minerals
<b>Cal</b>	As veins and patches	Fine to coarse grained	Chl-Ser <sub>2</sub>	Shows mutual crosscutting relationships with Ser <sub>2</sub> ; see above for Chl
<b>Ank</b>	Both within the altered wall rock and in the veins	Minor amounts along the Cal veinlets, relict fragments in the intense sericitized zones and inclusions in Py	Q <sub>2</sub> -Ser <sub>1</sub> -rt-py	Replaced and brecciated by Ser <sub>2</sub> and by cal-chl veins
<b>Sd</b>	Along the calcite veinlets	Minor amounts along the Cal veinlets	Cal	N/A
<b>Ap</b>	Within the altered wall rock	Sub-rounded to rounded, anhedral to euhedral, fine-grained to coarse grained (< 1 mm) crystals	Q <sub>2</sub> -ser <sub>1</sub> -ank-rt-py	Crosscut by Ser <sub>2</sub> , Cal and Chl; locally, overgrows Cal and Chl
<b>Mnz</b>	Scarce, disseminated within the altered wall rock and rarely along the Cal-Chl veins	Fine grained ( $\leq 20 \mu\text{m}$ ), irregular to rounded shapes	All the other alteration minerals	Brecciated by Cal-Chl veins but also hosted by them
<b>Xtm</b>	Disseminated within the altered wall rock and rarely along the Cal-Chl veins	Fine grained ( $\leq 40 \mu\text{m}$ ), irregular to rounded shapes	All the other alteration minerals	Brecciated by Cal-Chl veins but also hosted by them

**Table V.14.** – Summary CL characteristics of the quartz generations observed in samples from the Juliet South zone of the Romeo & Juliet prospect. The texture terminologies are used according to Rusk et al. (2004) and Rusk (2012).

Quartz (Q) generation	Optical properties	CL colour and intensity	CL texture	Crosscutting relationships	Association with other alteration minerals	Related vein set
Q <sub>1</sub>	Undistinguishable from Q <sub>2</sub>	Blue/yellow (medium to high CL intensity)	Occurs as relict fragments of Q crystals that are either yellow or blue or which show patchy zoning defined by blue and yellow areas and euhedral growth zones with alternating yellow-blue CL response	Brecciated and enclosed in Q <sub>2</sub> ; brecciated by Q <sub>3</sub>	N/A	Observed in the VS <sub>1</sub> veins and in the laminated Qtz-Cal vein
Q <sub>2</sub>	Shows multiple sub-generations: coarse-grained crystals in thick veins and brecciated, fine-grained crystals or no visible crystals in thin veins; inclusion trails	All sub-generations are dark purple (low intensity)	Networks of interconnected veins with random orientations that brecciate Q <sub>1</sub> and as homogenous/massive zones with mottled aspect given by the presence of Q <sub>1</sub> fragments	It is crosscut by Q <sub>3</sub> ; Ser <sub>2</sub> ; Chl; Cal; Hem	Ser <sub>1</sub> -rt-py-ap-ank	Observed in the VS <sub>1</sub> veins, in the laminated Qtz-Cal vein, in the and in the altered wall rock
Q <sub>3</sub>	Undistinguishable from the thin Q <sub>2</sub> veinlets	Low to very low CL response displaying dark blue to black colours	Scarce, very thin veinlets	Crosscuts Q <sub>1</sub> , Q <sub>2</sub> and Rt	Ser <sub>2</sub> and Chl	Observed in the VS <sub>1</sub> veins and in the thin veins from the altered wall rock (sample RJ <sub>4</sub> )

The quartz is the main component in the studied veins, and it also occurs in silicified and sericitized altered wall rock (*Table V.14*). In the veins is distributed in domains composed of coarse-grained, blocky to elongate blocky crystals and areas of fine-grained, anhedral to subhedral crystals (*Plate V.19- A*). Regardless of their shape and size, all the quartz crystals show the common undulatory extinction and diffuse or lobate to serrated crystal borders (*Plate V.19- B, C*).

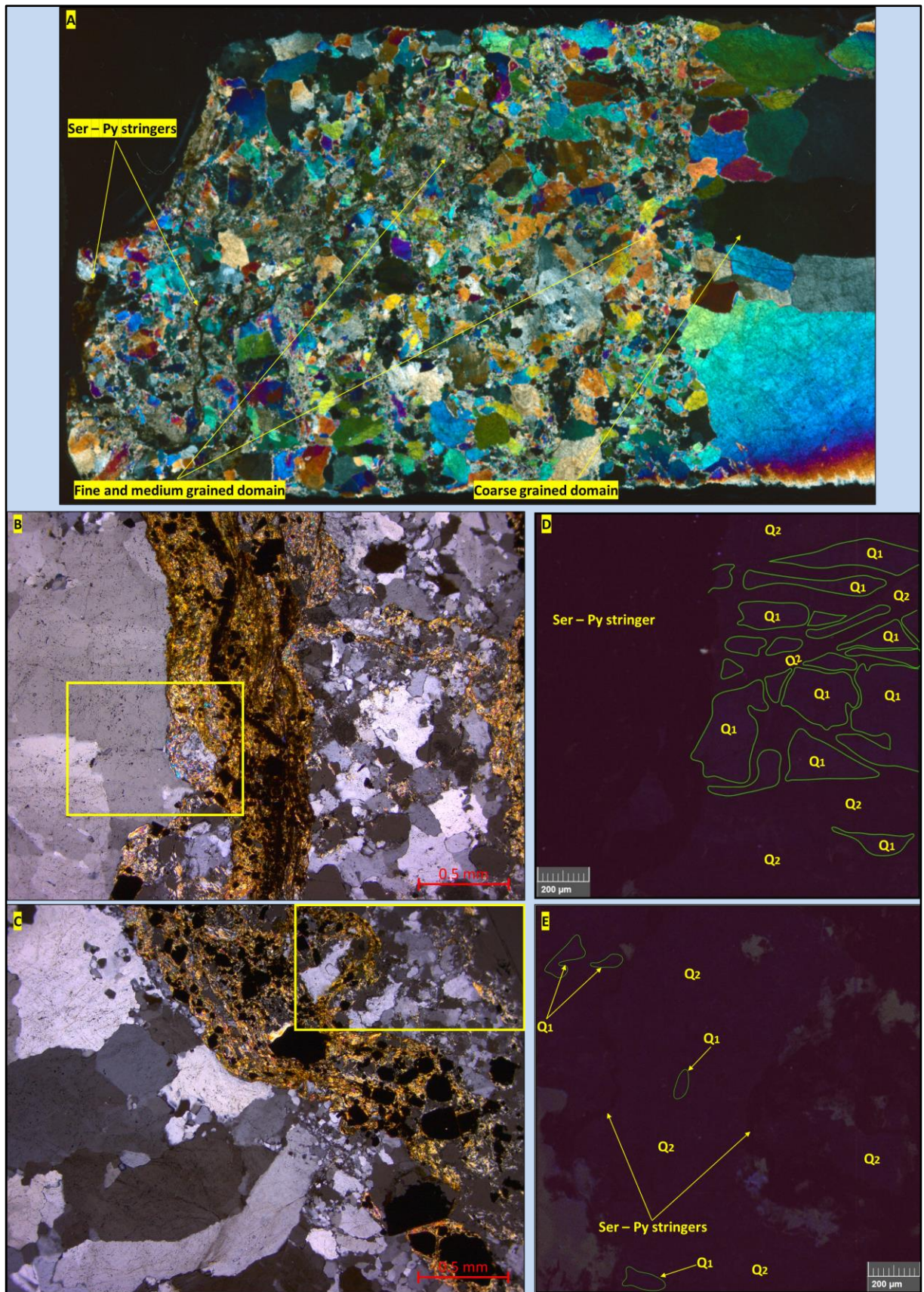
SEM-CL investigations showed that similarly to the previously described deposits, at least 3 main generations of quartz are present in the mineralised veins from the Juliet South zone (*Table V.14*). These are referred to as Q<sub>1</sub> to Q<sub>3</sub>, Q<sub>1</sub> being the earliest and Q<sub>3</sub> the latest, based on their crosscutting relationships and of their interpreted relative timing.

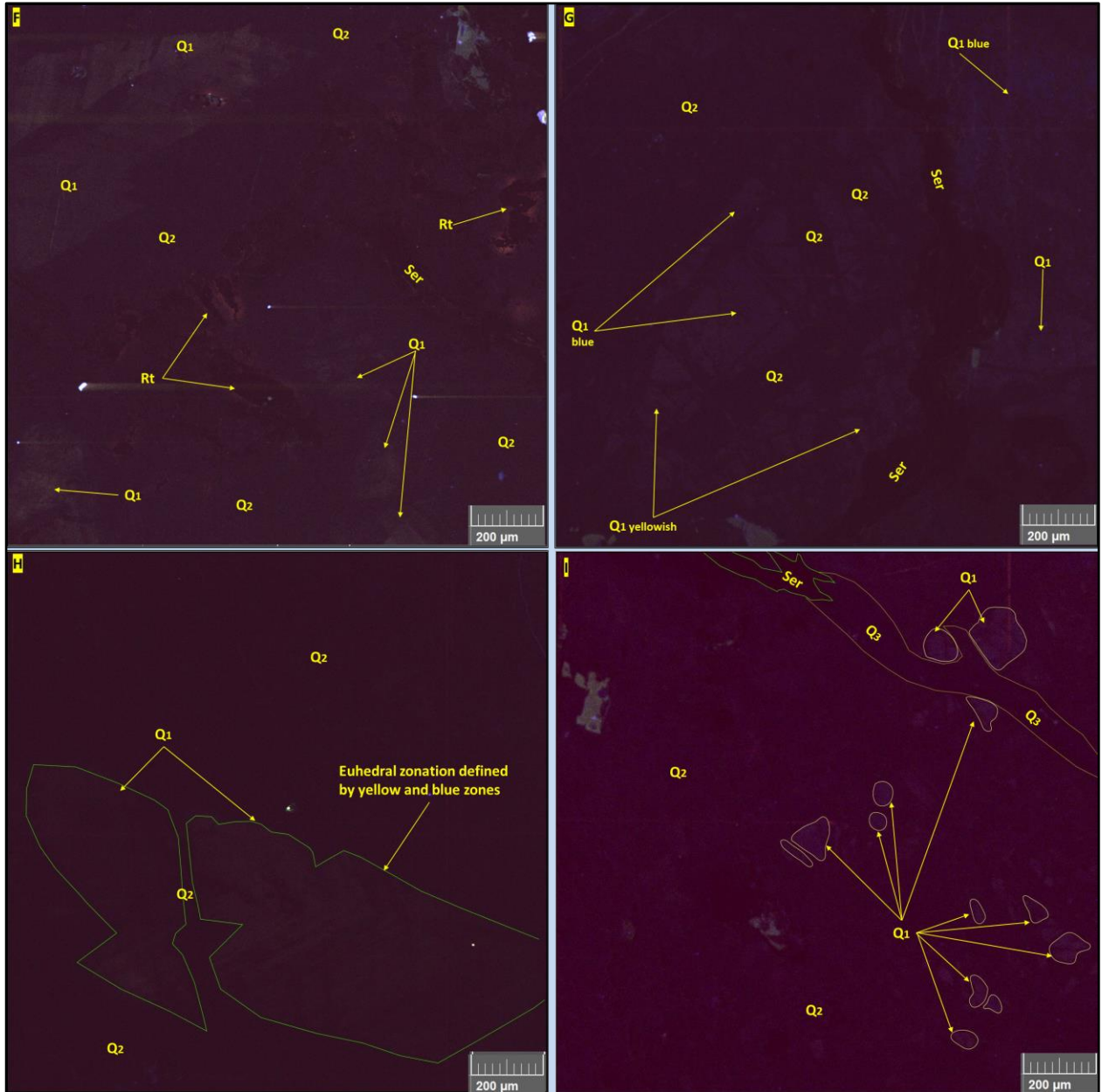
The 1<sup>st</sup> quartz generation (Q<sub>1</sub>) has a moderate to high CL response showing yellow and/or blue colours when imaged by coloured CL (*Table V.14; Plate V.19- D, F*). Q<sub>1</sub> crystals show blue and yellow patchy/irregular zonation or euhedral growth zones defined by alternating yellow and blue colours (*Plate V.19- G, H*). All the Q<sub>1</sub> crystals occur as brecciated fragments of quartz crystals fully enclosed in the second quartz (Q<sub>2</sub>) generation (*Plate V.19- D, F, G, H*). In contrast to the previously described deposits, Q<sub>1</sub> is significantly more abundant. In one sample comprises approximately half of the vein volume, whereas in other, approximately thirty percent. The rest of the volume, in both samples is composed mostly by Q<sub>2</sub> and small amounts of Q<sub>3</sub>. Both samples come from veins pertaining to VS<sub>1</sub>.

The second quartz generation (Q<sub>2</sub>) was observed as vein material in all the analysed samples and even as part of the alteration mineral assemblage together with sericite, pyrite, and rutile in the altered wall rock material (*Table V.14*). It has a low CL response and displays a dark purple colour. In samples where Q<sub>2</sub> comprises most of the vein volume it occurs as homogenous/massive masses (*Plate V.19- H*). In contrast, in samples where Q<sub>1</sub> is abundant, Q<sub>2</sub> was observed as networks of interconnected veins with random orientations that brecciate Q<sub>1</sub> and as restricted homogenous zones (*Plate V.19- D, G*). In transmitted light, Q<sub>1</sub> and Q<sub>2</sub> crystals are both coarse-grained, blocky to elongate blocky and fine-grained, anhedral to subhedral, and display undulatory extinction and diffuse or lobate to serrated crystal borders (*A, B, C*). Q<sub>2</sub> also corresponds to very thin veinlets with no visible crystals or as inclusion trails.

Q<sub>3</sub> from the Juliet samples shows a low to very low CL response displaying dark blue to black colours and occurs as very thin veinlets (< 1mm) that brecciate both Q<sub>1</sub> and Q<sub>2</sub> (*Table V.14; Plate V.19- I*). Overall, in the studied samples, very few Q<sub>3</sub> veinlets were observed. However, the difference in the CL response between Q<sub>2</sub> and Q<sub>3</sub> is very subtle and in areas where Q<sub>2</sub> occurs as veins, the separation between the two quartz generation can be equivocal. In contrast to the previous described deposits, in the studied samples from Juliet zone, no spatial association was observed between Q<sub>3</sub> and calcite. In very few places, Q<sub>3</sub> was seen in association with chlorite (see below) along veinlets that crosscut rutile (*Plate V.21- A*).

*Plate V.19 (next two pages)* – Representative images of different quartz generations related to the Juliet South mineralisation: *A* – Microscope image scan (cross polarized light) of section RJ2, **note** the different granulometry of the quartz crystals, from fine to coarse-grained, the quartz has anomalous colours because the section is thick (~100 µm); *B, C* – Microscope images (cross polarised light) showing oxidized sericite-pyrite stringers crosscutting quartz, **note** the undulatory extinction and the crystal borders (diffuse, lobated to serrated), yellow rectangles show the location of CL images *D & E* – Q<sub>1</sub> (bright blue, green contour lines) crosscut by Q<sub>2</sub> (dark purple) veins and everything crosscut by sericite stringer (*D*), Q<sub>2</sub> homogenous mass crosscut by sericite (*E*), **note** Q<sub>1</sub> and Q<sub>2</sub> cannot be differentiated in cross polarised light; *B, C, D, E* – section RJ3; *F* – CL image showing yellow Q<sub>1</sub> in Q<sub>2</sub> groundmass, section RJ4; *G* – CL image showing a Q<sub>1</sub> crystal with yellow and blue CL colours (sector zoning) strongly brecciated by Q<sub>2</sub> veins, **note** the Q<sub>2</sub> veins cannot be observed in the Q<sub>2</sub> mass that encloses Q<sub>1</sub>, both Q<sub>1</sub> and Q<sub>2</sub> are crosscut by sericite stringer, section RJ3; *H* – CL image showing a Q<sub>1</sub> crystal with euhedral growth zones defined by alternating yellow and dark blue colours enclosed in Q<sub>2</sub> homogenous mass, section RJ5; *I* – CL image showing Q<sub>1</sub> and Q<sub>2</sub> crosscut by Q<sub>3</sub> vein (dark blue to black, yellow contour), **note** the sericite along the same vein (green contour) with Q<sub>3</sub> and the very subtle difference between Q<sub>2</sub> and Q<sub>3</sub>. **Note**, for all the CL images the contrast was increased to better highlight the different quartz generations.





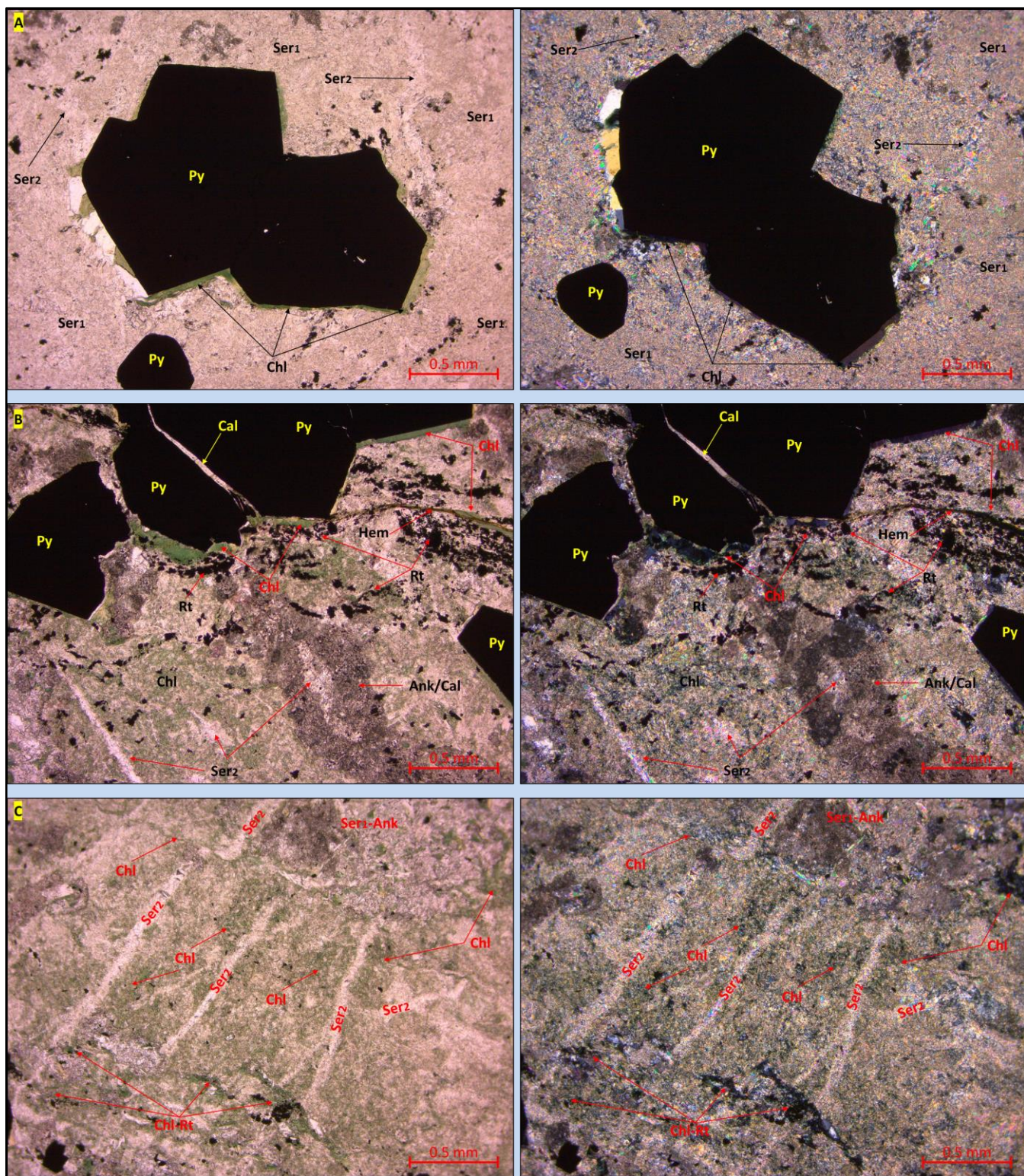
Sericite is the most abundant alteration mineral observed in the Juliet samples (*Table V.13*). In the altered wall rock, two types of sericites with different morphologies were observed: i) a pervasive, very fine-grained phase termed **Ser<sub>1</sub>** (*Plate V.20– A*); and ii) a coarser phase that occurs as veins and patches named **Ser<sub>2</sub>** (*Plate V.20– A, B, C*). The second phase crosscuts and overprints the first one (*Plate V.20– A, C*). The main mica that composes both sericite phases is phengite, but Ser<sub>2</sub> has ~ 2-3% more Al compared to Ser<sub>1</sub>. Relict albite crystals were seen within the sericitized areas. Oxidised sericite (coarse grained) stringers within quartz veins are common and crosscut both Q<sub>1</sub> and Q<sub>2</sub> (*Table V.13, Plate V.19 – B, C, D, E, G*). Q<sub>3</sub> and sericite were observed together only in one place, along the same vein but in different sections of the vein (*Plate V.19- I*). It is inferred that the sericite that composes the stringers which crosscut the quartz veins is Ser<sub>2</sub>. This assumption is based on the coarse grained texture of the sericite, on the high Al content, and on the fact that both Q<sub>3</sub> and Ser<sub>2</sub> show a close spatial association with chlorite (see below and *Table V.13 & Table V.14*).

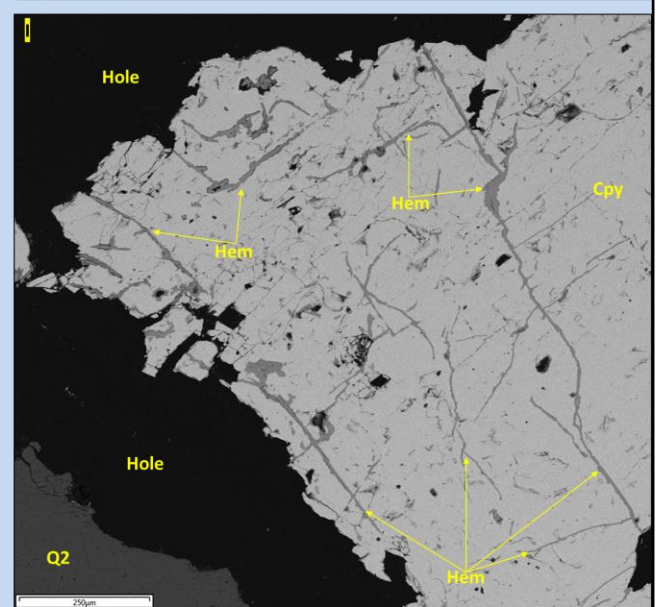
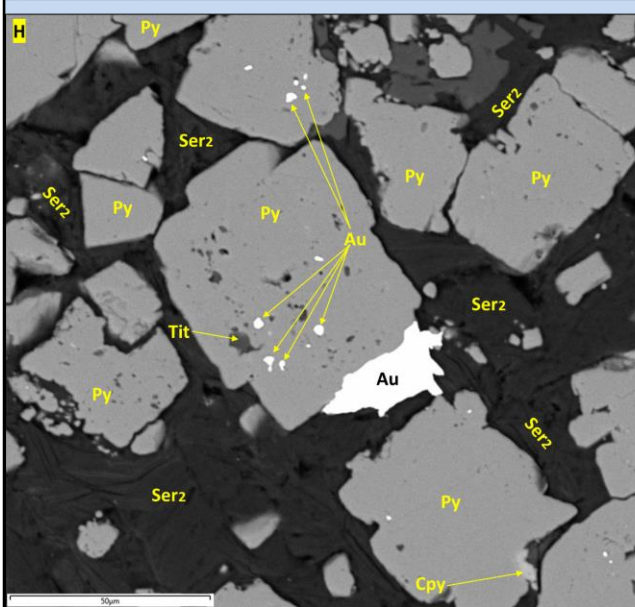
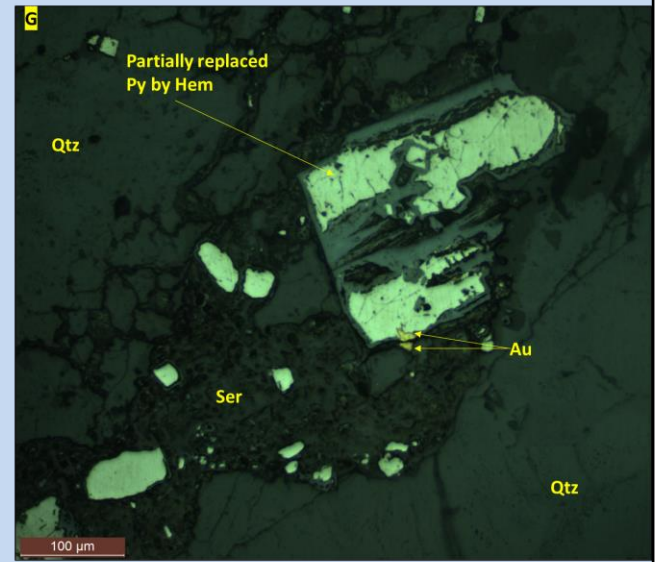
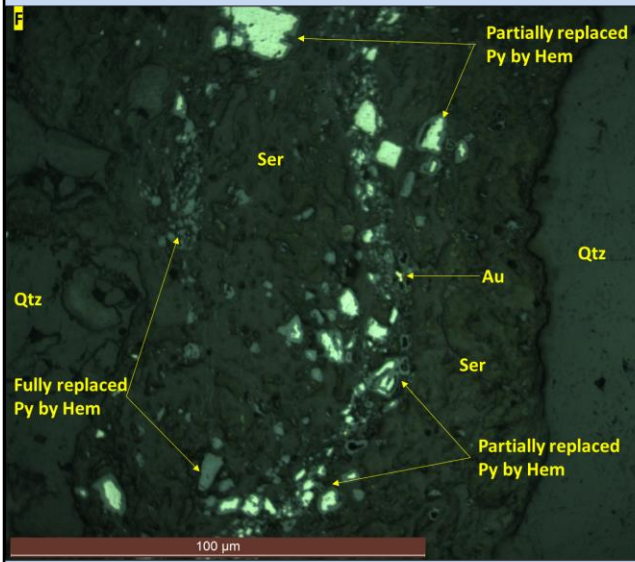
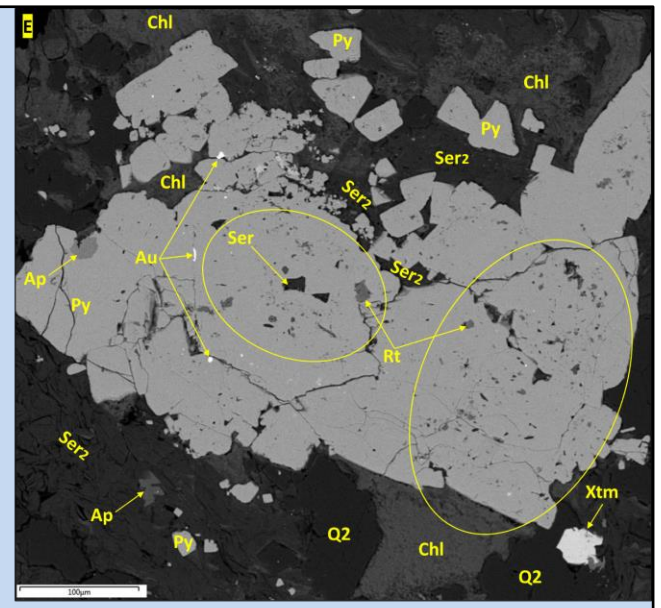
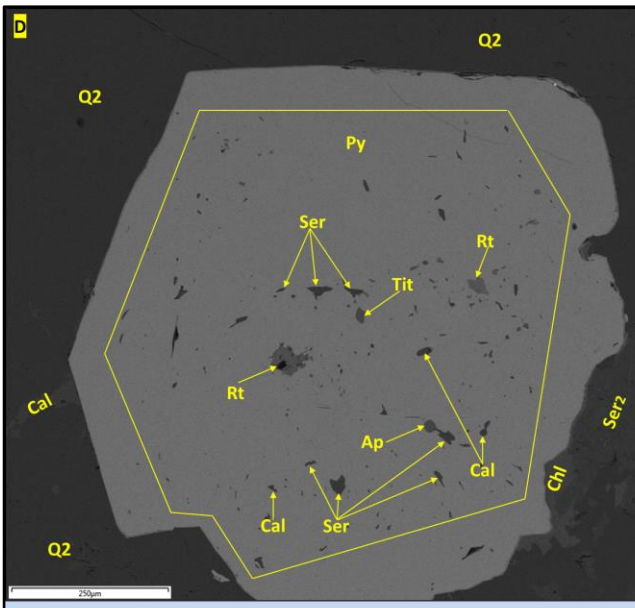
Pyrite was observed in the altered wall rock, in the sericite stringers that crosscut the veins, and directly within the quartz veins (*Table V.13*). In the alteration selvages that surround the veins, it occurs disseminated, mostly as fine to coarse grained (from a few microns to 1-2 mm) euhedral crystals, and secondary as polycrystalline aggregates with visible crystal margins (*Plate V.20 – B, D, E*). The crystals have inclusion-rich cores mantled by inclusion-free euhedral rims or contain both inclusion-rich and inclusion-poor domains (*Plate V.20- D*). The latter is also common for the pyrite aggregates (*Plate V.20- E*). In the sericite stringers that crosscut the veins, pyrite was often seen as fine to moderately grained (from 1 µm up to a few hundred µm), anhedral to euhedral, inclusion-poor crystals (*Plate V.20– F, G*). In the quartz veins, pyrite was observed rarely, and usually in association with the second quartz generation (Q<sub>2</sub>). Under CL it was observed that the pyrite crystals overgrow Q<sub>1</sub>. No relationship between the pyrite crystals and Q<sub>3</sub> was seen. The pyrite is crosscut by chlorite and/or calcite veinlets, and by sericite<sub>2</sub> (*Plate V.20– B, H*). However, all the alteration minerals (*Table V.13*), including the afore-mentioned ones, were observed as inclusions within the pyrite crystals and aggregates. In addition, albite and titanite were often seen as inclusions in pyrite.

The hematite is a major component in the alteration halo (*Table V.13*). It occurs as very thin wires that partially or fully replace pyrite (hematite pseudomorphs on pyrite are common) within the sericite stringers that crosscut the quartz veins (*Plate V.20– F, G*). It was also seen as veinlets that brecciate both pyrite and chalcopyrite but also as inclusions in pyrite (*Plate V.20- I*). Hematite veinlets that seem to follow and to crosscut at a low angle the chlorite veinlets were also noticed (*Plate V.20– B*). Hematite staining on outcrop surfaces or along open fractures is a common feature in the entire Juliet zone.

*Plate V.20 (next two pages)* – Representative images of different ore and alteration minerals observed in the Juliet South zone: **A** – Microscope image (PPL left, XPL right) showing a pyrite aggregate in a sericitized (Ser<sub>1</sub>, fine grained; dirty aspect in PPL) ground mass crosscut by Ser<sub>2</sub> stringer (clean in PPL, coarser than Ser<sub>1</sub>), **note** the Chl shadow pressure along the Py margins; **B** - Microscope image (PPL left, XPL right) showing a Chl-Cal veinlet fracturing Py, Chl patches overprinting Ser<sub>1</sub>, fine grained Rt patches associated with Chl, Ank/Cal patch – the Cal overprints the Ank, and Ser<sub>2</sub> stringer crosscutting the Chl patches, **note** the Hem along the Chl veinlet; **C** - Microscope image (PPL left, XPL right) showing mutual crosscutting relationships between Ser<sub>2</sub> and Chl – Ser<sub>2</sub> crosscuts the Chl patches that overprint Ank-Ser<sub>1</sub> and Chl veinlets crosscut the Ser<sub>2</sub> stringers; **A, B, C** – section RJ5; **D** – BSE image showing a coarse-grained pyrite crystal with inclusion rich core and inclusion-free euhedral rims, **note** the Rt, Ap, Tit inclusions, section RJ1; **E** - BSE image showing a Py aggregate with inclusion-free and inclusion-rich zones (yellow circles), **note** the Rt inclusions, and the presence of Au in the inclusion free domains, section RJ4; **F, G** – Microscope images (reflected light) showing partial and full replacement of Py crystals by Hem, note the free Au grain in **F** and the Au grains on the Py border in **G**, section RJ3; **H** – BSE image showing Py crystals hosted and brecciated by Ser<sub>2</sub>, the pyrite crystals are part of a larger aggregate, **note** the coarse-grained Au between the Py crystals, the fine-grained inclusions of Au in Py, and the Cpy grain between Py crystals, sample RJ4; **I** - BSE image showing a part of a Cpy patch brecciated by Hem veinlets, section RJ3.







Rutile was observed in both the altered wall rock and within the quartz veins (*Table V.13*). It occurs as patches composed of fine-grained, irregular to acicular crystals with random orientations, and as anhedral to euhedral (bladed/prismatic), coarse-grained (up to 400 µm length) crystals (*Plate V.20– B; Plate V.21– A, B*). Similar to the previously described deposits, the rutile observed in the Juliet zone also shows a close spatial association with pyrite: rutile crystals that are intergrown with pyrite, inclusions of rutile in pyrite, and inclusions of pyrite in rutile are common (*Plate V.20– D, E; Plate V.21– C, D, E*). The coarse-grained rutile was seen in Q<sub>2</sub> and sericite<sub>1</sub> and is crosscut and consumed by Q<sub>3</sub>, sericite<sub>2</sub>, chlorite, and calcite veinlets (see below) (*Plate V.21– A, E*). Nonetheless, very fine grained rutile crystals and patches were seen in association with sericite<sub>2</sub> and with chlorite veins and patches and overprint the rest of the minerals (*Plate V.20– B; Plate V.21- B*).

One type of chlorite was identified within the studied samples (*Table V.13*). It has the same optical and geochemical properties as the chlorite<sub>2</sub> from Pine Cove and Stog'er Tight deposits and as the chlorite observed in the Argyle deposit (see previous descriptions). As in the other deposits, it occurs as veins and patches that brecciate and overprint most of the alteration minerals and it shows mutual crosscutting relationships with Ser<sub>2</sub> (*Plate V.20 – A, B, C; Plate V.21 – A, B, E*). The chlorite veins and patches are crosscut by the Ser<sub>2</sub> stringers, but at the same time, some of the Ser<sub>2</sub> stringers are crosscut by the chlorite veinlets (*Plate V.20– C*). The chlorite was also seen to form shadow pressures around euhedral pyrite crystals (*Plate V.20 – A*).

Three carbonate phases were identified in the Juliet samples based on EDS analysis: calcite, ankerite, and siderite (*Table V.13*). The calcite is the more abundant and occurs as veins and patches. It overprints most of the alteration minerals and as in the previously described deposits, it was observed in association with chlorite along the same veins (*Plate V.20 - B*). However, it was also seen to crosscut the chlorite patches and to infill them replacing the chlorite (*Plate V.21– F*). As the chlorite, the calcite also shows mutual crosscutting relationships with Ser<sub>2</sub>. Both the ankerite and siderite were observed along calcite veins as minor components (*Table V.13*). Ankerite was also seen as patches of fine-grained crystals with Ser<sub>1</sub> in the altered ground mass, usually overprinted by calcite, and as inclusions in pyrite (*Plate V.20– B, C*).

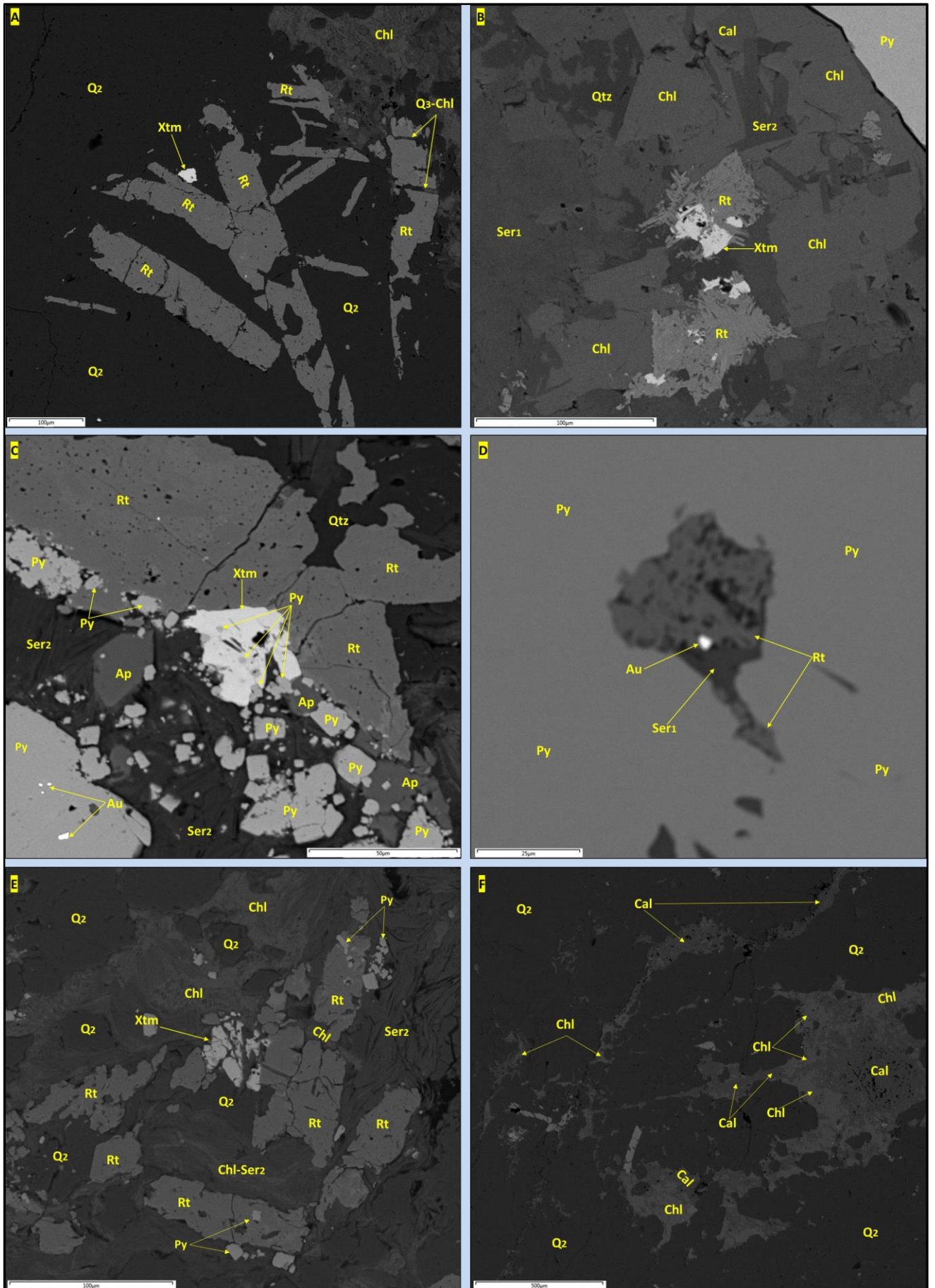
Apatite, monazite, and xenotime were observed disseminated in the altered wall rock material (*Table V.13*). In contrast to the previously described deposits, the phosphate minerals from the Juliet samples are less abundant and smaller in size (apatite < 1mm; monazite  $\leq 20 \mu\text{m}$ ; and xenotime  $\leq 40 \mu\text{m}$ ). The apatite shows various relationships with the rest of the alteration minerals: i) it is hosted by Q<sub>2</sub> and Ser<sub>1</sub>; ii) it occurs as inclusions in pyrite and intergrown with it (*Plate V.20– D*; *Plate V.21– C*); and iii) it is crosscut and overprint by the sericite<sub>2</sub>, chlorite, and calcite veins and patches but also overgrows them (*Plate V.21– G*). The monazite and the xenotime occur free in the altered ground mass or as inclusions in apatite, pyrite, and rutile (*Table V.13*). The monazite grains are scarce and small, whereas the xenotime grains are more abundant and slightly bigger. Pyrite, rutile, and sericite inclusions in xenotime were observed (*Plate V.21– C*). Both the monazite and xenotime are brecciated by chlorite and calcite, but locally also hosted by them (*Plate V.21– E*). Xenotime that is brecciated and overgrown by the fine-grained rutile associated with the chlorite veinlets was also seen (*Plate V.21 – B*).

#### **V.1.4.4. Mineralisation**

The ore mineralogy from the Juliet South zone is composed of native gold, chalcopyrite and trace amounts of undifferentiated gold, gold-silver, and bismuth tellurides, galena and scheelite. Descriptions for these minerals are provided in *Table V.15*, whereas representative images in *Plate V.20– E, F, G, H, I* and *Plate V.21– C, D, I, J*.

The gold was observed free in the quartz veins, in the sericite stringers that crosscut the quartz veins, in the sericitized altered ground mass and in calcite patches and veins (*Table V.15, Plate V.20– F, G, H*). It was also seen as wires and irregular to rounded inclusions in pyrite crystals and along fractures in pyrite in association with chlorite and calcite (*Plate V.20– E; Plate V.21– C, D, I*). Inclusions of pyrite in gold were also seen (*Plate V.21– J*). As in the previously described deposits, within the pyrite crystals the gold occurs in both the inclusion rich and poor domains. It is also coarser and more abundant in the brecciated, coarse-grained, inclusion-poor pyrite crystals and aggregates, compared to gold observed in the finer grained, inclusion rich crystals and aggregates. It was also seen in a close spatial association with rutile within the pyrite crystals (*Plate V.21- D*).

Chalcopyrite was often seen in the studied samples (*Plate V.15 Table V.15*). It occurs as patches in the quartz veins, as disseminated grains in the altered ground mass within sericite, and as inclusions in pyrite (*Plate V.20– H, I*). Chalcopyrite in association with gold and with undifferentiated gold telluride was observed along chlorite-calcite veinlets that brecciate the pyrite (*Plate V.21– I*).



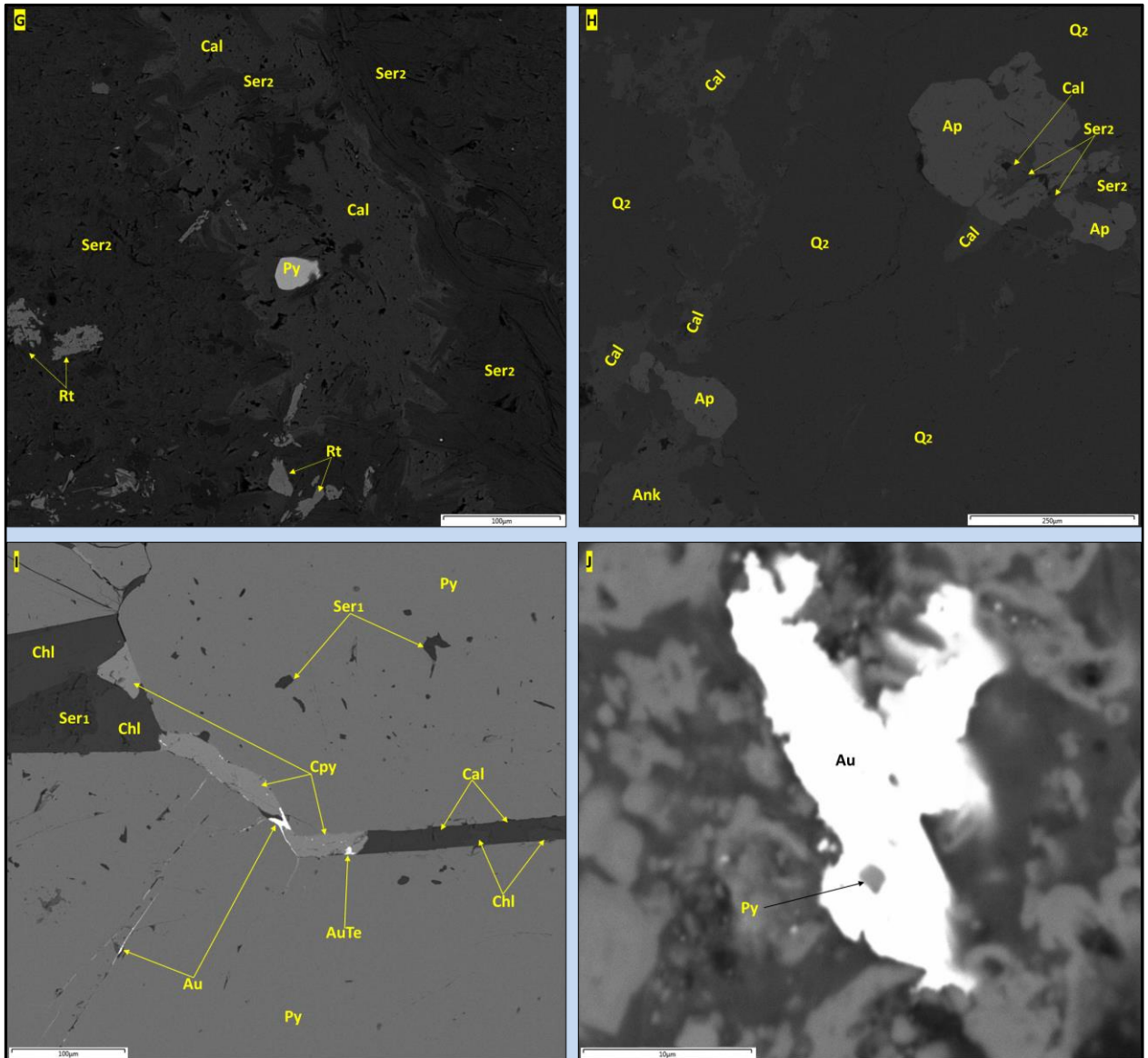


**Plate V.21** – Representative images of different ore and alteration minerals observed in the Juliet South zone: **A** – BSE image showing coarse-grained bladed rutile crystals within Q<sub>2</sub> brecciated and overprinted by Q<sub>3</sub>-Chl veins and Chl patches, **note** the Xtm grain in Q<sub>2</sub> with Rt, section RJ4; **B** – BSE image showing fine-grained rutile patches associated with Chl-Ser<sub>2</sub>, **note** the xenotime grains brecciated and replaced by rutile, section RJ5; **C** – BSE image showing coarse grained rutile intergrown with Xtm, Py and Ap, **note** the Au inclusions in Py, and the Py inclusions in Ap and in Xtm, section RJ4; **D** – BSE image showing Au associated with Rt and Ser<sub>1</sub> in Py, section RJ1; **E** – BSE image showing coarse grained rutile brecciated and consumed by Chl and Ser<sub>2</sub>, **note** the brecciated Xtm grain by Chl, section RJ4; **F** – BSE image showing Cal brecciating and replacing Chl, section RJ4; **G** – BSE image showing Ser<sub>2</sub> crosscutting and infiltrating into a Cal patch, section RJ5; **H** – BSE image showing Ap hosted by Q<sub>2</sub> and crosscut by Ser<sub>2</sub> and Cal but partially overgrowing the latter minerals, sample RJ1; **I** – BSE image showing Au, Cpy and undifferentiated Au telluride along a Chl-Cal veinlet that brecciates Py, section RJ5; **J** – BSE image showing Py inclusion in a free gold grain in Ser<sub>2</sub>-Hem stringer, section RJ3.

*Table V.15. – Summary characteristics of the ore minerals from the Juliet South zone of the Romeo & Juliet prospect.*

<b>Mineral</b>	<b>Occurrence, Morphology</b>
Au	Irregular to rounded inclusions in py; free as wires and irregular to rounded grains along Cal-Chl fractures that brecciate the py or at the interface of py crystals; free in the quartz veins, in the sericite stringers that crosscut the quartz veins, in the sericitized altered ground mass and in calcite patches and veins; sizes from 1 µm to up to 50 µm
Cpy	Inclusions in the py crystals; patches in the quartz veins (up to 1x1 cm in size); free in the altered groundmass or along Chl-Cal veinlets that brecciate the Py;
Gn	Small inclusions (1-10 µm) in the Py crystals; free along Chl-Cal veinlets that brecciate the Py;
Undifferentiated Au & Au-Ag telluride	Trace* amounts, irregular to rounded inclusions in Py; free as wires and irregular to rounded grains along Cal-Chl fractures that brecciate the Py; small sizes 1 - 20 µm
Undifferentiated Bi telluride	Trace* amounts, small (1-10 µm) inclusions within and at the interface of py crystals; free along Cal-Chl <sub>2</sub> fractures that brecciate the Py
Scheelite	Trace* amounts, small (1-10 µm) inclusions in Py

*\*trace = none, or very few grains / studied thin section*



### V.1.5. The Deer Cove prospect

The structural observations provided below for the Deer Cove area were collected from outcrops located along the coastline (within the cove), and from the nearby surroundings of the southern part of the Main Zone, including here the entrance of the old Deer Cove exploration adit (**Figure V.5 - A**). No field observations were gathered from the AK2 Zone because of poor exposure but descriptions for this mineralised block can be found in **Appendix I** of this thesis based on literature data, in Patey & Wilton (1993) and in Dubé et al. (1993). A summarised characterisation of the lithologies that host the mineralised intervals from the Deer Cove area is provided in **Table AI.1**, whereas detailed descriptions can be found in Gower et al. (1991) and in Patey & Wilton (1993).

#### V.1.5.1. Structural setting

Most of the structural elements presented in **Tables IV.1 and IV.2** were also observed in the Deer Cove area. All the mineralised zones that compose the Deer Cove prospect are located in the hanging wall of the D<sub>2a</sub> Deer Cove thrust (**Figure V.5- A**). The proven reserves extends from the thrust towards north, over a strike length of approximately 300 meters (**Figure V.5- A**). Over this distance, the host rocks are affected by dense, E-W, NW-SE, and N-S oriented D<sub>2b</sub> faults and shear zones (**Table IV.1 - Vi**) and show a strong composite S<sub>2a/2b</sub> foliation fabric that dips moderately to steeply from N to ENE (**Figure V.5 - B**). Generally, the S<sub>2a</sub> fabric is visible only under the microscope within the hinges of F<sub>2b</sub> microfolds (**Plate IV.5 - C**). However, in low D<sub>2b</sub> strain domains where both the S<sub>2a</sub> and the S<sub>2b</sub> fabrics are macroscopically visible, it can be observed that the S<sub>2b</sub> is steeper than the S<sub>2a</sub> and oriented clockwise at a very low angle from the latter dipping towards NE. On the main composite foliation fabric, a well-developed, oblique to down-dip plunging, stretching mineral L<sub>2</sub> lineation is characteristic (**Figure V.5- B**).

Along the coastline, a few meters wide D<sub>2b</sub> shear zones host quartz-pyrite veins associated with an intense iron oxide – fuchsite alteration halo (**Figure V.5– A; Plate V.22– A, B**). Mesoscale F<sub>2b</sub> folds are visible in the hanging wall of the Deer Cove thrust, in association with D<sub>2b</sub> shear zones and affect barren quartz-carbonate veins. The F<sub>2b</sub> folds are in general dismembered and refolded by D<sub>3</sub> and D<sub>4</sub> structural elements.

The  $F_3$  folds occur with a high density within the Deer Cove fault zone and overprint the  $D_2$  structures. Commonly, the  $F_3$  folds show wavelengths of tens of centimetres to maximum one meter and are spatially associated with extensional shears and kink bands related to the reactivation of the Deer Cove thrust as a normal fault. Along the coastline, some of the mineralised intervals hosted within the  $D_{2b}$  shears are affected by  $D_3$  shear bands and  $F_3$  folds.

The  $D_4$  structures are represented by a NNE to NE, moderately to steeply plunging crenulation lineation that is well developed in the entire area and by mesoscopic to large scale (wavelengths of a couple of centimetres to tens of meters)  $F_4$  folds (*Plate V.5– C, F*). As previously mentioned, it is considered that at least partially, the undulate shape of the Deer Cove thrust is the result of the  $F_4$  folding event, and that the reactivation of the  $D_{2b}$  structures with reverse kinematic motion compared to their initial one, is related to the  $D_4$  deformation. The mineralised intervals that are subparallel to the main foliation fabric are in general deformed by the  $F_4$  folds.

The syn-to-post  $D_4$  faults (*Table IV.1 – xiii, xiv*) were observed throughout the Deer Cove area, especially along the coastline, where dense sets of south dipping kink bands are very well developed (*Plate IV.8 - B, C*). These kink bands affect the  $D_{2b}$  faults that host mineralised, foliation-parallel, quartz-pyrite veins (*Plate V.22– A*). As in the rest of the PRC, late brittle joints are also present in the Deer Cove area and crosscut all the pre-existent structures and mineralised intervals (*Table IV.1 - xv*).

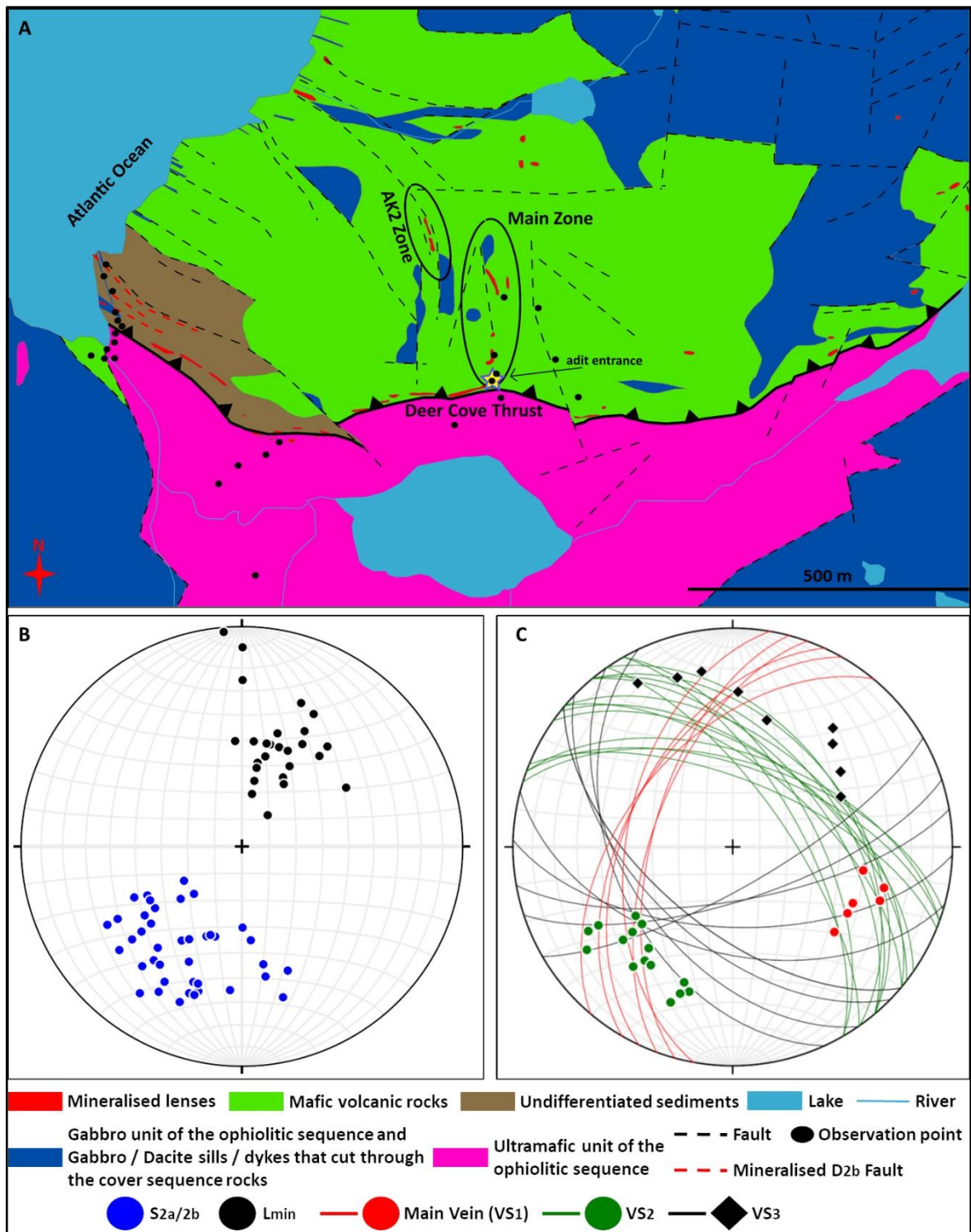


**Figure V.5:** *A* – Simplified geological map of the Deer Cove area after the unpublished geological map of Anaconda Mining (2018) and Pitman et al. (2020). *B*, *C* - Southern-hemisphere, equal-area, stereographic projections of the poles to the foliation planes and of the stretching mineral lineation (*B*), and of the poles to the main mineralised vein sets (*C*) from the Deer Cove area.

### V.1.5.2. Veins observed in the Deer Cove area

Three main vein sets, VS<sub>1</sub> to VS<sub>3</sub> (listed from old to young), were observed in the Deer Cove area. The main characteristics of these vein sets can be found in **Table V.16**.

The Main Zone represents the most important exploration target within the Deer Cove area and consists of multiple, discontinuous, quartz-carbonate breccia veins (**Figure V.5– A**) (Dearin et al., 2009). These veins are here attributed to VS<sub>1</sub> (**Table V.16**). During this study, a continuous 5 meters long, and half to one-meter-wide vein, part of the southern section of the Main Zone, was observed (**Plate V.22– C**). This segment strike from N to NE and dip moderately to steeply (50° to 75°) to W-NW (**Figure V.5– A, C**). The observed vein is composed of milky-white quartz and subordinate carbonate. It has a sheared to laminated aspect and shows multiple opening domains separated by aligned, squeezed, and intensively altered (silica-sericite) wall rock fragments. Around the vein, a few meters wide, strong alteration halo composed of silica, sericite, disseminated subhedral to euhedral auriferous pyrite, carbonate, and iron oxides is visible. The vein displays intense internal deformation and is affected by a NNE to NE, moderately to steeply dipping cleavage, interpreted herein as the S<sub>2b</sub> fabric (**Plate V.22- C**). Moreover, the NW plunging, isoclinal folds described by Gower et al. (1991) and by Dearin et al. (2009) for the southern-most part of the Main Zone (**Fig. A1.6 – B**) have similar characteristics to the F<sub>2b</sub> folds presented in this study (*see chapter IV*). Thereby, it is inferred that these folds can be corelated.

The relationships between the F<sub>3</sub> and F<sub>4</sub> folds and the Main Zone are not clear because of poor vertical exposure of the veins. Furthermore, considering the orientation of the Main Zone approximately parallel to the extensional field of both the D<sub>3</sub> and D<sub>4</sub> events, the vein deformation may be limited to necking and swelling.

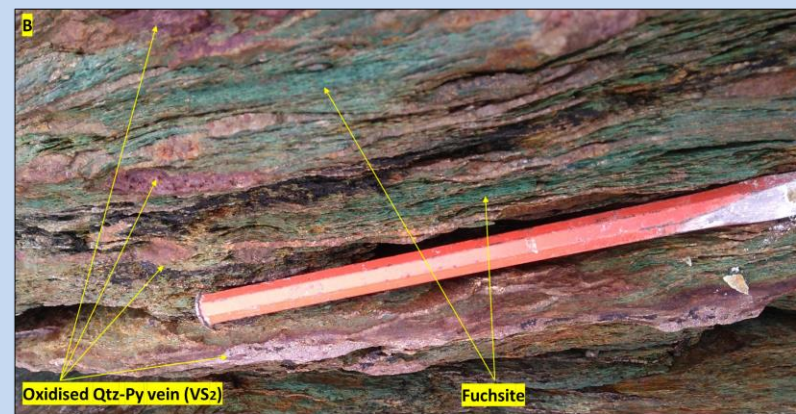
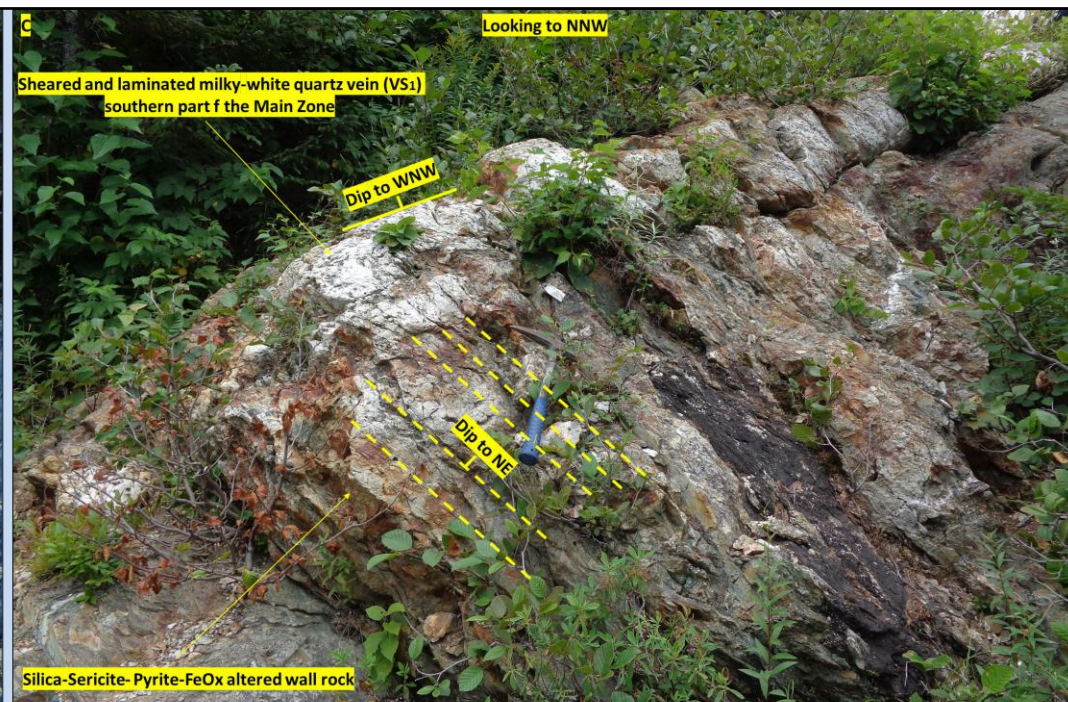
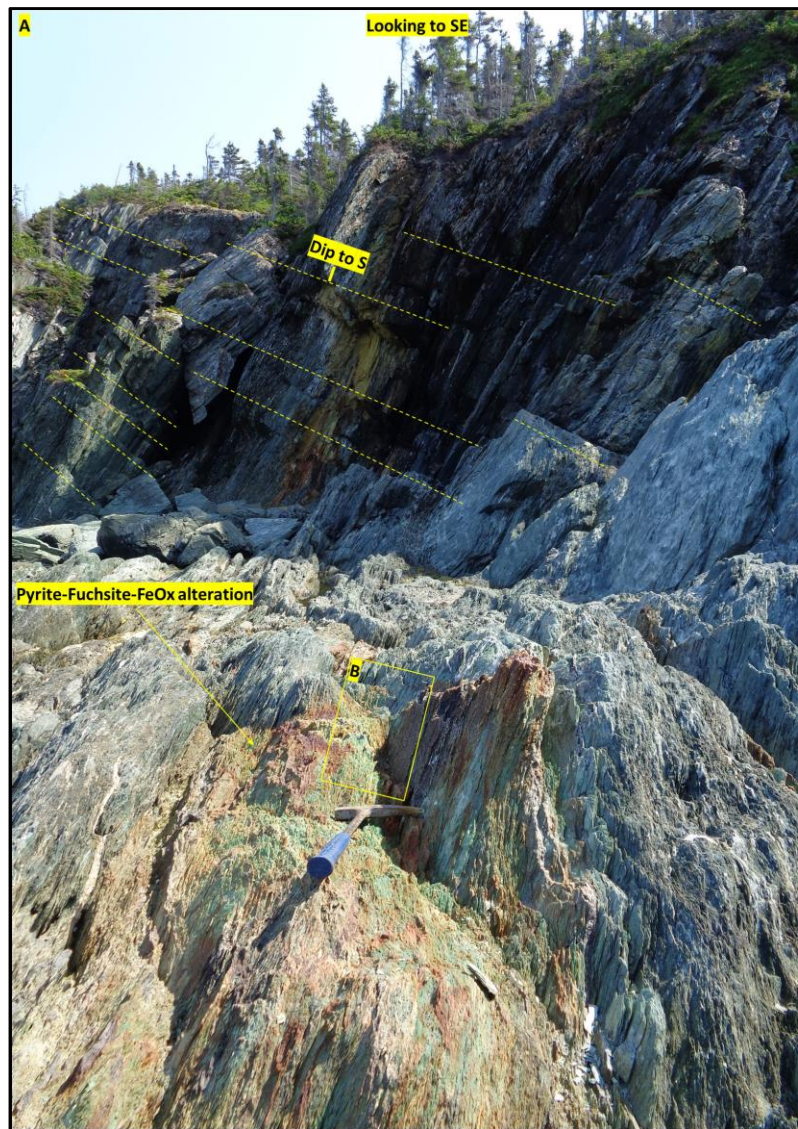
The second vein set (VS<sub>2</sub> - **Table V.16**) was observed mostly along the coastline and is composed of dense networks of foliation-parallel quartz-pyrite veins hosted by intensively altered (silica-fuchsite-iron-oxide) D<sub>2b</sub> shear zones (**Figure V.5– A, C, Plate V.22– A, B, D**). The mineralised faults vary in thickness from 1 meter to approximately 7 meters, whereas the veins show widths of a few centimetres to approximately half a meter (**Plate V.22– A, B, D**). Within the widest intervals, the veins show multiple opening domains characterised by different growth morphologies

(sheared, syntaxial, breccia, and ataxial/stretched) and composed of fine to coarse grained quartz crystals with variable textures: massive, sugary, comb, and fibrous (*Plate V.22– B, E*). Internal folding is visible and open spaces are common. Where the shears affect more rigid rocks, such as mafic dykes, the veins occur in dense stockwork networks, locally forming areas of silica flooding or replacement zones (*Plate V.22 – F*).

The third vein set (VS<sub>3</sub>) is composed of SSE to SW dipping quartz-carbonate tension gashes (*Table V.16; Plate V.22– G, H*). Some of these are subparallel to the syn-to-post D<sub>4</sub> faults and associated fracture sets (*Table IV.1 – xiii, xiv*). These veins are usually barren but associated with a narrow halo of iron-oxides and locally disseminated euhedral Py crystals.

**Table V.16** - . – Descriptions of vein sets identified in the Deer Cove area Terminologies regarding vein and crystal morphologies are used according to Bons (2000) and Bons et al. (2012)

<b>Vein set</b>	<b>Characteristics</b>	<b>Alteration / Mineralisation</b>	<b>Crosscutting relationships</b>	<b>Structural constrains</b>
<b>VS<sub>1</sub></b> <i>Fig. V-A; Plate V.22 - C</i>	Main Zone – quartz-carbonate vein with segments characterised by different growth morphologies: sheared to laminated and breccia type segments that overall have a cumulate strike to NNE; it shows multiple opening domains separated by aligned, squeezed, and intensively altered wall rock fragments	Strong alteration halo composed of silica, sericite, disseminated subhedral to euhedral auriferous pyrite, carbonate, and iron oxides; free Au was reported within the vein by previous workers	Unclear relationships with VS <sub>2</sub> and VS <sub>3</sub>	Crosscuts S <sub>2a</sub> foliation; affected by D <sub>2b</sub> structures (faults and cleavage); unclear relationships with D <sub>3</sub> and D <sub>4</sub> structures
<b>VS<sub>2</sub></b> <i>Plate V.22 – A, B, D, E, F</i>	Foliation-parallel quartz-pyrite veins that show multiple opening domains with different growth morphologies (sheared, syntaxial, breccia, and ataxial/stretched); composed of fine to coarse grained quartz crystals with variable textures: massive, sugary, comb, and fibrous; internal folding is visible and open spaces are common	Associated with strong fuchsite-pyrite-FeOx alteration; Free Au and auriferous Py	Unclear relationships with VS <sub>1</sub> ; crosscut by VS <sub>3</sub>	Hosted by D <sub>2b</sub> shear zones; affected by D <sub>3</sub> to syn-to-post D <sub>4</sub> kink bands and faults
<b>VS<sub>3</sub></b> <i>Plate V.22 – G, H</i>	SSE to SW dipping, quartz-carbonate tension gashes; open to massive and syntaxial vein textures with coarse-grained crystals	No visible mineralisation within the veins but associated with a narrow FeOx alteration halo and disseminated euhedral Py crystals	Unclear relationships with VS <sub>1</sub> ; crosscuts VS <sub>2</sub>	Crosscuts the S <sub>2a-2b</sub> composite foliation; occurs along or subparallel to the syn-to-post D <sub>4</sub> faults/fractures



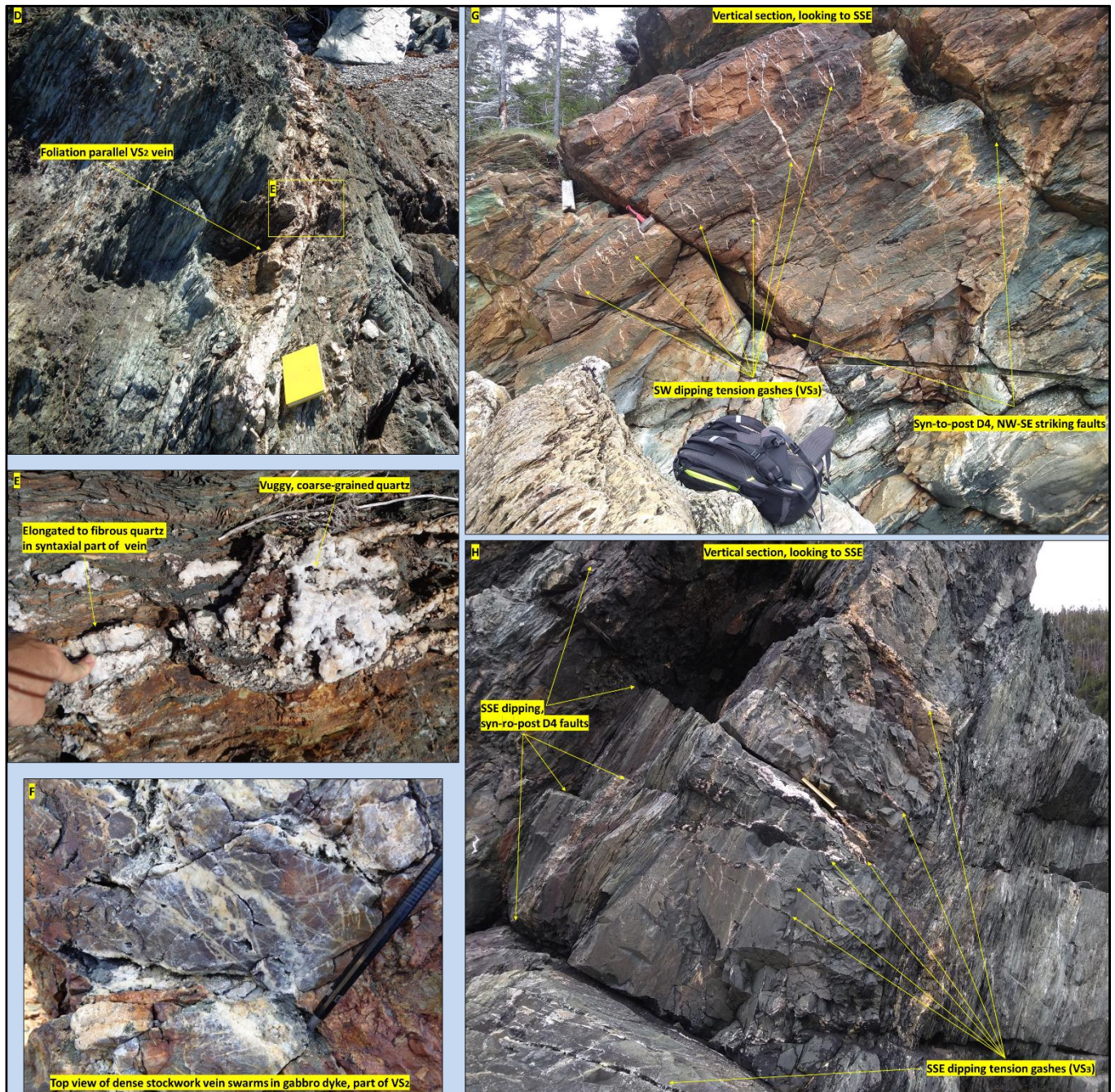


**Plate V.22** – Representative images for the main vein sets identified in the Deer Cove area: **A**, **B** – Intensively altered (pyrite-fuchsite-iron oxides) D<sub>2b</sub> shear zone that hosts thin, subparallel quartz-pyrite veins (VS<sub>2</sub>) (**B**), **note** the south dipping faults (yellow dashed lines) that crosscut the D<sub>2b</sub> fault; **C** – Sheared and laminated, milky-white quartz vein (VS<sub>1</sub>), southern part of the Main Zone, **note** the NE dipping fabric (interpreted as S<sub>2b</sub>) that affects both the vein and the altered (silica-sericite-pyrite-iron oxides) host rocks; **D**, **E** – Thicker, foliation-parallel quartz vein (VS<sub>2</sub>), **note** the overall laminated and sheared aspect of the vein (**D**) the syntaxial domains (**E**) and the different quartz morphologies (**E**); **F** – Dense stockwork quartz-vein network (VS<sub>2</sub>) associated with intense silicification; **G**, **H** – SSE and SW dipping tension gash arrays (VS<sub>3</sub>) formed along or subparallel to the syn-to-post D<sub>4</sub> south dipping, E-W striking (**G**) and NW-SE striking (here SW dipping) faults and fractures (**H**).



### V.1.5.3. Alteration

Most rocks observed in the Deer Cove area show at least a moderate hydrothermal alteration which overprints the initial textures and mineral assemblages. However, as well as the Romeo & Juliet gold bearing veins, the mineralised intervals from the Deer Cove area are also hosted by basaltic lava flows and associated volcanoclastic facies of the Mount Misery Formation. Therefore, the least altered rocks from the Romeo & Juliet (**Plate V.18 - F, G**) are also considered representative for the Deer Cove area. In the studied outcrops and core sections two main alteration halos were observed based on macroscopical observations: i) a proximal halo (~10 m) composed of sericite (including fuchsite)-silica-pyrite-chlorite-hematite  $\pm$  leucoxene-carbonate around VS<sub>1</sub> and VS<sub>2</sub> (**Plate V.22- B, C, F; Plate V.23- A**); and ii) a distal alteration (~ 10 to 50 m) composed of epidote-chlorite-carbonate-hematite  $\pm$  pyrite (**Plate V.23 - B**). In the distal alteration halo, intervals characterised by dense networks of quartz-epidote-hematite veins that generate intense brecciated to even “flooded/replacement” zones are common (**Plate V.23- C, D**). Overall, these are very similar to the alteration types described in precedent studies (Dubé et al., 1993; Patey & Wilton, 1993; Dearin et al., 2009). As for the previously described deposits, detailed petrographic and geochemical analysis (BSE-CL, EDS) were conducted only on samples collected from the ore zone (for rationale see *chapter III – Methodology, and for sample descriptions Appendix 2*). Thereby, for more descriptions related to the distal alteration halo the reader is referred to the afore-mentioned authors.

It is interpreted that samples DCD1 and DC3 (**Appendix 2**) come from veins pertaining to VS<sub>1</sub> based on their texture (breccia veins), composition, or drill hole location and depth interval. The vein and wall rock material from samples DC4 and DC5 (**Appendix 2**) are associated to VS<sub>2</sub> based on their textures and occurrence type (foliation parallel). It is not clear from which vein set the sample DC2 (**Appendix 2**) comes from because of complex overprinting relationships of multiple thin veins.

In the studied samples (**Appendix 2**) the host lithologies show a strong pervasive alteration. The volcanic textures and the mineral assemblages related to the initial composition of the host rocks, as well as the metamorphic related minerals, have been replaced by the alteration minerals. A few relict fragments of chromite and ilmenite were however observed. The main alteration minerals identified are quartz, sericite, chlorite, leucoxene (rutile-titanite), carbonate, albite, pyrite and hematite.

Summarised descriptions for all these minerals are presented in *Table V.18* & *Table V.19*. In contrast to the previously described deposits, apatite, monazite, and xenotime were observed in trace amounts (none or very few grains/section) and are very fine grained.

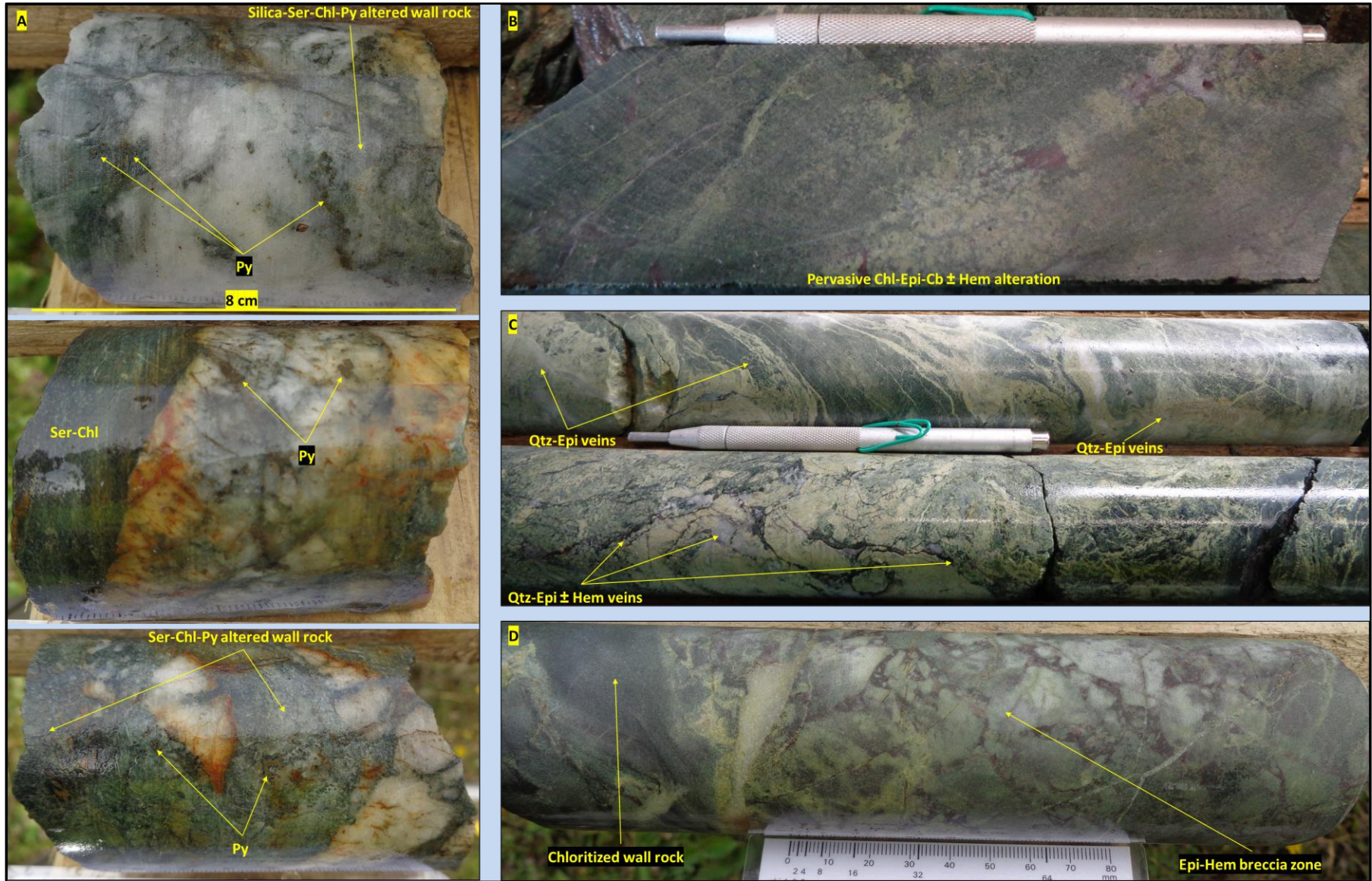


**Plate V.23 (see above)** – Representative images for the proximal and distal alteration halos observed in the Deer Cove area: **A** – Core segments from breccia type vein (VS1) within the Deer Cove Main Zone (low to medium gold grade interval), and associated Silica-Ser-Chl-Py proximal alteration halo, drill hole DC-86-24; **B** – Core section showing pervasive distal alteration composed of Chl-Epi-Cb ± Hem; **C, D** – Core sections showing intensively brecciated intervals and flooded/replacement zones by Qtz and/or Epi and/or Hem veins; **B,C, D** - drill hole DC-88-118.

**Table V.17**– Summary characteristics of the alteration minerals identified in the proximal alteration halo of the Deer Cove prospect.

<b>Mineral</b>	<b>Occurrence</b>	<b>Texture</b>	<b>Spatial association with other alteration minerals</b>	<b>Overprinting relationships</b>
<b>Qtz</b>	As vein material and in the altered wall rock in association with albite and sericite	Multiple generations (Q <sub>1</sub> , Q <sub>2</sub> , Q <sub>3</sub> ), see <i>Table V.18</i>	See <i>Table V.18</i>	See <i>Table V.18</i>
<b>Ser</b>	Main alteration mineral in the altered wall rock, usually defines the foliation fabric	Pervasive fine-grained; coarse-grained stringers and patches	Q <sub>2</sub> -Q <sub>3</sub> -Rt-Tit-Py-Chl-Cal	Crosscuts and replaces Q <sub>1</sub> and Ab; shows mutual crosscutting relationships with Q <sub>2</sub> -Q <sub>3</sub> -Chl-Cal
<b>Chl</b>	Within the alteration halo	Fine-grained crystals disseminated within the sericite groundmass; Py fringes; stringers and patches	Q <sub>3</sub> -Cal-Ser-Py	Overprint most of the other alteration minerals; shows mutual crosscutting relationships with Ser; occurs together with Cal as Py fringes and in patches, but is also crosscut by Cal
<b>Rt</b>	Within the alteration halo	Fine to coarse grained (1 up to ~ 60 µm) relict crystal fragments within the sericite or as inclusions in pyrite and in titanite	Q <sub>2</sub> -Ser-Tit-Py-Ank	Overprinted and replaced by Ser-Chl-Cal-Tit (coarse grained)
<b>Tit</b>	Within the alteration halo	Very fine grained crystals disseminated within the sericite and coarse-grained crystals	Q <sub>2</sub> -Ser-Rt-Py-Ank	The coarse grained crystals overgrow Rt and are crosscut and replaced by Ser-Cal-Chl

<b>Epi</b>	Occurs as a relict phase in the altered wall rock	Consumed by calcite and chlorite	N/A	Overprinted by the rest of the alteration minerals
<b>Ank</b>	Within the alteration halo	Minor amounts disseminated within the sericite ground mass and inclusions in Py	Q <sub>2</sub> -Ser-Rt-Py	Overprinted by Ser-Chl-Cal
<b>Dolo</b>	Vein material	Fine to coarse-grained	Chl-Cal	Brecciated by Cal
<b>Cal</b>	Veins and patches within both Qtz veins and altered wall rock	Fine to coarse-grained veins and patches and as Py fringes	Ser-Chl-Py	Overgrows and crosscuts most of the other alteration minerals; reopens and infills the Q <sub>2</sub> and Q <sub>3</sub> veins; shows mutual crosscutting relationships with Ser and Chl
<b>Ab</b>	Within the alteration halo	Brecciated and relict crystal fragments in the altered ground mass; inclusions in the pyrite crystals	Q <sub>1</sub>	Replaced by Ser and Chl
<b>Py</b>	Within the veins and in the altered wall rock	Fine and coarse grained, irregular to euhedral crystals with various textures: oscillatory zoned with inclusion-rich core and inclusion-poor euhedral rims defined by rhythmic growth of thin As-rich, and thick As-poor bands; crystals with multiple inclusion rich domains hosted in an inclusion-free matrix; un-zoned crystals without or with very few inclusions; patches of brecciated or annealed polycrystalline aggregates with both inclusion rich/poor domains	All the other alteration minerals	Hosted by Q <sub>1</sub> but also overgrows it; hosted by Q <sub>2</sub> but also brecciated by it; brecciated and consumed by Q <sub>3</sub> , sericite, calcite, chlorite, and locally by titanite but also overgrows these minerals; all the other alteration minerals were observed as inclusions in Py

<b>Hem</b>	Within the veins and in the altered wall rock	Inclusions in Py; staining on Py rims and along fractures within Py; partial to full replacement of chromite and Py	Ser-Cal-Chl	Replaces Chromite and Py crystals
------------	---	---	-------------	-----------------------------------

**Table V.18** – Summary CL characteristics of the quartz generations observed in samples from the Deer Cove prospect. The texture terminologies are used according to Rusk et al. (2004) and Rusk (2012).

<b>Quartz (Q) generation</b>	<b>Optical properties</b>	<b>CL colour and intensity</b>	<b>CL texture</b>	<b>Crosscutting relationships</b>	<b>Association with other alteration minerals</b>	<b>Related vein set</b>
<b>Q<sub>1</sub></b>	Blocky, coarse grained crystals; undulatory extinction; sharp, diffuse, and lobate to serrated crystal boundaries	Blue/yellow (medium to high CL intensity)	Brecciated coarse-grained crystals with patchy zonation defined by yellow and blue areas and euhedral growth zones with alternating yellow-blue CL response	Brecciated by both Q <sub>2</sub> and Q <sub>3</sub> ; overprinted by Ser-Chl-Cal	Ab-Py	Observed in the VS <sub>1</sub> veins (compose most of the vein volume) and in the altered wall rock material
<b>Q<sub>2</sub></b>	Fine-grained crystals in thin veins; medium to coarse-grained elongate to fibrous crystals when forms Py fringes; and moderate to fine-grained in mosaic domains; undulatory extinction; sharp, diffuse, and lobate to serrated crystal boundaries	Multiple sub-generations that are very dark to dark purple (low intensity)	Networks of interconnected veins with random orientations that brecciate Q <sub>1</sub> , and homogenous/massive zones with mottled aspect given by the presence of Q <sub>1</sub> fragments	Mutual crosscutting relationship with Ser; crosscuts Py but also overgrown by it; crosscut by Q <sub>3</sub> , Ser, Chl, Cal	Ser-Rt-Py-Tit-Ank	Comprises most of the VS <sub>2</sub> vein volume

Q <sub>3</sub>	Undistinguishable from the thin Q <sub>2</sub> veinlets	Moderate to high CL response displaying blue to bright blue colours with massive or patchy to brecciated (by Cal) internal structure	Networks of interconnected veins with random orientations that brecciate Q <sub>1</sub> & Q <sub>2</sub> ; Incorporate Q <sub>2</sub> fragments and locally re-uses Q <sub>2</sub> hosting structures	Crosscuts most of the other alteration minerals; mutual crosscutting relationships with Ser and Chl; crosscut by Cal; brecciates Py but also overgrown by it	Ser-Chl-Py	Observed in both VS <sub>1</sub> and VS <sub>2</sub> veins
----------------	---	--	---	--	------------	--

The quartz is the main component in the studied veins, and rarely it also occurs in the altered wall rock in silicified areas (*Table V.17, Table V.18*). In the veins the quartz displays various morphologies: coarse-grained, blocky to elongate blocky and fibrous crystals; fine-grained, anhedral to subhedral crystals locally forming mosaic domains (*Plate V.24– A, B, C*). Regardless of their shape and size, all the quartz crystals show the common undulatory extinction and sharp, diffuse, and lobate to serrated crystal borders (*Plate V.24– A, B, C*). Microstructural investigations of VS<sub>2</sub> veins showed that in general, the elongate to fibrous quartz crystals form as pressure fringes around pyrite and suggest both up-dip and down-dip motion directions (*Plate IV.5 – J; Plate V.24– A, B*). The quartz pyrite fringes show internal bending/folding and either overgrow the fine to medium-grained mosaic quartz domains or transit gradually into them (*Plate V.24– A, C*).

SEM-CL investigations showed that within the studied samples at least 3 main generations of quartz are present. These are referred to as Q<sub>1</sub> to Q<sub>3</sub>, Q<sub>1</sub> being the earliest and Q<sub>3</sub> the latest, based on their crosscutting relationships and of their interpreted relative timing.

The 1<sup>st</sup> quartz generation (Q<sub>1</sub>) observed in the Deer Cove samples has a moderate to high CL response showing yellow and blue colours when imaged by coloured CL (*Table V.18*). The yellow colour is characteristic for most part of the crystal surface, whereas the blue colour occurs as patchy/irregular zones or as euhedral growth zones alternating with the yellow zones (*Plate V.24– D, E, F*). Q<sub>1</sub> is strongly brecciated by both Q<sub>2</sub> and Q<sub>3</sub> (see below), but in contrast to the previously described deposits, Q<sub>1</sub> observed in the Deer Cove samples comprises most of the VS<sub>1</sub> vein volume (up to ~70% based on optical estimations). In the VS<sub>2</sub> veins it was observed only as a minor component. It was also observed in the altered wall rock material in association with albite. Under the microscope, Q<sub>1</sub> corresponds to the coarse-grained crystals.

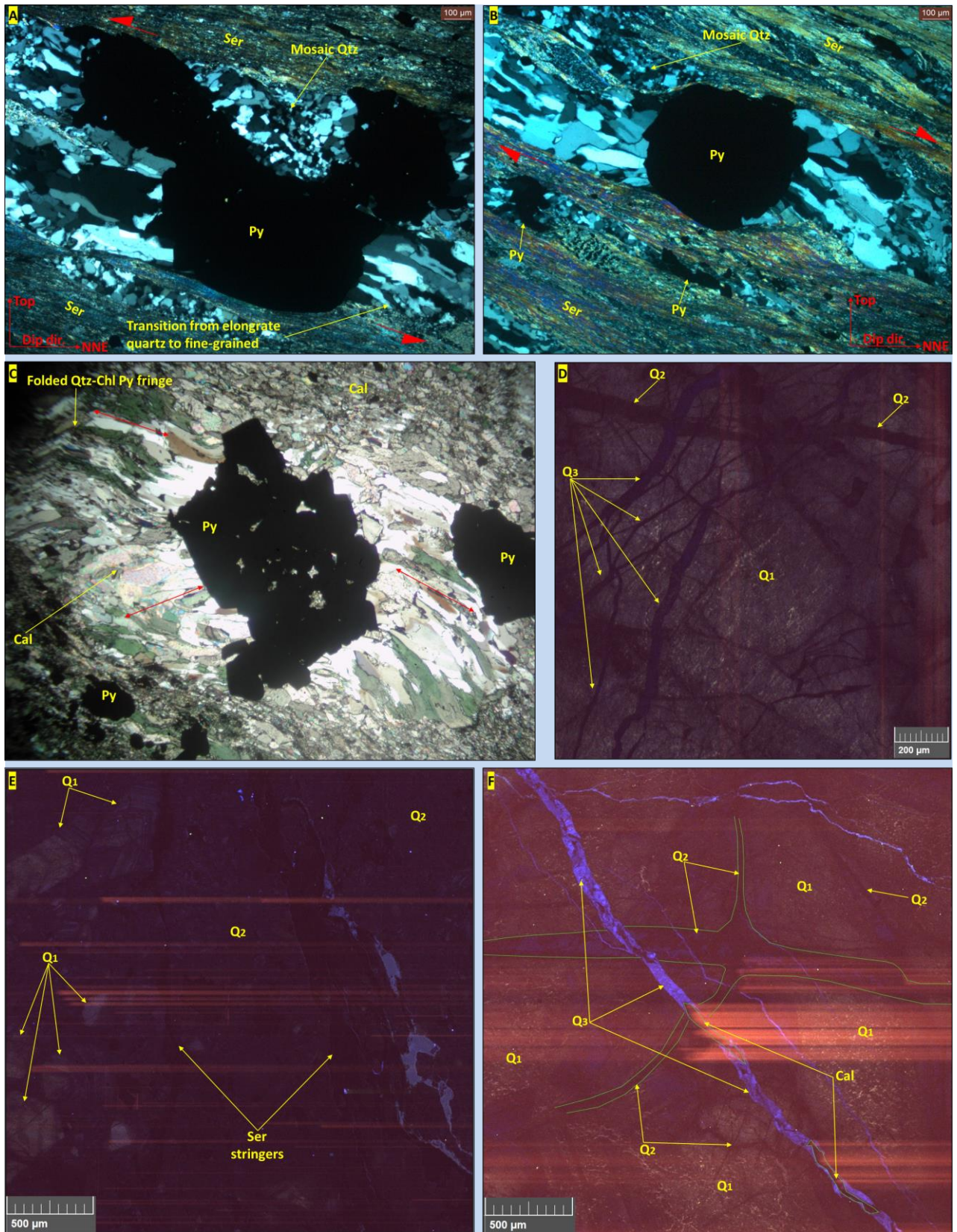
The second and third quartz generations (Q<sub>2</sub>, Q<sub>3</sub>) identified in the Deer Cove samples occurs as veins with random orientations (multiple sub-generations) and rarely as patches or large masses that fill in open spaces in Q<sub>1</sub> dominated domains (*Table V.18*). Under CL, Q<sub>2</sub> shows a very dark to dark purple colour with homogenous internal structure, as in the rest of the described deposits (*Plate V.24– D, E, G, H, I*). Q<sub>2</sub> comprise most volume of the VS<sub>2</sub> veins. The third quartz generation (Q<sub>3</sub>) crosscuts

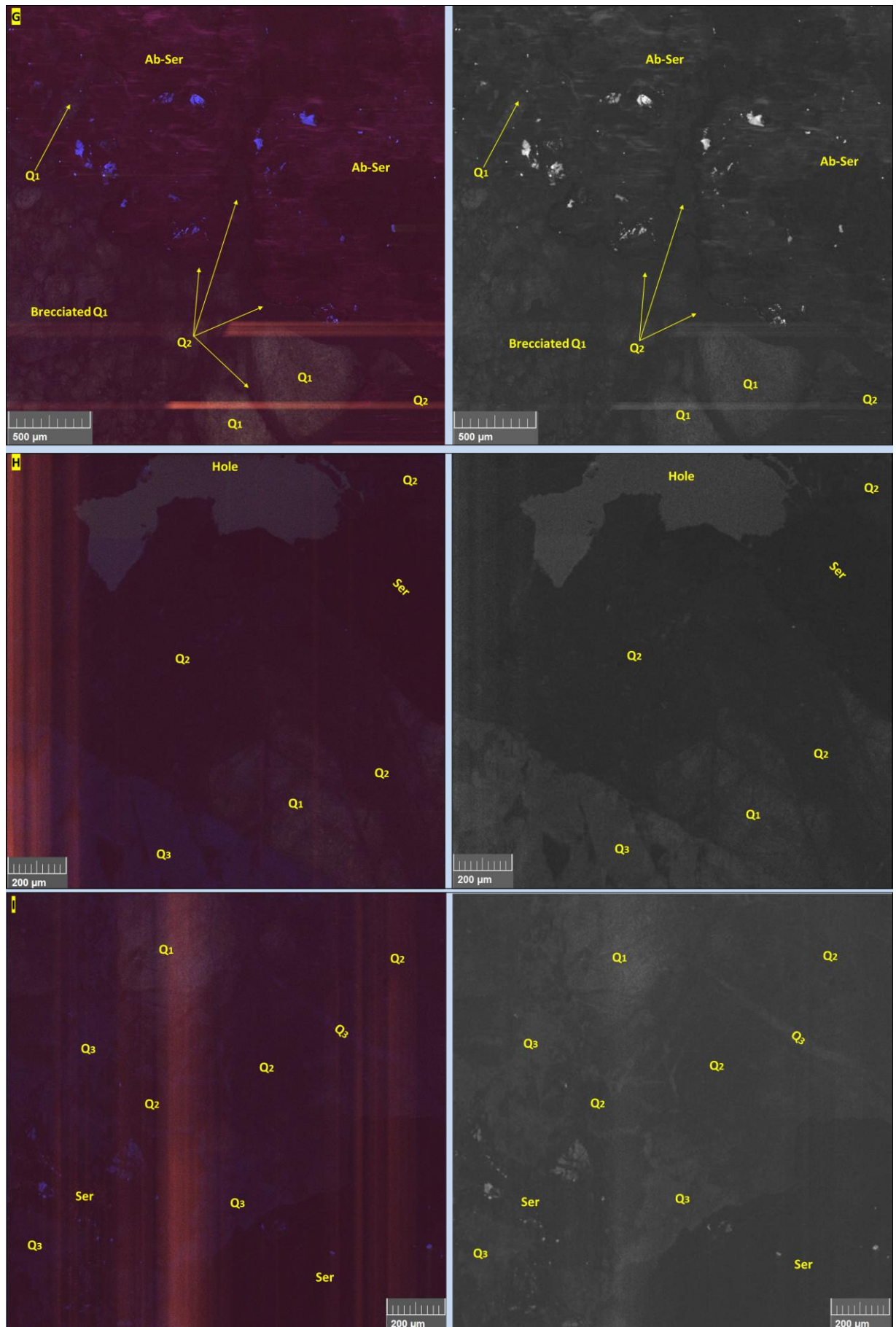


both Q<sub>1</sub> and Q<sub>2</sub> and under CL it displays a moderate to bright blue colour and a massive to patchy and brecciated (by calcite) internal structure (*Plate V.24– D, F, G, H, I, J*). In general, the Q<sub>3</sub> veins have different orientations compared to the Q<sub>2</sub> veins, but locally Q<sub>3</sub> also reopens and infill the structures that host the Q<sub>2</sub> veins. When analysed under optical microscope, both Q<sub>2</sub> and Q<sub>3</sub> coincide with fine-grained quartz domains.

Sericite is the main alteration product in the altered wall rock material (*Table V.17*). It usually defines the foliation fabric replacing albite and biotite, and shows multiple textures, from a pervasive fine-grained phase to coarse-grained stringers and patches (*Plate V.24– A, B, E, G, H, I, J; V.25 – A, D*). No clear crosscutting relationships was observed between the fine and coarse grained phases. Phengite is the main mica that compose the sericite, although fuchsite (Cr rich mica) is also abundant around the VS<sub>2</sub> veins (*Plate V.22 - B*). The sericite crosscuts and overprints Q<sub>1</sub> (*Plate V.24– E, G, H*) and shows mutual crosscutting relationships with both Q<sub>2</sub> and Q<sub>3</sub> (*Plate V.24– E, G, H, I, J*).

Chlorite occurs as fine-grained crystals disseminated within the sericite groundmass, and as stringers and patches together with Q<sub>3</sub> and/or calcite and/or sericite (coarse-grained) overprinting most of the other alteration minerals, including the fine-grained sericite (*Table V.17*) (*Plate V.25– J; Plate V.26– D, E*). It also forms shadow pressures around pyrite crystals either overgrowing pre-existent calcite and/or quartz pyrite fringes or growing together with the calcite and/or quartz (*Plate V.24– C; Plate V.25 – B, F*). In plane polarised light, the chlorite has a moderate pleochroism, varying from pale green to bright green, whereas in crossed polarised light it shows light to dark brown anomalous interference colours (*Plate V.25– E, F*). EDS analysis of different chlorite crystals showed that it has similar Mg and Al contents, with ranges of 9 to 12%, and Fe between 15 to 25%.





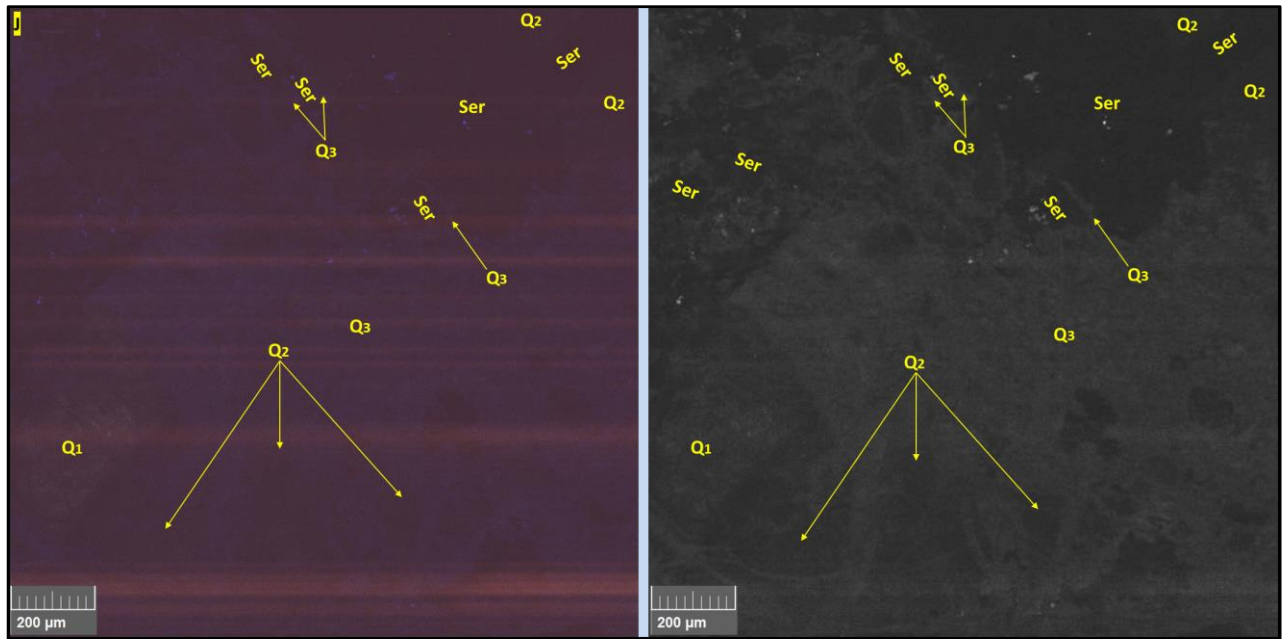


**Plate V.24 (previous two pages)** – Representative images of different quartz generations related to the Deer Cove mineralisation: **A, B, C** – Microscope images (cross polarized light) showing fibrous to elongated quartz crystals forming pyrite fringes (A, B, C) and mosaic quartz as vein material and Py fringes (A, B), **note1** the transition from fibrous quartz to mosaic, the undulate extinction, and the crystals boundaries, **note2** the orientation of the Py fringes that show opposing movement directions and the elongated and curved Py crystals in images **A** and **B**, **note3** the folded fringes, and the calcite crystals that have different orientation (red doubled arrows) compared to the Qtz-chl crystals (**C**); **A, B** section DC30, **C** section DC4; **D** – CL image showing Q<sub>1</sub> ground mass (yellow) brecciated by Q<sub>2</sub> (black to dark purple) and Q<sub>3</sub> (blue) veins, **note** Q<sub>3</sub> crosscuts both Q<sub>1</sub> & Q<sub>2</sub>, section DC2; **E** - CL image showing fragments of Q<sub>1</sub> crystals with euhedral growth zones (yellow and blue bands) in a mass of Q<sub>2</sub> (dark purple), **note** the presence of the two sericite stringers that crosscut both Q<sub>1</sub> and Q<sub>2</sub>, section DC3; **F** - CL image showing calcite infills in different portions of a Q<sub>3</sub> vein (bright blue) that crosscuts both Q<sub>1</sub> ground mass (yellow with blue zones) and Q<sub>2</sub> veins (black to dark blue/purple), red stripes are caused by the intense response of Cal in CL, section DCD1; **G – J** – CL images (left side - original colored image, right side – same as left but monochrome CL using only the blue colour channel) that show: albite (bright magenta) – sericite (black) patch crosscut by Q<sub>2</sub> and Q<sub>1</sub> brecciated by Q<sub>2</sub> (**G**); Q<sub>3</sub> vein and sericite stringer (black) overprinting both Q<sub>1</sub> and Q<sub>2</sub> (**H**); Q<sub>3</sub> brecciating Q<sub>1</sub> and Q<sub>2</sub> but overgrown by Ser stringers and patches (black) (**I**); Q<sub>1</sub> and Q<sub>2</sub> fragments in Q<sub>3</sub> ground mass and Ser growing over Q<sub>3</sub> but further brecciated by it (**J**); **G** – section DC3; **H-J** – section DC2; the monochrome images are included in order to better emphasize the difference between sericite and Q<sub>2</sub>. Note, for all the coloured CL images the initial contrast was enhanced to better highlight the differences of various quartz generations.

Leucoxene patches composed of titanite, and rutile are abundant in the altered wall rock material (*Table V.17*). The rutile occurs mostly as fine to coarse grained (1 up to ~ 60 µm) relict crystal fragments within the sericite ground mass or as inclusions in pyrite and in titanite (*Plate V.25– A, C, G*). The titanite was observed as very fine grained crystals disseminated within the sericite ground mass or as coarse-grained crystals and aggregates (up to 100 µm in length) that usually overgrow rutile, but which are brecciated and consumed by sericite, chlorite, and calcite (*Plate V.25– B, C, D*). Inclusions of ilmenite are also common within the titanite crystals.

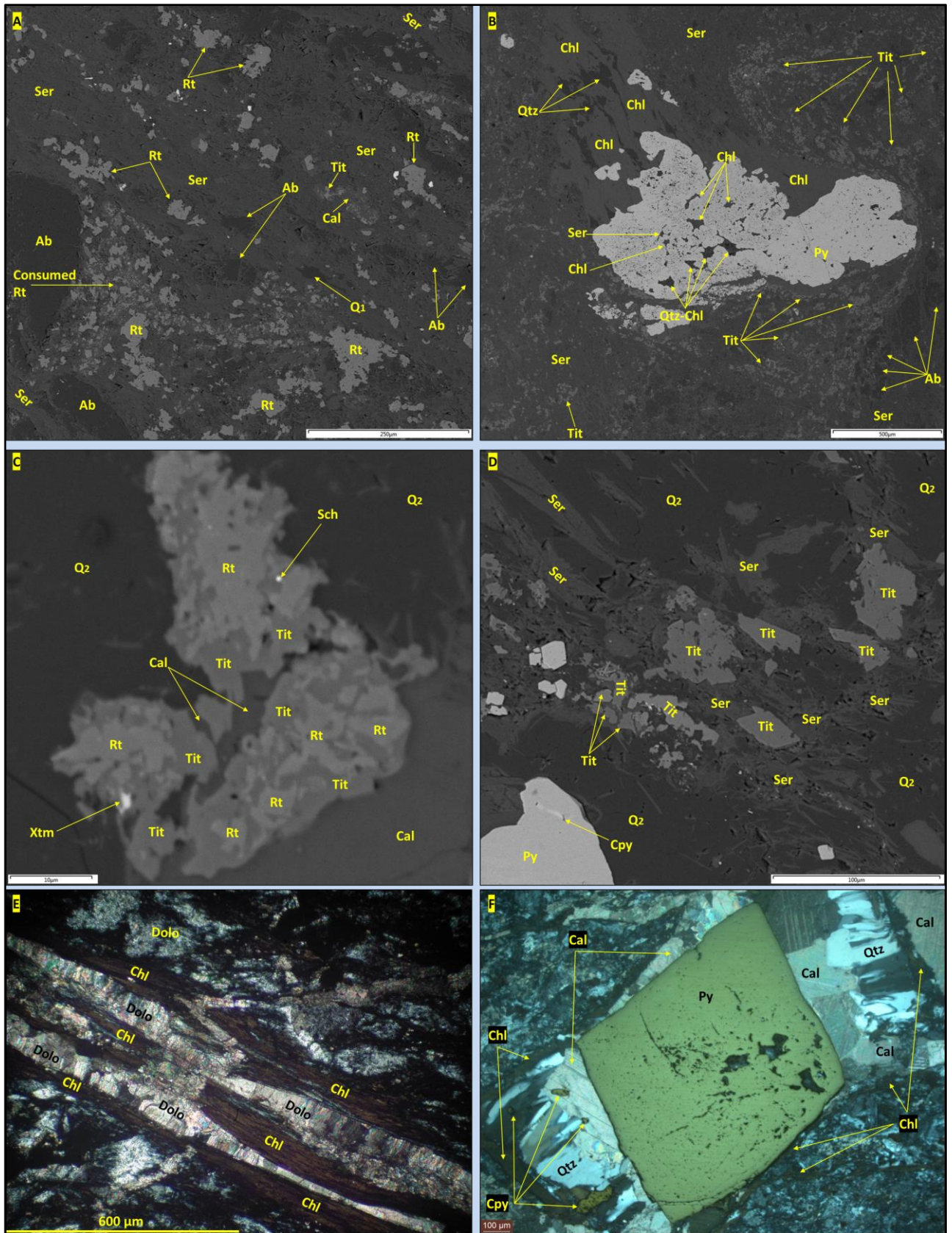
EDS analysis on different carbonate crystals showed that ankerite, dolomite, and calcite are present in the studied samples (*Table V.17*). The ankerite was seen only as inclusions in pyrite and as fine-grained crystals disseminated in the sericitized ground mass. The dolomite was observed in veins that crosscut at a low angle the composite S<sub>2a-2b</sub> foliation fabric. The veins show multiple opening domains some of which are infilled with chlorite or with coarse-grained calcite crystals (*Plate V.25– E*). Calcite was also seen as shadow pressures around pyrite crystals, and as mono or poly mineral patches and veinlets in association with chlorite (*Plate V.24 – C; Plate V.25 – F, K*). When calcite occurs as part of the pyrite fringes, it either grows together with chlorite and/or quartz or it overgrows the pre-existent quartz fringes usually showing different growing direction (*Plate V.24– C; Plate V.25– F*). The calcite overgrows and crosscuts most of the other alteration minerals, reopens and infills the Q<sub>2</sub> and Q<sub>3</sub> veins, and shows mutual crosscutting relationships with sericite and chlorite (*Plate V.24– F*).

Albite was observed only in the altered wall rock material (*Table V.17*). It occurs as brecciated and relict crystal fragments being replaced by both sericite and chlorite, or as inclusions in the pyrite crystals (*Plate V.24– G; Plate V.25- A*). When imaged by CL it has a moderate CL response and shows a homogenous magenta colour (*Plate V.24– G*). The albite has a close spatial association with Q<sub>1</sub> when the latter is present in the alteration halo and is crosscut by Q<sub>2</sub>.

Pyrite was observed disseminated in the alteration halo of the VS<sub>1</sub> and VS<sub>2</sub> veins and within the veins (*Table V.17*) (*Plate V.23– A*). The pyrite crystals vary in size from a few microns to a few millimetres, whereas the pyrite aggregates can form masses of several centimetres. The crystals vary in shape from irregular to euhedral and show various textures: oscillatory zoned crystals with inclusion-rich core, mantled

by inclusion-poor euhedral rims characterised by rhythmic growth of thin arsenic-rich, and thicker arsenic-poor bands (*Plate V.25- G*); crystals that contain multiple inclusion rich domains, usually bordered by euhedral arsenic-rich bands, hosted in an inclusion-free matrix (*Plate V.25- H*); un-zoned crystals without or with very few inclusions. The pyrite aggregates are either inclusion-poor/rich or contain inclusion-rich and inclusion-free domains. The pyrite shows diverse relationships with the rest of the above-mentioned vein and alteration minerals: i) it was seen fully enclosed in Q<sub>1</sub>; ii) it was observed hosted by Q<sub>2</sub> but also brecciated by it; iii) it is brecciated and consumed by Q<sub>3</sub>, sericite, calcite, chlorite, and locally by titanite but also overgrows these minerals (*Plate V.25- I, J, K*); and iv) all the minerals described in *Table V.17* plus epidote, chromite, and ilmenite occur as inclusions in pyrite. Within the VS<sub>2</sub> veins and in their alteration halo, the pyrite crystals and aggregates are usually bordered by shadow pressures, have elongated or curved/bent shapes and contain high amounts of inclusions with random or concentric to even helical distribution (*Plates IV.5 - K; Plate V.24 - A, B; Plate V.25- B*). The implications of the afore-mentioned pyrite textures for the growth history of the pyrite are discussed in the interpretation section of this chapter.

Hematite was observed both within the veins and in the altered wall rock (*Table V.17*). It occurs as inclusions in pyrite, as staining on pyrite rims and along fractures within pyrite, as partial replacement of chromite and as pseudomorphs after pyrite (*Plate V.25- L*).



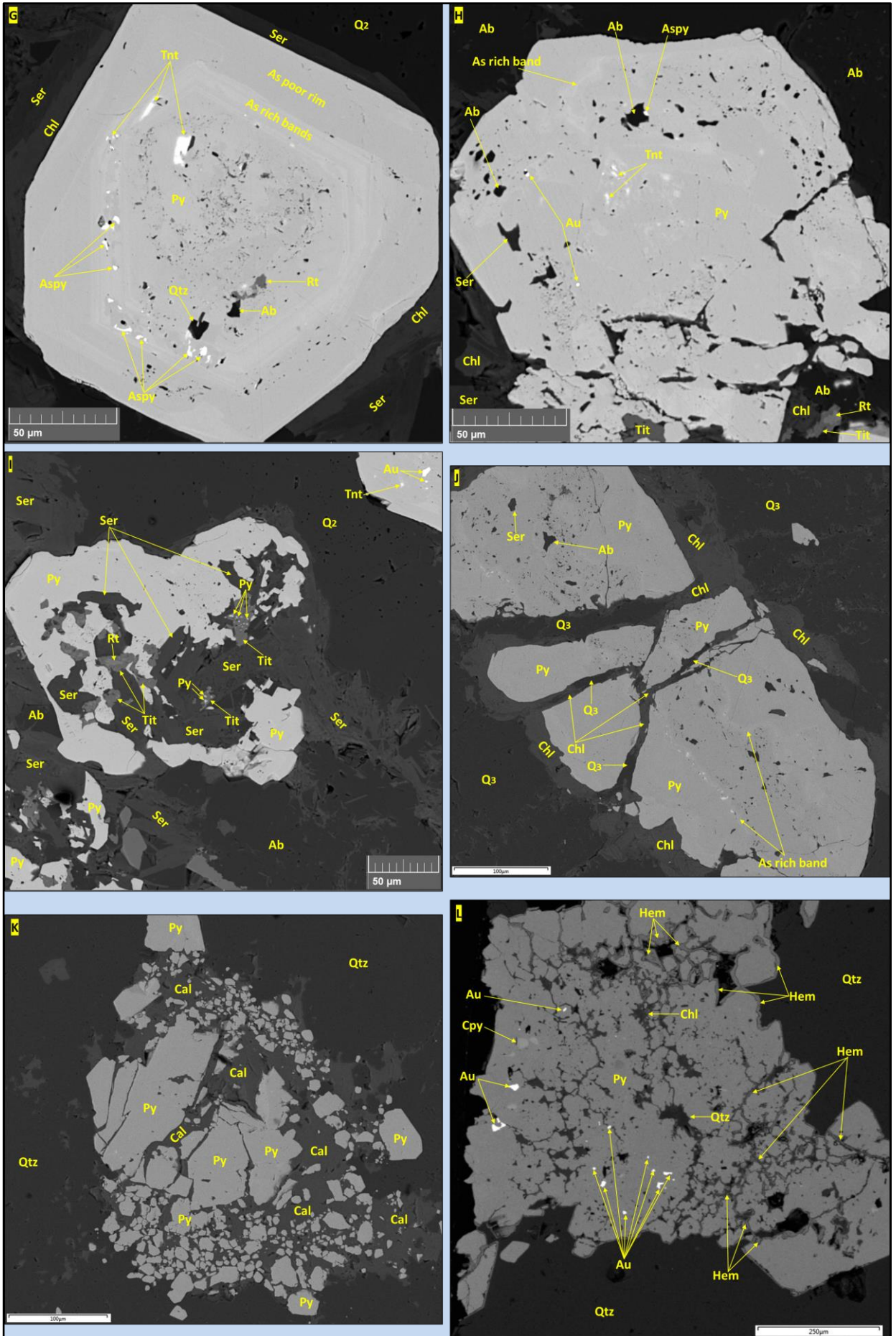




**Plate V.25 (previous two pages)** – Representative images of different alteration and ore minerals observed in the Deer Cove samples: **A to D** and **G to N** - BSE images; **E & F** - microscope images (cross polarised light); **A** – Rutile patches composed of both coarse and fine-grained crystals in a sericitized ground mass, **note** the brecciation and consumption of Rt, Ab, and Q<sub>1</sub> by Ser, section DC5; **B** – Fine-grained titanite crystals in sericitized ground mass, **note1** the fine grained inclusions from the Py crystals are Tit, **note2** the bending of the ground mass around the curved Py crystal and the associated fringe (Chl-Qtz), and the roughly circular inclusion pattern within the Py, section DC4; **C** - Rutile (central parts, light grey) replaced by Tit (on borders, darker grey), **note** the presence of Cal around Tit, section DC5; **D** – Coarse-grained Tit crystals brecciated and consumed by Ser, section DC5; **E** - Dolomite vein with multiple opening domains, some infilled by Chl; **E** - Calcite overgrowing fibrous quartz within Py fringes, **note** the different orientations of the Cal crystals, the presence of Chl overgrowing both Cal and Qtz, and the Cpy within the fringe zone, section GC60; **G** – Oscillatory zoned euhedral Py crystal with inclusion-rich core and inclusion-poor rims defined by As-rich (thin and light) and As-poor bands (thick), note the Aspy, Tnt, Qtz, Ab, and Rt inclusions; **H** – Py crystal with multiple inclusion rich domains hosted in an inclusion-free matrix, **note** the presence of Aspy, Tnt, and of the Au blebs in the inclusion-rich areas; **I** – Consumed Py by Ser and Tit, **note** the Au and tnt inclusions in Py; **G, H, I** – section DC3; **J** – Brecciated Py crystal by Chl-Q<sub>3</sub> veins, section DC2; **K** - Brecciated Py aggregate by Cal, section DC2; Brecciation and consumption of Py by Ser and Tit; **L** – Hematite staining along fractures in Py and on Py rims, note the Au and Cpy inclusions in Py, section DCD1.

#### **V.1.5.4. Mineralisation**

The main ore minerals observed in the Deer Cove samples are native gold, chalcopyrite, tennantite and arsenopyrite. Minor amounts of barite and trace amounts of scheelite, galena, and sphalerite are common. Detailed characterisation of the gold grains is provided below, whereas summarised descriptions for all the aforementioned minerals can be found in **Table V.19**. Representative images are presented in **Plate V.25– F, G, H, I, J, M** and in **Plate V.26**.

The gold was observed free, as fine to coarse-grained (from a few  $\mu\text{m}$  up to  $150 \times 100 \mu\text{m}$ ), irregular to rounded particles in Q<sub>1</sub> and Q<sub>2</sub>, in calcite veinlets and patches, in the sericite ground mass, and, in and between pyrite crystals along chlorite-sericite-calcite-Q<sub>3</sub> veins that brecciate the pyrite (**Plate V.26– A, B**). It also occurs as small (mostly  $<10 \mu\text{m}$ ), subrounded to rounded inclusions in pyrite, in both the inclusion rich and poor domains, and along the arsenic rich bands (**Plate V.25– I, L, M**). Gold inclusions in chalcopyrite were also seen (**Plate V.26– C**).

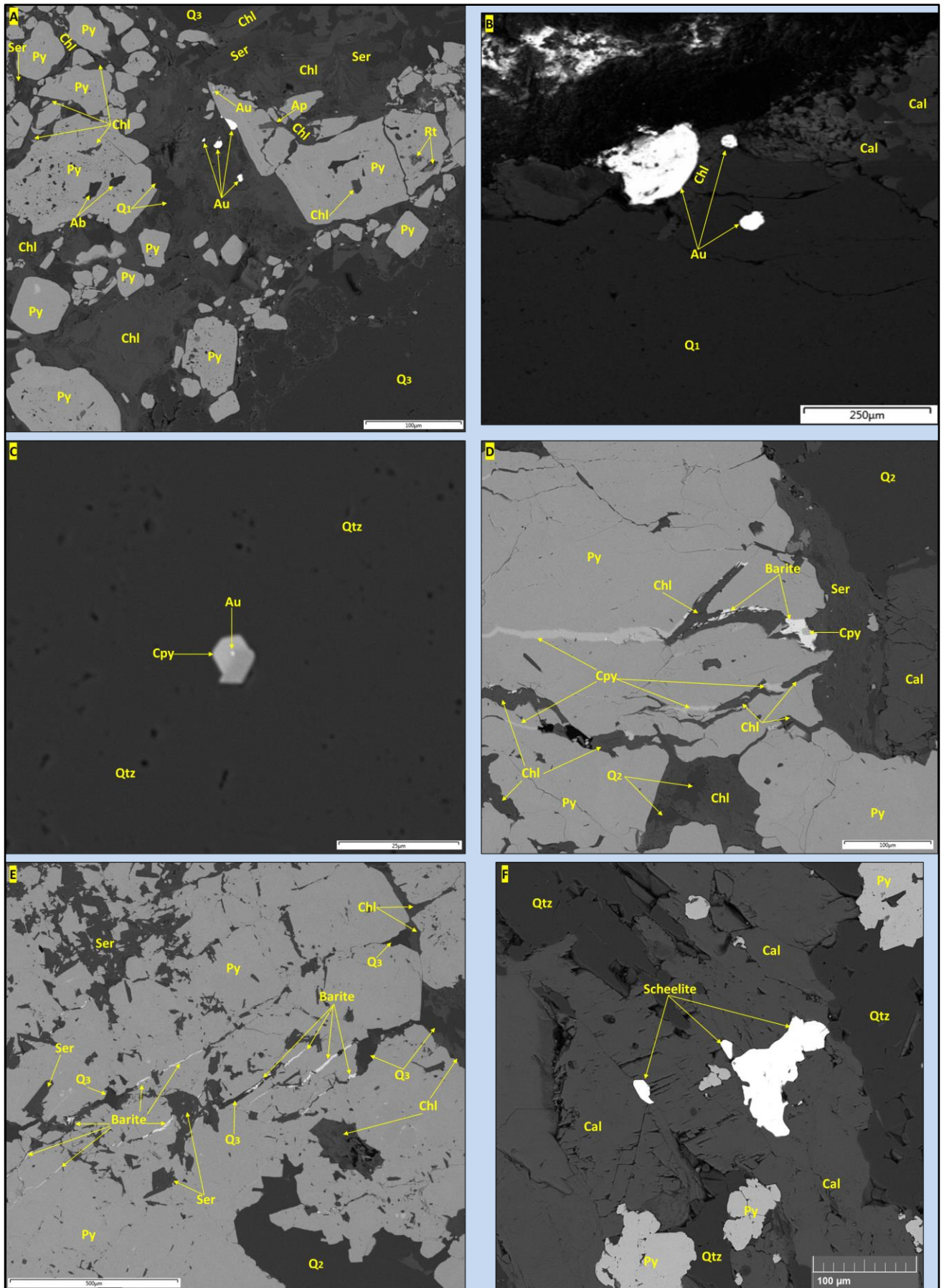


**Plate V.26 (previous page)** – Representative images of different alteration and ore minerals observed in the Deer Cove samples: **A** to **F** - BSE images; **A** – Brecciated Py crystals by chlorite and sericite, **note** the free coarse-grained Au grains, section DC2; **B** – Free, coarse-grained Au grains in Q<sub>1</sub> and between Q<sub>1</sub> and Chl, section DCD1; **C** – Au inclusion in Cpy, section DC2; **D** – Pyrite brecciated by Chl veins, note the presence of Cpy and barite along the Chl veins; **E** – Pyrite brecciated by Q<sub>3</sub>-Chl veins and by Ser patches and veins, **note** the Ser crosscuts the Q<sub>3</sub> veins, and the presence of barite along the Q<sub>3</sub> veins; **D, E** – section DC5; **F** – Coarse-grained scheelite in calcite patches, section DC4.

**Table V.19** – Summary characteristics of the ore minerals from the Deer Cove prospect.

Mineral	Occurrence, Morphology
Au	Free as irregular to rounded grains in: Q <sub>1</sub> , Q <sub>2</sub> , calcite veinlets and patches, sericite; free between and within pyrite crystals along chlorite-calcite-Q <sub>3</sub> veins that brecciate the pyrite; as subrounded to rounded inclusions in pyrite and chalcopryrite; fine-grained in Py (usually < 10 µm) and coarse-grained when free (up to 150x100 µm); <b>Plate V.25– I, L, M; Plate V.26– A, B, C</b>
Cpy	Inclusions in the py crystals; free in the quartz-calcite-chlorite pyrite fringes; free in the calcite veins and patches; free in quartz (Q <sub>1</sub> , Q <sub>2</sub> ) and in sericite; free at the interface of pyrite crystals and as wires along chlorite-calcite-Q <sub>3</sub> veins that brecciate the Py; vary in size from a few microns (usually in pyrite) up to a few hundred µm along the Cal-Chl-Q <sub>3</sub> veinlets; <b>Plate V.25– D, F; Plate V.26– C, D</b>
Aspy	As thin bands that define euhedral growth zones in pyrite, and as small (<30 µm) irregular to subhedral inclusions in Py; <b>Plate V.25– G, H</b>
Tnt	Occurs as small (<20 µm), irregular inclusions in pyrite, usually in the inclusion rich domains in association with chalcopryrite and arsenopyrite; <b>Plate V.25– G, H</b>
Barite	Minor* amounts (compared to the previously described deposits is more abundant); occurs as wires and irregular grains along calcite-chlorite-quartz <sub>3</sub> veinlets that brecciate pyrite and free in the sericite ground mass and at the interface of calcite and Q <sub>2</sub> -Q <sub>3</sub> crystals; <b>Plate V.26– F</b>
Scheelite	Trace** amounts, fine to coarse-grained (10 up to 100x100 µm), seen free in calcite, sericite, and chlorite; has inclusions of titanite and pyrite
Gn	Trace*** amounts, small grains (<10 µm) free in calcite and quartz and inclusions in pyrite
Sph	Trace*** amounts, small grains (<10 µm) inclusions in pyrite

\*minor = observed in all sections but with a low frequency (2 to 30 grains / per section)

\*\*trace = none, or <10 grains / studied thin section

### V.1.6. Geochemical signature of gold populations

This section characterises the geochemical signature of all gold populations based on its alloy composition. Details regarding methodology background and its aims for this study, together with descriptions of used samples, analytical procedures and data presentation can be found in the *Methodology chapter (III)*. The raw data is provided in *Appendix III*. Summarized descriptions related to the gold setting (including its particle size and morphology) in each of the studied sites, can be found in *Table V.4, Table V.8, Table V.11, Table V.15, and Table V.18*.

#### V.1.6.1. Comparison of in-situ gold particles

The compositional differences between the gold that occurs as inclusions within pyrite (termed below *inclusion Au*) and the one that is free, either along fractures within and between pyrite crystals or in the altered ground mass (termed below as *free Au*), were evaluated through the alloy compositions of the in-situ gold particles (gold analysed directly in thin sections, *see Methodology chapter*). Within the Pine Cove and Argyle deposits, some of the gold that occurs as inclusions in pyrite is hosted within partially healed fractures (*Plate V.5 – K; Plate V.15– L*). This type of gold is here referred to as *annealed Au*. It is expected that if any differences exist between the inclusion, annealed, and the free gold, these will group on different regions of the Ag/Hg/Cu profiles in the cumulative percentile vs increasing Ag/Hg/Cu plots or will form clusters in the binary plots.

The Ag, Hg, and Cu contents of the analysed in-situ gold particles from Pine Cove, Argyle, and Romeo & Juliet, show a random distribution on all types of plots. Hence, in these sites no significant compositional differences were observed between the inclusion Au, the annealed Au, and the free Au (*Figure V.6– A, B, C*), except for two free Au particles in the Argyle deposit that show higher Cu contents compared to the other analysed particles (*Figure V.6 – D*). Moreover, the in-situ gold particles from Pine Cove and Romeo & Juliet distribute between the liberated gold particles, which suggest that similar particles were liberated during the sample preparation process and are represented within the liberated gold particle population.

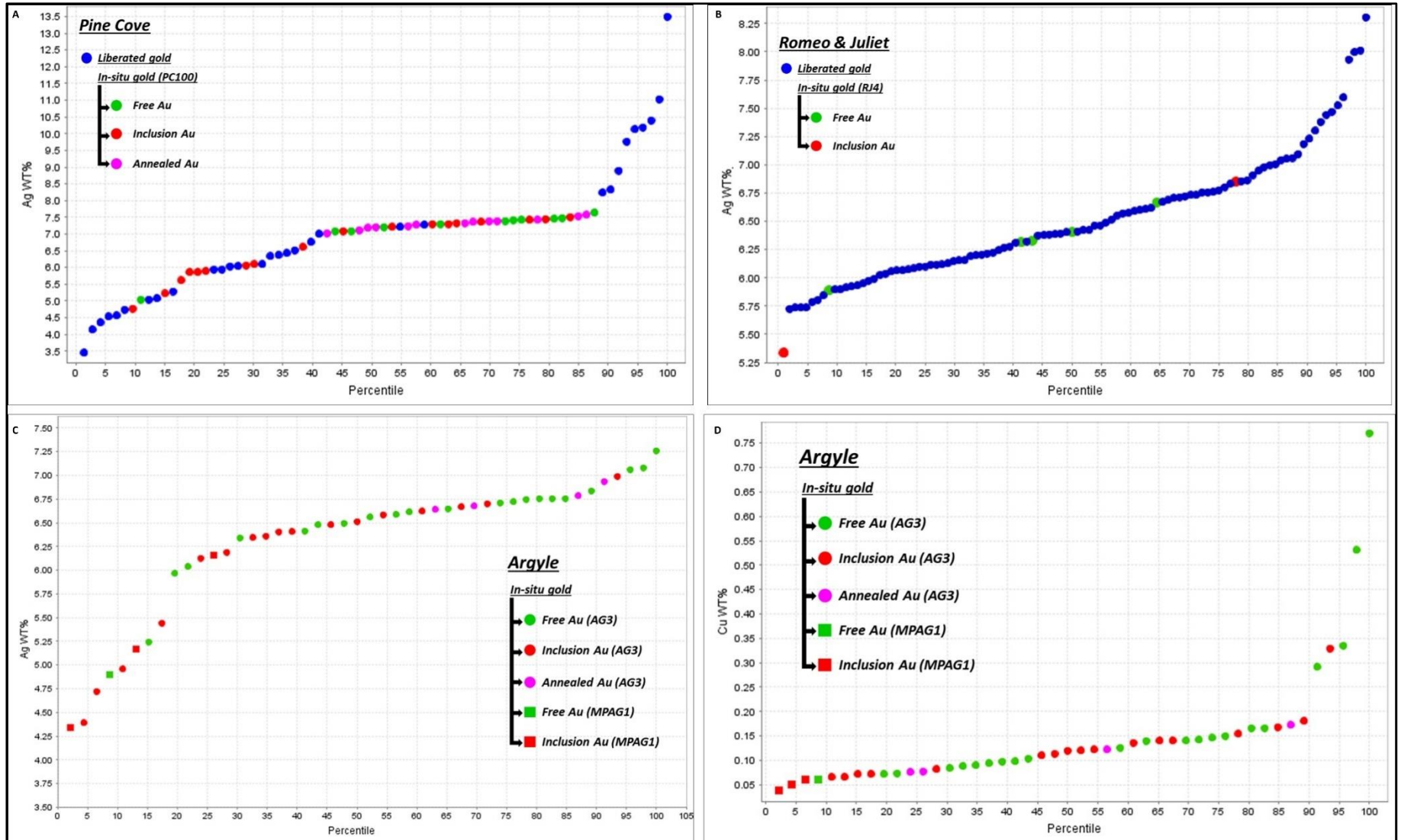


**Figure V.6** – Representative plots that show the random distribution of the inclusion, annealed, and free Au on the Ag or Cu profiles in the Pine Cove (A), Romeo & Juliet (B) and Argyle (C, D) deposits/prospects: **note** the two free Au grains with high Cu content in Argyle (D). The codes in parentheses represent the name of the section from which the in-situ gold particles were analysed.

In the in-situ gold particles from Stog'er Tight, some differences have been observed between the Ag and Cu concentrations of the inclusion Au and of the free Au (*Figure V.7*). A higher Cu content was recorded in some of the free Au particles that occur along the late quartz<sub>3</sub>-calcite-chlorite-chalcopyrite veinlets that brecciate pyrite masses in sample BN215 (*Plate V.11 – D, E*) (*Figure V.7- B*). Free gold that occurs along quartz<sub>3</sub>-calcite-chlorite veinlets but with no associated chalcopyrite was also analysed in section SOZ2 (*Plate V.10– C; V.7 – A*). In this section, the free Au shows low Cu contents same as the inclusion Au, but slightly higher Ag values compared to the latter (*Figure V.7 – A, B*).

At Deer Cove, some differences between the inclusion Au and the free Au can be highlighted based on their Ag and Hg contents (*Figure V.8*). All the inclusion Au particles from section DCD1 (*Plate V.25– L*) show a small range in their Ag concentrations, between 8 and 9 wt%, whereas the free Au particles from section DC2 (*Plate V.26– A*) show slightly higher Ag concentrations that range from 10.5 to 13 wt% (*Figure V.8*). Two inclusion Au particles from DC2 were also analysed and show very distinct Ag contents, ~6 and ~13 wt% (*Figure V.8*). The inclusion Au from DCD1 covers a gap in the Ag profile of the liberated gold (*Figure V.8 - A*). This means that this type of gold was not recovered during the extraction process, probably due to its small size ~ 10 µm, and so is underrepresented within the liberated gold population.

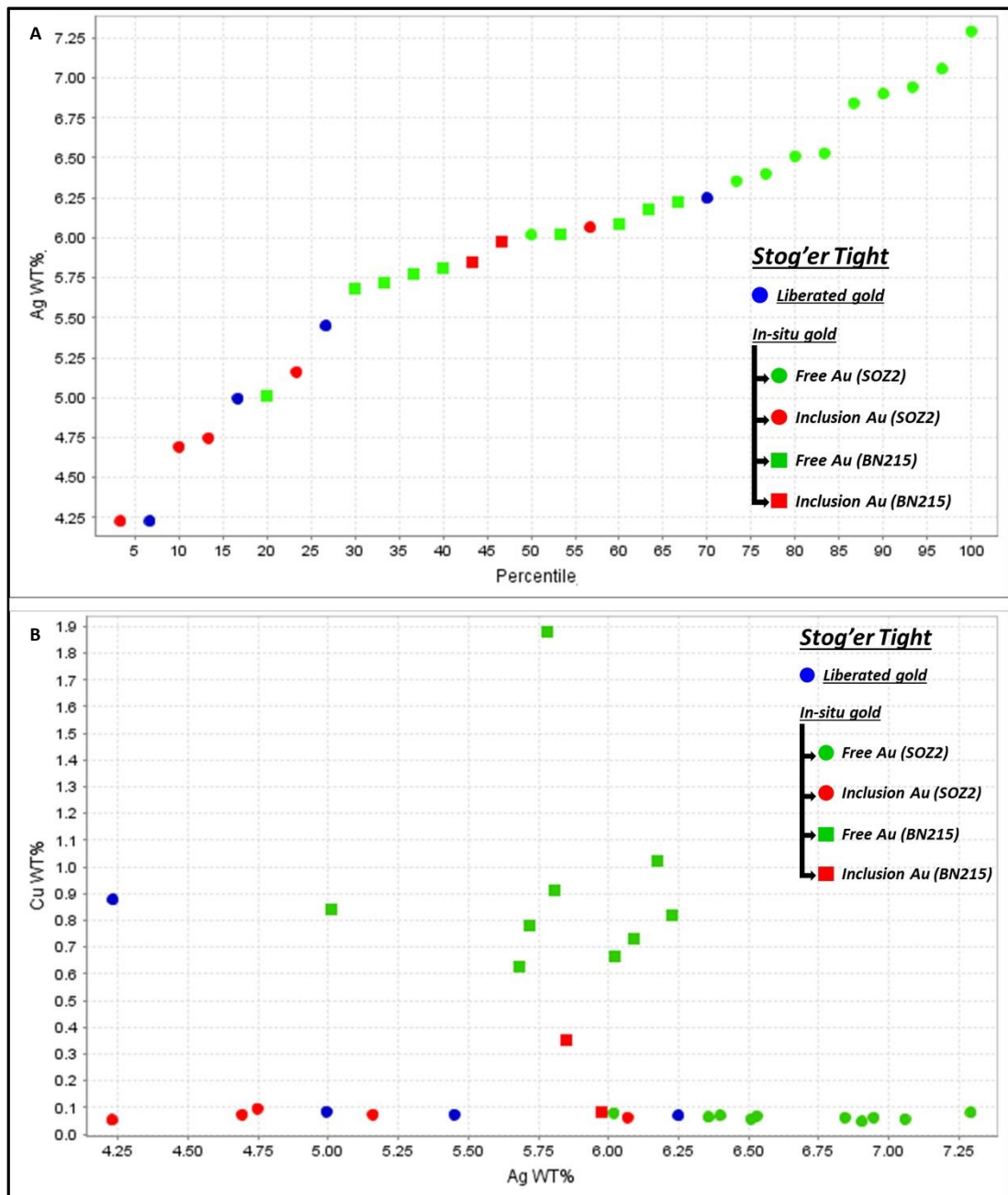


**Figure V.7** – Representative plots that show differences in the Ag and Cu concentrations of the inclusion Au and the free Au from Stog'er Tight: **A** – Cumulative percentile vs increasing Ag content plot; **B** - Ag-Cu binary plot; **note** the free Au from section SO22 shows slightly higher Ag content and the same amounts of Cu compared to the inclusion Au from the same section, whereas the free Au from section BN215 shows higher Cu contents compared to the inclusion Au from both SO22 and BN215 sections; the codes in parentheses represent the name of the section from which the in-situ gold particles were analysed.

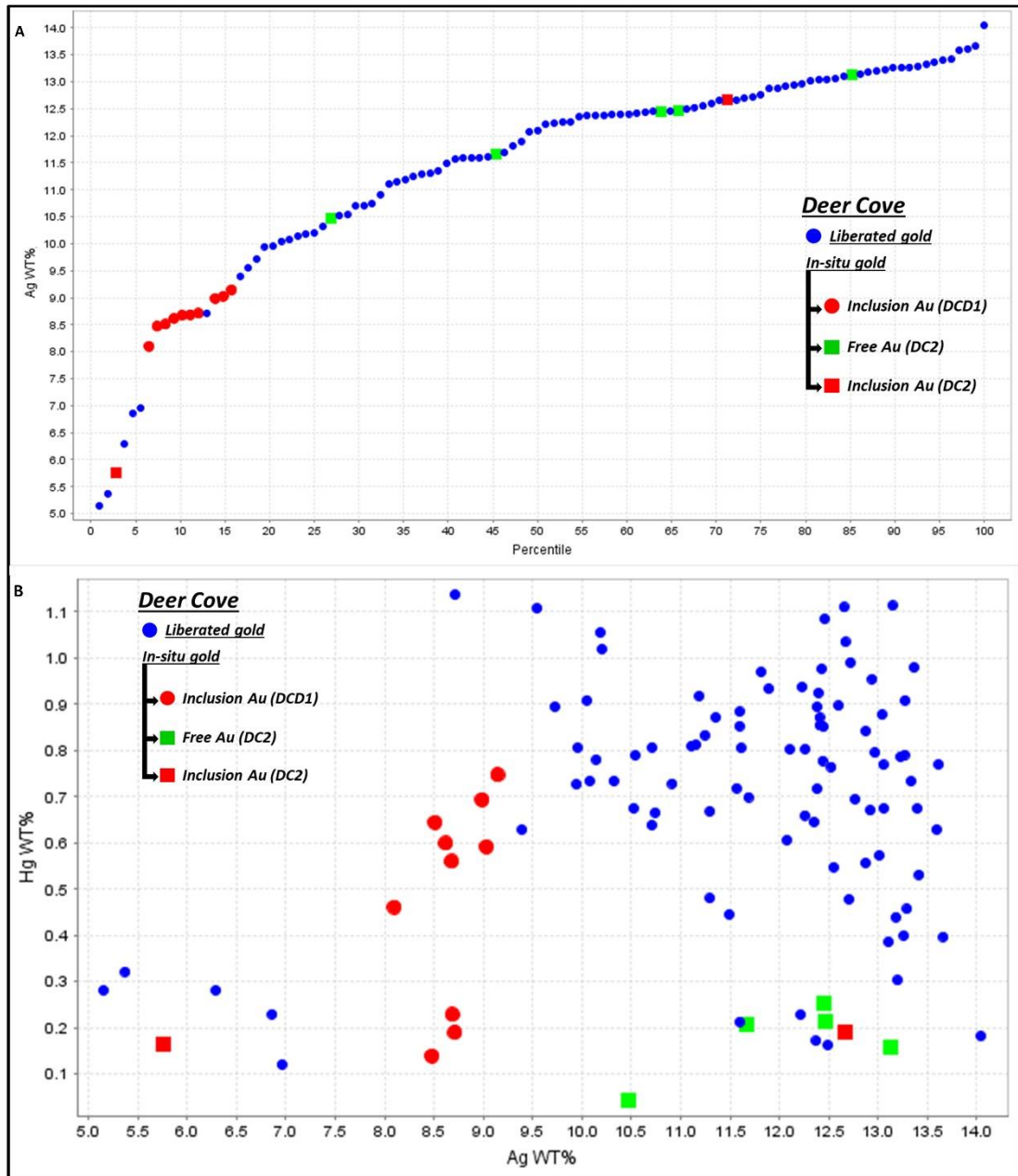


**Figure V.8** – Representative plots that show some differences in the Ag and Hg concentrations of the inclusion Au and the free Au from Deer Cove: **A** – Cumulative percentile vs increasing Ag content plot; **B** – Ag-Hg binary plot; **note** the free Au from section DC2 which shows slightly higher Ag content compared to the inclusion Au from section DCD1 (**A**, **B**) and 60% of the inclusion Au particles from section DCD1 show higher Hg contents compared to the rest of the analysed in-situ gold particles; the codes in parentheses represent the name of the section from which the in-situ gold particles were analysed (**B**).



#### *V.1.6.2. Description and comparison of gold populations by deposit/prospect*

The Ag, Hg, and Cu concentrations of the Au-Ag alloy from all the studied deposits/prospects are presented in **Figure V.9**. In **Figure V.9- A**, the Ag profiles from Pine Cove, Stog'er Tight, Argyle, and Romeo & Juliet are almost the same (shallowly inclined to horizontal), ranging between 4 and 8 wt% in all locations, except for 12% of the particles from Pine Cove that show higher Ag values, up to 13 wt%. In contrast, the Ag profile for the Deer Cove population shows a more convex shape due to the gradual increase in the Ag concentration from 5 to 14 wt% (**Figure V.9- A**).

The Hg content can be evaluated in **Figure V.9 - B**. The Hg profiles from Argyle, Stog'er Tight, Pine Cove and Romeo & Juliet look alike, most of the gold particles (70%, 90%, 71%, and 76%, respectively) showing values above the detection limit (LOD). At Argyle no gold particles contain Hg above the quantifiable limit (LQD), whereas 10%, 11% and, 13% of the gold particles from Stog'er Tight, Pine Cove, and Romeo & Juliet, respectively, have Hg contents above the LQD. In contrast to the rest of the deposits, the gold from Deer Cove shows higher Hg concentrations with 81% of the gold particles recording Hg values above the LQD.

The gold particles from all the analysed gold populations show Cu contents above the LOD, with 77%, 87%, 96%, 90%, and 41% of the gold particles from Pine Cove, Stog'et Tight, Argyle, Romeo & Juliet, and Deer Cove, respectively, having Cu concentrations above the LQD (**Figure V.9 - C**). Significant breaks in the slopes of the Stog'er Tight and Romeo & Julitet gold populations can be observed at 0.64 wt% and 7.47 wt%, respectively. 10% of the gold particles from Argyle also show an increase in the Cu content at ~0.3 wt% (**Figure V.9 - C**).

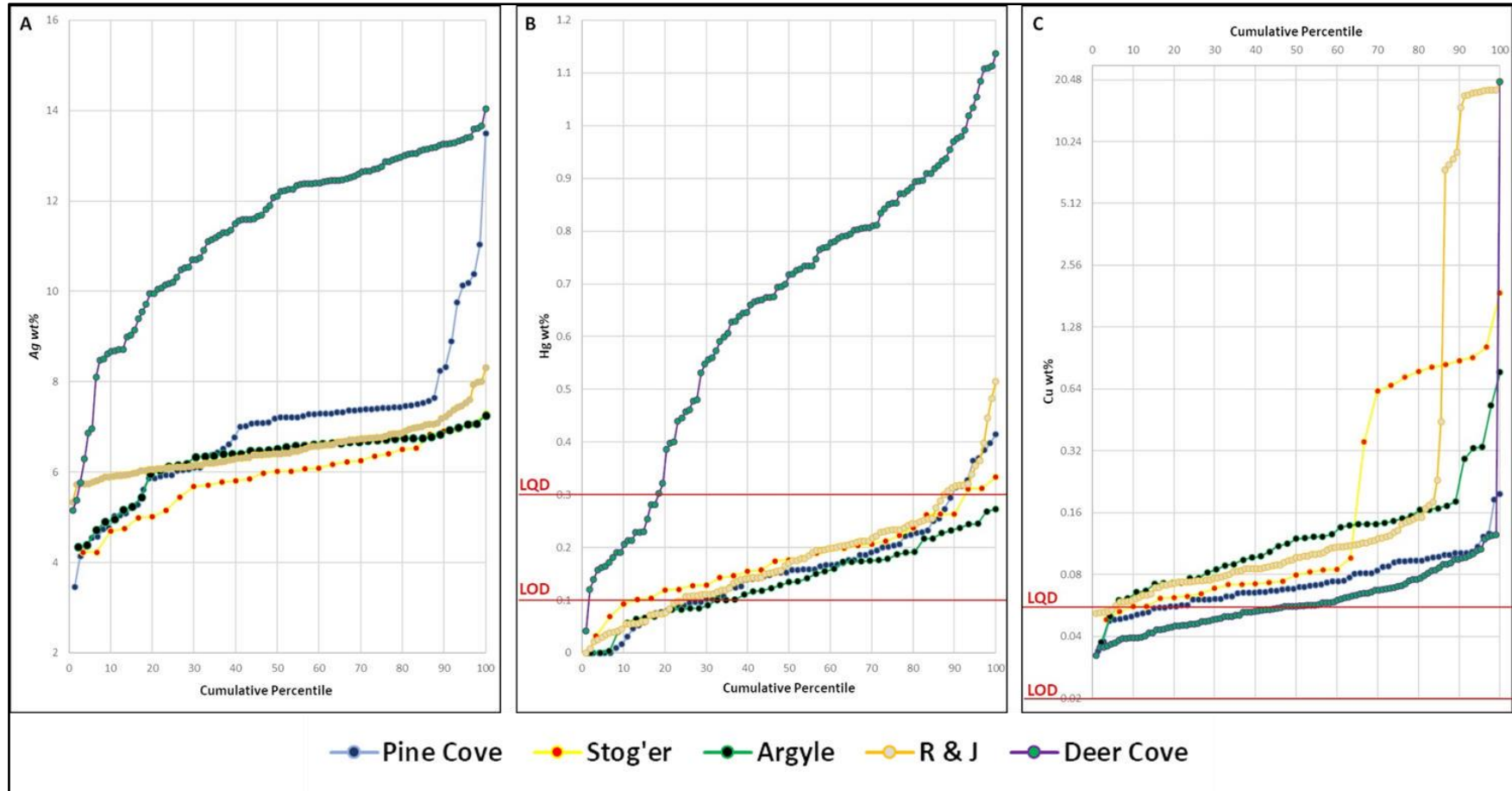


**Figure V.9** – Plots between the cumulative percentile and the increasing values of Ag (A), Hg (B), and Cu (C) for all the studied deposits.

### V.1.6.3. Gold types

Four gold types with different chemical signatures can be separated based on the Ag, Hg, and Cu concentrations of the analysed gold particles (**Figure V.10- B**). The compositional ranges of each gold type together with details regarding their occurrence are presented in **Table V.20**.

**Table V.20** – Characteristics of gold types identified in the studied gold populations

Au types	Ag(wt%)	Hg(wt%)	Cu(wt%)	Occurrence
<b>Type I</b>	<8	<0.55 (majority of gold particles below LQD)	<0.2	All gold occurrences in both in-situ (inclusion, annealed, and free) and in the liberated gold
<b>Type II</b>	8 to 14	0 to 1.15 (majority of gold particles above LQD)	<0.15	Deer Cove (in both in-situ and liberated gold) and in Pine Cove (only in some of the liberated gold particles)
<b>Type III</b>	3.5 to 8	0 to 0.3	0.5 to 2	Identified in the in-situ gold particles (free Au) from the Stog'er Tight and Argyle deposits
<b>Type IV</b>	6 to 8	0 to 0.3	7 to 20	Romeo & Juliet in some of the liberated gold particles

On the Hg-Ag plot, the data clusters in two main compositional fields that correspond to low Ag - low Hg contents (*CF1*) and high Ag with low to high Hg contents (*CF2*) (**Figure V.10 - A**). *CF1* comprises most gold particles from Pine Cove, a few particles from Deer Cove, and all the gold particles from Stog'er Tight, Argyle, and Romeo & Juliet populations. *CF2* is composed by most of the gold particles from Deer Cove and a few from Pine Cove. No clear covariance is visible in neither of the two compositional fields (**Figure V.10- A**). On the Cu-Ag plot, the data clusters in four compositional fields which define the four gold types (**Table V.20; Figure V.10 – B**). The gold particles clustered in *CF1* on the Hg-Ag plot correspond to three types of gold (Type1, Type3, and Type4) on the Ag-Cu plot, whereas the gold particles from *CF2* are representative for the Type2 gold (**Figure V.10 – A, B**).

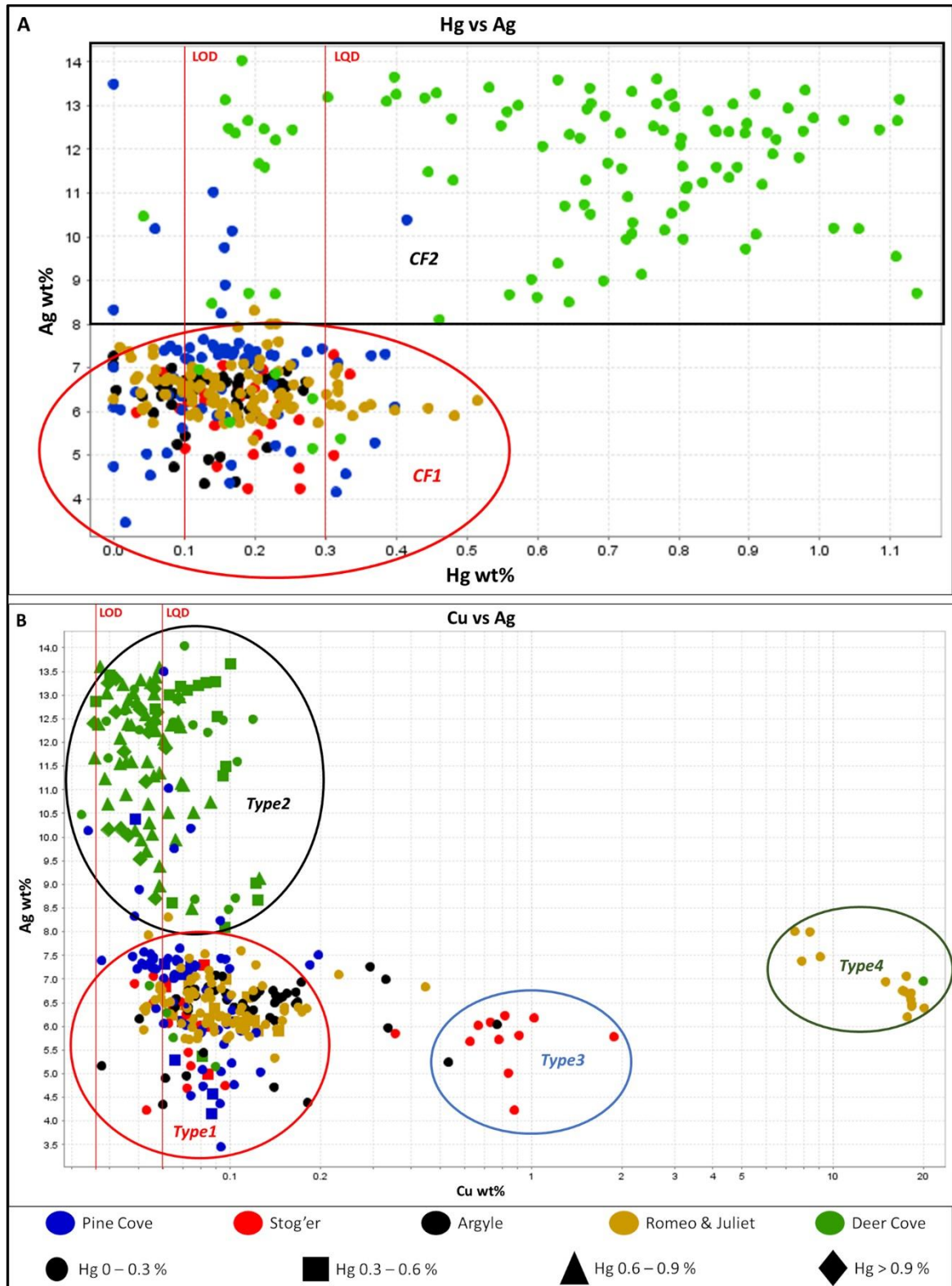


**Figure V.10** – Hg vs Ag (A) and Cu vs Ag (B) binary plots for gold particles from all the studied gold populations; the color coding is representative for the gold populations for both A & B, whereas the shapes in (B) represent the Hg content in a particular gold particle; see text and *Table V.20* for discussion about the highlighted compositional fields and the gold types; note the logarithmic scale for Cu in image B.

Most gold particles from Pine Cove (90%), Stog'er Tight (63%), Argyle (91%), Romeo & Juliet (85%) and a few particles from Deer Cove (6%) show the chemical characteristics of gold TypeI (**Table V.20; Figure V.10 - B**). From all deposits, both liberated and in-situ (inclusion, annealed, and free) gold particles fall in this category.

The majority of Deer Cove gold particles (94%) show a distinct signature characteristic of gold TypeII (**Figure V.10-B**). From the inclusion gold, both in-situ and free gold particles fall in this category. A few gold particles (12%) from the Pine Cove deposit also show the characteristics of gold TypeII. These particles are from the liberated gold, so their place in the paragenetic sequence is unknown.

Gold particles that show a TypeIII chemical signature were recorded only within the Stog'er Tight (37% of particles) and Argyle (2 particles) gold populations (**Figure V.10 - B**). These particles were analysed in-situ (section BN215 – **Figure V.7- B** and section AG3 – **Figure V.6 - C**) and correspond to free gold hosted by quartz<sub>3</sub>-chlorite-calcite-chalcopyrite veinlets.

Gold particles that show the TypeIV chemical signature pertain to Romeo & Juliet gold population (**Table V.20; Figure V.10- B**). These particles are from the liberated gold suite, so their in-situ characteristics are unknown. Interestingly, the majority of these particles show a particular sub-spheric shape.

#### V.1.6.4. Mineral inclusions

Mineral inclusions were observed within gold particles from all the studied deposits/prospects, but these are in general scarce. provides a list of the inclusions identified in both the liberated and the in-situ gold particles from each of the studied sites. Further discussion related to the identified mineral inclusion suites are presented in the interpretation section of this chapter.

**Table V.21 (below)** – Mineral inclusion species identified in both the in-situ and liberated gold particles from all the studied localities. The number of a specific inclusion identified in each site is marked in parentheses.

Deposit	Liberated gold	In-situ gold
Pine Cove	Py (5); Cpy (2); undifferentiated Bi telluride (1); Rt (1)	Py (2)
Stog'er Tight	Py (1)	Not observed
Argyle	Not applicable	Aspy (1)
Romeo & Juliet	Py (5); Ank (2); undifferentiated FeNiCoAsS (1)	Py (1)
Deer Cove	Py (5); Cal (1)	Not observed

## V.2. Interpretations

This section provides interpretations and assumptions about the relative timing of the studied deposits, to their vein and mineral paragenetic evolution, and to the fluid phases involved in their formation based on the structural, mineralogical, and geochemical observations listed in the first part of this chapter. These are presented in a compare-contrast manner to highlight the factors that led to the formation of gold mineralisation at a district scale.

### V.2.1. Vein development and relative timing

The relative timing of the studied gold occurrences is here evaluated based on the interaction between the mineralised vein sets and the local structural features observed in each of the studied sites (*Figure V.11*). The Pine Cove, Stog'er Tight, and the Argyle deposits show many similarities and thus, interpretations for these deposits are provided together, whereas the Romeo & Juliet and the Deer Cove prospects are assessed separately.

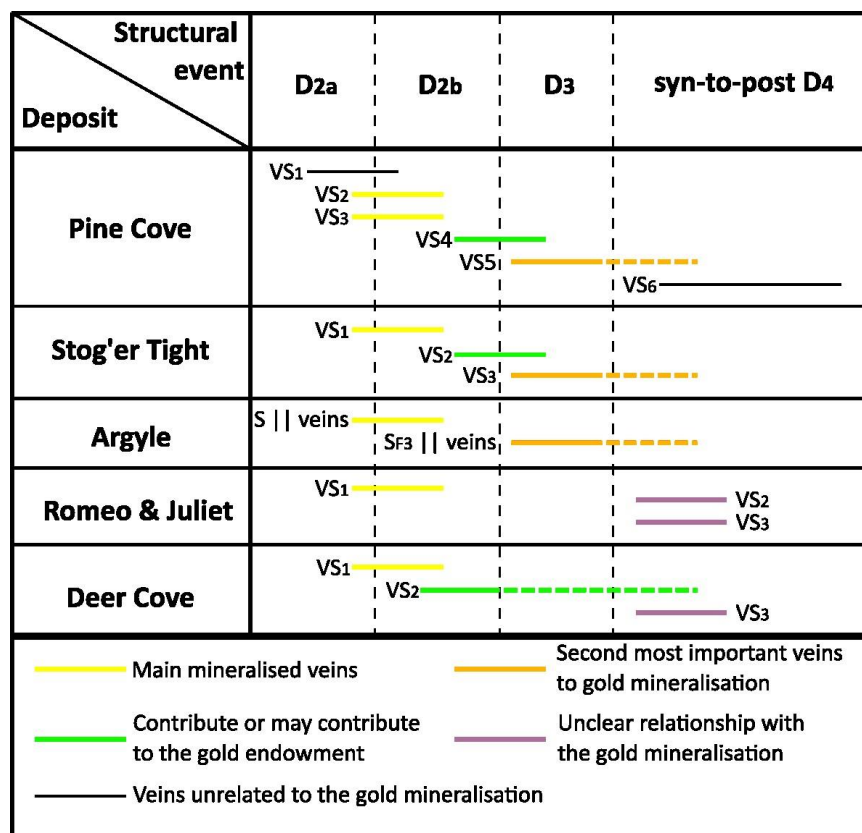


*Figure V.11* – The relative timing of the vein sets observed in each of the studied gold deposits/prospects. S || = foliation parallel; SF3 || = veins parallel to the axial planes of F3 folds.

### *V.2.1.1. Pine Cove, Stog'er Tight, and Argyle*

As presented in *section V.1.1.2*, VS<sub>1</sub> veins from the Pine Cove deposit are affected by all the post D<sub>2a</sub> structures, do not host any mineralisation within, nor around them, and are not associated to any alteration selvages (*Table V.1; Plate V.1 – D*). Hence, it is inferred that these veins are unrelated to the gold mineralisation and that these formed syn-D<sub>2a</sub> to early D<sub>2b</sub> deformational events (*Figure V.11*).

The VS<sub>2</sub> and VS<sub>3</sub> vein sets from the Pine Cove deposits, show textural differences (breccia vs sheared and laminated) but similar orientations and alteration halos (*Figure V.1– D*) (*Table V.1*). The textural differences between these two vein sets can be explained by the rheological properties of the lithologies that host them. In stratigraphic units with heterogenous lithological intervals each layer will have different failure and mechanical properties and even variable fluid pressures (Bons et al., 2012). It is common that shear and extensional fractures (and if filled, veins) which combine into stockwork and breccia domains to occur irrespective to the anisotropy plane in the more competent/massive layers. Also, in the softer and foliated rocks mixed extensional-shear fractures usually develop parallel to foliation or at the contact between competent-incompetent layers if the angle between  $\sigma_1$  and the anisotropy plane is below 60° (Robert & Poulsen, 2001; Bons et al., 2012). These features were observed at Pine Cove, where the breccia type veins (VS<sub>2</sub>) occur in the massive rocks, pillow basalts and greywackes, whereas the sheared and laminated veins (VS<sub>3</sub>) occur between soft and hard lithologies or parallel to the foliation in tuffs and in mudstone/siltstone units. Thereby, even though the VS<sub>2</sub> and VS<sub>3</sub> are described separately, these are interpreted to be genetically linked, being “sub-types” of the same vein set.

The vein sets VS<sub>2</sub> and VS<sub>3</sub> from the Pine Cove deposit are considered correlative to VS<sub>1</sub> from the Stog'er Tight deposit and to the foliation-parallel veins from the Argyle deposit. This is based on the following observations: the veins have similar orientations, mineralogy, internal textures, alteration halos, and most of their volume is occupied by a second quartz generation which in CL shows the same characteristics for all deposits (*Figure V.1– D & Figure V.2 – C; Table V.1, Table V.3, Table V.5, Table V.7, Table V.10*). These vein sets together with their associated disseminated wall-rock mineralisation and proximal alteration selvages constitute the bulk of the ore volume and therefore, are considered the main veins related to the

formation of the deposits. These vein sets are crosscut by most of the other vein sets (*Table V.1 & Table V.5*) and for simplification, henceforward these will be referred to as “early veins”.

The early veins formed pre-to-syn the  $D_{2b}$  structural event that affected the entire Point Rousse Complex, but before the latest movements associated to this stage have ceased (*Figure IV.9 – B, C; Figure V.11*). This interpretation is supported by the following aspects: i) the veins are parallel to subparallel to the  $S_{2a}$  foliation fabric but locally crosscut this fabric (*Plate V.1 – B, D, F*); ii) in high  $D_{2b}$  strain domains the veins are transposed into parallelism to the composite  $S_{2a-2b}$  foliation; iii) the veins are folded by the  $F_{2b}$  folds (*Plate V.1 – H*); iv) the  $D_{2b}$  faults host and also crosscut the veins; and v) the veins are affected by all the post- $D_{2b}$  structural features (*Plate V.1 – I, J, R; Plate V.6 – G, H; Plate V.12 - A*). These interpretations and observations agree with previous conclusions of Pitman et al. (2020) that most of the mineralisation was formed during the  $D_2$  structural phase. The vein textures (laminated, sheared, breccia/stockwork), their parallelism to the bedding and to the  $S_{2a}$  foliation planes, together with the orientation of the  $L_2$  stretching mineral lineation and associated striations normal to the veins and to the  $F_{2b}$  hinges, suggest that cyclic periods of high fluid pressure combined with layer-parallel flexural slip during  $D_{2b}$  folding enabled fluid flow and vein formation (*Figure V.12*). The shallow dipping veins observed in the Pine Cove deposit (*Plate V.1 – P, Q*) may have formed once the limbs of the  $F_{2b}$  folds achieved high dips and the flexural slip along layers have ceased (*Figure V.12*).

The presence of veins along both the  $S_{2b}$  cleavage and  $D_{2b}$  faults suggest that fluid flow was facilitated by these structures also. However, the timing of the veins hosted by the  $D_{2b}$  structures may have not been coeval across all deposits. In the Pine Cove area, where high  $D_{2b}$  strain was reached, these veins are transposed into parallelism with the composite  $S_{2a-2b}$  foliation, are mineralised and associated to proximal alteration halos. This suggests that in this locality the veins are syn- $D_{2b}$  and they have formed during the tightening of the  $F_{2b}$  folds. Thus, these are also catalogued as early veins (*Fig. V.12*). In the Stog’er Tight area, the  $VS_2$  veins are hosted by  $D_{2b}$  faults and locally folded by the  $F_3$  folds. These veins cut the early veins and the proximal alteration halos. Thereby, it is inferred that the  $VS_2$  veins from Stog’er Tight are slightly younger than the early veins. These veins could have developed either late



in the D<sub>2b</sub> event, or during the reactivation of the D<sub>2b</sub> reverse faults as normal faults early in the evolution of D<sub>3</sub> event before the formation of the F<sub>3</sub> folds (**Figure V.11**).

The timing of the VS<sub>4</sub> mineralised veins and tension gashes observed in the Pine Cove deposit is also seen as late D<sub>2b</sub> to early D<sub>3</sub> because these veins crosscut the composite S<sub>2a-2b</sub> foliation and are locally folded by the F<sub>3</sub> folds (**Figure V.11; Plate V.1–M, N; Table V.1**). Moreover, the steeply dipping to vertical nature of the veins/gashes combined with their syntaxial textures suggest a vertical orientation of the maximum compressional stress characteristic to the D<sub>3</sub> event (**Figure IV.12**). The steep veins observed in the high strain D<sub>3</sub> domains from the Stog'er Tight area show similar orientations and characteristics and so the same interpretation applies (**Plate V.6–G – box 1**).

The exact input of the VS<sub>2</sub> and VS<sub>4</sub> veins to the gold endowment in the Stog'er Tight and the Pine Cove deposits, respectively, cannot be assessed based on the available data. However, considering that pyrite and chalcopyrite occur within and around the veins suggest that these may have contributed to some degree to the gold mineralisation.

Vein set VS<sub>5</sub> from the Pine Cove deposit, VS<sub>3</sub> from the Stog'er Tight deposit, and the veins that are parallel to the F<sub>3</sub> axial cleavage in the Argyle deposit are considered equivalent, and their relative timing is interpreted as syn D<sub>3</sub> to early D<sub>4</sub> (**Figure V.11**). These interpretations are supported by the following observations: i) the veins crosscut both the S<sub>2a</sub> and the S<sub>2a-2b</sub> foliation fabrics; ii) occur subparallel or along the axial planes of the F<sub>3</sub> folds and along the D<sub>3</sub> extensional shears; iii) are affected by post-D<sub>3</sub> structural elements; and iv) display similar internal textures, mineral compositions, and associated alteration halos (**Figure V.1–D & Figure V.2 – C; Table V.1 & Table V.5; Plate V.1 – K, L, R and Plate V.6 – G, J**). In the high-grade zones, these veins host most of the observed gold and so, are considered the second most important veins that contribute to the gold endowment (see further interpretations related to paragenetic evolution). Multiple mechanisms can be inferred for the emplacement of these vein sets based on their textures and orientations: i) these formed as steep syntaxial veins during the early stages of D<sub>3</sub> and subsequently rotated by F<sub>3</sub> folds to a sub-horizontal position becoming sub-parallel to the F<sub>3</sub> axial planes; ii) vein emplacement was facilitated by high fluid pressures and fracture developed in the hinge zones of F<sub>3</sub> folds within most competent rocks (gabbro and pillow basalts)

during  $F_3$  folding; and iii) the veins were injected along the  $F_3$  axial planes during the early stages of  $D_4$  event but before the development of  $F_4$  folds. As presented above and in *chapter V*, both the  $D_2$  and  $D_3$  structural elements show signs of reactivation during the  $D_4$  structural event and all the pre-to-syn  $D_3$  veins are folded by  $F_4$  folds. Furthermore, the syn-to-post  $D_4$  south dipping faults form along, or at a low-angle to the  $F_3$  axial planes and  $D_3$  shears. Therefore, it is possible that subsequent fluid flow and mineral precipitation occurred along the above-mentioned veins during their brecciation and folding syn-to-post the  $D_4$  structural phase (**Figure V.11**; see further interpretations).

The  $VS_6$  veins from Pine Cove do not show any correspondent in the rest of the deposits and their lack of mineralisation and alteration suggest that these do not contribute to the gold endowment. These veins crosscut the early veins, the  $D_{2b}$  and the  $D_3$  structures and so, are interpreted as syn-to-post  $D_4$  (**Figure V.11**).

#### **V.2.1.2. Romeo & Juliet**

The veins from Juliet zone, termed here as  $VS_1$ , crosscut the  $S_{2a}$  foliation and are bordered and segmented by  $D_{2b}$  faults. Hence, the relative timing of this vein set is interpreted herein as pre-to-syn  $D_{2b}$  (**Fig. V.11**). As presented above, the Romeo & Juliet veins are subparallel to a regional-scale  $D_{2b}$  shear zone that strike from NNE to NE and dips moderately to steeply from WNW to NW. The genetic relationships between this shear zone and the veins are ambiguous because of poor field exposure. However, the overall morphology of the Juliet zone (multiple quartz lenses of various thickness with massive to laminated textures that dip steeply to ESE – SE) support the interpretations of Calon & Weick (1990). These authors inferred that the Romeo & Juliet veins represent a tension gash array emplaced in shear zone related dilatational sites formed in a competent lithological unit (pillow basalts).

The relative time of formation for the vein sets  $VS_2$  and  $VS_3$  is inferred herein as syn-to-post  $D_4$ . This is supported by their cross-cutting relationships with the  $S_{2a/2b}$  and  $VS_1$ , by their mutual cross-cutting relationships, and by their association with the syn-to-post  $D_4$  faults and shear zones (**Figure V.11**; **Table V.13**). The exact contribution of these veins for the gold mineralisation cannot be assessed based on the available data.

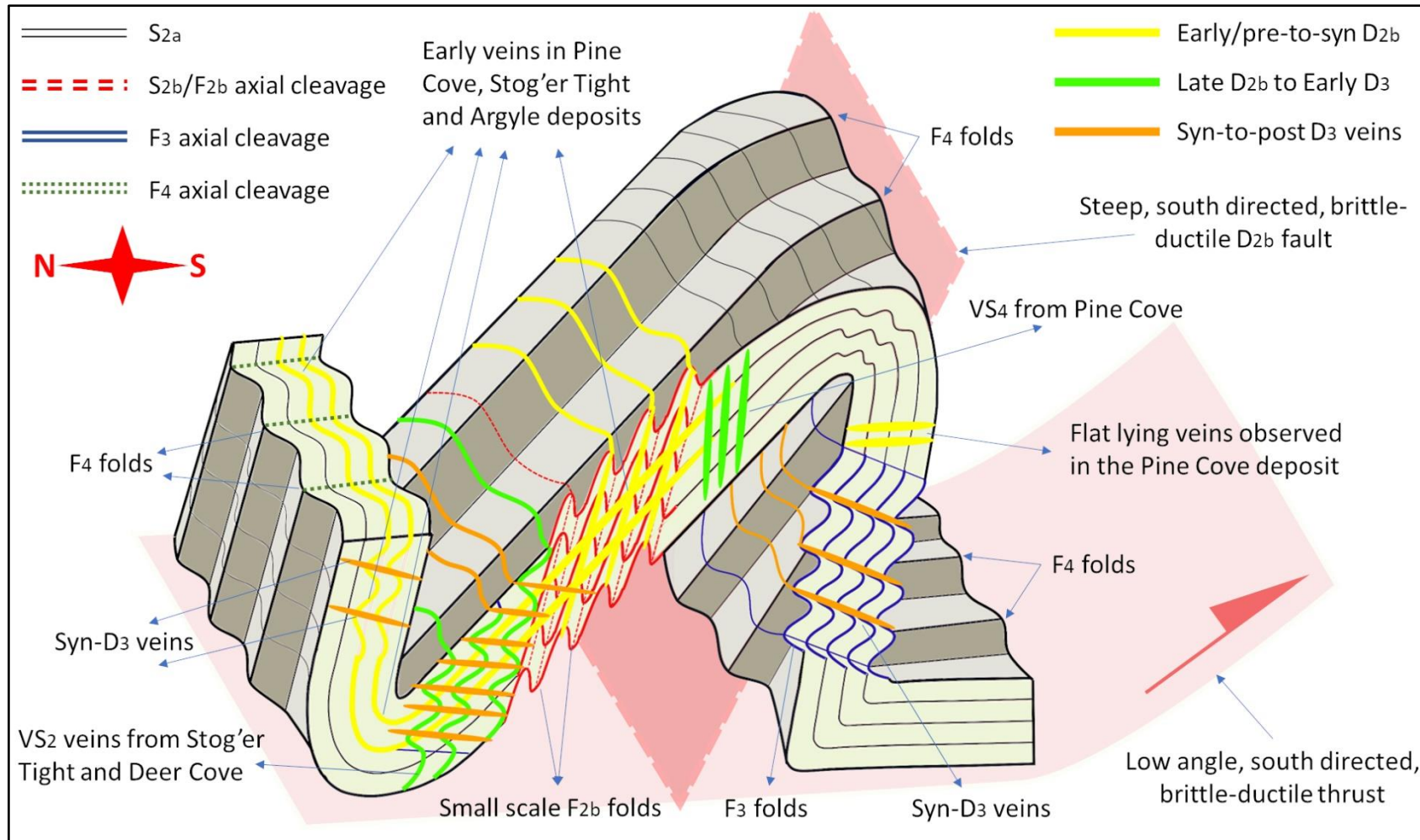


**Figure V.12** – 3D sketch diagram illustrating the overall relationships between the F<sub>2b</sub>, F<sub>3</sub>, and F<sub>4</sub> fold generations and some of the vein sets observed in the Pine Cove, Stog'er Tight, Argyle, and Deer Cove areas; **note** the relationships between the early veins (yellow) with the S<sub>2a</sub> and S<sub>2b</sub> foliations and their folding by F<sub>3</sub> and F<sub>4</sub> folds; **note** that the late D<sub>2b</sub> to early D<sub>3</sub> veins crosscut the early veins and are folded by F<sub>3</sub> and F<sub>4</sub> folds; **note** the formation of syn-to-post D<sub>3</sub> veins along the axial planes of F<sub>3</sub> folds and their folding by F<sub>4</sub> folds.

### V.2.1.3. Deer Cove

The relative age of the veins that compose the Main Zone of the Deer Cove prospect, termed here as VS<sub>1</sub>, is inferred to be pre-to-syn D<sub>2b</sub> based on their crosscutting relationships with both the S<sub>2a</sub> foliation and the D<sub>2b</sub> structures (**Figure V.11; Table V.17**). The orientation of the veins with respect to the Deer Cove fault (perpendicular to the E-W oriented segment) combined with their textures (**Fig. V.5; Table V.17**) suggest that the vein formation is related to the development of two types of structures. The shear to laminated veins are interpreted as fault filled veins related to the N to NNE oriented D<sub>2b</sub> tear faults. The breccia type veins are seen as tension gash arrays emplaced in dilatational sites controlled by the development of the ramp system associated to the Deer Cove thrust. These interpretations are in accordance with the models proposed by Gower et al (1991) and by Dubé et al (1993) (**Figure A1.7-A, B**).

It is inferred that the veins pertaining to VS<sub>2</sub> vein set, formed initially as shear type veins during the formation of the D<sub>2b</sub> structures, but further reopened and recrystallised during later deformational events (**Figure V.11**). This is supported by the following observations: i) the veins are hosted by D<sub>2b</sub> shears (**Plate V.22 – A, B, D**); ii) quartz pyrite fringes suggest both up-dip and down-dip motion (**Plate V.2– O**); iii) locally, the recrystallisation of pyrite is associated with down-dip motion (**Plate V.2 – N**); and iv) syntaxial textures and open domains suggest dilatation perpendicular to the D<sub>2b</sub> shears (**Plate V.22 – D, E**). As presented in **chapter IV**, the D<sub>2b</sub> structures were reactivated during both the D<sub>3</sub> and D<sub>4</sub> events and so, vein recrystallisation, subsequent fluid flow and mineral precipitation could have occurred during both these deformational phases (**Figure V.11**). Gold grains in trace amounts have been observed within these veins, so it is inferred that these contribute to some degree to the overall gold endowment.

It is considered that the tension gashes catalogued herein as VS<sub>3</sub>, formed during the development of the syn-to-post D<sub>4</sub> structures (**Figure V.11**). This is based on the crosscutting relationships that the VS<sub>3</sub> veins show with both the composite S<sub>2a-2b</sub> foliation and the VS<sub>2</sub> veins, and by their association to the syn-to-post D<sub>4</sub> faults and fractures (**see Table V.17; Plate V.22 - G, H**). Based on the available data, it remains unclear if these veins have any connection to the gold mineralisation.

### V.2.2. Mineral paragenetic evolution

The petrographic observations presented in the first section of this chapter suggest that in all the studied deposits/prospects the gold mineralisation is related to at least two distinct hydrothermal stages (*Figure V.5.13-17*). Each stage shows a complex evolution and is characterised by a distinct association of alteration minerals formed during the development of veins and structural features of different relative age (*Figure V.5.13-17*). This is the first study that presents the hydrothermal evolution of the study deposits/prospects with respect to the local and regional structural setting of the Point Rouse Complex.

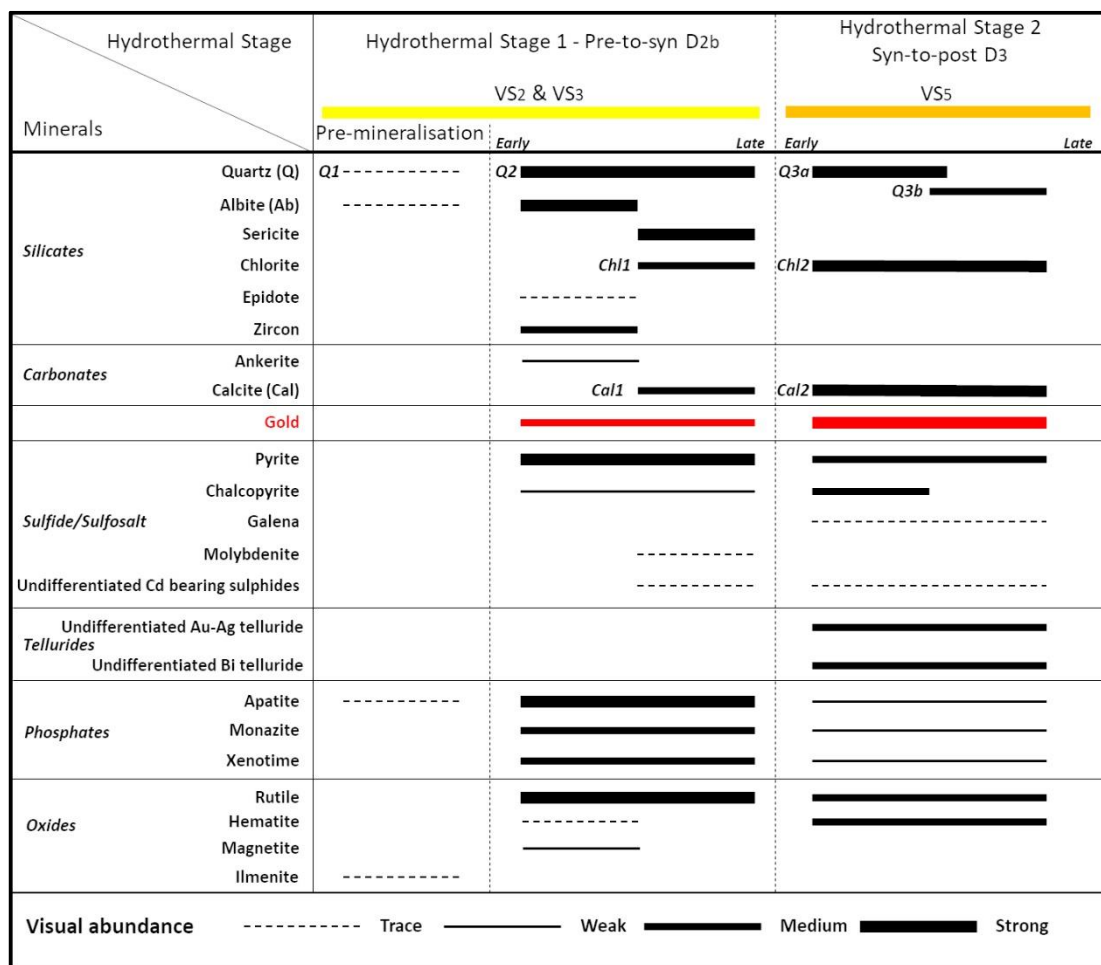


*Figure V.13* – Mineral paragenetic sequence for the Pine Cove deposit. The abundance scale applies for *Figure V.14*, *Figure V.15*, *Figure V.16*, and *Figure V.17* as well.

316 | Chapter V - Gold mineralisation in the Point Rouse Complex (Results and Interpretations)



Figure V.14 – Mineral paragenetic sequence for the Stog'er Tight deposit.



Figure V.15 – Mineral paragenetic sequence for the Argyle deposit. SF3 || = veins parallel to the axial planes of F3 folds.

317 | Chapter V - Gold mineralisation in the Point Rousse Complex (Results and Interpretations)

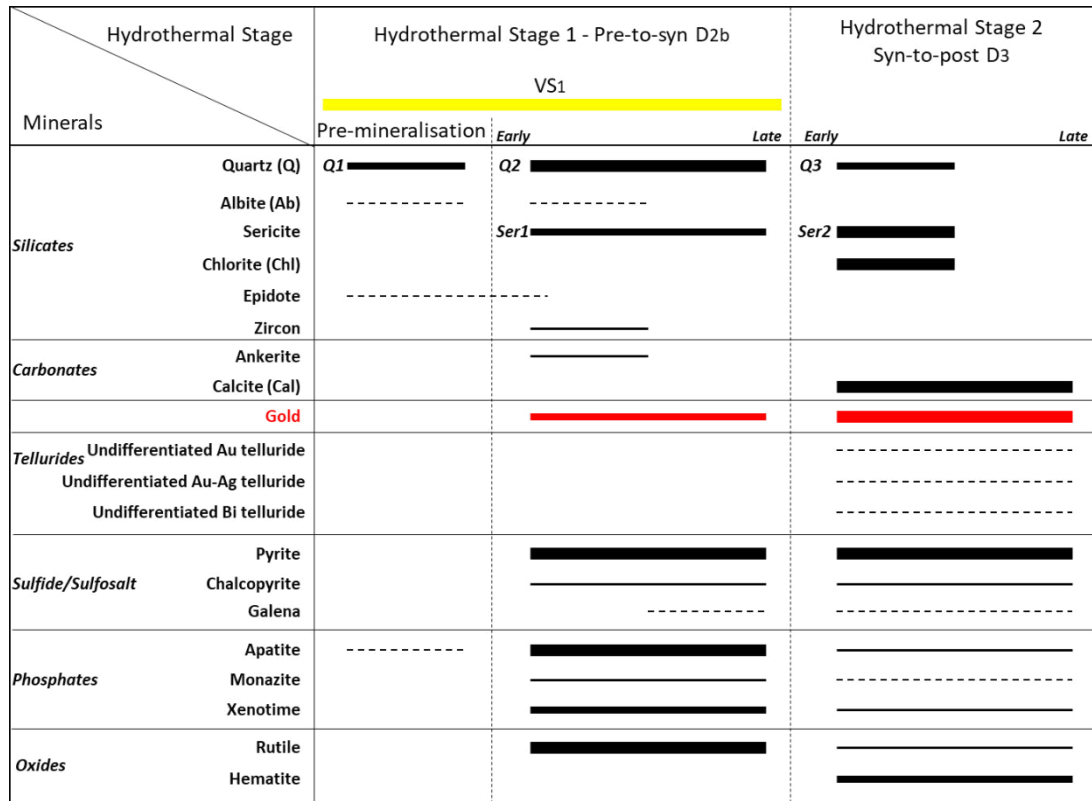


Figure V.16 – Mineral paragenetic sequence for the Romeo & Juliet prospect.

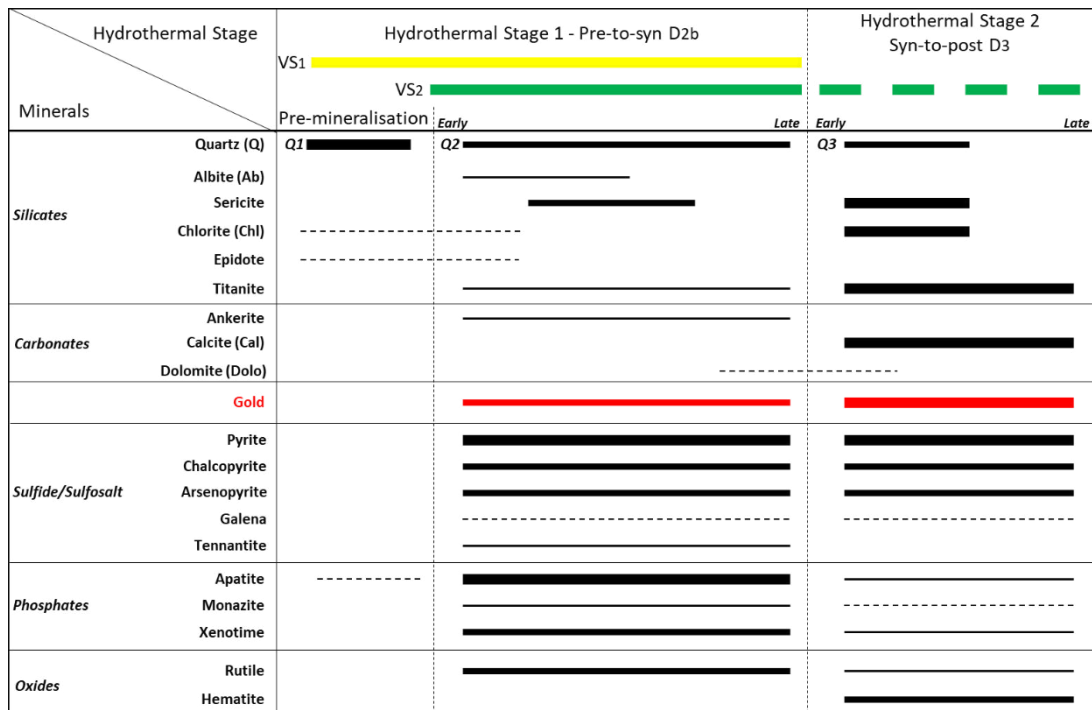


Figure V.17 – Mineral paragenetic sequence for the Deer Cove prospect.

### V.2.2.1. 1<sup>st</sup> hydrothermal stage

In all deposits/prospects, the first hydrothermal stage led to the development of the pre-to-syn D<sub>2b</sub> veins and to their associated pervasive alteration halos composed from the following alteration minerals: albite-ankerite-sericite-rutile-pyrite-phosphates-zircon ± calcite-chlorite-epidote-titanite-hematite (**Figure V.13, Figure V.14, Figure V.15, Figure V.16, Figure V.17**). An early generation of gold and other ore related minerals also formed during this event (**Figure V.13, Figure V.14, Figure V.15, Figure V.16, Figure V.17**).

In all deposits, an early quartz generation (Q<sub>1</sub>) that is intensively brecciated by late quartz generations is preserved within pre-to-syn D<sub>2b</sub> veins (**Table V.3, Table V.7, Table V.10, Table V.15, Table V.17**). The textures of Q<sub>1</sub> (coarse grained fragments, blocky to elongated crystals with euhedral growth zones) suggest that crystal growth occurred in open space under constant conditions. As previously mentioned, the evolution of the pre-to-syn D<sub>2b</sub> veins is related to faulting and folding during the D<sub>2b</sub> event in a brittle-ductile environment under a horizontal maximum principal stress ( $\sigma_1$ ). Therefore, it is inferred that high fluid pressures exceeded the lithostatic load sufficiently to permit the fractures to remain open long enough to favour growth of Q<sub>1</sub> crystals (**Fig. V.18-A**). The CL colours alone cannot provide accurate insights into the physio-chemical conditions active during Q<sub>1</sub> precipitation. However, heterogenous, bright blue to greenish-yellow CL colours in quartz are considered characteristic to quartz of pegmatitic or hydrothermal origin precipitated during metamorphism (Sittner & Götze, 2018). As presented above, under CL, Q<sub>1</sub> is blue in the Pine Cove and in the Stog'er deposits and blue-yellow in the rest of the studied gold occurrences, and so, it is here inferred that Q<sub>1</sub> precipitated from metamorphic related fluids generated during the D<sub>2a</sub> event.

It is not clear if the relict albite, epidote, apatite, chlorite, and/or ilmenite observed in the proximal alteration halo of some of the studied deposits pertain to an early alteration stage associated to Q<sub>1</sub> precipitation, or remnants of the mineral assemblages related to the initial lithologies or to the greenschist facies metamorphism (**Figs. V.13-17**). However, for the Argyle deposit, Pawlukiewicz (2019) attested that these minerals are cogenetic to an early, vein related quartz generation, and formed during a hydrothermal event which postdate the greenschist facies mineral assemblage



and pre-date the gold precipitation. Hence, an early hydrothermal alteration origin of the mentioned relict minerals is also favoured herein (*Fig. V.18 - A*).

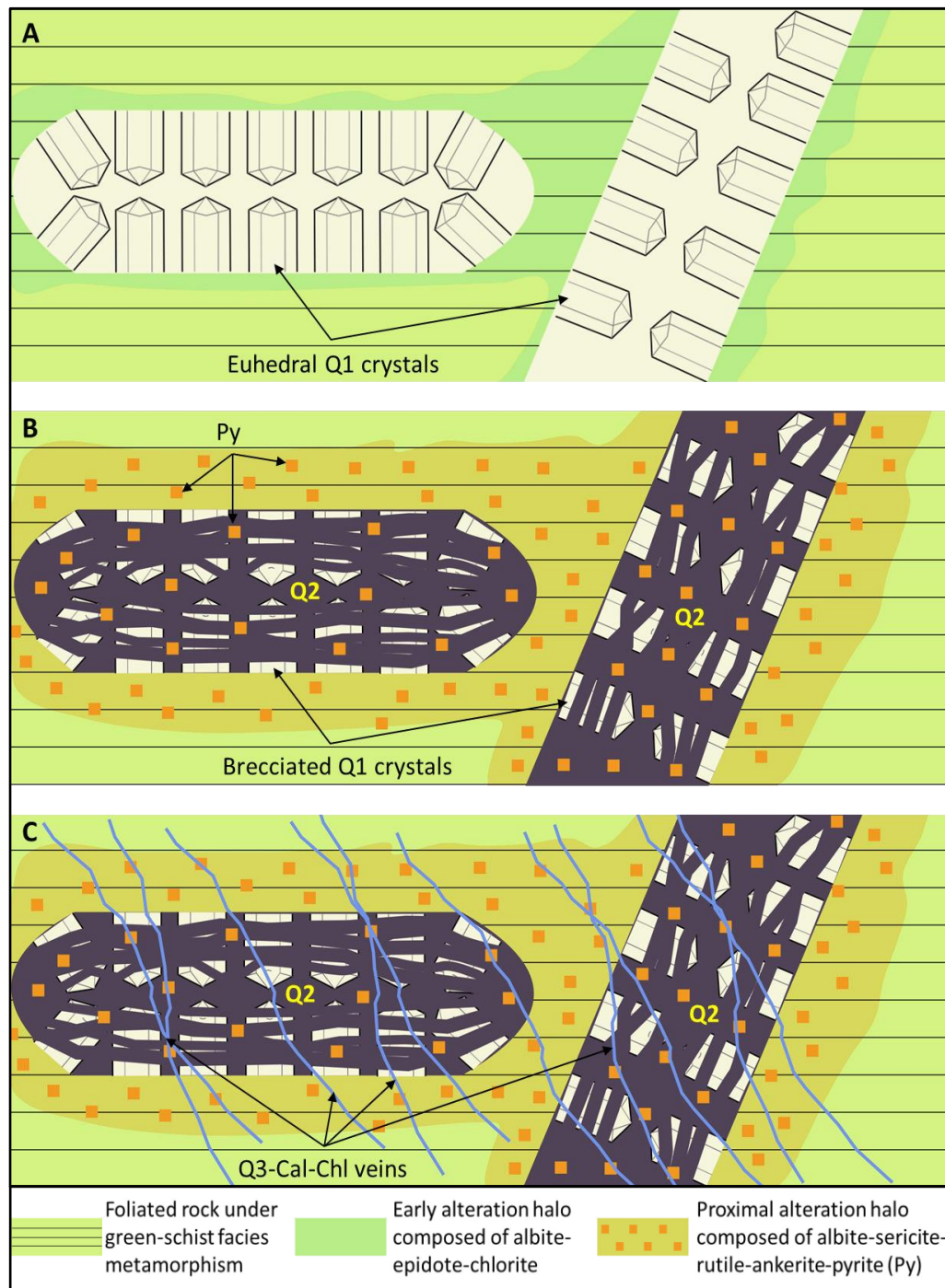


**Figure V.18** – Schematic cartoons that show the development of the first and second generations of quartz ( $Q_1$ ,  $Q_2$ ) with respect to the evolution of the syn-to-post  $D_{2b}$  veins (**A** & **B**) and the formation of the third generation of quartz ( $Q_3$ ) during the development of the syn-to-post  $D_3$  veins (**C**). **Note** the relationships between  $Q_1$ ,  $Q_2$ , and  $Q_3$  and of their associated alteration halos.  $Q_1$  pre-dates the pyrite and gold precipitation (**A**), whereas  $Q_2$  is related to the formation of the pervasive alteration halos and of the first generation of gold (**B**). The late  $Q_3$ -Cal-Chl veins brecciate all the pre-existent minerals and are associated to a second generation of gold (**C**). Cal – calcite; Chl – chlorite.

In the pre-to-syn D<sub>2b</sub> veins from the Pine Cove, Stog'er Tight, Argyle, Romeo & Juliet areas, the sulphides overgrow Q<sub>1</sub>. Also, no gold was observed in association, or within Q<sub>1</sub>. In the Deer Cove prospect, sulphides and gold do occur between Q<sub>1</sub> crystals or within it. However, in this case, both the sulphides and the gold are associated with Q<sub>2</sub> veins and fill in open spaces within Q<sub>1</sub> or at their crystal interfaces. Thereby, it is inferred that Q<sub>1</sub> predate the sulphide and gold precipitation (**Figure V.13, Figure V.14, Figure V.15, Figure V.16, Figure V.17 & Figure V.18 - A**).

A second quartz generation (Q<sub>2</sub>) comprise most of the volume of the pre-to-syn D<sub>2b</sub> veins from the Pine Cove, Stog'er Tight, Argyle and the Romeo & Juliet gold occurrences (**Figure V.13, Figure V.14, Figure V.15, Figure V.16**). In the Deer Cove area, Q<sub>2</sub> is less abundant than Q<sub>1</sub> in the VS<sub>1</sub> veins and cover the entire volume of the VS<sub>2</sub> veins (**Figure V.17**). Under CL, Q<sub>2</sub> has a low response and lack of any peculiar textures. Rusk et al. (2004) and Rusk (2014) attested that quartz with low CL intensity and with homogenous CL textures is of metamorphic origin and common in orogenic gold deposits. According to the same authors the lack of CL texture is due to annealing of initial textures during metamorphism. In the gold occurrences studied herein, both Q<sub>1</sub> and Q<sub>2</sub> show evidence of subsequent deformation and recrystallisation processes (undulatory extinction, serrated and lobate borders, sub-grain formation and rotation, etc.; e.g. **Plate V.19 – A, B, C**). Thus, it is inferred that the CL characteristics of Q<sub>2</sub> reflect its recrystallisation during deformation and metamorphism. The intense brecciation of Q<sub>1</sub> by Q<sub>2</sub> suggests that Q<sub>2</sub> post-date Q<sub>1</sub> (**Figure V.18 – B, C**). Q<sub>2</sub> infills within Q<sub>1</sub> crystals, rounded fragments of Q<sub>1</sub> fully enclosed by Q<sub>2</sub>, and the presence of dense interconnected networks of Q<sub>2</sub> veins, suggest that dissolution of Q<sub>1</sub> facilitated the input of hydrothermal fluids and precipitation of Q<sub>2</sub> in newly formed space (**Plate V.8 – B; Plate V.13– C; Figure V.18 – B, C**). Furthermore, based on the multigenerational nature of Q<sub>2</sub>, as clearly observed in the Stog'er Tight and Romeo & Juliet gold occurrences (**Plate V.7 – D; Plate V.19 – D, G**) it is inferred that influx of Q<sub>2</sub>-precipitating fluids corresponds to a time interval characterised by cyclic episodes of high fluid pressures (near-lithostatic) that led to the hydro-brecciation of Q<sub>1</sub> dominated-veins and of their host-rocks (**Figure V.18 – B**). During this stage, intense fluid-rock interaction resulted with the formation of the first generation of gold and of the associated pervasive alteration halos that overprint both the greenschist facies and the early alteration mineral assemblages (**Figure V.13, Figure V.14, Figure V.15,**

*Figure V.16, Figure V.17; Figure V.18 – B*). This is based on the close spatial association that Q<sub>2</sub> shows with the ore and alteration minerals both within the veins and in the altered wall-rocks.

With few exceptions, a very similar alteration history can be inferred for all deposits based on the textures presented in the first part of this chapter. The intergrowth of albite, ankerite, rutile, titanite (where present), and Q<sub>2</sub> suggest that these minerals started to precipitate together in the early phases (*Figure V.13, Figure V.14, Figure V.15, Figure V.16, Figure V.17*). As presented in *chapter II*, the studied gold occurrences are hosted by mafic to ultramafic rocks that contain significant amounts of Fe-Ti oxides (e.g. titanomagnetite, ilmenite). It is inferred that the albite replaced the pre-existent plagioclase phases, whereas the ankerite and rutile formed on the Fe-Ti oxides. The co-existence of two albite phases observed in some deposits, and the intergrowth of ankerite and rutile on one or two crystallographic directions support the afore-mentioned statement (*Plate V.11 - C*). Similar interpretations were also proposed by Ramezani (1992), Pawlukiewicz (2019), and Ybarra (2019) for the Stog'er Tight, Argyle, and Pine Cove deposits respectively. The albite is brecciated by Q<sub>2</sub> and overprinted by ankerite and sericite patches (e.g. Stog'er Tight and Argyle, *Plate V.14 - A*) which indicates that albite precipitation has ceased before the final stages of the first hydrothermal pulse (*Figure V.13, Figure V.14, Figure V.15, Figure V.16, Figure V.17*). The ankerite, as Q<sub>2</sub>, shows a protracted evolution in all deposits, except for Pine Cove where its precipitation ends while the hydrothermal system is still active (*Figure V.13, Figure V.14, Figure V.15, Figure V.16, Figure V.17*).

In the Pine Cove, Stog'er Tight and Argyle deposits the sericite replaces albite (*Plate V.4 – A, B; Plate V.14 – A, B*) and shows mutual crosscutting relationships with Q<sub>2</sub> which suggest that it formed during the late stages of the first hydrothermal stage (*Figure V.13, Figure V.14, Figure V.15*). In the Romeo & Juliet prospect, no clear crosscutting relationships were observed between Q<sub>2</sub> and sericite<sub>1</sub> because of the fine-grained and disseminated nature of the latter mineral. Nonetheless, the pervasive nature of the sericite around Q<sub>2</sub> dominated veins suggest that these two minerals had a common evolution (*Figure V.16*). In the Deer Cove prospect, sericite<sub>1</sub> overgrows albite and is crosscut by Q<sub>2</sub>, meaning that Q<sub>2</sub> precipitation continued after the formation of sericite<sub>1</sub> (*Plate V.24 – G, Figure V.17*).

Calcite and chlorite related to the first hydrothermal event are present only in the Pine Cove deposit and show cogenetic relationships with Q<sub>2</sub> and sericite (after albite; *Plate V.4–B*). It is inferred that these minerals replaced ankerite during the late stages of the first paragenetic sequence (*Figure V.13*).

Phosphate minerals are present in all deposits and their mutual overgrowing relationships with all the other alteration minerals suggest that these formed during the entire evolution of the first hydrothermal event (*Figure V.13, Figure V.14, Figure V.15, Figure V.16, Figure V.17*). Zircon is a common alteration product in the Stog'er Tight and Argyle deposits where it replaces pre-existent baddeleyite (*Plate V.10–J*). It is both intergrown and overgrown with/by xenotime and monazite and overgrown by sericite and pyrite. Thus, precipitation of zircon ceased before the late stages of the first hydrothermal event (*Figure V.14; Figure V.15*).

The crosscutting relationships that the pyrite shows with the rest of the alteration minerals combined with its internal textures (inclusion-rich cores, clear rims, pyrite aggregates) suggest a protracted evolution which resulted with the development of multiple pyrite generations (*Figure V.19*). The inclusion-rich cores are considered herein the first pyrite generation (*Figure V.19-A*). The presence of albite, ankerite, rutile, and Q<sub>2</sub> inclusions in the pyrite cores indicate that these are cogenetic and formed through the expansion of pre-existent Fe-bearing minerals in the early stages of the first hydrothermal event. The presence of ilmenite, usually replaced by rutile, as inclusions in pyrite also support the aforementioned statement. The pyrite-rims, either un-zoned or oscillatory zoned (arsenic rich bands in Deer Cove), are interpreted as the second generation of pyrites and their development is associated to successive fluid flow episodes (*Figure V.19-A*). The pyrite aggregates are seen as a third generation of pyrite (*Figure V.19-A*). These overgrow the pre-existent pyrites and the rest of the alteration minerals which suggest that these formed in the late stages of the first hydrothermal event (*Plate V.5-D, E; Plate V.9-I*). The clearing of inclusion-rich domains in the pyrite aggregates may result from prolonged interaction between fluid and pyrite through coupled-dissolution-precipitation processes (Putnis, 2009; Velásquez et al., 2014; Hastie et al., 2020).

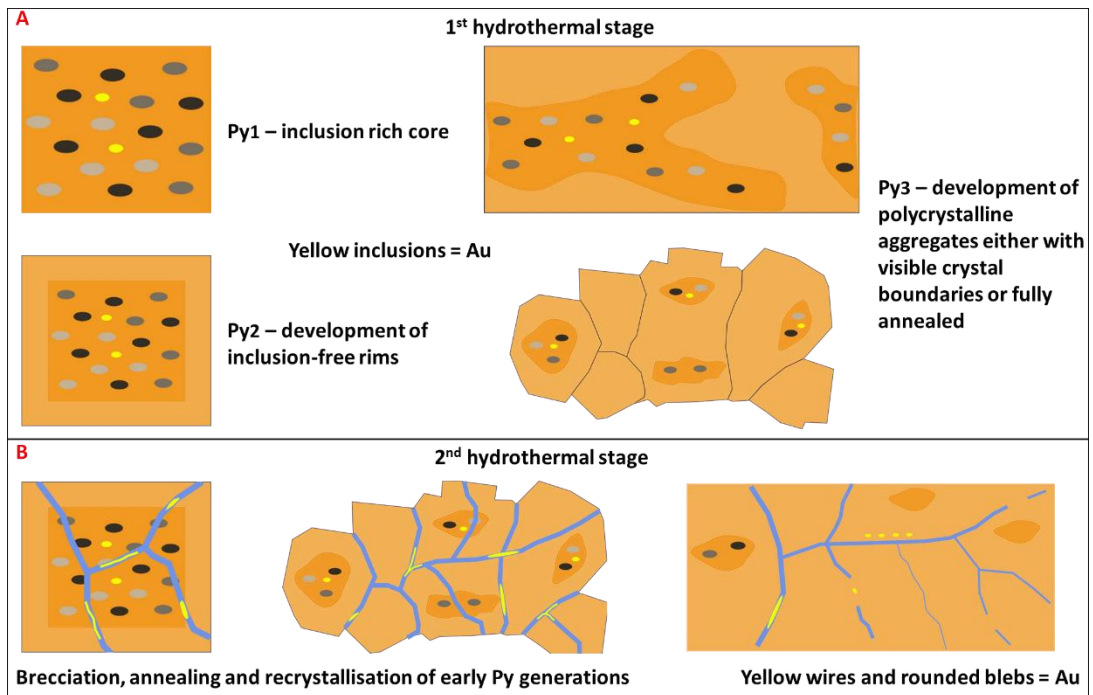
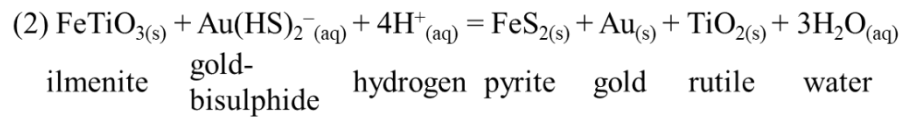
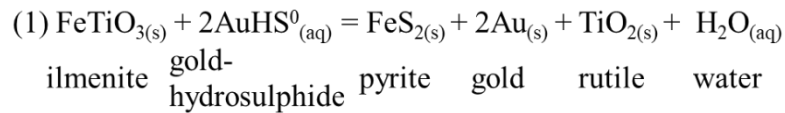


**Figure V.19** – Schematic cartoons that show the development of pyrite (Py) during both the first (A) and second (B) hydrothermal events.

The fine grained gold particles that occur as inclusions in porous-rich domains in pyrite, or the free particles (less common) from Q<sub>2</sub> or from other early alteration minerals are ascribed here to the first hydrothermal stage (*Plate V.10–B; Plate V.14–B; Figure V.19*). The presence of pyrite, rutile, and ankerite inclusions in gold also suggest that these minerals are cogenetic (*Table V.21; Figure V.13, Figure V.14, Figure V.15, Figure V.16, Figure V.17*). The close spatial association between gold, pyrite, and other sulphide phases (e.g. chalcopyrite) indicate that gold was transported in gold-sulphide complexes and that wall rock sulphidation was one of the mechanisms for gold precipitation (Williams-Jones et al., 2009; Phillips & Powell 2010). Also, the common association between gold and rutile, and locally relict ilmenite, support the interpretations of other authors (Ramezani, 1992; Pawlukiewicz, 2019; Ybarra, 2019) that the high content of Fe-Ti oxides of the host rocks acted as a chemical trap and facilitated the co-precipitation of pyrite, gold, and rutile through the destabilisation of AuHS<sup>0</sup> or Au(HS)<sub>2</sub><sup>-</sup> complexes as presented in the following equations: (1) from Ramezani et al. (2000) and (2) from Pawlukiewicz (2019).



Considering that free gold also exists within the pre-to-syn D<sub>2b</sub> veins, especially in the Romeo & Juliet and Deer Cove prospects, precipitation of gold may have also been controlled by flash vaporisation processes (Ybarra, 2019; Weatherley and Henley et al., 2013). Rapid pressure drops resulted from multiple brittle-ductile slip events can drive the precipitation of silica and other metals from solution, including gold (Williams-Jones et al., 2009; Weatherley and Henley et al., 2013). The direct spatial association between free gold, auriferous pyrite, and Q<sub>2</sub> sub-generations in all the studied deposits/prospects indicate that both flash vaporisation and wall rock sulphidation processes facilitated the precipitation of gold during the D<sub>2b</sub> deformation phase.

#### V.2.2.2. 2<sup>nd</sup> hydrothermal stage

In all the deposits/prospects, the second hydrothermal stage led to the development of quartz<sub>3</sub>-calcite-chlorite/chlorite<sub>2</sub> ± sericite<sub>2</sub>-hematite veins and patches that crosscut and overprint the alteration minerals related to the first hydrothermal stage (**Figure V.13, Figure V.14, Figure V.15, Figure V.16, Figure V.17, Figure V.18 - C**). Based on the observed textures, alteration and recrystallisation of pre-existent phosphates and rutile is also associated to this stage. Moreover, neo-formation of titanite occurs in Argyle and Deer Cove through the replacement of early rutile and titanite (**Plate V.15 – G; Plate V.25 -C; Figure V.15 & Figure V.17**). A second generation of gold and chalcopyrite was also formed during this hydrothermal stage in all the studied gold occurrences, whereas undifferentiated Au/Au-Ag/Pb/Pb-Bi/Bi tellurides and other sulphides formed only in some localities (**Figure V.13, Figure V.14, Figure V.15, Figure V.16, Figure V.17**). An overall mineral precipitation order for both the ore and the alteration minerals was established based on the crosscutting relationships that these minerals show with Q<sub>3</sub> and between

themselves and is presented for each of the studied gold occurrences in *Figure V.13*, *Figure V.14*, *Figure V.15*, *Figure V.16*, *Figure V.17*.

The relative timing of the second hydrothermal event is interpreted as syn-to-post D<sub>3</sub>. This is based on the following observations: i) in the Pine Cove, Stog' er Tight, and the Argyle deposits these minerals were observed within and around the syn-to-post D<sub>3</sub> veins (*Plate V.1 – L*; *Plate V.6 - J*); ii) the chlorite<sub>2</sub> from Pine Cove and Stog' er Tight, as well as the chlorite from Romeo & Juliet, were seen as neo-formation minerals aligned along the F<sub>3</sub> axial planes (*Plate V.9- D*), as pyrite fringes of euhedral pyrite crystals bordered by syn-D<sub>3</sub> extensional shear bands (*Plate V.4– F, G*), and as a shear related fabric formed during the reactivation of the D<sub>2b</sub> faults as normal faults (*Plate V.7 – G, H, I*); iii) in the Stog' er Tight area, some of the carbonates form in the hinges of F<sub>3</sub> folds and along the foliation planes during the reactivation of D<sub>2b</sub> faults with a down-dip motion to N (*Plate V.9 - E*); and iv) in the Deer Cove area, calcite veinlets crosscut the composite S<sub>2a-2b</sub> foliation, whereas syn-kinematic recrystallised pyrite crystals/aggregates together with their associated calcite-chlorite-quartz fringes overgrow the S<sub>2a-2b</sub> foliation and indicate a down-dip motion to N (*Plate V.24 – B, C*).

The CL textures displayed by Q<sub>3A</sub> (euhedral growth zones, laminated/banded) in the Pine Cove, Stog' er Tight, and Argyle deposits indicate that quartz precipitation occurred in open spaces close to hydrostatic conditions (*Plate V.3 – D*; *Plate V.8- E*). When Q<sub>3</sub> occurs together with chlorite and calcite along the same vein, their internal distribution suggest that these minerals precipitated successively, likely due to multiple fluid flows, rather than simultaneously. However, these minerals also occur along mono-mineral veins with mutual crosscutting relationships, suggesting that these formed during the same hydrothermal event (*Figure V.13*, *Figure V.14*, *Figure V.15*, *Figure V.16*, *Figure V.17*). The presence of Q<sub>3</sub> on both conjugate structures and in randomly distributed stockworks (*Plate V.8– D*; *V.13- D, H*) indicate that high fluid pressures combined with a high differential stress contributed to fracture development, dilation, fluid flow, and mineral precipitation.

In all deposits, the pyrite generations formed during the first hydrothermal event are intensively brecciated and locally even pulverised by Q<sub>3</sub>-Cal-Chl veinlets (*Figure V.19 - B*). However, it is inferred that annealing and the formation of at least one new pyrite generation also took place during this hydrothermal stage (*Figure V.19*

– **B**). This is based on the following observations: i) irregular patches and wires of pyrite which overprint and brecciate early alteration minerals were observed in association with late Q<sub>3</sub>-Cal-Chl veinlets (**Plate V.5- H**); and ii) discontinuous Q<sub>3</sub>-Cal-Chl veinlets or inclusions of these minerals occur within some pyrite crystals/aggregates (**Figure V.19– B**).

The free gold particles found along mono or poly mineral Q<sub>3</sub>-Cal-Chl veinlets, whether within pyrite or not, are here interpreted to have formed during the second hydrothermal event (**Figure V.19 – B**). Moreover, some of the gold observed as inclusions within pyrite is also interpreted as late stage gold, based on its distribution within the pyrite and on its textural characteristics. Compared to the first generation of gold, the former occurs in inclusion-free, annealed, and recrystallised domains in pyrite or is aligned parallel to Q<sub>3</sub>-Cal-Chl veinlets (**Figure V.19 – B; Plate V.5 – K, L**). In all deposits, the second generation of gold is characteristic of the high-grade gold intervals, which at least visually, comprise most of the gold endowment. Based on the available data, it is not clear whether the late gold is remobilized from pre-existing mineralization or if it is a product of the newly introduced fluid. Therefore, this topic will be further discussed in Chapter VII (**Discussions and Synthesis**).

### V.2.3. Insights from gold geochemistry

Gold alloy composition is controlled by both P-T-X conditions at the site of deposition and by the chemistry of the mineralising fluid (Gammons and Williams-Jones, 1995). In the Pine Cove, Stog’er Tight, Argyle, and Romeo & Juliet gold occurrences, a *type I* signature was recorded in all the gold particles attributed to the first generation of gold, as well as in the majority of the gold particles interpreted as late stage gold (**Table V.20; Figure V.10**). Based on this, it is believed that the same mineralising fluid contributed to the early development of these deposits/prospects, and that the physio-chemical conditions at the precipitation sites were similar. Interestingly, some of the gold particles interpreted as late gold from the Stog’er Tight and Argyle deposits also exhibit a *type III* signature (**Table V.20; Figure V.10**). The presence of both *type I* and *type III* signatures in the second generation of gold from some localities suggests that either the early mineralising system evolved over time and/or an input of fluids with different origins may have occurred, at least locally, during the late development of the deposits. Elevated Cu contents (>1%) in the gold



alloy are uncommon for orogenic gold-style mineralisation and usually point towards a magmatic origin of the mineralising fluid (Chapman et al., 2011; Moles et al., 2013). This topic will be further addressed in chapter VII (*Discussions and Synthesis*).

The majority of gold particles from the Deer Cove prospect show a type II chemical signature, while a few display the *type I* signature (**Table V.20; Figure V.9 & Figure V.10**). It remains unclear whether the limited number of gold particles with a *type I* signature reflects an underrepresentation of this gold type in the sample suite due to sample processing protocols or a volumetrically limited gold phase within the deposit. Regardless of the case, the prevalence of type II signature in the gold from Deer Cove prospect, suggest the presence of different mineralising factors compared to the other studied gold occurrences. These factors could include different P-T-X conditions at the precipitation site, fluids with distinct chemical characteristics, and/or temporal variations of the mineralising system.

A decrease of temperature could lead to an increase in the Ag content of the Au-Ag alloy (Gammons and Williams-Jones, 1995). The controls of Hg contents in the gold alloys are still poorly constrained (Chapman et al., 2021). However, an increase of Hg contents in the gold alloys due to temperature reduction was inferred by some authors (Knight et al., 1999; Gas'kov, 2017). The gold bearing veins from Deer Cove are situated at a higher structural level in the stratigraphic stack and hosted by splays of the Deer Cove thrust, in contrast to the other studied occurrences which are hosted by splays of the Scrape Thrust and which are located lower in the stratigraphy (**Figure IV.1**). Considering the depth difference, the Deer Cove prospect could have formed under lower temperatures compared to the other gold occurrences, which in turn could explain the higher Ag-Hg levels of the gold alloy.

The chemistry of fluids can change during transport from the source to the deposition site as a consequence of fluid-rock interaction. The major fluid conduits involved in the formation of *type I* and *type II* gold signatures are different, and therefore, it is possible that these signatures to reflect a change of fluid chemistry that occurred along distinct fluid paths.

Input of fluids with distinct origins or a different temporal evolution of the mineralizing system can also explain the presence of both type I and type II signatures in the Deer Cove gold particles. Nevertheless, the continuum in the data distribution suggests a transition between these two signatures, which supports a temporal

evolution of the mineralising system, rather than fluids of different origin (**Figure V.10**). Based on all the afore-mentioned aspects, it is inferred herein that the mineralised veins from Deer Cove represent a spatial and/or temporal variation of the same hydrothermal system that generated the *type I* gold in the other localities.

Several gold particles from the Romeo & Juliet samples show a *type IV* signature (**Figure V.10**). These particles are from the liberated gold suite, so their setting in the paragenetic sequence is unknown. The data distribution and the significantly higher Cu contents of the *type IV* gold suggest that this gold type precipitated from a mineralising fluid with different characteristics compared to the fluids that generated the other types of gold. The high Cu content, up to 20 wt%, suggest that these particles are intermetallic Au-Cu compounds close to tetraauricupride (AuCu) composition. Occurrences of such compounds are known in altered ultramafic rocks (e.g. rodingites, serpentinites) from the Ural Mountains, Russia (Murzin et al., 2019, 2018; Pal'yanova et al., 2018). Their origin was linked to fluids derived during the alteration of the ultramafic rocks or of serpentinites/rodingites by fluids with various sources (metamorphic or metamorphic-meteoric mixed fluids - Murzin et al., 2019, 2018; metamorphic and/or magmatic - Pal'yanova et al., 2018). Intermetallic Au-Cu compounds were also reported in association with porphyry copper-gold mineralisation in Bulgaria (Cioaca et al., 2020). Nearby the Romeo & Juliet prospect, both altered ultramafic rocks and granodioritic intrusions exist. Thereby, the source of the *type IV* gold can be related to fluids derived directly from a magmatic source or from the metasomatised ultramafic rocks. Currently, no assumptions favoring one option over the other can be made based on the available data.

### **V.3. Summary**

The studied gold occurrences show a very similar structural and mineralogical evolution. Two main mineralising moments, each related to gold deposition, were identified, and can be related to structural features of different relative age (**Figs. V.13-17**).

The first hydrothermal event led to the formation of foliation-parallel and fault-filled quartz  $\pm$  carbonate veins associated with a proximal pervasive alteration halo composed of albite-ankerite-sericite-rutile-pyrite-phosphates-zircon  $\pm$  calcite-

chlorite-epidote-titanite-hematite (*Figure V.13, Figure V.14, Figure V.15, Figure V.16, Figure V.17*). The veins together with their associated alteration halos comprise the bulk of the ore volume. The gold associated to this event occurs as inclusions in pyrite (*Figure V.19*), and to a lesser degree free within the veins. The relative age of this event is considered pre-to-syn D<sub>2b</sub>.

The second hydrothermal event is characterised by the presence of narrow quartz<sub>3</sub>-calcite-chlorite ± sericite-hematite veins and patches that crosscut and overprint the pre-existent minerals. The gold related to this stage occurs mostly free along the veins in brecciated pyrite (*Figure V.19*). It is unclear if the gold is remobilised from the pre-existent mineralisation or represents a distinct phase introduced by the new fluid. The age of this hydrothermal event is considered syn-to-post D<sub>3</sub>.

The gold geochemistry suggests the presence of a single mineralizing system that exhibited spatial and/or temporal variations during the first hydrothermal event. The existence of two chemical signatures in the second gold generation indicates that fluids from multiple sources might have contributed to the mineralisation stage.

## **VI. Timing of gold mineralisation in the Point Rouse Complex based on in-situ LA-ICP-MS U-Th-Pb analysis of monazite, xenotime and titanite (Results & Interpretations)**

As presented in *chapter II*, geochronological ages for gold occurrences from the Baie Verte Peninsula are scarce and the relationship between gold forming processes and the tectonic evolution of the area are poorly constrained. Therefore, in this chapter the formation and the subsequent evolution of the Stog' er Tight, Argyle, Romeo & Juliet, and Deer Cove gold deposits/prospects are assessed based on new in-situ LA-ICP-MS U-Th-Pb isotope analysis of monazite, xenotime, and titanite. Description of the analytical techniques together with information on the engaged workflow and utilised software are provided in the *Methodology chapter (III)*.

The data are interpreted with respect to the mineral paragenetic sequences presented in *chapter V*. The obtained ages are integrated with previous published data and discussed with respect to the regional tectonic evolution of the Baie Verte Peninsula in *chapter VII*. Summarised theoretical aspects regarding both the advantages and limitations of using monazite, xenotime, and titanite as geochronometers are provided in the same chapter.

### **VI.1. Description of analysed grains**

For the Stog' er Tight and the Argyle deposits both monazite and xenotime were analysed, whereas for the Romeo & Juliet and the Deer Cove prospects analysis were made on xenotime and titanite, respectively. The spatial relationships between the monazite, xenotime, and titanite grains and the alteration and ore related minerals alongside their setting within the paragenetic sequences of each of the studied deposits/prospects are presented in *chapter V*. Descriptions related to the external and internal morphology of the analysed grains are provided in *Table VI.1*, whereas their high-resolution BSE and/or CL images can be found in *Appendix IV*.

*Table VI.1 – Summarised descriptions of the analysed grains*

Deposit	Mineral	Description
Stog'er Tight	Monazite	Vary in shape and size, from ~20x20 µm to 110x60 µm (length and width) ( <i>Appendix IV - Plates AIV.1; AIV.2; AIV.3</i> ). The smaller grains are usually subrounded to rounded or slightly elongated, whereas the larger grains are anhedral to euhedral with both rounded and orthogonal corners (e.g. <i>Plates AIV.2 – K; AIV.3 – E, F</i> ). Embayed and serrated borders were observed in both large and small grains, but more often in the small grains (e.g. <i>Plates AIV.2 – A; AIV.3 - C</i> ). All grains show cracks and fractures, some partially annealed, and/or porous and/or inclusion rich domains. Where Chl <sub>2</sub> -Cal-Q <sub>3</sub> veins and patches overprint earlier alteration minerals, monazites occur in clusters of 5 to 20 grains, show very irregular shapes, and are brecciated. Jigsaw textures suggest that these grain clusters were part of larger grains before brecciation ( <i>Plate AIV.1 – A, C</i> ). Regardless their size and shape, no zoning patterns were seen in either BSE or CL. However, EPMA intensity maps of five grains show internal compositional zonation in Th, Y, and to a lesser degree in Sm ( <i>Plates AIV.2 – B, C; AIV.3 – E, F, K</i> ). Four of the investigated grains show moderate to high Th intensities on the rims and low intensities towards the central parts ( <i>Plates AIV.2 – B, C; AIV.3 – E, F</i> ). In the same four monazites, Y is heterogeneous, forming either sector or patchy zoning patterns, whereas Sm shows high intensities over the entire grain surface, with high peaks corresponding to high Th zones. These four monazites are entirely or almost surrounded by alteration minerals characteristic to the first paragenetic stage of the Stog'er Tight deposit ( <i>Figure V.14</i> ). In contrast, the fifth monazite analysed by EPMA is partially hosted by a late calcite vein and shows moderate to high Th intensity and low Y and Sm intensities over the entire surface of the grain ( <i>Plate AIV.3 – K</i> ).
	Xenotime	Vary in size from 20x10 µm to 50x40 µm (length and width) and have bean, subrounded, lobate and subhedral shapes ( <i>Appendix IV - Plates AIV.6; AIV.7; AIV.8</i> ). Serrated and embayed grain borders are a common feature (e.g. <i>Plate. AIV.8 – C</i> ). One grain shows core-rim zonation under BSE, whereas all the others are homogenous ( <i>Plate AIV.7 – D</i> ). However, under CL, most grains show dark cores and fully or partially grown, bright thin rims ( <i>Plates AIV.6 – C; AIV.7 – B, C; AIV.8 – B</i> ). Like monazite, the xenotime grains are also brecciated by Q <sub>3</sub> -Chl <sub>2</sub> -Cal veinlets ( <i>Plate AIV.6 – D</i> ).
Argyle	Monazite	Show subhedral to irregular shapes with serrated and embayed margins and variable sizes from 35x20 µm to 180x100 µm (length and width) ( <i>Appendix IV - Plates AIV.4; AIV.5</i> ). Most grains show cracks and/or porous and inclusion rich domains. Some have tails consisting of aligned and very fine-grained monazite particles ( <i>Plate AIV.5 – D</i> ). No zoning pattern was observed in BSE or CL.

		However, some monazites exhibit auto-radiation halos around them when imaged by CL ( <i>e.g. Plate AIV.5 – A, B, N</i> ).
<b>Argyle</b>	Xenotime	Vary in size from 20x20 µm to 50x50 µm, occur as subrounded to rounded, elongated to subhedral crystals, and as irregular aggregates composed of several small grains ( <i>Appendix IV - Plates AIV.9; AIV.10</i> ). The grains show straight, serrated, and embayed margins and are either homogenous, or contain porous and inclusion rich domains. No zonation was observed under BSE, but in CL, except for one grain which is homogenous ( <i>Plate AIV.9 – A</i> ) all crystals show either a patchy or a core –rim (dark-bright) zoning pattern ( <i>Plates AIV.9 – D, E, F; AIV.10</i> ). Both xenotimes and monazites brecciated by Q <sub>3</sub> -Chl-Cal veinlets have been observed ( <i>Plates AIV.5 – C, G; AIV.9 - A</i> ).
<b>Romeo &amp; Juliet</b>	Xenotime	Vary in size from 20x10 µm to 40x30 µm (length and width), are subrounded to rounded, subhedral with both rounded and straight corners, spherical to elongated and irregular ( <i>Appendix IV - Plates AIV.11 &amp; AIV.12</i> ). Most grains have serrated and embayed borders, are cracked and fractured, and are porous or inclusion rich. All xenotimes imaged by CL show either patchy zoning or core-rim domains. Are both brecciated and hosted by Cal-Chl veins.
<b>Deer Cove</b>	Titanite	The grains are very irregular, show rounded, serrated, and embayed margins and variable sizes, from 40x40 µm to 200x50 µm ( <i>Appendix IV – Plate AIV.13</i> ). Aggregates composed of multiple small crystals with visible grain boundaries are common ( <i>e.g. Plate AIV.13 – A</i> ). Most crystals and aggregates are porous or contain very small rutile and/or ilmenite inclusions. All grains are either intergrown with sericite and chlorite or are crosscut by both these minerals and by calcite.

## **VI.2. Data quality assessment**

The mineral type and the number of analysed grains together with the total number of data points per each analysed section are provided in *Table VI.2*. Not all the obtained monazite and xenotime dates were considered geologically relevant (*see below and Appendix IV*). The number of accepted and rejected data points are provided in *Table VI.2*. The raw data and the computed dates for each of the analysed spots are provided in *Appendix IV* together with their corresponding high-resolution BSE and/or CL images.

*Table VI.2 – List of sections, analysed minerals and number of data points*

Deposit	Section Code	Analysed mineral (no.)	No. of data points (spot analysis)
Stog'er Tight	BN215	Monazite (13)	15; 6 accepted / 9 rejected
		Xenotime (8)	16; 13 accepted / 3 rejected
	SOZ1	Monazite (16)	30; 21 accepted / 9 rejected
		Xenotime (9)	10; 6 accepted / 4 rejected
	SOZ2	Monazite (11)	33; 27 accepted / 6 rejected
		Xenotime (4)	8; 6 accepted / 2 rejected
Argyle	AG3	Monazite (2)	16; 9 accepted / 7 rejected
		Xenotime (8)	11; 8 accepted / 3 rejected
	AG4	Monazite (19)	43; 26 accepted / 17 rejected
		Xenotime (10)	14; 8 accepted / 6 rejected
Romeo & Juliet	RJ4	Xenotime (9)	9; 4 accepted / 5 rejected
	RJ5	Xenotime (7)	8; 4 accepted / 4 rejected
Deer Cove	DC5	Titanite (18)	24; all accepted

### VI.2.1. Excluded monazite and xenotime data points

The following analysis spots were not used for age interpretation.

- i) Data points that correspond to analysed spots in which extra material was ablated from underneath the grain (the laser burned through the entire thickness of the analysed grain), from the grain's surroundings (when the analysis point landed slightly off grain), or from mineral inclusions hosted within the analysed grain (*see Appendix IV*).
- ii) Data points that have large uncertainties (>10% of the obtained date) (*e.g. Plate AIV.2 – D*).
- iii) Data points that generated either very old or young dates that are not geologically plausible (*e.g. Plate AIV.1 – C, D*).
- iv) Data points that show high discordance values between individual U-Th-Pb dates.

Discordance filters vary between studies according to different processing techniques and interpretation rationale, but U-Pb dates with  $\leq 10\%$  discordance are commonly considered concordant (Spencer et al., 2016). The discordance value is calculated herein based on the ratio between two different U-Pb dates multiplied by 100 (*e.g.*  $(^{207}\text{Pb}/^{235}\text{U} \text{ date} / ^{206}\text{Pb}/^{238}\text{U} \text{ date}) * 100$ ). Compared to discordance in the U-Pb system (*i.e.* between the two decay chains of  $^{235}\text{U}$  and  $^{238}\text{U}$ ), discordance between the U-Pb and Th-Pb decay chains lacks an established methodology and is

less commonly investigated. However, most of the analysed monazites show discordance higher than 10% between their individual U-Th-Pb dates. Hence, the degree of deviation from the concordia curve was evaluated based on how the data distribute on: i) the U-Th-Pb concordia diagram of Vermeesch (2020) which combines three isotopic ratios ( $^{208}\text{Pb}/^{232}\text{Th}$ ,  $^{207}\text{Pb}/^{235}\text{U}$ , and the  $^{206}\text{Pb}/^{238}\text{U}$ ) but displays the results on a  $^{208}\text{Pb}/^{232}\text{Th}$  vs  $^{206}\text{Pb}/^{238}\text{U}$  plot; and ii) on the two commonly used U-Pb concordia diagrams of Tera & Wasserburg, (1972a, b) and of Wetherill, (1956) (**Figure VI.1 & Figure VI.2**). The points that are significantly shifted on all three concordia plots suggest a disturbance of their Th-Pb and/or U-Pb isotope systems and so, these were excluded. For xenotime, all points with a discordance >10% between the  $^{207}\text{Pb}/^{235}\text{U}$  and  $^{206}\text{Pb}/^{238}\text{U}$  dates were not included in the interpretation stage (**Figure VI.3**). More than 90% of the monazite and xenotime dates with high discordance levels correspond to analysis that incorporated extra material (*point i*), have high uncertainties (*point ii*), or generated very old/young dates that are geologically improbable (*point iii*). A discussion related to the potential factors that can lead to the disturbance of the U-Th-Pb isotopic system, and consequently to unreliable dates, is provided in the interpretation section of this chapter (*section VI.3.2*).



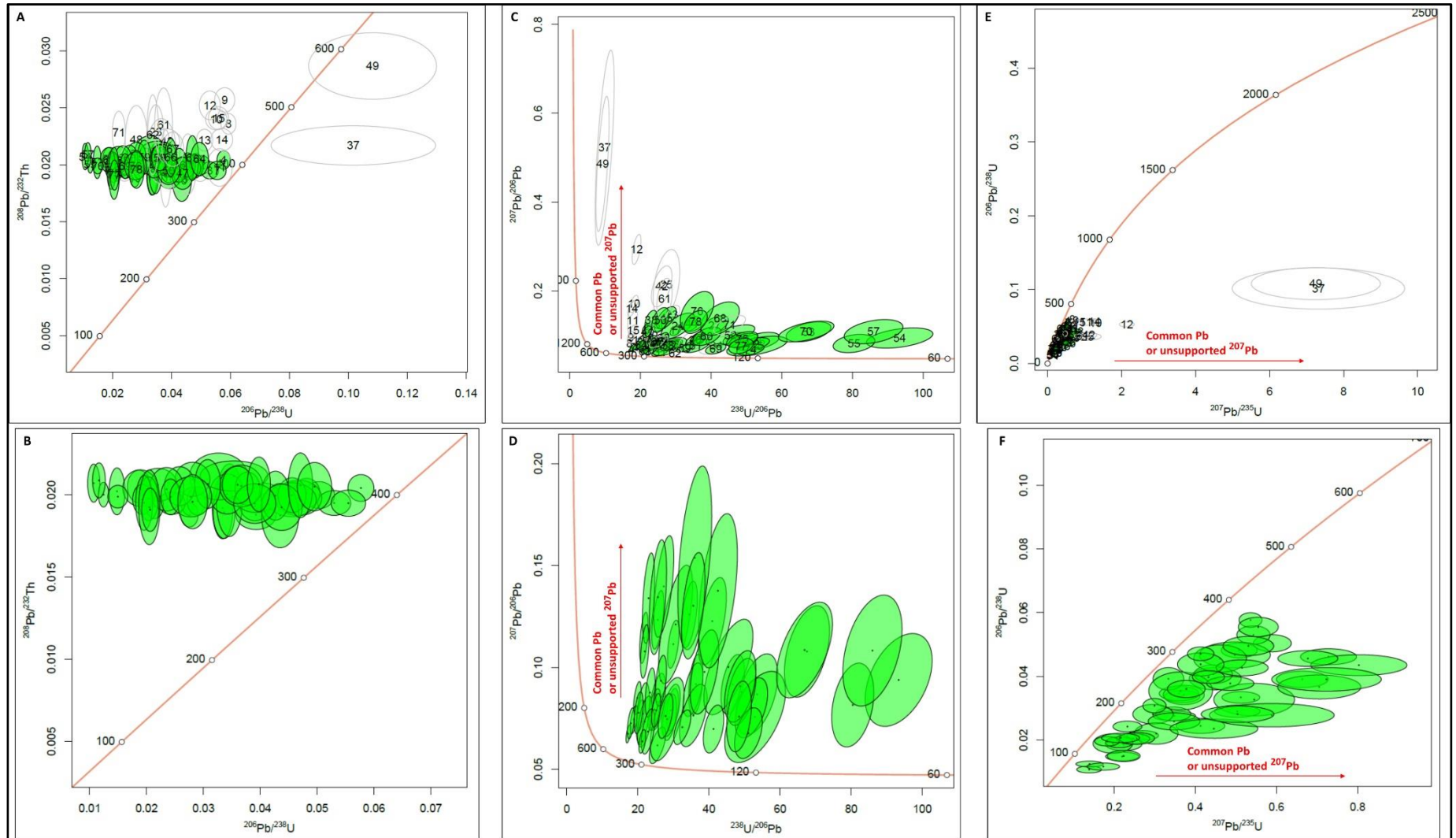


**Figure VI.1-** Stog'ier Tight monazite data plotted on  $^{208}\text{Pb}/^{232}\text{Th}$  vs  $^{206}\text{Pb}/^{238}\text{U}$  (A, B), Tara-Wasserburg (C, D), and Wetherill (E, F) concordia diagrams; empty ellipses represent the excluded points, whereas the green ellipses the used ones. The ellipse number corresponds to the position of the data point within the excel spreadsheets (Appendix IV – Table AIV.3).

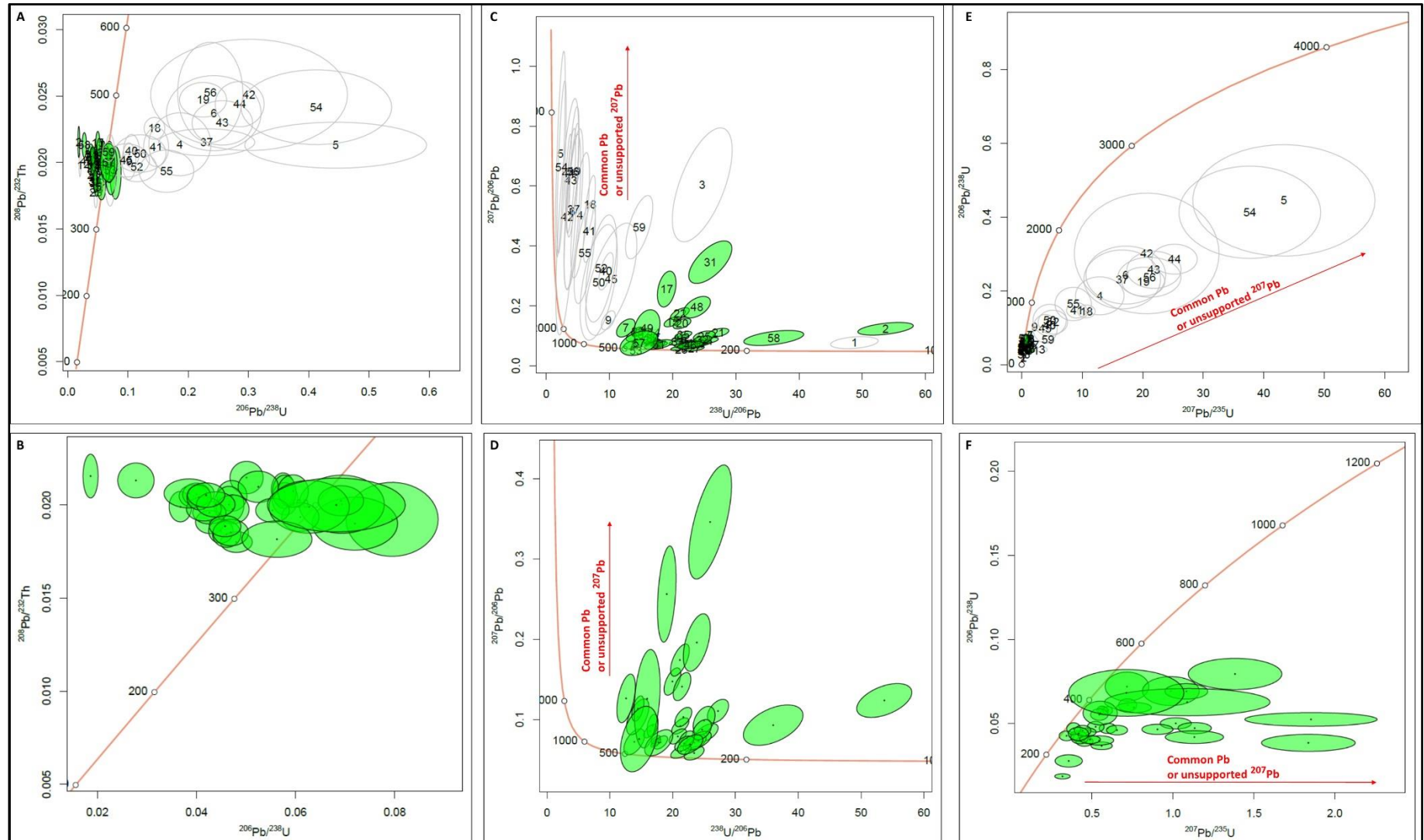


**Figure VI.2-** Argyle monazite data plotted on  $^{208}\text{Pb}/^{232}\text{Th}$  vs  $^{206}\text{Pb}/^{238}\text{U}$  (A, B), Tara-Wasserburg (C, D), and Wetherill (E, F) concordia diagrams; empty ellipses represent the excluded points, whereas the green ellipses the used ones. The ellipse number corresponds to the position of the data point within the excel spreadsheets (Appendix IV – Table AIV.6).

337 | Chapter VI – Timing of gold mineralisation in the Point Rouse Complex based on in-situ LA-ICP-MS U-Th-Pb analysis of monazite, xenotime, and titanite (Results and Interpretations)

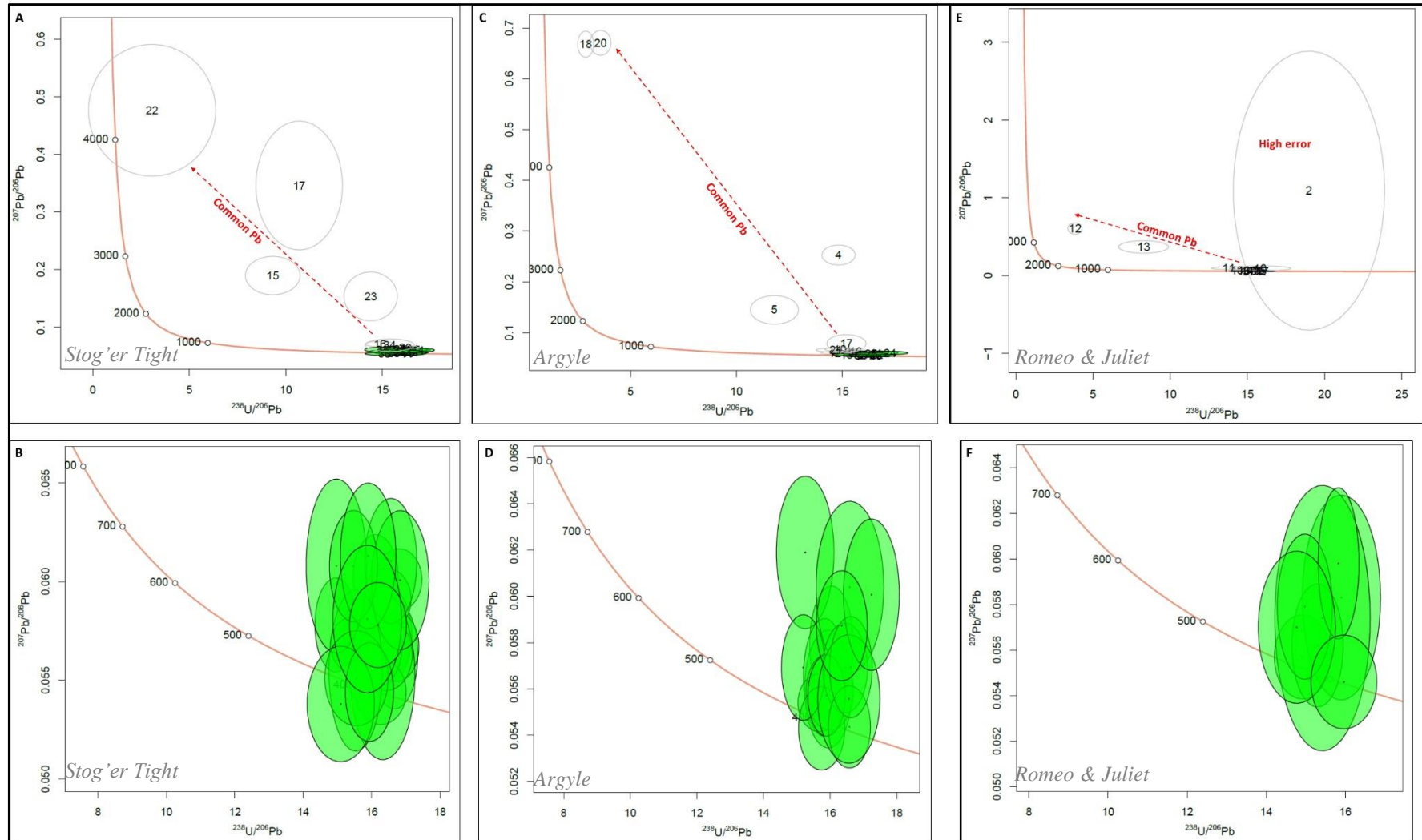


**Figure VI.3** – Xenotime data plotted on Tara-Wasserburg concordia diagram; A, B – Stog'er Tight; C, D – Argyle; E, F – Romeo & Juliet; empty ellipses represent the excluded points (discordance >10%), whereas the green ellipses show the points with discordance  $\leq$ 10%. The ellipse number corresponds to the position of the data point within the excel spreadsheets (Appendix IV – Tables AIV.8; AIV.10; AIV.12).

### VI.2.2. Monazite data (Stog' er Tight and Argyle)

A total of 61 monazite grains were analysed, 40 from the Stog' er Tight deposit and 21 from the Argyle deposit (*Table VI.2*). Five different U-Th-Pb dates were calculated for each analysed spot (*Tables AIV.3 & AIV.6*). The minimum and the maximum values of the obtained dates are listed in *Table VI.3*, whereas the minimum and the maximum values of the total Pb, Th, and U contents are provided in *Table VI.4*.

For both deposits, the  $^{208}\text{Pb}/^{232}\text{Th}$  dates show the lowest time span compared to the rest of the obtained dates (*Table VI.3*) and are considered geologically relevant (*see interpretations below*). Most of the  $^{207}\text{Pb}/^{235}\text{U}$  dates are significantly older or younger than the  $^{208}\text{Pb}/^{232}\text{Th}$  dates, whereas the  $^{206}\text{Pb}/^{238}\text{U}$  dates show the youngest values compared to all the other U-Th-Pb dates (*Table VI.3*). Both the  $^{207}\text{Pb}/^{235}\text{U}$  and the  $^{206}\text{Pb}/^{238}\text{U}$  dates cover large time intervals and show minimum and maximum values which are geologically unpalusible in the context of the geological history of the study area (*Table VI.3; see chapter II*). The  $^{207}\text{Pb}/^{206}\text{Pb}$  dates are anomalously old in both deposits (except for two dates from the rejected points in Argyle). Concordia dates are slightly older than the  $^{206}\text{Pb}/^{238}\text{U}$  dates and usually significantly younger than the  $^{207}\text{Pb}/^{235}\text{U}$  dates. Overall, in both deposits, the individual U-Th-Pb dates show high levels of disagreement (“*discordance*”).

In both deposits, Th values show a linear relationship with the Pb concentrations, consistent with a closed system whereby the Pb content is dominantly from decay of Th. In contrast, U does not present any covariance with *Figure VI.2* either Pb or Th (*Figure VI.4*). In the accepted data points from the Stog' er Tight monazites, the U contents display a direct relationship with the  $^{206}\text{Pb}/^{238}\text{U}$  dates and a reverse correlation with the discordance values between the  $^{208}\text{Pb}/^{232}\text{Th}$  and the  $^{206}\text{Pb}/^{238}\text{U}$  dates (*Figure VI.5*). Given the large range in the geologically implausible  $^{206}\text{Pb}/^{238}\text{U}$  dates, these are considered highly disturbed and the reasons for this are discussed later. No other relationships have been observed between the Pb, Th, and U contents and the individual U-Th-Pb dates and discordances.

In the Stog' er Tight and the Argyle deposits the accepted  $^{208}\text{Pb}/^{232}\text{Th}$  monazite dates cover a time span of 48 Ma and 70 Ma (without errors), respectively (*Table VI.3*). The largest variation of the  $^{208}\text{Pb}/^{232}\text{Th}$  dates (without errors) recorded

within a single grain is 36 Ma for the Stog'er Tight deposit and 50 Ma for the Argyle deposit (*Plates AIV.2 – E; AIV.4 - A*). In the five monazites analysed by EPMA from the Stog'er Tight deposit, the  $^{208}\text{Pb}/^{232}\text{Th}$  dates show a random distribution with respect to the Th, Y, and Sm zoning patterns (*Plates AIV.2 – B, C; AIV.3 – E, F, K*). Also, in both the Stog'er Tight and the Argyle deposits, the variability of the  $^{208}\text{Pb}/^{232}\text{Th}$  dates do not show any connection with the sizes and morphologies of the analysed grains.

*Table VI.3 – Minimum (min) and maximum (max) U-Th-Pb monazite dates*

Deposit	Monazite		<sup>208</sup> Pb/ <sup>232</sup> Th	Error	<sup>207</sup> Pb/ <sup>235</sup> U	Error	<sup>206</sup> Pb/ <sup>238</sup> U	Error	<sup>207</sup> Pb/ <sup>206</sup> Pb	Error	Concordia	Error
			Date (Ma)	(2σ)	Date (Ma)	(2σ)	Date (Ma)	(2σ)	Date (Ma)	(2σ)	Date (Ma)	(2σ)
Stog'er Tight	Accepted points	Min.	<b>375.28</b>	<b>31.39</b>	131.77	21.96	68.67	5.55	666.6	249.94	72.16	5.4
		Max.	<b>423.01</b>	<b>14.6</b>	598.56	53.76	361.54	11.24	2387.49	401.69	386.81	9.2
	Rejected points	Min.	<b>372.5</b>	<b>21.17</b>	<b>231.66</b>	<b>37.98</b>	<b>141.04</b>	<b>11.22</b>	<b>608.38</b>	<b>221.66</b>	<b>157.3</b>	<b>10.79</b>
		Max.	<b>571.24</b>	<b>46.23</b>	<b>2151.28</b>	<b>229.02</b>	<b>662.4</b>	<b>101.62</b>	<b>4305.11</b>	<b>497.32</b>	<b>726.85</b>	<b>102.28</b>
Argyle	Accepted points	Min.	<b>360.6</b>	<b>8.94</b>	280.02	29.56	118.97	7.75	535.37	263.56	127.34	7.58
		Max.	<b>430.83</b>	<b>18.72</b>	1064.43	117.08	492.96	44.71	3688.51	252.19	534.96	43.01
	Rejected points	Min.	<b>355.64</b>	<b>18.74</b>	<b>200.87</b>	<b>36.37</b>	<b>130.86</b>	<b>8.06</b>	<b>181.8</b>	<b>613.02</b>	<b>133.84</b>	<b>7.9</b>
		Max.	<b>504.56</b>	<b>59.9</b>	<b>3850</b>	<b>277.67</b>	<b>2372.32</b>	<b>541.93</b>	<b>4743.89</b>	<b>561.39</b>	<b>3173.64</b>	<b>444.61</b>

**Table VI.4** – Minimum (min) and maximum (max) values for Pb, Th, and U concentrations of the analysed monazite, xenotime and titanite grains

Deposit	Mineral / data point / value	Pb (ppm)	Th (ppm)	U (ppm)		
Stog'er Tight	Monazite	Accepted points	Min.	12.75	679.48	58.39
			Max.	92.79	5867.13	384.21
		Rejected points	Min.	6.41	298	49.87
			Max.	80.55	4498.58	271
	Xenotime	Accepted points	Min.	1.14	10.17	15.6
			Max.	19.46	371.82	385.56
		Rejected points	Min.	0.21	0.47	0.65
			Max.	21.54	137.68	373.16
Argyle	Monazite	Accepted points	Min.	5.8	427.94	4.73
			Max.	145.42	7573.51	130.8
		Rejected points	Min.	3.02	205.53	3.08
			Max.	249.79	11653.67	124.5
	Xenotime	Accepted points	Min.	8.12	79.54	71.08
			Max.	36.13	655.14	574.48
		Rejected points	Min.	3.56	9.14	32.7
			Max.	38.98	366.82	165.10
Romeo & Juliet	Xenotime	Accepted points	Min.	1.52	2.44	66.58
			Max.	23.22	595.37	639.39
		Rejected points	Min.	0.77	12.15	23.17
			Max.	22.27	424.36	826.88
Deer Cove	Titanite	All points	Min.	0.01	0.00	1.16
		Max.	0.08	0.28	2.48	

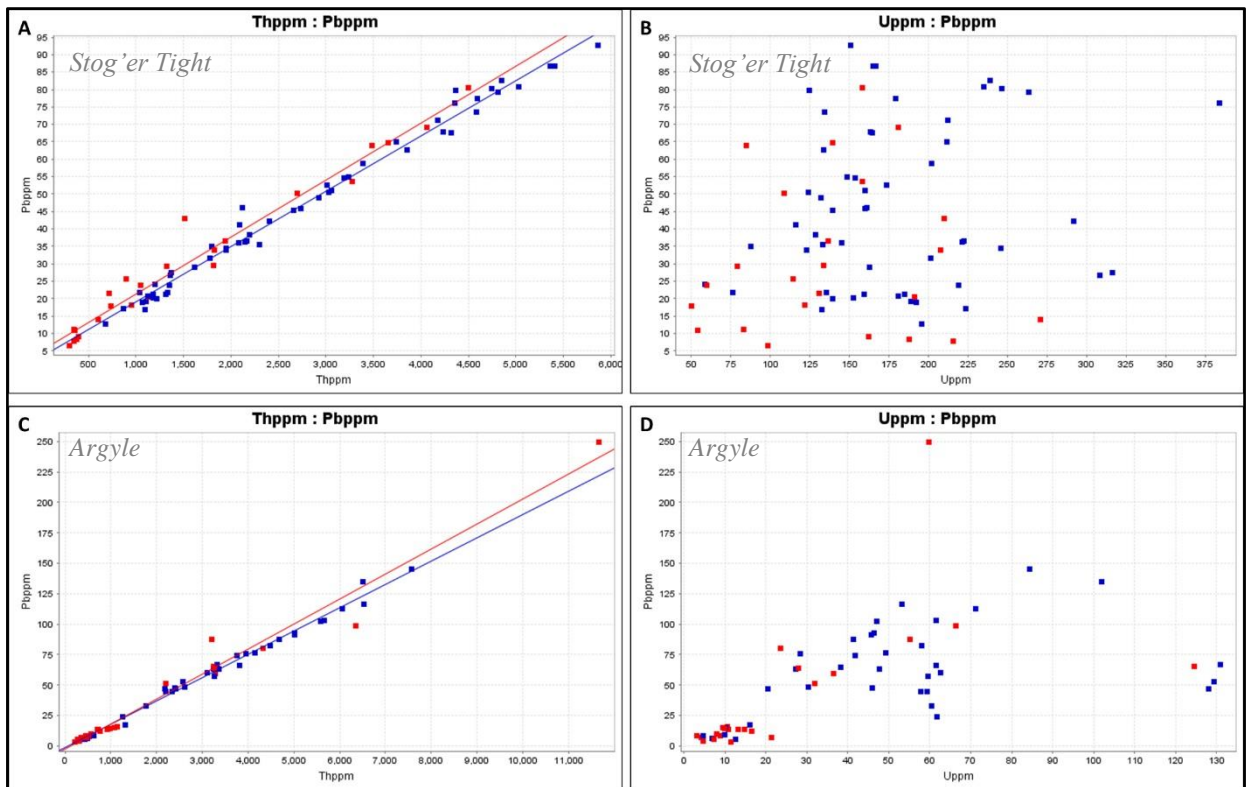


**Figure VI.4** – Th-Pb and U-Pb binary plots for the Stog'er Tight (A, B) and Argyle (C, D) monazites. Red and blue squares correspond to rejected and accepted data points, respectively.

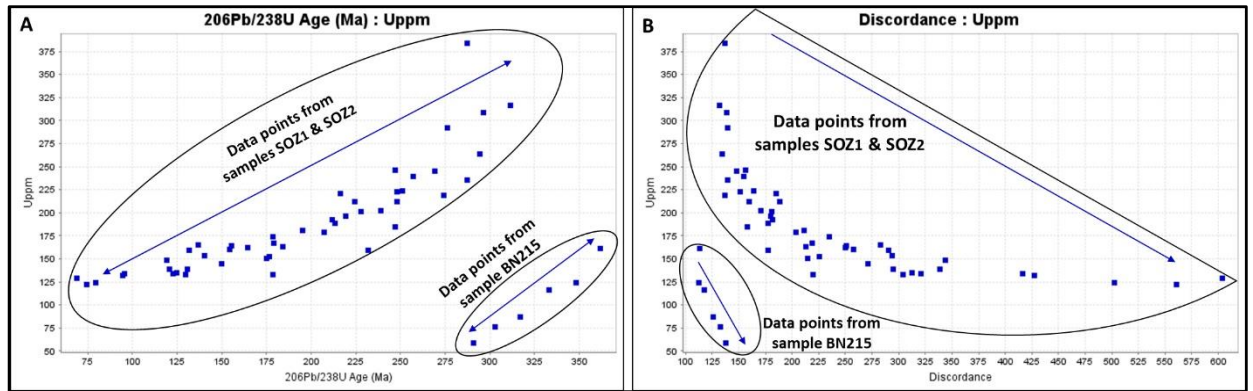


**Figure VI.5** – Binary plots of U vs  $^{206}\text{Pb}/^{238}\text{U}$  dates (A) and U vs Discordance (between the  $^{208}\text{Pb}/^{232}\text{Th}$  and the  $^{206}\text{Pb}/^{238}\text{U}$  dates) (B) for the accepted Stog’er Tight monazites; note the separation of the data points from the SOZ<sub>1</sub> & SOZ<sub>2</sub> samples and from sample BN215 in two separate clusters based on the  $^{206}\text{Pb}/^{238}\text{U}$  dates.

### VI.2.3. Xenotime data (Stog’er Tight, Argyle, and Romeo & Juliet)

A total of 55 xenotime grains were analysed, 21 from the Stog’er Tight deposit, 18 from the Argyle deposit, and 16 from the Romeo & Juliet deposit (**Table VI.2**). Four different U-Pb dates were generated for each analysed spot (**Tables AIV.8, AIV.10, AIV.12**), as  $^{208}\text{Pb}/^{232}\text{Th}$  dates are not considered for this Th-poor mineral. The minimum and the maximum dates are listed in **Table VI.5**, whereas the minimum and the maximum values of the total Pb, Th, and U contents are provided in **Table VI.4**.

In the Stog’er Tight xenotimes, there is a positive correlation between the Pb and U contents of both the accepted and rejected data points, whereas in the Argyle xenotimes, the Pb and U contents show a correlation only for the accepted data points (**Figure VI.6**). These correlations are a sign that the U-Pb system is not disturbed or dominated by the incorporation of inherited lead and that most of the radiogenic Pb resulted from the decay of U. No covariance was observed between Th and U in either of the two deposits. In contrast, the accepted data points from the Romeo & Juliet xenotimes, exhibit a direct relationship between Pb and both U and Th values, and between U and Th concentrations (**Figure VI.7**). This suggest that the radiogenic Pb comes from both the U and Th decay and that no common Pb influence the accepted dates. No clear covariance is observable between these elements in the rejected data points (**Figure VI.7**).

In none of the three deposits, the Pb, Th, and U contents do not show any covariance with any of the four recorded U-Pb dates and neither with the



discordance values between the  $^{207}\text{Pb}/^{235}\text{U}$  and  $^{206}\text{Pb}/^{238}\text{U}$  dates. Also, no connection has been observed between the variability of the U-Pb dates and the external or internal morphological characteristics (including the CL zoning pattern) of the analysed xenotimes.

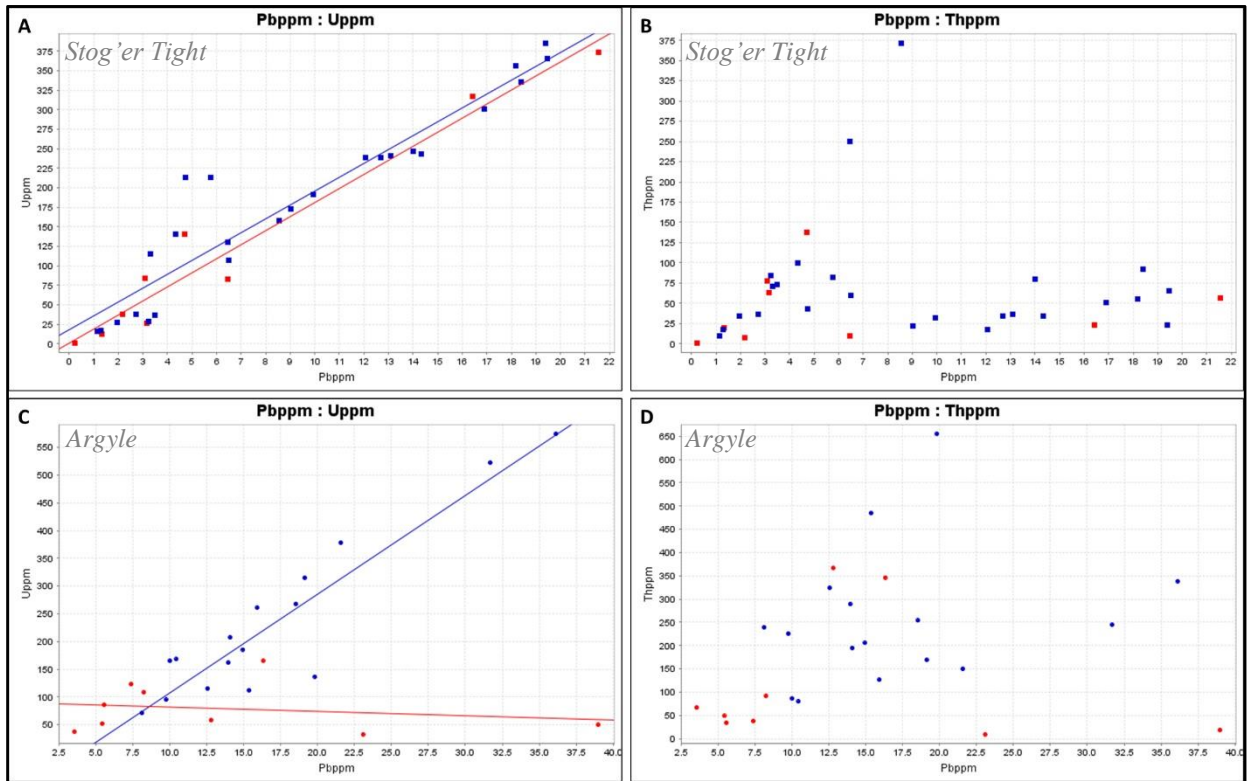


**Figure VI.6** –Pb-U and Pb-Th binary plots for the Stog'er Tight (A, B) and Argyle (C, D) xenotimes. Red and blue squares correspond to rejected and accepted data points, respectively.

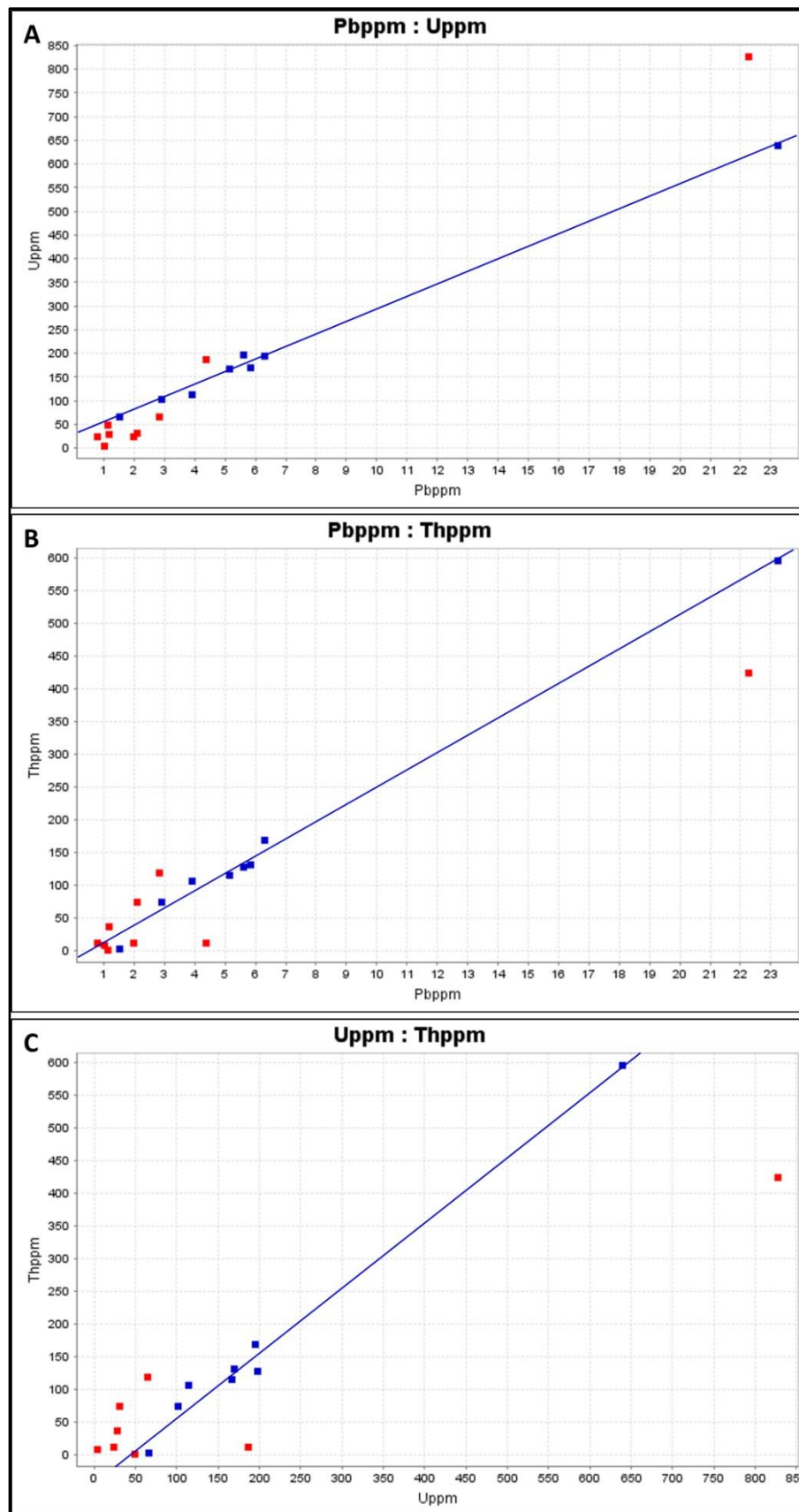


**Figure VI.7** – Binary plots between Pb and U (**A**), Pb and Th (**B**), and between U and Th (**C**) for the Romeo & Juliet xenotimes. Red and blue squares correspond to rejected and accepted data points, respectively.

*Table VI.5 – Minimum (min) and maximum (max) U-Pb xenotime dates*

Deposit	Xenotime		Concordia	Error	<sup>207</sup> Pb/ <sup>235</sup> U	Error	<sup>206</sup> Pb/ <sup>238</sup> U	Error	<sup>207</sup> Pb/ <sup>206</sup> Pb	Error
			Date (Ma)	(2σ)	Date (Ma)	(2σ)	Date (Ma)	(2σ)	Date (Ma)	(2σ)
Stog'er Tight	Accepted points	Min.	373.1	14.9	384.9	14.4	371.9	14.8	361.7	100.2
		Max.	419.6	13.5	451.3	27.9	417.2	13.5	648.8	105.7
	Rejected points	Min.	122.3	434.8	402.4	14.4	386.5	12.4	490.5	63.1
		Max.	500.8	70.9	3156	858	1816.9	1366.7	4169.4	286
Argyle	Accepted points	Min.	364.6	14.2	378.8	13	363.5	14.1	382.5	60.9
		Max.	413	14	451.1	23.1	410.9	14	669.7	93.1
	Rejected points	Min.	134.1	54.2	448.7	19.9	399.9	13.7	613.4	78.7
		Max.	488.2	38.5	3548.1	108.8	1919.4	176.2	4668.3	42.4
Romeo & Juliet	Accepted points	Min.	391.8	15.5	392.1	16.8	391.7	16	394.9	68
		Max.	424.5	21.6	433.7	20.5	422.2	21.7	595.4	96.6
	Rejected points	Min.	323.84	66.38	421.6	78.03	330.86	67.03	566.12	489.16
		Max.	900.4	110.7	3173.6	131.5	1495.6	127.8	5361.13	1847.54

*Table VI.6 – Minimum (min) and maximum (max) U-Pb titanite dates*

Deposit	Titanite	Concordia	Error	<sup>207</sup> Pb/ <sup>235</sup> U	Error	<sup>206</sup> Pb/ <sup>238</sup> U	Error	<sup>207</sup> Pb/ <sup>206</sup> Pb	Error
		Date (Ma)	(2σ)	Date (Ma)	(2σ)	Date (Ma)	(2σ)	Date (Ma)	(2σ)
Deer Cove	Min.	264.6	30.8	1243.8	110.1	459.3	46	3093.8	180.5
	Max.	800.8	37	2824.5	58.6	1164.1	41.5	4394.5	69.6

#### VI.2.4. Titanite data (Deer Cove)

A total of 18 titanite grains were analysed from the Deer Cove deposit (*Table VI.2*). Four different U-Pb dates were generated for each analysed spot, and as with xenotime,  $^{208}\text{Pb}/^{232}\text{Th}$  data were not considered (*Table AIV.15*). The minimum and the maximum values of the obtained dates are listed in *Table VI.6*, whereas the minimum and the maximum values of the total Pb, Th, and U contents are provided in *Table VI.4*. All the obtained U-Pb dates spread on large time intervals (>500 Ma) and show minimum and maximum values that are geologically meaningless (*Table VI.6*). However, on a Tera-Wasserburg diagram, the data align perfectly along a discordia line, indicating mixing between radiogenic and initial lead (*Figure VI.8*). The variability of the obtained dates do not show any association with the Pb, Th and U concentrations. Moreover, no clear covariance has been observed between the Pb, Th, and U contents.

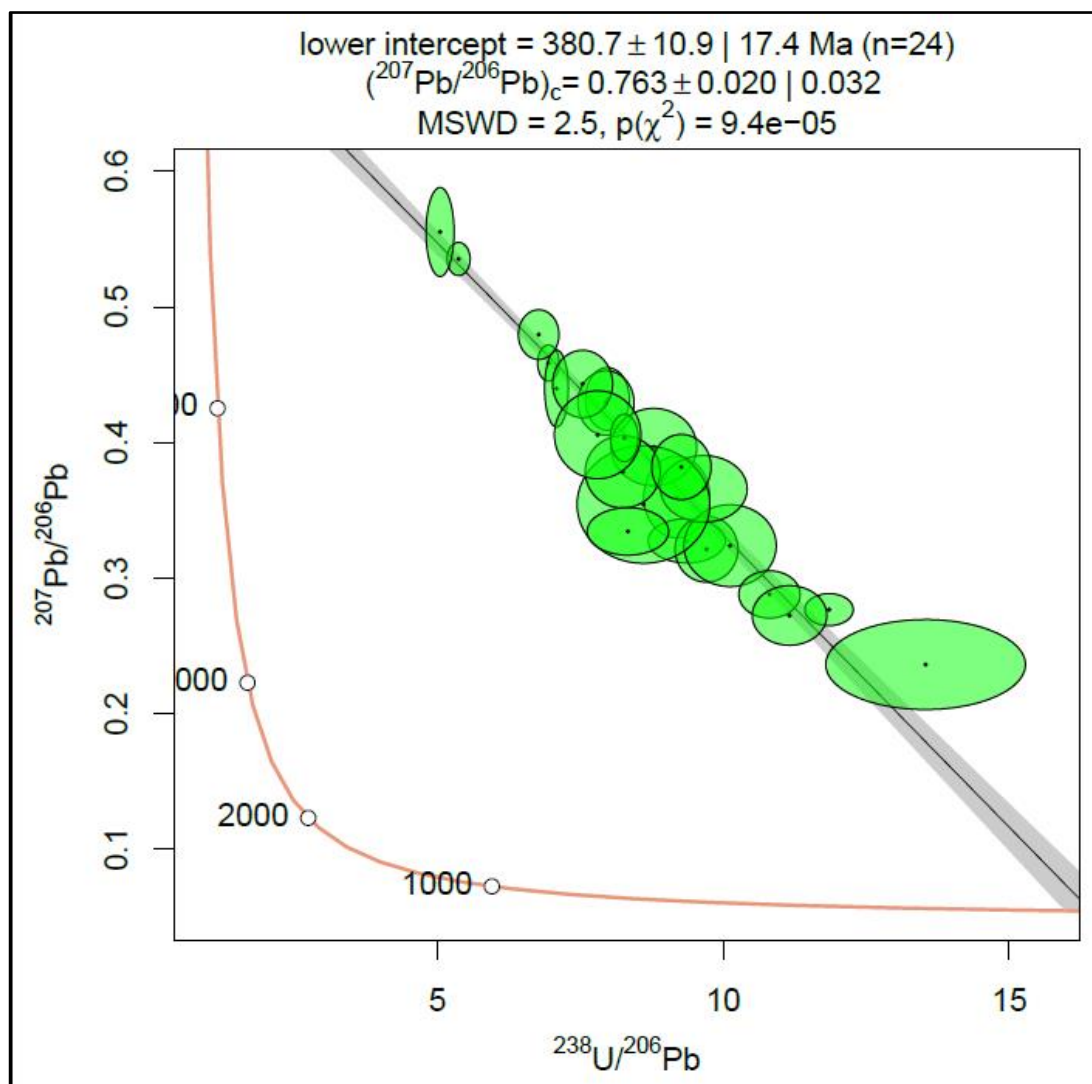


**Figure VI.8** – Deer Cove titanite data plotted on Tera-Wasserburg concordia diagram; *note* the lower intercept age of  $380.7 \pm 17.4$  interpreted as best estimate for titanite crystallization.

### **VI.3. Interpretations**

#### **VI.3.1. Grain textures and morphologies**

Resorbed and serrated grain boundaries, polycrystalline aggregates, porous and inclusion rich domains, presence of cracks and fractures, patchy and sector zoning patterns, and heterogenous compositional zonation are textures suggestive of alteration and recrystallisation through fluid-mediated coupled dissolution-precipitation reactions (Putnis, 2009; Hetherington et al., 2009; Li et al., 2021; Schulz, 2021). Both the monazite and xenotime grains analysed herein show these types of textures and thus, were assumably affected by similar processes (Table VI.1 and Plates AIV.1 - AIV.12). This is also supported by the significant spread of dates over several million years both within separate grains and in the same grain. It is interpreted that the alteration and recrystallization of the monazite and xenotime occurred during the second mineralising event that contributed to the formation of the studied deposits (*see chapter V*). This is based on the paragenetic setting of the analysed grains which formed during the first hydrothermal stage but were subsequently brecciated and overprinted by late alteration minerals (*see Table VI.1 and chapter V*).

As presented in *chapter V*, the coarse grained titanite crystals and aggregates formed through recrystallisation of fine-grained titanite and replacement of rutile crystals during the early stage of the second hydrothermal event that affected the Deer Cove deposit (*Figure. V.17*). All the analysed titanites show textures and morphologies that support their formation during the second paragenetic stage and thus, their relative timing is interpreted accordingly (*Table VI.1; Plate AIV.13*). Subsequent grain alteration may have also occurred considering that some titanites are overgrown and brecciated by calcite, sericite, and chlorite (*Table VI.1; Plate AIV.13*).

#### **VI.3.2. Reasons for date discordance in the excluded points**

There are several factors that can lead to discordance between the U-Th-Pb dates, the most common being the following: incorporation of initial Pb (also referred to as non-radiogenic or common); intermediate daughter product disequilibrium; Th, Pb, and U loss or gain; mixing between two crystal growth episodes; and Th, U, or Pb mobility within the crystal lattice (Harrison et al., 2002;

Williams et al., 2011; Seydoux-Guillaume et al., 2012; Spencer et al., 2016; Reiners et al., 2018; Barnes et al., 2021; Budzyń et al., 2022). For the analytical points in which extra material was ablated during the data acquisition stage (*point i*), contamination with common Pb and/or unsupported radiogenic Pb incorporated from other minerals (e.g. zircon, rutile) are considered the main causes for the disturbance of the U-Th-Pb dates. This interpretation is supported by the high  $^{207}\text{Pb}/^{206}\text{Pb}$  ratios of these data points, and consequently by their old  $^{207}\text{Pb}/^{206}\text{Pb}$  dates which are almost the same or older than the age of the earth (e.g. *points 37, 49 - Figure VI.1- C; point 5 - Figure VI.2- C; point 22 – Figure VI.3 – A; points 18 & 20 – Figure VI.3– C; point 12 – Figure VI.3 – E, and others*).

For the rest of the excluded points (*ii, iii, and iv*), the lack of covariance between the Th, U, and Pb contents and the U-Th-Pb dates and discordances suggest that a combination of the above-listed factors affected the recorded dates. However, without more detailed investigations (e.g. transmission electron microscopy – TEM; LA-ICP-MS compositional maps) the degree to which these factors affect the U-Th-Pb isotopic system of the studied grains cannot be quantified. Incorporation of common Pb can explain the old  $^{207}\text{Pb}/^{206}\text{Pb}$  dates or the high errors in some points but should not drive concordant or near concordant  $^{206}\text{Pb}/^{238}\text{U}$  dates to significantly older or younger ages.

Excess of  $^{206}\text{Pb}$  and  $^{207}\text{Pb}$  resulted from the decay of  $^{230}\text{Th}$  and from  $^{231}\text{Pa}$ , intermediate daughter isotopes of  $^{238}\text{U}$  and  $^{235}\text{U}$ , respectively, can lead to overestimation of the  $^{206}\text{Pb}/^{238}\text{U}$  and  $^{207}\text{Pb}/^{235}\text{U}$  dates in monazite, whereas either deficit or excess of  $^{206}\text{Pb}$  due to low or high concentrations of  $^{230}\text{Th}$  can generate underestimated or overestimated  $^{206}\text{Pb}/^{238}\text{U}$  dates in xenotime (Schärer, 1984; Harrison et al., 2002; Grand'Homme et al., 2016; Barnes et al., 2021). In this study, excess of  $^{206}\text{Pb}$  in monazite or a deficit/excess of  $^{206}\text{Pb}$  in xenotime is unlikely because the  $^{206}\text{Pb}/^{238}\text{U}$  monazite dates are anomalously young in both Stog'er Tight and Argyle deposits, rather than anomalously old, and the  $^{206}\text{Pb}/^{238}\text{U}$  xenotime dates are similar to the concordia dates in all deposits (*Tables AIV.3; AIV.6; AIV.8; AIV.10; AIV.12*). In both Stog'er Tight and Argyle deposits, excess of  $^{207}\text{Pb}$  is a potential cause for the disturbance of the U-Pb isotopic system in monazite as some data extend to older  $^{207}\text{Pb}/^{235}\text{U}$  ratios at fixed  $^{208}\text{Pb}/^{232}\text{Th}$  and  $^{206}\text{Pb}/^{238}\text{U}$  ratios (*Figure VI.1 and Figure VI.2*). However, for some data points significant young

$^{206}\text{Pb}/^{238}\text{U}$  dates correlate to young  $^{207}\text{Pb}/^{235}\text{U}$  dates, which implies that unsupported  $^{207}\text{Pb}$  cannot be the dominant cause of isotopic disturbance in the excluded points (**Figure VI.1– C, E; Figure VI.2– C, E**).

Several studies showed that internal remobilisation and/or partial gain/loss of Th/U/Pb are processes that can disturb the initial U-Th-Pb isotopic system of both monazite and xenotime during fluid-mediated grain alteration and/or recrystallisation (Williams et al., 2011; Seydoux-Guillaume et al., 2012; Grand’Homme et al., 2016; Budzyń and Sláma, 2019). Considering the altered and the recrystallized nature of the analysed grains, it is inferred that similar processes also contributed to the date disturbance of the excluded points.

As presented above, some of the analysed xenotime grains show a core-rim zoning pattern under CL (**Plates AIV.8 – B; AIV.9 – D; AIV.11 - H**). In these grains, mixing of different growth zones may be one of the causes that led to high discordance values in the analytical points that fell on two domains. Still, concordant dates were also recorded in laser spots that cover both core and rim zones (*e.g.* **Plate AIV.8 – B**). Thus, mixing effect alone may not be enough to generate high discordance values and probably other of the previously mentioned factors also contributed.

### **VI.3.3. Age interpretation of monazite data**

A few studies showed that for monazite, the  $^{208}\text{Pb}/^{232}\text{Th}$  dates are more reliable than the U-Pb dates because: i) monazite incorporates more Th than U; ii) the high amounts of  $^{232}\text{Th}$  result with high concentrations of radiogenic  $^{208}\text{Pb}$  which diminish the effect of initial Pb; iii) unsupported  $^{206}\text{Pb}$  and  $^{207}\text{Pb}$  resulted from the disequilibrium of the U decay chain can lead to the overestimation of the  $^{206}\text{Pb}/^{238}\text{U}$  and  $^{207}\text{Pb}/^{235}\text{U}$  dates, respectively; and iv) the high solubility of U in oxidised fluids can lead to U depletion during fluid-mediated alteration and recrystallisation processes (Seydoux-Guillaume et al., 2012; Grand’Homme et al., 2016; Barnes et al., 2021; Budzyń et al., 2022). In this study, the distribution of the accepted data points on all three concordia diagrams suggest that both the U-Pb and the Th-Pb isotopic systems are disturbed (**Figure VI.1 and Figure VI.2**). However, as in the above mentioned studies, several observations indicate that the Th-Pb dates are less affected than the U-Pb dates: i) the data points form linear trends in the U-Th-Pb

concordia space but are randomly distributed on the Wetherill and Tera-Wasserburg diagrams (*Figure VI.1 and Figure VI.2*); ii) the Th and Pb contents show positive covariance, whereas the U and Pb do not show any correlation (*Figure VI.4*); and iii) the U-Pb dates cover larger time intervals than the Th-Pb dates and show minimum and maximum values which are geologically unpalatable (*Table VI.3*). U depletion during the alteration and recrystallisation is considered the primary process that affected the U-Pb system of the analysed monazites, followed by incorporation of common Pb and excess of  $^{207}\text{Pb}$ . The positive covariance between the U contents and the  $^{206}\text{Pb}/^{238}\text{U}$  dates, combined with the reverse correlation between the U values and the discordance between the  $^{208}\text{Pb}/^{232}\text{Th}$  and the  $^{206}\text{Pb}/^{238}\text{U}$  dates observed in the Stog'er Tight monazites combined with the overall distribution of the accepted points on the concordia diagrams support the afore-mentioned statement (*Figure VI.1 and Figure VI.2; Figure VI.5*).

The weighted mean ages of the  $^{208}\text{Pb}/^{232}\text{Th}$  dates for both the Stog'er Tight ( $398.2 \pm 3.12$ ) and for the Argyle ( $396.07 \pm 6.3$ ) monazites have associated mean square weighted deviations (MSWD) higher than  $1+2\sqrt{\frac{2}{f}}$  ( $f$  is the degree of freedom = number of averaged dates – 1; Wendt and Carl, 1991) (*Figure VI.9- A & Figure VI.10- A*). This suggests that either the uncertainties are underestimated, or that there is a high degree of natural variation in the data due to open system behaviour or to a complex crystallisation history (Spencer et al., 2016). Thus, based on the high MSWD, combined with the large time intervals covered by the obtained dates (> 40 Ma) and with the altered/recrystallised nature of the analysed monazites, the weighted mean ages of the Th-Pb dates are considered, for both deposits, a combination of partially reset or mixed ages which reflect the protracted evolution of the mineralising systems.

The lack of correlation between the Th-Pb dates and either the observed textures or the Th/U/Pb contents, do not permit to evaluate the degree of resetting/mixing of the Th-Pb isotopic system, or to establish the exact cause of disturbance (Th and/or Pb loss/gain, nano to micron scale remobilisation, incorporation of initial Pb, etc.). Hence, there is no unique way to separate the dates to obtain geologically meaningful ages representative for multiple mineralisation events. However, considering the paragenetic evolution of the analysed grains (see interpretations above and *chapter V*) some assumptions can be made.



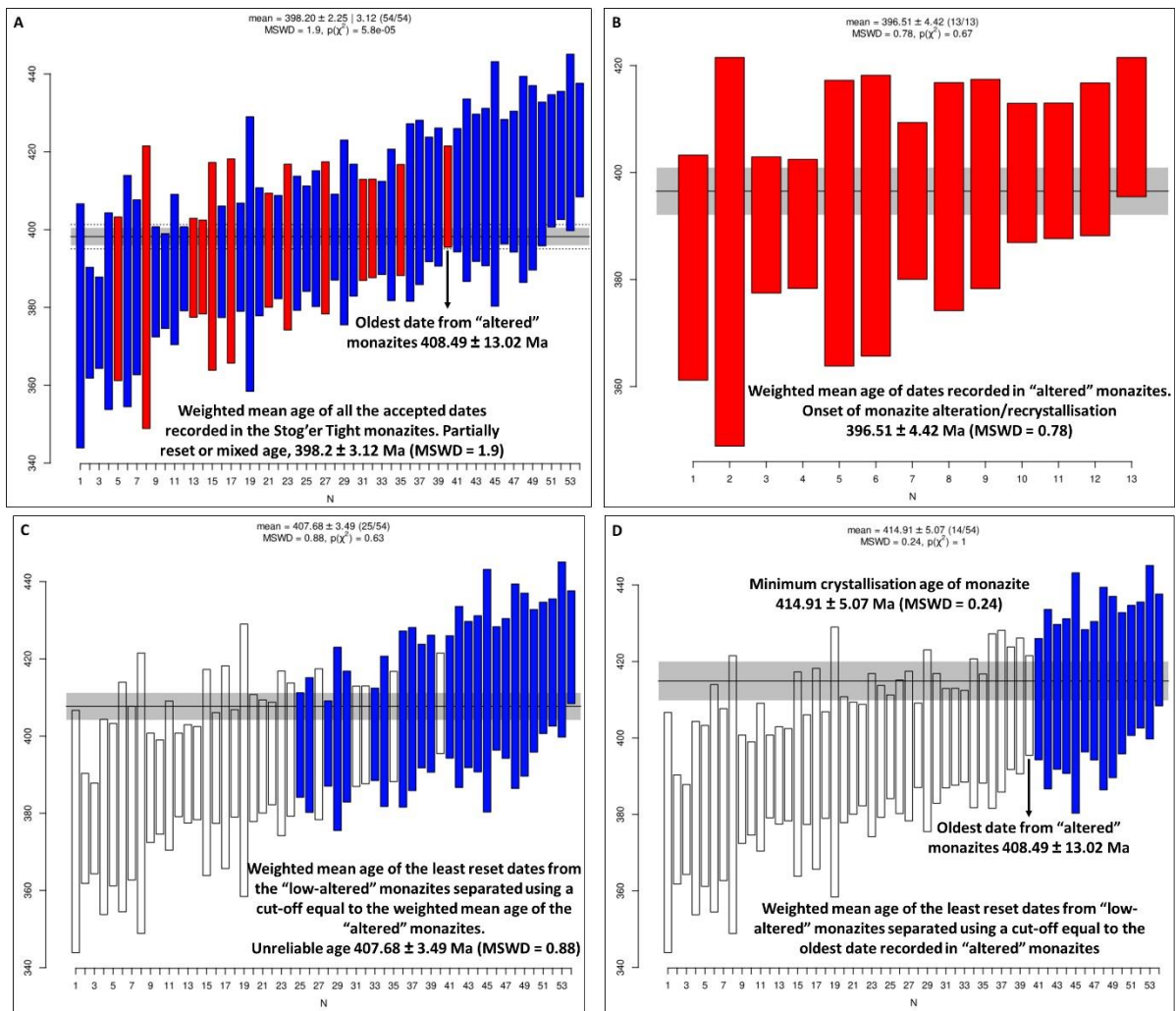


**Figure VI.9** – Interpreted weighted mean ages for the accepted Th-Pb dates recorded in the Stog'er Tight monazites. The length of the bars represents the date uncertainty (in  $2\sigma$ ). The blue bars correspond to dates recorded in "low-altered" monazites. The red bars represent dates from "altered" monazites. See text for explication of "low-altered" and "altered" terminologies. The white/empty bars show the dates that were not included in the mean. N = number of dates.

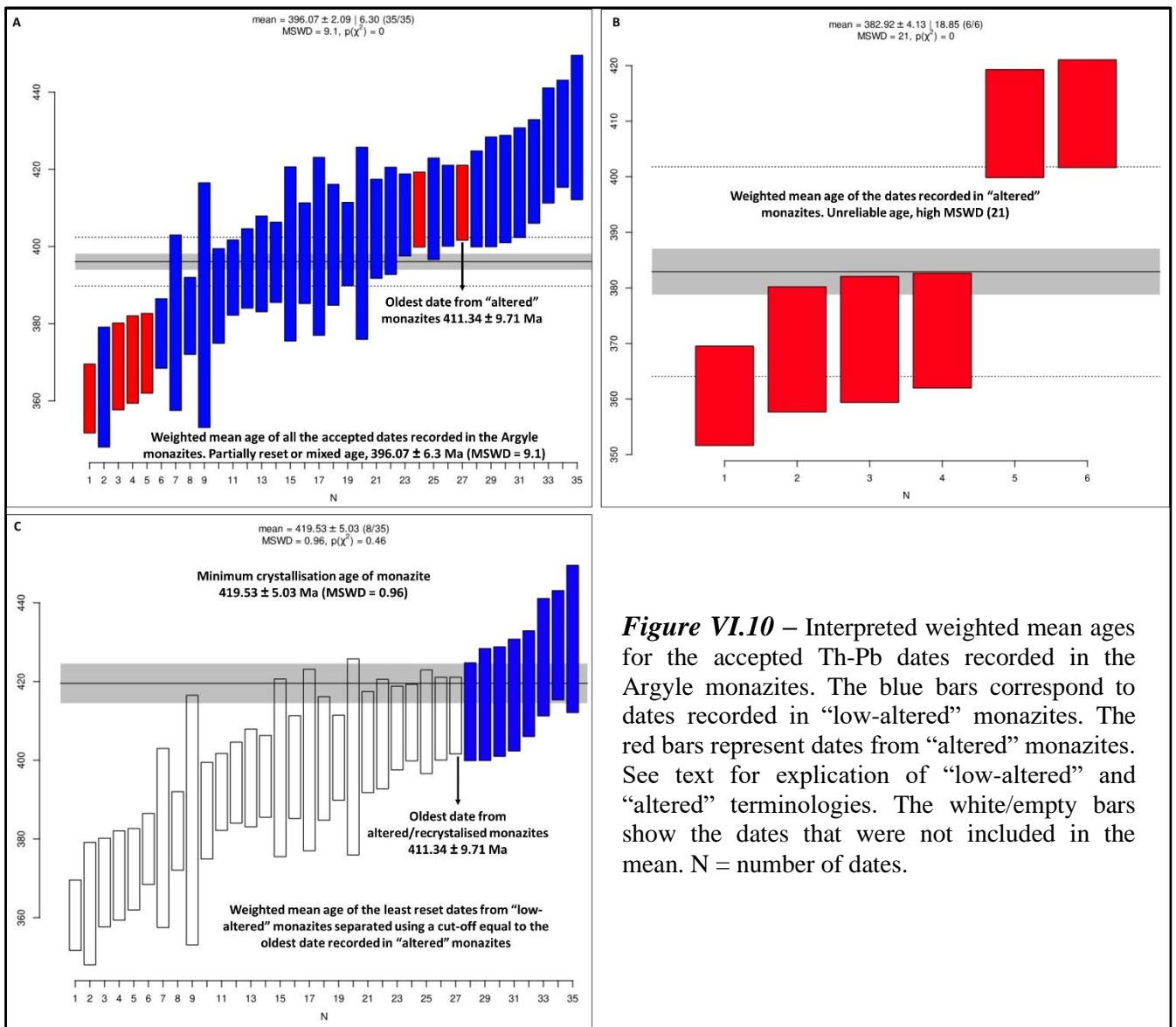


**Figure VI.10** – Interpreted weighted mean ages for the accepted Th-Pb dates recorded in the Argyle monazites. The blue bars correspond to dates recorded in “low-altered” monazites. The red bars represent dates from “altered” monazites. See text for explication of “low-altered” and “altered” terminologies. The white/empty bars show the dates that were not included in the mean. N = number of dates.

The oldest dates from both the Stog'er Tight and Argyle deposits correspond to the onset of monazite crystallisation, whereas the youngest dates reflect the recrystallisation processes and in turn, the resetting of the isotopic system. The monazites that show very little or no surface contact (in 2D) with minerals formed during the second hydrothermal stage have a low chance to be altered/recrystallised (henceforward “low-altered”) and so, record an age approximate to to their crystallisation age. In contrast, the monazites that have at least one face in direct contact with late alteration minerals or which are brecciated by these minerals have a high chance to be altered/recrystallised (henceforward “altered”), and record an age related to their alteration and/or recrystallisation. Beside the paragenetic context, these assumptions are also supported by the following observations. No dates older than ~411 Ma were recorded in the “altered” monazites, while dates that are both older and younger than ~411 Ma were recorded in the “low-altered” grains (**Figure VI.9– A; Figure VI.10– A**). The EPMA analysed monazite that shows homogenous Th, Y, and Sm zonation has high contact with late calcite veins (so “altered”) and record young dates (397 Ma to 382 Ma, **plate AIV.3 – K**). The other four monazites analysed by EPMA, show heterogenous Th, Y, and Sm zoning patterns, have very little or no contact with late alteration minerals (“low-altered”) and show either old dates (400 Ma to 419 Ma, **Plate AIV.3 – E**; 410 Ma to 413 Ma, **plate AIV.3 - F**) or young dates (384 to 379 Ma, **plate AIV.B**; 391 Ma to 376 Ma, **plate AIV.2 – C**). The homogenous zoning pattern observed in the altered monazite combined with its young ages suggest that the grain recrystallised almost completely and consequently, its isotopic system was reset almost totally. In contrast, the heterogenous nature of the “low-altered” monazites and their associated dates suggest that these grains are altered/recrystallised to various degrees and that their isotopic system is only partially reset. Moreover, considering the 2D nature of the analysed thin sections, it is possible that some of the “low-altered” grains to be in contact with late alteration minerals in the 3<sup>rd</sup> dimension. This can explain their various degrees of alteration/recrystallisation and why some of these grains do not consistently show older dates.

For the Stog'er Tight deposit, the weighted mean age of the dates recorded in the “altered” grains show an acceptable MSWD value, and this age is interpreted as the onset (maximum age) of the alteration and/or recrystallisation of monazites

( $396.51 \pm 4.42$  Ma, *Figure VI.9- B*). This is considered only a maximum age and not a best estimate because, as previously mentioned, the degree of reset cannot be quantified, and so, it is considered that the isotopic system did not reach total reset. For the Argyle deposit, the obtained weighted mean age of the dates recorded in the “altered” monazites show a very high MSWD and is therefore considered an unreliable age estimate (*Figure VI.10- B*).

Because the isotopic system of the “low-altered” monazites is reset to various degrees, it is considered that a weighted mean age of the dates recorded in these monazites would represent a partially reset age, and so, a geologically meaningless age. Therefore, to obtain a relevant age for the monazite crystallisation, the least reset dates (closest to crystallisation) from the low-altered monazite must be extracted. Depending on how the data are handled, this can be done using two different approaches. For the first option it is inferred that the least reset dates of the “low-altered” grains should be older than the weighted mean age of the “altered” monazites (the maximum age of the alteration/recrystallisation processes), while for the second approach, the least reset dates of the “low-altered” grains should be older than the oldest date recorded in the “altered” monazites (*Figure VI.9- C, D; Figure VI.10- C*). Thus, for the Stog’er Tight deposit, two weighted mean ages with reasonable MSWD values were obtained for the “low-altered” monazites (*Figure VI.9 - C, D*). Out of these, the weighted mean age ( $414.91 \pm 5.07$  Ma) calculated using the second approach, is considered more reliable because it has a lower chance of incorporating partially reset or mixed dates. Moreover, because the used dates may still be slightly reset, this age is interpreted as a minimum age for monazite crystallisation (*Figure VI.9- D*). For the Argyle monazites, only the second approach can be used to select the least reset dates from the “low-altered” grains. The weighted mean age ( $419.53 \pm 5.03$ ) of these dates has a reasonable MSWD value and, as for the Stog’er Tight deposit, it is interpreted as a minimum crystallisation age (*Figure VI.10- C*).

#### VI.3.4. Age interpretation of xenotime data

Concordia dates are considered more reliable than the rest of the U-Pb dates because make the best use of all U-Pb ratios and contain a quantifiable measure of concordance (Ludwig, 1998; Spencer et al., 2016). Thus, the concordia dates are used herein to compute the mean ages of the analysed xenotime grains from the Stog' er Tight, Argyle, and Romeo & Juliet deposits (*Figure VI.11 – A; Figure VI.12– A; Figure VI.13– A*). The high MSWD values of the obtained weighted mean ages, combined with the large time intervals covered by the used dates (~46, ~48, ~33 Ma for Stog' er Tight, Argyle, in Romeo & Juliet, respectively, *Table VI.5*) and with the altered/recrystallised nature of the analysed xenotimes, indicate that the resulted ages are partially reset or mixed.

As for the monazite grains, the lack of correlation between the concordia dates and either the U/Pb contents and the observed grain morphologies and textures (including CL zoning) do not permit an evaluation of the degree of resetting/mixing of the U-Pb isotopic system and neither the exact cause of distortion (U/Pb loss/gain, nano to micron scale remobilisation, incorporation of initial Pb, etc.). However, the xenotimes show a similar paragenetic evolution as the monazites and thus, the same assumptions and systematics are used to separate and interpret the data.

In all deposits, no dates older than ~396 Ma were recorded in the xenotime grains that are brecciated, have high surface contact ( $\geq$  half grain) or are fully surrounded by alteration minerals related to the second hydrothermal stage (henceforward “altered”; *Figure VI.11– A; Figure VI.12 – A; Figure VI.13 – A*). It is considered that these xenotimes have the highest chance of being altered and/or recrystallised during the second hydrothermal stage and their associated dates are most likely reset. Thereby, the weighted mean age of these dates is interpreted as the onset of their alteration and/or recrystallisation (*Figure VI.11– A; Figure VI.12 – A; Figure VI.13– B*).

As for the monazites, two cut-off values can be used to separate the least reset dates from the “low-altered” grains: the weighted mean age of the dates recorded in the “altered” xenotimes, or the oldest date recorded in the aforementioned xenotimes. In the Stog' er Tight deposit, the weighted mean age obtained using the second approach is considered more reliable because it has a lower probability to include partially reset or mixed dates (*Figure VI.11 – C, D*). For the

Argyle deposit, the two computed weighted mean ages of the least reset dates from the “low-altered” grains overlap within error with the weighted mean age of the “altered” xenotimes, and so are considered unreliable (*Figure VI.12– C, D*). For the Romeo & Juliet deposit, only one weighted mean age can be calculated for the least reset dates because these are older than both cut-off values described above (*Figure VI.13 – C*). The resulted weighted mean ages of the least reset dates recorded in the “low-altered” xenotimes from both the Stog’er Tight and Romeo & Juliet deposits are interpreted as minimum crystallisation ages (*Figure VI.11– D; Figure VI.13– C*).

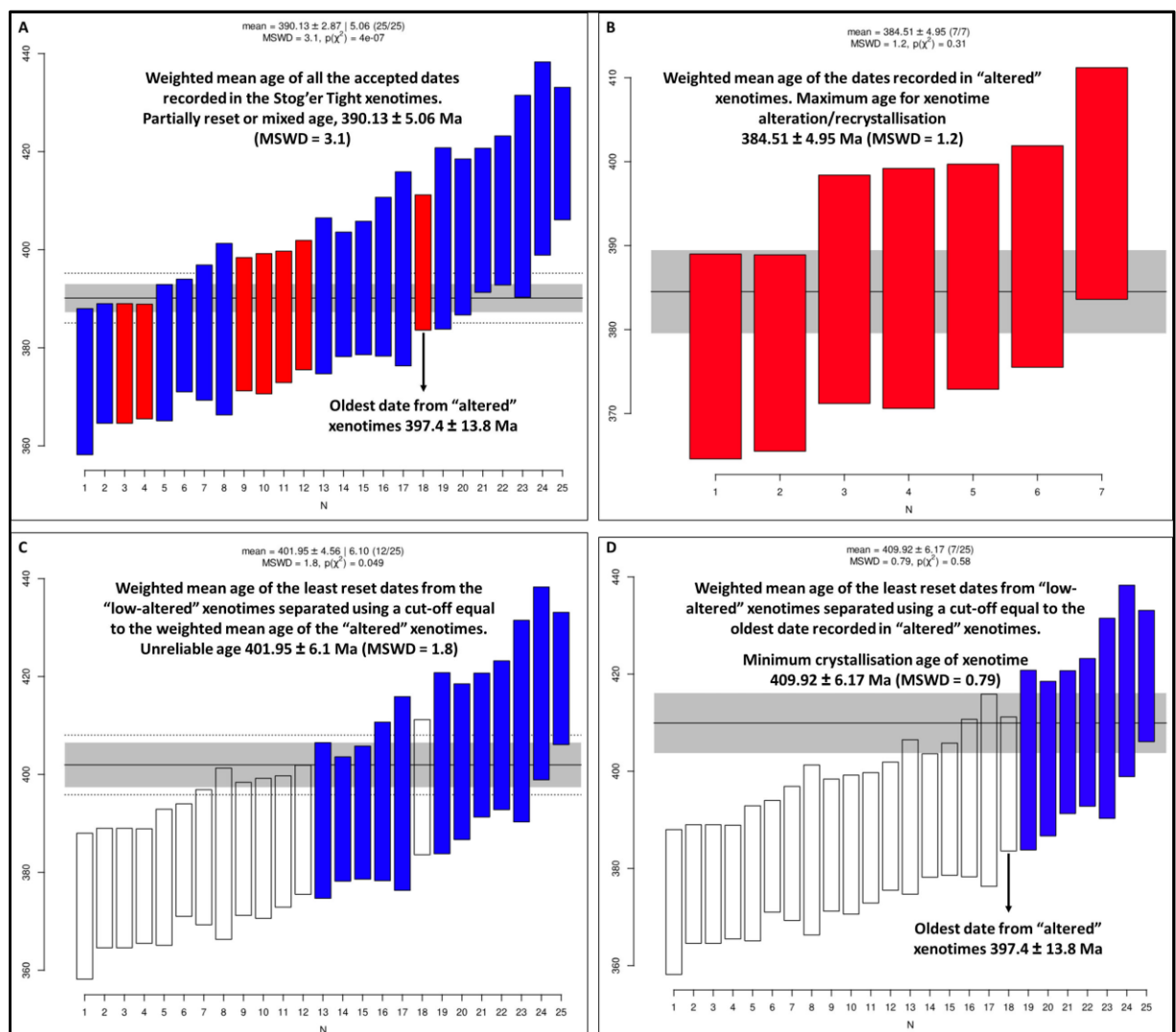


**Figure VI.11** – Interpreted weighted mean ages for the accepted concordia dates recorded in the Stog’er Tight xenotimes. The length of the bars represents the date uncertainty (in  $2\sigma$ ). The blue bars correspond to dates recorded in “low-altered” grains. The red bars represent dates from “altered” xenotimes. See text for explication of “low-altered” and “altered” terminologies. The white/empty bars show the dates that were not included in the mean. N = number of dates.

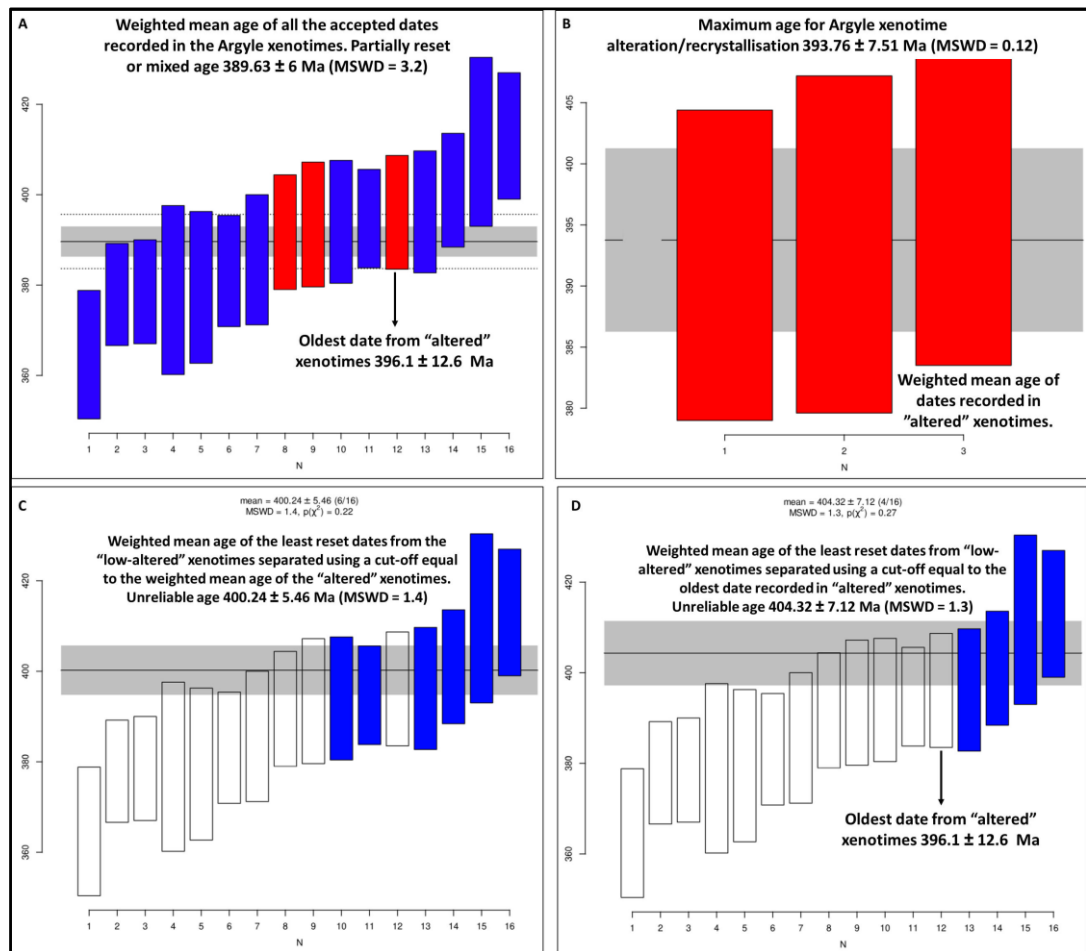


**Figure VI.12** – Interpreted weighted mean ages for the accepted concordia dates recorded in the Argyle xenotimes. The length of the bars represents the date uncertainty (in  $2\sigma$ ). The blue bars correspond to dates recorded in "low-altered" grains. The red bars represent dates from "altered" xenotimes. See text for explication of "low-altered" and "altered" terminologies. The white/empty bars show the dates that were not included in the mean. N = number of dates.

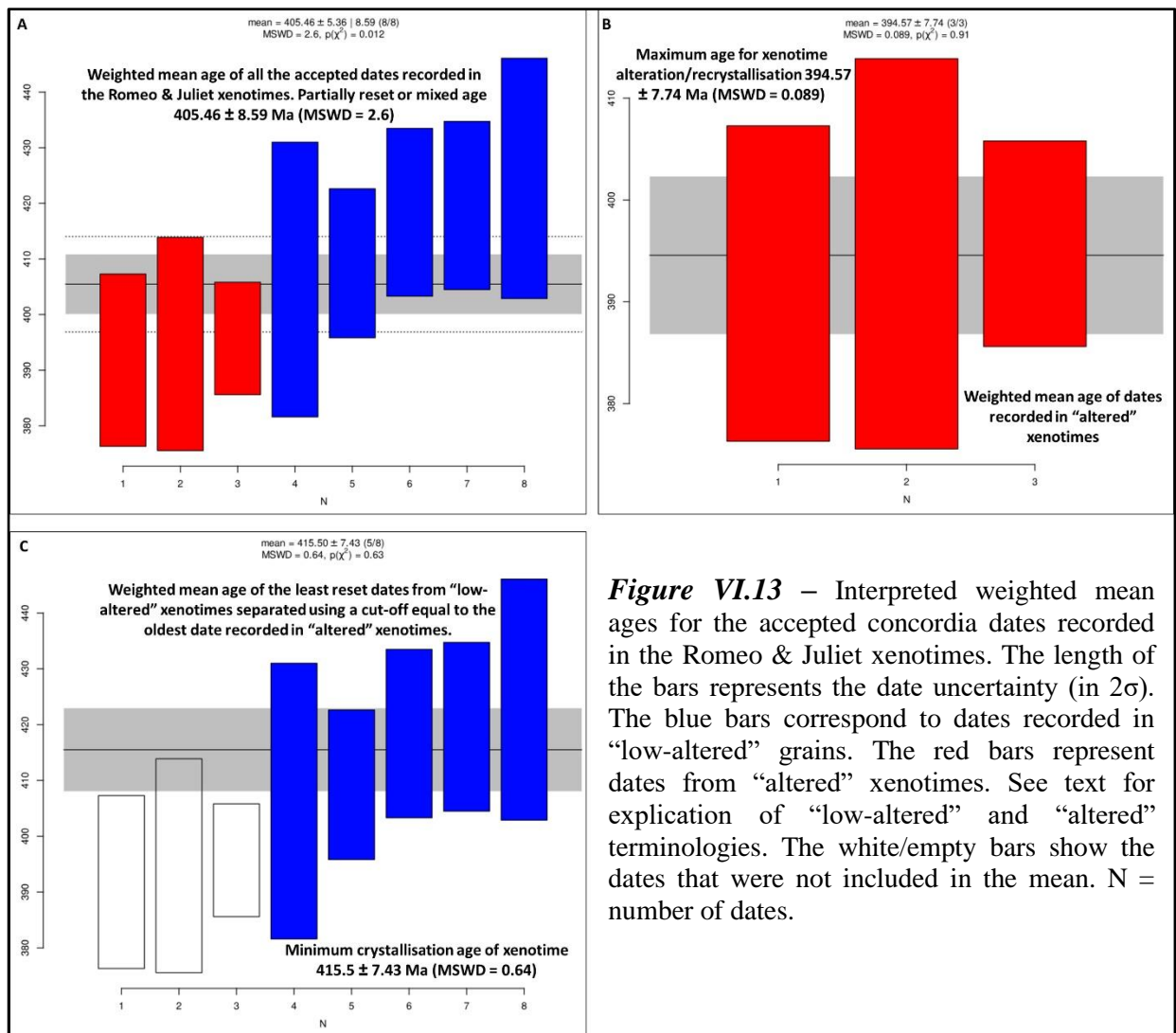


**Figure VI.13** – Interpreted weighted mean ages for the accepted concordia dates recorded in the Romeo & Juliet xenotimes. The length of the bars represents the date uncertainty (in  $2\sigma$ ). The blue bars correspond to dates recorded in "low-altered" grains. The red bars represent dates from "altered" xenotimes. See text for explication of "low-altered" and "altered" terminologies. The white/empty bars show the dates that were not included in the mean. N = number of dates.

### VI.3.5. Age interpretation of titanite data

It is known that titanite can incorporate significant amounts of common Pb, experience Pb and U loss and/or inherit radiogenic Pb from precursor phases during both initial crystallisation and subsequent alteration/recrystallisation processes (Kirkland et al., 2018; Gordon et al., 2021; Walters et al., 2022). As mentioned above, the coarse grained titanite crystals and aggregates formed through replacement of pre-existent titanite and rutile crystals during the second hydrothermal stage that affected the Deer Cove deposit. Thus, inheritance of both common and radiogenic Pb from the two precursor phases during titanite growth is a feasible process. Subsequent alteration of the titanites may have also occurred by the end of the second hydrothermal phase, but to what degree this process affects the U-



Pb isotopic systems of the analysed grains cannot be inferred based on the current data. Regardless of these uncertainties, the reasonable alignment of the titanite data (MSWD = 2.5) and the geologically reasonable lower intercept age, suggest they largely represent a simple two component mixing between radiogenic and initial components (**Figure VI.8**). Therefore, it is interpreted herein that the lower intercept age of  $380.7 \pm 17.4$  Ma, reflects the crystallisation age of the coarse grained titanite crystals and aggregates.

#### **VI.4. Timing of gold mineralisation**

The above presented ages represent the time of initial crystallisation and subsequent alteration and/or recrystallisation of the monazite, xenotime, and titanite grains. Considering the paragenetic setting of these grains (see above and **chapter V**), their ages can be used to infer the timing of gold mineralisation within each of the studied deposits (**Table VI.7**). The uncertainties associated with the ages presented in **Table VI.7** are slightly higher than the ones presented in **Figure VI.8**, **Figure VI.9**, **Figure VI.10**, **Figure VI.11**, **Figure VI.12**, **Figure VI.13**. This is due to the addition of three extra uncertainties which IsoplotR does not include in the primary age calculation algorithm. These uncertainties are related to the decay constant estimate, to the uncertainty of the reference material used, and to the long term reproducibility of this analytical method for the laboratory.

For the Stog'er Tight deposit, the ages of the “low-altered” monazite and xenotime grains overlap within uncertainty of both the U-Pb zircon age of Ramezani (1992), and with the Re-Os pyrite age of Kerr & Selby (2012) (**Table VI.7**). As presented in **chapter V**, the zircon together with the monazite, xenotime, and the early pyrite are cogenetic and formed during the first hydrothermal stage of the Stog'er Tight deposit (**Figure VI.14**). Zircon inclusions are common in the other three minerals and so, it is possible that it started to crystallise slightly earlier. Furthermore, zircon is more resilient to alteration and recrystallisation processes compared to the other three minerals (Harrison et al., 2002). Therefore, it is interpreted herein that for the Stog'er Tight deposit, the hydrothermal zircon age of Ramezani (1992) represents the maximum age or the onset of the first gold mineralising event, whereas the minimum crystallisation age of xenotime is considered the minimum age of the same event (**Table VI.7**).

**Table VI.7** – Interpreted ages of gold mineralisation; N/A – not applicable; \*Ramezani, 1992; \*\* Kerr & Selby, 2012

Deposit	Mineral	Age of 1 <sup>st</sup> hydrothermal stage / gold mineralisation	Age of 2 <sup>nd</sup> hydrothermal stage / gold mineralisation
Stog' er Tight	Zircon*	420 ± 5 maximum age	N/A
	Pyrite**	411 ± 7	N/A
	Monazite	414.91 ± 7.78	396.51 ± 7.17 maximum age
	Xenotime	409.92 ± 7.76 minimum age	384.51 ± 6.63 best estimate
Argyle	Monazite	419.53 ± 7.81 minimum age	N/A
	Xenotime	N/A	393.76 ± 8.76 maximum age
Romeo & Juliet	Xenotime	415.5 ± 8.83 minimum age	394.57 ± 8.96 maximum age
Deer Cove	Titanite	N/A	380.7 ± 17.88 best estimate
Pine Cove	Pyrite**	420 ± 7	N/A

The ages obtained from the Stog' er Tight “altered” monazites and xenotimes are considered representative for the second hydrothermal stage. However, between the monazite and xenotime ages there is a difference of 12 Ma with uncertainties that barely overlap (**Table VI.7**). It is not clear what causes the age difference between the two phosphate phases. The Th-Pb and the U-Pb dates of the “low-altered” monazites and xenotimes generated similar ages, and so, a methodological problem that would occur from the comparison of two different isotopic systems is less probable. Considering that the analysed xenotimes are in general smaller than the monazites and show a higher degree of brecciation and contact with the late alteration minerals, it seems likely that the xenotimes were more affected by alteration and recrystallisation processes and so, their U-Pb isotopic system records a higher degree of resetting. Therefore, it is here inferred that the Th-Pb age of the “altered” monazites represents the onset of the second hydrothermal event that affected the Stog' er Tight deposit, whereas the U-Pb xenotime age reflects the best estimate for the timing of this event (**Table VI.7**).

For the Argyle deposit, the minimum crystallisation age of the “low-altered” monazites is interpreted as the minimum age (cessation) of the first gold mineralising event, whereas the maximum age obtained for the alteration/recrystallisation of xenotimes is interpreted as the onset of the second

hydrothermal stage (*Table VI.7*). The same approach is applied for the Romeo & Juliet xenotimes. The minimum crystallisation age of xenotime is interpreted as the minimum age of the first gold mineralising event, whereas the maximum age of the xenotime alteration/recrystallisation marks the onset of the second hydrothermal phase (*Table VI.7*).

As presented above, in the Deer Cove deposit, both the growth and subsequent alteration/recrystallisation of the analysed titanite crystals and aggregates occurred during the second hydrothermal event. Thereby, the titanite crystallisation age is interpreted as the best estimate age for the second gold mineralising event that occurred in the Deer Cove area (*Table VI.7*).

No geochronological data was obtained in this study for the Pine Cove deposit. However, a Re-Os pyrite age of  $420 \pm 7$  MA determined by Kerr & Selby (2012) exist in literature (*Table VI.7*). This age is within error with the monazite, xenotime, zircon, and pyrite ages used to interpret the first gold mineralising event within the Stog'er Tight, Argyle, and Romeo & Juliet (*Table VI.7*). Moreover, the structural and mineral paragenetic characteristics of the Pine Cove deposit mirrors the geological characteristics of the afore-mentioned gold occurrences. Thus, it is interpreted that the Re-Os pyrite age of Kerr & Selby (2012) reflects the time of the first gold mineralising event from the Pine Cove deposit (*Table VI.7*).

## **VI.5. Summary**

The U-Th-Pb ages of monazite, xenotime, and titanite obtained in this study combined with pre-existent geochronological data and with the paragenetic observations presented above and in *chapter V* suggest that the studied deposits have a very similar evolution and resulted from two hydrothermal events that were active at ~15 Ma apart (*Figure VI.14*). The first gold mineralising event potentially covers a time span of ~10 Ma and is best constrained by the maximum and minimum ages (~420 and ~410 Ma) of the first hydrothermal event of the Stog'er Tight deposit (*Figure VI.14*). The second gold mineralising event likely started around 396 Ma. This is reflected by the maximum alteration/recrystallisation ages of the monazite/xenotime grains from Stog'er Tight, Argyle and Romeo & Juliet deposits/prospects (*Figure VI.14*). The best estimate time for this event is marked

by the alteration/recrystallisation age of xenotime in the Stog’er Tight deposit and by the titanite crystallisation age in the Deer Cove deposit (*Figure VI.14*).

No geochronological data exist for the second hydrothermal event of the Pine Cove deposit and neither for the first hydrothermal stage of the Deer Cove prospect. However, these gold occurrences show structural and mineral paragenetic characteristics comparable to the rest of the studied deposits/prospects. Therefore, it is inferred that the first hydrothermal stage of Deer Cove and the second hydrothermal event of Pine Cove, formed during the same gold mineralising events that contributed to the formation of the other studied deposits/prospects (*Figure VI.14*).

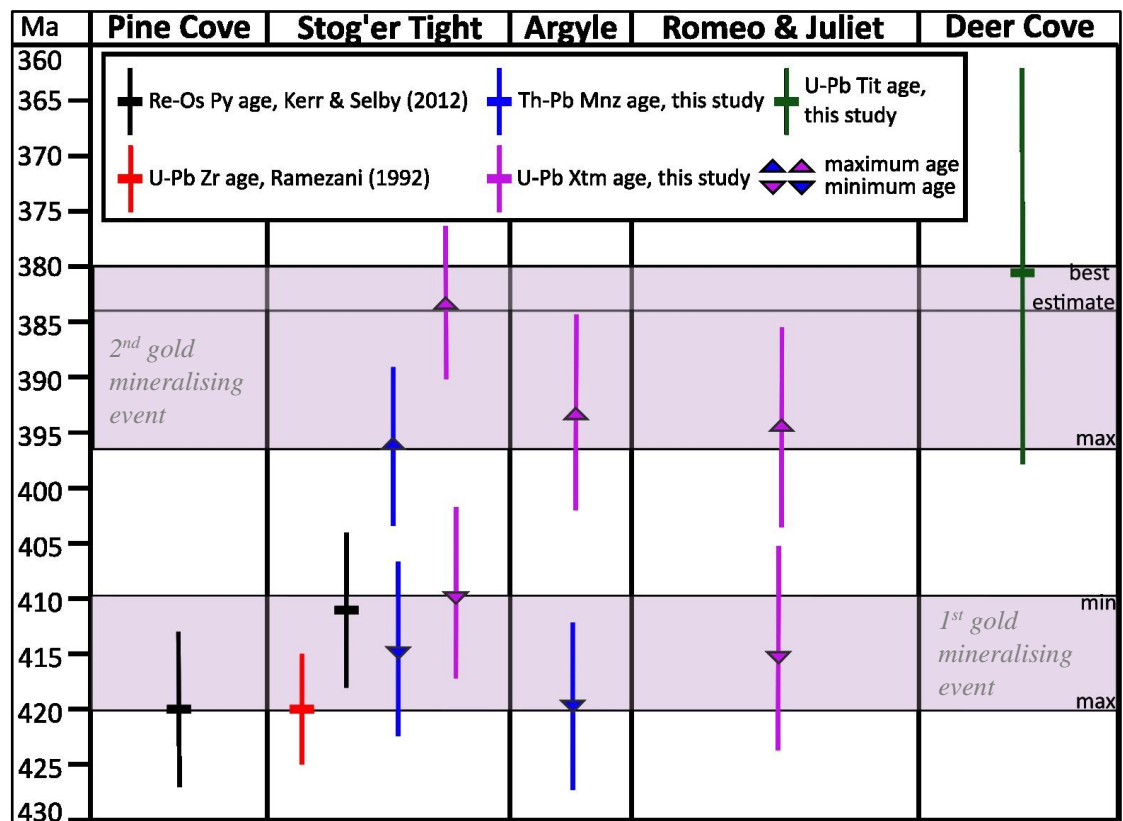


*Figure VI.14* – Compilation of geochronological data for the Pine Cove, Stog’er Tight, Argyle, Romeo & Juliet, and Deer Cove gold occurrences; shaded intervals represent the timing of the two gold mineralising events; ages provided in million years (Ma); the length of the bars represent the age uncertainties.

## **VII. Discussions and Synthesis**

This chapter integrates the structural, mineralogical, geochemical, and geochronological results and interpretations from the preceding chapters into a comprehensive model that brings new understandings regarding the formation of gold mineralisation in relation to the structural evolution of the entire district. It also links the timing of gold precipitation to distinct orogenic phases, and therefore, to different tectonic processes. The implications of the proposed model are discussed with respect to both local and regional scale exploration strategies in Newfoundland, and also in other regions within the Appalachian-Caledonian belt (e.g. Nova Scotia, Northern Ireland, Scotland, etc.).

### **VII.1. Implications for the structural evolution of the Baie Verte Peninsula**

The BVP records a protracted structural evolution related to four orogenic cycles developed during Cambrian to late Paleozoic times: Taconic (~495-450 Ma), Salinic (~445-420), Acadian (~420-395), and Neo-Acadian (~395-350) (Anderson et al., 2001; van Staal et al., 2007, 2009; Skulski et al., 2010; van Staal & Barr, 2012; Castonguay et al., 2014; Wilner et al., 2018, 2022). Summarised descriptions of the regional tectonic processes associated with these orogenic events are provided in *chapter II*. The existent theories regarding the structural evolution of the BVP during these times are presented in *chapter II* and also discussed below in the light of the results obtained in this study. This is needed in order to reconcile the regional tectonometamorphic context for the development of gold mineralisation.

The first deformation phase that affected the BVP is associated with the Ordovician Taconic Orogeny (Waldron et al., 1998; Castonguay et al., 2009, 2014; Skulski et al., 2010, 2015a). According to the same authors, this phase involved the westward obduction of the Baie Verte Oceanic Tract (including the Point Rouse Complex) on the Laurentian margin (*Figure. II.4*). The Baie Verte Line (BVL) started to form during this event, and acted as the root for the obduction of ophiolitic complexes over the Humber Zone (western part of the BVP; *Figure. II.4*; Hibbard, 1983; Anderson, 1998). During this stage, the western side of BVP was metamorphosed up to eclogite facies conditions (Castonguay et al., 2014). The

structural elements related to the Taconic phase are best developed west of the BVL, in the Fleur de Lys and Birchy Complex (**Figure II.4**; Skulski et al., 2010, 2015a; Castonguay et al., 2009, 2014). East of the BVL, the aforementioned authors interpreted the earliest observable fold generation and associated foliation as Taconic, whereas Anderson (1998) ascribed these structures to the Salinic phase. In this study, based on the observations presented in **chapter IV**, all the structural elements recorded in the Point Rousse Complex (PRC) are interpreted as post Ordovician in age and consequently, unrelated to the Taconic event. However, the presence of Taconic structures east of the BVL cannot be ruled out based on the available data. It is possible that during subsequent deformation, the Taconic structures were overprinted and totally transposed into parallelism with younger structures, thus, becoming indistinguishable. Nonetheless, the gold mineralisation post-dates the Taconic event by ~30Ma (**Figure VII.1**). Furthermore, up to the present date, there are no records of Ordovician gold mineralisation in the BVP. Thereby, it is assumed that none of the metamorphic and/or magmatic fluids generated during this phase could have contributed to the formation of the studied gold occurrences.

During the Silurian Salinic orogenic event, the western part of the BVP experienced rapid uplift, whereas the eastern side of the peninsula was subject to widespread plutonism and associated volcanism, followed by subsidence and metamorphism during regional-scale folding and S-SE directed thrusting (**Figure VII.1 & Figure VII.2–A**); Anderson, 1998; Waldron et al., 1998; Castonguay et al., 2009, 2014; Skulski et al., 2010, 2015a). The same authors attested that these processes occurred under a sinistral transpressional regime localised along the BVL. According to Hibbard (1983) and to Bélanger et al. (1996), the E-SE directed reverse faults that dip steeply to west (e.g. the Baie Verte Road Fault system), which overprint the BVL and imbricate parts of the Advocate Complex (AC) with the Flat Water Pond Group (FWPG) and the Burlington Granodiorite (BG), also formed during this event and may represent splays of the BVL (**Figure VII.2**).

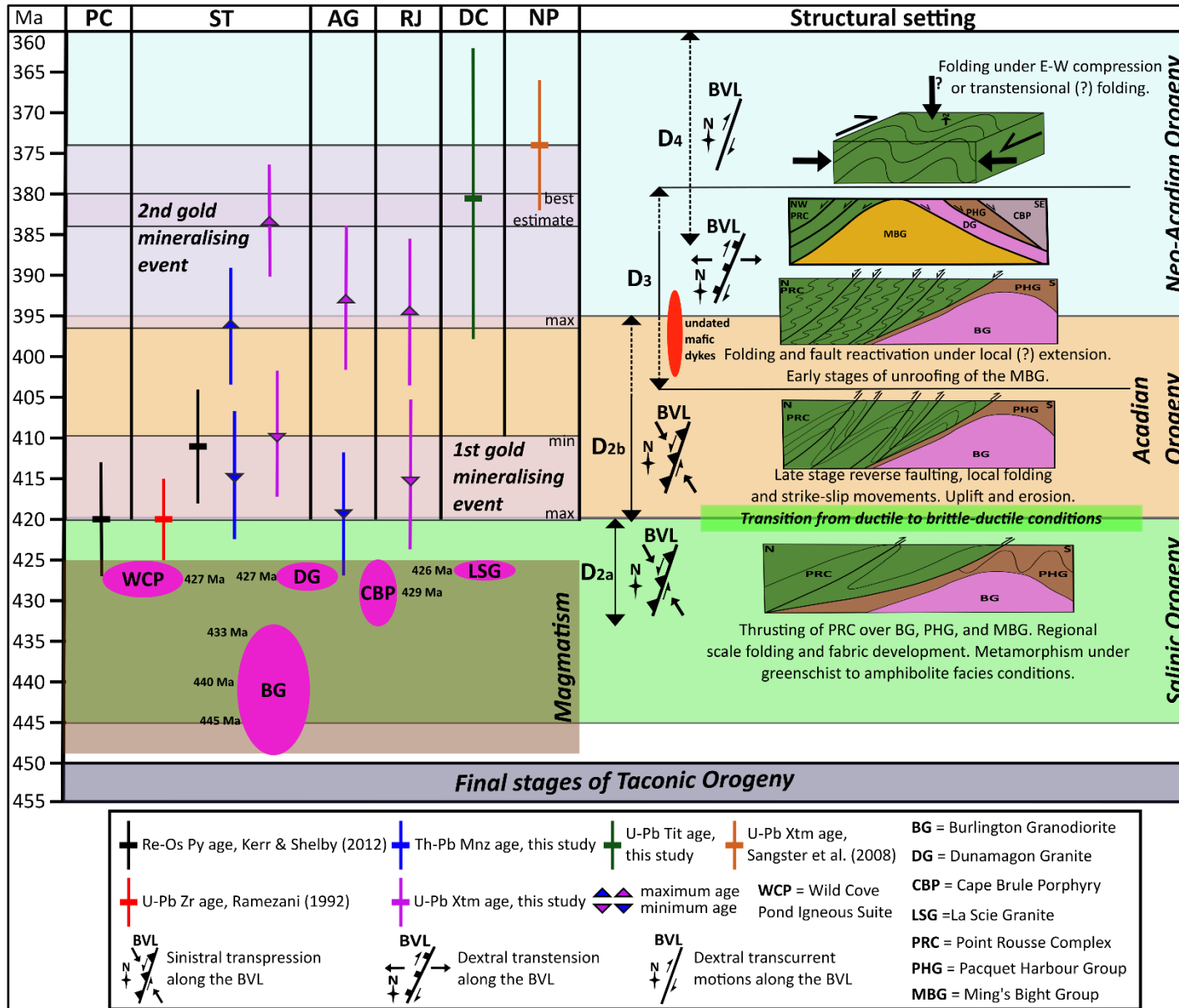


**Figure VII.1** – Time correlation chart between the main orogenic events that affected the Baie Verte Peninsula (BVP), structural setting, local magmatic activity, and gold mineralisation. PC – Pine Cove, ST – Stog’er Tight, Ag – Argyle, RJ – Romeo & Juliet, DC – Deer Cove, NP – Nugget Pond gold occurrences; mnz – monazite; xtm – xenotime; zr – zircon; py – pyrite.

The vertical size of the magmatic plutons shows their age including the analytical uncertainty of their respective age (U-Pb on Zircon). BVL – Baie Verte Line. The cartoon illustrating the exhumation of the MBG is modified after Anderson et al. (2001).

In contrast to prior hypotheses regarding the tectono-metallogenic evolution of the BVP, the current study brings the following new interpretations. The earliest deformation fabrics from the Point Rouse Complex and probably from most of the eastern part of the BVP post-date the Taconic Orogeny. During the Salinic Orogeny and probably throughout the entire Acadian Orogeny, a sinistral transpressional setting was active along the BVL, whereas dextral transtension started during late stages of Acadian - early stages of Neo-Acadian Orogenies. This is the first study to demonstrate the existence of a second gold mineralising event within the BVP and its genetic link with Devonian extensional structures.

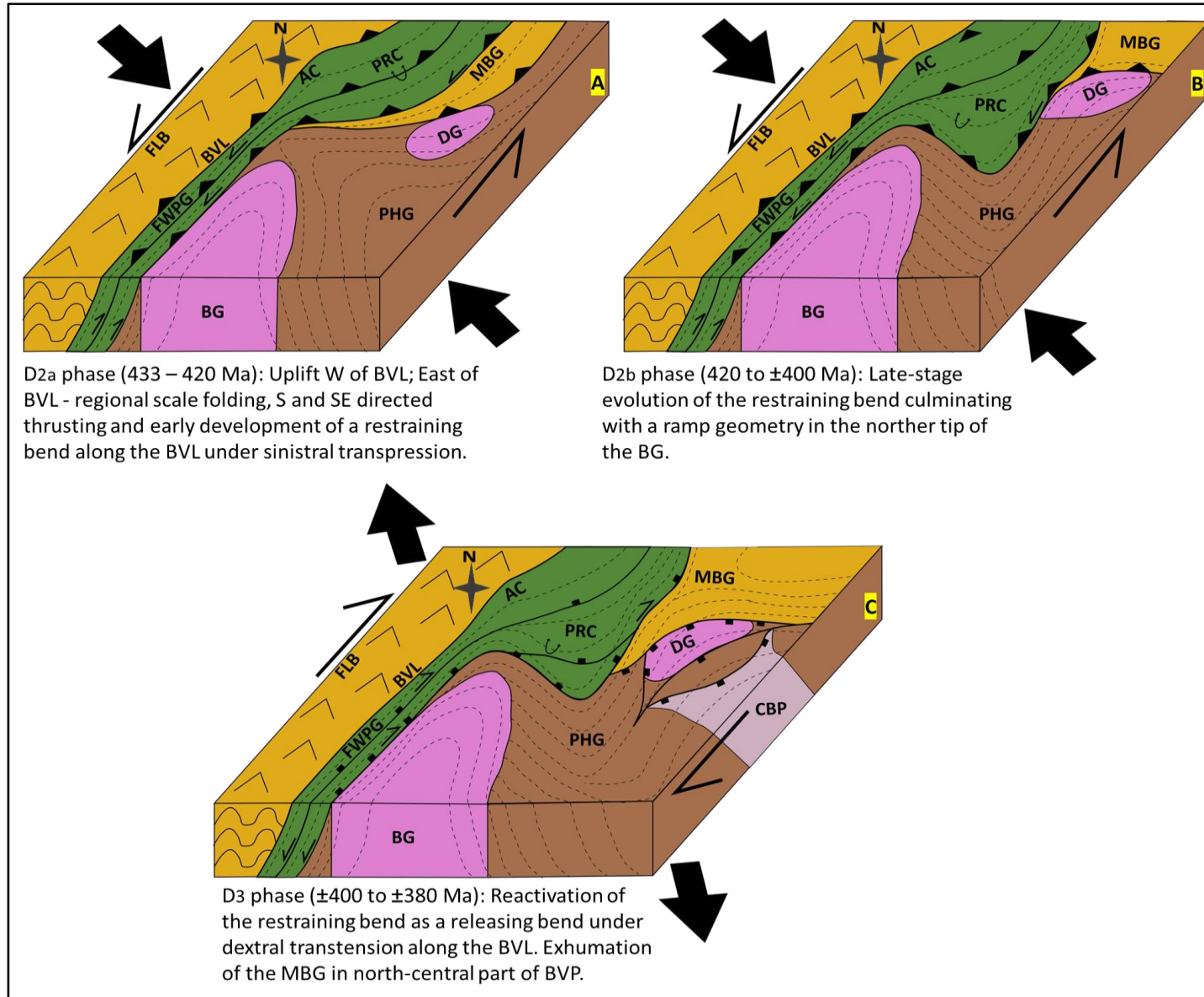


**Figure VII.2** – Cartoons illustrating the structural evolution of the Baie Verte Peninsula (BVP) during Mid to Late Silurian (A), Early Devonian (B), late Early to Mid-Devonian (C). D<sub>2a</sub>, D<sub>2b</sub>, and D<sub>3</sub> represent the deformation phases described during this study. Image adapted after Anderson (1998). In contrast to Anderson’s model, who proposed a dextral transpressional setting localized along the BVL during 420 to ±388 Ma, the findings of this study indicate that sinistral transpression likely prevailed along the BVL until at least ±400 Ma. Subsequently, a dextral transtensional setting was active until around 380Ma.



Anderson (1998) argued that during this stage, the north-central part of the BVP, including the PRC, evolved as a restraining bend formed in response to the presence of the BG in the footwall of the BVL (*Figure VII.2A*). In the model proposed by the aforementioned author, the BG acted as a major rheological heterogeneity, which under a NW-SE oriented shortening (present day coordinates), deflected the structural trends, including that of the BVL, from an initial NNE orientation to a nearly E-W strike (*Figure VII.2-A*). In turn, the strain was portioned in domains characterised by reverse dip-slip motion and sinistral strike-slip to oblique motion. Continuous shortening resulted with the formation of oblique, frontal, and lateral ramp geometry (from W to E) around the northern tip of the BG (*Figure VII.2-B*).

The evolution of the BVP during the Acadian and Neo-Acadian orogenic events is linked to dextral transcurrent motions localised along the BVL (Waldron et al., 1998; Anderson, 1998; Anderson et al., 2001; Castonguay et al., 2009, 2014; Skulski et al., 2010, 2015 a,b). Same authors described a dextral transpressional regime during the Early Devonian followed by a dextral transtensional regime which resulted with the inversion of the Salinic structures, and with the extensional exhumation of the MBG during Mid Devonian to Early Carboniferous (*Figure VII.1; Figure VII.2-C*). Exhumation processes were associated with metamorphism under amphibolite facies conditions (Anderson et al., 2001).

Overall, the findings of this research support the previously mentioned theories. However, there are a few exceptions concerning the timing of these events, as well as regarding the processes and the sequence in which certain structural features have formed. Thereby, an updated view on the evolution of the BVP during the Early Silurian to the Carboniferous times is provided below and summarised in *Figure VII.1*.

### VII.1.1. Evolution of the PRC during Salinic & Acadian orogenic cycles

As presented in *chapter IV*, the earliest deformation phase (D<sub>2</sub>) that affected the PRC was a progressive event that accommodated early (D<sub>2a</sub>) regional scale folding associated to the south directed thrusting of the PRC over the Paquet Harbour Group (PHG), the BG, and over the Ming's Bight Group (MBG; *Figure VII.2-A*). The late stage of this event (D<sub>2b</sub>) culminated with the development of a ramp geometry observed in the southern part of the PRC (*Figure VII.2-B*). As noted in *chapter IV*, E-W oriented shear zones interpreted as D<sub>2a</sub> have been observed in the northern tip of

the BG. This part of the granodiorite yielded a zircon U-Pb age of ~433 Ma (Skulski et al., 2012; 2015a). Thereby, this places a maximum age for the D<sub>2a</sub> deformation phase of the PRC (**Figure VII.1**). Furthermore, as mentioned in **chapter V**, the veins related to the first gold mineralising event are interpreted as pre-to-syn D<sub>2b</sub>. Thus, the maximum age of the first gold mineralising event (~420 Ma) is considered the minimum age for the D<sub>2a</sub> phase and the maximum age for the D<sub>2b</sub> event (**Figure VII.1**). Based on the available data, the minimum age of the D<sub>2b</sub> event, and consequently, the maximum age of the D<sub>3</sub> phase cannot be determined with certainty. However, some assumptions can be made. As noted in **chapter V**, D<sub>2b</sub> structures affect the veins related to the first gold mineralising event. This means that PRC was still subject of D<sub>2b</sub> deformation after ~410 Ma (minimum age of first mineralising moment; **Figure VII.1**). The syn-to-post D<sub>3</sub> veins described in **chapter V**, are related to the second gold mineralising event which has a maximum age of ~396 Ma. However, it is possible that these veins formed either during the late stages of D<sub>3</sub> or the early stages of D<sub>4</sub> (**see subchapter V.2**), meaning that the D<sub>2b</sub> event might have ceased before ~396 Ma. Anderson (1998) attested that the maximum age for normal oblique motion along the eastern side of PRC is 405±8 Ma. This statement is based on an Ar-Ar age obtained from amphibole porphyroblasts that overgrow the foliation fabric related to sinistral transpressional shearing within the contact between the PRC and MBG. Based on these considerations it is interpreted that in the PRC the transition from the D<sub>2b</sub> to the D<sub>3</sub> deformation phases occurred sometime between 405 and 396 Ma (**Figures VII.1, VII.2**). Taking into account the mentioned ages and the progressive nature of the D<sub>2</sub> event in the PRC, it is interpreted that deformation of the BVP under a sinistral transpressional regime extended beyond the Salinic orogenic cycle and persisted throughout the Acadian (**Figures VII.1, VII.2**). Sinistral transpression associated to the Acadian event was reported elsewhere in Newfoundland along several NNE-NE striking major shear zones or terrane boundary faults (e.g. *Valentine Lake Shear Zone*, Honsberger et al., 2022; *Dover Fault*, Kellett et al., 2016). Moreover, according to Waldron et al. (2022) both the Salinic and the Acadian orogenic cycles involved NW dipping subduction, which in turn, would result with sinistral motions along NNE-NE oriented structures. Thereby, dextral motions along the BVL are unlikely to have occurred until at least the late phases of the Acadian event.

In literature, most of the exhumation history of the rocks lying east of the BVL is related to extensional tectonics during Mid-Late Devonian (see summarised

theories above). However, the different nature of the structural elements that characterise the D<sub>2a</sub> and the D<sub>2b</sub> deformations phases, suggest a transition between ductile to brittle-ductile conditions. Hence, it is likely that rock exhumation commenced as early as Late Silurian to Early Devonian (**Figure VII.1**) as a result of uplift and erosional processes. Rapid extension-related uplift following the Grander margin slab break-off under composite Laurentia at ~425 to 418 Ma (**Figure VII.3**) was reported elsewhere in North American Appalachians (e.g. in New-Brunswick, Wilson et al., 2017; and in central Newfoundland, Honsberger et al., 2022). However, in the study area, the absence of evidence for extensional deformation suggests that uplift probably occurred due to thrusting and syn-orogenic erosion. The diachronous nature of the uplift related processes is unclear at this stage, but it might be related to the varying positions of the compared areas relative to the collisional front. Notably, the Baie Verte Peninsula being situated further from the suture zone.

### VII.1.2. Evolution of the PRC during the Neo-Acadian orogeny

During the D<sub>3</sub> deformation phase that affected the PRC, the D<sub>2a/2b</sub> south directed thrusts and reverse faults were reactivated as normal faults. Asymmetric recumbent folds that verge to north were also formed (**Figures VII.1; VII.2-C**). As discussed in **chapter IV**, these structures developed under an extensional regime which was manifested either at a local- or at a regional-scale. The exact time span in which this deformation phase was active is uncertain, but some relative estimations can be inferred. The onset of this event corresponds to the transition between the Acadian and Neo-Acadian orogenic cycles and might have been active until ~380 Ma (**Figure VII.1**). This minimum age is here interpreted based on several considerations. The titanite age from Deer Cove represents a crystallisation age during the second gold mineralising event which based on structural constraints is interpreted as syn-to-post D<sub>3</sub>. Thereby, there is a possibility that the titanite formed after the D<sub>3</sub> deformation had ceased. Hence, this puts a minimum age limit on the D<sub>3</sub> stage. Moreover, the titanite age from Deer Cove closely matches the U-Pb ages of hydrothermal titanite (388±4) and rutile (380±2) obtained by Anderson (1998) and Anderson et al. (2001) on samples collected from the Northern Ming's Tickle Shear Zone (NMTSZ) which affects the PRC at the contact with the MBG. The same authors considered that these minerals formed slightly before or during the early evolution of this shear zone. As noted in **chapter IV**, the syn-to-post D<sub>4</sub> south dipping structures identified in the PRC

may be genetically related to the south dipping branches of this shear zone (*Table IV.I-xiii*). Consequently, this indicates a transition between the D<sub>3</sub> and the D<sub>4</sub> deformation phases sometime between 388 and 380 Ma (*Figure VII.1*).

Anderson (1998) and Anderson et al. (2011) argued that dextral transcurrent motions localised along the BVL led to the reactivation of the Salinic restraining bend as a releasing bend during Mid to Late Devonian times (*Figure VII.2-C*). Same authors attested that the MBG represents a symmetrical core complex exhumed under a localised transtensional regime. Considering the extensional nature of the D<sub>3</sub> structures and the probable time interval in which these have formed, it is interpreted that the D<sub>3</sub> deformation phase within the PRC was coeval with the early exhumation stages of the MBG (*Fig. VII.1, VII.2-C*). Moreover, evidence for deformation under dextral transtension has also been observed in the PRC. As noted in *chapter IV*, the NNE to NE striking D<sub>2b</sub> faults from the Pine Cove coast are reactivated with a dextral oblique-normal motion (*Plate IV.6–M*). These faults continue offshore towards SW and may represent splays of the BVL.

The exact geodynamic conditions in which the dextral transtensional setting occurred are unclear. The Neo-Acadian orogeny is associated to an overall dextral transpressional regime (van Staal, 2019). However, extension-related recumbent folds associated with a gently dipping to flat lying foliation that post-date quartz veins of ~410 Ma, have been reported in central Newfoundland close to the Red Indian Line (*Fig. II.1*; Honsberger et al., 2020, 2022). This suggests that during the early Neo-Acadian period (Mid Devonian), one of two scenarios may have occurred: i) this period was primarily characterized by a transtensional tectonic regime rather than a transpressional one; or ii) localized transtensional domains might have occurred due to the structural complexity of specific areas, as proposed by Anderson et al. (2001) for the Baie Verte Peninsula (BVP).

As presented in *chapter IV*, the D<sub>4</sub> deformation phase that occurred in the PRC is mostly characterised by NNE to NE trending, broad, open folds (*Fig. VII.1*). The age, and consequently, the structural setting in which these folds developed is poorly constrained in literature. Initially, the relative age of these folds was interpreted by Castonguay et al. (2009) as post-Silurian. Subsequently, Skulski et al., (2010, 2015a) and Castonguay et al. (2014) associated the genesis of these folds with the development of the Late Silurian-Early Devonian sinistral restraining bend (*Fig. VII.2*).

The results of this study support the interpretation of Castonguay et al., (2009). The onset of this event occurred sometime in late-Early Devonian during the Neo-Acadian Orogeny (**Fig. VII.1**). However, the minimum age of this phase remains undetermined, as the available data does not provide enough information to make any speculations.

The orientation of the F<sub>4</sub> folds and the configuration of the syn-to-post D<sub>4</sub> faults, which resembles a partial *Riedel* system, suggest that this deformation phase occurred under an E-W compression (**Figs. IV.8; VII.1**). Consequently, E-W oriented shortening would have generated dextral motions along the BVL. Although the aforementioned model is preferred, the possibility that these folds formed under a dextral transtensional setting cannot be ruled out. Based on experimental data, strain modelling, and structural analysis of field data, several authors attested that folds can form during transtension (e.g. Venkat-Ramani & Tikoff, 2002; De Paola et al., 2005; Fossen et al., 2013). In such cases the folds are usually oriented towards the divergence vector (Fossen et al., 2013). Given the orientation of the ramp system in the southern part of the PRC, the local divergence vector under dextral transtension would be oriented towards N-NE, same as the orientation of the F<sub>4</sub> fold axis (**Fig. IV.3–A**). Regardless the model, both of these suggest that the BVL accommodated dextral transcurrent motions in the last phases of the Neo-Acadian event. Moreover, compared to the preceding D<sub>3</sub> deformation phase, the D<sub>4</sub> stage shows a more brittle nature, which indicates that the BVP was largely exhumed by Late Devonian times. This also aligns with existing interpretations based on cooling ages of biotite that suggest regional cooling gradients below 300 °C by early Carboniferous (Anderson, 1998 and references therein).

## **VII.2. A regional genetic framework for gold mineralisation within the Baie Verte Peninsula (BVP)**

Over a hundred structurally controlled epigenetic gold occurrences are known in the BVP (Evans, 2004). Most of these are located in the eastern part, either along the BVL or along splays of this major terrane boundary fault (Evans, 2004). These gold occurrences, including the ones studied herein, were catalogued as orogenic gold type deposits (Dubé et al. 1993; Evans 2004; Pawlukiewicz, 2019; Ybarra, 2019; Pitman et al. 2020). Although the exact fluid sources involved in the formation of the studied gold occurrences cannot be determined based on the available data, their structural

setting and the textural characteristics of their gold bearing veins support the interpretations of the afore-mentioned authors (*see chapter V*).

*Chapters V & VI* provide evidence that the studied gold occurrences have a similar structural and mineralogical evolution and that their formation is related to at least two separate hydrothermal stages (*Figs. V.13-17, VI.14, VII.2*). This confirms previous hypothesis regarding the presence of two distinct gold mineralising events within the BVP (Kerr et al., 2012). Each of these two mineralising events are characterised by a specific association of alteration minerals formed during the development of veins and structural features of different relative age (*Figs. V.13-17*). This indicate that mineralising conditions have evolved through time with respect to the structural evolution of the BVP.

Based on the results presented in *chapters V & VI* it is inferred that the first gold mineralising moment occurred in Early Devonian times during the late stages of the progressive D<sub>2</sub> deformation phase that affected the PRC (*Fig. VII.1*). As noted in *chapter V*, the gold bearing veins that formed during this phase record a progressive evolution and are composed of two generations of quartz (Q<sub>1</sub> and Q<sub>2</sub>; *Fig. V.18–A, B*). Both their optical and CL characteristics suggest that Q<sub>1</sub> formed under constant hydrothermal conditions at supralithostatic fluid pressures, while Q<sub>2</sub> precipitated during a period characterised by cyclic episodes of high fluid pressures (near-lithostatic) that resulted with the hydro-brecciation of both Q<sub>1</sub> and host lithologies. These differences suggest that the quartz veins related to the first gold mineralising event started to form during the D<sub>2a</sub> event, under more ductile conditions, probably just below the brittle-ductile transition zone. Uplift processes resulted with the upward migration of rocks into the brittle ductile domain during the D<sub>2b</sub> phase (*Fig. VII.1*). During Q<sub>2</sub> deposition, intense fluid-rock interaction resulted with the formation of the first generation of gold and of the associated pervasive alteration halos. As interpreted in *chapter V*, gold precipitation was controlled by combined wall-rock sulphidation and flash vaporisation processes. As mentioned by other authors, and in alignment with the results presented in this study, the physicochemical properties of the host rocks played a major role in the localisation of mineralised sites (Ramezani 1992; Pawlukiewicz, 2019; Ybarra, 2019). The most competent rocks (gabbros, basalts) favoured the development of discrete interconnected shears which increased the local permeability, whereas the high content of Fe-Ti oxides of host rocks triggered the precipitation of pyrite and gold within the altered wall rock. The geochemical

signatures of the *type I and type II* gold suggest that overall, a common hydrothermal system contributed to the early development of the studied gold occurrences.

While not conclusive, several pieces of evidence point to a metamorphic origin for the mineralising fluids involved in the early development of the studied gold occurrences: i) the CL textures of Q<sub>2</sub> are typical to quartz of metamorphic origin (Rusk et al., 2004; Rusk, 2012); ii) the *type I* and *type II* gold signatures do not suggest any magmatic component; and iii) the mineralisation post-date the magmatic activity and is syn-to-post peak metamorphic conditions which are bracketed between ~433-425 Ma (**Figure VII.1**; Skulski et al., 2015 a, b).

The results presented in **chapters V and VI** indicate that the second gold mineralising event occurred in Mid-Late Devonian during the D<sub>3</sub> and the D<sub>4</sub> deformational phases that affected the PRC (**Figure VII.1**). The gold bearing veins associated with this event are composed of quartz (Q<sub>3</sub>)-chlorite-calcite (**Fig. V.18-C**). The internal distribution of these minerals within the veins, together with the CL textures of Q<sub>3</sub> indicate that these minerals precipitated successively rather than simultaneously, in dilatational sites close to hydrostatic pressure conditions. These features are suggestive of a shallower depositional environment, under brittle-ductile to brittle conditions. In turn, this suggests that at the time of gold deposition the BVP was probably in an advanced stage of exhumation, close to the transition between the D<sub>3</sub> to D<sub>4</sub> deformation phases (**Figure VII.1**).

As outlined in **chapters IV and V**, the D<sub>2</sub> and D<sub>3</sub> structures were reactivated during the D<sub>4</sub> phase. This enabled fluid migration and vein development along both D<sub>4</sub> and pre-existing structures. This led to intense brecciation of pre-existing minerals, especially of pyrite (**Fig. V.19-B**). Gold associated with this event occurs mostly free, on and along fractures in pyrite (**Fig. V.19-B**). In all the studied gold occurrences, the second generation of gold is characteristic of the high-grade gold intervals, and at least visually, at microscopic scale, comprise most of the gold endowment. Based on the available data, the origin of this late gold cannot be determined. This gold could either be remobilised from the pre-existing mineralisation and/or a product of the newly introduced fluid.

The source of the mineralising fluids related to this gold mineralising event is also unclear. The presence of both *type I* and *type III* signatures in the late gold from the Stog'er Tight and Argyle deposits could suggest that two mineralising fluids with different sources contributed, at least locally, to the second mineralising event.

Anderson (1998) proved that during the exhumation of the MBG, amphibolite facies conditions have been reached. *Type I* signature is also characteristic for the first gold generation, which as mentioned above, it may be related to fluids of metamorphic origin. As explained in *chapter V*, the *type III* signature may be indicative of magmatic related fluids. Although, no Mid-Late Devonian intrusive rocks are known in the BVP, magmatic intrusions of this age are known in both central and eastern parts of Newfoundland (Kellett et al., 2021). Thus, the presence of unexposed intrusions within the BVP cannot be excluded. Thereby, it is possible that at least at a local scale both metamorphic and magmatic fluids might have contributed to the formation of the second gold phase.

### **VII.3. Implications for exploration strategies**

The results of this study build upon the most recent compilation of geochronological data for orogenic gold mineralisation in Newfoundland (Sandeman et al., 2022) and provide new evidence for the existence of two distinct gold mineralisation events across the entire island (*Figure VII.3*). The first gold event covers a time interval ranging from ~433 to ~405 Ma. However, most data falls between ~420 to 405 Ma suggesting an association with the Acadian orogenic event (*Figure VII.3*). The second phase ranges from ~395 to 370 Ma and show best estimate ages of ~380 Ma (*Figure VII.3*). This phase is related to the Neo-Acadian orogeny.

This study showed that each of these events are related to different geodynamic settings, which in turn, has significant implications for both exploration and development strategies. Firstly, the recognition of Mid to Late Devonian mineralisation opens new exploration opportunities in areas covered by Silurian and Devonian rocks, which were less explored in the past, partially due to poor temporal constraints between the mineralisation and host lithologies. Secondly, the link between the mineralisation and structures of different ages permit the identification of better exploration targets at both regional and local scales.

As mentioned earlier, in Newfoundland, both the Salinic and the Acadian orogenic cycles are associated with an overall sinistral transpressional setting localized along major NNE to NE striking faults. Groves et al. (2018) suggested that, on a regional scale, compressional jogs or restraining bends along major crustal faults are ideal sites for the formation of orogenic gold deposits. As previously discussed,



the studied deposits and prospects are situated within a Salinic-Acadian sinistral restraining bend. Therefore, one of the initial steps in a regional exploration program in Newfoundland can be to identify the locations of compressional jogs or restraining bends of Mid Silurian–Early Devonian age. Orogenic gold deposits of Mid Silurian age, genetically linked with sinistral restraining bends, are known in both Ireland and Northern Ireland (e.g., the Cavanacaw deposit, Northern Ireland, Shaw et al., 2022). Therefore, this approach may have applicability elsewhere along the Appalachian-Caledonian belt.

In the study area, the hydrothermal systems that contributed to the formation of both gold events overlap in space. Furthermore, within the deposits, the highest gold grade zones coincide with the locations where the gold bearing veins related to the second gold mineralising event overprint the early mineralisation. As noted above, the late veins formed during the inversion of early structures. Thereby, at a regional scale, Salinic/Acadian restraining bends that were reactivated as releasing bends during the Neo-Acadian could potentially host well-endowed deposits, making them promising exploration targets. Additionally, at the district and deposit scale, identifying intersection sites between early and late gold-bearing veins can inform drilling exploration campaigns as well as mine or open pit designs.

In Nova Scotia, current geochronological data indicate the same time intervals for gold mineralisation (Kerr and Selby, 2012 and references therein). Thereby, all the recommendations for potential exploration can also be applied.

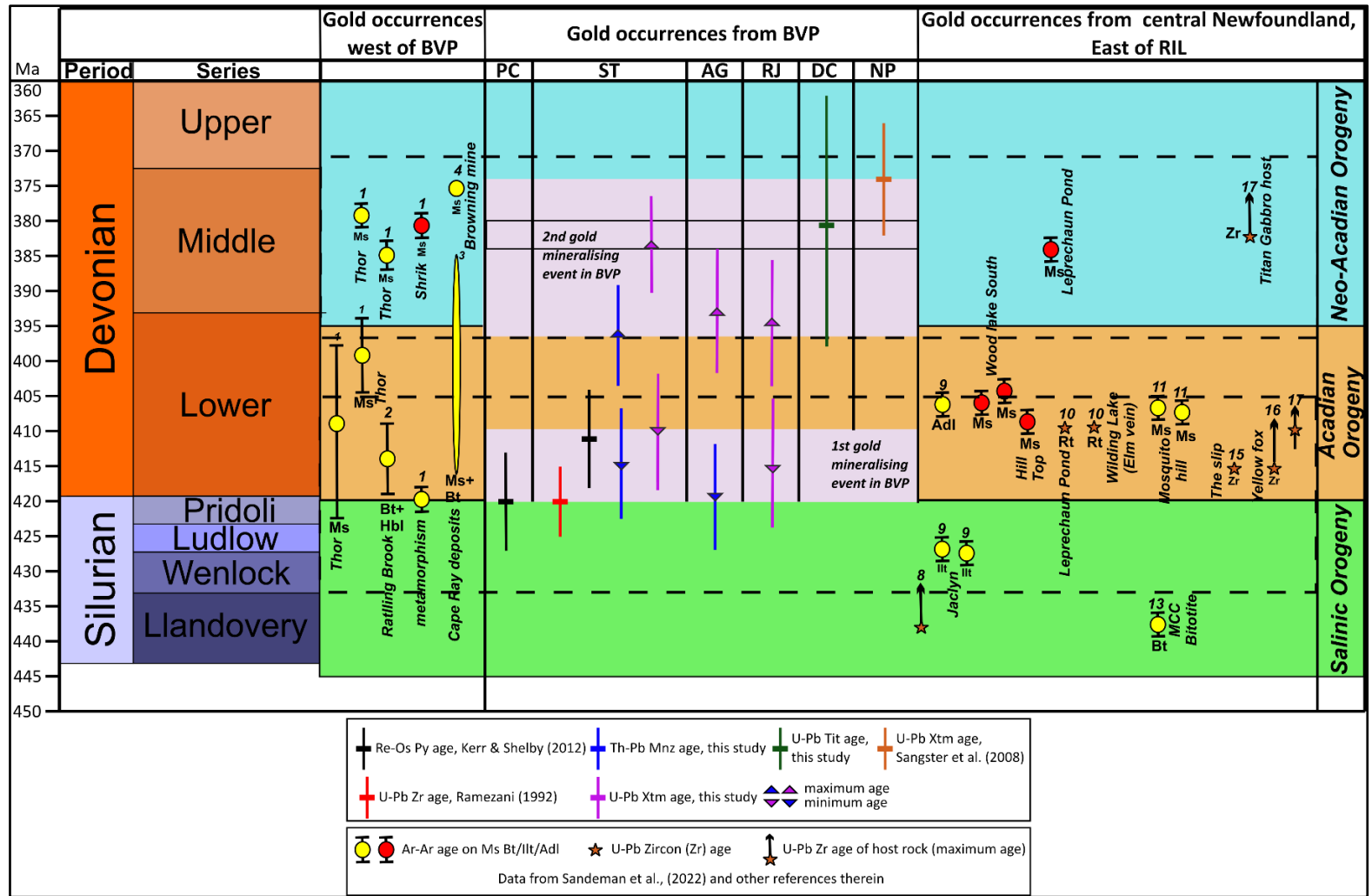


**Figure VII.3** – Compilation of geochronological data for orogenic gold occurrences from west and central Newfoundland and comparison with ages presented in this study (Column - Gold occurrences from BVP). This study agrees with the existent knowledge and provide new evidence for the existence of two distinct gold mineralising events across the entire island. Dashed rectangles mark the two gold mineralising moments at a regional scale. BVP – Baie Verte Peninsula; RIL – Red Indian Line; monazite (Mnz); xenotime (Xtm); zircon (Zr); titanite (Tit); muscovite (Ms); biotite (Bt); illite (Ilt); adularia (Adl).

#### **VII.4. Recommendations for future work**

The present study has emphasized some uncertainties concerning both the structural evolution of the BVP and the sources of fluids and metals involved in the formation of the studied gold occurrences. However, there are ways in which future studies could cover these knowledge gaps.

As noted earlier, the minimum age of the D<sub>2b</sub> event and consequently, the maximum age of the D<sub>3</sub> phase, are relative and come with a considerable degree of uncertainty. However, there is a solution to obtain a more accurate age for the end/beginning of these deformation phases. In the Stog'er Tight area, there are some mafic dykes that cut the mineralisation, and are folded by the F<sub>3</sub> folds (*Plate V.6 – B, C*). These dykes are interpreted as late D<sub>2b</sub> – early D<sub>3</sub> (*Figure VII.1*). Thereby, direct geochronological ages obtained for these dykes would provide a more accurate minimum and maximum ages for the D<sub>2b</sub> and D<sub>3</sub> deformation phases, respectively.

A similar approach can be used to determine the minimum age for the D<sub>4</sub> event, which currently is unclear (*Figure VII.3*). In both the Romeo & Juliet and the Deer Cove areas, there are veins that occur along the syn-to-post D<sub>4</sub> structures (*Plates V.17–E,G,F; V.22–G,H*). Consequently, these veins are interpreted herein as syn-to-post D<sub>4</sub>. Locally, these structures crosscut the F<sub>4</sub> folds. Therefore, if geochronological ages were to be determined for these veins, they could also serve to estimate the minimum age of the F<sub>4</sub> folds.

As previously stated, none of the available data can be used to accurately determine the fluid and metal sources that were involved in the formation of the studied deposits/prospects. Several geochemical analyses can be conducted on various mineral phases in order to gain insights into the physio-chemical properties of the mineralising fluids, which in turn could be used to infer the fluid and metal sources. Some of these methods are listed below.

- Coupled trace element and fluid inclusion analysis on Q<sub>2</sub> and Q<sub>3</sub>. Can be used to characterise the fluids involved in the formation of both gold events and in turn would provide the setting for speculating potential fluid sources. Carbon isotope analysis on the gaseous phases from the fluid inclusions can highlight the potential source for the fluids.
- Oxygen isotope analysis conducted on both Q<sub>2</sub> and Q<sub>3</sub> quartz generations in conjunction with sulfur isotope analysis on both early and late stages of pyrite

can provide insights into the source of the fluids related to both gold generations.

- Pyrite can contain, primary, invisible gold within its lattice. BSE imaging combined with EPMA and/or LA-ICP-MS spot analysis and element mapping of different pyrite generations can be used to determine both the textural and geochemical characteristics of pyrite. In turn, this can be used to speculate if the late gold generation was liberated from pyrite (remobilized).

## **VIII. Conclusions**

This PhD project is the first to integrate regional- to deposit scale structural observations with paragenetic associations, gold geochemistry, and in-situ U-Th-Pb geochronology of multiple gold occurrences from the Baie Verte Peninsula (BVP) of Newfoundland. This chapter summarises the key conclusions of this study.

- The Point Rouse Complex (PRC) was affected by at least three main deformational moments.
  - The first deformation phase, termed here as D<sub>2</sub>, records a progressive nature. During the early stage (D<sub>2a</sub>), the PRC was thrust towards south, over the Paquet Harbour Group (PHG), the Burlington Granodiorite (BG), and over the Ming's Bight Group (MBG). This resulted with regional scale folding and south directed thrusts. The main foliation fabric observable in the area was also formed during this phase. During the late stages (D<sub>2b</sub>), further shortening was accommodated by brittle-ductile reverse faults associated with south verging mesoscale folds. The entire D<sub>2</sub> phase developed during the Salinic (D<sub>2a</sub>) and the Acadian (D<sub>2b</sub>) orogenic cycles under an overall sinistral transpressional setting.
  - During the D<sub>3</sub> deformational phase, recumbent, north verging mesoscale folds were formed in association with the inversion of the south directed thrusts and reverse faults as normal faults. This event corresponds to the onset of the Neo-Acadian Orogeny and developed under a dextral transtensional setting localised along the BVL.
  - The D<sub>4</sub> event shows a more brittle nature compared to the preceding deformational stages, and is characterised by the presence of broad, open, north trending folds. The onset of this event is constrained at early Late Devonian times. At this stage, dextral transcurrent motions were accommodated by the BVL.
- Two gold mineralising events contributed to the formation of the studied gold occurrences.
  - The age of the first gold mineralising moment is constrained between 420 to 410 Ma. Pre-to-syn D<sub>2b</sub>, sheared to laminated and breccia type quartz ± carbonate veins are related to this event. The veins formed at mesozonal conditions. The veins are enveloped by a few meters wide, pervasive alteration

halo composed of albite-ankerite-sericite-rutile-pyrite-phosphates-zircon ± calcite-chlorite-epidote-titanite-hematite. The gold associated to this mineralising moment occurs mostly as inclusions in pyrite, and to a lesser degree, free within the veins. Gold precipitation was controlled by wall-rock sulphidation and flash vaporisation processes. This mineralising stage resulted from a single mineralising system that exhibited spatial and/or temporal variations. Fluids of metamorphic origin may be related to this event.

- The maximum age of the second gold mineralising event is ~396 Ma, whereas the best estimate age is ~380 Ma. Syn-to-post D<sub>3</sub> quartz<sub>3</sub>-calcite-chlorite ± sericite-hematite veins are associated to the late generation of gold. The veins formed under epizonal conditions. The gold related to this stage occurs mostly free on and along the veins within brecciated pyrite crystals. At least locally, fluids of both magmatic and metamorphic origin might have contributed to this mineralising stage.

## **Bibliography**

**Aerden, D.G., 1996.** The pyrite-type strain fringes from Lourdes (France): indicators of Alpine thrust kinematics in the Pyrenees. *Journal of Structural Geology*, v. 18(1), p. 75-91, [https://doi.org/10.1016/0191-8141\(95\)00084-Q](https://doi.org/10.1016/0191-8141(95)00084-Q).

**Aerden, D.G. and Sayab, M., 2017.** Probing the prodigious strain fringes from Lourdes. *Journal of Structural Geology*, v. 105, p. 88-106, <https://doi.org/10.1016/j.jsg.2017.11.001>.

**Alsop, G.I., 1992.** Progressive deformation and the rotation of contemporary fold axes in the Ballybofey Nappe, north-west Ireland. *Geological Journal*, v. 27(3), p. 271-283, <https://doi.org/10.1002/gj.3350270305>.

**Alsop, G.I., and Holdsworth, R.E., 2002.** The geometry and kinematics of flow perturbation folds. *Tectonophysics*, 350, 99-125.

**Alsop, G.I., Cheer, D.A., Strachan, R.A., Krabbendam, M., Kinny, P.D., Holdsworth, R.E. and Leslie, A.G., 2010.** Progressive fold and fabric evolution associated with regional strain gradients: a case study from across a Scandian ductile thrust nappe, Scottish Caledonides. *Geological Society, London, Special Publications*, v. 335(1), p. 255-274, <https://doi.org/10.1144/SP335.12>.

**Alsop, G.I. and Holdsworth, R.E., 1999.** Vergence and facing patterns in large-scale sheath folds. *Journal of Structural Geology*, v. 21(10), p. 1335-1349, [https://doi.org/10.1016/S0191-8141\(99\)00099-1](https://doi.org/10.1016/S0191-8141(99)00099-1).

**Anderson, S.D., 1998.** Structure, metamorphism, and U–Pb and <sup>40</sup>Ar/<sup>39</sup>Ar geochronology of the Ming's Bight Group, and the Paleozoic tectonic evolution of the Baie Verte Peninsula, Newfoundland. Ph.D. thesis, Dalhousie University, Dartmouth, Nova Scotia, p. 452.

**Anderson, S.D., Jamieson, R.A., and Reynolds, P.H., 2001.** Devonian extension in northwestern Newfoundland: <sup>40</sup>Ar/<sup>39</sup>Ar and U-Pb data from the Ming's Bight area, Baie Verte Peninsula. *Journal of Geology*, v.10, p.191–211.

**Baird, D.M., 1951.** The Geology of the Burlington Peninsula Newfoundland. *Geological Survey of Canada, Paper 51-21*, p. 70.

**Baranov, V., 1957.** A new method for interpretation of aeromagnetic maps: pseudo-gravimetric anomalies. *Geophysics*, v. 22(2), p. 359-382.

**Baranov, V. and Naudy, H., 1964.** Numerical calculation of the formula of reduction to the magnetic pole. *Geophysics*, v. 29(1), p. 67-79.

**Barnes, C.J., Majka, J., Jeanneret, P., Ziemniak, G., Kooijman, E., Kósmińska, K., Kielman-Schmitt, M., and Schneider, D.A., 2021.** Using Th-U-Pb geochronology to extract crystallization ages of Paleozoic metamorphic monazite contaminated by initial Pb. *Chemical Geology*, v. 582, p. 120450.

**Bastida, F., Aller, J., Fernández, F.J., Lisle, R.J., Bobillo-Ares, N.C. and Menéndez, O., 2014.** Recumbent folds: key structural elements in orogenic belts. *Earth-science reviews*, v. 135, p. 162-183, <https://doi.org/10.1016/j.earscirev.2014.05.002>.

**Bédard, J.H., Lauzière, K., Sangster, A., Tellier, M., Tremblay, A., and Dec, T., 1999.** Geology, Betts Cove Ophiolite and its cover rocks, Newfoundland. Geological Survey of Canada, Map 1969A, scale 1:20 000. doi:10.4095/211851.

**Bédard, J.H., Lauzière, K., Tremblay, A., Sangster, A., Douma, S.L., and Dec, T., 2000.** Betts Cove ophiolite and its cover rocks, Newfoundland. Geological Survey of Canada, Bulletin 550, p. 76.

**van Berkel, J.T., Currie K.L., 1988.** Geology of the Puddle Pond(12A/5) and Little Grand Lake (12A/12) map areas, southwestern Newfoundland. Newfoundland Department of Mines and Energy Report, v. 88-1, p. 99-107.

**Berthé, D., Choukroune, P. and Jégouzo, P., 1979.** Orthogneiss, mylonite and non-coaxial deformation of granites: the example of the South Armorian Shear Zone. *Journal of Structural Geology*, v. 1(1), p. 31-42, [https://doi.org/10.1016/0191-8141\(79\)90019-1](https://doi.org/10.1016/0191-8141(79)90019-1).

**Blenkinsop, T.G., 2002.** Deformation microstructures and mechanisms in minerals and rocks. Kluwer Academic Publishers.

**Boyle, R.W., 1979.** The geochemistry of gold and its deposits: Geological Survey of Canada Bulletin 280, p. 584.

**Bons, P.D., Elburg, M.A. and Gomez-Rivas, E., 2012.** A review of the formation of tectonic veins and their microstructures. *Journal of structural geology*, v. 43, p. 33-62, <https://doi.org/10.1016/j.jsg.2012.07.005>.

**Bons, P.D., 2000.** The formation of veins and their microstructures. *Journal of the Virtual Explorer*, v. 2, p. 12,

**Budzyń, B., Wirth, R., Sláma, J., Kozub-Budzyń, G.A., Rzepa, G. and Schreiber, A., 2022.** A detailed and comprehensive TEM, EPMA and Raman characterization of high-metamorphic grade monazites and their U-Th-Pb systematics (the Góry Sowie Block, SW Poland). *Chemical Geology*, v. 607, p.121015, <https://doi.org/10.1016/j.chemgeo.2022.121015>.

**Budzyń, B., Wirth, R., Sláma, J., Birski, Ł., Tramm, F., Kozub-Budzyń, G.A., Rzepa, G. and Schreiber, A., 2021.** LA-ICPMS, TEM and Raman study of radiation damage, fluid-induced alteration and disturbance of U-Pb and Th-Pb ages in experimentally metasomatised monazite. *Chemical Geology*, v. 583, p. 120464, <https://doi.org/10.1016/j.chemgeo.2021.120464>.

**Budzyń, B. and Sláma, J., 2019.** Partial resetting of U–Pb ages during experimental fluid-induced re-equilibration of xenotime. *Lithos*, v. 346, p. 105163, <https://doi.org/10.1016/j.lithos.2019.105163>.

**Bursnall, J.T., 1975.** Stratigraphy, structure and metamorphism west of Baie Verte, Burlington Peninsula, Newfoundland. Unpublished Ph.D. thesis, Cambridge University, England, p. 337.

**Burg, J.-P., 2018.** Script to Structural Geology. ETH Zürich, Lectures 651-3422-00L and 651-3422-00V, Zurich, Switzerland, p. 235-256.

**Butt, C.R. and Hough, R.M., 2009.** Why gold is valuable. *Elements*, v. 5(5), p. 277-280, <https://doi.org/10.2113/gselements.5.5.277>.



**Calon, T.J. and Weick, J., 1990.** Structural evolution of the Pine Cove Gold Deposit. Preliminary report of a detailed structural analysis on behalf of the Corona Corporation. Unpublished report.

**Cardozo, N. and Allmendinger, R.W., 2013.** Spherical projections with OSXStereonet. *Computers & Geosciences*, v.51, p. 193-205. <https://doi.org/10.1016/j.cageo.2012.07.021>.

**Carmignani L., & Kligfield R., (1990).** Crustal extension in the northern Apennines: The transition from compression to extension in the Alpi Apuane Core Complex *Tectonics*, 9, 1275-1303.

**Castonguay, S., vanStaal, C.R., Joyce, N., Skulski, T., and Hibbard, J., 2014.** Taconic metamorphism preserved in the Baie Verte Peninsula, Newfoundland Appalachians: geochronological evidence for ophiolite obduction and subduction and exhumation of the leading edge of the Laurentian (Humber) margin during closure of the Taconic Seaway. *Geoscience Canada*, v. 41, p. 459–482.

**Castonguay, S., Skulski, T., McNicoll, V., and van Staal, C.R., 2012.** Eastern Baie Verte Peninsula Revisited: from Early Paleozoic suprasubduction zone ophiolite, through syn-orogenic continental volcanism, to later Paleozoic extensional collapse. *Geological Association of Canada–Mineralogical Association of Canada, Program with Abstracts, St. John's, Newfoundland, May 27–29, 2012*, v. 35, p. 22.

**Castonguay, S., Skulski, T., van Staal, C.R., 2009.** New insights on the structural geology of the Paquet Harbour Group and Point Rouse Complex, Baie Verte Peninsula, Newfoundland. Newfoundland and Labrador Department of Natural Resources, Geological Survey, Current Research, Report 09-1, p. 147-158.

**Cawood, P.A., Hawkesworth, C.J. and Dhuime, B., 2013.** The continental record and the generation of continental crust. *GSA Bulletin*, v. 125(1-2), p. 14-32, <https://doi.org/10.1130/B30722.1>.

**Cawood, P.A., Kröner, A., Collins, W.J., Kusky, T.M., Mooney, W.D., and Windley, B.F., 2009.** Accretionary orogens through Earth history. *Geological Society, London, Special Publications*, v. 318, p. 1-36.

**Cawood, P.A., McCausland, P.J. and Dunning, G.R., 2001.** Opening Iapetus: constraints from the Laurentian margin in Newfoundland. *Geological Society of America Bulletin*, v. 113(4), p. 443-453.

**Cawood, P.A. and Nemchin, A.A., 2001.** Paleogeographic development of the east Laurentian margin: Constraints from U-Pb dating of detrital zircons in the Newfoundland Appalachians. *Geological Society of America Bulletin*, v. 113(9), p. 1234-1246.

**Cawood, P. A., and Dunning, G. R. 1993.** Silurian age for movement on the Baie Verte Line: implications for accretionary tectonics in the northern Appalachians. *Geological Society of America, Program with Abstracts*, 25, p. 422.

**Chapman, R., Torvela, T. and Savastano, L., 2023.** Insights into Regional Metallogeny from Detailed Compositional Studies of Alluvial Gold: An Example from the Loch Tay Area, Central Scotland. *Minerals*, v. 13(2), p. 140, <https://doi.org/10.3390/min13020140>.

**Chapman, R.J., Mortensen, J.K., Allan, M.M., Walshaw, R.D., Bond, J. and MacWilliam, K., 2022.** A new approach to characterizing deposit type using mineral inclusion assemblages in gold particles. *Economic Geology*, v. 117(2), p. 361-381, doi: <https://doi.org/10.5382/econgeo.4863>.

**Chapman, R.J., Banks, D.A., Styles, M.T., Walshaw, R.D., Piazzolo, S., Morgan, D.J., Grimshaw, M.R., Spence-Jones, C.P., Matthews, T.J. and Borovinskaya, O., 2021.** Chemical and physical heterogeneity within native gold: implications for the design of gold particle studies. *Mineralium Deposita*, v. 56, p. 1563-1588, <https://doi.org/10.1007/s00126-020-01036-x>.

**Chapman, R.J., Allan, M.M., Mortensen, J.K., Wrighton, T.M. and Grimshaw, M.R., 2018.** A new indicator mineral methodology based on a generic Bi-Pb-Te-S mineral inclusion signature in detrital gold from porphyry and low/intermediate sulfidation epithermal environments in Yukon Territory, Canada. *Mineralium Deposita*, v. 53, p. 815-834, <https://doi.org/10.1007/s00126-017-0782-0>.

**Chapman, R., Mileham, T., Allan, M. and Mortensen, J., 2017.** A distinctive Pd-Hg signature in detrital gold derived from alkalic Cu-Au porphyry systems. *Ore Geology Reviews*, v. 83, p. 84-102, <https://doi.org/10.1016/j.oregeorev.2016.12.015>.

**Chapman, R.J. and Mortensen, J.K., 2016.** Characterization of gold mineralization in the Northern Cariboo gold district, British Columbia, Canada, through integration of compositional studies of lode and detrital gold with historical placer production: A template for evaluation of orogenic gold districts. *Economic Geology*, v. 111(6), p. 1321-1345, doi: <https://doi.org/10.2113/econgeo.111.6.1321>.

**Chapman, R., Mortensen, J., and LeBarge, W., 2011.** Styles of lode gold mineralization contributing to the placers of the Indian River and Black Hills Creek, Yukon Territory, Canada as deduced from microchemical characterization of placer gold grains: *Mineralium Deposits*, v. 46, p. 881–903.

**Chapman, R.J., Mortensen, J.K., Crawford, E.C. and Lebarge, W., 2010.** Microchemical studies of placer and lode gold in the Klondike District, Yukon, Canada: 1. Evidence for a small, gold-rich, orogenic hydrothermal system in the Bonanza and Eldorado Creek area. *Economic Geology*, v. 105(8), p. 1369-1392, doi: <https://doi.org/10.2113/econgeo.105.8.1369>.

**Chapman, R.J., Leake, R.C., Bond, D.P.G., Stedra, V. and Fairgrieve, B., 2009.** Chemical and mineralogical signatures of gold formed in oxidizing chloride hydrothermal systems and their significance within populations of placer gold grains collected during reconnaissance. *Economic Geology*, v. 104(4), p. 563-585, <https://doi.org/10.2113/gsecongeo.104.4.563>.

**Chapman, R.J., Leake, R.C. and Moles, N.R., 2000a.** The use of microchemical analysis of alluvial gold grains in mineral exploration: experiences in Britain and Ireland. *Journal of Geochemical Exploration*, v. 71(3), p. 241-268, [https://doi.org/10.1016/S0375-6742\(00\)00157-6](https://doi.org/10.1016/S0375-6742(00)00157-6).

**Chapman, R.J., Leake, R.C., Moles, N.R., Earls, G., Cooper, C., Harrington, K. and Berzins, R., 2000b.** The application of microchemical analysis of alluvial gold grains to the understanding of complex local and regional gold

mineralization: a case study in the Irish and Scottish Caledonides. *Economic Geology*, v. 95(8), p. 1753-1773, doi: <https://doi.org/10.2113/gsecongeo.95.8.1753>.

**Chew, D.M., Daly, J.S., Flowerdew, M.J., Kennedy, M.J., and Page, L.M., 2004.** Crenulation-slip development in a Caledonian shear zone in NW Ireland: evidence for a multi-stage movement history. In *Flow Processes in Faults and Shear Zones* edited by Alsop, G.I., Holdsworth, R.E., McCafrey, K.J.W. and Hand, M., Geological Society, London, special Publications, 224, p. 337-352.

**Church, W.R., 1969.** Metamorphic rocks of the Burlington Peninsula and adjoining areas of Newfoundland and their bearing on continental drift in North Atlantic. In *North Atlantic Geology and Continental Drift*, edited by Kay, M., American Association of Petroleum Geologists, Memoir 12, p. 212-233.

**Cioacă, M.E., Munteanu, M., Lynch, E.P., Arvanitidis, N., Bergqvist, M., Costin, G., Ivanov, D., Milu, V., Arvidsson, R., Iorga-Pavel, A. and Högdahl, K., 2020.** Mineralogical setting of precious metals at the Assarel porphyry copper-gold deposit, Bulgaria, as supporting information for the development of new drill core 3D XCT-XRF scanning technology. *Minerals*, v. 10(11), p. 946, <https://doi.org/10.3390/min10110946>.

**Colman-Sadd, S.P., Stone, P., Swinden, H.S. and Barnes, R.P., 1992.** Parallel geological development in the Dunnage Zone of Newfoundland and the Lower Palaeozoic terranes of southern Scotland: an assessment. *Earth and Environmental Science Transactions of The Royal Society of Edinburgh*, v. 83(3), p. 571-594.

**Cook R.B., Cochrane, L.B., 2006.** Technical report on the Rambler Property, Baie Verte Peninsula, Newfoundland, Canada. Rambler Metals and Mining PLC., NI 43-101 report, p. 82.

**Copeland, D., Pitman, C., Evans, D.T.W., McNeill, P., and Slepcev, G., 2015.** Mineral resource and mineral reserve update on the Pine Cove mine and mineral resource estimate on the Stog'er Tight deposit, Point Rouse Project, Baie Verte. Anaconda Mining INC., Newfoundland and Labrador, Canada, NI 43-101 Technical Report, p. 249.

**Coyle, M., 1990.** Geology, geochemistry and geochronology of the Springdale Group, an Early Silurian caldera in central Newfoundland. Ph.D. thesis, Memorial University of Newfoundland, St. John's, Newfoundland and Labrador, p. 310.

**Currie, K.L., 1995.** Plutonic rocks; Geology of the Appalachian—Caledonian Orogen in Canada and Greenland. Geological Survey of Canada, Geology of Canada, p. 629-680.

**Cullen, M., Pitman, C., Copeland, D.A., McNeill, P., and Slepcev, G., 2018.** Mineral resource and mineral reserve update on the Point Rouse Project, Baie Verte. Anaconda Mining Inc., Newfoundland and Labrador, Canada, NI-43-101 Technical Report. p. 285.

**Cutts, J.A., Zagorevski, A., McNicoll, V. and Carr, S.D., 2012.** Tectono-stratigraphic setting of the Moreton's Harbour Group and its implications for the

evolution of the Laurentian margin: Notre Dame Bay, Newfoundland. *Canadian Journal of Earth Sciences*, v. 49(1), p. 111-127, <https://doi.org/10.1139/e11-040>.

**De Paola, N., Holdsworth, R.E., McCaffrey, K.J.W., Barchi, M.R., 2005.** Partitioned transtension: an alternative to basin inversion models. *Journal of Structural Geology*, v. 27, Issue 4, p. 607-625.

**de Wit, M.J., 1980.** Structural and metamorphic relationships of pre-Fleur de Lys and Fleur de Lys rocks of the Baie Verte Peninsula, Newfoundland. *Canadian Journal of Earth Sciences*, v. 17, p. 1559-1575.

**Dearin, C., Geo, P., 2009.** Eighth Year Assessment Report: Rock Sampling of Main vein: Surface, Adit & Stockpiles. Deer Cove Gold Project, Baia Verte, Newfoundland. Unpublished report, Fortis GeoServices Ltd.

**Dearin, C., 2003.** First year assessment report: digital geochemical, geophysical and geological compilation. Deer Cove gold project, Baie Verte, Newfoundland,. Unpublished report, Fortis GeoServices Ltd.

**Dimmell, P. and Hartley, C., 1991.** Gold mineralization and exploration potential of the Pine Cove property, Baie Verte peninsula. *Ore Horizons*, v. 1, p. 51-62.

**Dimmell, P. and Hartley, C., 1991.** Sixth year work: Geology, Geochemistry, Geophysics, Trenching and Diamond Drilling on the Project 7432, Varna Option Property, Baie Verte, Newfoundland. Unpublished report, Corona Corporation.

**Dubé, B., Lauzière, K., and Poulsen, H.K., 1993.** The Deer Cove deposit: an example of “thrust”-related breccia-vein type gold mineralization in the Baie Verte Peninsula, Newfoundland. *Geological Survey of Canada, Current Research*, part D, Paper 93-1D, p. 1-10.

**Duncan, D.R. and Graves, R.M., 1992.** Assessment report (7th year) on geology and diamond drilling at the Pine Cove property, Baie Verte area. Novagold Resources. *Geological Survey File*, (12H/16), p. 1278.

**Dunning, G.R., O'brien, S.J., Colman-Sadd, S.P., Blackwood, R.F., Dickson, W.L., O'neill, P.P. and Krogh, T.E., 1990.** Silurian orogeny in the Newfoundland Appalachians. *The Journal of Geology*, v. 98(6), p. 895-913,

**Dunning, G.R. and Krogh, T.E., 1985.** Geochronology of ophiolites of the Newfoundland Appalachians. *Canadian Journal of Earth Sciences*, v. 22(11), p. 1659-1670.

**Ene, V.V., 2021.** Crustal recycling in the magmatic evolution of post-subduction provinces: The South Apuseni Mountains, Romania. Ph.D. thesis, University of Leicester.

**Engi, M., 2017.** Petrochronology based on REE-minerals: monazite, allanite, xenotime, apatite. *Reviews in Mineralogy and Geochemistry*, v. 83(1), p. 365-418, <https://doi.org/10.2138/rmg.2017.83.12>.

**Evans, D.T.W., 2004.** Epigenetic gold occurrences, Baie Verte Peninsula, Newfoundland. Newfoundland and Labrador Department of Natural Resources, *Geological Survey, Mineral Resource Report 11*, p. 177.

**Evans, D.T.W., 1999.** Epigenetic gold mineralization, Baie Verte Peninsula, Newfoundland. Newfoundland Department of Mines and Energy, Geological Survey, Report 99-1, p. 163-182.

**Evans, D., 2013.** Exploration Summary Report Anaconda Mining Inc. Tenacity Option, Mineral Exploration Licence 7513M, Baie Verte Peninsula, Newfoundland, NTS 12H/16, Silvertip Exploration Consultants Incorporated, p. 34.

**Evans, D. T. W., & Wilson, M., 1996.** Epigenetic Gold Occurrences in the Eastern Dunnage Zone, Newfoundland. Mineral Resource Report 9. Government of Newfoundland and Labrador, Department of Mines and Energy.

**Feng, H., Shen, P., Zhu, R., Ma, G., Li, C. and Li, J., 2020.** SIMS U-Pb dating of vein-hosted hydrothermal rutile and carbon isotope of fluids in the Wulong lode gold deposit, NE China: Linking gold mineralization with craton destruction. *Ore Geology Reviews*, v. 127, p. 103838, <https://doi.org/10.1016/j.oregeorev.2020.103838>.

**Fielding, I.O.H., Johnson, S.P., Zi, J.-W., Rasmussen, B., Muhling, J.R., Dunkley, D.J., Sheppard, S., Wingate, M.T.D., Rogers, J.R., 2017.** Using In Situ SHRIMP U-Pb Monazite and Xenotime Geochronology to Determine the Age of Orogenic Gold Mineralization: An Example from the Paulsens Mine, Southern Pilbara Craton. *Economic Geology*, v. 112(5), p. 1205–1230. doi: <https://doi.org/10.5382/econgeo.2017.4507>

**Fossen, H., Cavalcante, G.C.G., Pinheiro, R.V.L. and Archanjo, C.J., 2019.** Deformation–progressive or multiphase?. *Journal of Structural Geology*, v. 125, p. 82-99, <https://doi.org/10.1016/j.jsg.2018.05.006>.

**Fossen, H., 2016.** Structural geology. Cambridge university press.

**Fossen, H., Teyssier, C., & Whitney, D. L. 2013.** Transtensional folding. *Journal of Structural Geology*, 56, 89-102.

**Frelinger, S.N., Ledvina, M.D., Kyle, J.R. and Zhao, D., 2015.** Scanning electron microscopy cathodoluminescence of quartz: Principles, techniques and applications in ore geology. *Ore Geology Reviews*, v. 65, p. 840-852, <https://doi.org/10.1016/j.oregeorev.2014.10.008>.

**Frimmel, H.E., 2008.** Earth's continental crustal gold endowment. *Earth and Planetary Science Letters*, v. 267(1-2), p. 45-55, <https://doi.org/10.1016/j.epsl.2007.11.022>.

**Froitzheim, N., 1992.** Formation of recumbent folds during synorogenic crustal extension (Austroalpine nappes, Switzerland). *Geology*, v. 20(10), p. 923-926.

**Gale G.H., 1971.** An investigation of some sulphide deposits of the Rambler area, Newfoundland. Ph.D. thesis, Durham University, p. 279.

**Gammons, C.H. and Williams-Jones, A.E., 1995.** Hydrothermal geochemistry of electrum; thermodynamic constraints. *Economic Geology*, v. 90(2), p. 420-432, <https://doi.org/10.2113/gsecongeo.90.2.420>.

**Gas'kov, I. V., 2017.** Major impurity elements in native gold and their association with gold mineralization settings in deposits of Asian folded areas. *Russian Geology and Geophysics*, v. 58, p. 1080-1092.

**Goldfarb, R.J. and Pitcairn, I., 2023.** Orogenic gold: is a genetic association with magmatism realistic?. *Mineralium Deposita*, v. 58(1), p. 5-35, <https://doi.org/10.1007/s00126-022-01146-8>.

**Goldfarb, R.J., 2021.** Lode Gold Deposits in Time and Space, in: Alderton, D., Elias, S.A., *Encyclopedia of Geology*, (Second Edition), Academic Press, Oxford, p. 663–679.

**Goldfarb, R.J. and Groves, D.I., 2015.** Orogenic gold: Common or evolving fluid and metal sources through time. *Lithos*, v. 233, p. 2-26, <https://doi.org/10.1016/j.lithos.2015.07.011>.

**Gonçalves, G.O., Lana, C., Scholz, R., Buick, I.S., Gerdes, A., Kamo, S.L., Corfu, F., Marinho, M.M., Chaves, A.O., Valeriano, C. and Nalini Jr, H.A., 2016.** An assessment of monazite from the Itambé pegmatite district for use as U–Pb isotope reference material for microanalysis and implications for the origin of the “Moacyr” monazite. *Chemical Geology*, v. 424, p. 30-50.

**Gordon, S.M., Kirkland, C.L., Reddy, S.M., Blatchford, H.J., Whitney, D.L., Teyssier, C., Evans, N.J. and McDonald, B.J., 2021.** Deformation-enhanced recrystallization of titanite drives decoupling between U-Pb and trace elements. *Earth and Planetary Science Letters*, v. 560, p. 116810, <https://doi.org/10.1016/j.epsl.2021.116810>.

**Gower, D., Graves, G., Walker, S., and MacInnis, D. 1991.** Lode gold mineralization at Deer Cove, Point Rouse Complex, Baie Verte Peninsula in Metallogenic framework of base and precious metal deposits, central and western Newfoundland. Geological Survey of Canada, Open File 2156.

**Götze, J., Pan, Y., & Müller, A. 2021.** Mineralogy and mineral chemistry of quartz: A review. *Mineralogical Magazine*, v. 85(5), p. 639-664, doi:10.1180/mgm.2021.72

**Götze, J., 2002.** Potential of cathodoluminescence (CL) microscopy and spectroscopy for the analysis of minerals and materials. *Analytical and bioanalytical chemistry*, v. 374, p. 703-708, <https://doi.org/10.1007/s00216-002-1461-1>.

**Grandell, L., Lehtilä, A., Kivinen, M., Koljonen, T., Kihlman, S., Lauri, L.S., 2016.** Role of critical metals in the future markets of clean energy technologies. *Renewable Energy*, v. 95, p. 53-62, <https://doi.org/10.1016/j.renene.2016.03.102>.

**Grand’Homme, A., Janots, E., Seydoux-Guillaume, A.M., Guillaume, D., Bosse, V. and Magnin, V., 2016.** Partial resetting of the U-Th-Pb systems in experimentally altered monazite: Nanoscale evidence of incomplete replacement. *Geology*, v. 44(6), p. 431-434, <https://doi.org/10.1130/G37770.1>.

**Grand’Homme, A., 2016.** Hydrothermal monazite: the unavoidable accessory. PhD thesis, Université Grenoble Alpes.

**Grasemann, B., Stüwe, K. and Vannay, J.C., 2003.** Sense and non-sense of shear in flanking structures. *Journal of Structural Geology*, v. 25(1), p. 19-34, [https://doi.org/10.1016/S0191-8141\(02\)00012-3](https://doi.org/10.1016/S0191-8141(02)00012-3).

**Grasemann, B., Wiesmayr, G., Draganits, E. and Füsseis, F., 2004.** Classification of refold structures. *The Journal of geology*, v. 112(1), p. 119-125.

**Grimshaw, M.R., 2018.** Gold Mineralisation in the Lone Star area of the Klondike Gold District, Yukon, Canada. PhD thesis, University of Leeds.

**Groves, D.I., Santosh, M., and Zhang, L., 2020a.** A scale-integrated exploration model for orogenic gold deposits based on a mineral system approach. *Geoscience Frontiers*, v. 11(3), p. 719-738.

**Groves, D.I., Santosh, M., Deng, J., Wang, Q., Yang, L. and Zhang, L., 2020b.** A holistic model for the origin of orogenic gold deposits and its implications for exploration. *Mineralium Deposita*, v. 55, p. 275-292, <https://doi.org/10.1007/s00126-019-00877-5>.

**Groves, D.I., Santosh, M., Goldfarb, R.J. and Zhang, L., 2018.** Structural geometry of orogenic gold deposits: Implications for exploration of world-class and giant deposits. *Geoscience Frontiers*, v. 9(4), p. 1163-1177, <https://doi.org/10.1016/j.gsf.2018.01.006>.

**Groves, D.I. and Santosh, M., 2015.** Province-scale commonalities of some world-class gold deposits: implications for mineral exploration. *Geoscience Frontiers*, v. 6(3), p. 389-399, <https://doi.org/10.1016/j.gsf.2014.12.007>.

**Groves, D.I. and Bierlein, F.P., 2007.** Geodynamic settings of mineral deposit systems. *Journal of the Geological Society*, v. 164(1), p. 19-30, <https://doi.org/10.1144/0016-76492006-065>.

**Groves, D.I., Goldfarb, R.J., Robert, F., and Hart, C.J.R., 2003.** Gold Deposits in Metamorphic Belts: Overview of Current Understanding, Outstanding Problems, Future Research, and Exploration Significance. *Economic Geology*, v. 98, p. 1-29.

**Groves, D.I., Goldfarb, R.J., Gebre-Mariam, M., Hagemann, S.G. and Robert, F., 1998.** Orogenic gold deposits: a proposed classification in the context of their crustal distribution and relationship to other gold deposit types. *Ore geology reviews*, v. 13(1-5), p. 7-27, [https://doi.org/10.1016/S0169-1368\(97\)00012-7](https://doi.org/10.1016/S0169-1368(97)00012-7).

**Hagemann, S.G., and Cassidy, K.F., 2000.** Archean orogenic lode gold deposits. *Reviews in Economic Geology* v. 13, p. 9-68.

**Hagemann, S.G., Lisitsin, V.A. and Huston, D.L., 2016.** Mineral system analysis: Quo vadis. *Ore Geology Reviews*, v. 76, p. 504-522, <https://doi.org/10.1016/j.oregeorev.2015.12.012>.

**Harris, L. B., Koyi, H. A., & Fossen, H., 2002.** Mechanisms for folding of high-grade rocks in extensional tectonic settings. *Earth-Science Reviews*, 59(1-4), 163-210.

**Harrison, T.M., Catlos, E.J. and Montel, J.M., 2002.** U-Th-Pb dating of phosphate minerals. *Reviews in Mineralogy and Geochemistry*, v. 48(1), p. 524-558, <https://doi.org/10.2138/rmg.2002.48.14>.

**Hart, C.J.R. and Goldfarb, R.J., 2005.** Distinguishing intrusion-related from orogenic gold systems. In *New Zealand Minerals Conference Proceedings*, v. 2005, p. 125-133.

**Hastie, E.C., Kontak, D.J. and Lafrance, B., 2020.** Gold remobilization: Insights from gold deposits in the Archean Swayze greenstone belt, Abitibi

Subprovince, Canada. *Economic Geology*, v. 115(2), p. 241-277, <https://doi.org/10.5382/econgeo.4709>.

**Haworth, R.T., Poole, W.H., Grant, A.C., and Sandford, B.V., 1976.** Marine geoscience survey northeast of Newfoundland. Geological Survey of Canada, Paper 76-1A, p. 7-15.

**Herzog, M., LaFlamme, C., Beaudoin, G., Marsh, J. and Guilmette, C., 2023.** U–Pb vein xenotime geochronology constraints on timing and longevity of orogenic gold mineralization in the Malartic-Val-d'Or Camp, Abitibi Subprovince, Canada. *Mineralium Deposita*, v. 58(1), p. 105-133, <https://doi.org/10.1007/s00126-022-01131-1>.

**Hetherington, C.J., Harlov, D.E. and Budzyń, B., 2010.** Experimental metasomatism of monazite and xenotime: mineral stability, REE mobility and fluid composition. *Mineralogy and Petrology*, v. 99, p. 165-184, <https://doi.org/10.1007/s00710-010-0110-1>.

**Hibbard, J., 1983.** Geology of the Baie Verte Peninsula, Newfoundland. Department of Mines and Energy, Government of Newfoundland and Labrador, Memoir 2, p. 279.

**Hibbard, J., 1982.** Significance of the Baie Vene Flexure, Newfoundland. *Geological Society of America Bulletin*, v. 93, p. 790-797.

**Holder, R.M., and Hacker, B.R., 2019.** Fluid-driven resetting of titanite following ultrahigh-temperature metamorphism in southern Madagascar. *Chemical Geology*, v. 504, p. 38-52.

**Holder, R.M., Hacker, B.R., Seward, G.G. and Kylander-Clark, A.R., 2019.** Interpreting titanite U–Pb dates and Zr thermobarometry in high-grade rocks: empirical constraints on elemental diffusivities of Pb, Al, Fe, Zr, Nb, and Ce. *Contributions to Mineralogy and Petrology*, v. 174, p. 1-19, <https://doi.org/10.1007/s00410-019-1578-2>.

**Holdsworth, R.E., 1990.** Progressive deformation structures associated with ductile thrusts in the Moine Nappe, Sutherland, N. Scotland. *Journal of Structural Geology*, 12, 443-52.

**Holdsworth, R.E., 1989.** Late brittle deformation in a Caledonian ductile thrust wedge: new evidence for gravitational collapse in the Moine Thrust sheet, Sutherland, Scotland. *Tectonophysics*, v. 170(1-2), p. 17-28.

**Honsberger, I.W., Bleeker, W., Kamo, S.L., Sandeman, H.A.I., Evans, D.T.W., Rogers, N., van Staal, C.R. and Dunning, G.R., 2022.** Latest Silurian syntectonic sedimentation and magmatism and Early Devonian orogenic gold mineralization, central Newfoundland Appalachians, Canada: Setting, structure, litho-geochemistry, and high-precision U-Pb geochronology. *GSA Bulletin*, v. 134(11-12), p. 2933-2957, <https://doi.org/10.1130/B36083.1>.

**Honsberger, I.W., Bleeker, W., Kamo, S.L., Sandeman, H.A., Evans, D.T., Mercier-Langevin, P., Lawley, C.J.M. and Castonguay, S., 2020.** The emerging Paleozoic gold district of central Newfoundland: New insights on structural controls and tectonic drivers of gold mineralization and preservation. *Targeted Geoscience Initiative*, v. 5, p. 193-210.



**Honsberger, I.W., Bleeker, W., Sandeman, H.A., Evans, D.T., Kamo, S.L., Mercier-Langevin, P., Lawley, C.J.M. and Castonguay, S., 2020.** Vein-hosted gold mineralization in the Wilding Lake area, central Newfoundland: Structural geology and vein evolution. Targeted Geoscience Initiative, v. 5, p. 179-192.

**Hough, R.M., Butt, C.R.M., and Fischer-Bühner, J., 2009.** The Crystallography, Metallography and Composition of Gold. Elements, v. 5, p. 297-302.

**Ibraheem, I.M., Haggag, M., and Tezkan, B., 2019.** Edge Detectors as Structural Imaging Tools Using Aeromagnetic Data: A Case Study of Sohag Area, Egypt. Geosciences, v. 9(5), p. 211.

**Isles, D.J. and Rankin, L.R., 2013.** Geological interpretation of aeromagnetic data. Society of Exploration Geophysicists and Australian Society of Exploration Geophysicists.

**Jackson, C., 1992.** A microstructural kinematic study of selected shear zones in the Hartbees River Thrust Belt, northeastern Namaqua Tectonic Province. MSc thesis, Rhodes University.

**Kellett, D. A., Warren, C., Larson, K. P., Zwingmann, H., van Staal, C. R., & Rogers, N., 2016.** Influence of deformation and fluids on Ar retention in white mica: Dating the Dover Fault, Newfoundland Appalachians. Lithos, v. 254, p. 1-17.

**Kellett, D. A., Piette-Lauzière, N., Mohammadi, N., Bickerton, L., Kontak, D., Rogers, N., Schetselaar, E., 2021.** Spatio-temporal distribution of Devonian post-accretionary granitoids in the Canadian Appalachians: Implications for tectonic controls on intrusion-related mineralization. Targeted geoscience initiative, 5, 7-23.

**Kerr, A., and Selby, D., 2012.** The timing of epigenetic gold mineralisation on the Baie Verte Peninsula, Newfoundland, Canada: new evidence from Re–Os pyrite geochronology. Mineralium Deposita, v. 47, p. 325-337.

**Kerr, A., van Nostrand, T.S., Dickson, W.L., and Lynch, E.P., 2009.** Molybdenum and tungsten in Newfoundland: A geological overview and a summary of recent exploration developments. Newfoundland and Labrador Department of Natural Resources, Geological Survey. Current Research, Report 09-1, p.43-80.

**Kerr, A., Wardle, R.J., O'Brien, S.J., Evans, D.W. and Squire, G.C., 2005.** Gold Metallogeny in the Newfoundland Appalachians. Geological Association of Canada, Annual Meeting, Halifax, Nova Scotia. Field Trip Guidebook B9, p. 99.

**Kerrich, R., Goldfarb, R.J., and Richards, P.R. 2005.** Metallogenic Provinces in an Evolving Geodynamic Framework. *In* Economic Geology: One Hundredth Anniversary Volume, edited by Hedenquist, J.W., Thompson, J.F.H., Goldfarb, R.J., Society of Economic Geologists, p. 1097-1136.

**Kessler, L.G., and Bédard, J.H., 2000.** Epiclastic volcanic debrites-evidence of flow transformations between avalanche and debris flow processes,

Middle Ordovician, Baie Verte Peninsula, Newfoundland, Canada. *Precambrian Research*, v. 101, p. 135-161.

**Kidd, W.S.F., Dewey, J.F. and Bird, J.M., 1978.** The Mings Bight ophiolite complex, Newfoundland: Appalachian oceanic crust and mantle. *Canadian Journal of Earth Sciences*, v. 15(5), p. 781-804.

**Kidd, W.S.F., 1974.** The evolution of the Baie Verte lineament, Burlington Peninsula, Newfoundland. Ph.D. thesis, University of Cambridge, Cambridge, England, p. 294.

**Kilfoil, G.J., 2009.** Geophysical Data From Recent Airborne Surveys, Newfoundland and Labrador. Current Research, Newfoundland and Labrador Department of Natural Resources, Geological Survey, Report 09-01, p. 305-314.

**Kirkland, C.L., Fougereuse, D., Reddy, S.M., Hollis, J. and Saxey, D.W., 2018.** Assessing the mechanisms of common Pb incorporation into titanite. *Chemical Geology*, v. 483, p. 558-566, <https://doi.org/10.1016/j.chemgeo.2018.03.026>.

**Kirkwood, D. and Dubé, B., 1992.** Structural control of sill-hosted gold mineralization: the Stog'er Tight gold deposit, Baie Verte Peninsula, northwestern Newfoundland. Current research, pt. D, *Geol. Surv. Can. Pap.*, p. 211-221.

**Knight, J.B., Mortensen, J.K. and Morison, S.R., 1999.** Lode and placer gold composition in the Klondike District, Yukon Territory, Canada; implications for the nature and genesis of Klondike placer and lode gold deposits. *Economic Geology*, v. 94(5), p. 649-664, doi: <https://doi.org/10.2113/gsecongeo.94.5.649>.

**Koehn, D., Bons, P.D. and Passchier, C.W., 2003.** Development of antitaxial strain fringes during non-coaxial deformation: an experimental study. *Journal of Structural Geology*, v. 25(2), p. 263-275, [https://doi.org/10.1016/S0191-8141\(02\)00022-6](https://doi.org/10.1016/S0191-8141(02)00022-6).

**Koehn, D., Hilgers, C., Bons, P.D. and Passchier, C.W., 2000.** Numerical simulation of fibre growth in antitaxial strain fringes. *Journal of Structural Geology*, v. 22(9), p. 1311-1324 [https://doi.org/10.1016/S0191-8141\(00\)00039-0](https://doi.org/10.1016/S0191-8141(00)00039-0).

**Lang, J.R., and Baker, T., 2001.** Intrusion-related gold systems: the present level of understanding. *Mineralium Deposita*, v. 36, p. 477-489. <https://doi.org/10.1007/s001260100184>

**Leake, R.C., Chapman, R.J., Bland, D.J. and Condliffe, E., 1997.** Microchemical characterization of alluvial gold from Scotland. *Transactions of the Institution of Mining and Metallurgy. Section B. Applied earth science*, p. 106.

**Li, X.C., Yang, K.F., Spandler, C., Fan, H.R., Zhou, M.F., Hao, J.L. and Yang, Y.H., 2021.** The effect of fluid-aided modification on the Sm-Nd and Th-Pb geochronology of monazite and bastnäsite: Implication for resolving complex isotopic age data in REE ore systems. *Geochimica et Cosmochimica Acta*, v. 300, p. 1-24, <https://doi.org/10.1016/j.gca.2021.02.028>.

**Lipson, R., 2014.** The promise and perils of porphyry deposits in the future of gold production. *SEG Newsletter*, v. 98, p. 1-21, <https://doi.org/10.5382/SEGnews.2014-98.fea>.

**Lister, G.S. and Snoke, A.W., 1984.** SC mylonites. *Journal of Structural Geology*, v. 6(6), p. 617-638.

**Ludwig, K.R., 1998.** On the treatment of concordant uranium-lead ages. *Geochimica et Cosmochimica Acta*, v. 62(4), p. 665-676, [https://doi.org/10.1016/S0016-7037\(98\)00059-3](https://doi.org/10.1016/S0016-7037(98)00059-3).

**Malo, M., Kirkwood, D., de Broucker, G., and St. Julien, P., 1992.** A reevaluation of the position of the Baie Verte - Brompton Line in the Quebec Appalachians: the influence of Middle Devonian strike-slip faulting in Gaspé Peninsula. *Canadian Journal of Earth Sciences*, v. 29, p. 1265-1273.

**Martin, A.J., Gehrels, G.E. and DeCelles, P.G., 2007.** The tectonic significance of (U, Th)/Pb ages of monazite inclusions in garnet from the Himalaya of central Nepal. *Chemical Geology*, v. 244(1-2), p. 1-24, <https://doi.org/10.1016/j.chemgeo.2007.05.003>.

**Mason, S., 2023.** All eyes on Newfoundland's 'gold rush' as exploration spending heats up in the province. Proactive Group Holdings. [Press release]. Available from: <https://www.proactiveinvestors.com/companies/news/1018944/all-eyes-on-newfoundland-s-gold-rush-as-exploration-spending-heats-up-in-the-province-1018944.html>

**Meade J., Evans D.T.W., and Wilton D.H.C., 1998.** Newfoundland Department of Mines and Energy geological Survey, Report 9801, p. 77-83.

**Meffre, S., Large, R.R., Steadman, J.A., Gregory, D.D., Stepanov, A.S., Kamenetsky, V.S., Ehrig, K. and Scott, R.J., 2016.** Multi-stage enrichment processes for large gold-bearing ore deposits. *Ore Geology Reviews*, v. 76, p. 268-279, <https://doi.org/10.1016/j.oregeorev.2015.09.002>.

**Miller, H.G., and Wiseman, R., 1994.** Potential field interpretation of the Baie Verte Peninsula, Newfoundland, utilizing constraints from Lithoprobe East Seismic Line 89-13. *Atlantic Geology*, v. 30, p. 25-36.

**Miller, H.G. and Singh, V., 1994.** Potential field tilt—a new concept for location of potential field sources. *Journal of applied Geophysics*, v. 32(2-3), p. 213-217. [https://doi.org/10.1016/0926-9851\(94\)90022-1](https://doi.org/10.1016/0926-9851(94)90022-1)

**Mitra, S., 1990.** Fault-propagation folds: geometry, kinematic evolution, and hydrocarbon traps. *AAPG bulletin*, v. 74(6), p. 921-945.

**Moles, N.R., Chapman, R.J. and Warner, R.B., 2013.** The significance of copper concentrations in natural gold alloy for reconnaissance exploration and understanding gold-depositing hydrothermal systems. *Geochemistry: Exploration, Environment, Analysis*, v. 13(2), p. 115-130, <https://doi.org/10.1144/geochem2011-114>.

**Mohammadi, N., McFarlane, C.R.M, and Lentz, D.R., 2019.** U–Pb Geochronology of Hydrothermal Monazite from Uraniferous Greisen Veins Associated with the High Heat Production Mount Douglas Granite, New Brunswick, Canada. *Geosciences*, v. 9, p. 224.

**Molnár, F., Middleton, A., Stein, H., Hugh, O., Lahaye, Y., Huhma, H., Pakkanen, L. and Johanson, B., 2018.** Repeated syn-and post-orogenic gold mineralization events between 1.92 and 1.76 Ga along the Kiistala Shear Zone in the

Central Lapland Greenstone Belt, northern Finland. *Ore Geology Reviews*, v. 101, p. 936-959, <https://doi.org/10.1016/j.oregeorev.2018.08.015>.

**Morrison, G.W., Rose, W.J., and Jaireth, S., 1991.** Geological and geochemical controls on the silver content (fineness) of gold in gold-silver deposits. *Ore Geology Reviews*, v. 6, p. 333-364.

**Mottram, C.M., Warren, C.J., Regis, D., Roberts, N.M., Harris, N.B., Argles, T.W. and Parrish, R.R., 2014.** Developing an inverted Barrovian sequence; insights from monazite petrochronology. *Earth and Planetary Science Letters*, v. 403, p. 418-431.

**Murzin, V., Chudnenko, K., Palyanova, G., & Varlamov, D. (2019).** Formation of Au-bearing antigorite serpentinites and magnetite ores at the massif of ophiolite ultramafic rocks: thermodynamic modeling. *Minerals*, v. 9, p. 758.

**Murzin, V. V., Chudnenko, K. V., Palyanova, G. A., Varlamov, D. A., Naumov, E. A., & Pirajno, F. (2018).** Physicochemical model for the genesis of Cu-Ag-Au-Hg solid solutions and intermetallics in the rodingites of the Zolotaya Gora gold deposit (Urals, Russia). *Ore Geology Reviews*, v. 93, p. 81-97.

**Nassif T.M., Monecke, T., Reynolds, T.J., Kuiper, Y.D., Goldfarb, R.J., Piazzolo, S. and Lowers, H.A., 2022.** Formation of orogenic gold deposits by progressive movement of a fault-fracture mesh through the upper crustal brittle-ductile transition zone. *Scientific Reports*, v. 12(1), p. 17379, <https://doi.org/10.1038/s41598-022-22393-9>.

**Newfoundland government pamphlet, 2021.** Gold in Newfoundland: <https://www.findnewfoundlandlabrador.com/files/mines-investments-commodity-flyers-gold-nl-flyer.pdf>

**Norman, R.E., and Strong, D.F., 1975.** The Geology and geochemistry of ophiolitic rocks exposed at Ming's Bight, Newfoundland. *Canadian Journal of Earth Sciences*, v.12, p.777-797.

**Palyanova, G. A., Murzin, V. V., Zhuravkova, T. V., & Varlamov, D. A. (2018).** Au–Cu–Ag mineralization in rodingites and nephritoids of the Agardag ultramafic massif (southern Tuva, Russia). *Russian Geology and Geophysics*, v. 59, p. 238-256.

**Parrish, R.R., 1990.** U–Pb dating of monazite and its application to geological problems. *Canadian Journal of Earth Sciences*, v. 27(11), p. 1431-1450.

**Patey, K.S. and Wilton, D.H., 1993.** The Deer Cove deposit, Baie Verte Peninsula, Newfoundland, a Paleozoic mesothermal lode-gold occurrence in the northern Appalachians. *Canadian Journal of Earth Sciences*, v. 30(7), p. 1532-1546.

**Pawlukiewicz, M., 2019.** Hydrothermal Reconstruction and Lithogeochemistry of the Argyle Orogenic Gold Deposit, Baie Verte, Newfoundland. MSc thesis, Memorial University of Newfoundland, p. 421.

**Passchier, C.W. and Simpson, C., 1986.** Porphyroclast systems as kinematic indicators. *Journal of Structural Geology*, v. 8(8), p. 831-843, [https://doi.org/10.1016/0191-8141\(86\)90029-5](https://doi.org/10.1016/0191-8141(86)90029-5).

**Phillips, G.N. and Powell, R., 2010.** Formation of gold deposits: a metamorphic devolatilization model. *Journal of Metamorphic geology*, v. 28(6), p. 689-718, <https://doi.org/10.1111/j.1525-1314.2010.00887.x>.

**Pi, Q., Hu, R., Xiong, B., Li, Q., and Zhong, R., 2017.** In situ SIMS U-Pb dating of hydrothermal rutile: reliable age for the Zhesang Carlin-type gold deposit in the golden triangle region, SW China. *Mineralium Deposita*, v. 52, p. 1179-1190.

**Picazo, S.M., Ewing, T.A., and Müntener, O., 2019.** Paleocene metamorphism along the Pennine–Austroalpine suture constrained by U–Pb dating of titanite and rutile (Malenco, Alps). *Swiss Journal of Geosciences*, v. 112, p. 517-542.

**Piercey, S.J., and Copeland, D.A., 2017.** Host rock reactivity in the generation of gabbro-hosted orogenic Au in the Baie Verte Peninsula, Newfoundland, Canada. *Atlantic Geology Spring Technical Meeting, Geological Association of Canada*, v. 53.

**Piercey S.J. and Hinchey, J., 2012.** Volcanic Massive Sulphide (VMS) deposits of the Central Mobile Belt, Newfoundland. *Geological Association of Canada–Mineralogical Association of Canada Joint Annual Meeting, Field Trip Guidebook B4. Newfoundland and Labrador Department of Natural Resources, Geological Survey, Open File NFLD/3173*, p. 56.

**Piercey S.J. and Wilton D.H.C., 1997.** The Stratigraphy and Geochemistry of the Southern Pacquet Harbour Group, Baie Verte Peninsula, Newfoundland: Implications for Mineral Exploration. Newfoundland Department of Mines and Energy, Geological Survey, Current Research, Report 97-1, pages 119-139.

**Pilote J.L., 2018.** Geology, Structure, Petrogenesis, and Hydrothermal Alteration Reconstruction of the Ming Volcanogenic Massive Sulphide Deposit, Baie Verte Peninsula, Newfoundland, Canada. PhD thesis, Memorial University of Newfoundland, p. 518.

**Pitman, C., Cullen, M., and Harrington, M., 2020.** NI 43-101 Technical Report, Mineral Resource and Mineral Reserve update on the Point Rouse project, Baie Verte, Newfoundland and Labrador, Canada, Anaconda Mining, p.300.

**Poblet, J. and Lisle, R.J., 2011.** Kinematic evolution and structural styles of fold-and-thrust belts. *Geological Society, London, Special Publications*, v. 349(1), p. 1-24, <https://doi.org/10.1144/SP349.1>.

**Powell, J., Eccles, R., Smith, S., Schulte, M., Merry, W.P.H., Russell, S., Anstey-Moore, C., Haghghi, B., Goode, J.R., Lipiec, I.A., Hernandez, S., and Raponi, T.R. 2022.** Valentine Gold Project NI 43-101 Technical Report and Feasibility Study, Marathon Gold, p.500.

**Putnis, A., 2009.** Mineral replacement reactions. *Reviews in mineralogy and geochemistry*, v. 70(1), p. 87-124, <https://doi.org/10.2138/rmg.2009.70.3>.

**Ramezani, J., Dunning, G.R., and Wilson, M.R., 2001.** Geologic Setting, Geochemistry of Alteration, and U-Pb Age of Hydrothermal Zircon from the Silurian Stog'er Tight Gold Prospect, Newfoundland Appalachians, Canada. *Exploration Mining Geology*, v. 9, p. 171-188.

**Ramezani, J., Dunning, G.R. and Wilson, M.R., 2000.** Geologic setting, geochemistry of alteration, and U-Pb age of hydrothermal zircon from the Silurian Stog'er Tight gold prospect, Newfoundland Appalachians, Canada. *Exploration and Mining Geology*, v. 9(3-4), p. 171-188, <https://doi.org/10.2113/0090171>.

**Ramezani, J., 1992:** The geology, geochemistry and U-Pb geochronology of the Stog'er Tight Gold Prospect, Baie Verte Peninsula, Newfoundland. Unpublished M.Sc. thesis, Memorial University of Newfoundland, St. John's, p. 256.

**Ramsay, J.G., 1967.** Folding and fracturing of rocks. Mc Graw Hill Book Company, p. 568.

**Rasmussen, C., Mundil, R., Irmis, R.B., Geisler, D., Gehrels, G.E., Olsen, P.E., Kent, D.V., Lepre, C., Kinney, S.T., Geissman, J.W. and Parker, W.G., 2021.** U-Pb zircon geochronology and depositional age models for the Upper Triassic Chinle Formation (Petriified Forest National Park, Arizona, USA): Implications for Late Triassic paleoecological and paleoenvironmental change. *GSA Bulletin*, v. 133(3-4), p. 539-558, <https://doi.org/10.1130/B35485.1>.

**Reiners, P.W., Carlson, R.W., Renne, P.R., Cooper, K.M., Granger, D.E., McLean, N.M. and Schoene, B., 2017.** Geochronology and thermochronology. John Wiley & Sons.

**Richard H. Sillitoe, 2020.** "Chapter 1: Gold Deposit Types: An Overview", in *Geology of the World's Major Gold Deposits and Provinces*, Richard H. Sillitoe, Richard J. Goldfarb, François Robert, Stuart F. Simmons

**Riedel, W., 1929.** Zur Mechanik Geologischer Brucherscheinungen. *Zentralblatt für Mineralogie. Geologie und Paleontologie B*, p. 354-368.

**Robert F. and Poulsen H.K., 2001.** Vein Formation and Deformation in Greenstone Gold Deposits in Structural Controls on Ore Genesis. Editors: Richards J.P. Tosdal, R.M.

**Rowland, S.M., Duebendorfer, E.M. and Gates, A., 2007.** Structural analysis and synthesis: a laboratory course in structural geology. John Wiley & Sons.

**Rusk, B., 2012.** Cathodoluminescent textures and trace elements in hydrothermal quartz in Quartz: Deposits, mineralogy and analytics, p. 307-329.

**Rusk, B., Reed, M., Bignall, G., & Tsuchiya, N. (2004).** Natural and synthetic quartz growth and dissolution revealed by scanning electron microscope cathodoluminescence. 14<sup>th</sup> International Conference on the Properties of Water and Steam in Kyoto.

**Sandeman, H.A., Honsberger, I.W. and Camacho, A., 2022.** Overview of age constraints for gold mineralization in central and western Newfoundland and new <sup>40</sup>Ar/<sup>39</sup>Ar ages for muscovite from selected auriferous zones. *Atlantic Geoscience*, v. 58, p. 267-289, <https://doi.org/10.4138/atlgeo.2022.012>.

**Sangster, A.L., Douma, S., and Lavigne, J., 2008.** Base metal and gold deposits of the Betts Cove Complex, Baie Verte Peninsula, Newfoundland. In *Mineral deposits of Canada: a synthesis of major deposit types, district metallogeny, the evolution of metallogenic provinces, and exploration methods*, edited by

Goodfellow, W.D., Geological Association of Canada, Mineral Deposits Division, Ottawa, special publication 5, p. 703–723.

**Schärer, U., 1984.** The effect of initial  $^{230}\text{Th}$  disequilibrium on young U-Pb ages: the Makalu case, Himalaya. *Earth and Planetary Science Letters*, v. 67, p. 191-204.

**Schulz, B., 2021.** Monazite microstructures and their interpretation in petrochronology. *Frontiers in Earth Science*, v. 9, p. 668566, <https://doi.org/10.3389/feart.2021.668566>.

**Seydoux-Guillaume, A.M., Montel, J.M., Bingen, B., Bosse, V., de Parseval, P., Paquette, J.L., Janots, E. and Wirth, R., 2012.** Low-temperature alteration of monazite: Fluid mediated coupled dissolution–precipitation, irradiation damage, and disturbance of the U–Pb and Th–Pb chronometers. *Chemical Geology*, v. 330, p. 140-158, <https://doi.org/10.1016/j.chemgeo.2012.07.031>.

**Schmitz, M.D. and Bowring, S.A., 2001.** U-Pb zircon and titanite systematics of the Fish Canyon Tuff: An assessment of high-precision U-Pb geochronology and its application to young volcanic rocks. *Geochimica et Cosmochimica Acta*, v. 65, p. 2571-2587.

**Schärer, U., 1984.** The effect of initial  $^{230}\text{Th}$  disequilibrium on young UPb ages: the Makalu case, Himalaya. *Earth and Planetary Science Letters*, v. 67(2), p. 191-204, [https://doi.org/10.1016/0012-821X\(84\)90114-6](https://doi.org/10.1016/0012-821X(84)90114-6).

**Shah, S.A., Shao, Y., Zhang, Y., Zhao, H., and Zhao, L., 2022.** Texture and Trace Element Geochemistry of Quartz: A Review. *Mineral*, v. 12, p. 1042.

**Sillitoe, R.H., 2020.** Gold Deposit Types: An Overview. *In* *Geology of the World's Major Gold Deposits and Provinces*, edited by Sillitoe, R.H., Goldfarb, R.J., Robert, F., and Simmons, S.F., The Society of Economic Geologists, Special Publication Number 23, p. 1-28.

**Skulski, T., Castonguay, S., Côté, N., McNicoll, V.J., Currie, M., Magee, A., Harris, B., and van Staal C.R., 2017.** Digital geoscience atlas of Baie Verte Peninsula, Newfoundland and Labrador.

**Skulski, T., Castonguay, S., Kidd, W.S.F., McNicoll, V.J., van Staal, C.R., and Hibbard, J.P., 2015a.** Geology, Baie Verte and parts of Fleur de Lys, Newfoundland and Labrador, NTS 12-H/16 and part of NTS 12-I/1. Geological Survey of Canada, Canadian Geoscience Map 159, scale 1:50000. doi:10.4095/295865.

**Skulski, T., Castonguay, S., Moussallam, Y., McNicoll, V.J., van Staal, C.R., and Bédard, J.H., 2015b.** Geology, Nippers Harbour and parts of Horse Islands, Cape St. John, and Little Bay Island, Newfoundland and Labrador, NTS2-E/13 and parts of NTS2-E/12, NTS2-E/14, and NTS2-L/4. Geological Survey of Canada, Canadian Geoscience Map 160, scale 1:50 000. doi:10.4095/295866.

**Skulski, T., Castonguay, S., Kidd, W.S.F., McNicoll, V.J., and van Staal, C.R., 2015c.** Geology, King's Point, Newfoundland and Labrador, NTS12-H /9. Geological Survey of Canada, Canadian Geoscience Map 156, scale 1:50 000. doi:10.4095/295864.

**Skulski, T., McNicoll, V., Whalen, J.B., Moussallam, Y., Dunning, G., Castonguay, S., Cawood, P., Kidd, W.S.F., and van Staal, C., 2012a.** Subduction to slab-break-off transition recorded in the timing, composition and setting of early Silurian volcano-plutonic complexes, Baie Verte Peninsula, Newfoundland. Geological Association of Canada–Mineralogical Association of Canada, Program with Abstracts, St. John's, Newfoundland, May 27–29, 2012, v. 35, p. 128.

**Skulski, T., Castonguay, S., McNicoll, V., and Kidd, W.S.F., 2012b.** Western Baie Verte Peninsula revisited: from ophiolite obduction onto Laurentia, the Notre Dame continental arc, to post-arc continental volcanism and the Salinic Orogeny. Geological Association of Canada–Mineralogical Association of Canada, Program with Abstracts, St. John's, Newfoundland, May 27–29, 2012, v. 35, p. 129.

**Skulski, T., Castonguay, S., McNicoll, V., van Staal, C.R., Kidd, W., Rogers, N., Morris, W., Ugalde, H., Slavinski, H., Spicer, W., Mousallam, Y., and Kerr, I., 2010.** Tectonostratigraphy of the Baie Verte Oceanic Tract and its ophiolite cover sequence on the Baie Verte Peninsula, Newfoundland. Newfoundland and Labrador Department of Natural Resources, Geological Survey, Current Research 2010, Report 10-1, p. 315–335.

**Skulski, T., Castonguay, S., van Staal, Rogers, N., McNicoll, V., Kerr, A., and Escayola, M., 2009.** Baie Verte Peninsula: An evolving geological story. Annual field trip, Geological Association of Canada Newfoundland and Labrador Section, p. 76.

**Soper, N.J., Strachan, R.A., Holdsworth, R.E., Gayer, R.A. and Greiling, R.O., 1992.** Sinistral transpression and the Silurian closure of Iapetus. *Journal of the Geological Society*, v. 149(6), p. 871-880, <https://doi.org/10.1144/gsjgs.149.6.087>.

**Spence-Jones, C.P., 2022.** Geochemical Signatures of Native Gold Alloys as a Tool for Understanding Auriferous Ore Deposits, Volume 1. PhD Thesis, University of Leeds.

**Spencer, C.J., Kirkland, C.L. and Taylor, R.J., 2016.** Strategies towards statistically robust interpretations of in situ U–Pb zircon geochronology. *Geoscience Frontiers*, v. 7(4), p. 581-589, <https://doi.org/10.1016/j.gsf.2015.11.006>.

**Spencer, K.J., Hacker, B.R., Kylander-Clark, A.R.C., Andersen, T.B., Cottle, J.M., Stearns, M.A., Poletti, J.E. and Seward, G.G.E., 2013.** Campaign-style titanite U–Pb dating by laser-ablation ICP: Implications for crustal flow, phase transformations and titanite closure. *Chemical Geology*, v. 341, p. 84-101.

**Spicer, B.J., 2010.** Geologically Constrained Geophysical modelling of Magnetism and Gravity – The Baie Verte Peninsula, Newfoundland. MSc. Thesis, McMaster University, Ontario, p.179.

**Stern, R.A. and Rayner, N.M., 2003.** Ages of several xenotime megacrysts by ID-TIMS: potential reference materials for ion microprobe U-Pb geochronology (p. 7). Natural Resources Canada, Geological Survey of Canada.

**Suppe, J., 1983.** Geometry and kinematics of fault-bend folding. *American Journal of science*, v. 283(7), p. 684-721.



**Suppe, J. and Medwedeff, D.A., 1990.** Geometry and kinematics of fault-propagation folding. *Eclogae Geologicae Helvetiae*, v. 83(3), p. 409-454.

**Suzuki, K. and Kurihara, T., 2021.** U–Pb ages and sandstone provenance of the Permian volcano-sedimentary sequence of the Hida Gaien belt, Southwest Japan: Implications for Permian sedimentation and tectonics in Northeast Asia. *Journal of Asian Earth Sciences*, v. 219, p. 104888, <https://doi.org/10.1016/j.jseas.2021.104888>.

**Swinden H.S., Evans D.T.W., Kean B.F., 1991.** Metallogenic framework of base and precious metal deposits, central and western Newfoundland, (Field Trip 1). Geological Survey of Canada, open file 2156, p. 245.

**Tavakoli, B., Pezeshk, S. and Cox, R.T., 2010.** Seismicity of the New Madrid seismic zone derived from a deep-seated strike-slip fault. *Bulletin of the Seismological Society of America*, v. 100(4), p. 1646-1658.

**Tera, F. and Wasserburg, G.J., 1972a.** U-Th-Pb systematics in three Apollo 14 basalts and the problem of initial Pb in lunar rocks. *Earth and Planetary Science Letters*, v. 14(3), p. 281-304, [https://doi.org/10.1016/0012-821X\(72\)90128-8](https://doi.org/10.1016/0012-821X(72)90128-8).

**Tera, F. and Wasserburg, G.J., 1972b.** U-Th-Pb systematics in lunar highland samples from the Luna 20 and Apollo 16 missions. *Earth and Planetary Science Letters*, v. 17(1), p. 36-51, [https://doi.org/10.1016/0012-821X\(72\)90257-9](https://doi.org/10.1016/0012-821X(72)90257-9).

**Tuach, J., Dean, P.L., Swinden, H.S., O'Driscoll, C.F., Kean, B.F. and Evans, D.T.W., 1988.** Gold mineralization in Newfoundland: a 1988 review. Newfoundland Department of Mines, Mineral Development Division, Report, p. 88-1.

**Tuach, J. and Kennedy, M.J. 1978:** The Geologic Setting of the Ming and Other Sulphide Deposits, Consolidated Rambler Mines, northeast Newfoundland. *Economic Geology*, v.73, p.192-206.

**Townley, B.K., Hérail, G., Maksaev, V., Palacios, C., Parseval, P.D., Sepulveda, F., Orellana, R., Rivas, P. and Ulloa, C., 2003.** Gold grain morphology and composition as an exploration tool: application to gold exploration in covered areas. *Geochemistry: Exploration, Environment, Analysis*, v. 3(1), p. 29-38, <https://doi.org/10.1144/1467-787302-04>.

**Townsend, K.J., Miller, C.F., D'Andrea, J.L., Ayers, J.C., Harrison, T.M., and Coath, C.D., 2000.** Low temperature replacement of monazite in the Ireteba granite, Southern Nevada: geochronological implications. *Chemical Geology*, v. 172, p. 95-112.

**Twiss, R.J. and Moores, E.M., 1992.** *Structural geology*. Macmillan.

**Upadhyay, H.D., 1973.** The Betts Cove Ophiolite and Related Rocks of the Snooks Arm Group, Newfoundland. Ph.D. thesis, Memorial University of Newfoundland, p. 248.

**van Staal, C.R., 2021.** Northern Appalachians. *Encyclopedia of Geology* (Second Edition), v. 2 p 80-92.

**van Staal, C. R., Barr, S. M., Waldron, J. W., Schofield, D. I., Zagorevski, A., & White, C. E. 2021.** Provenance and Paleozoic tectonic evolution

of Ganderia and its relationships with Avalonia and Megumia in the Appalachian-Caledonide orogen. *Gondwana Research*, v. 98, p. 212-243.

**van Staal, C.R., 2019.** North American Regional Geology Northern Appalachians. Geological Survey of Canada.

**van Staal, C.R., Chew, D.M., Zagorevski, A., McNicoll, V., Hibbard, J., Skulski, T., Castonguay, S., Escayola, M.P., and Sylvester, P.J., 2013.** Evidence of Late Ediacaran hyperextension of the Laurentian Iapetan margin in the Birchy Complex, Baie Verte Peninsula, northwest Newfoundland: implications for the opening of Iapetus, formation of peri-Laurentian microcontinents and Taconic–Grampian orogenesis. *Geoscience Canada*, v. 40, p. 94–117.

**van Staal, C.R. and Barr, S.M. 2012.** Litosphere architecture and tectonic evolution of the Canadian Appalachians and associated Atlantic margin. Chapter 2 in *Tectonic Styles in Canada: The LITOPROBE Perspective*. Edited by J.A. Percival; F.A. Cook, and R.M. Clowes. Geological Association of Canada, Special Paper 49, p. 41-95

**van Staal, C.R., Whalen, J.B., Valverde-Vaquero, P., Zagorevski, A. and Rogers, N., 2009.** Pre-Carboniferous, episodic accretion-related, orogenesis along the Laurentian margin of the northern Appalachians. Geological Society, London, Special Publications, v. 327(1), p. 271-316, <https://doi.org/10.1144/SP327.13>.

**van Staal, C.R., Whalen, J.B., McNicoll, V.J., Pehrsson, S., Lissenberg, C.J., Zagorevski, A., van Breemen, O., and Jenner, G.A., 2007.** The Notre Dame arc and the Taconic orogeny in Newfoundland. In *4-D Framework of Continental Crust*, edited by Hatcher, R.D.Jr., Carlson, M.P., McBride, J.H., and Martínez Catalán J.R., Geological Society of America, Memoir 200, p. 511–552.

**Vasconcelos, A.D., Gonçalves, G.D.O., Lana, C., Buick, I.S., Kamo, S.L., Corfu, F., Scholz, R., Alkmim, A., Queiroga, G. and Nalini Jr, H.A., 2018.** Characterization of Xenotime From Datas (Brazil) as a Potential Reference Material for In Situ U-Pb Geochronology. *Geochemistry, Geophysics, Geosystems*, v. 19, p. 2262-2282.

**Velásquez, G., Béziat, D., Salvi, S., Siebenaller, L., Borisova, A.Y., Pokrovski, G.S. and De Parseval, P., 2014.** Formation and deformation of pyrite and implications for gold mineralization in the El Callao District, Venezuela. *Economic Geology*, v. 109(2), p. 457-486, <https://doi.org/10.2113/econgeo.109.2.457>.

**Venkat-Ramani, M., Tikoff, B., 2002.** Physical models of transtensional folding. *Geology* 2002; 30 (6): 523–526. doi: [https://doi.org/10.1130/0091-7613\(2002\)030<0523:PMOTF>2.0.CO;2](https://doi.org/10.1130/0091-7613(2002)030<0523:PMOTF>2.0.CO;2).

**Verduzco, B., Fairhead, J.D., Green, C.M., and MacKenzie, C., 2004.** New insights into magnetic derivatives for structural mapping. *The Leading Edge*, v. 23, p. 116-119. <https://doi.org/10.1190/1.1651454>

**Vermeesch, P., 2020.** Unifying the U–Pb and Th–Pb methods: joint isochron regression and common Pb correction. *Geochronology*, v. 2(1), p. 119-131.

**Vermeesch, P., 2018.** IsoplotR: A free and open toolbox for geochronology. *Geoscience Frontiers*, v. 9(5), p. 1479-1493, <https://doi.org/10.1016/j.gsf.2018.04.001>.

**Vielreicher, N., Groves, D., McNaughton, N. and Fletcher, I., 2015.** The timing of gold mineralization across the eastern Yilgarn craton using U–Pb geochronology of hydrothermal phosphate minerals. *Mineralium Deposita*, v. 50, p. 391-428, <https://doi.org/10.1007/s00126-015-0589-9>.

**Vielreicher, N.M., Groves, D.I., Fletcher, I.R., McNaughton, N.J. and Rasmussen, B., 2003.** Hydrothermal monazite and xenotime geochronology: a new direction for precise dating of orogenic gold mineralization. *SEG Newsletter*, v. 53, p. 1-16, <https://doi.org/10.5382/SEGnews.2003-53.fea>.

**Waldron, J.W., McCausland, P.J., Barr, S.M., Schofield, D.I., Reusch, D. and Wu, L., 2022.** Terrane history of the Iapetus Ocean as preserved in the northern Appalachians and western Caledonides. *Earth-Science Reviews*, p.104-163, <https://doi.org/10.1016/j.earscirev.2022.104163>.

**Waldron, J.W.F., and van Staal, C.R., 2001.** Taconian orogeny and the accretion of the Dashwoods block: A peri-Laurentian microcontinent in the Iapetus Ocean. *Geology*, v. 29, p. 811–814.

**Waldron, J.W.F., Anderson, S.D., Cawood, P.A., Goodwin, L.B., Hall, J., Jamieson, R.A., Palmer, S.E., Stockmal, G.S., and Williams, P.F., 1998.** Evolution of the Appalachian Laurentian margin: Lithoprobe results in western Newfoundland. *Canadian Journal of Earth Sciences*, v. 11, p.1271–1287.

**Waldron, J.W. and Milne, J.V., 1991.** Tectonic history of the central Humber Zone, western Newfoundland Appalachians: post-Taconian deformation in the Old Man's Pond area. *Canadian Journal of Earth Sciences*, v. 28(3), p. 398-410.

**Wardle, R.J., 2005.** Gold. In press: Newfoundland Department of Mines and Energy, Geological Survey, Commodity Series Report 4.

**Walters, J.B., Cruz-Uribe, A.M., Song, W.J., Gerbi, C. and Biela, K., 2022.** Strengths and limitations of in situ U–Pb titanite petrochronology in polymetamorphic rocks: An example from western Maine, USA. *Journal of Metamorphic Geology*, v. 40(6), p. 1043-1066, <https://doi.org/10.1111/jmg.12657>.

**Weatherley, D.K. and Henley, R.W., 2013.** Flash vaporization during earthquakes evidenced by gold deposits. *Nature Geoscience*, v. 6(4), p. 294-298, <https://doi.org/10.1038/ngeo1759>.

**Wendt, I. and Carl, C., 1991.** The statistical distribution of the mean squared weighted deviation. *Chemical Geology: Isotope Geoscience Section*, v. 86(4), p. 275-285, [https://doi.org/10.1016/0168-9622\(91\)90010-T](https://doi.org/10.1016/0168-9622(91)90010-T).

**Wetherill, G.W., 1956.** Discordant uranium-lead ages, I. *Eos, Transactions American Geophysical Union*, v. 37(3), p. 320-326, <https://doi.org/10.1029/TR037i003p00320>.

**White, W.M., 2015.** *Isotope Geochemistry*. New York: Wiley Blackwell.

**Wiest, J.D., Fossen, H. and Jacobs, J., 2020.** Shear zone evolution during core complex exhumation—Implications for continental detachments. *Journal of Structural Geology*, v. 140, p. 104139, <https://doi.org/10.1016/j.jsg.2020.104139>.

**Williams, H., 1964.** The Appalachians in northeastern Newfoundland; a two-sided symmetrical system. *American Journal of Science*, v. 262(10), p. 1137-1158.

**Williams, H., and St. Julien, P., 1978.** The Baie Verte - Brompton Line in Newfoundland and regional correlations in the Canadian Appalachians. Geological Survey of Canada, current Research Part A, Paper 78-1A, p. 225-229.

**Williams, H., Colman-Sadd, S.P., and Swinden, H.S., 1988.** Tectonostratigraphic divisions of central Newfoundland. In *Current Research, Part B*. Geological Survey of Canada, Paper 88-1B, p. 91-98.

**Williams, H., 1995.** Temporal and Spatial divisions; Geology of the Appalachian—Caledonian Orogen in Canada and Greenland. Geological Survey of Canada, *Geology of Canada*, p. 21-44.

**Williams, S. H., Boyce, W. D., & Colman-Sadd, S. P. (1992).** A new Lower Ordovician (Arenig) faunule from the Coy Pond Complex, central Newfoundland, and a refined understanding of the closure of the Iapetus Ocean. *Canadian Journal of Earth Sciences*, v. 29, p. 2046-2057.

**Williams, M.L., Jercinovic, M.J., Harlov, D.E., Budzyń, B. and Hetherington, C.J., 2011.** Resetting monazite ages during fluid-related alteration. *Chemical Geology*, v. 283(3-4), p. 218-225, <https://doi.org/10.1016/j.chemgeo.2011.01.019>.

**Willner, A.P., van Staal, C.R., Glodny, J., Sudo, M. and Zagorevski, A., 2022.** Conditions and timing of metamorphism near the Baie Verte Line (Baie Verte Peninsula, NW Newfoundland, Canada): Multiple reactivations within the suture zone of an arc-continent collision in New Developments in the Appalachian-Caledonian-Variscan Orogen. Editors: Kuiper Y.D., Murphy J.B., Nance, R.D., Strachan R.A., Thompson M.D.

**Willner, A.P., van Staal, C.R., Zagorevski, A., Glodny, J., Romer, R.I., and Sudo, M., 2018.** Tectonometamorphic evolution along the Iapetus suture zone in Newfoundland: Evidence for polyphase Salinic, Acadian and Neoacadian very low- to medium-grade metamorphism and deformation. *Tectonophysics*, v. 742-743, p. 137-167.

**Williams-Jones, A. E., Bowell, R. J., & Migdisov, A. A. (2009).** Gold in solution. *Elements*, v. 5, p. 281-287.

**Willner, A.P., van Staal, C.R., Zagorevski, A., Glodny, J., Romer, R.I. and Sudo, M., 2018.** Tectonometamorphic evolution along the Iapetus suture zone in Newfoundland: Evidence for polyphase Salinic, Acadian and Neoacadian very low-to medium-grade metamorphism and deformation. *Tectonophysics*, v. 742, p. 137-167, <https://doi.org/10.1016/j.tecto.2018.05.023>.

**Wilson, R.A., van Staal, C.R. and Kamo, S.L., 2017.** Rapid transition from the Salinic to Acadian orogenic cycles in the northern Appalachian orogen: evidence from northern New Brunswick, Canada. *American Journal of Science*, v. 317(4), p. 449-482, <https://doi.org/10.2475/04.2017.02>.

**Winchester, J.A., Williams, H., Max, M.D., and van Staal, C.R., 1992.** Does the Birchy complex of Newfoundland extend into Ireland?. *Journal of the Geological Society, London*, v. 149, p. 159-162.

**World Gold Council, 2022.** <https://www.gold.org/goldhub/research/gold-demand-trends/gold-demand-trends-q1-2022>

**Woodhead, J.D. and Hergt, J.M., 2001.** Strontium, neodymium and lead isotope analyses of NIST glass certified reference materials: SRM 610, 612, 614. *Geostandards Newsletter*, v.25, p. 261-266.

**World Gold Council, 2020.** Gold supply and demand statistics (available at: [www.gold.org/goldhub/data/demand-and-supply](http://www.gold.org/goldhub/data/demand-and-supply))

**Ybarra S., 2019.** Hydrothermal alteration and litogeochemistry of the Pine Cove orogenic gold deposit, Baie Verte Peninsula, Newfoundland, Canada. Unpublished MSc thesis, St. John's, Newfoundland and Labrador, p. 172.

**Zack, T. and Kooijman, E., 2017.** Petrology and geochronology of rutile. *Reviews in Mineralogy and Geochemistry*, v. 83(1), p. 443-467, doi: <https://doi.org/10.2138/rmg.2017.83.14>.

**Zagorevski, A., and van Staal, C.R., 2011.** The record of Ordovician arc-arc and arc-continent collisions in the Canadian Appalachians during the closure of Iapetus. Chapter 12, in *Arc-Continent Collision*, edited by Brown, D., and Ryan, P.D., *Frontiers in Earth Sciences*, p. 341–371.

**Zagorevski, A., van Staal, C.R., McNicoll, V., Rogers, N. and Valverde-Vaquero, P., 2008.** Tectonic architecture of an arc-arc collision zone, Newfoundland Appalachians in *Formation and Applications of the Sedimentary Record in Arc Collision Zones*. Editors: Draut, A.E., Clift, P.D., Scholl, D.W.

**Zhang, F., Li, W., Fu, T., and Qiao, X., 2022.** Late Permian orogenic gold mineralization at Haoyaoerhudong, northern China: Constraints from hydrothermal titanite and apatite chemistry. *Ore Geology Reviews*, v. 144, p. 104858.

**Zhang, W., Zhang, Y., Chen, H. and Yu, Y., 2022.** Using titanite to constrain geochronology and physicochemical conditions of hydrothermal mineralization events: A case study of the Duotoushan Fe–Cu deposit, Eastern Tianshan, NW China. *Geological Journal*, v. 57(8), p. 3333-3350, <https://doi.org/10.1002/gj.4476>.

**Zhang, Q. and Fossen, H., 2020.** The dilemma of asymmetric porphyroblast systems and sense of shear. *Journal of Structural Geology*, v. 130, <https://doi.org/10.1016/j.jsg.2019.103893>.

## **Appendix I – Geological characteristics of the studied gold occurrences**

This appendix provides a compilation of the results and conclusions from previous works conducted on each of the study cases. The simplified geological map of the Point Rousse Complex with the marked location of each of the studied gold occurrences is also provided here (*Figure A1.1*). Summarised descriptions for each of the gold occurrences are provided in *Table A1.1*.

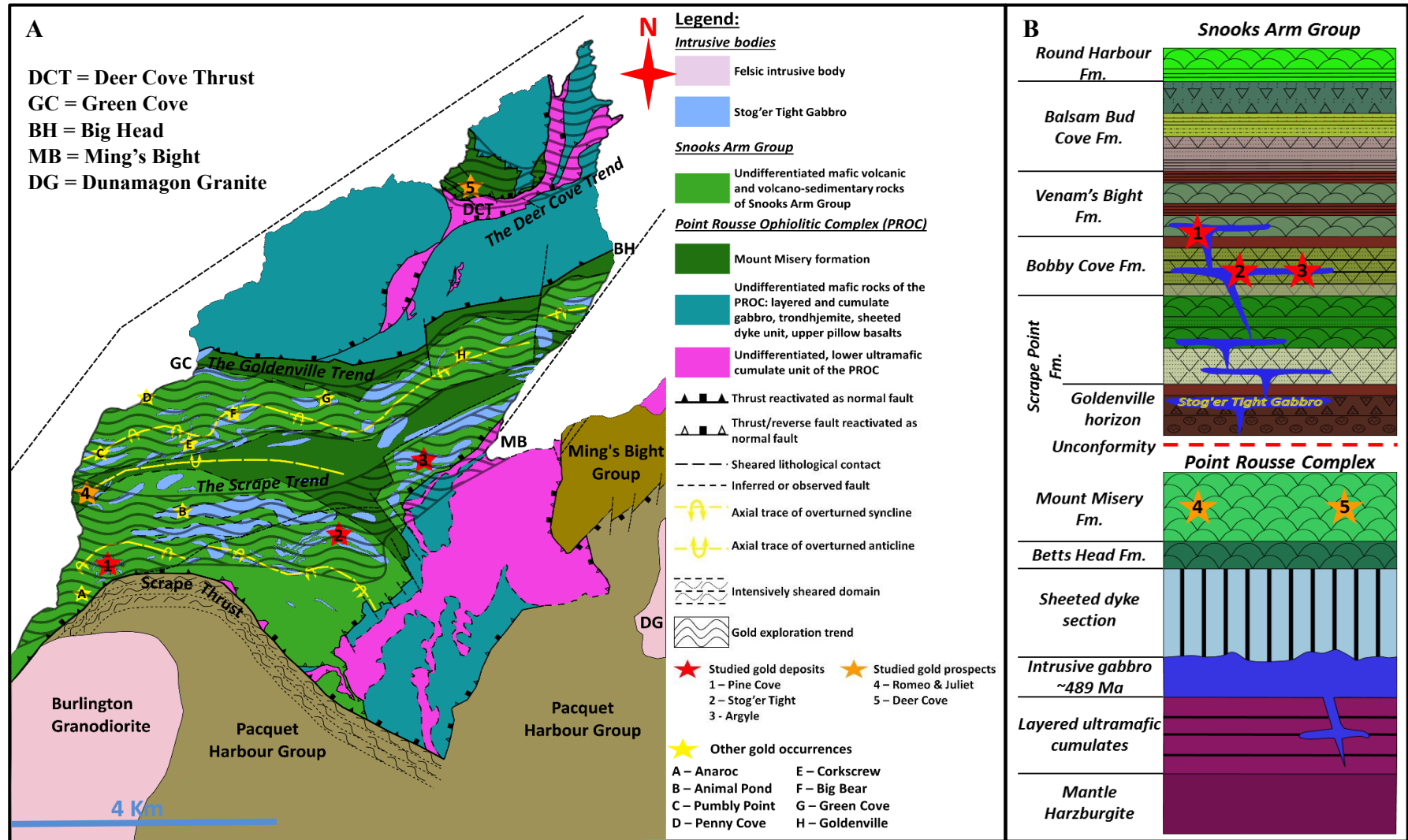


**Figure A1.1 A** - Geological map of the Point Rousse Complex (PRC) after Anderson et al. (2001), Skulski et al. (2015) and after the unpublished geological map of Anaconda Mining (2018). **B** – Representative stratigraphic column of the PRC modified after Hibbard (1983), Bédard et al. (2000) and Skulski et al. (2009, 2010) and the location of the study deposits/prospects within it.

Table A1.1 – Summarised descriptions of the studied gold deposits/prospects

Study Case	Major Structure	Local structural controls	Alteration mineral assemblage	Associated veins	Ore minerals	Host rocks	Relative timing	Absolute timing
<b>Pine Cove</b>	The Scrape Thrust (1,2)	The mineralisation is associated with D <sub>3</sub> shear zones that are subparallel to the axial plane of the F <sub>3</sub> folds of (1).	After (3), from distal to proximal: i) epidote–chlorite–albite ± carbonate; ii) carbonate – chlorite; and iii) sericite–rutile-chlorite	According to (1), three types of veins: i) S <sub>1-2</sub> foliation parallel, thin, barren quartz veins composed of recrystallised quartz aggregates related to D <sub>1</sub> -D <sub>2</sub> deformation; ii) E-W striking tension gash system composed of, steeply dipping, thick (up to several meters in width), parallel, dilational veins which cut both the regional cleavage and the S <sub>3</sub> cleavage; and iii) thick quartz-breccia veins and massive quartz pods and lenses that dip moderately to steeply to N, locally steeply dipping to S – overall sub-parallel to the F <sub>3</sub> axial planes. Both ii & iii vein sets are interpreted to be related to the D <sub>3</sub> deformation	Au ± Ccp, Gn, CoAsS, AuTe, AuAgTe (3; 4)	According to (2), at the mine scale, the host lithologies can be divided in five stratigraphic units: i) Pyroxene, crystal-tuff breccia, and volcanoclastic rocks; ii) Maroon Argillite; iii) Quartz-granule bearing greywacke and siltstone; iv) Mafic volcanic and volcanoclastic rocks and fine grained intrusives; and v) Mafic intrusive bodies	Mid Silurian to Early Devonian (2)	420 ± 7 Ma (5)
<b>Stog'er Tight</b>	The Scrape Thrust (2,6,7,8)	The mineralization is spatially associated with D <sub>1</sub> shear zones of (6), interpreted as splays of the Scrape Thrust	From distal to proximal there are four main alteration zones (7,8): i) chlorite-calcite; ii) sericite-ankerite; iii) red albite – pyrite (± gold); and iv) chlorite-magnetite	Four types of veins after (6): the “Va” veins strike to ESE and dip steeply to SSW, are composed of quartz-ankerite-chlorite-pyrite, are perpendicular to the mineral stretching lineation and are interpreted as extensional veins; the “Vb” veins strike E-W, dip moderately to steeply to N and are composed of quartz-ankerite-pyrite; the “Vc” veins follow the F <sub>2</sub> axial planes and consist of quartz-carbonate; and the “Vd”	Au ± Ccp (7)	Fe-Ti oxide rich gabbro sills - the Stog'er Tight gabbro (2,6,7,8)	Mid Silurian to Early Devonian (2)	420 ± 5 Ma (7,8); 411 ± 7 Ma (5)



				quartz veins strike SSE to SE and dip moderately to steeply to SW; Two types of veins after (7): <i>i</i> ) centimeter wide shear parallel quartz-ankerite-albite veins that are common in the red albite-pyrite (+gold) alteration zone, and <i>ii</i> ) barren, late, dilational, tension quartz veins that crosscut the alteration zones.				
<b>Argyle</b>	The Scrape Thrust (2,9)	Meter scale damage zones interpreted as splays of the Scrape Thrust (9)	From (9) i) a broadly symmetrical distal envelope composed of chlorite-calcite-rutile ± epidote-albite; ii) an intermediate, diffuse zone of chlorite-epidote-albite-calcite ± ankerite-rutile-hematite-sericite-pyrite; and iii) a proximal/ore zone characterised by sericite-quartz-ankerite ± albite-chlorite-rutile-inclusion-rich pyrite-gold	High density of quartz – carbonate veins with random orientations in the proximal alteration zone (9)	Au ± AuTe Ccp Aspy Sph (9)	Fe-Ti oxide rich gabbro sills – Stog’er Tight gabbro (2,9)	Mid Silurian to Early Devonian (2)	Not yet determined

*Table A1.1 (continuation) – Summarised descriptions of the studied gold deposits/prospect*

Study Case	Major Structure	Local structural controls	Alteration mineral assemblage	Associated veins	Ore minerals	Host rocks	Relative timing	Absolute timing
Romeo & Juliet	Scrape Thrust (1)	N-NE trending shear zone (2)	Intense Fe-carbonate alteration $\pm$ sericite and hematite which usually occur along the vein margins and/or on the slip planes (2)	The gold bearing quartz veins are composed of multiple, parallel, milky-white quartz vein generations indicative of crack-seal type processes (1,2,10)	Au	Weakly deformed, pillow basalts and their associated volcanic facies, and fine-grained gabbroic rocks pertaining to the Mount Misery formation (1,2,10,11)	Mid Silurian to Early Devonian (2)	Not yet determined
Deer Cove	Deer Cove Thrust (2,12,13, 10)	NW, NNW, E-W and N oriented reverse faults and strike-slip shears - interpreted as ramps or Riedel faults associated with the Deer Cove Thrust by (7, 8, 13)	Sericite-silica alteration proximal to veins (2,14,15); chlorite-carbonate alteration overprinting / post-dating the gold mineralization (15)	Quartz-carbonate breccia veins at high angle to the Deer Cove fault (e.g. the Main and the AK2 zones) and shear type quartz veins oriented parallel to the Deer Cove fault (2,12,13,14,15)	Au $\pm$ Ccp Aspy (15)	Basaltic flows associated with hyaloclastites, mafic volcanoclastic facies, and thin layers of jasper - iron banded formation (2,12,15) which according to (11) are part of the Mount Misery Formation; Parts of the mineralisation are hosted by gabbro sills which are geochemically similar to the Stog'er Tight gabbro (14)	Mid Silurian to Early Devonian (2)	Not yet determined

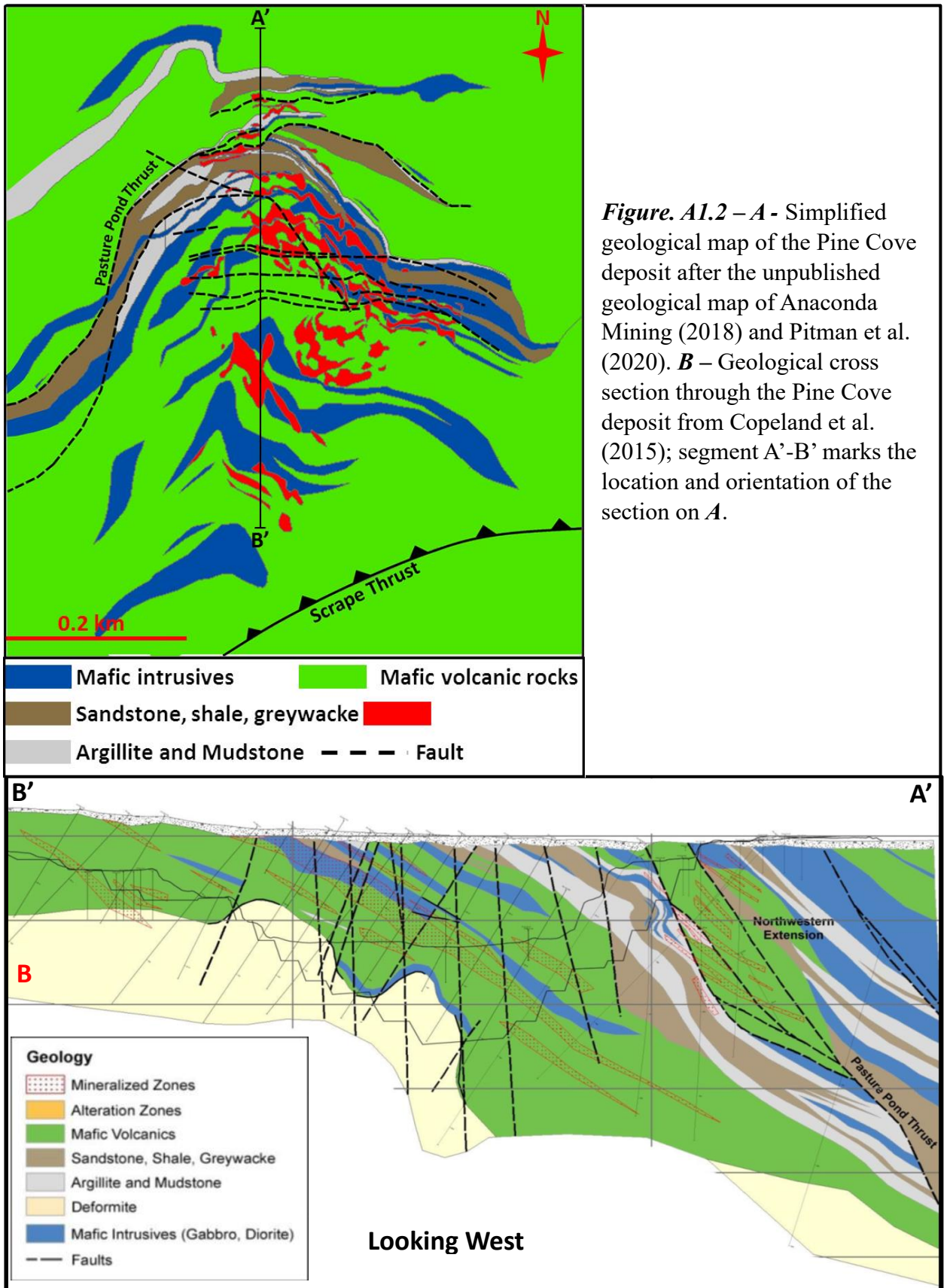
1 = Calon & Weick (1990); 2 = Pitman et al., (2020); 3 = Ybarra (2019); 4 = Piercey (2015); 5 = Kerr & Shelby (2011); 6 = Kirkwood & Dubé, (1992); 7 = Ramezani (1992); 8 = Ramezani et al., (2001); 9 = Pawlukiewicz (2019); 10 = Meade et al., 1998; 11 = Skulski et al. (2015); 12 = Gower et al. (1991); 13 = Dubé et al. (1993); 14 = Patey and Wilton (1993); 15 = Dearin et al. (2009). Au = gold; Ccp = chalcopyrite; Gn = Galena; CoAsS = cobalite; AuTe = gold tellurides; AuAgTe = gold-silver-tellurides; Aspy = Arsenopyrite; Sph = Sphalerite.

### **AI.1. The Pine Cove deposit**

The Pine Cove deposit is located in the southwestern part of the Point Rouse Complex, ~ 6 Km NE from the Baie Verte Town and ~ 6 Km WSW from the Ming's Bight town (**Fig. AI.1**) (Duncan & Graves, 1992). Mineralisation in the area was first discovered in 1988 and the mining started in 2011 (Dimmell & Hartley, 1991; Evans, 2004). The production is now finished, but brown-field exploration continues for potential extension. Detailed information regarding the geological characteristics of the deposit (mineralogy, geochemistry, host rocks, alteration halos, structural setting) can be found in the following studies and exploration reports: Calon & Weick (1990), Dimmell & Hartley (1991), Duncan & Graves (1992), Copeland et al. (2015), Ybarra (2019), and Pitman et al. (2020).

The Pine Cove deposit consists of multiple N dipping mineralised zones hosted in rock sequences that correspond to both the Bobby Cove and the Venam's Bight Formations (**Figs. AI.1; AI.2**) (Ybarra, 2019; Pitman et al., 2020). Geological mapping led by the Anaconda Mining geologists, together with lithogeochemical analyses conducted by Ybarra (2019) have shown that the local stratigraphic sequence is overturned to the south. Summary descriptions for the main rock units that outcrop in the Pine Cove area can be found in **Table AI.1**.

The mineralisation is hosted directly in quartz-carbonate veins or is disseminated in the altered wall rocks (Ybarra, 2019; Pitman et al., 2020). The gold occurs as free grains in silicates and along fractures within pyrite crystals or as small inclusions within pyrite (Ybarra, 2019; Pitman et al., 2020). The gold precipitation is considered to be favoured by both rheological and chemical characteristics of the host rocks: the more rigid rocks (e.g. gabbro and basalts) were deformed in a brittle manner and reached higher permeability rates, whereas their high Fe-Ti oxide content triggered de-sulfidation processes within the fluids which resulted with the precipitation of pyrite and gold (Ybarra, 2019). The main alteration hallos that surround the mineralisation and a list with other subordinate ore minerals are presented in **Table AI.1**.



The mineralised zones are subparallel to the Scrape Thrust and located approximately 50 to 200 m above the fault zone (**Fig. A1.2**) (Dimmell & Hartley, 1991; Ybarra, 2019). In the northern part of the area, the down-dip section of the mineralisation is imbricated with the hanging wall rocks by the Pasture Pond Thrust, a splay of the Scrape fault (**Fig. A1.2**) (Callon et al., 2017; Pitman et al., 2020). A thorough structural assessment of the deposit was conducted by Calon & Weick (1990) and according to these authors the Pine Cove area was affected by four deformational moments: i & ii) a D<sub>1</sub>-D<sub>2</sub> progressive deformation characterised by high strain rates, which resulted with the overturning and the repetition of the rock units in a north – south direction, with the development of the main foliation fabric and the associated mineral stretching lineation, and with the development of two generations of small to large scale folds; iii) a D<sub>3</sub> event that led to the development of the Scrape Thrust and an associated south verging “*fault propagation fold system*”; and iv) a D<sub>4</sub> phase which generated mesoscale folds that plunge gently to steeply towards north. This structural succession was later adjusted by the Anaconda Mining geologists (Copeland et al., 2015; Pitman et al., 2020) after the structural deformation sequence proposed by Castonguay et al. (2009). It is considered herein that the D<sub>1</sub>-D<sub>2</sub> and the D<sub>3</sub> events of Calon & Weick (1990) correlate with the D<sub>1</sub> and the D<sub>2</sub> stages of Castonguay et al. (2009), whereas the D<sub>4</sub> event of the first authors correlates to the D<sub>4</sub> of the latter. Calon & Weick (1990) associated the formation of the mineralised veins to the development of the Scrape Thrust and to its subsidiary structures and interpreted the relative age of the deposit as syn-D<sub>3</sub>, which according to Castonguay et al. (2009) and Skulski et al. (2010) would correspond to the Silurian period. The absolute age of the deposit,  $420 \pm 7$ , was determined by Kerr & Shelby (2011) based on Re-Os geochronological analysis and support these interpretations.

Currently there are no studies that aimed to determine the fluid and metal reservoirs involved in the formation of the Pine Cove deposit. Two assumptions do however exist based on field observations: i) Calon & Weick (1990) inferred that the mineralisation can be related to a syn-D<sub>3</sub> porphyry granitic sill that occurs along the outcrop trace of the Scrape Thrust, whereas ii) Ybarra (2019) mentioned that the amphibolitic rocks of the Pacquet Harbour Group might have liberated the mineralising fluids during their transition from greenschist to amphibolite facies.

## **AI.2. The Stog'er Tight deposit**

The Stog'er Tight area is located in the southeastern part of the Point Rouse Complex, approximately 2 kilometres WSW from the Ming's Bight City (*Fig. AI.1*) (Pitman et al., 2020). The region accommodates the Stog'er Tight deposit and seven other mineralised zones (East, West and South extensions, Gabbro zone, Gabbro West and Gabbro East zones and Cliff zone) (*Fig. AI.3 - A*) (Pitman et al., 2020). The Stog'er Tight deposit and the Eastern zones were extracted, whereas the rest of the zones are still under exploration. The mineralisation is hosted within layered, Fe-Ti oxide rich gabbro sills which display the following mineralogical composition: plagioclase (60-45%); amphibole (30-45%); titanomagnetite (7-20%); and epidote ( $\leq 5\%$ ) (Kirkwood & Dubé, 1992; Ramezani 1992; Pitman et al., 2020). The gabbroic bodies have intact chilled northern margins and weakly to strongly sheared southern contacts and show a significant variation in their grain-size which range from fine-grained to almost pegmatitic (Kirkwood & Dubé, 1992; Ramezani 1992; Pitman et al., 2020). The sills strike NW-SE, dip to NE, reach up to 70 meters in thickness and are conformable with the volcano-sedimentary rocks of the Bobby Cove Formation (*Fig. AI.1B; Fig. AI.3 - B, C*) (Kirkwood & Dubé, 1992; Pitman et al., 2020).

The structural setting of the deposit was initially described by Kirkwood & Dubé (1992) and later revised by the Anaconda Mining geologists in accordance with the deformational sequence proposed by Castonguay et al. (2009). Kirkwood & Dubé (1992) described three deformational events that affected the Stog'er Tight area: i) a regional ductile  $D_1$  phase that generated regional scale folding associated with the development of a main  $S_1$  foliation fabric, a down-dip  $L_1$  mineral stretching lineation, south directed major thrusts (e.g. the Scrape Thrust) and small scale shear zones sub-parallel to the foliation; ii) a brittle-ductile  $D_2$  event characterised by the presence of south verging, asymmetric,  $F_2$  kink folds and reverse faults that dip steeply to north and are sub-parallel to the  $F_2$  axial planes; and iii) a  $D_3$  stage represented by broad, local to large scale,  $F_3$  open folds that affect both the  $D_1$  and the  $D_2$  fabrics. It is considered herein that the  $D_1$  and  $D_2$  stages of Kirkwood & Dubé (1992) corresponds with the  $D_2$  phase of Castonguay et al. (2009), whereas the  $D_3$  event of the first authors correlates to the  $D_4$  of the latter. In this structural framework, the relative timing of the mineralisation was interpreted as post  $D_1$  but

pre D<sub>2</sub> by Kirkwood & Dubé (1992) and as pre- to syn D<sub>2</sub> of Castonguay et al. (2009) by the Anaconda Mining Geologists (e.g. Pitman et al., 2020).

The mineralised zones are surrounded by a wide alteration halo of up to 40 meters in width that overprint the regional green-schist facies mineral assemblage (Ramezani et al., 2001). Within the whole alteration envelope, Ramezani (1992) identified four zones characterised by distinct mineral assemblages and of different intensities and spatial distributions with respect to the mineralisation (**Table A1.1; Fig. A1.3 - D**). The ore zone is characterised by the red albite – pyrite (+ gold) alteration and is bordered in the footwall, and locally even overprinted by the chlorite–magnetite zone (**Fig. A1.3 - D**) (Ramezani, 1992; Ramezani et al., 2001). The mineralogical and textural characteristics of the chlorite-magnetite zone suggest that this phase occurred late in the mineralisation history of the deposit (Ramezani, 1992; Ramezani et al., 2001).

Kirkwood & Dubé (1992) identified four types of veins (“*Va, Vb, Vc, Vd*”) in the Stog’er Tight area, two of which considered to be associated with the mineralisation (“*Va & Vb*” veins). A short description of the veins can be found in **Table A1.1**. Ramezani (1992) also identified two classes of veins within the Stog’er Tight area (**Table A1.1**). The relationships between the “*Va*” and the “*Vb*” veins of Kirkwood & Dubé (1992) and the shear parallel quartz-ankerite-albite veins of Ramezani (1992) are not clear since the former are considered “*extensional*”, whereas the latter, “*shear-parallel*”. Regardless the vein type, no gold was reported directly within the veins, the gold being hosted within the altered wall rocks (Ramezani 1992; Kirkwood & Dubé, 1992; Ramezani et al., 2001).

The gold occurs as small inclusions in pyrite crystals and aggregates, along thin fractures within brecciated pyrite, and rarely, as inclusions within silicate phases (Ramezani 1992; Ramezani et al., 2001). It is considered that the gold precipitation was favoured by the physicochemical properties of the hosting gabbro sills (Ramezani 1992; Ramezani et al., 2001). The rigidity of the gabbro favoured the development of discrete shear zones that brecciated the sills and acted as fluid paths for the mineralising fluids (Ramezani 1992; Ramezani et al., 2001). Moreover, the high content of Fe-Ti oxides of the gabbro triggered oxidation processes (desulphidation) of the gold-sulphur bearing fluids which in turn resulted in the precipitation of pyrite and gold within the altered wall rock (Ramezani 1992; Ramezani et al., 2001).

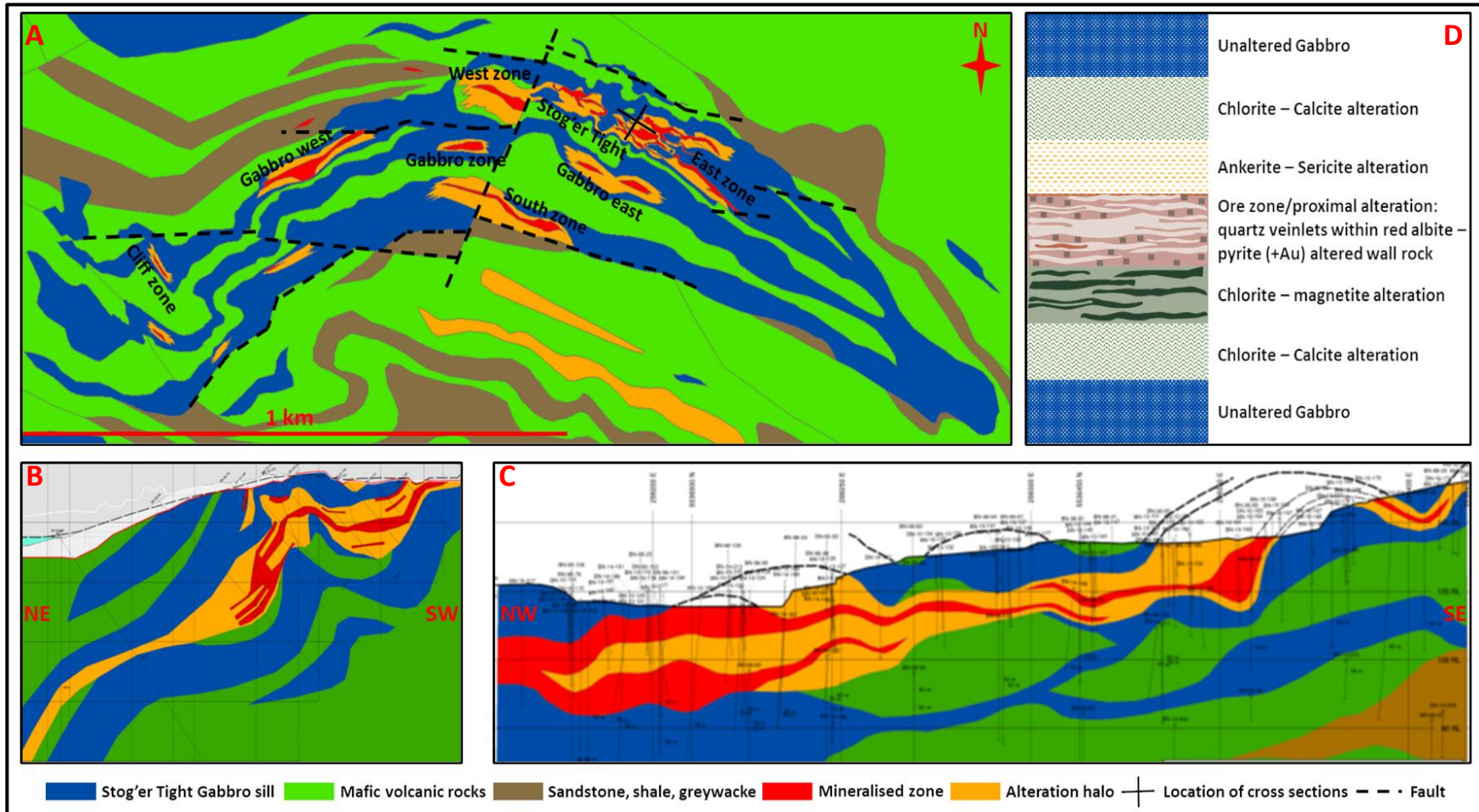


**Figure A1.3** – **A** – Simplified geological map of the Stog'er Tight area after the unpublished geological map of Anaconda Mining (2018) and Pitman et al. (2020); **B, C** – Geological cross sections through the Stog'er Tight deposit from Copeland et al. (2015); **D** - Representative section showing the ore zone and the alteration halos of the deposit after Ramezani (1992) and Ramezani et al. (2001).



Ramezani (1992) dated hydrothermal zircon crystals from the red albite–pyrite (+gold) alteration zone through U-Pb geochronological techniques and obtained a late Silurian age of  $420 \pm 5$  Ma. More recent Re-Os geochronological studies conducted by Kerr & Shelby (2012) on gold bearing pyrite crystals yield an Early Devonian age of  $411 \pm 7$  Ma. Ramezani et al. (2001) concluded that the gold bearing fluids that generated the Stog’er Tight deposit originated at least partially from Silurian I-type magmatic bodies based on trace element compositions and on oxygen and carbon isotope studies of vein and altered wall rock samples. This interpretation is debatable because the zircon age reported for the Stog’er Tight deposit barely overlaps with the youngest existing ages for the plutonic suites from the Baie Verte Peninsula and the pyrite age of the deposit post-date the youngest intrusions with  $\sim 10$  Ma.

### **AI.3. The Argyle deposit**

The Argyle deposit is located  $\sim 1$  km W from the Ming’s Bight City,  $\sim 1.5$  Km NW from the Stog’er Tight deposit and  $\sim 300$  meters N from the NE trending segment of the Scrape Thrust (**Figs. AI.1; AI.4 - A**). The mineralised zones in the Argyle area were discovered in 2012 (Pitman et al., 2020) and their extraction started in 2020. The litho-geochemistry of the host lithologies, and the mineralogical and the geochemical properties of the deposit have been described by Pawlukiewicz (2019). There are no academic studies that documented the deformation history of the Argyle area. Limited information regarding the structural controls on the mineralisation can be found in Pawlukiewicz (2019) and in Pitman et al. (2020). The following paragraphs are summarised from Pawlukiewicz (2019) and Pitman et al. (2020).

The Argyle deposit is hosted within gabbro sills and dykes that cut through both the Scrape and the Bobby Cove formations (Pitman et al., 2020) (**Fig. AI.1- B**). The gabbroic bodies from the Argyle area show many similarities with the gabbro sills that host the mineralised zones from the Stog’er Tight area, and thereby, these were interpreted to be part of the same intrusive sequence (Pawlukiewicz, 2019; Pitman et al., 2020). As of 2020, the Argyle mineralised zone has a strike of 685 m and a down-dip continuity of 225 m (Pitman et al., 2020). The mineralisation and the associated alteration hallos are strata-bound to a gently dipping to N, E-W trending

gabbro sill of ~50 m in thickness (Pawlukiewicz, 2019) (*Fig. A1.4*). The gabbroic body is heterogenous displaying variable mineralogical compositions, textures, and grain sizes (chilled, aphanitic margins at the contact with the surrounding rocks and coarse-grained to pegmatitic in the central part) (Pawlukiewicz, 2019; Pitman et al., 2020). Overall, the hosting gabbro sill show magnetic properties, except for the hydrothermally altered zones and the gold mineralised areas where magnetite destruction is common (Pitman et al., 2020). Deformation within the Argyle gabbro is weak, but in the proximity of shear zones a strong mylonitic foliation is developed (Pawlukiewicz, 2019). The coarse-grained parts of the gabbro are significantly more faulted and damaged compared to the aphanitic margins (Pawlukiewicz, 2019). The alteration and mineralisation increase in the most deformed parts of the gabbro, being most intense within, and in the proximity of meter scale damage zones that brecciate the coarse-grained to pegmatitic, central parts of the sill (Pawlukiewicz, 2019). The small-scale faults that brecciate the gabbro are considered the main control on hydrothermal fluid flow and are interpreted to represent splays of the Scarpe Thrust (Pawlukiewicz, 2019; Pitman et al., 2020).

Pawlukiewicz (2019) attested that there were two main hydrothermal events that affected the Argyle area: i) a pre-mineralisation phase that generated an epidote-albite alteration halo which is not related to the gold mineralisation; and ii) a late stage, cogenetic with the gold mineralisation, characterised by carbonate and sericite alteration mineral assemblages. The latter was further divided by the same author in three subzones which are defined by different alteration mineral assemblages (see *Table A1.1*).

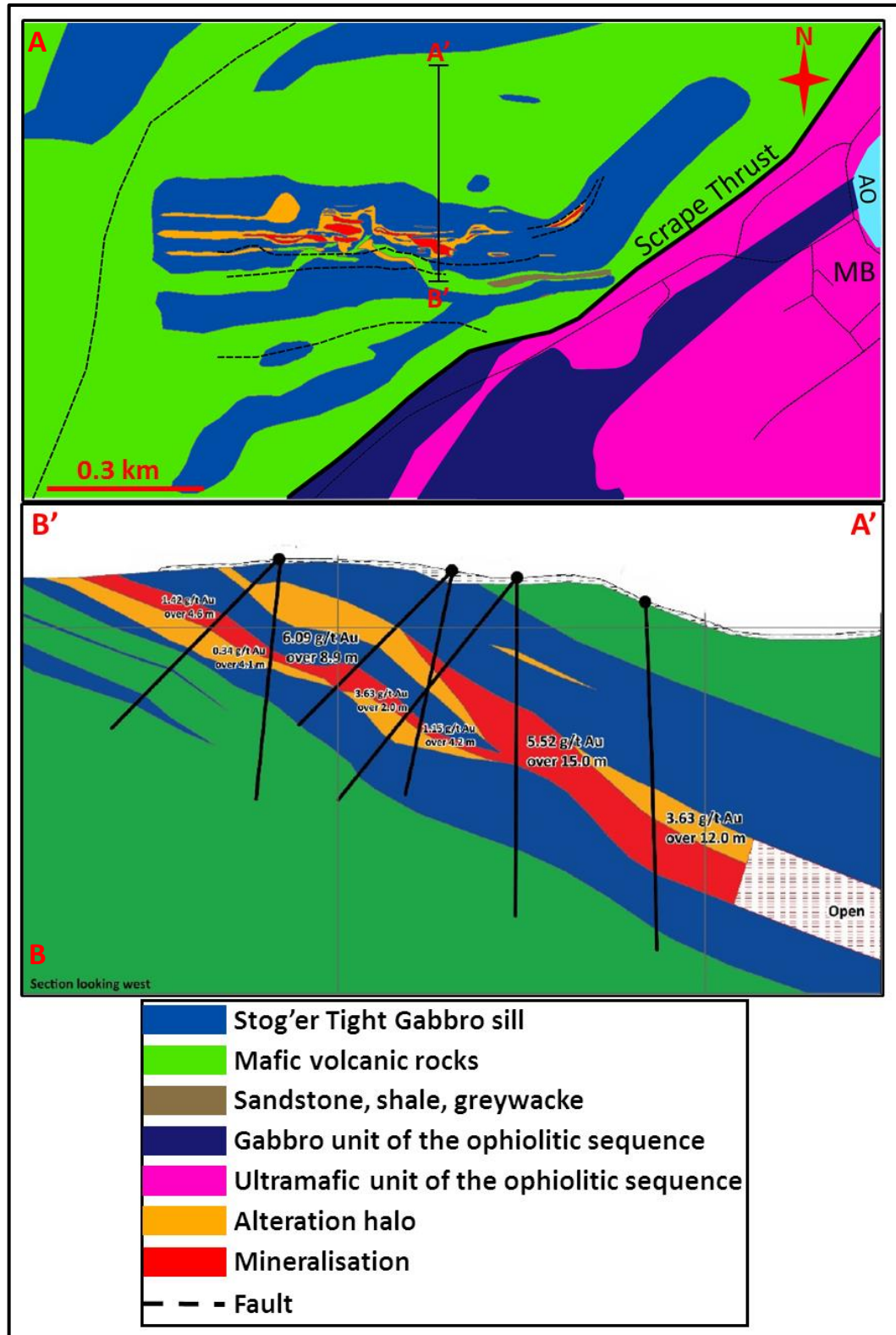


**Figure A1.4 – A** – Simplified geological map of the Argyle area after the unpublished geological map of Anaconda Mining (2018) and Cullen et al. (2018); **B** – Geological cross section through the Argyle deposit from Cullen et al. (2018).

The gold occurs as inclusions in pyrite crystals, along cracks within brecciated pyrite crystals and intergrown with alteration minerals (Pawlukiewicz, 2019). Gold along late chlorite fractures that post-date the mineralisation was also reported and is interpreted to be remobilised (Pawlukiewicz, 2019). Like the Stog'er Tight deposit, the physiochemical properties of the hosting gabbro sill are interpreted to represent the main controls on gold precipitation: the competent coarse-grained parts of the gabbro favoured the development of brecciated zones that increased the local permeability, whereas the high content of Fe-Ti oxides generated de-sulphidation reactions which led to the co-precipitation of gold and pyrite (Pawlukiewicz, 2019).

Pitman et al. (2020) attested that the relative timing of the gold deposits located along the Scrape Trend is pre- to syn D<sub>2</sub> of Castonguay et al. (2009) because the mineralised zones are subsequently deformed by D<sub>3</sub> and D<sub>4</sub> events. D<sub>2</sub> of Castonguay et al. (2009) is interpreted to be of Silurian to Early Devonian age, and thus, the relative timing of the Argyle deposit is inferred to be the same (*Fig. A1.1*). However, up to date, there are no detailed studies that aimed to determine the relative and/or the absolute age of the Argyle deposit. Likewise, there are no information regarding the fluid and metal sources involved in the formation of the Argyle deposit.

#### **A.II.4. The Romeo & Juliet prospect**

The Romeo & Juliet prospect is located close to the western shore of the Point Rousse area, ~1 km N from the Pine Cove deposit (*Fig. A1.1*). The prospect was discovered in 1987, is still under exploration and consists of three subparallel gold bearing quartz veins that trend to NE (30° N): i) the Juliet Zone which is subdivided into Juliet South and Juliet North zones; ii) the Connecting Zone; and iii) the Romeo Zone (*Fig. A1.5*) (Meade et al., 1998; Evans, 2004; Pitman et al., 2020). The veins have a cumulate strike length of over 250 meters, dip 60° to SE and follow a N-NE trending topographic lineament that correspond to an intense shear zone which outcrops for a couple of kilometres (Meade et al., 1998; Evans, 2004; Pitman et al., 2020). Gold was reported to occur free, as flecks within the quartz veins, and as blebs or fine grained in association with sericite along the vein margins

(Meade et al., 1998; Pitman et al., 2020). Information regarding the host rocks, alteration type and associated veins can be found in *Table A1.1*.

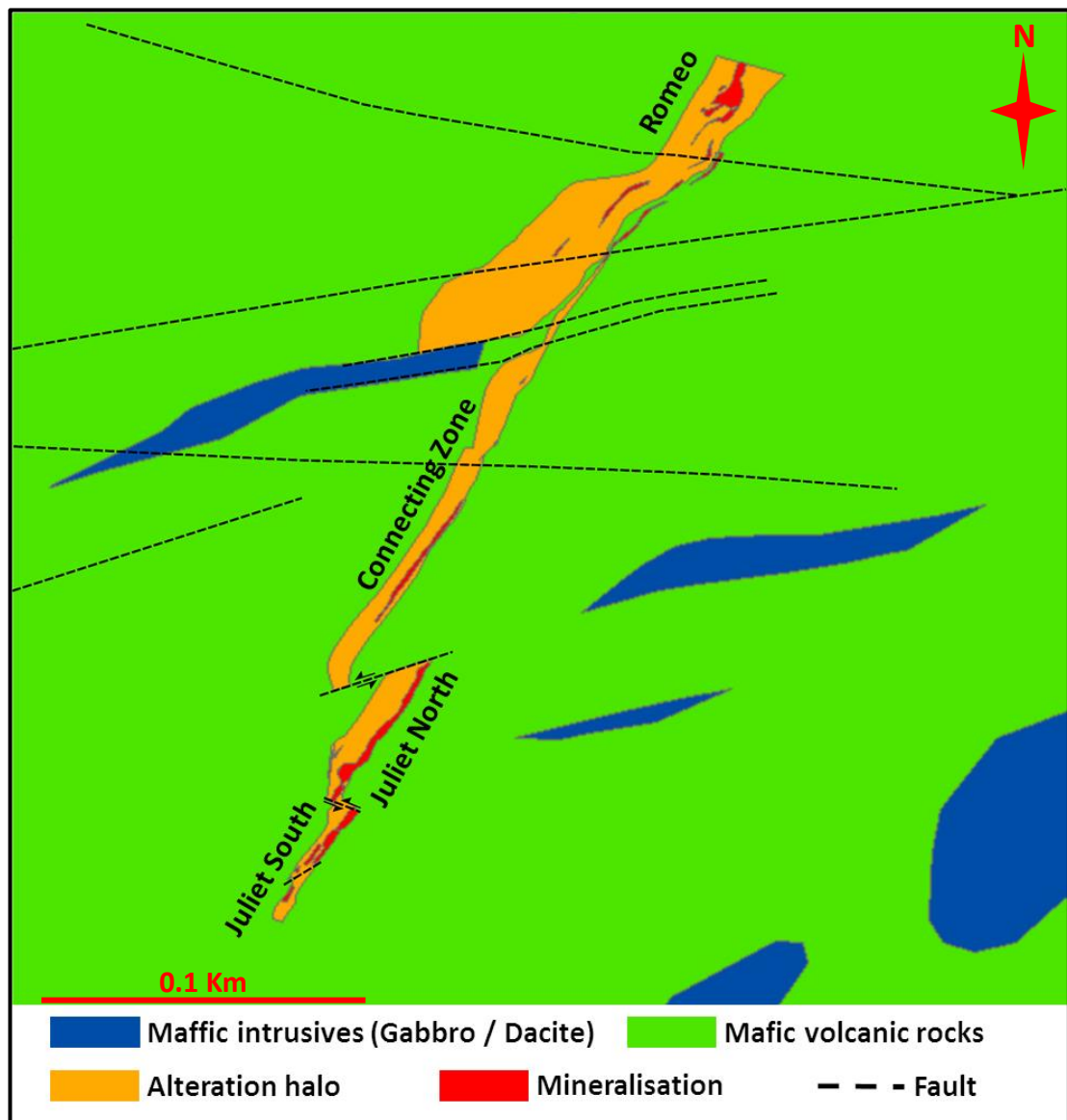


*Figure A1.5* - Simplified geological map of the Argyle area after Duncan (1994), Meade et al. (1998) and after the unpublished geological map of Anaconda Mining (2018).

There have been no detailed academic studies regarding the structural, mineralogical, and/or geochemical characteristics of the mineralised veins from the Romeo & Juliet prospect. Thereby the timing of the gold mineralisation and the structural controls on the vein formation are poorly constrained, whereas the sources of the fluid and metals that contributed to the gold mineralisation are mostly unknown. Calon & Weick (1990) attested that the Romeo & Juliet vein system show

similarities with the dilational veins from the Pine Cove area that formed during the development of the Scrape Thrust. This event would correspond to the D<sub>2</sub> of Castonguay et al. (2009), so Mid Silurian – Early Devonian like the rest of the gold prospects located within the Scrape exploration trend (**Fig. A1.1**).

Another mineralised zone, named the Balcony Zone, is also present in the area and was discovered by the Anaconda Mining Inc. in 2013 (in press). The Balcony Zone is located at depth between the Connecting and the Romeo zones, it was defined for ~100 m in strike and is still open in both strike and dip (Pitman et al., 2020). Compared to the rest of the mineralised zones from the Romeo & Juliet area, the Balcony zone is characterised by a different mineralisation style, the gold being disseminated in an altered pyritic mafic dyke associated to a NE trending lineament that cut through the rest of the zones. There are no structural studies that assessed this mineralised zone, and thus, any structural correlations to rest of the gold bearing quartz veins from the Romeo & Juliet prospect are yet to be determined.

#### **A.A1.1. The Deer Cove prospect**

The Deer Cove block is located in the northern part of the Point Rouse Complex, ~13 Km N from the Baie Verte city and ~4 Km NNW from the Ming's Bight town (**Fig. A1.1**) (Patey, et al., 1993; Dearin, 2009). The area hosts a total of 16 gold showings, including the Deer Cove deposit which currently represents the main exploration target (Pitman et al., 2020). The structural setting of the area was described by Gower et al. (1988) and by Dubé et al. (1993), whereas the geological characteristics (mineralogy, alteration, geochemistry, etc) of the mineralised zones were assessed by Patey and Wilton (1993). Geological information regarding the Deer Cove area can also be found in Anaconda Mining's technical reports (e.g. Cullen et al., 2018; Pitman et al., 2020). A summarised geological description for the Deer Cove prospect was compiled from the afore-mentioned studies and is presented below and in **Table A1.1**.

The main structural feature within the area is represented by the Deer Cove fault zone (**Figs. A1.1; A1.6**) (Dearin, 2009). The hanging wall compartment is characterised by the presence of three, moderately to steeply dipping fault sets that trend to E, SE, and to S, and which show mutual cross-cutting relationships with the Deer Cove fault (**Fig. A1.6**) (Gower et al., 1988; Dubé et al., 1993). Most of these

faults display an oblique reverse movement, and as well as the Deer Cove fault accommodate a south directed transport direction (Gower et al., 1988; Dubé et al., 1993). Gower et al. (1988) and Dubé et al. (1993) interpreted the NW trending faults as oblique ramps, whereas the N-S striking faults as “tear faults” or “lateral ramps” formed during thrusting. An E-W oriented penetrative cleavage that dips  $\sim 40\text{-}60^\circ$  to N is characteristic in the high strain zones, but less pronounced further away from the fault zone (Dearin, 2003). The fabric represents the axial planar cleavage of folds that plunge steeply to N and NW and is associated with a well-developed, down-dip to oblique plunging stretching mineral lineation (Gower et al., 1991; Dubé et al., 1993).

Within the Deer Cove area, the gold mineralisation is associated with both quartz breccia veins and with shear parallel quartz veins (Pitman et al., 2020). The Deer Cove deposit consist of two main gold bearing quartz – carbonate breccia veins named the “Main Zone” and the “AK2 Zone” (**Fig. A1.6**) (Patey and Wilton, 1993). The stratigraphic package that hosts the two mineralised zones was attributed by Skulski et al. (2015) to the Mount Misery Formation (**Fig. A1.1**). Further details regarding host rocks and alteration types can be found in **Table A1.1**. Below and along the Deer Cove thrust, sheared and intensively serpentinised and talc-carbonate (litwanite) altered ultramafic ophiolitic rocks underlie the Deer Cove mineralisation (Gower et al., 1991; Pitman et al., 2020).

The “Main Zone” has a strike length of more than 500 meters, is open in the northern part, and is composed of multiple quartz-breccia vein lenses that show variable individual orientations ranging from  $40^\circ\text{N}$  to  $65^\circ\text{N}$ , but overall composing a mineralised zone that dips between  $45^\circ$  to  $70^\circ$  to W and which has an approximate N-S orientation (**Fig. A1.6**) (Dearin et al., 2009; Pitman et al., 2020). The high-grade gold zones correspond to the intersection of crosscutting structures and to a strongly folded interval of approximately 30 m length which represent to the southern-most termination of the mineralised zone against the Deer Cove Fault (**Fig. A1.6 - B**) (Gower et al., 1991; Dubé et al., 1993; Dearin, 2009).

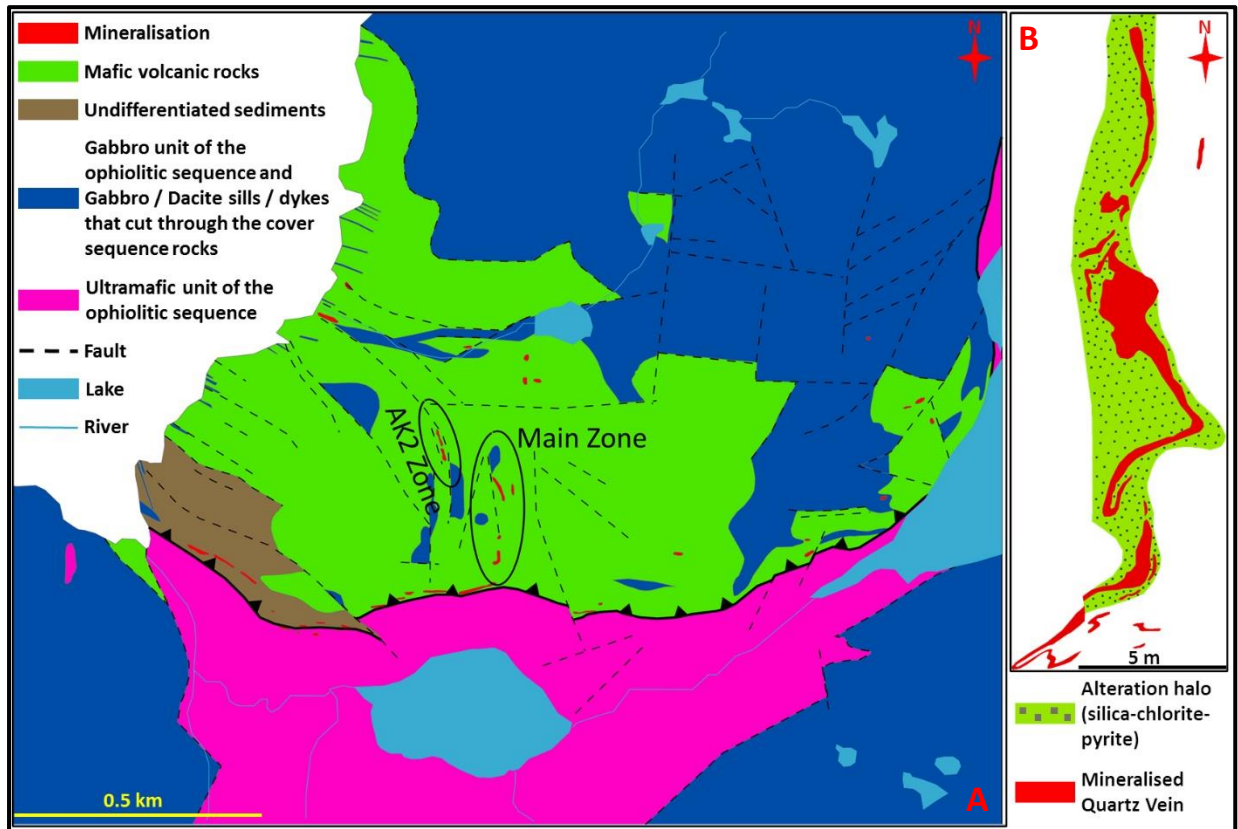


**Figure A1.6 - A** – Simplified geological map of the Deer Cove area after the unpublished geological map of Anaconda Mining (2018) and Pitman et al. (2020); **B** – Detailed map of the southernmost part (30 m length) of the Main Zone simplified from Dearin (2009).

The gold bearing quartz-breccia vein from the “AK2 Zone” strikes to NW and dip  $\sim 50^\circ$  to NE (**Fig. A1.6 - A**) (Dubé et al., 1993; Pitman et al., 2020). The vein contains up to 40% chloritized wall rock material and is associated with a dextral shear zone developed at the contact between gabbroic and volcanoclastic rocks (Dubé et al., 1993; Pitman et al., 2020). Low gold grade values were also reported to be within intensively sheared and chloritized wall rock intervals (Patey and Wilton, 1993).

The formation of the mineralisation within the Deer Cove area was linked with the evolution of the Deer Cove thrust (Gower et al., 1991; Dubé et al., 1993). Based on structural observations, the previous mentioned authors, concluded that the quartz-breccia veins from the Deer Cove area formed after the initial development of the Deer Cove fault, but before the movement along the fault has ended. Gower et al. (1991) proposed that the gold was sourced from the underlying serpentinitised ultramafic rocks through dehydration processes during their alteration into listwanite (talc – magnesite – carbonate altered ultramafic rocks) and that the Deer Cove fault,



and its associated branches acted as the main conduits for the fluids (*Fig. A1.7 - A*). However, based on oxygen and carbon isotope measurements and trace element analysis, Patey and Wilton, (1993) favoured a genetic model in which the fluids responsible for the gold mineralisation have a metamorphic and/or a magmatic origin and were derived from a heterogeneous crustal reservoir. Furthermore, Dubé et al. (1993) argued that the formation of the gold bearing quartz breccia veins was triggered by rapid decompression of H<sub>2</sub>O/CO<sub>2</sub> fluids within extensional structures that formed at a right angle to the E-W segment of the Deer Cove fault in response to heterogeneous strain distribution between different segments of the fault (*Fig. A1.7 - B*). Currently, the relative age of the deposit is considered to be syn-to-post-Silurian based on the structural observations of Patey and Wilton (1993) and of Anaconda Mining geologists (e.g. Pitman et al., 2020). No absolute geochronological ages exist at the moment.

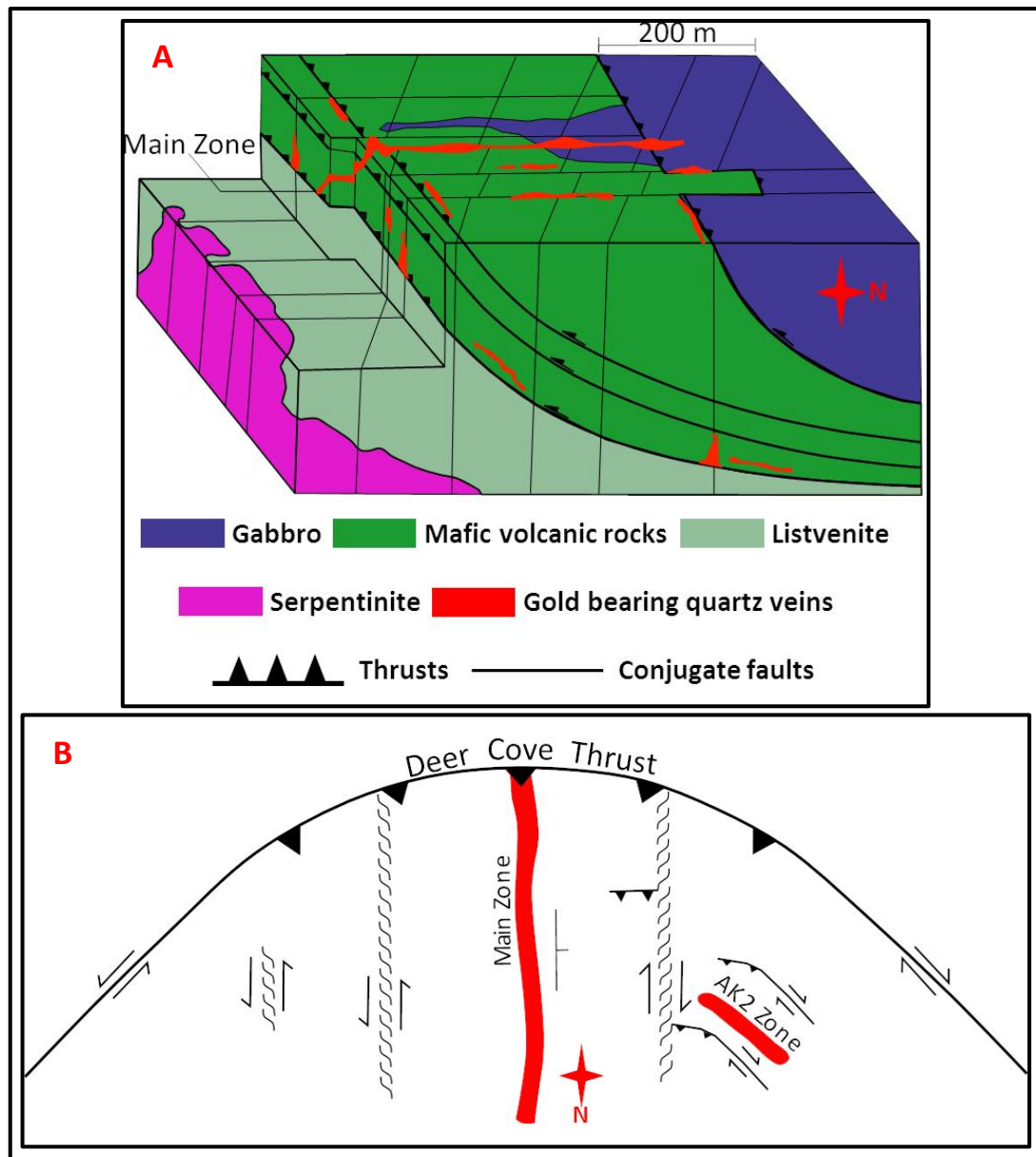


**Figure. A1.7** – Genetic models proposed for the Deer Cove deposit: **A** – after Gower et al. (1991); **B** – after Dubé et al. (1993).

## **Appendix II – List of samples and summary descriptions**

This appendix provides a summary description for each sample from which a thin section has been made and studied for this PhD thesis. The samples are listed according to their provenance area.

Coordinate system – datum: NAD 1983; projection: UTM, Zone 21N.

<b>Abbreviations</b>	
<b>PTS</b>	polished thin section
<b>PTkS</b>	polished thick section
<b>TS</b>	unpolished thin section
<b>OM</b>	optical microscopy (includes both reflected and transmitted light analysis)
<b>MsA</b>	microstructural analysis
<b>BSE</b>	backscattered electron microscope
<b>EDS</b>	electron dispersive microscopy
<b>CL</b>	cathodoluminescence
<b>EPMA</b>	electron probe micro analyzer
<b>U-Pb LA-ICP-MS</b>	uranium – lead laser-ablation inductively-coupled-plasma mass-spectrometer analysis
<b>Au</b>	gold
<b>Chl</b>	chlorite
<b>Ser</b>	sericite (fine grained muscovite/phengite)
<b>Lx</b>	leucoxene (alteration of titanium bearing minerals; in the studied samples occurs mostly as fine-grained rutile or titanite)
<b>Rt</b>	rutile
<b>Py</b>	pyrite
<b>Cb</b>	carbonate
<b>Qtz</b>	quartz
<b>Hem</b>	hematite
<b>Ab</b>	albite
<b>Cpy</b>	chalcopyrite
<b>Cal</b>	calcite
<b>FeOx</b>	iron oxides
<b>Mnz</b>	monazite
<b>Xtm</b>	xenotime
<b>Tit</b>	titanite
<b>Epi</b>	epidote
<b>Amph</b>	amphibole
<b>Plg</b>	Plagioclase
<b>g/t</b>	grams / ton
<b>m</b>	meters
<b>cm</b>	centimetres
<b>PHG</b>	Paquet Harbour Group

**Table A2.1** – List of samples collected from the Pine Cove area

Sample code	Sample origin	Coordinates (m) E / N	Sample description	Image	Section type	Analysis
PC04-19	Outcrop (Pine Cove pit)	562,268.804; 5,534,769.023	Foliation-parallel quartz breccia veins (355°/36°)* associated with an intense dark-green and orange-brown wall-rock alteration composed of chl-ser-lx-py and crosscut by steeply dipping Qtz-cb-hem-chl veins	<i>Plate A1 – A, B</i>	Oriented PTS*	OM; MsA; BSE; EDS; CL
PC-100	Drill core (PC-92-100; sampled interval 16.7 - 16.82 m)	562,350.649; 5,534,620.659	High Au grade interval (19.8 g/t) characterized by Qtz-cb-chl veinlets that cut through a strongly altered, pink, dark-green and orange-brown wall rock material composed of ab-py-ser-chl-lx ± cb	<i>Plate A1 – C</i>	PTkS	OM; BSE; EDS; EPMA
PC-102	Drill core (PC-92-102; sampled interval 12.9 - 13 m)	562,373.791; 5,534,692.959	High Au grade interval (18.6 g/t) with a brecciated aspect due to white-milky quartz veins associated with intensively altered, orange-brown wall rock fragments composed of ser-py-lx ± chl and late cb. veinlets	<i>Plate A1 – D</i>	PTkS	OM; BSE; EDS; CL
PC-167	Drill core (PC-05-167; sampled interval 109.65-109.75 m)	562,447,728; 5,543,828.128	Medium Au grade interval (4.8 g/t) characterized by Qtz veins with strongly altered, dark-green and orange-brown altered wall rock composed of py-ser-lx-chl	<i>Plate A1 - E</i>	PTkS	OM; BSE; EDS; CL
PCHG	Float (Pine Cove pit)	N/A	Float sample (blast residue) from high Au grade interval characterized by massive, milky-white quartz veins with wall rock fragments totally replaced by chl. and py. (patchy to massive aspect, both fine grained and euhedral)	<i>Plate A1 – F</i>	PTkS	OM; BSE; EDS; CL
PCC	Float (Pine Cove pit)	N/A	Float sample (blast residue) characterized by massive, milky-white quartz veins with large patches of cpy., locally massive aspect; everything cut by cal. veinlets	<i>Plate A1 - G</i>	PTkS	OM; BSE; EDS; CL

G12	Outcrop (south from the Pine Cove pit, along the Scrape thrust)	562,319.947; 5,534,155.409	Intense sheared and altered outcrop with a dark grey upper part (moderate grained, chloritized rock with visible actinolite phenocrystals and with massive zones of undeformed, coarse-grained gabbro), an intense altered middle part (chl-hem-py, and traces of fuchsite), and a fine grained chloritized lower part; in the contact zones, along the foliation planes there are acicular phenocrysts of actinolite, up to 3-4 centimetres in length	<i>Plate A1</i> <i>- H</i>	Oriented PTS**	OM; MsA
-----	---	-------------------------------	--	-------------------------------	-------------------	---------

\*Measurements as dip direction / dip; section cut perpendicular to the foliation and parallel to the down-dip stretching mineral lineation

\*\*Oriented sample (strike 36°, dip 40° to NW), section cut perpendicular to the foliation and parallel to the stretching mineral lineation (rake: 36° / 40°)

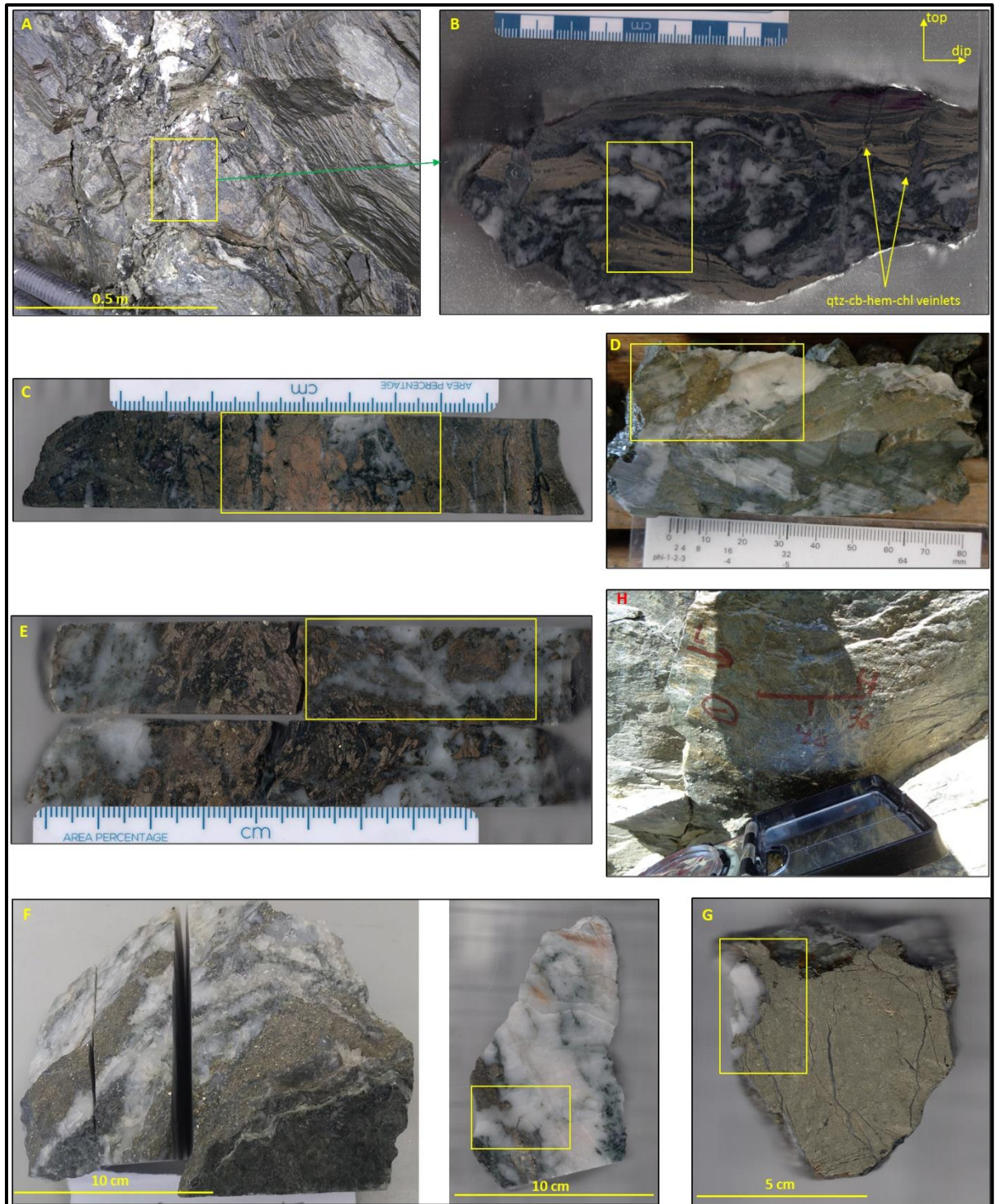


**Plate AII.1** – Representative images of samples collected from the Pine Cove area used for this study. The yellow rectangles show the location of thin sections on the samples. Descriptions in *Table A2.1*.

*Table A2.2 – List of samples collected from the Stog'er Tight area*

Sample code	Sample origin	Coordinates (m) E / N	Sample description	Image	Section type	Analysis
SOZ1 SOZ2	Outcrop (Stog'er Tight pit)	566,124.769 5,535,242.258	Medium Au grade zone (blast zone of 3 g/t average grade) characterized by a strong and pervasive alteration composed of ab (pink) – pyrite – quartz (translucent) ± cb (patches). The pyrite occurs as large patches, or even as massive zones and is both fine and coarse grained. The quartz veins show random orientations (stock-work zone).	<b>Plate A2 – A, B</b>	PTkS x 2	OM; BSE; EDS; CL; EPMA; U-Pb LA-ICP-MS analysis on mnz/xtm
ST07-Ore	Float (Stog'er Tight pit)	N/A	Intensively veined sample with complicated crosscutting relationships: 1 <sup>st</sup> vein – translucent qtz – cb (cream-white) – ab (pink) cut by 2 <sup>nd</sup> vein - translucent qtz with fine grained, euhedral py crystals; 3 <sup>rd</sup> – qtz-chl-cal veinlets oriented at a high angle to 1 <sup>st</sup> and 2 <sup>nd</sup> vein sets; 4 <sup>th</sup> calcite veinlets that cut the previously mentioned veins (not visible macroscopically)	<b>Plate A2 – C</b>	PTkS	OM; BSE; EDS; CL
ST-Ore-Chl	Float (Stog'er Tight pit)	N/A	Ore sample consisting of translucent qtz and white cb veins associated with a strong alteration halo composed of pink ab and py; everything is strongly brecciated by black chlorite veins that locally replace all the pre-existent minerals and form large patches of a few tens of centimeters	<b>Plate A2 – D</b>	PTS	OM; BSE; EDS
BN215	Drill core (BN-14-215; sampled interval (18.17-18.24 m))	565,931.748 5,535,171.995	High Au grade interval (up to 18.6 g/t) from the Gabbro Zone; Dense network of quartz-carbonate veins associated with an intense orange-pink alteration halo composed of ab-ser-lx-py ± cpy and overprinted by chl (black) – calcite veins and patches	<b>Plate A2 – E</b>	PTkS	OM; BSE; EDS; CL; EPMA; U-Pb LA-ICP-MS analysis on mnz/xtm

ST07V	Outcrop (Stog'er Tight pit)	566,086.668 5,535,272.949	Contact between mineralised gabbro (ore zone) and volcanics; Intense sheared rock affected by multiple generations veins associated with a moderate chlorite-carbonate alteration: qtz-ab-cb veins subparallel to the foliation that are folded by F <sub>3</sub> microfolds and qtz-cb vein that are flat lying and parallel to the axial planes of F <sub>3</sub> folds; all veins are folded by F <sub>4</sub> folds	<b>Plate A2</b> - <b>F</b>	Oriented PTS*	OM; MsA
ST07-19	Outcrop (East Zone pit)	566,433.035 5,534,996.839	Strongly sheared and folded (by F <sub>3</sub> folds) outcrop; the rocks show an intense chlorite-carbonate alteration and supergene oxidation	<b>Plate A2</b> - <b>G</b>	Oriented PTS**	OM; MsA

\*Oriented sample (strike 318°, dip 58° to NE); section cut perpendicular to the foliation and parallel to the oblique stretching mineral lineation (rake: 135° / 58)

\*\*Oriented sample (strike 300°, dip 60° to NE), section cut perpendicular to the foliation and parallel to the down-dip stretching mineral lineation



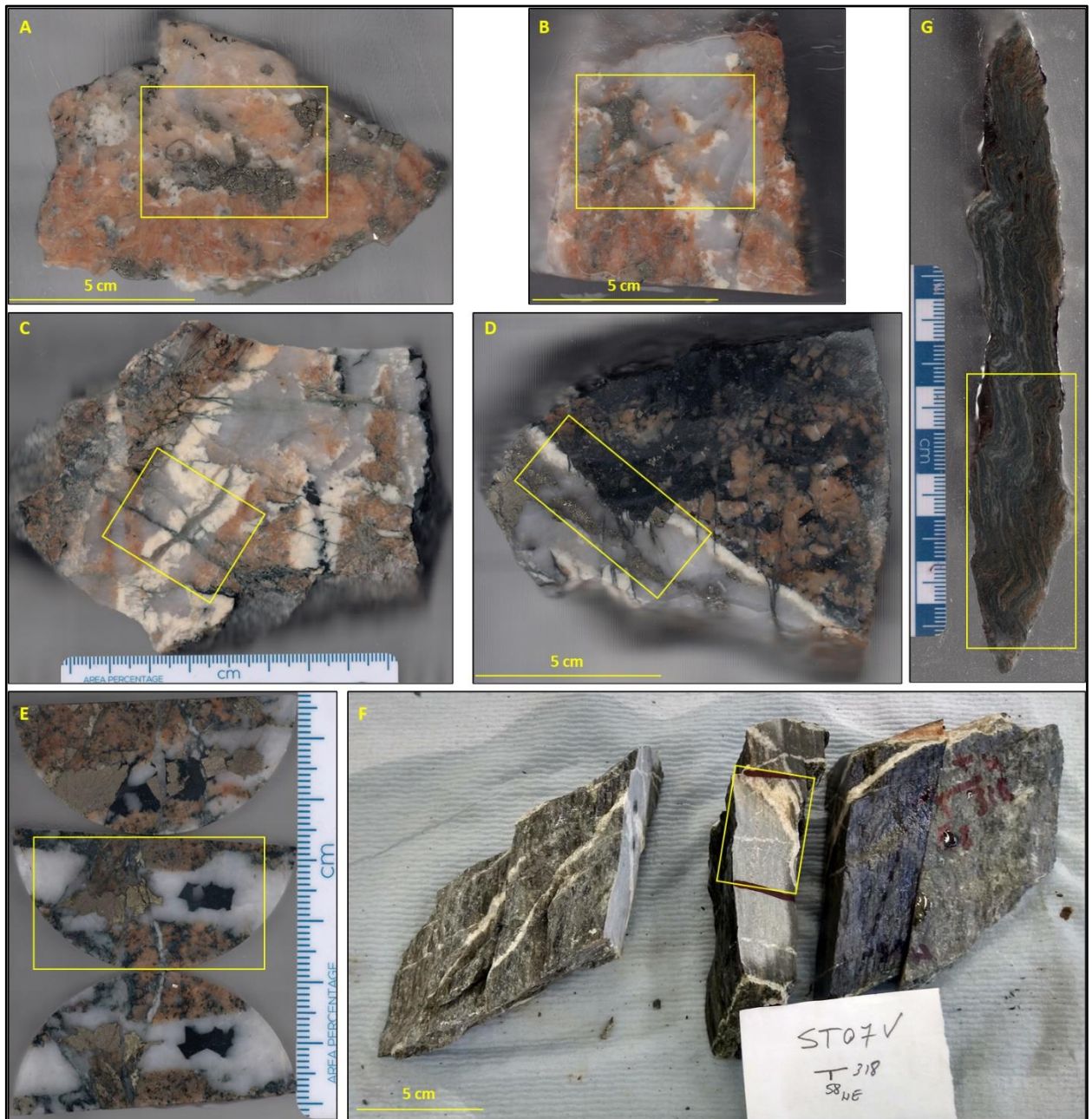


**Plate AII.2** – Representative images of samples collected from the Stog'er Tight area used for this study. The yellow rectangles show the location of thin sections on the samples. Descriptions in *Table A2.2*.

*Table A2.3 – List of samples collected from the Argyle area*

Sample code	Sample origin	Coordinates (m) E / N	Sample description	Image	Section type	Analysis
AG1	Drill core (AE-18-64A; sampled interval: 69.13-69.3 m)	567,620.3129 5,536,552.019	High Au grade zone (up to 18 g/t) characterised by high density, almost “flooding” of quartz – carbonate veins associated with beige-brown alteration patches composed of ab – ser – lx (bladed) ± py, everything strongly brecciated by late dark green - black chlorite veins with fine grained pyrite	<i>Plate A3 – A</i>	PTkS	OM; BSE; EDS; CL
AG2	Drill core (AE-17-46; sampled interval 61.2 - 61.32 m)	567,620.5897 5,536,552.698	Medium Au grade zone (4.5 g/t); dense network of quartz-albite-carbonate veins associated with intensively altered, white-cream coloured, albitised wall rock with orange/orange-red and green spots of carbonates, chlorite, and clay minerals; patches of coarse-grained pyrite and small, beige aggregates of leucoxene are common	<i>Plate A3 – B</i>	PTS	OM
AG3 AG4	Drill core (AE-17-46; sampled interval 68-68.4 m)	567,620.5897 5,536,552.698	Medium Au grade zone (8.3 g/t) characterised by high density of quartz – carbonate veins associated with an intense, white to cream/beige alteration halo composed mainly of albite and large patches of pyrite, and small patches of ser-cb-lx; everything is cross-cut by late chlorite (black) – pyrite (fine grained) veins	<i>Plate A3 – C, D</i>	PTS x 2	OM; BSE; EDS; CL; EPMA; U-Pb LA-ICP-MS analysis on mnz/xtm
MPAG1	Drill core (AE-16-23; sampled interval 35.35 m)	567,266.684 553,6459.378	Sample consisting of milky-white quartz vein material crosscut by late veinlets of chl (black)-cal within a moderately altered (chl-ab-cal ± cb-rt-hem-ser-pyrite) gabbro; sample collected by Maciej Pawlukiewicz, former MSc student at Memorial University of Newfoundland	<i>Plate A3 – E</i>	PTS	OM; BSE; EDS; CL; EPMA

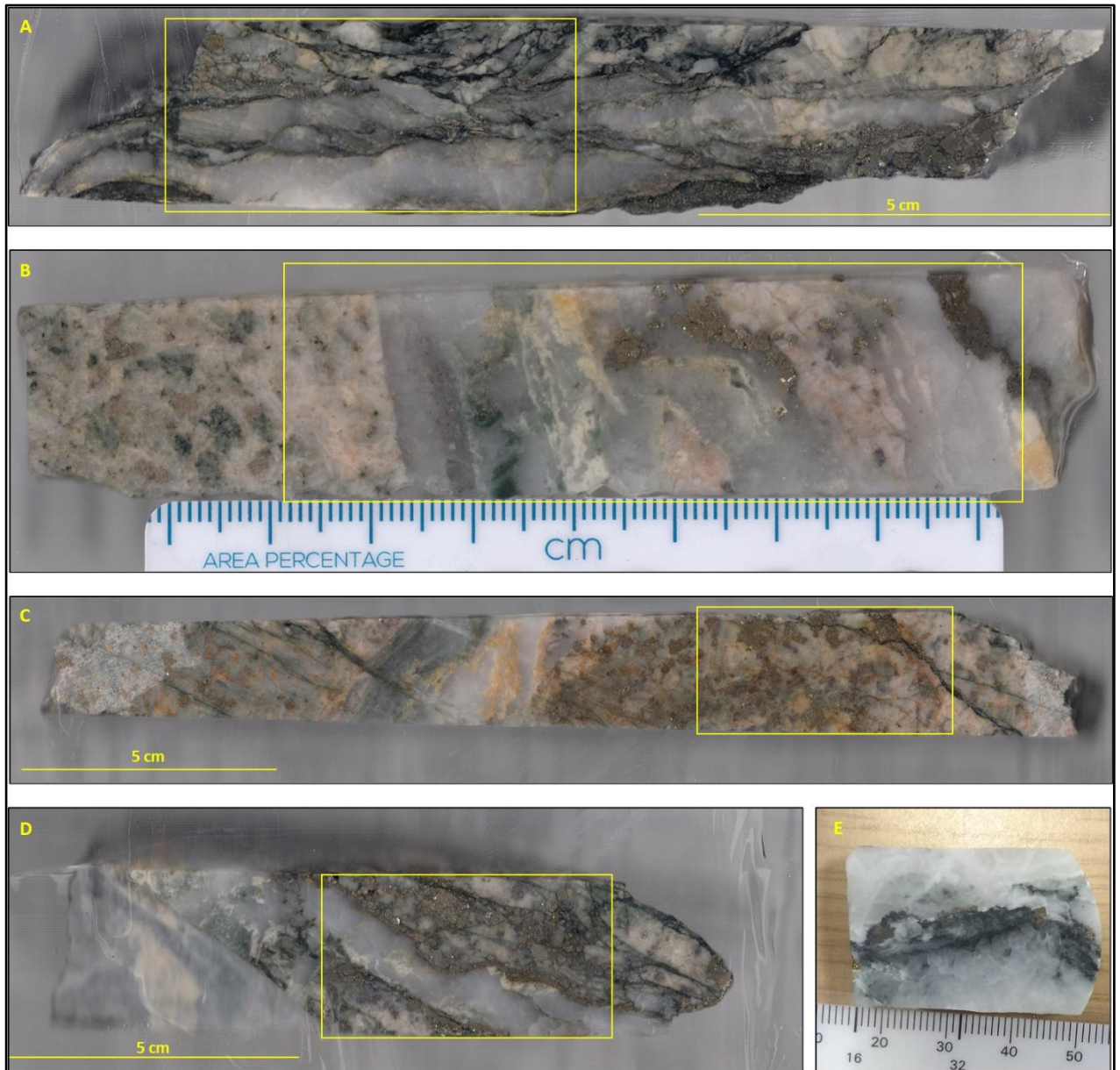


**Plate A2.3** – Representative images of samples collected from the Argyle area used for this study. The yellow rectangles show the location of thin sections on the samples. Descriptions in **Table A2.3**.

*Table A2.4 – List of samples collected from the Romeo & Juliet area*

Sample code	Sample origin	Coordinates (m) E / N	Sample description	Image	Section type	Analysis
RJ1	Drill core (RJ-00-06; sampled interval 11.6 – 11.83 m)	561,900 5,535,613	Medium Au grade zone (3.8 g/t) from Juliet South; Thin (<10 cm) milky white to orange-brown quartz-carbonate veins associated with a strong alteration halo composed of chl-ser-py ± cal	<i>Plate A4 – A</i>	PTkS	OM; BSE; EDS; CL
RJ2	Drill core (RJ-00-05; sampled interval 5.44-5.6 m)	561,899 5,535,615	Vein collected from a medium Au grade zone (6 g/t) from Juliet South; narrow (10 cm), milky-white to rusty (due to iron oxides) quartz vein with coarse grained crystals and massive texture, crosscut by dark-grey ser-py stringers	<i>Plate A4 – C</i>	PTkS	OM; BSE; EDS; CL
RJ3	Drill Core (RJ-00-06; sampled interval 6.5-6.655 m)	561,900 5,535,613	High Au grade interval (36.5 g/t) from Juliet South; half a meter thick, massive, milky white, quartz vein with oxidized fractures and ser-py stringers associated with a strong orange-brown alteration halo composed of ser-cb-FeOx	<i>Plate A4 – D</i>	PTkS	OM; BSE; EDS; CL
RJ4	Drill core (RJ-00-08; sampled interval 21.1 – 21.4 m)	561,890 5,535,590	Medium Au grade interval (7 g/t) from Juliet South; greenish grey, strongly altered wall rock (ser-qtz-chl-py ± cb) with narrow qtz-cal veinlets	<i>Plate A4 – E</i>	PTS	OM; BSE; EDS; CL; EPMA; U-Pb LA-ICP-MS analysis on mnz/xtm
RJ5	Drill core (RJ-00-06; sampled interval 11.6 – 11.83 m)	561,900 5,535,613	Medium Au grade zone (3.8 g/t) from Juliet South; Sample collected from strongly altered wall rock (chl-ser- patchy py) with narrow (<1 cm) calcite veinlets	<i>Plate A4 – B</i>	PTS	OM; BSE; EDS; CL; U-Pb LA-ICP-MS analysis on mnz/xtm
CL8-19	Outcrop (along the coastline ~200 m NW from the RJ prospect)	566,433.035 5,534,996.839	Dense network of shear-type qtz-cb veins associated with a strong chl (black) – cb – py alteration halo within a steeply dipping, NNE striking shear zone visible	<i>Plate A4 – F</i>	Oriented PTS (strike 30°, dip 85° to WNW)	OM; MsA; BSE; EDS

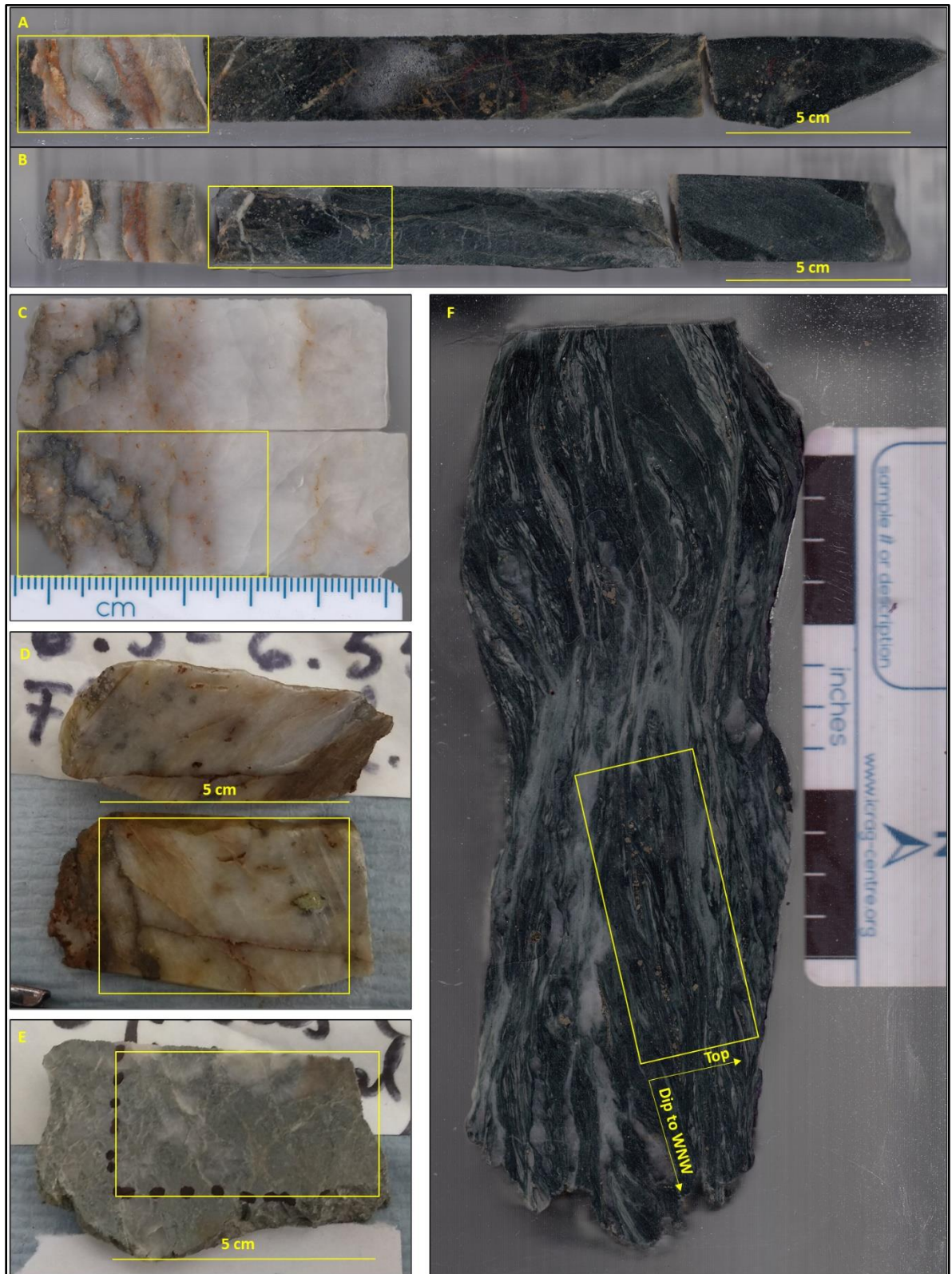


**Plate AII.4** – Representative images of samples collected from the Romeo & Juliet area used for this study. The yellow rectangles show the location of thin sections on the samples. Descriptions in **Table A2.4**.

*Table A2.5 – List of samples collected from the Deer Cove area*

Sample code	Sample origin	Coordinates (m) E / N	Sample description	Image	Section type	Analysis
DCD1	Float from the Deer Cove ore-stock pile	568,558 5,540,824	Milky white quartz vein fragment with visible Au, patchy py and fragments of altered (chl-py) wall rock material	<i>Plate A5 – A</i>	PTkS	OM; BSE; EDS; CL; EPMA
DC2	Drill core (DC-14-150 sampled interval 87.68-87.74 m)	568,382.7 5,540,591	Low to medium Au grade section (2 - 3 g/t) characterized by a dense network of wispy quartz-carbonate veins associated with an intense alteration halo composed of chl-ser-lx and fine grained py	<i>Plate A5 – B</i>	PTkS	OM; BSE; EDS; CL; EPMA
DC3	Drill Core (DC-86-24; sampled interval 23.2 – 23.7 m)	568,420 5,540,860	Low to medium Au grade zone (2 - 3 g/t) with high density of milky white quartz – carbonate veins associated with a strong chl-cb-ser-py alteration halo	<i>Plate A5 – C</i>	PTkS	OM; BSE; EDS; CL
DC4	Drill core (DC-87-94; sampled interval 87.4 – 87.6 m)	568,460 5,540,760	High Au grade interval (35.5 g/t) characterized by foliation parallel Qtz-cb-py veins associated with a strong alteration halo composed of chl-ser-py (patchy and disseminated) and minor epi	<i>Plate A5 - D</i>	PTS	OM; BSE; EDS
DC5	Drill core (DC-87-94; sampled interval 103.1 – 103.2 m)	568,460 5,540,760	Medium Au grade zone (5.18 g/t) characterized by cm thick Qtz-py stringers associated with an intense alteration halo composed of chl-ser-cb-lx-py and minor epi	<i>Plate A5 – E</i>	PTS	OM; BSE; EDS; CL; U-Pb LA-ICP-MS analysis on tit
GC60	Outcrop (At the entrance of the Deer Cove exploration adit)	568,507.322 5,540,865.946	Strongly foliated rock in the Deer Cove fault zone affected by south verging folds and steeply dipping, E-W striking kink bands; the rocks are moderately to strongly altered (chl – cb and py); there are two types of Qtz-cal veins: foliation parallel and steeply dipping veins that are subparallel to the E-W oriented kink bands	<i>Plate A5 – F</i>	Oriented PTS*	OM; MsA; BSE; EDS

DC19	Outcrop (along the coastline in the cove)	567,841.491 5,540,945.023	Strongly foliated rock in the hanging-wall of the Deer Cove fault, just above a thick (1-3 m) qtz vein; The rocks show a composite foliation, are strongly crenulated and are affected by a dense network of qtz-cb foliation parallel veins and a strong alteration composed of chl-cb ± py	<b>Plate A5 - G</b>	Oriented PTS**	OM; MsA
DC30 / DCF	Outcrop (along the coastline in the cove)	567,804.079 5,541,078.162	Intensively altered and mineralised D <sub>2b</sub> shear zones; foliation parallel qtz-py veins associated with pervasive fuchsite-FeOx alteration and disseminated cpy	<b>Plate A5 - H</b>	Unoriented & Oriented PTS***	OM; MsA; BSE; EDS

\*Oriented sample (strike 165°, dip 40° to ENE); section cut perpendicular to the foliation and parallel to the oblique stretching mineral lineation

\*\*Oriented sample (strike 290°, dip 60° to NNE), section cut perpendicular to the foliation and parallel to the down-dip stretching mineral lineation

\*\*\*Oriented sample (strike 320°, dip 50° to NE) section cut perpendicular to the foliation and parallel to the oblique to down-dip stretching mineral lineation (trend/plunge 25°/50°)

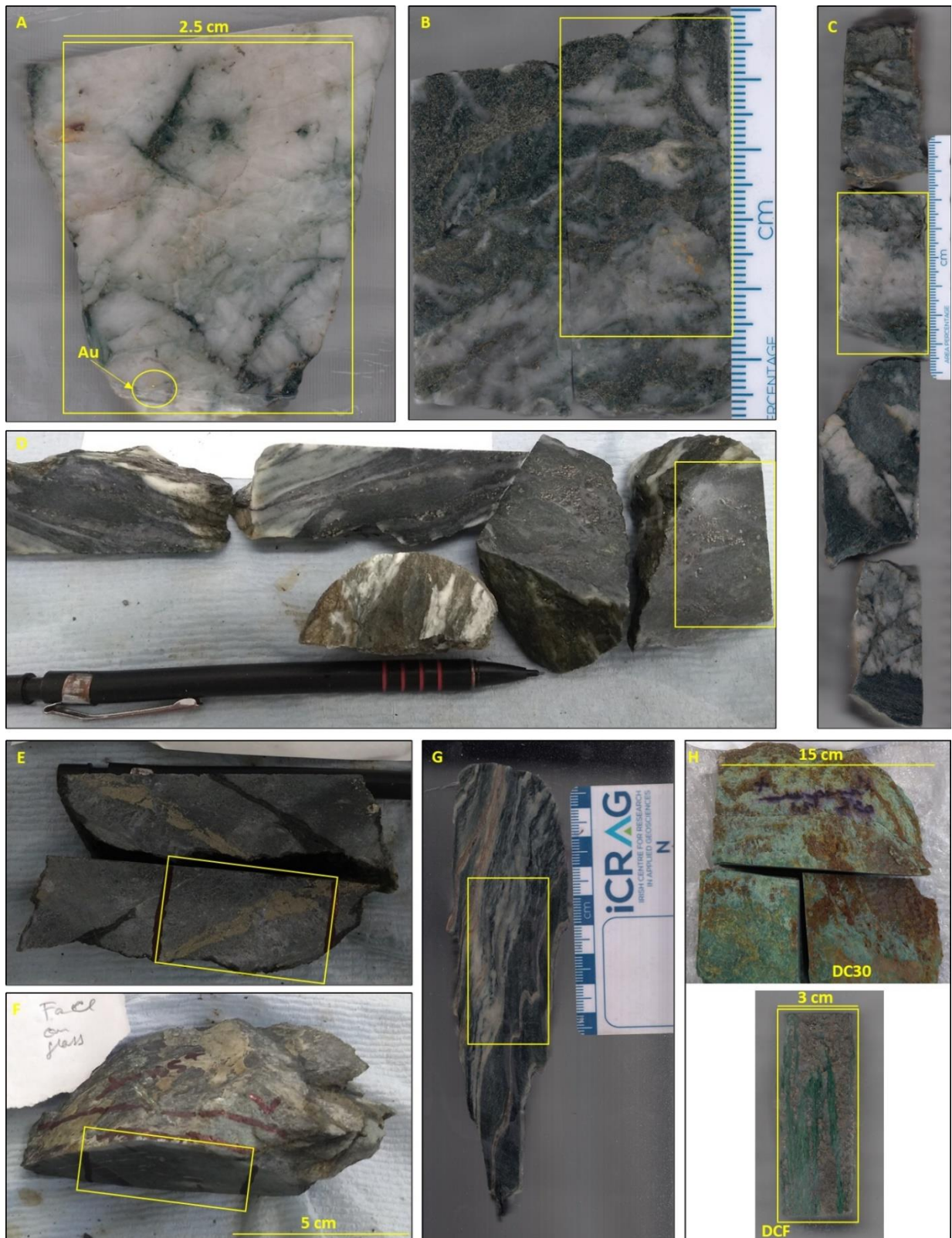


**Plate AII.5** – Representative images of samples collected from the Deer Cove area used for this study. The yellow rectangles show the location of thin sections on the samples.

Descriptions in **Table A2.5**.



**Table A2.6** – List of samples collected from the Point Rousse Complex, Paquet Harbour Group and the Flat Water Pond Group and used for regional correlations

Sample code	Sample origin	Coordinates (m) E / N	Sample description	Section type	Analysis
CS1	Outcrop (along the Ming's Bight Road)	5531932; 565811	Strongly sheared rock, medium grained, dark grey colour rich in quartz and white micas; Footwall of Scrape thrust (~500 m S from thrust in the PHG)	Oriented PTS (strike 295°, dip 75° to N)	OM, M <sub>S</sub> A
GC18	Outcrop (quarry entrance)	5527505; 555117	Strongly sheared outcrop, contact between the upper part of the ophiolite sequence and the lower part of the cover sequence; dark green coloured, fine grained rock, looks like a slate.	Oriented PTS (strike 250°, dip 70° to NW)	OM, M <sub>S</sub> A
GC19	Outcrop (Along the NNW oriented segment of the Deer Cove thrust)	5540644; 568017	Strongly sheared and altered outcrop; grey-cream coloured rock, strongly magnetic (tested with mag pen), shows a pervasive alteration composed of: needle shaped, white, soft minerals – possibly talc, chrysotile or tremolite; soft dark minerals - most probably serpentine minerals; patches of sericite and iron oxides; relict plagioclase feldspars are still visible)	Oriented TS (strike 340°, dip 45° to SW)	OM, M <sub>S</sub> A
GC32	Outcrop (Ming's Bight area)	5536960; 568697	Outcrop with massive and strongly sheared intervals at the contact between middle and upper part of ophiolites; the more massive part has a dark purple – green colour, is strong magnetic and fine grained; the sheared part is white-cream in colour and shows a pervasive alteration composed of sericite, iron oxides, talc, and serpentinite minerals	Oriented PTS (strike 30°, dip 60° to NW)	OM, M <sub>S</sub> A
GC52K	Outcrop (along the coastline in the Baie Verte town)	5532392; 558531	Grey-greenish rock, chloritized schist with disseminated cubic pyrite and quartz-epidote veinlets along the foliation planes; affected by a horizontal to oblique crenulation	Oriented PTS (strike 62°, dip 80° to NW)	OM, M <sub>S</sub> A, BSE

GC76	Outcrop (along the 410 road)	5526671; 554298	Very fine grained, black - dark green rock, intense chloritized, close to the contact between ophiolite and cover rocks	Oriented PTS (strike 40°, dip 70° to NW)	OM, M <sub>S</sub> A
GC107	Outcrop (in the Baie Verte town)	5532229; 558141	Grey-greenish rock, chloritised schist with disseminated cubic pyrite and quartz-epidote veinlets along the foliation planes; affected by two visible crenulations, an oblique to horizontal one crosscut by a steep one	Oriented PTS (strike 55°, dip 80° to NW)	OM, M <sub>S</sub> A
MBR10-19	Outcrop (PHG – Ming’s Bight Road)	5532494 565798	Grey to dark-green, strongly foliated rock, with well-developed down-dip stretching mineral lineation defined by stretched amph-plg	Oriented TS (strike 55°, dip 80° to NW)	OM, M <sub>S</sub> A
PCL1-19.2	Outcrop (on the Pine Cove coast)	5535110 561902	Grey to dark-green, strongly foliated rocks, fine- to moderately grained; well-developed down-dip stretching mineral lineation defined by (Chl-plg). Aligned along the lineation – garnet porphyroclasts (?)	Oriented PTS (strike 55°, dip 80° to NW)	OM, M <sub>S</sub> A
CLE7-19	Outcrop (on the East Coast, ~1 km S from Big Head cove)	5538563 569897	A few meters wide, strongly sheared and altered (FeOx–Py–ser-silica), NNW dipping fault.	Oriented PTS (strike 245°, dip 30° to 335°)	OM, M <sub>S</sub> A, EDS, BSE
G23-19	Outcrop (on the 410 road ~ 2 km south from the intersection with 414 road)	5526121 554223	Strongly sheared and altered (FeOx-Py-Silica-Ser) fault zone (a few meters wide).	Oriented PTS (strike 15°, dip 75° to 285°)	OM, M <sub>S</sub> A, EDS, BSE

## **Appendix III - EPMA gold data**

*Table A3.1 – EPMA gold compositional data for the Pine Cove deposit; sample codes starting with PC100... correspond to in-situ gold particles, whereas the sample codes starting with RJC... correspond to liberated gold particles*

SAMPLE CODE	Au WT%	Ag WT%	Hg WT%	Cu WT%	Pd WT%	TOTAL
PC100_Site5_2	92.8914	7.50594	0.07996	0.196969	-0.07225	100.602
PC100_Site1_2	93.3091	7.08923	0.204186	0.065733	-0.07047	100.598
PC100_Site19_2	92.9692	7.3702	0.201421	0.066646	-0.05073	100.557
PC100_Site23	92.8744	7.36061	0.273116	0.06108	-0.03514	100.534
PC100_Site1_1	92.8993	7.07482	0.185496	0.065299	-0.02177	100.203
PC100_Site19_1	92.606	7.20717	0.194288	0.056766	-0.02198	100.042
PC100_Site5_3	92.5137	7.28224	0.22764	0.077321	-0.07928	100.022
PC100_Site3	92.3606	7.41193	0.089701	0.06661	-0.01808	99.9107
PC100_Site16	92.3405	7.10689	0.317165	0.07073	-0.01573	99.8195
PC100_Site21	92.1076	7.52653	0.139724	0.05465	-0.00944	99.8191
PC100_Site9	92.0526	7.42519	0.152482	0.096696	-0.0512	99.6758
PC100_Site21_1	91.9302	7.64462	0.126744	0.068235	-0.10247	99.6674
PC100_Site14	92.2167	7.21353	0.101931	0.069551	-0.07637	99.5253
PC100_Site15	93.4281	5.86483	0.158606	0.080454	-0.01015	99.5218
PC100_Site24_1	91.5923	7.43234	0.294505	0.062456	-0.0482	99.3334
PC100_Site10	91.7487	7.32776	0.158279	0.050981	-0.09435	99.1913
PC100_Site7	91.5944	7.37673	0.170108	0.06754	-0.03122	99.1776
PC100_Site18_2	92.962	6.05405	0.123933	0.060518	-0.0574	99.1431
PC100_Site23_2	91.6699	7.38746	0.090074	0.055056	-0.06011	99.1423
PC100_Site19_3	91.6601	7.29415	0.147517	0.060253	-0.03694	99.125
PC100_Site23_3	91.7614	7.18436	0.10667	0.073239	-0.05142	99.0742
PC100_Site17_2	92.1755	6.6193	0.224258	0.099415	-0.06535	99.0532
PC100_Site16_2	93.1585	5.62043	0.096507	0.095603	-0.02786	98.9432
PC100_Site14_1	91.3708	7.46049	0.107553	0.055905	-0.07063	98.9241
PC100_Site5_1	91.2876	7.44068	0.15867	0.0934	-0.05674	98.9236
PC100_Site15_1	91.3768	7.29496	0.167246	0.052356	-0.09766	98.7937
PC100_Site12	93.7119	4.76723	0.166773	0.103288	-0.02922	98.7199
PC100_Site6	91.0959	7.47733	0.141455	0.047603	-0.04867	98.7137
PC100_Site24	91.0845	7.31856	0.384321	0.060771	-0.13707	98.7111
PC100_Site24_3	91.2475	7.38959	0.071267	0.037598	-0.03758	98.7084
PC100_Site22	90.9472	7.42139	0.190664	0.055776	-0.00946	98.6056
PC100_Site8	92.464	5.86802	0.176109	0.122406	-0.04912	98.5814
PC100_Site20	93.0156	5.22418	0.228853	0.101501	-0.13604	98.4341
PC100_Site18_1	91.1974	7.20815	0.102728	0.04919	-0.14404	98.4134
PC100_Site23_1	91.1757	7.01528	0.20606	0.06053	-0.06585	98.3917
PC100_Site12_1	92.0184	5.89976	0.145604	0.109144	-0.03218	98.1408
PC100_Site2	92.8802	5.03293	0.046533	0.126253	-0.00752	98.0784
PC100_Site5	90.5501	7.23747	0.123907	0.055179	-0.11919	97.8474
PC100_Site15_2	89.8406	7.57171	0.176777	0.051876	-0.14984	97.4911

PC100_Site11	89.7004	7.29994	0.222025	0.184576	-0.04057	97.3664
PC100_Site10_1	91.1345	6.09674	-0.00508	0.101857	-0.14653	97.1815
PC100_Site19_4	89.9047	7.08466	0.254374	0.068344	-0.13326	97.1788
RJC141_16_1	89.7494	10.3856	0.414951	0.048574	0.133293	100.732
RJC141_16_2	94.8551	4.56611	0.328135	0.087749	0.0474	99.8845
RJC141_16_3	93.8865	5.28407	0.369539	0.065792	0.124057	99.7299
RJC141_16_4	91.4289	7.28426	0.364544	0.074521	0.015158	99.1674
RJC141_16_5	93.4528	6.09977	0.39778	0.069627	0.084049	100.104
RJC140_17_01	95.1494	4.36556	0.164186	0.092805	0.079458	99.8514
RJC140_17_02	91.655	8.89418	0.157641	0.050092	0.048335	100.805
RJC140_17_03	91.439	7.21851	0.186106	0.099742	0.050343	98.9937
RJC140_17_04	86.9455	13.495	-0.00008	0.060521	-0.01423	100.487
RJC140_17_05	95.2456	5.03961	0.075022	0.09345	0.1716	100.625
RJC140_17_06	88.5733	10.1316	0.167553	0.033909	0.115025	99.0214
RJC140_17_07	93.4445	5.93117	0.199669	0.091323	0.060349	99.727
RJC140_17_08	91.9953	8.32554	-0.07447	0.048282	0.091122	100.386
RJC140_17_09	95.4766	4.14693	0.315021	0.087249	0.172458	100.198
RJC140_17_10	90.1421	10.1861	0.058233	0.074121	0.076853	100.538
RJC140_17_11	96.951	3.45396	0.01631	0.093368	0.12293	100.638
RJC140_17_12	90.2232	8.23944	0.151984	0.093016	0.039792	98.7475
RJC140_17_13	93.2846	6.04377	0.009615	0.097903	0.103476	99.5394
RJC140_17_14	92.3775	6.33885	0.095732	0.101819	0.037858	98.9518
RJC140_17_15	95.7679	4.53705	0.051955	0.074178	0.047967	100.479
RJC140_17_16	92.7466	6.76277	0.084925	0.083643	0.061667	99.7396
RJC140_17_17	88.5655	11.0299	0.141	0.062723	0.09275	99.8919
RJC140_17_18	92.5172	6.43381	0.031338	0.071518	0.049016	99.1029
RJC140_17_19	89.7694	9.75345	0.15686	0.06542	0.073908	99.8191
RJC140_17_20	94.4816	6.02994	0.096911	0.07128	0.097975	100.778
RJC140_17_21	94.4941	6.51254	0.152714	0.064814	0.044247	101.268
RJC140_17_22	95.1655	5.08398	0.250654	0.081301	0.081602	100.663
RJC140_17_23	95.1585	4.73508	-0.02713	0.081413	0.07613	100.024
RJC140_17_24	91.5431	6.37751	0.077088	0.056928	0.056207	98.1108
RJC140_17_25	93.7269	7.00854	-0.02445	0.065293	0.083127	100.86
RJC140_17_26	94.5381	5.93614	0.231977	0.081203	0.033176	100.821

*Table A3.2 – EPMA gold compositional data for the Stog’er Tight deposit; sample codes starting with SOZ2 & BN215... correspond to in-situ gold particles, whereas the sample codes starting with RJC... correspond to liberated gold particles*

SAMPLE CODE	Au WT%	Ag WT%	Hg WT%	Cu WT%	Pd WT%	TOTAL
BN215_S12_1	93.5809	5.68065	0.142919	0.626161	-0.04181	99.9888
BN215_S12_2	92.8645	6.22576	0.104159	0.817603	-0.0865	99.9255
SOZ2_S4_1	92.6272	6.8441	0.334097	0.061185	-0.04164	99.825
SOZ2_S5_5	95.3136	4.22775	0.263261	0.052853	-0.14564	99.7118
BN215_SX	93.6754	5.00957	0.198161	0.839881	-0.08512	99.6379
BN215_SX_1	92.0335	6.17462	0.236915	1.02135	0.00451	99.4709

SO22_S5_1	94.4851	4.74653	0.145949	0.096462	-0.09971	99.3743
BN215_S7	92.0335	6.09067	0.174049	0.730481	-0.06318	98.9656
BN215_S24_2	91.8031	5.8076	0.262346	0.911293	-0.05049	98.7338
SO22_S10	91.7815	6.90347	0.069033	0.0483	-0.08189	98.7204
SO22_S9	92.156	6.39958	0.127783	0.071633	-0.06756	98.6875
SO22_S5_3	93.3411	5.15916	0.100696	0.074289	-0.06471	98.6106
BN215_S9	92.1238	5.85186	0.206219	0.353275	-0.04934	98.4858
SO22_S5_4	92.3489	6.06796	0.09233	0.062763	-0.12011	98.4519
BN215_S12_3	91.8445	5.7166	0.222665	0.779375	-0.1377	98.4255
SO22_S10_3	89.9953	7.29319	0.311227	0.082368	-0.05466	97.6274
SO22_S4_2	90.4749	7.05759	0.15468	0.055828	-0.12272	97.6203
SO22_S10_1	91.5404	6.01884	0.120701	0.079676	-0.14938	97.6102
SO22_S5_2	92.6051	4.69135	0.262699	0.072186	-0.08425	97.5471
SO22_S10_4	90.3587	6.94521	0.211474	0.061748	-0.06071	97.5164
BN215_S30	91.4304	5.97732	0.032266	0.084388	-0.14096	97.3834
BN215_S6_1	90.5901	6.02222	0.119191	0.666796	-0.04167	97.3566
BN215_S24_1	89.4624	5.77864	0.157676	1.88182	-0.03443	97.2461
SO22_S5_6	90.518	6.50943	0.176438	0.055922	-0.02909	97.2307
SO22_S5_7	90.6274	6.35713	0.179711	0.064546	-0.0364	97.1923
SO22_S10_2	90.5514	6.52858	0.198491	0.068577	-0.19194	97.1551
RJC141_15_1	94.502	5.45095	0.20412	0.072953	0.089874	100.32
RJC140_16_01	95.3552	4.99359	0.311727	0.084655	0.086591	100.832
RJC140_16_02	94.2787	6.24924	0.128507	0.071458	0.05476	100.783
RJC140_16_03	96.1763	4.22979	0.189959	0.879024	0.060007	101.535

*Table A3.3 – EPMA compositional data for in-situ gold particles from the Argyle deposit*

SAMPLE CODE	Au WT%	Ag WT%	Hg WT%	Cu WT%	Pd WT%	TOTAL
AG3_S21	94.1952	6.75307	0.141485	0.072849	-0.08031	101.082
AG3_S31	93.2671	6.83592	0.227014	0.084661	-0.00547	100.409
AG3_S40_2	93.6359	6.40917	0.084431	0.072499	-0.03267	100.169
AG3_S39	93.2505	6.70805	0.10051	0.096864	-0.02224	100.134
AG3_S23	93.4082	6.40278	0.19056	0.065702	-0.06309	100.004
AG3_S15_4	92.6386	6.93611	0.245275	0.172614	-0.13426	99.8583
AG3_S32	92.6975	7.05847	-0.01618	0.094453	-0.01965	99.8146
AG3_S20	92.8431	6.56281	0.243626	0.09803	-0.02673	99.7208
AG3_S35_3	94.8915	4.7192	0.084877	0.14039	-0.11666	99.7193
AG3_S35	92.6626	6.67717	0.272768	0.122436	-0.06937	99.6656
AG3_S19	92.0179	7.08042	0.186727	0.089873	-0.07627	99.2987
AG3_S37	92.3185	6.69911	0.069083	0.154612	0.048758	99.2901
AG3_S15_2	92.3556	6.78666	0.154641	0.076559	-0.08539	99.2881
AG3_S36	92.9039	6.33867	0.040449	0.072552	-0.10521	99.2503
AG3_S14	92.8713	5.96773	0.056616	0.334596	0.009492	99.2397
AG3_S18	92.4928	6.58237	0.118276	0.066479	-0.04092	99.219
AG3_S35_4	92.2423	6.75278	0.122376	0.139177	-0.12753	99.1291

MPAG1_Site15	94.6242	4.34402	0.128248	0.060046	-0.13382	99.0227
AG3_S17	92.0888	6.75246	0.178402	0.088703	-0.10665	99.0017
MPAG1_S3	92.6798	6.15632	0.082144	0.050152	-0.04242	98.926
AG3_S34	92.143	6.58925	0.074953	0.146182	-0.05006	98.9033
AG3_S24	91.8382	6.74591	0.216547	0.125594	-0.07521	98.851
AG3_S19_2	91.9441	6.62273	0.174879	0.120181	-0.08679	98.7751
AG3_S34_2	93.9721	4.39013	0.172248	0.18122	-0.06313	98.6526
AG3_S27	92.0767	6.35901	0.067113	0.112993	-0.06961	98.5462
AG3_S25_2	91.7657	6.47907	0.003039	0.165372	-0.0365	98.3767
MPAG1_Site5	93.1424	4.90112	0.134133	0.06113	-0.08917	98.1496
AG3_S35_2	91.2735	6.61684	0.064403	0.149381	-0.01703	98.0871
AG3_S35_5	91.1568	6.49497	0.231724	0.141002	-0.11857	97.9059
AG3_S19_3	91.3446	6.12636	0.175935	0.140879	-0.01643	97.7714
AG3_S28_2	90.9067	6.4799	0.268614	0.11028	-0.10764	97.6578
AG3_S2	90.71	6.04067	0.19161	0.770471	-0.08009	97.6327
AG3_S13	90.6284	6.64865	0.237241	0.1423	-0.09241	97.5641
AG3_S28_1	90.6348	6.6706	0.159123	0.122125	-0.04229	97.5444
AG3_S40	91.1	6.18693	0.17357	0.135752	-0.05205	97.5442
AG3_S15	90.751	6.64107	0.11032	0.076969	-0.05891	97.5204
AG3_S29_2	91.7085	5.24088	0.090057	0.530903	-0.06462	97.5057
AG3_S38	90.1547	6.9893	0.082479	0.329019	-0.15098	97.4045
AG3_S5	90.4096	6.72273	0.13557	0.165812	-0.06324	97.3705
AG3_S18_2	90.8191	6.34689	0.100572	0.11964	-0.09004	97.2961
AG3_S36_2	90.6876	6.4105	0.173291	0.103334	-0.10314	97.2716
AG3_S28_3	90.4216	6.51274	0.116116	0.167842	-0.02743	97.1909
AG3_S12_2	92.1072	4.95828	0.150506	0.071845	-0.10509	97.1828
MPAG1_Site4_1	91.7557	5.16553	0.217056	0.037528	-0.00602	97.1698
AG3_S22	91.5037	5.44208	0.100939	0.081891	-0.03473	97.0939
AG3_S1	89.643	7.2594	-0.31971	0.291875	0.166421	97.041

**Table A3.4** – EPMA gold compositional data for the Romeo & Juliet prospect; sample codes starting with RJ4... correspond to in-situ gold particles, whereas the sample codes starting with RJC... correspond to liberated gold particles

SAMPLE CODE	Au WT%	Ag WT%	Hg WT%	Cu WT%	Pd WT%	TOTAL
RJ4_site3_4	93.7447	5.88776	0.119591	0.088777	-0.09664	99.7442
RJ4_site3_10	92.4739	6.66577	0.094397	0.101	-0.07045	99.2646
RJ4_site3_7	92.455	6.40508	0.178969	0.168322	-0.12895	99.0785
RJ4_site3_2	92.2424	6.32944	0.21191	0.151727	-0.03909	98.8964
RJ4_site6_2	90.6339	6.84961	0.132435	0.128268	-0.05527	97.6889
RJ4_site3_3	90.9427	6.31412	0.143202	0.108131	-0.09315	97.415
RJ4_site1_1	91.8353	5.33649	0.198034	0.141025	-0.13982	97.371
RJC141_14_1	93.4558	5.9264	0.150798	0.051838	0.069738	99.6545
RJC141_14_3	93.7063	6.07353	0.445601	0.110671	0.071955	100.408
RJC141_13_1	93.9347	6.02435	0.3982	0.112261	0.071198	100.541
RJC141_13_2	93.4267	6.09693	0.354799	0.100564	0.065732	100.045

RJC141_13_3	92.9308	6.46083	0.317946	0.070918	0.090322	99.8708
RJC141_13_4	93.6043	6.14703	0.364128	0.074856	0.064158	100.255
RJC141_13_5	92.8549	6.37553	0.212007	0.052035	0.09266	99.5871
RJC141_13_6	93.5195	5.89923	0.482173	0.123628	0.083571	100.108
RJC141_13_7	92.4106	7.18354	0.207053	0.085423	-0.00014	99.8865
RJC141_13_8	94.1975	5.80219	0.209592	0.100009	0.051064	100.36
RJC141_13_9	92.8403	6.24434	0.514806	0.064251	0.106568	99.7703
RJC141_13_10	92.8093	6.42318	0.237279	0.053043	0.13271	99.6555
RJC141_13_11 (v. small particle)	92.7816	6.37906	0.234061	0.179566	0.096377	99.6706
RJC141_13_12	93.5934	6.11813	0.320037	0.120586	0.073353	100.226
RJC141_13_13	92.6854	6.99591	0.317662	0.096697	0.113743	100.209
RJC141_13_14	92.8556	6.61723	0.317248	0.114244	0.16019	100.064
RJC141_13_15	93.1573	6.71227	0.072134	0.072325	0.0993	100.113
RJC141_13_16	93.8318	6.38725	0.300594	0.089061	0.145	100.754
RJC141_13_17	92.4571	7.05413	0.249517	0.076799	0.076757	99.9143
RJC141_13_18	94.1331	5.89635	0.337786	0.145493	0.100464	100.613
RJC141_13_19	93.1079	6.32229	0.245821	0.052454	0.029957	99.7585
RJC140_13i_05	93.1009	6.7552	0.076256	0.119654	-0.00924	100.043
RJC140_13i_04	93.7537	6.59186	0.12214	0.086484	0.057781	100.612
RJC140_13i_03	92.6587	6.60775	0.25446	0.082912	0.153869	99.7577
RJC140_13i_02	92.3851	7.09378	0.184053	0.22974	0.083791	99.9765
RJC140_13i_01	91.0629	6.85462	0.190642	0.058608	0.041982	98.2088
RJC140_13i_06	93.6242	6.11557	0.152451	0.149263	0.072161	100.114
RJC140_13i_07	92.6813	6.97855	0.112161	0.074784	0.051212	99.898
RJC140_13i_08	93.4883	6.55336	0.119195	0.056519	0.032821	100.25
RJC140_13i_09	92.5754	6.27508	-0.02302	0.079885	0.074207	98.9815
RJC140_13i_10	93.8573	6.57579	0.141421	0.073361	0.023551	100.671
RJC140_13i_11	93.3179	6.05591	0.251041	0.069088	0.078575	99.7725
RJC140_13i_12	93.7222	6.09979	0.253363	0.110055	0.032169	100.218
RJC140_13i_13	92.6035	7.44105	0.05577	0.07337	0.129612	100.303
RJC140_13i_14	93.735	6.51463	0.097514	0.063544	0.094032	100.505
RJC140_13i_15	92.3635	7.93159	0.175682	0.053596	0.022652	100.547
RJC140_13i_16	92.6353	7.59657	0.233443	0.108987	0.04037	100.615
RJC140_13i_17	92.4755	6.67158	0.275001	0.076602	0.04626	99.5449
RJC140_13i_18	93.5496	5.99117	0.202101	0.088642	0.052864	99.8843
RJC140_13i_19	93.3129	6.48752	0.194689	0.060911	0.088293	100.144
RJC140_13i_20	92.2444	7.52724	0.217759	0.082658	0.042487	100.115
RJC140_13ii_01	92.5779	6.77453	0.14269	0.058629	0.061135	99.6149
RJC140_13ii_02	92.5012	7.30117	0.05547	0.122056	0.053147	100.033
RJC140_13ii_03	93.0098	6.76153	0.143236	0.059624	0.076049	100.05
RJC140_13ii_04	91.4428	6.22229	0.110691	0.09392	0.066242	97.9359
RJC140_13ii_05	93.1142	6.06711	0.232419	0.102433	0.089833	99.606
RJC140_13ii_06	91.801	6.86146	0.313726	0.073386	0.085857	99.1354
RJC140_13ii_07	92.4016	6.80217	0.034004	0.093749	0.060367	99.3919
RJC140_13ii_08	91.7532	8.30495	0.198817	0.062365	0.082369	100.402
RJC140_13ii_09	93.593	6.20263	0.241474	0.091805	0.08834	100.217

RJC140_13ii_10	93.7902	6.26576	0.199831	0.063502	0.035645	100.355
RJC140_13ii_11	94.2128	5.72288	0.156369	0.073418	0.093589	100.259
RJC140_13ii_12	93.2957	6.03684	0.041409	0.131342	0.010016	99.5153
RJC140_13ii_13	93.7867	6.15623	0.307425	0.085363	0.020696	100.356
RJC140_13ii_14left	92.6698	6.90927	0.232938	0.086922	0.050375	99.9493
RJC140_13ii_14right	91.5526	7.23012	0.024589	0.068899	0.08844	98.9646
RJC140_13ii_15	92.6408	7.00501	0.110821	0.074236	0.085035	99.9159
RJC140_13ii_16	94.6152	5.73761	0.288669	0.098036	0.052853	100.792
RJC140_13ii_17	92.0815	6.40266	0.135318	0.109431	0.084556	98.8135
RJC140_13ii_18	92.8966	6.60197	0.107348	0.05908	0.041219	99.7062
RJC140_13ii_19	73.7836	6.39051	0.07176	20.1223	0.047392	100.416
RJC140_13ii_20	93.7672	6.08232	0.170757	0.096864	0.080466	100.198
RJC140_13ii_21	93.8555	6.15445	0.245736	0.085559	0.001471	100.343
RJC140_13ii_22	93.3906	6.41028	0.10668	0.152113	0.00502	100.065
RJC140_13ii_23	93.4792	6.2148	0.138842	0.113676	0.039151	99.9857
RJC140_13iii_01	91.5596	7.04291	0.205238	0.085642	0.016314	98.9097
RJC140_13iii_02	94.0183	5.84625	0.193856	0.078973	0.097637	100.235
RJC140_13iii_03	93.743	6.38197	0.073757	0.07245	0.065393	100.337
RJC140_13iii_04	92.9096	6.1153	0.045312	0.117409	0.110909	99.2985
RJC140_13iii_05	93.7331	6.19192	0.155244	0.098057	0.066144	100.245
RJC140_13iii_06	83.7647	7.99701	0.221486	8.39583	0.030325	100.409
RJC140_13iii_07	75.4106	6.42397	0.037962	18.2918	0.101251	100.266
RJC140_13iii_08	76.0859	6.2013	0.140875	17.7047	0.089378	100.222
RJC140_13iii_09	83.241	7.46946	0.008276	9.09185	0.084012	99.8946
RJC140_13iii_10	76.1412	7.06053	0.166073	17.5569	0.097441	101.022
RJC140_13iii_11	78.2834	6.94767	0.05901	14.9784	0.037308	100.306
RJC140_13iii_12	75.2433	6.70643	0.059397	18.1986	0.038673	100.246
RJC140_13iii_13	75.2857	6.56919	0.150388	18.1597	0.004554	100.17
RJC140_13iii_14	84.8551	8.01128	0.22976	7.47188	0.039229	100.607
RJC140_13iii_15	75.49	6.68742	0.073227	17.8915	0.022609	100.165
RJC140_13iii_16	94.0702	6.06512	0.03984	0.083392	0.082476	100.341
RJC140_13iii_17	91.9262	6.73436	0.203872	0.075371	0.07007	99.0098
RJC140_13iii_18	93.1213	5.9491	0.228831	0.143471	0.024919	99.4676
RJC140_13iii_19	76.2774	6.73388	0.083753	17.2819	0.048524	100.425
RJC140_13iii_20	76.5783	6.75417	0.054171	17.0823	0.04469	100.514
RJC140_14_01	94.0087	6.12892	0.195154	0.10572	0.146791	100.585
RJC140_14_03	93.8481	5.78542	0.21191	0.116239	0.067686	100.029
RJC140_14_04	91.6987	6.3103	0.111301	0.173456	0.049051	98.3428
RJC140_14_05	76.2282	6.46104	0.09721	18.2962	0.042449	101.125
RJC140_14_02	93.5076	5.73953	0.178669	0.071132	-0.03344	99.4634
RJC140_14_06	93.6572	5.73595	0.055171	0.077921	0.109443	99.6357
RJC140_14_07	93.6485	5.97397	0.115196	0.075142	0.068441	99.8812
RJC140_14_08	92.7305	6.83229	0.108796	0.444824	0.061604	100.178
RJC140_14_09	93.8271	6.71995	0.029977	0.085363	0.065775	100.728
RJC140_14_10a	94.3929	5.93476	0.175007	0.107983	0.049225	100.66
RJC140_14_10b	94.4333	5.91337	0.107989	0.111828	0.106949	100.673



RJC140_14_11	85.6728	7.37806	0.021336	7.8981	0.046842	101.017
--------------	---------	---------	----------	--------	----------	---------

*Table A3.5 – EPMA compositional data for liberated gold particles from the Deer Cove prospect*

SAMPLE CODE	Au WT%	Ag WT%	Hg WT%	Cu WT%	Pd WT%	TOTAL
RJC141_11_1	73.4701	6.95624	0.120848	20.0094	0.098589	100.655
RJC141_11_2	87.0199	12.4574	1.08388	0.056058	0.114176	100.732
RJC141_11_3	86.8539	12.4252	0.976159	0.035295	0.046983	100.338
RJC141_11_4	86.1172	13.5878	0.628704	0.058443	0.040662	100.433
RJC141_11_5	86.5354	13.33	0.733532	0.05052	0.076789	100.726
RJC141_11_6	87.0755	12.2558	0.65974	0.056708	0.071946	100.12
RJC141_11_7	86.9152	12.7192	0.990964	0.050103	0.077029	100.753
RJC141_11_8	87.0696	13.6589	0.397407	0.100922	0.06839	101.295
RJC141_11_8	85.8217	13.2916	0.457044	0.08973	0.102957	99.763
RJC141_11_9	87.9011	11.3554	0.871474	0.058614	0.07911	100.266
RJC141_11_10	86.1607	13.3979	0.674196	0.056779	0.070667	100.36
RJC141_11_11	85.9994	13.6143	0.769437	0.037061	0.081066	100.501
RJC141_11_12	86.4677	13.1453	1.11271	0.05603	0.054977	100.837
RJC141_11_13	89.849	9.54668	1.10771	0.050099	0.059971	100.614
RJC141_11_14	88.6789	11.5929	0.853125	0.045247	0.103266	101.274
RJC141_11_15	90.3198	8.71458	1.1368	0.056401	0.042505	100.27
RJC141_11_16	86.6778	12.8763	0.842037	0.049036	0.061799	100.507
RJC141_11_17	86.5758	12.6525	1.10956	0.041735	0.101734	100.481
RJC140_11i_1	86.8283	13.05	0.76881	0.047621	0.05312	100.748
RJC140_11i_2	87.8816	12.548	0.548022	0.090901	0.029808	101.098
RJC140_11i_3	86.8826	12.9688	0.794879	0.067821	0.006997	100.721
RJC140_11i_4	86.944	13.266	0.790762	0.054512	0.056485	101.112
RJC140_11i_5	89.1633	10.5383	0.790029	0.075557	0.047594	100.615
RJC140_11i_6	87.9095	12.2292	0.938138	0.053418	0.040218	101.171
RJC140_11i_7	87.0642	13.1798	0.440064	0.06857	0.079891	100.833
RJC140_11i_8	90.3533	9.94692	0.726183	0.050744	0.044966	101.122
RJC140_11i_9	87.8717	12.3473	0.645706	0.068251	0.099597	101.033
RJC140_11i_10	85.5935	12.373	0.172033	0.075475	0.026992	98.241
RJC140_11i_11	88.9433	10.1998	1.01891	0.043325	0.059534	100.265
RJC140_11i_12	89.138	10.7089	0.807103	0.039301	0.032182	100.726
RJC140_11i_13	88.819	11.4903	0.445464	0.096935	0.036202	100.888
RJC140_11i_14	89.4643	11.297	0.480411	0.095025	0.077953	101.415
RJC140_11i_15	88.6256	10.1466	0.780007	0.04853	0.044839	99.6456
RJC140_11i_16	87.1652	13.1958	0.30252	0.078851	0.074304	100.817
RJC140_11i_17	87.4333	12.8696	0.556598	0.036013	0.017312	100.913
RJC140_11i_18	88.8351	10.7018	0.638075	0.053717	0.035644	100.264
RJC140_11i_19	89.2025	11.5969	0.213709	0.106008	0.074997	101.194
RJC140_11i_20	89.6068	10.5206	0.674928	0.062367	0.031499	100.896
RJC140_11i_21	87.7394	12.5258	0.764556	0.056388	0.067668	101.154
RJC140_11i_22	87.9198	12.2158	0.228827	0.08434	0.074684	100.523

RJC140_11i_23	89.074	9.71901	0.894547	0.052688	0.041413	99.7816
RJC140_11i_24	88.9732	11.6082	0.804917	0.047197	0.070808	101.504
RJC140_11i_25	87.2839	11.6848	0.699143	0.035495	0.060314	99.7636
RJC140_11ii_01	89.7929	9.95154	0.806254	0.065881	0.033672	100.65
RJC140_11ii_02	86.4485	13.2721	0.908726	0.03945	0.053595	100.722
RJC140_11ii_03	88.1833	12.3907	0.925036	0.054814	0.000087	101.554
RJC140_11ii_04	86.3924	14.0405	0.181489	0.070765	0.017169	100.702
RJC140_11ii_05	86.7902	13.3618	0.978883	0.041706	0.055624	101.228
RJC140_11ii_06	87.0212	12.4487	0.850981	0.067356	0.038662	100.427
RJC140_11ii_07	86.612	12.4354	0.777743	0.06484	0.097857	99.9878
RJC140_11ii_08	86.4099	13.4145	0.531359	0.040073	0.043933	100.44
RJC140_11ii_09	88.3616	10.9146	0.728221	0.04523	0.043174	100.093
RJC140_11ii_10	87.6858	11.5944	0.883238	0.053059	0.027079	100.244
RJC140_11ii_11	87.0958	13.0377	0.877083	0.055845	0.008318	101.075
RJC140_11ii_12	94.6824	5.37389	0.321084	0.081046	0.026657	100.485
RJC140_11ii_13	86.8704	12.5997	0.896599	0.052547	0.042043	100.461
RJC140_11ii_14	89.1393	11.2455	0.833772	0.038372	0.051425	101.308
RJC140_11ii_15	86.1741	10.7418	0.666142	0.086311	0.087516	97.7559
RJC140_11ii_16	93.5984	6.29037	0.281186	0.061682	0.015789	100.247
RJC140_11ii_17	86.8437	13.2276	0.786354	0.044073	0.056968	100.959
RJC140_11ii_18	87.9966	12.103	0.802257	0.043162	0.090445	101.036
RJC140_11ii_19	89.7494	9.39434	0.628306	0.058383	0.074327	99.9047
RJC140_11ii_20	92.4768	6.86004	0.229566	0.054039	0.044889	99.6654
RJC140_11ii_21	89.2426	10.0738	0.73401	0.055134	0.057293	100.163
RJC140_11ii_22	88.2605	12.0776	0.606734	0.060192	0.059424	101.065
RJC140_11ii_23	88.7062	11.19	0.918088	0.052333	0.043752	100.91
RJC140_11iii_01	85.3207	12.405	0.85358	0.036696	0.055744	98.6717
RJC140_11iii_02	95.2622	5.15089	0.281096	0.089644	0.041367	100.825
RJC140_11iii_03	88.6007	11.8942	0.933053	0.061041	0.014244	101.503
RJC140_11iii_04	88.2335	11.8156	0.969939	0.044301	0.022763	101.086
RJC140_11iii_05	87.3551	11.1101	0.810066	0.069913	-0.00511	99.3401
RJC140_11iii_06	87.6139	13.0567	0.675306	0.039001	0.044133	101.429
RJC140_11iii_07	87.6466	12.2618	0.80361	0.050092	0.009586	100.772
RJC140_11iii_08	89.1535	11.2983	0.668076	0.055956	0.01197	101.188
RJC140_11iii_09	87.6112	12.7636	0.69519	0.045021	0.106531	101.222
RJC140_11iii_10	87.4392	13.0105	0.572585	0.06304	0.072575	101.158
RJC140_11iii_11	86.9518	12.9411	0.954507	0.067056	0.077952	100.992
RJC140_11iii_12	87.4907	12.3795	0.893725	0.047111	0.035023	100.846
RJC140_11iii_13	89.859	11.5658	0.718819	0.043077	0.112813	102.3
RJC140_11iii_14	87.6075	12.7034	0.478203	0.056558	0.038052	100.884
RJC140_11iii_15	86.6819	12.3779	0.716954	0.063718	0.06045	99.9009
RJC140_11iii_16	89.8583	10.3183	0.734335	0.05394	0.06436	101.029
RJC140_11iii_17	89.2965	11.1518	0.811883	0.068876	0.036069	101.365
RJC140_11iii_18	87.4649	12.6653	1.03448	0.057208	0.058087	101.28
RJC140_11iii_19	86.0596	12.9191	0.669959	0.046227	0.097148	99.792
RJC140_11iii_20	87.8958	12.4042	0.871269	0.045804	0.052791	101.27

RJC140_11iii_21	88.1469	13.2612	0.399855	0.08337	0.055639	101.947
RJC140_11iii_22	89.1911	10.0485	0.908948	0.045818	0.066003	100.26
RJC140_11iii_23	89.597	10.1799	1.05504	0.039459	0.00108	100.873
RJC140_11iii_24	85.2334	12.4901	0.162545	0.119135	0.039562	98.0448
RJC140_11iii_25	87.9335	13.1069	0.385939	0.072274	0.081831	101.581

*Table A3.6 – EPMA compositional data for in-situ gold particles from the Deer Cove prospect*

SAMPLE CODE	Au WT%	Ag WT%	Hg WT%	Cu WT%	Pd WT%	Fe WT%	S WT%	TOTAL
DC site 3.1	89.0107	8.67595	0.560385	0.12413	-0.02951	2.30438	0.278754	100.925
DC site 1.1	87.846	8.68516	0.228683	0.076597	-0.18055	2.4225	0.501261	99.5796
DC site 2.1	88.3285	8.70998	0.190599	0.104344	-0.14923	2.77762	0.776029	100.738
DC site 4.1	87.9187	8.47601	0.138932	0.099113	-0.12444	2.79218	0.318582	99.619
DC site 4.1a	88.8904	8.09748	0.461278	0.096174	-0.10928	1.76673	0.264169	99.467
DC site 5.1	87.829	8.50823	0.644185	0.074815	-0.01337	2.30262	0.129011	99.4745
DC site 6.1	87.2666	8.61817	0.599418	0.064376	-0.07663	3.25195	0.478724	100.203
DC site 7.1a	90.0408	8.98583	0.693059	0.058337	-0.05147	1.80536	-0.06194	101.47
DC site 8.1	90.6	9.14218	0.747295	0.125256	-0.04654	0.600326	0.19037	101.359
DC site 8.2	90.0235	9.02953	0.591075	0.122127	-0.08348	0.870612	0.080114	100.634
DC 2 3.1	88.3754	10.4748	0.042106	0.03219	-0.07567	0.947104	0.160225	99.9562
DC 2 3.2	85.6944	11.6669	0.206134	0.039567	-0.07377	0.955244	0.232687	98.7212
DC 2 3.3	85.5998	12.4502	0.253224	0.038954	-0.0195	1.29333	0.036861	99.6529
DC 2 2.1	81.8856	12.4716	0.213009	0.095048	-0.09753	3.88133	0.589106	99.0382
DC 2 1.1	82.7998	13.1316	0.157797	0.048291	-0.08287	3.39802	2.61612	102.069
DC 2 7.1b	88.2528	5.76179	0.164342	0.064997	-0.0869	3.99967	1.76591	99.9226
DC 2 6.1a	86.9592	12.6619	0.190247	0.044891	-0.0207	1.64071	0.339027	101.815

## **Appendix IV – Geochronology data**

This appendix provides the raw data obtained from the in-situ LA-ICP-MS U-Th-Pb isotope analysis of monazite, xenotime and titanite grains from the Stog' er Tight, Argyle, Romeo & Juliet, and Deer Cove gold occurrences. BSE and CL images for each analysed grain together with the location of each analytical spot are also presented. Large scale images that display the surrounding alteration minerals are also included to provide the paragenetic context of each analysed grain.

<b>Abbreviations</b>	
<b>LA-ICP-MS</b>	laser-ablation inductively-coupled-plasma mass-spectrometer
<b>U</b>	uranium
<b>Th</b>	thorium
<b>Pb</b>	lead
<b>Y</b>	yttrium
<b>Sm</b>	samarium
<b>BSE</b>	backscattered electron microscope
<b>CL</b>	cathodoluminescence
<b>ppm</b>	parts per million
<b>1s %</b>	confidence level of one sigma (68%)
<b>Mnz</b>	monazite
<b>Xtm</b>	xenotime
<b>Tit / Ttn</b>	titanite
<b>Chl</b>	chlorite
<b>Ser</b>	sericite (fine grained muscovite/phengite)
<b>Rt</b>	rutile
<b>Ank</b>	ankerite
<b>Qtz / Q</b>	quartz
<b>Py</b>	pyrite
<b>Cal</b>	calcite
<b>Ab</b>	albite
<b>Zr</b>	zircon
<b>Ap</b>	apatite
<b>Cpy</b>	chalcopyrite
<b>Au</b>	gold
<b>EPMA</b>	electron probe micro analyzer
<b>WDS</b>	wavelength dispersive X-ray spectroscopy

**AIV.1. Monazite data****AIV.1.1. Stog'er Tight***Table A4.1 – U-Th-Pb isotope ratios recorded in the Stog'er Tight monazites (red rows correspond to the rejected analysis spots)*

Sample code	$^{207}\text{Pb}/^{235}\text{U}$	1s %	$^{206}\text{Pb}/^{238}\text{U}$	1s %	$^{208}\text{Pb}/^{232}\text{U}$	1s %	$^{232}\text{Th}/^{238}\text{U}$	1s %
<b>BN215_S9_M1</b>	<b>0.475506</b>	<b>3.215029</b>	<b>0.049755</b>	<b>2.114596</b>	<b>0.019333</b>	<b>1.647793</b>	<b>51.047409</b>	<b>2.896417</b>
BN215_S9_M2	0.590057	3.188934	0.050364	2.152878	0.019994	1.644290	26.091625	2.930766
BN215_S9_M3	0.543449	3.040661	0.052988	2.219240	0.019512	1.561243	21.057200	2.869090
BN215_S9_M4	0.536169	2.125333	0.057687	1.598273	0.020426	1.610125	15.166050	2.447815
BN215_S9_M5	0.728350	3.819935	0.046135	2.196773	0.020013	1.599335	28.657256	3.065250
BN215_S9_M6	0.508403	3.516407	0.048137	1.952305	0.020122	1.791602	18.278135	2.894773
BN215_S11_M1	0.555292	3.573751	0.055486	2.204206	0.019503	1.647496	41.015973	5.339907
<b>BN215_S13_M1</b>	<b>0.667692</b>	<b>2.588624</b>	<b>0.059325</b>	<b>1.732061</b>	<b>0.023593</b>	<b>1.545681</b>	<b>7.483363</b>	<b>5.818579</b>
<b>BN215_S13_M2</b>	<b>0.759118</b>	<b>5.175979</b>	<b>0.058040</b>	<b>2.366916</b>	<b>0.025698</b>	<b>1.687733</b>	<b>13.395608</b>	<b>7.004645</b>
<b>BN215_S13_M3</b>	<b>1.298914</b>	<b>3.731978</b>	<b>0.055166</b>	<b>2.641104</b>	<b>0.023988</b>	<b>1.544454</b>	<b>21.270823</b>	<b>5.049577</b>
<b>BN215_S13_M4</b>	<b>1.034889</b>	<b>12.446036</b>	<b>0.056286</b>	<b>3.084081</b>	<b>0.019774</b>	<b>3.367353</b>	<b>28.330341</b>	<b>6.983629</b>
<b>BN215_S14_M1</b>	<b>2.142896</b>	<b>3.777900</b>	<b>0.052987</b>	<b>2.702242</b>	<b>0.025221</b>	<b>2.007577</b>	<b>10.455812</b>	<b>3.862678</b>
<b>BN215_S15_M1a</b>	<b>0.625319</b>	<b>3.203410</b>	<b>0.051221</b>	<b>2.174990</b>	<b>0.022164</b>	<b>1.747499</b>	<b>23.666940</b>	<b>4.405091</b>
<b>BN215_S15_M1b</b>	<b>1.262549</b>	<b>3.692232</b>	<b>0.057054</b>	<b>2.617886</b>	<b>0.022202</b>	<b>1.804022</b>	<b>22.282207</b>	<b>4.656096</b>
<b>BN215_S15_M2</b>	<b>0.860909</b>	<b>3.485924</b>	<b>0.055939</b>	<b>2.462938</b>	<b>0.024099</b>	<b>1.668227</b>	<b>6.077982</b>	<b>3.255242</b>
SOZ1_S4_M1	0.44930	5.73247	0.03924	3.63706	0.01879	1.91369	23.20600	0.31175
SOZ1_S4_M2a	0.51235	3.66151	0.03337	2.18161	0.01920	3.90751	12.84590	0.28228
SOZ1_S4_M2b	0.36769	4.75743	0.03363	2.29129	0.01894	3.36789	13.35930	0.26969
SOZ1_S4_M3a	0.34834	6.05870	0.02754	2.23717	0.01879	1.57758	89.54287	0.27359
SOZ1_S4_M3b	0.34582	5.06324	0.02816	3.13110	0.01958	1.84843	75.70759	0.27679
<b>SOZ1_S5_M1a</b>	<b>0.368416</b>	<b>4.0654739</b>	<b>0.037989</b>	<b>2.099025</b>	<b>0.019681</b>	<b>6.932446</b>	<b>3.59131295</b>	<b>0.298619</b>
SOZ1_S5_M1b	0.36024	5.44935	0.03458	2.68890	0.01968	4.52498	8.09154	0.28252
<b>SOZ1_S5_M1c</b>	<b>0.70012</b>	<b>4.77006</b>	<b>0.03463</b>	<b>3.14525</b>	<b>0.02289</b>	<b>4.19551</b>	<b>5.56420</b>	<b>0.31448</b>
SOZ1_S6_M1a	0.54526	7.34236	0.03267	6.29130	0.02113	2.71377	57.33970	0.35897

<b>SOZ1_S6_M1b</b>	1.08059	13.71148	0.03656	5.55092	0.02119	5.44108	45.89794	0.29814
SOZ1_S6_M1c	0.37169	5.47113	0.03416	3.60360	0.02006	2.45065	26.27166	0.34500
SOZ1_S6_M1d	0.41309	5.84313	0.02443	3.90310	0.01949	1.39995	64.61097	0.32783
SOZ1_S6_M1e	0.27066	5.77329	0.02142	2.85989	0.01933	1.59250	75.56488	0.28289
SOZ1_S6_M2a	0.44463	4.26812	0.04065	2.91835	0.01988	1.72022	45.16603	0.30731
SOZ1_S6_M2b	0.66370	3.87689	0.03905	2.64677	0.01932	1.85002	46.57442	0.29102
SOZ1_S8_M1a	0.33393	4.56118	0.03920	3.64124	0.01977	1.69701	48.13117	0.33895
SOZ1_S8_M1b	0.49745	7.09904	0.04670	3.53208	0.01982	2.19647	38.81480	0.31338
SOZ1_S8_M1c	0.36401	8.68484	0.03539	6.78780	0.02116	1.74332	42.13356	0.29813
<b>SOZ1_S8_M1d</b>	<b>0.25628</b>	<b>9.16775</b>	<b>0.02411</b>	<b>4.89021</b>	<b>0.01965</b>	<b>2.23238</b>	<b>52.24791</b>	<b>0.26756</b>
SOZ1_S10_M1a	0.46121	5.68841	0.04556	3.80301	0.01971	2.11016	29.19624	0.31245
SOZ1_S10_M1b	0.48639	4.82850	0.03775	2.34755	0.02039	1.98410	39.17592	0.28421
<b>SOZ1_S10_M2</b>	<b>7.32025</b>	<b>12.81826</b>	<b>0.10167</b>	<b>11.05921</b>	<b>0.02170</b>	<b>3.20724</b>	<b>65.72506</b>	<b>0.27574</b>
SOZ1_S13_M1	0.80308	5.94412	0.04349	3.03187	0.01875	4.22069	14.97276	0.34147
<b>SOZ1_S13_M2a</b>	<b>0.59182</b>	<b>9.86333</b>	<b>0.04554</b>	<b>2.60924</b>	<b>0.02005</b>	<b>5.35627</b>	<b>8.61581</b>	<b>0.42074</b>
<b>SOZ1_S13_M2b</b>	<b>0.59534</b>	<b>8.87165</b>	<b>0.04315</b>	<b>2.69574</b>	<b>0.01861</b>	<b>2.86754</b>	<b>23.19669</b>	<b>0.40568</b>
SOZ1_S15_M1	0.67751	4.39829	0.04558	2.18531	0.01999	2.14122	48.89818	0.28323
<b>SOZ1_S15_M2</b>	<b>1.11425</b>	<b>7.65372</b>	<b>0.03847</b>	<b>4.49560</b>	<b>0.02204</b>	<b>2.05421</b>	<b>59.44578</b>	<b>0.27484</b>
<b>SOZ1_S16_M1</b>	<b>0.45424</b>	<b>5.82257</b>	<b>0.03872</b>	<b>3.12459</b>	<b>0.01920</b>	<b>2.69925</b>	<b>34.45895</b>	<b>0.29795</b>
SOZ1_S16_M2	0.50358	4.49770	0.02900	2.61898	0.01964	1.78693	61.83356	0.30854
SOZ1_S17_M1	0.70553	5.85059	0.03664	4.15451	0.02055	2.48667	47.41326	0.30215
SOZ2_S15_M1a	0.51554	5.00838	0.04266	2.37736	0.01996	3.00344	18.20820	0.29674
SOZ2_S15_M1b	0.41348	5.57105	0.04375	3.32954	0.01925	2.94832	18.98837	0.29829
<b>SOZ2_S19_M1</b>	<b>0.35069</b>	<b>9.32147</b>	<b>0.02806</b>	<b>5.40977</b>	<b>0.02222</b>	<b>5.41126</b>	<b>6.84873</b>	<b>0.29838</b>
<b>SOZ2_S23_M1</b>	<b>7.24945</b>	<b>9.68772</b>	<b>0.10822</b>	<b>8.07149</b>	<b>0.02868</b>	<b>4.10359</b>	<b>16.68116</b>	<b>0.30461</b>
SOZ2_S25_M1	0.72339	7.51846	0.03903	3.81901	0.01948	2.50345	15.18175	0.30259
SOZ2_S27_M1a	0.29586	6.75577	0.02808	4.39921	0.02096	1.98832	40.24843	0.33089
SOZ2_S27_M1b	0.30388	7.13699	0.02200	6.11830	0.02062	1.95901	47.53645	0.30101
SOZ2_S27_M1c	0.21996	7.47658	0.01480	3.78602	0.02022	2.84786	48.52051	0.28249
SOZ2_S27_M1d	0.13857	8.88393	0.01071	4.06128	0.02072	2.25427	39.74625	0.28035

SOZ2_S27_M1e	0.13973	9.70576	0.01243	2.96221	0.02002	1.51157	55.59451	0.26970
SOZ2_S27_M1f	0.22357	8.09166	0.01868	4.39814	0.02051	1.95450	50.96301	0.28253
SOZ2_S27_M1g	0.17354	9.35349	0.01163	3.89862	0.02089	2.05849	35.88904	0.27453
SOZ2_S28_M1a	0.37803	4.95520	0.03601	3.02743	0.02062	2.21977	20.47678	0.27701
SOZ2_S28_M1b	0.29968	3.83372	0.03076	2.97110	0.02067	2.89693	14.04135	0.27011
SOZ2_S28_M1c	0.34793	7.39282	0.02581	4.18636	0.02054	2.32868	23.47506	0.27639
SOZ2_S28_M1d	0.93886	9.52637	0.03731	3.25377	0.02351	5.55798	18.42160	0.28810
SOZ2_S28_M1e	0.27875	4.52195	0.03362	2.41430	0.02264	6.24366	4.57193	0.27604
SOZ2_S28_M1f	0.41349	3.18164	0.04706	1.84126	0.02059	3.85566	9.98824	0.27434
SOZ2_S28_M1g	0.53096	4.74566	0.04953	2.44917	0.02051	2.88952	9.91298	0.27590
SOZ2_S29_M1	0.19707	9.95140	0.01888	6.50576	0.02042	2.19366	44.71060	0.29140
SOZ2_S31_M1a	0.43256	3.69395	0.03975	2.05784	0.02065	3.24143	9.06553	0.27745
SOZ2_S31_M1b	0.47699	5.18695	0.04047	3.67481	0.02136	2.85233	20.46843	0.28386
SOZ2_S31_M1c	0.44600	9.78231	0.02352	5.18518	0.02035	2.62090	33.80656	0.28337
SOZ2_S32_M1a	0.23302	6.16253	0.02422	2.81565	0.01988	2.21751	40.43815	0.28347
SOZ2_S32_M1b	0.22367	7.29948	0.01495	4.74325	0.01990	1.39980	78.10160	0.28555
SOZ2_S34_M1a	0.37677	5.71846	0.02212	4.02270	0.02282	3.32074	29.70781	0.29107
SOZ2_S34_M1b	0.21292	6.47112	0.01926	3.55541	0.01973	1.87486	65.46371	0.27891
SOZ2_S34_M2	0.24695	6.71964	0.02036	3.36515	0.01977	2.72202	38.07743	0.28440
SOZ2_S37_M1a	0.18282	6.72340	0.01957	3.05782	0.01952	3.45129	22.42620	0.27612
SOZ2_S37_M1b	0.25617	6.86698	0.02049	3.65497	0.01925	4.76151	19.92123	0.28415
SOZ2_S37_M1c	0.58850	10.52392	0.02777	5.32951	0.01989	2.48408	19.47965	0.34553
SOZ2_S37_M1d	0.21606	8.73454	0.02064	2.89013	0.01910	2.77865	19.79520	0.28826
SOZ2_S37_M1e	0.50427	7.15865	0.02809	3.72681	0.01959	3.38119	17.73434	0.27890

*Table A4.2 – U-Th-Pb contents recorded in the Stog'er Tight monazites (red rows correspond to the rejected analysis spots)*

Sample code	Th/U (ppm)	Pb (ppm)	Th (ppm)	U (ppm)
<b>BN215_S9_M1</b>	<b>41.04</b>	<b>63.87</b>	<b>3485.05</b>	<b>84.92</b>
BN215_S9_M2	20.51	35.02	1793.50	87.46
BN215_S9_M3	18.05	41.28	2091.74	115.90
BN215_S9_M4	13.15	46.13	2116.29	160.90
BN215_S9_M5	20.50	23.98	1196.96	58.39
BN215_S9_M6	13.73	21.70	1043.49	76.01
BN215_S11_M1	35.12	79.77	4368.04	124.37
<b>BN215_S13_M1</b>	<b>5.51</b>	<b>21.51</b>	<b>720.22</b>	<b>130.67</b>
<b>BN215_S13_M2</b>	<b>7.90</b>	<b>25.68</b>	<b>901.22</b>	<b>114.03</b>
<b>BN215_S13_M3</b>	<b>14.77</b>	<b>17.96</b>	<b>736.29</b>	<b>49.87</b>
<b>BN215_S13_M4</b>	<b>24.83</b>	<b>50.17</b>	<b>2696.53</b>	<b>108.60</b>
<b>BN215_S14_M1</b>	<b>6.58</b>	<b>10.97</b>	<b>353.74</b>	<b>53.75</b>
<b>BN215_S15_M1a</b>	<b>16.67</b>	<b>29.30</b>	<b>1321.96</b>	<b>79.28</b>
<b>BN215_S15_M1b</b>	<b>17.43</b>	<b>23.74</b>	<b>1045.06</b>	<b>59.97</b>
<b>BN215_S15_M2</b>	<b>4.16</b>	<b>11.09</b>	<b>344.84</b>	<b>82.80</b>
SOZ1_S4_M1	9.75	36.40	2171.57	222.66
SOZ1_S4_M2a	5.56	18.87	1069.30	192.19
SOZ1_S4_M2b	5.87	19.06	1108.47	188.80
SOZ1_S4_M3a	38.90	92.79	5867.13	150.83
SOZ1_S4_M3b	32.16	86.75	5357.38	166.61
<b>SOZ1_S5_M1a</b>	<b>1.606959</b>	<b>7.6916398</b>	<b>346.457</b>	<b>215.598</b>
SOZ1_S5_M1b	3.47	12.75	679.48	195.90
SOZ1_S5_M1c	2.47	9.05	399.27	161.90
SOZ1_S6_M1a	25.64	77.33	4593.99	179.18
<b>SOZ1_S6_M1b</b>	<b>20.71</b>	<b>53.59</b>	<b>3280.88</b>	<b>158.40</b>
SOZ1_S6_M1c	9.70	36.38	2145.44	221.08
SOZ1_S6_M1d	26.29	67.48	4320.92	164.35
SOZ1_S6_M1e	32.78	86.75	5406.93	164.93
SOZ1_S6_M2a	20.29	82.64	4847.99	238.89
SOZ1_S6_M2b	19.26	80.28	4748.12	246.52
SOZ1_S8_M1a	19.70	71.11	4176.38	211.95
SOZ1_S8_M1b	18.25	79.17	4809.87	263.61
SOZ1_S8_M1c	17.64	65.00	3738.61	211.88
<b>SOZ1_S8_M1d</b>	<b>22.43</b>	<b>69.01</b>	<b>4063.14</b>	<b>181.12</b>
SOZ1_S10_M1a	11.34	76.00	4356.41	384.21
SOZ1_S10_M1b	16.77	58.80	3390.27	202.16
<b>SOZ1_S10_M2</b>	<b>28.45</b>	<b>80.55</b>	<b>4498.58</b>	<b>158.14</b>
SOZ1_S13_M1	6.18	23.91	1352.54	219.01
<b>SOZ1_S13_M2a</b>	<b>2.24</b>	<b>14.07</b>	<b>606.38</b>	<b>271.00</b>
<b>SOZ1_S13_M2b</b>	<b>5.95</b>	<b>20.52</b>	<b>1136.62</b>	<b>190.93</b>
SOZ1_S15_M1	21.41	80.75	5032.77	235.10
<b>SOZ1_S15_M2</b>	<b>26.20</b>	<b>64.84</b>	<b>3651.36</b>	<b>139.38</b>
<b>SOZ1_S16_M1</b>	<b>13.61</b>	<b>29.63</b>	<b>1819.37</b>	<b>133.66</b>



SOZ1_S16_M2	25.96	67.74	4238.07	163.23
SOZ1_S17_M1	19.15	50.92	3057.52	159.66
SOZ2_S15_M1a	7.94	34.47	1950.32	245.62
SOZ2_S15_M1b	8.23	42.18	2402.24	291.91
SOZ2_S19_M1	3.03	6.41	298.00	98.32
SOZ2_S23_M1	7.22	42.87	1514.45	209.80
SOZ2_S25_M1	6.42	21.15	1186.58	184.96
SOZ2_S27_M1a	17.34	52.54	3011.85	173.67
SOZ2_S27_M1b	20.78	54.55	3186.89	153.40
SOZ2_S27_M1c	22.15	48.98	2926.40	132.13
SOZ2_S27_M1d	17.09	38.32	2196.73	128.53
SOZ2_S27_M1e	24.40	50.45	3031.77	124.25
SOZ2_S27_M1f	21.79	54.77	3237.91	148.62
SOZ2_S27_M1g	15.87	34.04	1946.00	122.61
SOZ2_S28_M1a	8.82	31.70	1777.46	201.60
SOZ2_S28_M1b	6.19	20.60	1121.68	181.14
SOZ2_S28_M1c	9.94	29.14	1615.14	162.46
SOZ2_S28_M1d	7.82	18.26	950.88	121.54
SOZ2_S28_M1e	2.00	8.30	376.49	187.78
SOZ2_S28_M1f	4.43	26.59	1365.93	308.55
SOZ2_S28_M1g	4.34	27.44	1373.37	316.10
SOZ2_S29_M1	19.09	45.27	2656.37	139.17
SOZ2_S31_M1a	3.89	16.98	867.91	223.35
SOZ2_S31_M1b	8.79	34.03	1823.67	207.42
SOZ2_S31_M1c	14.33	35.93	2080.12	145.11
SOZ2_S32_M1a	17.12	45.90	2738.09	159.92
SOZ2_S32_M1b	34.13	73.65	4580.66	134.23
SOZ2_S34_M1a	14.22	36.53	1943.55	136.71
SOZ2_S34_M1b	28.88	62.74	3852.47	133.41
SOZ2_S34_M2	17.28	35.44	2297.70	132.99
SOZ2_S37_M1a	9.84	21.76	1329.97	135.11
SOZ2_S37_M1b	8.76	20.07	1217.89	139.07
SOZ2_S37_M1c	7.76	20.28	1183.02	152.48
SOZ2_S37_M1d	8.26	21.26	1313.44	159.05
SOZ2_S37_M1e	8.27	16.91	1096.99	132.68

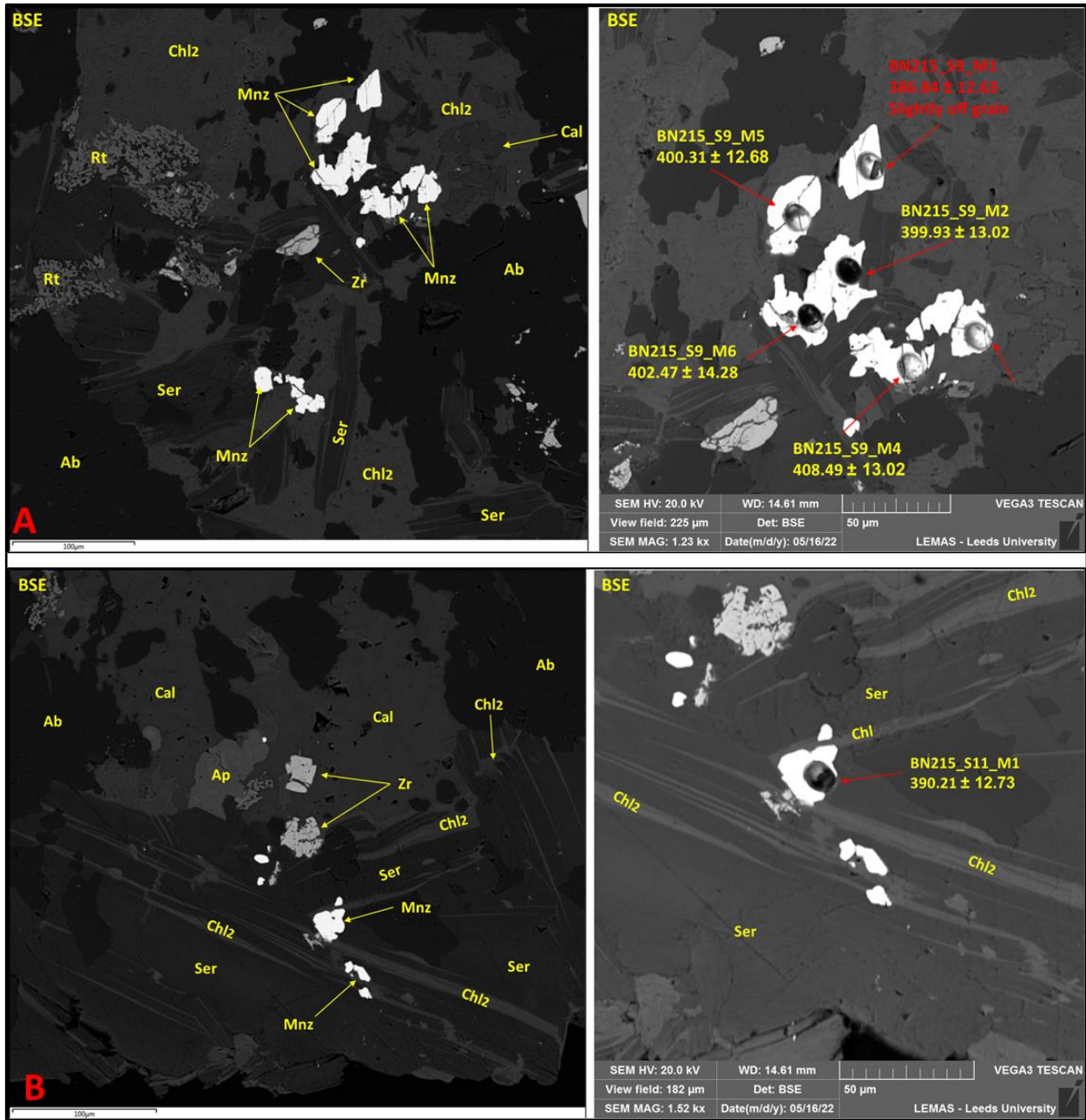
Table A4.3 – U-Th-Pb dates recorded in the Stog'er Tight monazites (red rows correspond to the rejected analysis spots)

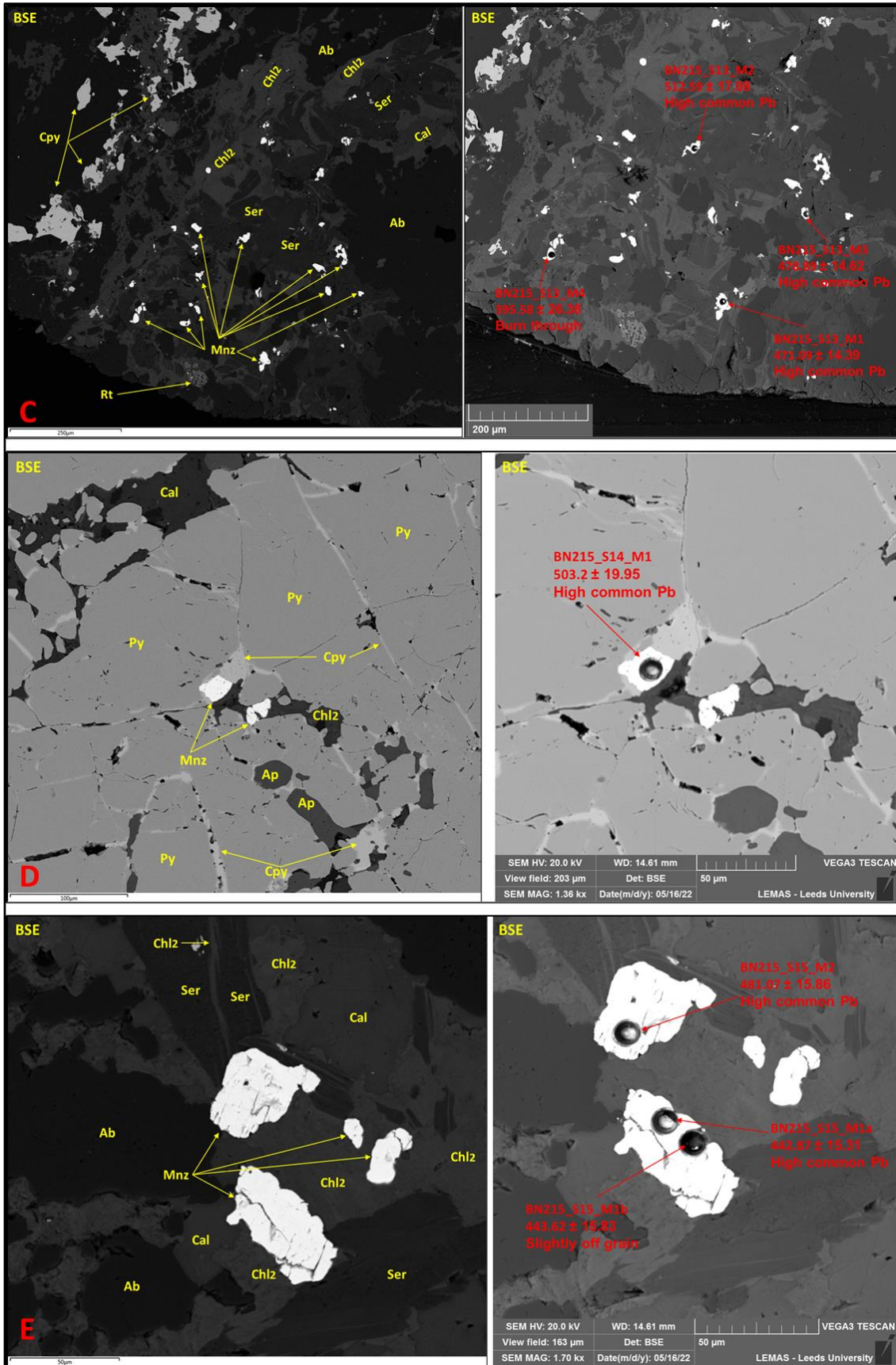
Sample code	No.	$^{208}\text{Pb}/^{232}\text{Th}$ Age (Ma)	Error ( $2\sigma$ )	$^{207}\text{Pb}/^{235}\text{U}$ Age (Ma)	Error ( $2\sigma$ )	$^{206}\text{Pb}/^{238}\text{U}$ Age (Ma)	Error ( $2\sigma$ )	$^{207}\text{Pb}/^{206}\text{Pb}$ Age (Ma)	Error ( $2\sigma$ )	Concordia Age (Ma)	Error ( $2\sigma$ )
<b>BN215_S9_M1</b>	1	<b>386.84</b>	<b>12.63</b>	394.99	21.04	313.02	12.92	908.09	158.53	333.95	11.23
BN215_S9_M2	2	399.93	13.02	470.9	24.03	316.76	13.31	1314.88	149.23	347.99	12.03
BN215_S9_M3	3	390.39	12.07	440.7	21.74	332.84	14.4	1051.91	151.7	363.01	12.34
BN215_S9_M4	4	408.49	13.02	435.9	15.06	361.54	11.24	850.46	110.55	386.81	9.2
BN215_S9_M5	5	400.31	12.68	555.58	32.69	290.75	12.49	1872.04	158.94	315.26	12.03
BN215_S9_M6	6	402.47	14.28	417.37	24.07	303.07	11.56	1110.79	160.66	322.09	10.64
BN215_S11_M1	7	390.21	12.73	448.46	25.91	348.11	14.94	1002.34	170.48	370.97	13.24
<b>BN215_S13_M1</b>	8	<b>471.09</b>	<b>14.39</b>	519.31	21.05	371.52	12.51	1236.6	122.16	405.29	11.12
<b>BN215_S13_M2</b>	9	<b>512.59</b>	<b>17.08</b>	573.5	45.36	363.69	16.74	1525.28	214.49	383.2	16.08
<b>BN215_S13_M3</b>	10	<b>478.89</b>	<b>14.62</b>	845.24	42.82	346.16	17.8	2565.19	152.93	386.39	17.38
<b>BN215_S13_M4</b>	11	<b>395.58</b>	<b>26.38</b>	721.37	128.54	353	21.19	2142.54	448.24	358.79	21.08
<b>BN215_S14_M1</b>	12	<b>503.2</b>	<b>19.95</b>	1162.76	52.31	332.83	17.53	3435.26	144.27	360.92	17.46
<b>BN215_S15_M1a</b>	13	<b>442.87</b>	<b>15.31</b>	493.18	25.03	322.01	13.66	1394.28	148.53	355.3	12.42
<b>BN215_S15_M1b</b>	14	<b>443.62</b>	<b>15.83</b>	829.05	41.84	357.68	18.22	2460.88	152.97	400.7	17.7
<b>BN215_S15_M2</b>	15	<b>481.07</b>	<b>15.86</b>	630.62	32.75	350.88	16.82	1825.96	154.81	394.49	15.74
SOZ1_S4_M1	16	376.07	14.26	376.79	36.09	248.12	17.71	1270.24	264.98	269.98	16.27
SOZ1_S4_M2a	17	384.2	29.74	420.03	25.19	211.61	9.08	1821.65	154.67	230.2	8.74
SOZ1_S4_M2b	18	379.05	25.29	317.94	25.97	213.23	9.61	1179.54	208.81	224.36	9.13
SOZ1_S4_M3a	19	376.07	11.76	303.47	31.79	175.13	7.73	1461.92	245.48	181.17	7.57
SOZ1_S4_M3b	20	391.73	14.34	301.57	26.42	179.02	11.06	1405.6	228.01	194.92	10.38
<b>SOZ1_S5_M1a</b>	21	<b>393.71</b>	<b>54.06</b>	318.48	22.23	240.36	9.9	938.15	187.61	252.26	9.16
SOZ1_S5_M1b	22	393.71	35.29	312.39	29.31	219.15	11.59	1083.32	243.73	230.47	10.91
<b>SOZ1_S5_M1c</b>	23	<b>457.21</b>	<b>37.93</b>	538.86	39.89	219.46	13.57	2306.98	196.21	241.61	13.23
SOZ1_S6_M1a	24	422.42	22.69	441.89	52.61	207.24	25.66	1971.71	344.65	242.35	24.01
<b>SOZ1_S6_M1b</b>	25	<b>423.61</b>	<b>45.62</b>	743.92	144.62	231.47	25.24	2938.84	478.08	238.83	25.15
SOZ1_S6_M1c	26	401.24	19.47	320.91	30.11	216.53	15.35	1170.01	259.43	235.93	13.95

SOZ1_S6_M1d	27	389.95	10.81	351.1	34.69	155.59	12	1994.93	249.79	172	11.57
SOZ1_S6_M1e	28	386.78	12.2	243.22	24.97	136.62	7.73	1460.02	244.94	144.77	7.46
SOZ1_S6_M2a	29	397.68	13.55	373.51	26.68	256.86	14.7	1180.38	204.44	281.18	13.2
SOZ1_S6_M2b	30	386.58	14.17	516.87	31.41	246.94	12.82	2004.05	166.7	275.03	12.29
SOZ1_S8_M1a	31	395.5	13.29	292.56	23.19	247.87	17.71	666.6	249.94	263.86	14.26
SOZ1_S8_M1b	32	396.49	17.25	409.97	47.89	294.23	20.32	1127.8	315.94	309.74	19.03
SOZ1_S8_M1c	33	423.01	14.6	315.2	47.07	224.19	29.91	1057.71	443.81	248.48	25.83
SOZ1_S8_M1d	34	393.12	17.38	231.66	37.98	153.58	14.84	1123.6	414.27	163.03	13.97
SOZ1_S10_M1a	35	394.31	16.48	385.1	36.46	287.2	21.37	1025.57	276.85	310.13	18.85
SOZ1_S10_M1b	36	407.78	16.02	402.45	32.09	238.87	11.01	1496.97	203.1	252.95	10.59
SOZ1_S10_M2	37	433.7	27.52	2151.28	229.02	624.19	131.59	4305.11	497.32	683.74	132.46
SOZ1_S13_M1	38	375.28	31.39	598.56	53.76	274.43	16.29	2150.09	233.06	292.31	15.97
SOZ1_S13_M2a	39	401.04	42.54	472.03	74.47	287.08	14.65	1513.19	385.12	292.41	14.48
SOZ1_S13_M2b	40	372.5	21.17	474.27	67.23	272.33	14.38	1625.3	344.89	279.02	14.18
SOZ1_S15_M1	41	399.86	16.96	525.27	36.07	287.33	12.28	1762.65	179.53	305.69	11.9
SOZ1_S15_M2	42	440.42	17.9	760.22	81.91	243.34	21.47	2906.07	287.69	259.86	21.29
SOZ1_S16_M1	43	384.2	20.55	380.24	36.93	244.89	15.02	1317.46	256.2	261.33	14.18
SOZ1_S16_M2	44	392.92	13.91	414.12	30.59	184.29	9.52	2042.07	184.01	199.39	9.26
SOZ1_S17_M1	45	410.94	20.23	542.09	49.15	231.97	18.93	2222.94	248.64	259.5	18.3
SOZ2_S15_M1a	46	399.26	23.75	422.17	34.6	269.3	12.54	1374.77	213.24	284.06	12
SOZ2_S15_M1b	47	385.19	22.5	351.38	33.09	276.04	17.99	885.07	268.34	292.04	16.06
SOZ2_S19_M1	48	443.97	47.53	305.24	49.15	178.4	19.04	1439.11	410.9	192.66	18.05
SOZ2_S23_M1	49	571.24	46.23	2142.61	172.89	662.4	101.62	4198.82	372.64	726.85	102.28
SOZ2_S25_M1	50	389.75	19.33	552.67	64.09	246.82	18.5	2156.54	294.33	262.55	18.15
SOZ2_S27_M1a	51	419.06	16.49	263.16	31.32	178.52	15.49	1106.01	322.27	193.79	14.11
SOZ2_S27_M1b	52	412.33	15.99	269.43	33.78	140.28	16.98	1627.42	349.57	163.13	15.55
SOZ2_S27_M1c	53	404.41	22.81	201.88	27.38	94.71	7.12	1762.4	306.36	100.6	6.94
SOZ2_S27_M1d	54	414.31	18.49	131.77	21.96	68.67	5.55	1504.85	369.14	72.16	5.4
SOZ2_S27_M1e	55	400.45	11.99	132.8	24.16	79.64	4.69	1234.25	398.12	81.43	4.61
SOZ2_S27_M1f	56	410.15	15.87	204.88	30.02	119.31	10.4	1356.13	355.15	127.57	9.92

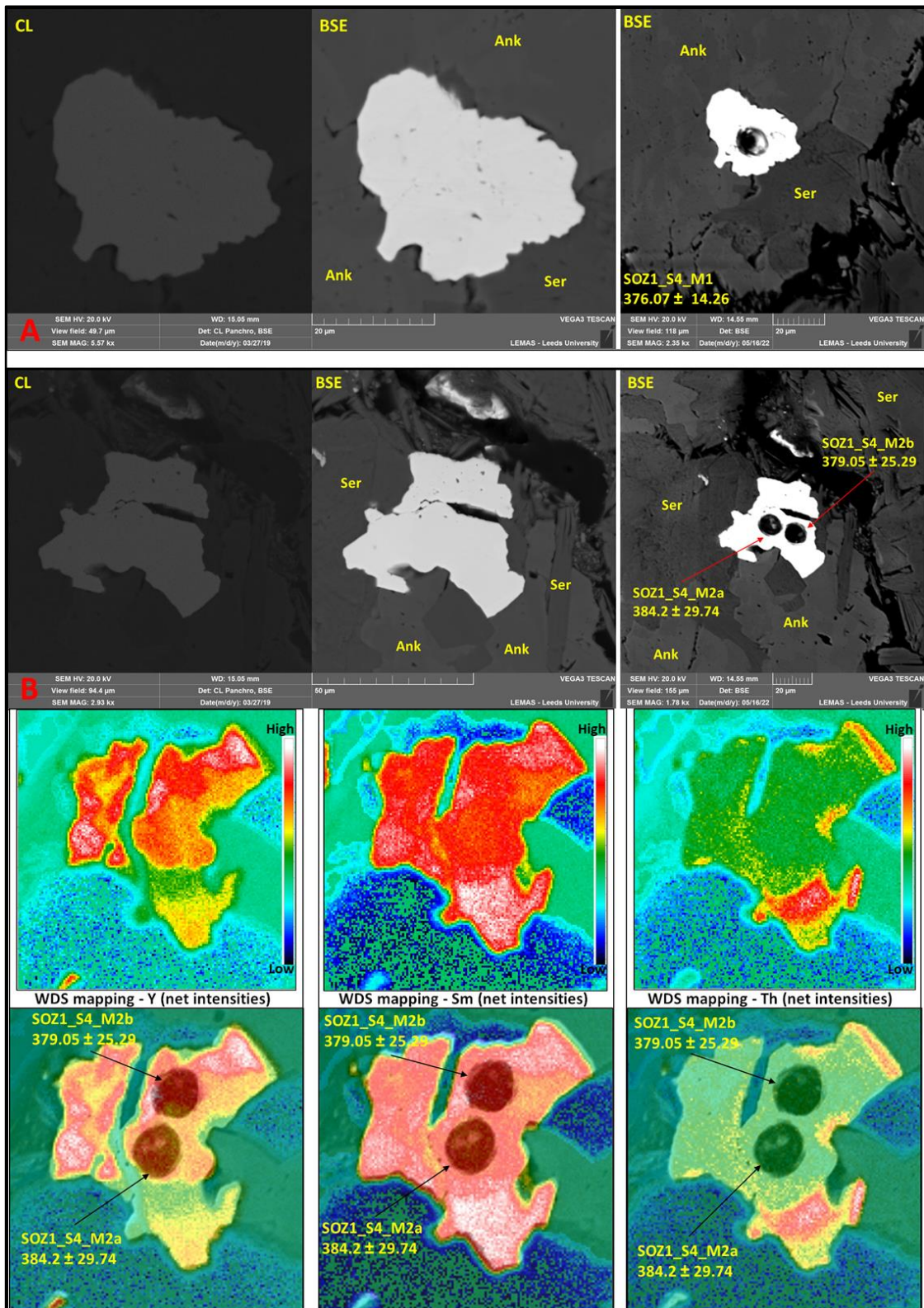
SOZ2_S27_M1g	57	<b>417.67</b>	<b>17.02</b>	162.49	28.09	74.54	5.78	1769.71	370.1	77.7	5.68
SOZ2_S28_M1a	58	<b>412.33</b>	<b>18.12</b>	325.59	27.61	228.05	13.57	1098.7	232.38	245.23	12.4
SOZ2_S28_M1b	59	<b>413.32</b>	<b>23.7</b>	266.15	17.95	195.3	11.43	947.58	198.59	214.59	9.82
SOZ2_S28_M1c	60	<b>410.75</b>	<b>18.94</b>	303.16	38.75	164.27	13.58	1582.01	317.8	177.09	13.01
SOZ2_S28_M1d	61	<b>469.45</b>	<b>51.58</b>	<b>672.29</b>	<b>93.68</b>	<b>236.14</b>	<b>15.09</b>	<b>2675.76</b>	<b>333.18</b>	<b>242.08</b>	<b>15.03</b>
SOZ2_S28_M1e	62	<b>452.27</b>	<b>55.85</b>	<b>249.67</b>	<b>20.02</b>	<b>213.16</b>	<b>10.12</b>	<b>608.38</b>	<b>221.66</b>	<b>220.34</b>	<b>9.1</b>
SOZ2_S28_M1f	63	<b>411.74</b>	<b>31.43</b>	351.39	18.9	296.45	10.67	732.53	155.73	309.08	9.41
SOZ2_S28_M1g	64	<b>410.15</b>	<b>23.46</b>	432.45	33.42	311.64	14.9	1140.45	212.39	329.19	13.88
SOZ2_S29_M1	65	<b>408.37</b>	<b>17.74</b>	182.64	33.27	120.57	15.54	1087.25	476.59	130.99	14.24
SOZ2_S31_M1a	66	<b>412.92</b>	<b>26.5</b>	364.99	22.65	251.28	10.14	1170.22	167.44	268.07	9.43
SOZ2_S31_M1b	67	<b>426.97</b>	<b>24.1</b>	<b>396.01</b>	<b>34.02</b>	<b>255.75</b>	<b>18.43</b>	<b>1326.5</b>	<b>246.15</b>	<b>283.53</b>	<b>16.68</b>
SOZ2_S31_M1c	68	<b>406.98</b>	<b>21.12</b>	374.47	61.27	149.86	15.36	2196.33	384.74	159.69	15.09
SOZ2_S32_M1a	69	<b>397.68</b>	<b>17.46</b>	212.69	23.65	154.27	8.58	921.82	278.52	160.62	8.13
SOZ2_S32_M1b	70	<b>398.07</b>	<b>11.04</b>	204.96	27.1	95.66	9.01	1774.53	317.75	105.16	8.64
SOZ2_S34_M1a	71	<b>455.83</b>	<b>29.93</b>	<b>324.66</b>	<b>31.78</b>	<b>141.04</b>	<b>11.22</b>	<b>2007.9</b>	<b>248.17</b>	<b>157.3</b>	<b>10.79</b>
SOZ2_S34_M1b	72	<b>394.7</b>	<b>14.66</b>	196	23.07	122.98	8.66	1201.39	291.05	131.26	8.19
SOZ2_S34_M2	73	<b>395.5</b>	<b>21.32</b>	224.1	27.03	129.93	8.66	1381.81	288.78	137.72	8.32
SOZ2_S37_M1a	74	<b>390.54</b>	<b>26.7</b>	170.48	21.1	124.94	7.57	861.02	306.53	129.85	7.16
SOZ2_S37_M1b	75	<b>385.19</b>	<b>36.33</b>	231.58	28.44	130.75	9.46	1439.77	296.56	139.62	9.07
SOZ2_S37_M1c	76	<b>397.87</b>	<b>19.57</b>	469.91	79.18	176.58	18.57	2387.49	401.69	186.83	18.33
SOZ2_S37_M1d	77	<b>382.22</b>	<b>21.04</b>	198.63	31.52	131.7	7.54	1092.99	368.49	135.01	7.36
SOZ2_S37_M1e	78	<b>391.93</b>	<b>26.25</b>	414.59	48.73	178.58	13.13	2100.66	283.45	190.26	12.87

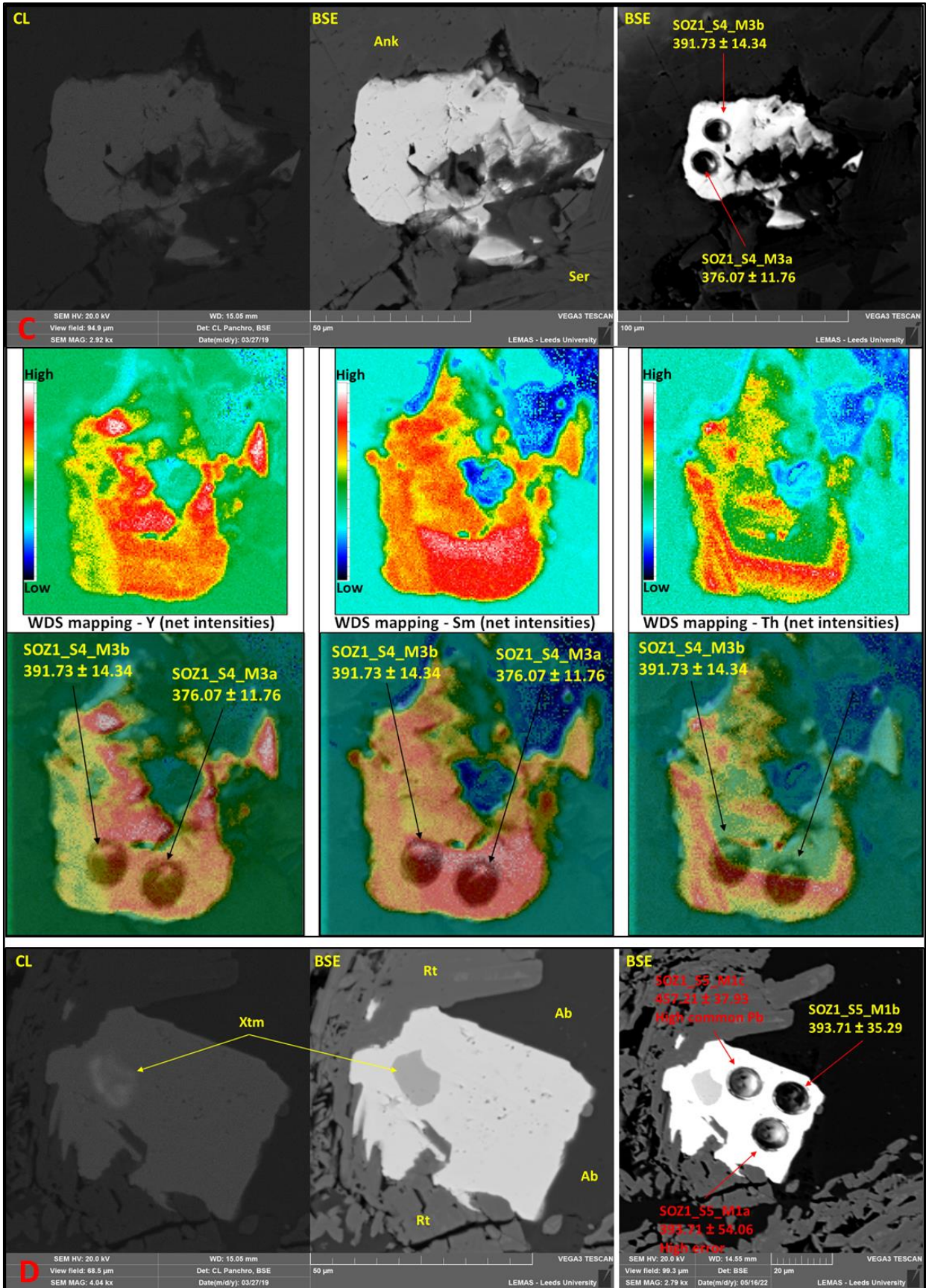
*Plate AIV.1 (next two pages) – BSE/CL images of analysed monazite grains from sample BN215 (Stog'er Tight deposit); red annotations correspond to the rejected analysis spots, whereas the yellow ones to the accepted analysis.*



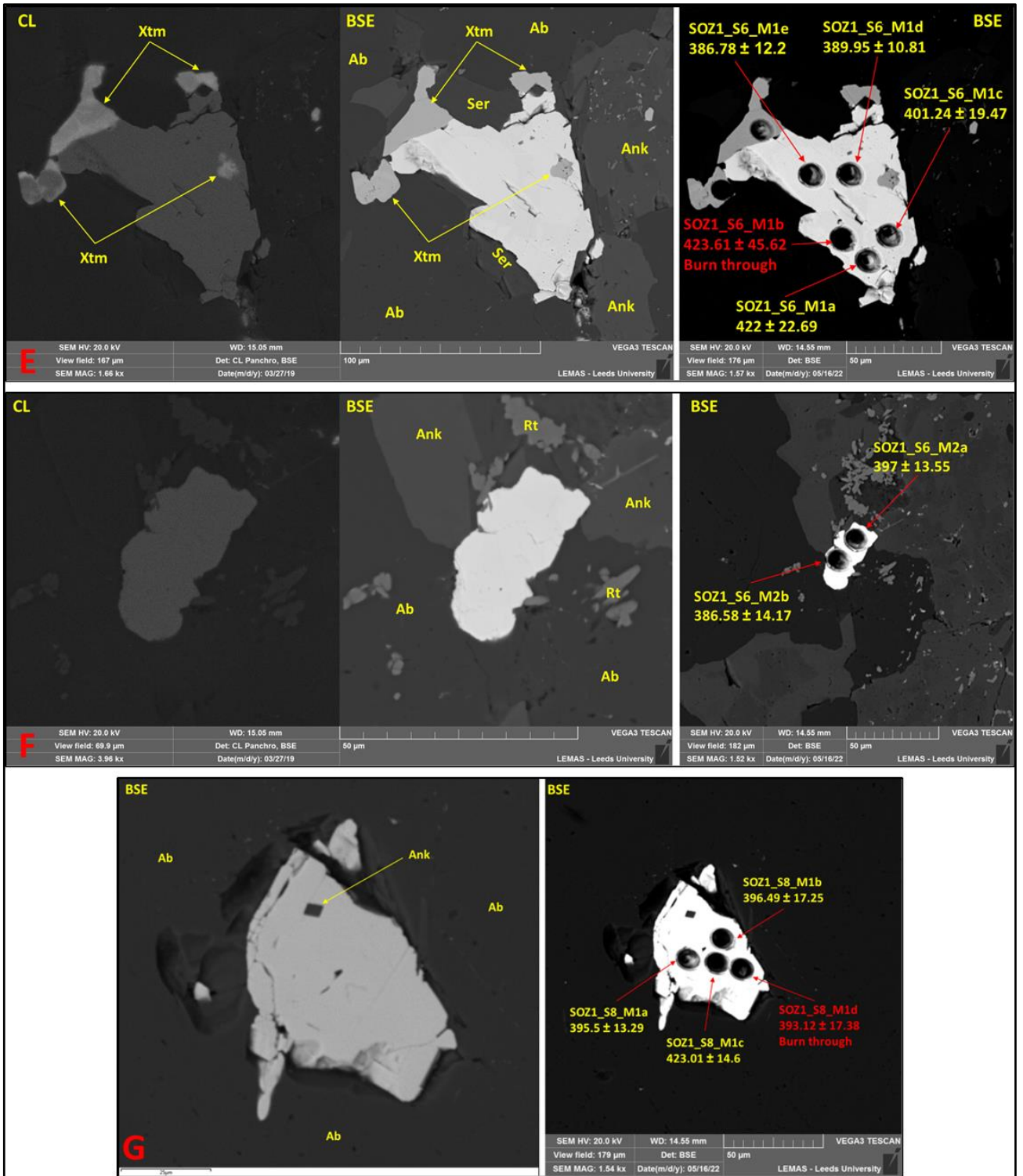


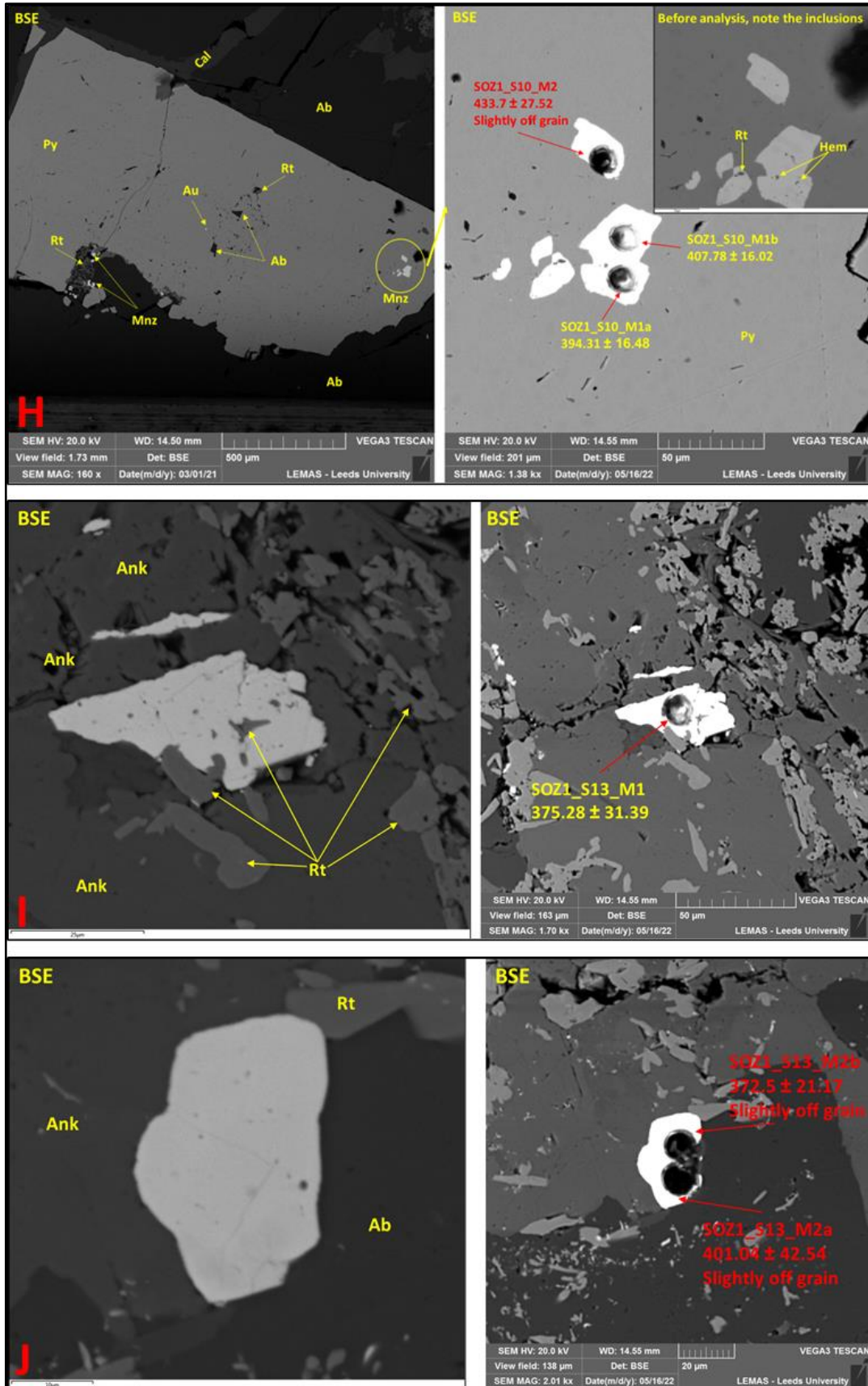
*Plate AIV.2 (next five pages) – BSE/CL images of analysed monazite grains from sample SOZ1 (Stog’er Tight deposit); red annotations correspond to the rejected analysis spots, whereas the yellow ones to the accepted analysis.*

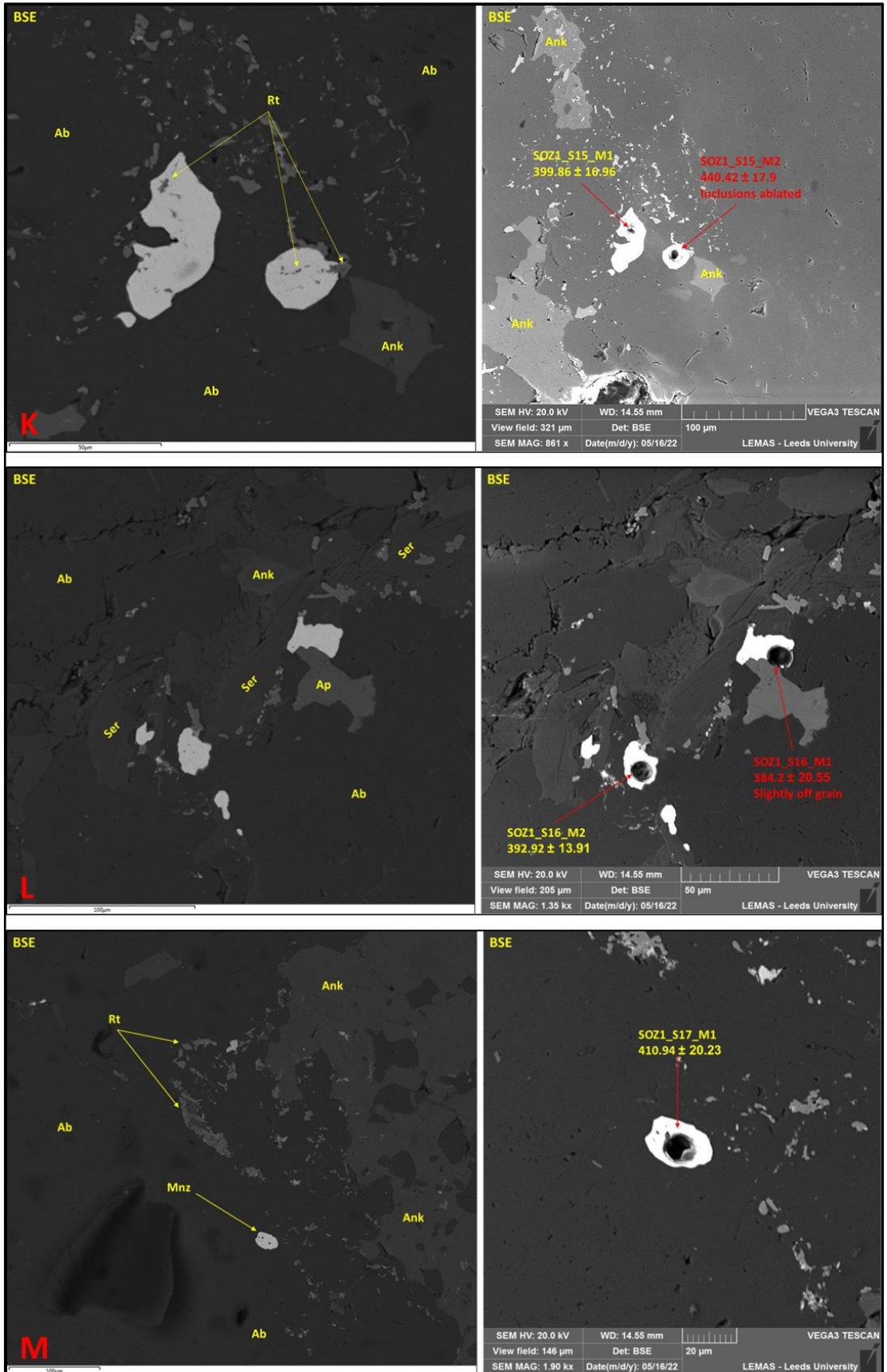




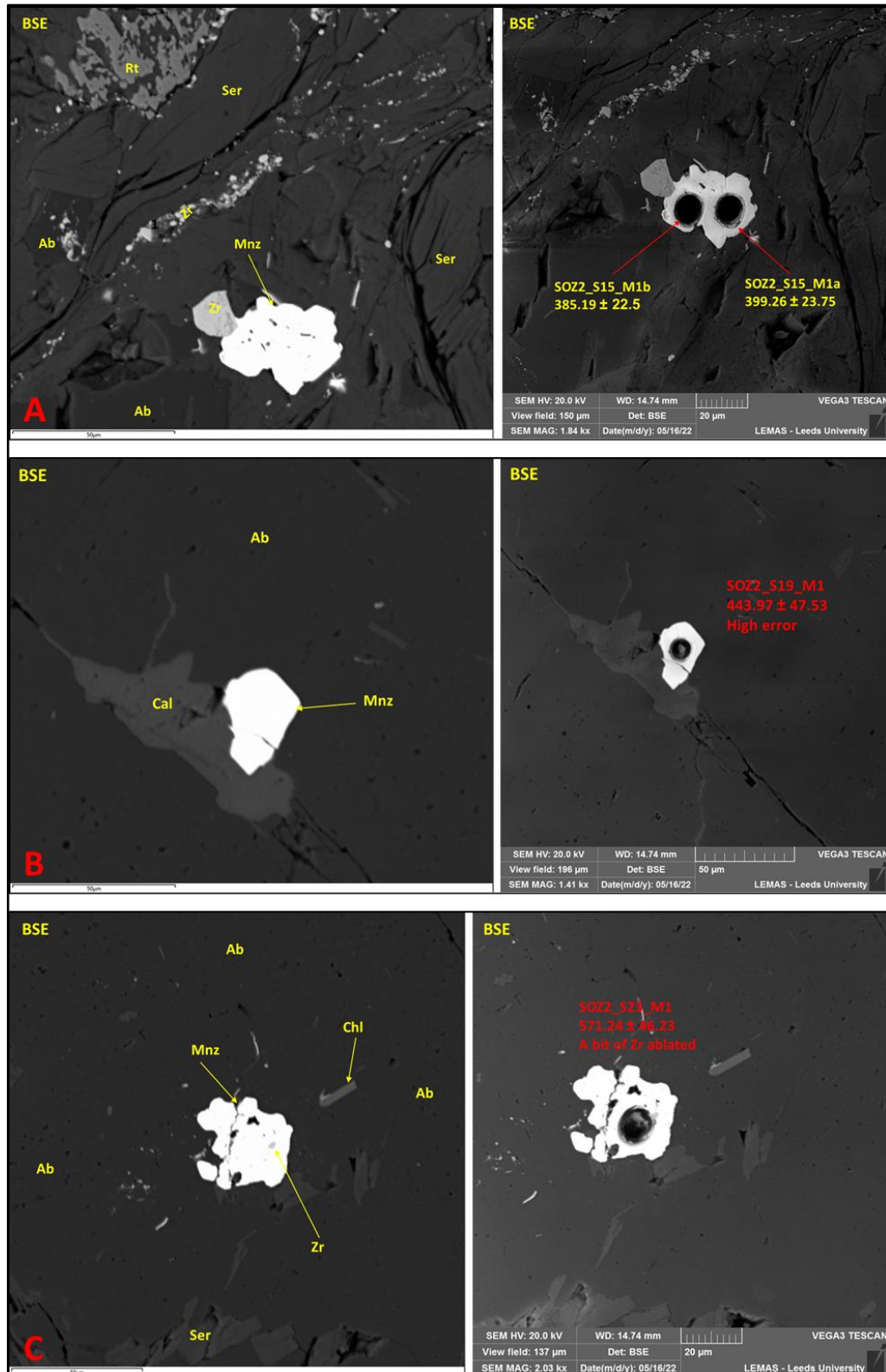


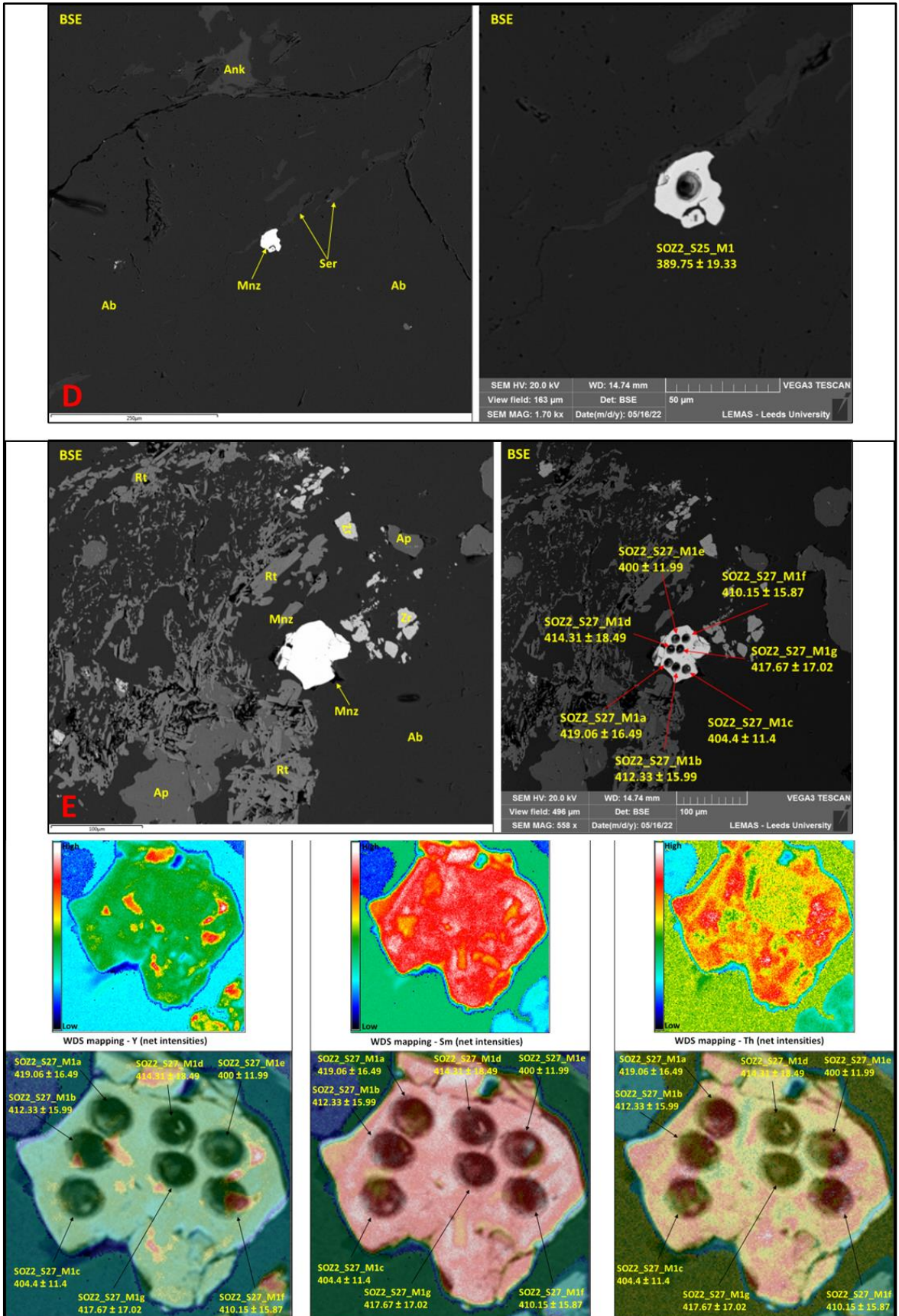


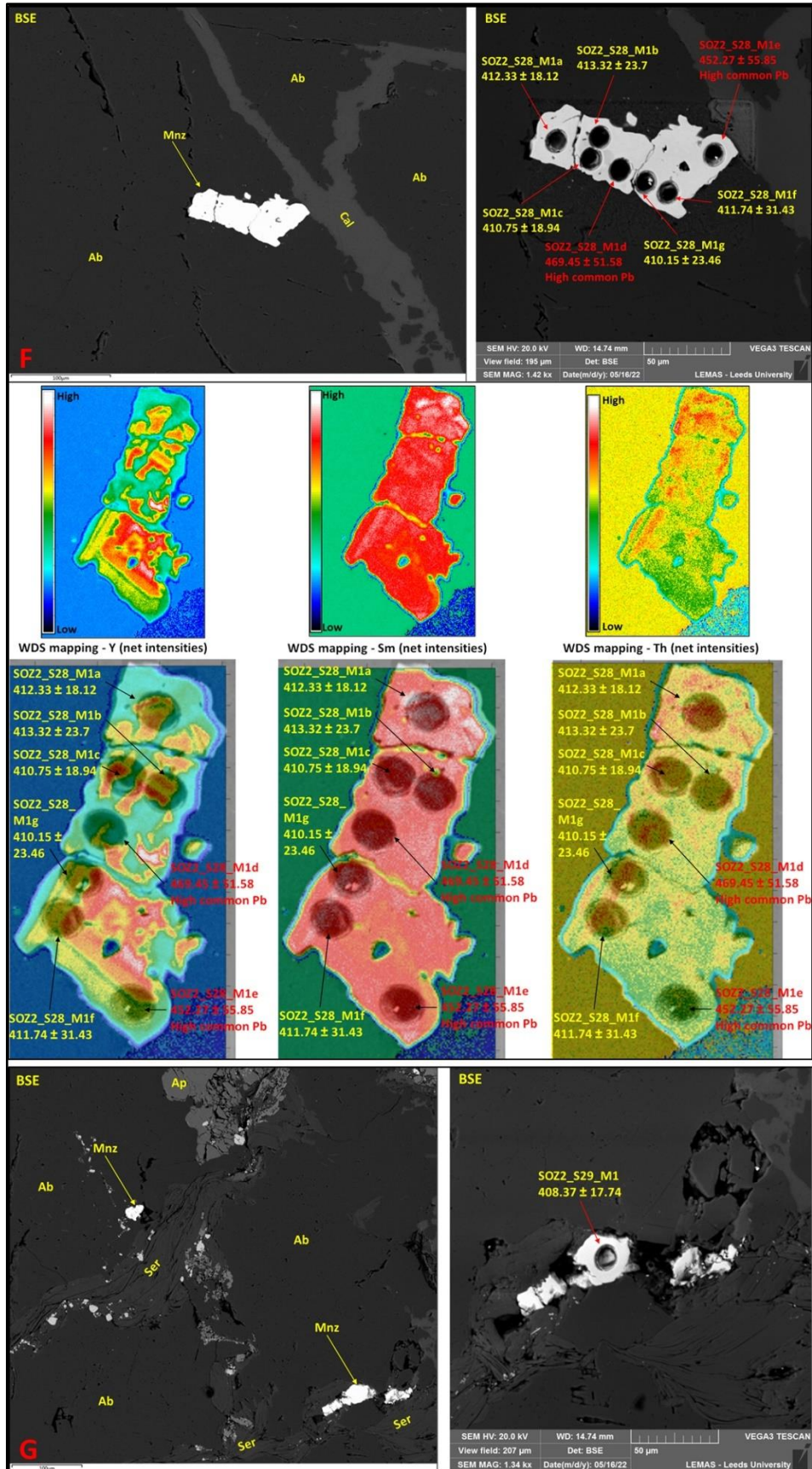


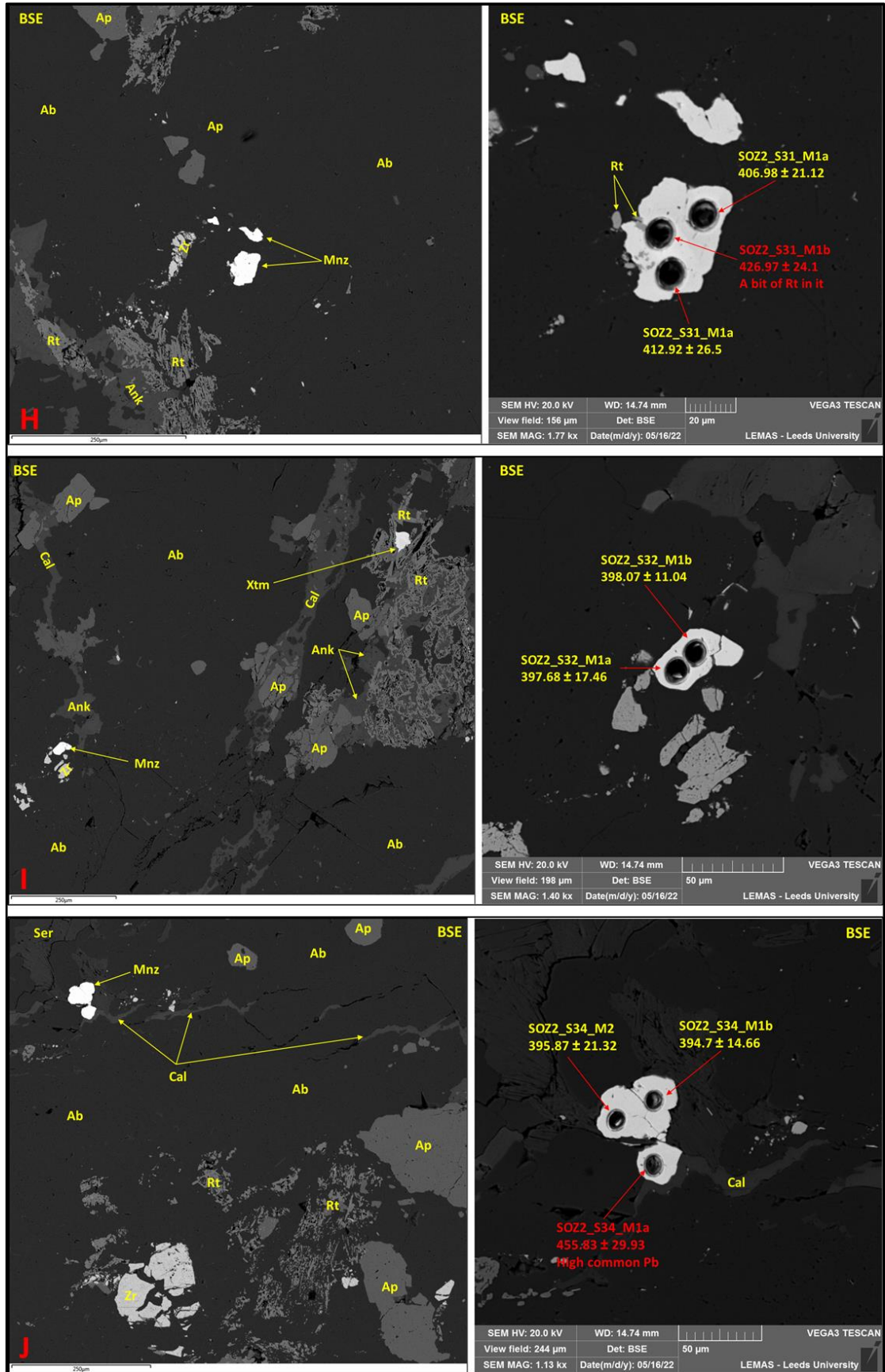


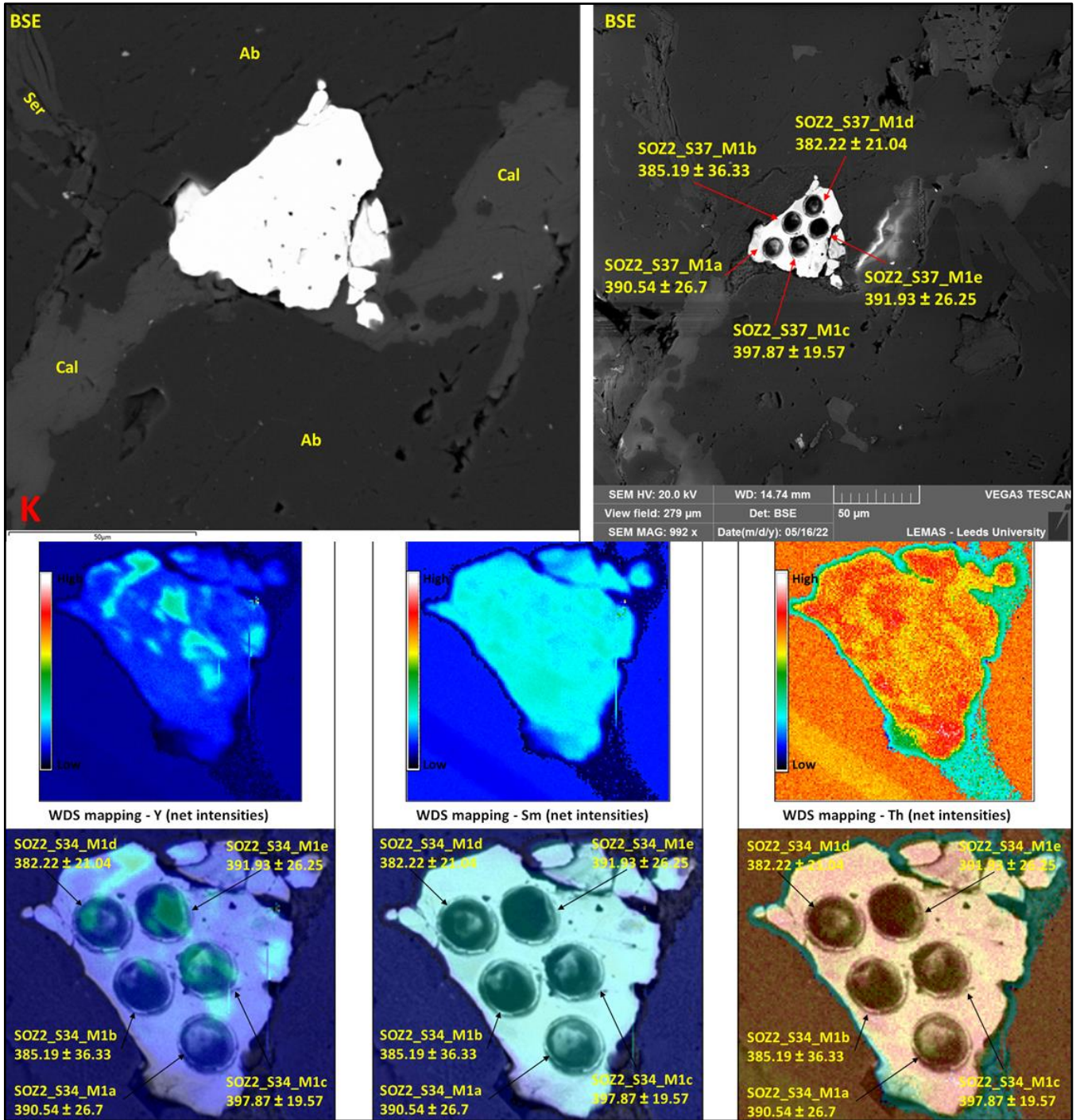
*Plate AIV.3 (next five pages) – BSE/CL images of analysed monazite grains from sample SOZ2 (Stog'er Tight deposit); red annotations correspond to the rejected analysis spots, whereas the yellow ones to the accepted analysis.*













## AIV.1.2. Argyle

Table A4.4 – U-Th-Pb isotope ratios recorded in the Argyle monazites (red rows correspond to the rejected analysis spots)

Sample code	$^{207}\text{Pb}/^{235}\text{U}$	1s %	$^{206}\text{Pb}/^{238}\text{U}$	1s %	$^{208}\text{Pb}/^{232}\text{U}$	1s %	$^{232}\text{Th}/^{238}\text{U}$	1s %
<b>AG3_S1_M1a</b>	<b>0.218753</b>	<b>9.978664</b>	<b>0.020507</b>	<b>3.111025</b>	<b>0.019824</b>	<b>1.800830</b>	<b>277.202974</b>	<b>4.176978</b>
AG3_S1_M1b	0.31756	6.0395773	0.018626	3.289314	0.021555	2.19622	311.956215	4.583876
<b>AG3_S1_M1c</b>	<b>3.373147</b>	<b>10.038371</b>	<b>0.040517</b>	<b>7.729021</b>	<b>0.020373</b>	<b>1.812661</b>	<b>285.098647</b>	<b>10.367459</b>
<b>AG3_S1_M1d</b>	<b>12.90300</b>	<b>12.51585</b>	<b>0.18629</b>	<b>11.13006</b>	<b>0.02138</b>	<b>4.46361</b>	<b>267.18325</b>	<b>0.31021</b>
<b>AG3_S1_M1e</b>	<b>43.33065</b>	<b>13.98884</b>	<b>0.44485</b>	<b>13.65223</b>	<b>0.02131</b>	<b>3.26924</b>	<b>424.79007</b>	<b>0.34558</b>
<b>AG3_S1_M1f</b>	<b>17.20530</b>	<b>15.42652</b>	<b>0.24256</b>	<b>13.02550</b>	<b>0.02372</b>	<b>4.80591</b>	<b>110.32401</b>	<b>0.28788</b>
AG3_S1_M1g	1.38347	8.41630	0.07947	4.71028	0.01923	4.15983	162.22709	0.29786
AG3_S1_M1h	0.71619	7.58139	0.07197	4.81872	0.01900	3.01926	73.20684	0.28189
<b>AG3_S1_M1i</b>	<b>2.13333</b>	<b>7.10956</b>	<b>0.10187</b>	<b>4.47383</b>	<b>0.02010</b>	<b>2.76502</b>	<b>52.23249</b>	<b>0.31476</b>
AG3_S1_M1j	0.98719	7.14430	0.06931	4.99495	0.02004	3.13861	144.62704	0.32783
AG3_S13_M1a	0.571587	2.275808	0.057486	1.661249	0.020834	1.721939	19.883438	2.653224
AG3_S13_M1b	0.562571	2.239433	0.057849	1.817006	0.020333	1.726991	22.326950	2.754468
AG3_S13_M1c	0.596860	1.972523	0.057729	1.669526	0.020713	1.735696	29.143610	3.041732
<b>AG3_S13_M1d</b>	<b>0.899698</b>	<b>2.821559</b>	<b>0.058535</b>	<b>1.884759</b>	<b>0.020376</b>	<b>2.012482</b>	<b>28.737470</b>	<b>2.922672</b>
AG3_S13_M1e	1.017281	3.809279	0.050105	2.688137	0.021473	1.636464	54.168785	3.336680
AG3_S13_M1f	0.597390	3.573676	0.047140	2.592884	0.020490	1.622176	53.951977	3.395208
AG4_s1_M1a	1.85280	8.87696	0.05247	3.11699	0.02098	1.61937	113.56375	4.35744
<b>AG4_s1_M1b</b>	<b>10.69822</b>	<b>5.42127</b>	<b>0.14416</b>	<b>4.80642</b>	<b>0.02258</b>	<b>1.46774</b>	<b>33.39336</b>	<b>6.11299</b>
<b>AG4_s1_M1c</b>	<b>20.09852</b>	<b>7.13710</b>	<b>0.22482</b>	<b>6.98929</b>	<b>0.02473</b>	<b>2.12472</b>	<b>22.57244</b>	<b>8.54902</b>
AG4_s4_M1a	0.90430	4.27377	0.04654	2.63138	0.02002	1.97594	98.38558	3.75474
AG4_s4_M1b	0.55990	4.70871	0.03675	2.49589	0.01991	1.65503	178.36267	3.38759
AG4_s4_M1c	1.13421	3.65793	0.04728	2.84727	0.01977	1.58395	109.23120	3.50666
<b>AG4_s5_M1</b>	<b>0.35190</b>	<b>4.87749</b>	<b>0.04676</b>	<b>2.60135</b>	<b>0.01776</b>	<b>2.65738</b>	<b>103.57880</b>	<b>4.15203</b>
AG4_s5_M2a	0.45314	4.71162	0.03942	2.96405	0.02048	1.19878	116.92153	3.61973
AG4_s5_M2b	0.54334	6.71140	0.03999	2.80551	0.02057	1.19206	81.48023	3.63182
AG4_s6_M1a	0.71981	3.14778	0.06095	2.48877	0.01935	1.60181	70.97810	3.58087
AG4_s6_M1b	0.34243	5.36144	0.04271	2.73887	0.01909	1.31774	135.56051	3.57655
AG4_s6_M1c	1.08274	4.92282	0.06915	2.66861	0.02023	1.60326	45.51665	5.03084

AG4_s8_M1a	0.41681	4.92290	0.04260	3.16254	0.01959	1.25684	179.95656	3.82797
AG4_s8_M1b	0.42335	5.08047	0.04149	3.42330	0.01979	1.32726	173.63268	6.21830
AG4_s9_M1a	1.83649	6.35228	0.03852	5.28970	0.02062	1.52268	203.58743	7.51428
AG4_s9_M1b	0.48753	5.30241	0.04051	2.42728	0.02041	1.31768	140.60278	3.35188
AG4_s10_M1a	0.52284	3.98583	0.04805	2.68678	0.01801	1.25086	73.84735	3.39664
AG4_s10_M1b	0.47193	4.57654	0.04492	2.20514	0.01860	1.40328	38.57185	2.87116
AG4_s10_M1c	0.65471	4.00647	0.04610	2.49932	0.01843	1.53937	67.46684	3.38808
AG4_s10_M1d	0.38635	4.50849	0.04692	3.06985	0.01852	1.54496	25.96473	3.77431
AG4_s10_M2	16.60912	15.34967	0.23082	13.91638	0.02153	1.90405	101.02171	17.65599
AG4_s13_M1	0.44238	4.65137	0.04578	2.80826	0.01886	1.20792	162.15290	3.36194
AG4_s16_M1	0.75869	5.74290	0.05951	2.07442	0.02075	1.69379	100.69190	3.23115
AG4_s17_M1	4.61009	6.19889	0.10601	4.99537	0.02088	2.39419	108.58565	0.29060
AG4_s17_M2a	9.09048	7.36904	0.14687	5.69032	0.02117	2.79386	152.25443	0.29143
AG4_s17_M2b	20.66070	23.29481	0.30114	21.82960	0.02510	6.72136	100.95620	0.28359
AG4_s17_M3	21.85931	8.24964	0.25675	7.87590	0.02299	2.93014	159.82361	0.30844
AG4_s17_M4	25.26417	5.97845	0.28557	5.71743	0.02440	2.81701	156.17503	0.29484
AG4_s17_M5	3.88107	20.63719	0.09736	15.90936	0.02016	2.49389	229.44506	0.29301
AG4_s18_M1a	0.41667	6.09869	0.04389	3.57637	0.02003	1.36154	170.39998	4.22123
AG4_s18_M1b	0.54518	3.98368	0.05534	2.47112	0.01971	1.31592	99.98443	3.21591
AG4_s18_M1c	1.13247	6.41107	0.04195	3.62503	0.02053	1.29238	230.88653	4.23717
AG4_s19_M1a	1.08847	18.91383	0.06274	5.20087	0.01990	2.86410	240.79677	0.27548
AG4_s19_M1b	4.62581	23.94057	0.12049	14.31635	0.02068	2.76005	226.81819	0.29806
AG4_s19_M1c	0.550692	7.7421243	0.05624	5.060829	0.018162	2.156309	186.375442	0.2910579
AG4_s19_M1d	5.15027	19.01999	0.11500	11.36314	0.01968	2.29254	257.93189	0.29225
AG4_s20_M1a	0.48321	11.99091	0.07049	5.41029	0.01943	5.61293	40.23939	0.30611
AG4_s20_M1b	37.70204	12.50286	0.41268	12.19716	0.02417	4.68974	169.14987	0.30812
AG4_s20_M1c	8.52130	14.21454	0.16414	11.11528	0.01935	3.31272	140.00927	0.32527
AG4_s20_M1d	21.10994	9.93378	0.23665	9.19997	0.02529	6.01025	82.52154	0.32215
AG4_s20_M1e	0.71186	20.11287	0.06822	8.20907	0.02000	2.91034	316.25593	0.33548
AG4_s21_M1a	0.35609	9.51870	0.02778	5.30895	0.02132	1.76915	315.59805	10.72021
AG4_s21_M1b	4.33653	7.07873	0.06801	5.88720	0.02080	1.38065	127.71284	7.86600

*Table A4.5 – U-Th-Pb contents recorded in the Argyle monazites (red rows correspond to the rejected analysis spots)*

Sample code	Th/U (ppm)	Pb (ppm)	Th (ppm)	U (ppm)
<b>AG3_S1_M1a</b>	<b>89.79</b>	<b>59.73</b>	<b>3278.30</b>	<b>36.51</b>
AG3_S1_M1b	86.21632	48.723507	2622.985	30.4233
<b>AG3_S1_M1c</b>	<b>184.07</b>	<b>80.28</b>	<b>4327.50</b>	<b>23.51</b>
<b>AG3_S1_M1d</b>	<b>113.87</b>	<b>8.02</b>	<b>526.69</b>	<b>4.63</b>
<b>AG3_S1_M1e</b>	<b>165.77</b>	<b>8.28</b>	<b>510.96</b>	<b>3.08</b>
<b>AG3_S1_M1f</b>	<b>50.69</b>	<b>8.13</b>	<b>449.44</b>	<b>8.87</b>
AG3_S1_M1g	72.82	6.40	496.52	6.82
AG3_S1_M1h	33.95	5.80	427.94	12.61
<b>AG3_S1_M1i</b>	<b>22.11</b>	<b>7.28</b>	<b>474.99</b>	<b>21.48</b>
AG3_S1_M1j	63.86	8.83	634.06	9.93
AG3_S13_M1a	17.00	47.14	2178.80	128.14
AG3_S13_M1b	19.97	52.95	2582.77	129.35
AG3_S13_M1c	25.45	66.50	3328.72	130.80
<b>AG3_S13_M1d</b>	<b>26.10</b>	<b>65.19</b>	<b>3248.87</b>	<b>124.50</b>
AG3_S13_M1e	38.04	44.38	2201.39	57.86
AG3_S13_M1f	39.23	44.98	2331.12	59.42
AG4_s1_M1a	90.17	74.05	3764.19	41.74
<b>AG4_s1_M1b</b>	<b>68.92</b>	<b>51.66</b>	<b>2194.18</b>	<b>31.83</b>
<b>AG4_s1_M1c</b>	<b>58.19</b>	<b>87.51</b>	<b>3210.18</b>	<b>55.17</b>
AG4_s4_M1a	77.20	82.08	4473.12	57.94
AG4_s4_M1b	108.17	92.42	5013.69	46.35
AG4_s4_M1c	84.23	76.59	4143.06	49.19
<b>AG4_s5_M1</b>	<b>95.90</b>	<b>98.41</b>	<b>6357.91</b>	<b>66.29</b>
AG4_s5_M2a	70.49	63.26	3366.71	47.76
AG4_s5_M2b	52.09	47.32	2398.09	46.04
AG4_s6_M1a	63.84	135.26	6514.21	102.04
AG4_s6_M1b	91.94	103.00	5661.90	61.59
AG4_s6_M1c	49.73	60.55	3110.66	62.55
AG4_s8_M1a	118.84	102.29	5581.56	46.97
AG4_s8_M1b	109.16	91.24	5006.05	45.86
AG4_s9_M1a	117.14	46.80	2413.95	20.61
AG4_s9_M1b	86.82	64.46	3329.33	38.35
AG4_s10_M1a	62.03	65.75	3813.31	61.48
AG4_s10_M1b	29.37	32.63	1772.51	60.36
AG4_s10_M1c	54.63	57.09	3253.65	59.56
AG4_s10_M1d	20.50	24.00	1265.84	61.76
<b>AG4_s10_M2</b>	<b>195.21</b>	<b>249.79</b>	<b>11653.67</b>	<b>59.70</b>
AG4_s13_M1	122.71	116.43	6538.36	53.28
AG4_s16_M1	89.67	145.42	7573.51	84.46
<b>AG4_s17_M1</b>	<b>46.00</b>	<b>12.02</b>	<b>763.38</b>	<b>16.60</b>

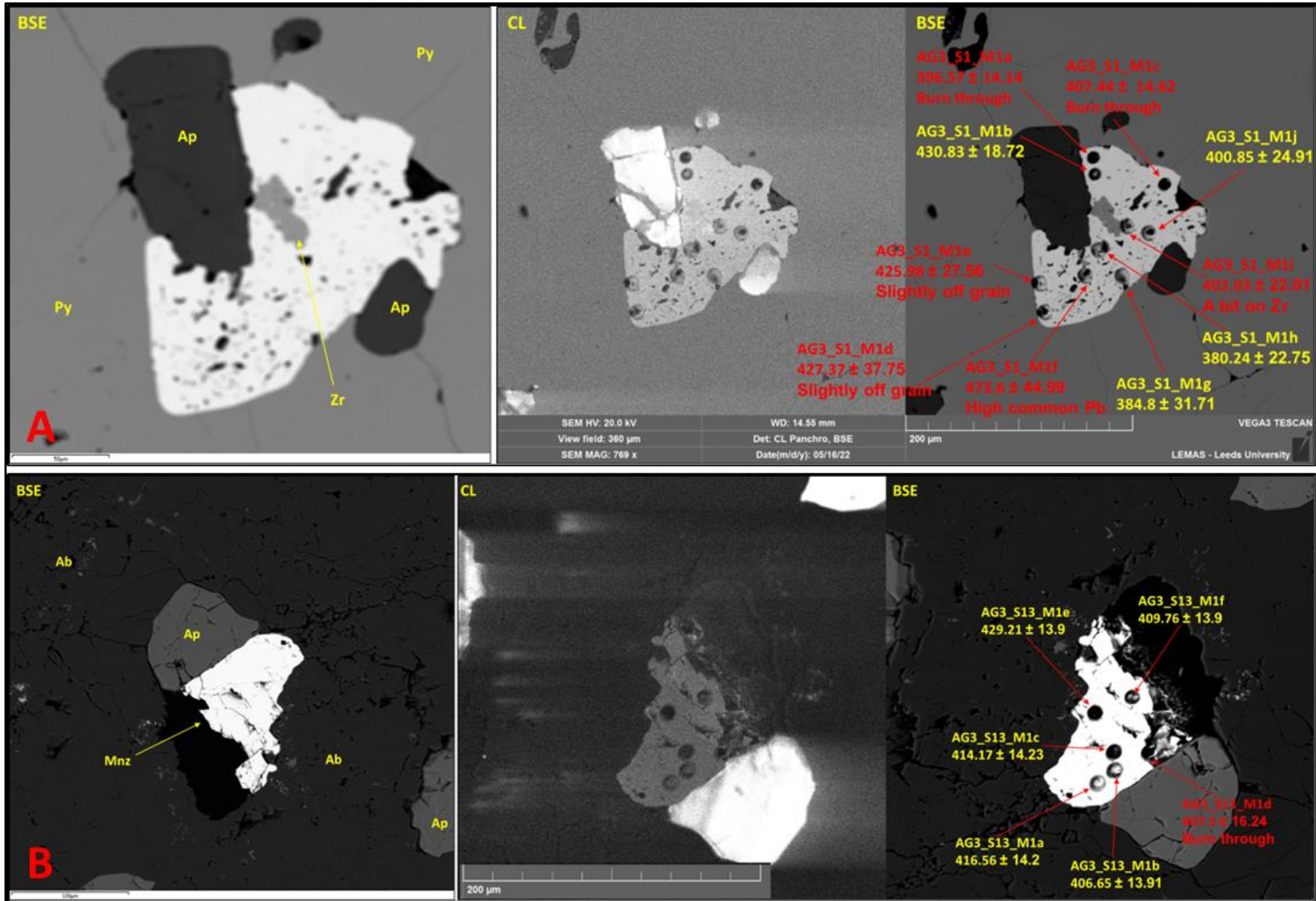
<b>AG4_s17_M2a</b>	68.52	13.69	917.04	13.38
<b>AG4_s17_M2b</b>	46.96	13.27	696.75	14.84
<b>AG4_s17_M3</b>	72.64	9.93	575.48	7.92
<b>AG4_s17_M4</b>	66.71	13.26	717.72	10.76
<b>AG4_s17_M5</b>	105.85	16.16	1134.78	10.72
<b>AG4_s18_M1a</b>	113.16	87.38	4673.41	41.30
<b>AG4_s18_M1b</b>	85.17	112.92	6064.22	71.20
<b>AG4_s18_M1c</b>	138.87	75.58	3947.50	28.43
<b>AG4_s19_M1a</b>	105.46	15.10	1080.61	10.25
<b>AG4_s19_M1b</b>	97.46	14.61	981.11	10.07
<b>AG4_s19_M1c</b>	81.4871	17.128037	1311.773	16.09792
<b>AG4_s19_M1d</b>	115.17	15.00	1089.55	9.46
<b>AG4_s20_M1a</b>	17.97	3.02	205.53	11.44
<b>AG4_s20_M1b</b>	82.49	6.84	357.79	4.34
<b>AG4_s20_M1c</b>	65.50	4.22	305.19	4.66
<b>AG4_s20_M1d</b>	37.45	5.19	275.17	7.35
<b>AG4_s20_M1e</b>	132.39	8.73	625.55	4.73
<b>AG4_s21_M1a</b>	118.78	63.41	3251.42	27.37
<b>AG4_s21_M1b</b>	116.18	63.92	3259.48	28.06

Table A4.6 – U-Th-Pb dates recorded in the Argyle monazites (red rows correspond to the rejected analysis spots)

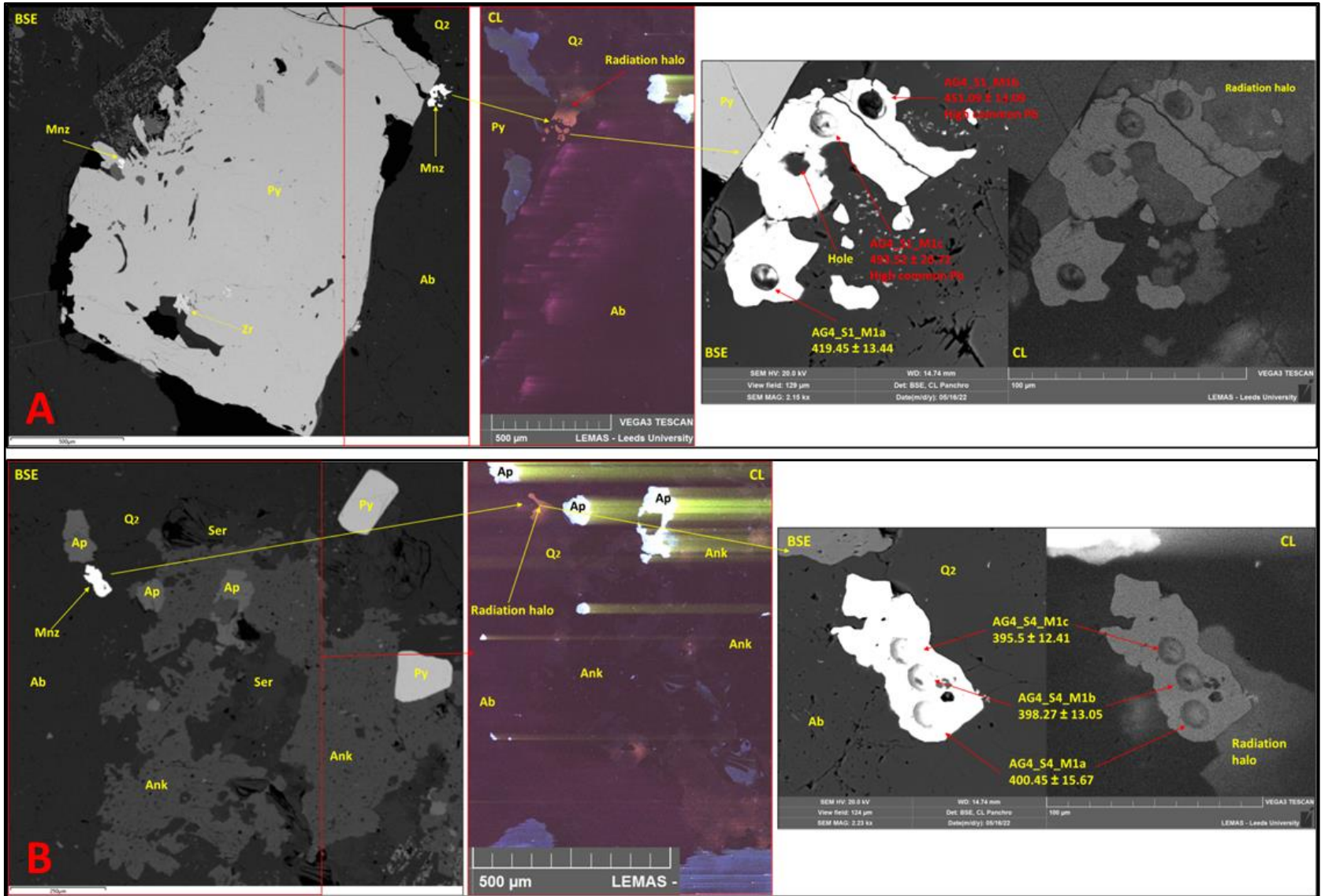
Sample code	No.	$^{208}\text{Pb}/^{232}\text{Th}$ Age (Ma)	Error ( $2\sigma$ )	$^{207}\text{Pb}/^{235}\text{U}$ Age (Ma)	Error ( $2\sigma$ )	$^{206}\text{Pb}/^{238}\text{U}$ Age (Ma)	Error ( $2\sigma$ )	$^{207}\text{Pb}/^{206}\text{Pb}$ Age (Ma)	Error ( $2\sigma$ )	Concordia Age (Ma)	Error ( $2\sigma$ )
AG3_S1_M1a	1	396.57	14.14	200.87	36.37	130.86	8.06	1130.64	416.31	133.84	7.9
AG3_S1_M1b	2	430.83	18.72	280.02	29.56	118.97	7.75	2009.59	244.06	127.34	7.58
AG3_S1_M1c	3	407.44	14.62	1498.18	157.24	256.04	38.8	4517.18	367.98	268.93	38.83
AG3_S1_M1d	4	427.37	37.75	2672.59	235.89	1101.25	225.34	4248.1	493.58	1268.76	229.25
AG3_S1_M1e	5	425.98	27.56	3850	277.67	2372.32	541.93	4743.89	561.39	3173.64	444.61
AG3_S1_M1f	6	473.6	44.99	2946.35	296.07	1399.99	327.83	4283.15	593.82	1634.89	334.19
AG3_S1_M1g	7	384.8	31.71	881.92	99.21	492.96	44.71	2046.53	340.82	534.96	43.01
AG3_S1_M1h	8	380.24	22.75	548.42	64.25	448.01	41.71	990.83	365.38	475.45	35.89
AG3_S1_M1i	9	402.03	22.01	1159.67	98.3	625.36	53.33	2367.24	286.64	693.76	51.28
AG3_S1_M1j	10	400.85	24.91	697.29	72.07	432	41.74	1684.26	321.81	483.72	38.22
AG3_S13_M1a	11	416.56	14.2	459.04	16.81	360.32	11.64	989.16	114.63	390.02	9.83
AG3_S13_M1b	12	406.65	13.91	453.2	16.37	362.53	12.81	943.85	118.15	394.99	10.36
AG3_S13_M1c	13	414.17	14.23	475.24	14.97	361.8	11.75	1068.11	103.89	401.93	9.55
AG3_S13_M1d	14	407.5	16.24	651.57	27.14	366.71	13.44	1823.61	123.11	408.07	12.64
AG3_S13_M1e	15	429.21	13.9	712.55	39.01	315.17	16.54	2314.25	159.98	353.02	16
AG3_S13_M1f	16	409.76	13.16	475.58	27.14	296.94	15.05	1465.55	167.73	332.32	13.66
AG4_s1_M1a	17	419.45	13.44	1064.43	117.08	329.67	20.03	3222.9	296.99	337.08	20
AG4_s1_M1b	18	451.09	13.09	2497.27	100.68	868.14	78.08	4349.48	212.31	971.27	79.09
AG4_s1_M1c	19	493.52	20.72	3096.11	138.07	1307.29	165.4	4620.34	288.64	1541.17	170.84
AG4_s4_M1a	20	400.45	15.67	654.02	41.21	293.24	15.09	2238.59	173.61	320.5	14.69
AG4_s4_M1b	21	398.27	13.05	451.46	34.32	232.66	11.41	1807.61	193.73	249.19	11.05
AG4_s4_M1c	22	395.5	12.41	769.76	39.48	297.8	16.57	2596.36	154.59	337.94	16.14
AG4_s5_M1	23	355.64	18.74	306.15	25.78	294.6	14.98	395.11	247.93	297.49	12.99
AG4_s5_M2a	24	409.56	9.72	379.48	29.84	249.24	14.49	1277.91	217.03	270.95	13.35
AG4_s5_M2b	25	411.34	9.71	440.62	47.98	252.77	13.91	1596.7	271.58	264.18	13.55
AG4_s6_M1a	26	387.18	12.29	550.55	26.75	381.4	18.43	1330.36	155.3	429.09	15.87
AG4_s6_M1b	27	382.02	9.97	299.01	27.77	269.61	14.46	535.37	263.56	275.71	12.91
AG4_s6_M1c	28	404.61	12.84	744.97	51.97	431.03	22.25	1857.17	202.33	464.83	21.34

AG4_s8_M1a	29	391.93	9.76	353.77	29.41	268.93	16.66	956.33	239.25	288	14.77
AG4_s8_M1b	30	395.89	10.41	358.44	30.69	262.06	17.58	1041.58	247.26	283.88	15.59
AG4_s9_M1a	31	412.33	12.43	1058.61	83.52	243.65	25.3	3688.51	252.19	266.65	25.2
AG4_s9_M1b	32	408.17	10.65	403.23	35.29	255.99	12.18	1366.79	224.55	269.08	11.7
AG4_s10_M1a	33	360.6	8.94	427.05	27.79	302.54	15.88	1170.07	190.35	329.87	14.17
AG4_s10_M1b	34	372.31	10.35	392.52	29.8	283.26	12.22	1100.25	203.25	297.15	11.49
AG4_s10_M1c	35	368.93	11.26	511.37	32.19	290.53	14.2	1678.91	174.44	318.61	13.43
AG4_s10_M1d	36	370.72	11.35	331.7	25.52	295.58	17.74	593.45	236.44	307.04	14.71
AG4_s10_M2	37	430.33	16.21	2912.54	294.01	1338.8	336.48	4304.23	608.67	1586.76	343.72
AG4_s13_M1	38	377.46	9.03	371.93	28.97	288.56	15.85	930.81	223.05	306.32	14.16
AG4_s16_M1	39	414.9	13.91	573.25	50.31	372.64	15.02	1476.94	231.61	385.32	14.63
AG4_s17_M1	40	417.47	19.79	1751.1	103.45	649.53	61.73	3547.55	245.27	731.89	61.61
AG4_s17_M2a	41	423.21	23.4	2347.15	134.82	883.39	93.95	4081.58	277.03	976.05	94.75
AG4_s17_M2b	42	500.81	66.5	3122.81	451.22	1696.96	651.39	4234.1	941.54	2146.97	638.76
AG4_s17_M3	43	459.19	26.61	3177.5	160.2	1473.19	207.45	4549.68	330.73	1771.29	214.31
AG4_s17_M4	44	487.01	27.11	3318.48	116.79	1619.35	163.74	4605.25	239.2	1978.89	169.41
AG4_s17_M5	45	403.22	19.91	1609.75	333.23	598.92	181.98	3412.85	810.67	670.18	181.16
AG4_s18_M1a	46	400.65	10.8	353.67	36.43	276.9	19.39	894.35	291.88	292.64	17.39
AG4_s18_M1b	47	394.31	10.28	441.83	28.54	347.22	16.71	970.3	191.27	369.41	14.74
AG4_s18_M1c	48	410.55	10.5	768.93	69.14	264.91	18.82	2791.43	241.16	282.57	18.64
AG4_s19_M1a	49	398.07	22.58	747.76	200.18	392.27	39.59	2040.45	693.67	400.42	39.28
AG4_s19_M1b	50	413.52	22.59	1753.94	399.76	733.38	198.48	3354.22	871.65	792	197.88
AG4_s19_M1c	51	363.58	15.54	445.45	55.83	352.72	34.74	957.89	378.11	376.65	30.18
AG4_s19_M1d	52	393.71	17.88	1844.44	323.45	701.72	151.1	3592.77	680.4	750.92	151.15
AG4_s20_M1a	53	388.76	43.22	400.27	79.33	439.11	45.93	181.8	613.02	429.03	39.39
AG4_s20_M1b	54	482.48	44.72	3712.13	247.34	2227.16	459.38	4651.66	503.91	2963.18	399.78
AG4_s20_M1c	55	387.18	25.41	2288.2	258.35	979.74	202.06	3817.87	545.79	1109.38	203.06
AG4_s20_M1d	56	504.56	59.9	3143.65	192.61	1369.26	226.98	4617.19	391.28	1597.27	234.13
AG4_s20_M1e	57	400.05	23.06	545.85	169.85	425.42	67.59	1086.62	870.89	439.75	63.84
AG4_s21_M1a	58	426.18	14.92	309.29	50.76	176.64	18.5	1487.2	412.84	189.9	17.66
AG4_s21_M1b	59	415.89	11.37	1700.34	116.82	424.16	48.33	4125.76	273.24	459.99	48.43

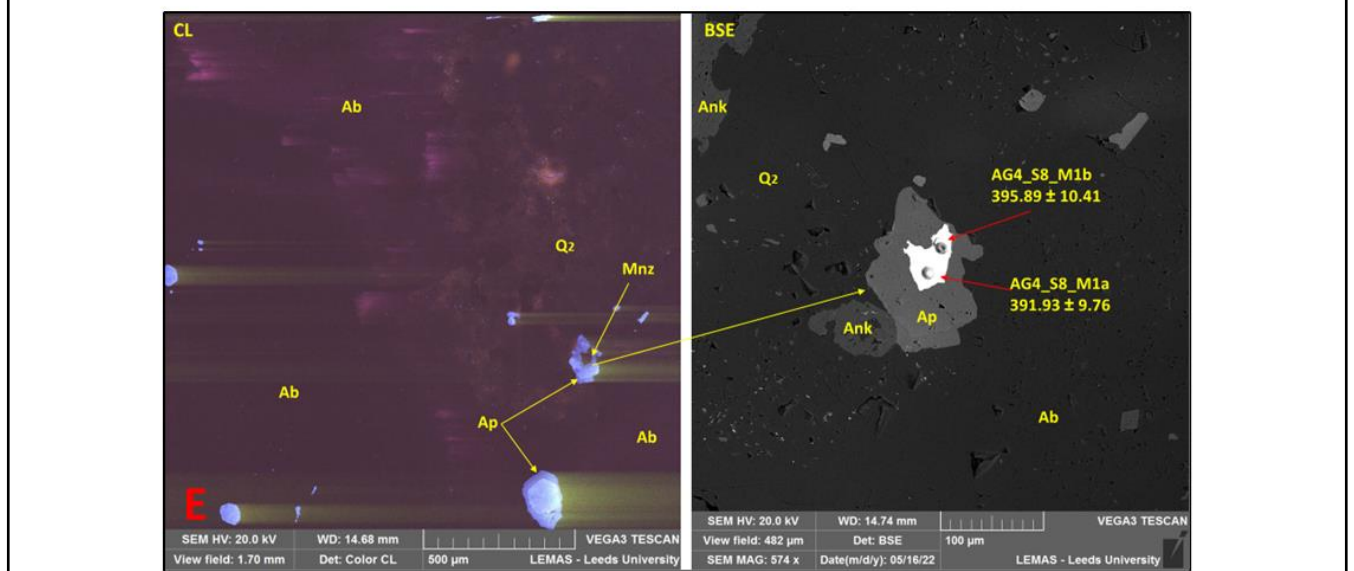
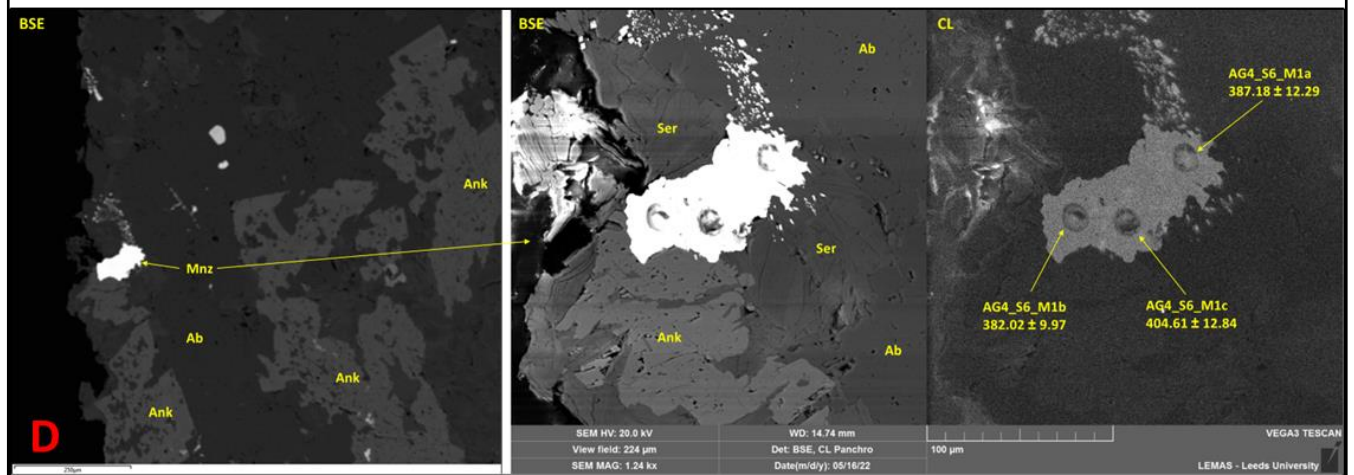
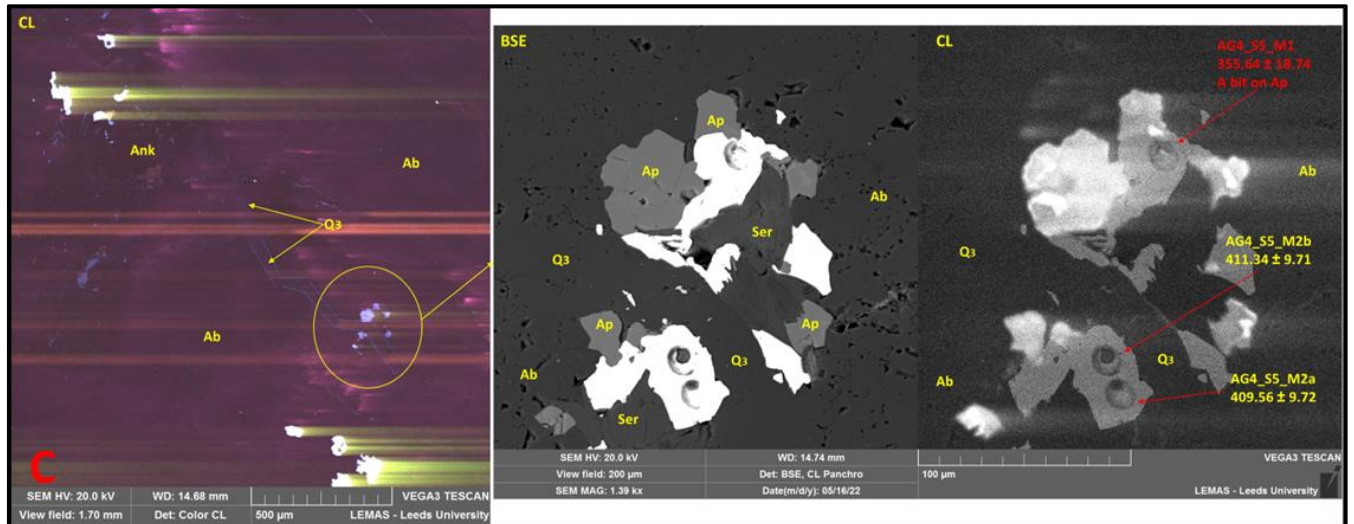
*Plate AIV.4 – BSE/CL images of analysed monazite grains from sample AG3 (Argyle deposit); red annotations correspond to the rejected analysis spots, whereas the yellow ones to the accepted analysis.*

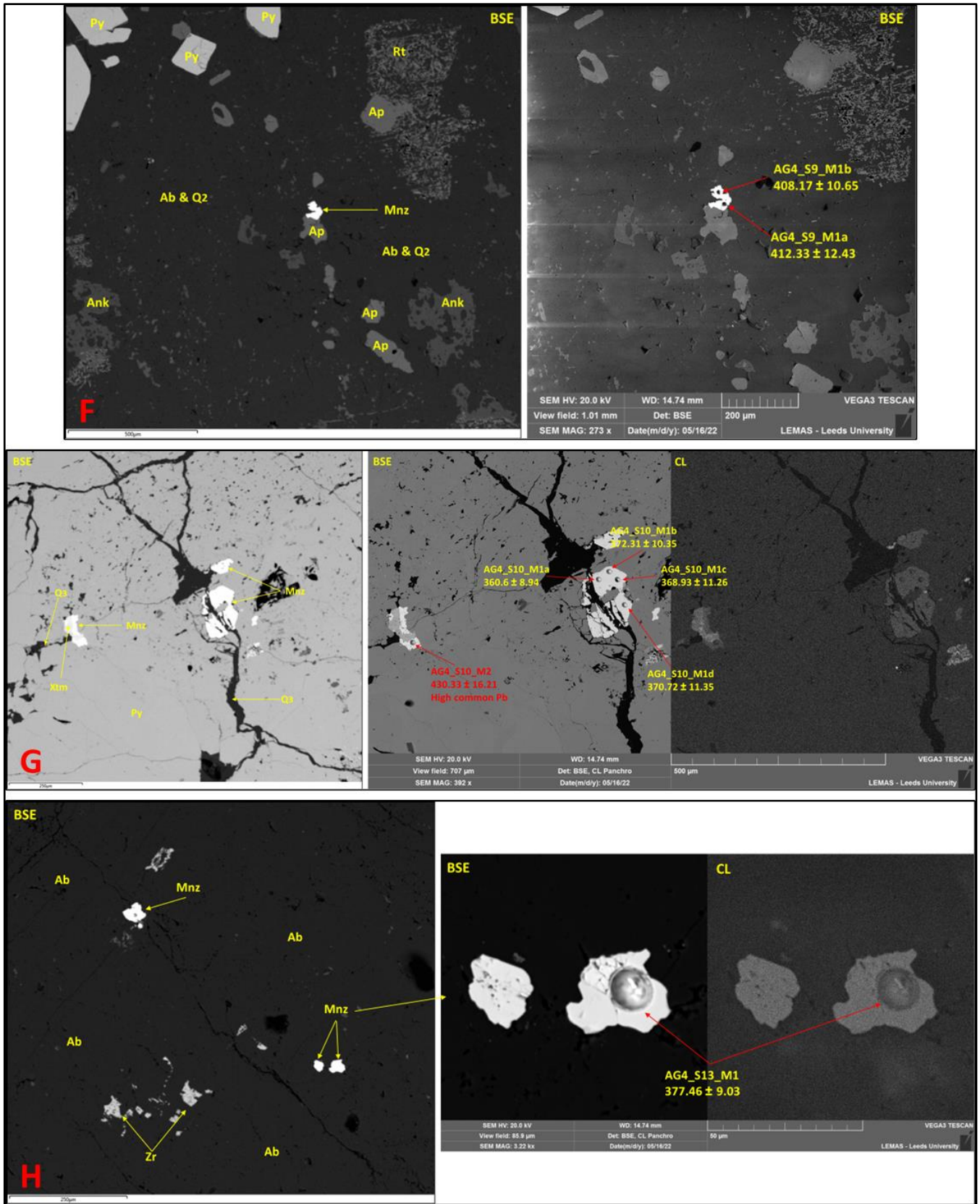


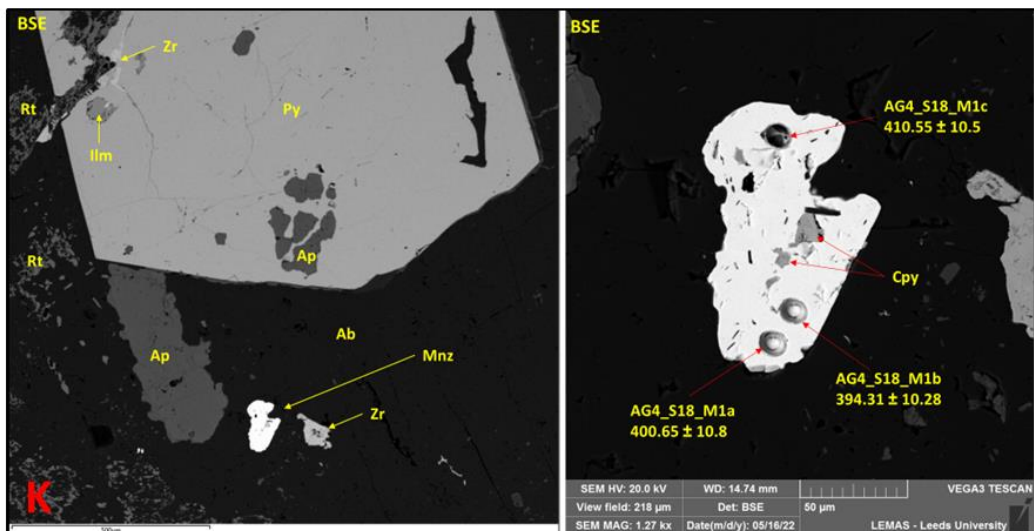
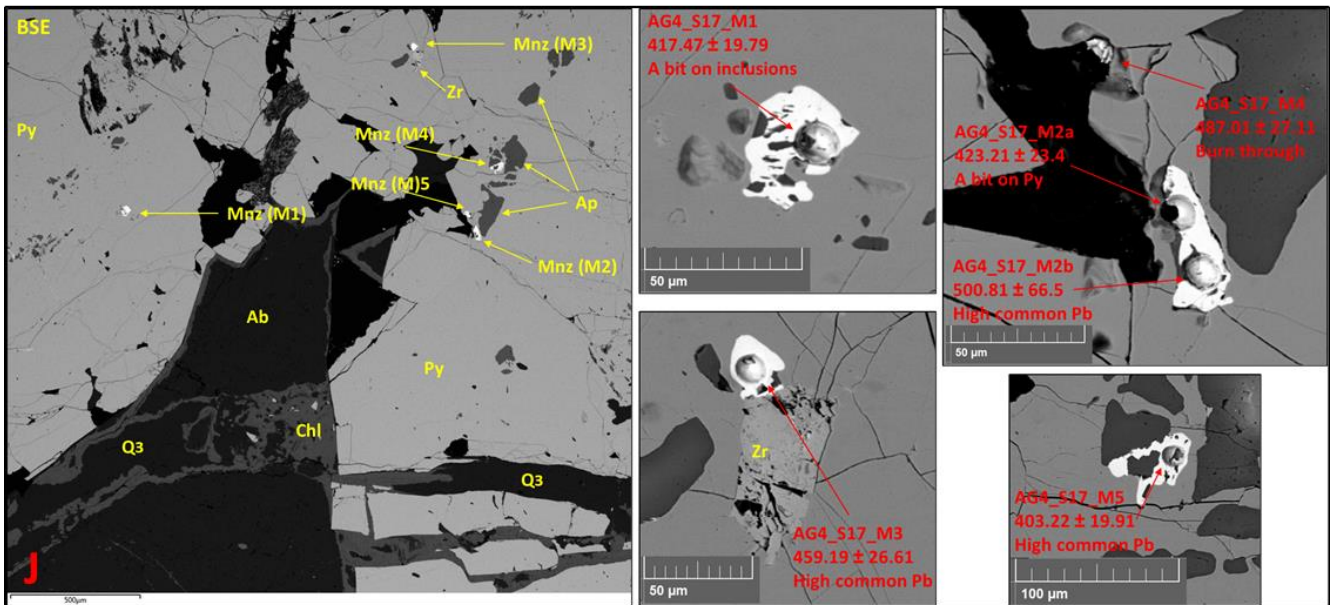
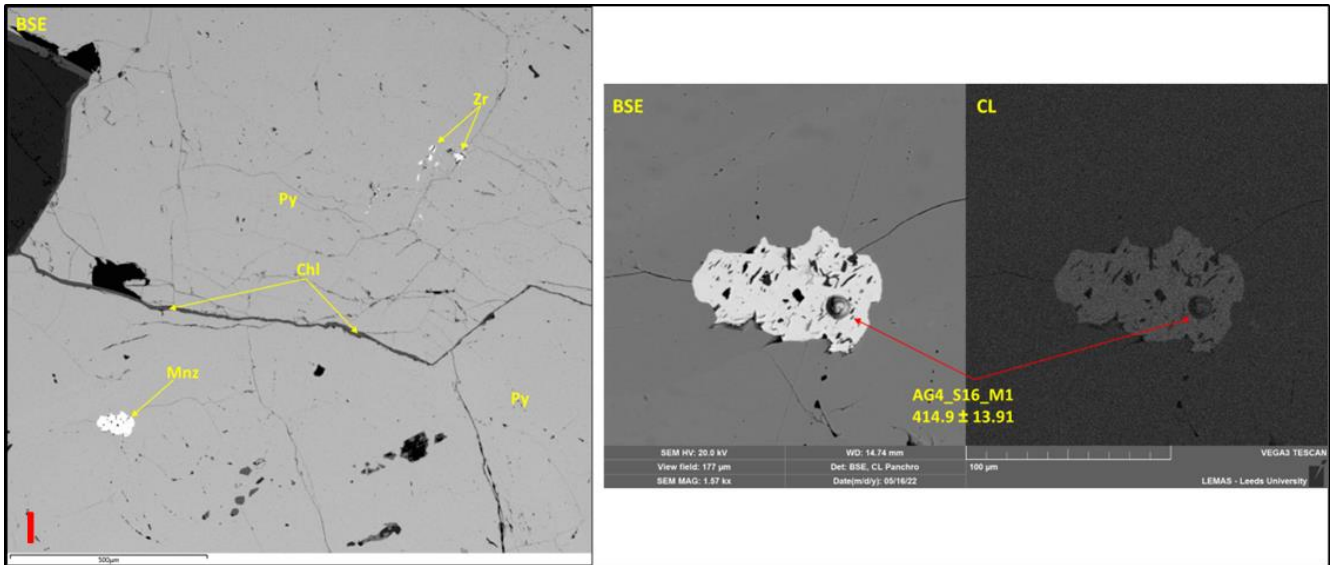
*Plate AIV.5 (next 5 pages) – BSE/CL images of analysed monazite grains from sample AG4 (Argyle deposit); red annotations correspond to the rejected analysis spots, whereas the yellow ones to the accepted analysis.*

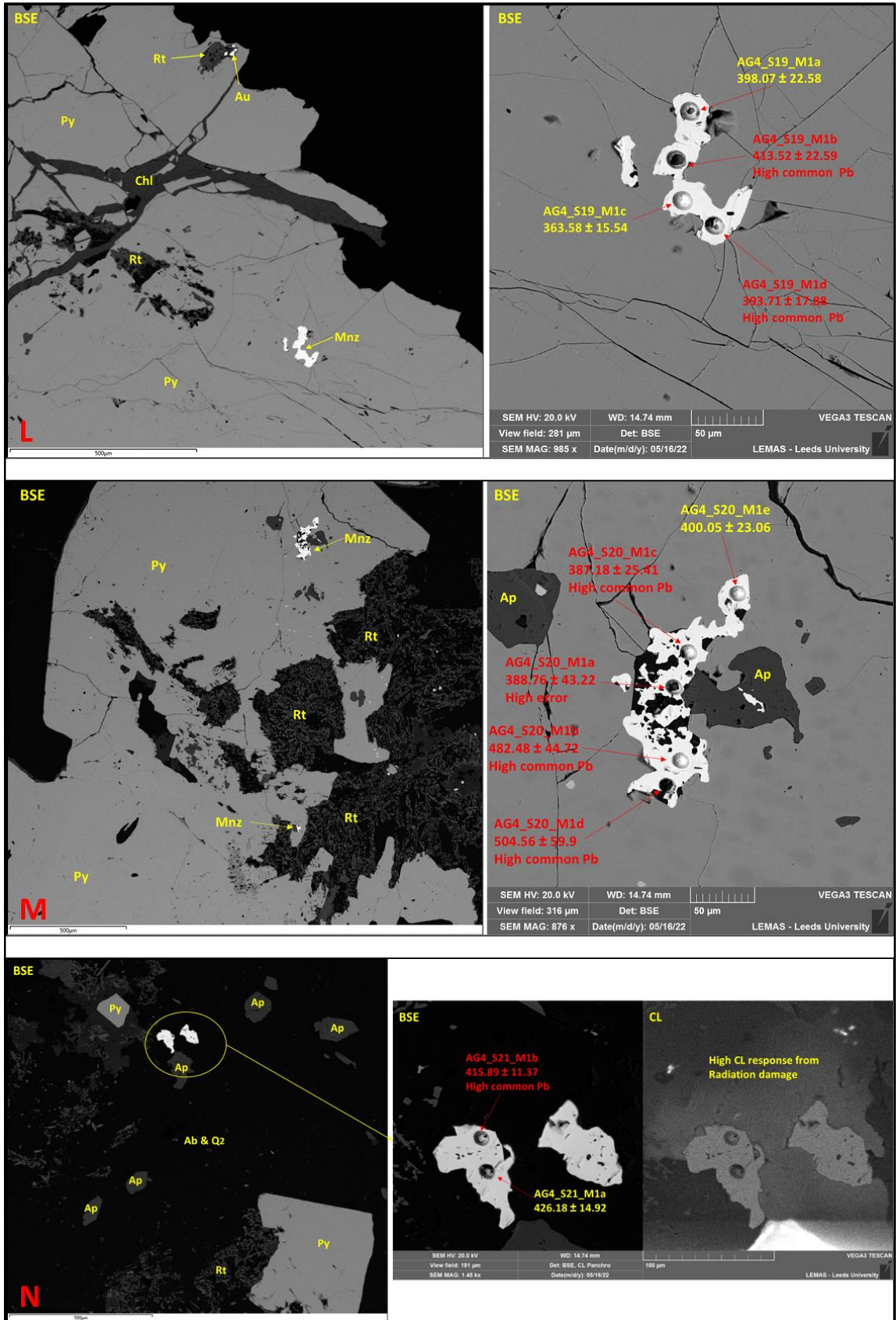












**AIV.2. Xenotime data****AIV.2.1. Stog'er Tight***Table A4.7 – U-Pb isotope ratios and U-Th-Pb contents recorded in the Stog'er Tight xenotimes (red rows correspond to the rejected analysis spots)*

Sample code	$^{238}\text{U}/^{206}\text{Pb}$	1s %	$^{207}\text{Pb}/^{206}\text{Pb}$	1s %	Th/U (ppm)	Pb (ppm)	Th (ppm)	U (ppm)
BN215_S1_X1	15.8889	1.8059	0.0575	1.3391	0.32	14.00	79.44	246.83
BN215_S3_X1a	14.9557	1.6759	0.0578	1.6845	0.14	14.34	33.87	243.66
BN215_S3_X1b	15.5448	1.9733	0.0568	1.0710	0.17	16.89	50.49	300.48
BN215_S3_X1c	16.4985	1.5632	0.0569	1.2096	0.27	18.40	92.07	335.79
BN215_S3_X1d	16.8010	1.6261	0.0601	1.0621	0.18	19.46	64.82	365.98
BN215_S3_X1e	16.1164	1.6542	0.0603	1.4085	0.15	13.10	36.00	240.94
BN215_S4_X1	16.4322	1.8541	0.0573	1.7604	0.55	6.50	59.51	107.64
BN215_S5_X1a	16.6661	1.6794	0.0563	1.9976	0.07	12.07	17.19	239.15
BN215_S5_X1b	16.7245	1.6053	0.0567	1.2732	0.06	19.39	23.57	385.56
BN215_S5_X1c	16.4450	1.7611	0.0591	1.0902	0.17	9.94	32.45	191.50
BN215_S5_X1d	16.2635	1.8714	0.0544	1.2373	0.13	9.01	22.07	172.70
BN215_S5_X2	16.1959	1.7595	0.0568	1.5220	0.14	12.70	33.84	238.32
BN215_S7_X1a	16.4078	1.9447	0.0563	1.3297	0.16	18.18	55.20	356.13
BN215_S7_X1b	16.1548	1.6223	0.0570	1.4304	0.07	16.41	23.49	317.64
BN215_S8_X1a	9.3191	6.1169	0.1895	7.0876	0.12	6.47	10.26	83.30
BN215_S8_X1b	14.8675	2.0001	0.0706	2.8171	0.15	21.54	56.62	373.16
SOZ1_s1_x1	10.69026	8.4405785	0.3459	13.02327	1.66	1.32	19.98	12.04
SOZ1_s3_x1	16.3234	2.3560	0.0552	3.1282	1.05	1.28	17.80	16.96
SOZ1_s6_x1	15.5323	2.0488	0.0555	3.0037	0.65	1.14	10.17	15.60
SOZ1_s6_x2	14.97212	2.4214454	0.060789	2.961356	0.962707	2.703602	36.8206893	38.24704
SOZ1_s7_x1	16.56285	1.8719578	0.061039	2.124396	1.978716	3.499615	72.9761362	36.88055
SOZ1_s7_x2	3.071461	43.158897	0.4765	9.66261	0.72	0.21	0.47	0.65
SOZ1_s9_x1	14.3883	3.8598	0.1533	11.1098	2.35	3.15	63.12	26.83
SOZ1_s12_x1a	16.83725	2.0415256	0.060067	2.397839	1.255648	1.960013	34.0212153	27.09455

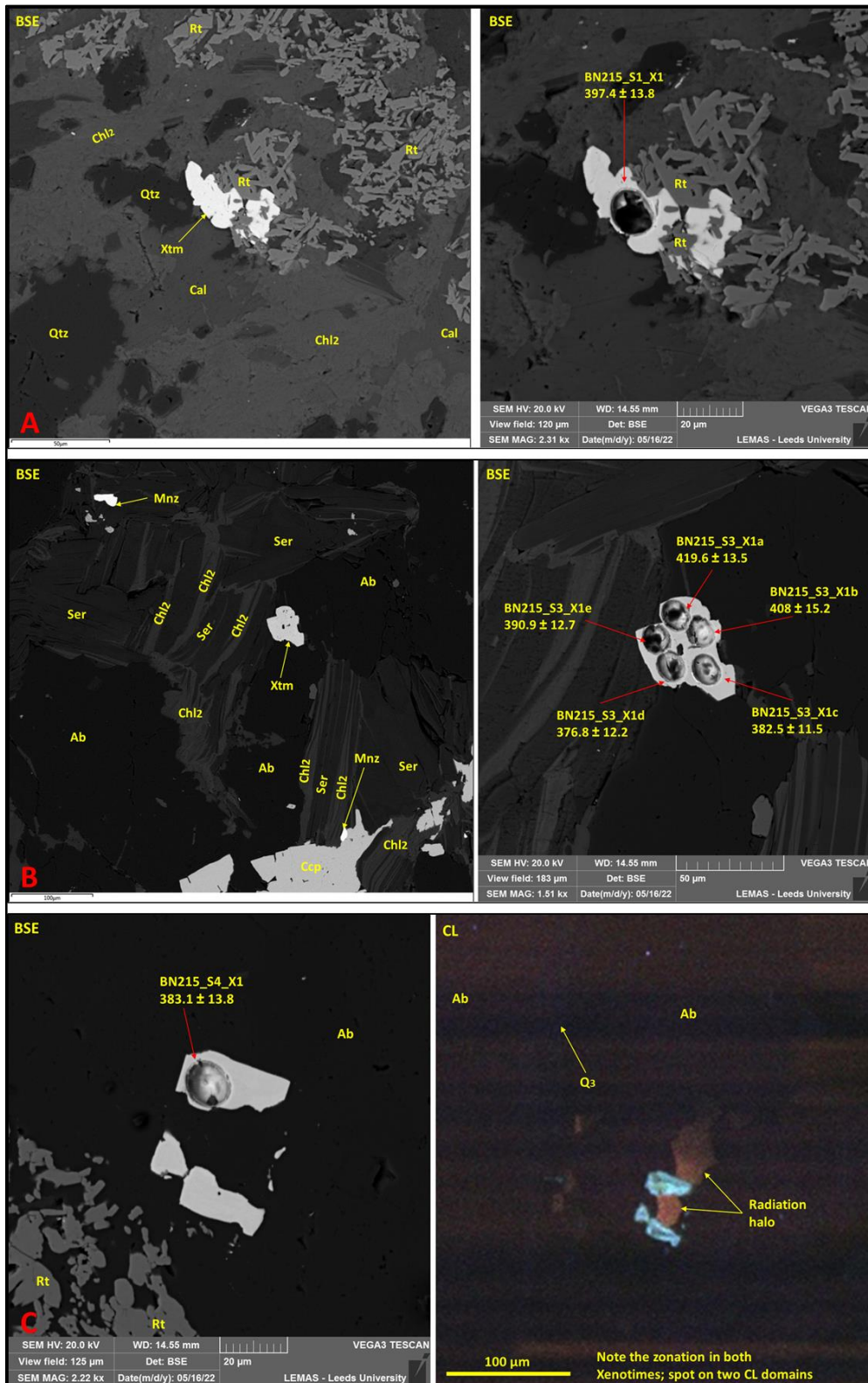
SOZ1_s12_x1b	15.46929	1.8509759	0.060781	1.896861	2.942895	3.247854	84.7204959	28.78815
SOZ1_s14_x1	16.1855	1.6547709	0.064411	2.322852	0.180769	2.157351	6.9557562	38.47874
SOZ2_S11_x1	15.9008	2.2610	0.0618	1.7174	0.98	4.71	137.68	140.80
SOZ2_S26_x1a	15.5577	2.4307	0.0551	1.7878	0.39	5.78	81.99	212.75
SOZ2_S26_x1b	15.8993	2.0911	0.0613	2.4601	0.71	4.33	100.43	140.62
SOZ2_S32_x1a	15.0972	2.6661	0.0538	2.2219	0.61	3.32	70.65	115.71
SOZ2_S32_x1b	15.9358	1.8050	0.0544	1.8808	2.35	8.53	371.82	158.20
SOZ2_S32_x1c	15.8720	2.5776	0.0581	2.6295	1.92	6.45	249.90	130.38
SOZ2_S33_x1a	16.1867	2.1037	0.0578	1.5267	0.20	4.74	42.76	213.16
SOZ2_S33_x1b	15.3749	3.3466	0.0687	6.2738	0.93	3.10	77.55	83.83

*Table A4.8 – U-Pb dates recorded in the Stog' er Tight xenotimes (red rows correspond to the rejected analysis spots); Discordance = ( $^{207}\text{Pb}/^{235}\text{U}$  date /  $^{206}\text{Pb}/^{238}\text{U}$  date) \* 100*

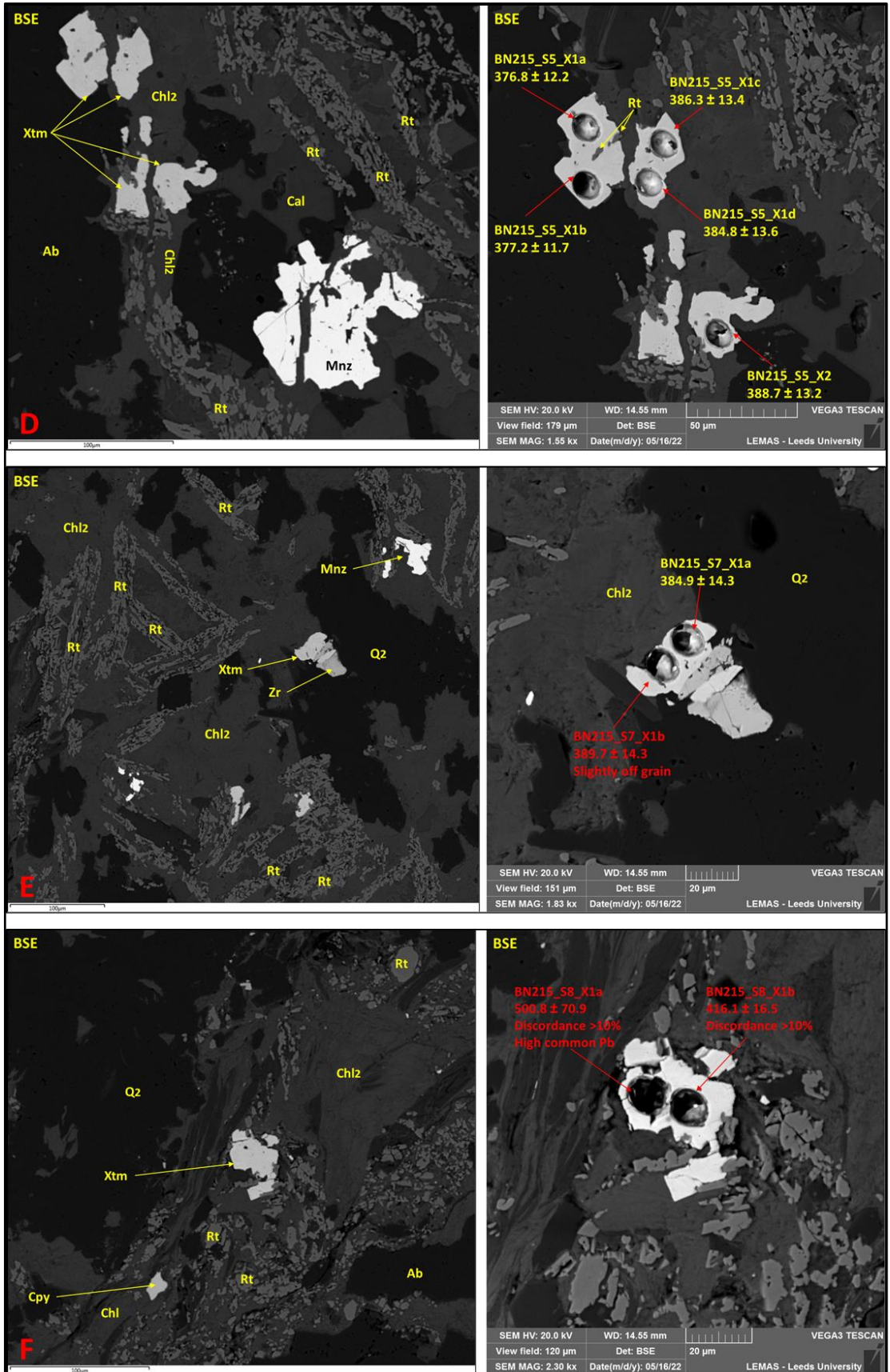
Sample code	No	Concordia Age (Ma)	Error (2 $\sigma$ )	$^{207}\text{Pb}/^{235}\text{U}$ Age (Ma)	Error (2 $\sigma$ )	$^{206}\text{Pb}/^{238}\text{U}$ Age (Ma)	Error (2 $\sigma$ )	$^{207}\text{Pb}/^{206}\text{Pb}$ Age (Ma)	Error (2 $\sigma$ )	Discordance
BN215_S1_X1	1	397.4	13.8	410.9	15.2	393.5	13.8	509.8	58.9	104.42186
BN215_S3_X1a	2	419.6	13.5	433.6	16.8	417.2	13.5	521.2	73.9	103.93097
BN215_S3_X1b	3	408	15.2	414.1	15.3	401.9	15.4	482.8	47.3	103.03558
BN215_S3_X1c	4	382.5	11.5	394.8	12.9	379.3	11.5	486.7	53.4	104.08648
BN215_S3_X1d	5	376.8	12.2	407	13	372.7	11.8	606.2	45.9	109.20311
BN215_S3_X1e	6	390.9	12.7	422.2	15	388.1	12.5	613.4	60.9	108.7864
BN215_S4_X1	7	383.1	13.8	398.5	16.9	380.8	13.7	502.1	77.5	104.64811
BN215_S5_X1a	8	376.8	12.2	388.1	16.8	375.6	12.3	463.2	88.5	103.32801
BN215_S5_X1b	9	377.2	11.7	389.3	13.3	374.4	11.7	478.9	56.3	103.9797
BN215_S5_X1c	10	386.3	13.4	408.5	13.9	380.5	13	569.8	47.4	107.35874
BN215_S5_X1d	11	384.8	13.6	384.9	14.4	384.7	14	386.6	55.6	100.05199
BN215_S5_X2	12	388.7	13.2	400.4	15.4	386.2	13.2	482.8	67.2	103.67685
BN215_S7_X1a	13	384.9	14.3	393.2	15.4	381.4	14.4	463.2	58.9	103.09386
BN215_S7_X1b	14	389.7	12.2	402.4	14.4	387.2	12.2	490.5	63.1	103.92562
BN215_S8_X1a	15	500.8	70.9	1356.2	140.1	657.1	76.4	2737.1	233.2	206.39172

<b>BN215_S8_X1b</b>	16	<b>416.1</b>	<b>16.5</b>	511.2	27.8	419.6	16.3	944.9	115.4	121.83031
<b>SOZ1_s1_x1</b>	17	<b>453.4</b>	<b>84.9</b>	1723.4	257.4	576.5	93.1	3688.3	397.3	298.94189
<b>SOZ1_s3_x1</b>	18	<b>383.8</b>	<b>17.5</b>	388.5	25.3	383.3	17.5	419.3	139.7	101.35664
<b>SOZ1_s6_x1</b>	19	<b>402.6</b>	<b>15.9</b>	406.6	24.4	402.2	16	431.4	133.9	101.09398
<b>SOZ1_s6_x2</b>	20	<b>418.6</b>	<b>19.7</b>	451.3	27.9	416.8	19.5	631.2	127.6	108.27735
<b>SOZ1_s7_x1</b>	21	<b>379</b>	<b>13.9</b>	416.8	19.4	377.9	13.7	638.3	91.4	110.29373
<b>SOZ1_s7_x2</b>	22	<b>122.3</b>	<b>434.8</b>	3156	858	1816.9	1366.7	4169.4	286	173.70246
<b>SOZ1_s9_x1</b>	23	<b>415.3</b>	<b>32</b>	917.5	142.1	433.1	32.3	2382.3	378.5	211.84484
<b>SOZ1_s12_x1a</b>	24	<b>373.1</b>	<b>14.9</b>	406.2	21.1	371.9	14.8	606.2	103.7	109.22291
<b>SOZ1_s12_x1b</b>	25	<b>406</b>	<b>14.7</b>	439.5	18.9	403.8	14.5	631.2	81.7	108.84101
<b>SOZ1_s14_x1</b>	26	<b>386</b>	<b>12.6</b>	443.9	20.5	386.5	12.4	753.8	98.1	114.85123
<b>SOZ2_S11_x1</b>	27	<b>395.9</b>	<b>17.8</b>	435.5	20.1	393.2	17.2	666.2	73.6	110.75788
<b>SOZ2_S26_x1a</b>	28	<b>402.3</b>	<b>18.5</b>	403.6	20.1	401.6	18.9	415.3	79.9	100.49801
<b>SOZ2_S26_x1b</b>	29	<b>394.5</b>	<b>16.2</b>	432.7	22.8	393.2	16	648.8	105.7	110.04578
<b>SOZ2_S32_x1a</b>	30	<b>410.9</b>	<b>20.6</b>	405.7	23.2	413.4	21.4	361.7	100.2	98.137397
<b>SOZ2_S32_x1b</b>	31	<b>392.2</b>	<b>13.6</b>	391.5	16.9	392.3	13.7	386.6	84.5	99.796074
<b>SOZ2_S32_x1c</b>	32	<b>396.1</b>	<b>19.8</b>	414.7	25.1	393.9	19.7	532.6	115.2	105.28053
<b>SOZ2_S33_x1a</b>	33	<b>390.6</b>	<b>15.9</b>	406.4	17.4	386.4	15.8	521.2	67	105.17598
<b>SOZ2_S33_x1b</b>	34	<b>404.8</b>	<b>26.6</b>	487.2	55	406.2	26.3	888.8	259.2	119.94092

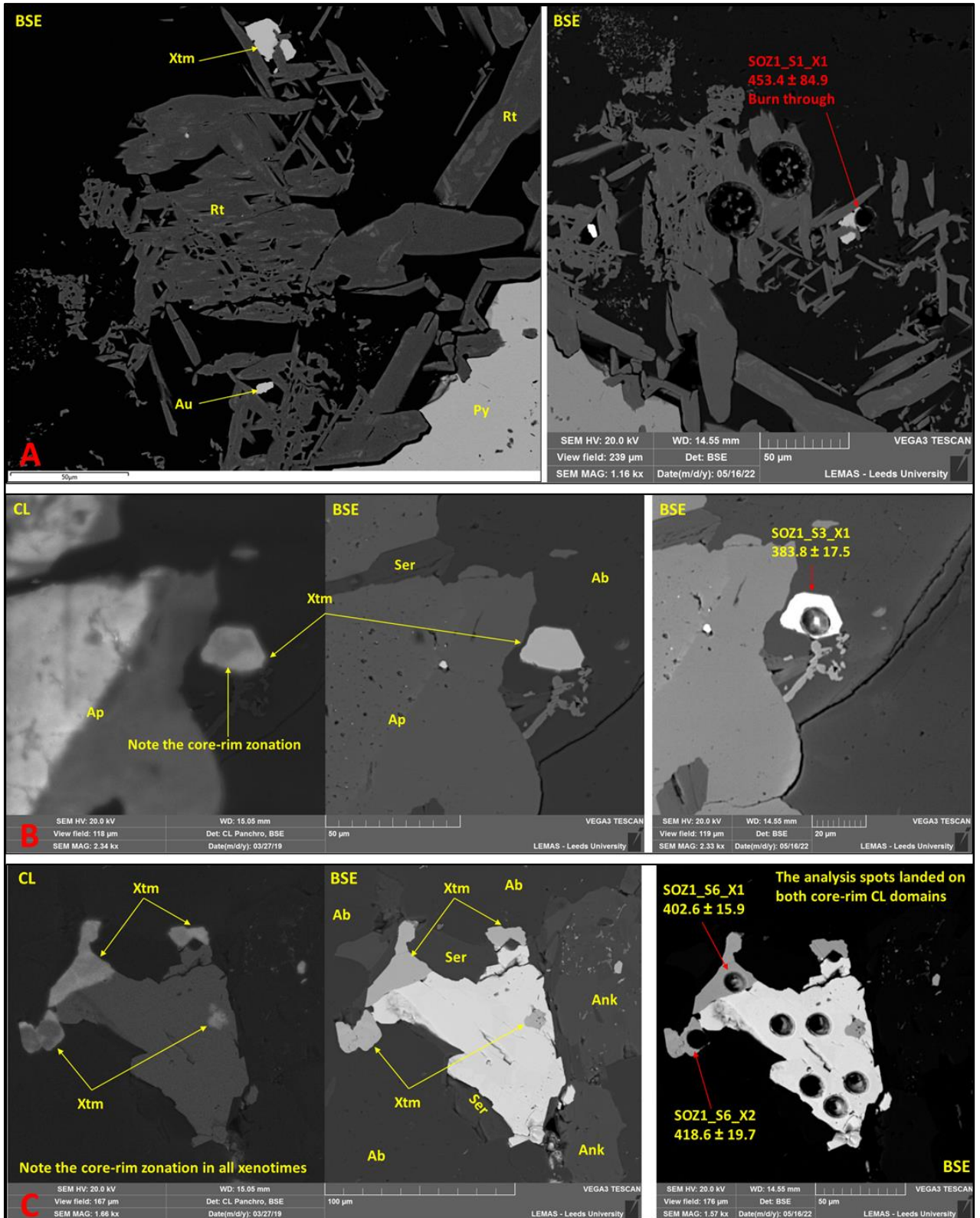
*Plate AIV.6 (next two pages) – BSE/CL images of analysed xenotime grains from sample BN215 (Stog'er Tight deposit); red annotations correspond to the rejected analysis spots, whereas the yellow ones to the accepted analysis.*

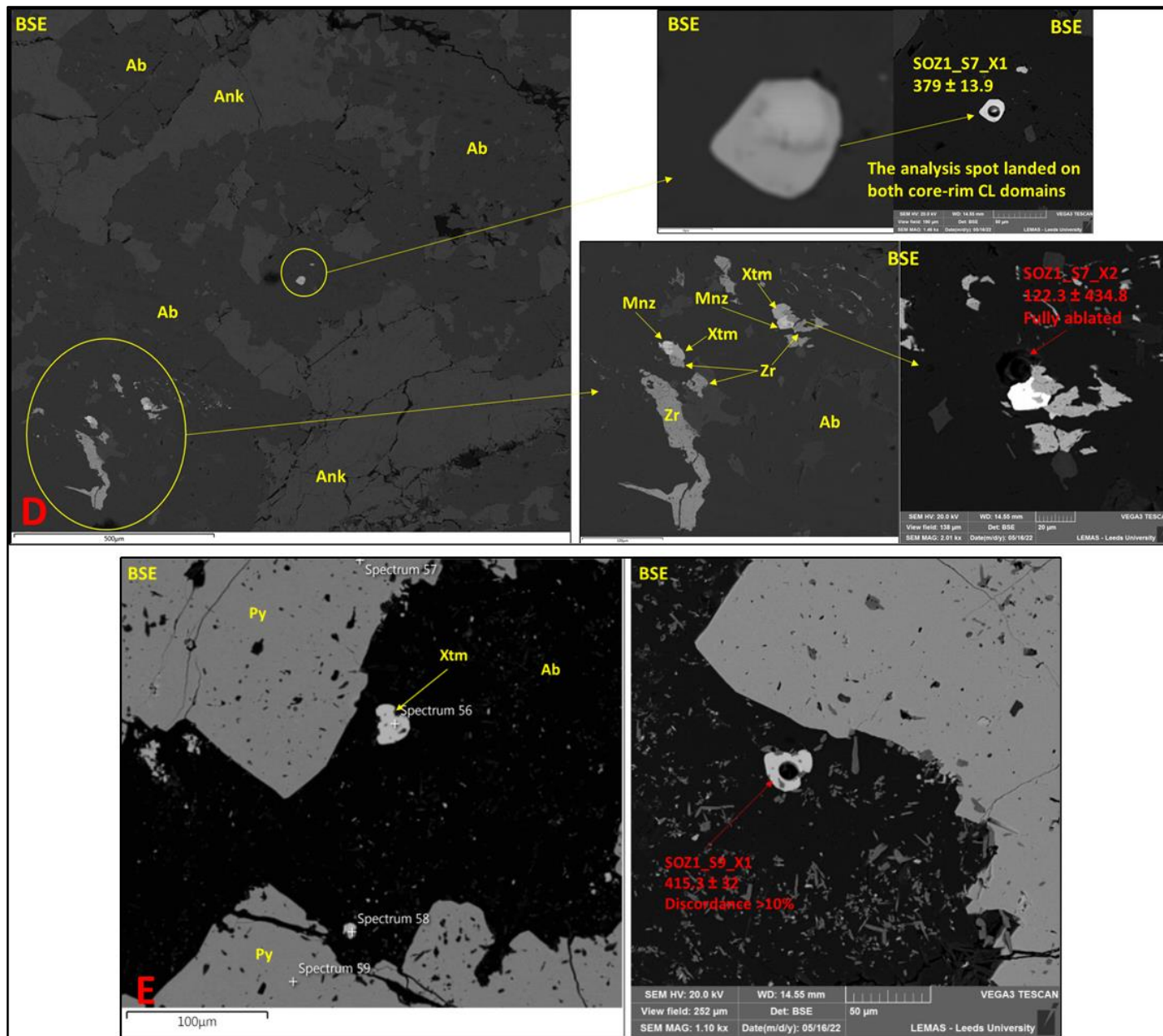


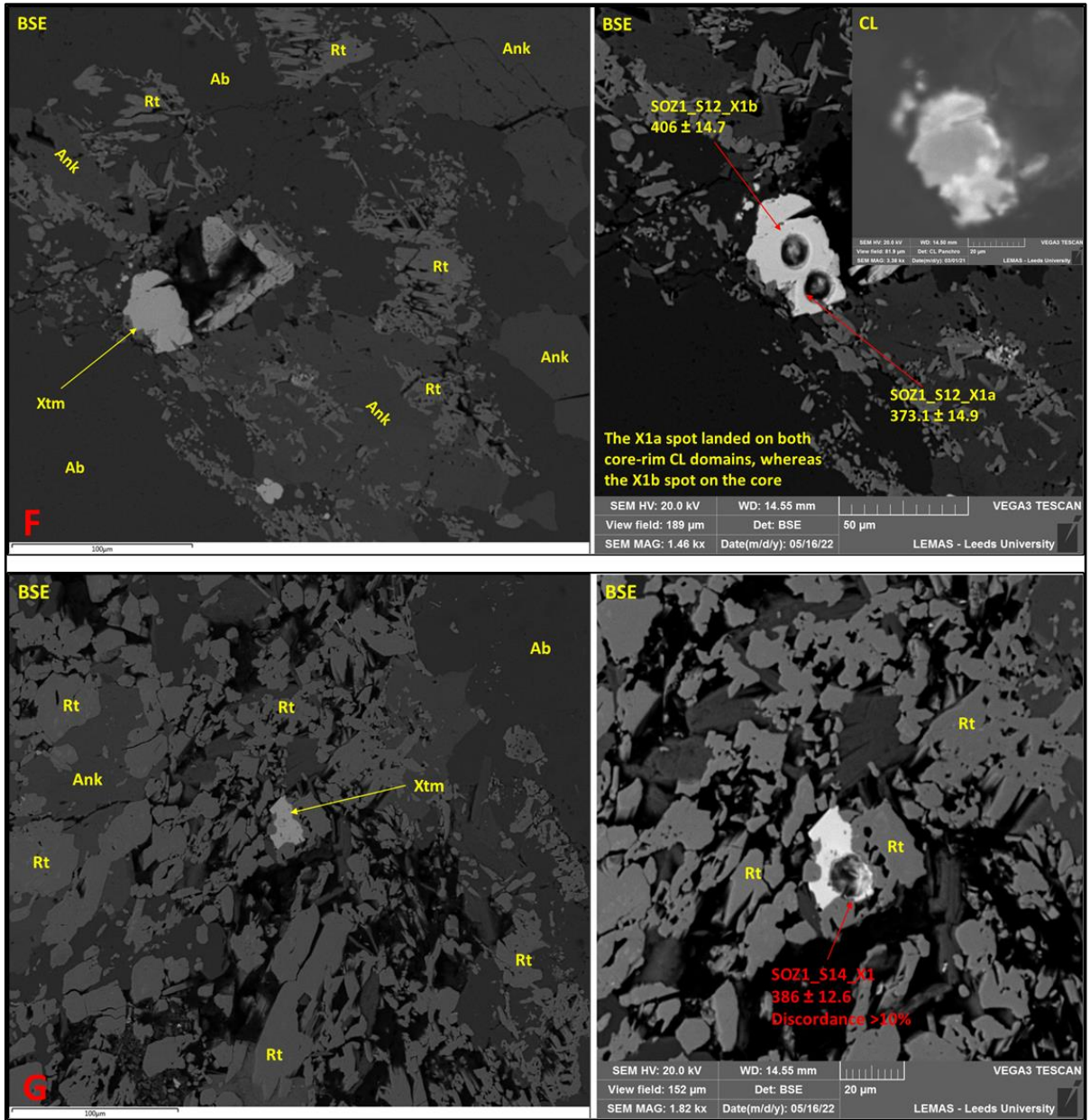




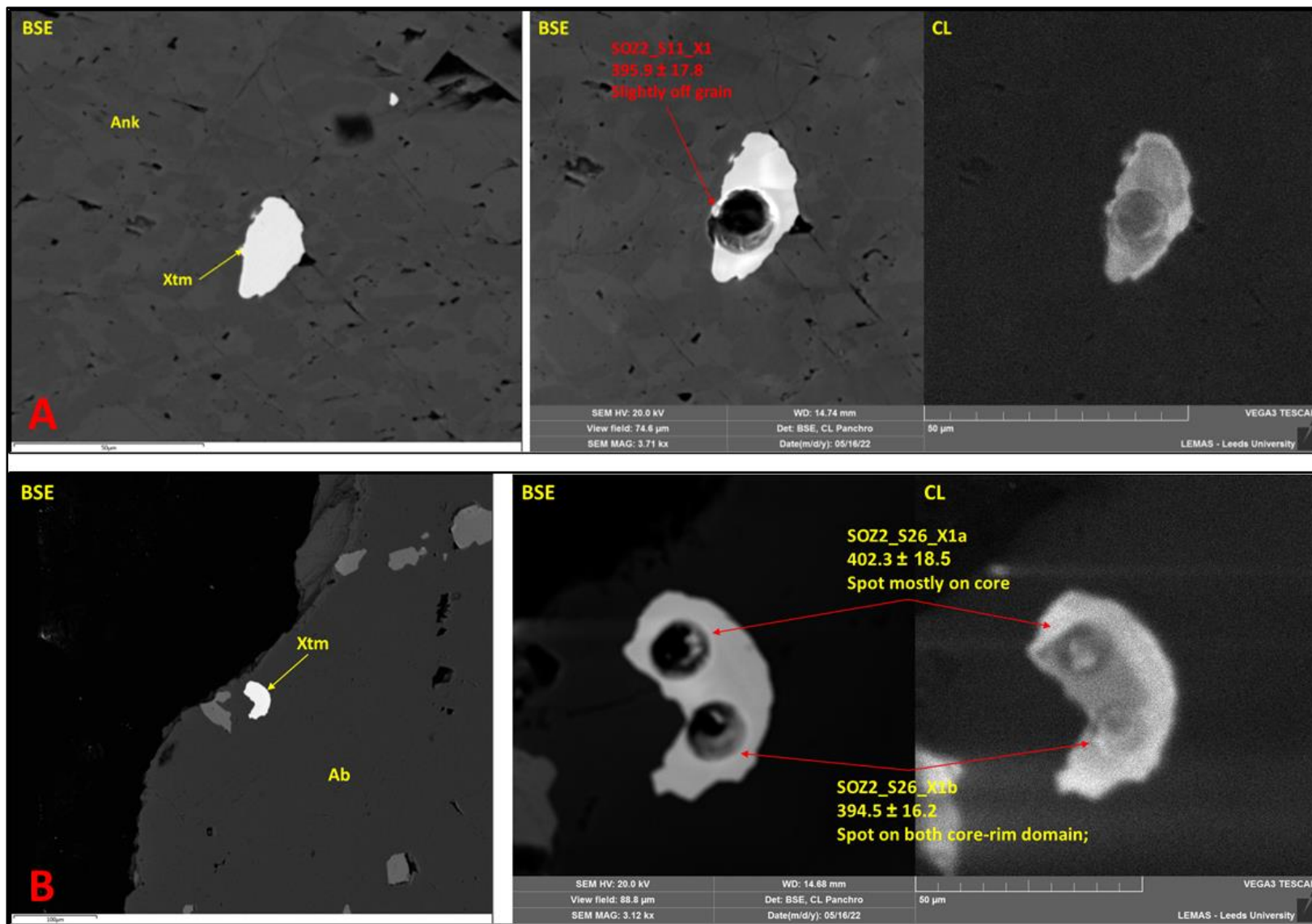
*Plate AIV.7 (next three pages) – BSE/CL images of analysed xenotime grains from sample SOZ1 (Stog'er Tight deposit); red annotations correspond to the rejected analysis spots, whereas the yellow ones to the accepted analysis.*

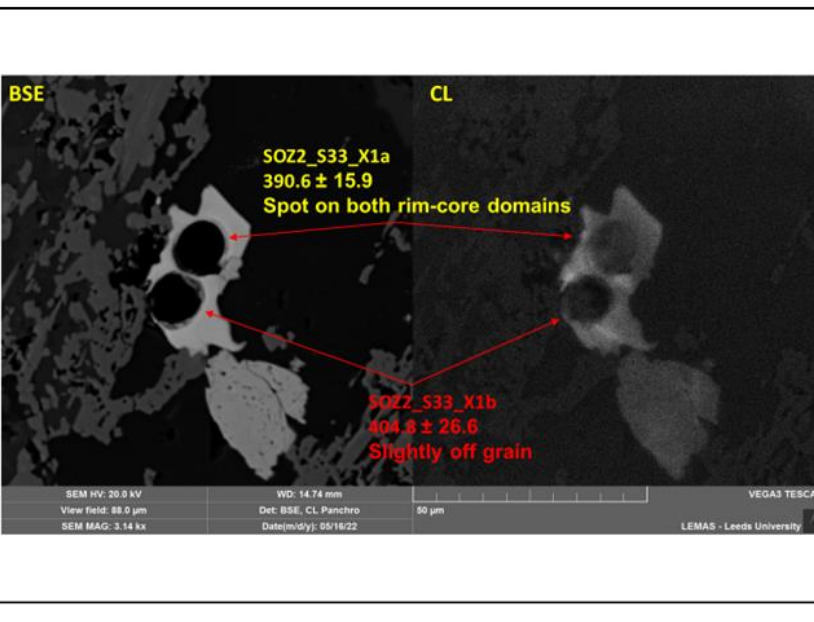
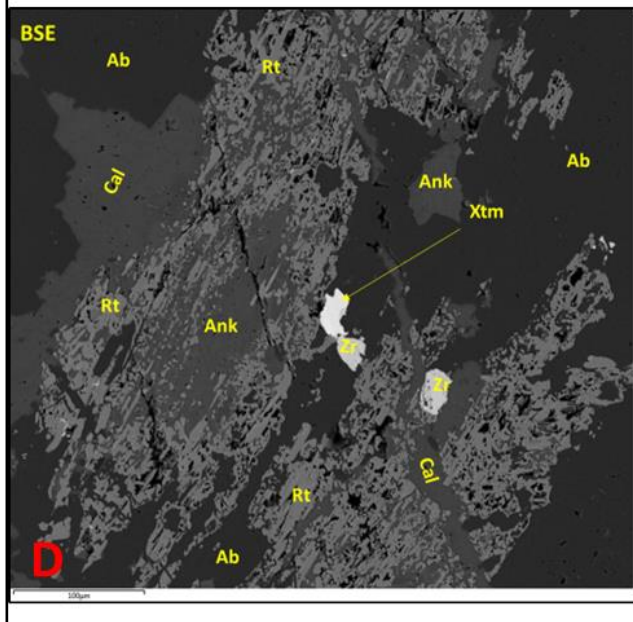
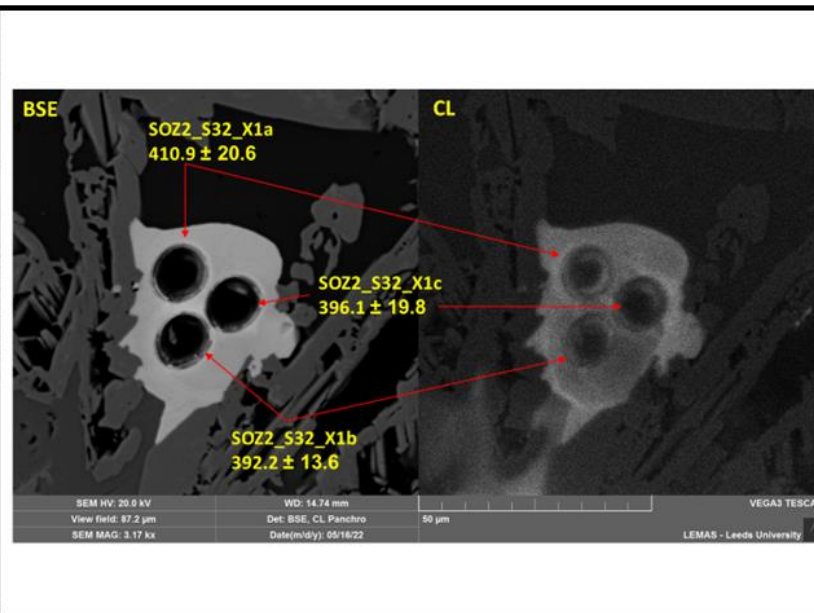
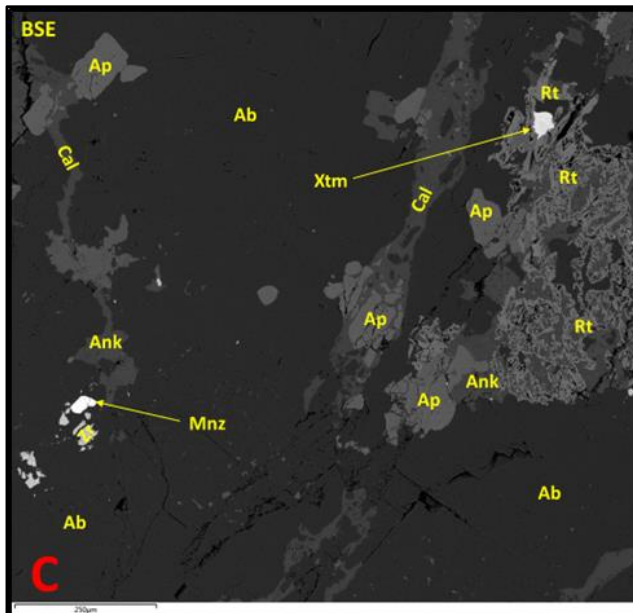






*Plate AIV.8 (next two pages) – BSE/CL images of analysed xenotime grains from sample SOZ2 (Stog'er Tight deposit); red annotations correspond to the rejected analysis spots, whereas the yellow ones to the accepted analysis.*





## AIV.2.2. Argyle

*Table A4.9 – U-Pb isotope ratios and U-Th-Pb contents recorded in the Argyle xenotimes (red rows correspond to the rejected analysis spots)*

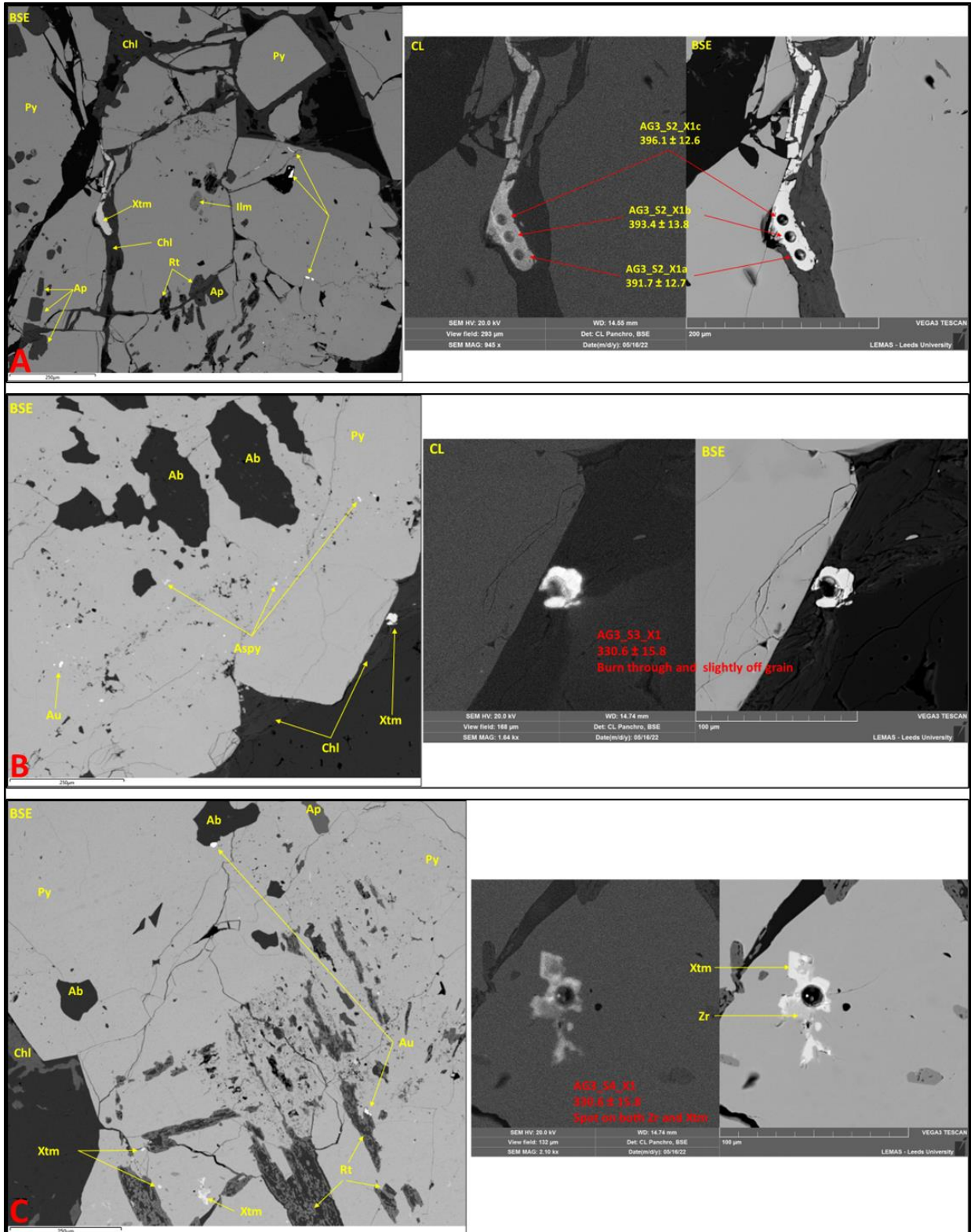
Sample code	$^{238}\text{U}/^{206}\text{Pb}$	1s %	$^{207}\text{Pb}/^{206}\text{Pb}$	1s %	Th/U (ppm)	Pb (ppm)	Th (ppm)	U (ppm)
AG3_S2_X1a	16.0426	1.6708	0.0579	1.8011	4.79	19.83	655.14	136.79
AG3_S2_X1b	15.9460	1.8280	0.0560	1.8588	2.80	12.55	323.86	115.52
AG3_S2_X1c	15.8360	1.6463	0.0565	1.8433	4.30	15.36	484.61	112.68
<b>AG3_S3_X1</b>	<b>14.8147</b>	<b>2.1357</b>	<b>0.2529</b>	<b>3.1129</b>	<b>6.28</b>	<b>12.79</b>	<b>366.82</b>	<b>58.39</b>
<b>AG3_s4_x1</b>	<b>11.7877</b>	<b>3.8745</b>	<b>0.1449</b>	<b>7.8002</b>	<b>0.93</b>	<b>5.42</b>	<b>48.58</b>	<b>52.40</b>
AG3_S8_X1a	15.6792	1.6832	0.0554	0.9165	0.59	36.13	338.63	574.48
AG3_S8_X1b	15.9889	1.8203	0.0559	1.2185	0.47	10.45	79.54	168.06
AG3_S8_X2	15.2526	2.3096	0.0619	2.1762	2.38	9.75	225.95	94.95
AG3_S10_X1	15.7451	1.8043	0.0543	1.3553	1.79	13.95	288.86	161.60
<b>AG3_S10_X2</b>	<b>14.8888</b>	<b>1.9646</b>	<b>0.0673</b>	<b>2.2927</b>	<b>2.10</b>	<b>16.31</b>	<b>346.13</b>	<b>165.10</b>
AG3_S11_X1	16.5930	2.5080	0.0604	2.5106	3.37	8.12	239.47	71.08
<b>AG4_S2_X1a</b>	<b>14.63929</b>	<b>1.8208064</b>	<b>0.060288</b>	<b>1.821163</b>	<b>0.84</b>	<b>8.26</b>	<b>91.42</b>	<b>108.28</b>
AG4_S2_X1b	15.19443	1.763406	0.056927	1.639327	1.11	14.95	205.53	185.82
AG4_S2_X2	16.45112	1.6673068	0.056906	1.391429	0.53	19.12	168.65	315.35
AG4_S3_X1a	15.89357	1.4383244	0.055716	1.289464	0.47	31.69	244.64	522.28
<b>AG4_S3_X1b</b>	<b>15.62595</b>	<b>1.7712732</b>	<b>0.062994</b>	<b>2.091429</b>	<b>0.30</b>	<b>7.38</b>	<b>37.33</b>	<b>123.10</b>
<b>AG4_S3_X1b</b>	<b>15.18679</b>	<b>2.4584462</b>	<b>0.078745</b>	<b>8.938757</b>	<b>0.40</b>	<b>5.57</b>	<b>33.99</b>	<b>85.87</b>
<b>AG4_S3_X2</b>	<b>2.883299</b>	<b>5.3065163</b>	<b>0.668022</b>	<b>1.547233</b>	<b>0.36</b>	<b>38.98</b>	<b>17.94</b>	<b>49.49</b>
AG4_S3_X3	16.57943	1.5606506	0.054361	1.33397	0.39	21.57	149.49	378.55
<b>AG4_S3_X5</b>	<b>3.584976</b>	<b>5.5710464</b>	<b>0.670644</b>	<b>1.47165</b>	<b>0.28</b>	<b>23.07</b>	<b>9.14</b>	<b>32.70</b>
<b>AG4_S7_X1a</b>	<b>14.6859</b>	<b>2.571992</b>	<b>0.06587</b>	<b>2.482948</b>	<b>1.75</b>	<b>3.56</b>	<b>66.57</b>	<b>38.01</b>
AG4_S7_X1b	16.62381	1.5733855	0.056939	1.569932	0.94	14.09	195.14	207.24
AG4_S15_X1	16.56353	2.3061055	0.055566	2.041916	0.52	10.03	86.56	164.98
AG4_S15_X2	17.23981	1.9901777	0.060074	2.228686	0.95	18.54	253.71	267.40
AG4_S15_X3	16.3516	1.92073	0.058732	1.657036	0.48	15.93	126.12	261.04

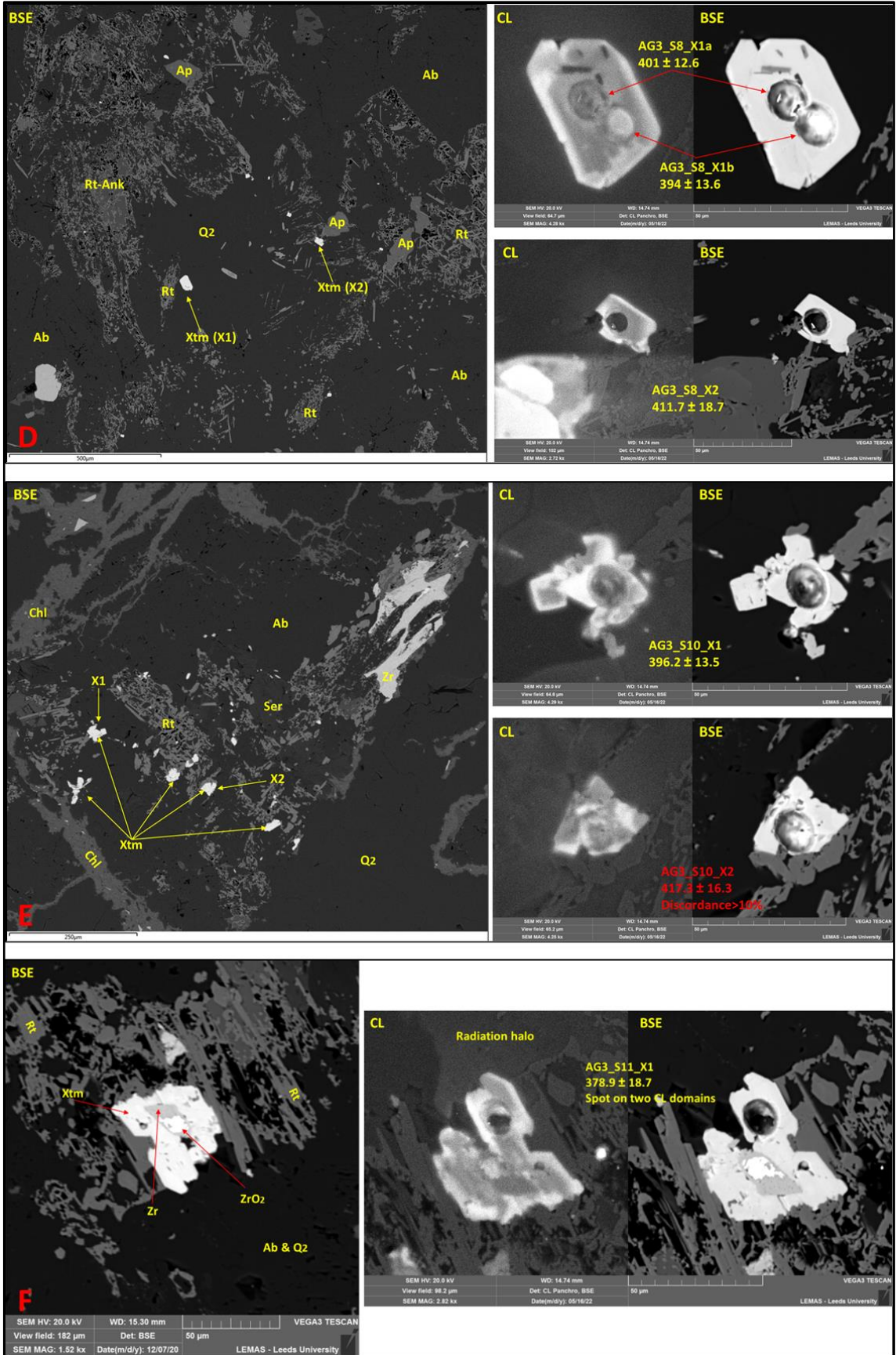
**Table A4.10** – U-Pb dates recorded in the Argyle xenotimes (red rows correspond to the rejected analysis spots);Discordance =  $(^{207}\text{Pb}/^{235}\text{U date} / ^{206}\text{Pb}/^{238}\text{U date}) * 100$ 

Sample code	No.	Concordia Age (Ma)	Error (2 $\sigma$ )	$^{207}\text{Pb}/^{235}\text{U}$ Age (Ma)	Error (2 $\sigma$ )	$^{206}\text{Pb}/^{238}\text{U}$ Age (Ma)	Error (2 $\sigma$ )	$^{207}\text{Pb}/^{206}\text{Pb}$ Age (Ma)	Error (2 $\sigma$ )	Discordance
AG3_S2_X1a	1	391.7	12.7	409.9	16.6	389.8	12.6	525	79	105.1564905
AG3_S2_X1b	2	393.4	13.8	400.8	17.3	392.1	13.9	451.4	82.6	102.2188217
AG3_S2_X1c	3	396.1	12.6	406.1	16.5	394.7	12.6	471.1	81.6	102.8882696
AG3_S3_X1	4	330.6	15.8	1228.4	53.8	421.1	17.4	3202.3	98.4	291.7121824
AG3_s4_x1	5	488.2	38.5	1006.3	111.2	524.9	39.1	2285.8	268.5	191.7127072
AG3_S8_X1a	6	401	12.6	402.8	12.7	398.6	13	427.4	40.9	101.0536879
AG3_S8_X1b	7	394	13.6	399.3	14.5	391.1	13.8	447.4	54.2	102.0966505
AG3_S8_X2	8	411.7	18.7	451.1	23.1	409.4	18.3	669.7	93.1	110.1856375
AG3_S10_X1	9	396.2	13.5	394.8	14.8	396.9	13.9	382.5	60.9	99.47089947
AG3_S10_X2	10	417.3	16.3	491.7	23.5	419.1	15.9	846.1	95.4	117.3228346
AG3_S11_X1	11	378.9	18.7	412.8	24.1	377.2	18.4	617	108.4	109.4379639
AG4_S2_X1a	12	429	15.2	456.5	18.9	426	15	613.4	78.7	107.1596244
AG4_S2_X1b	13	413	14	422.5	16.6	410.9	14	486.7	72.4	102.8230713
AG4_S2_X2	14	383.1	12.3	395.8	14.2	380.4	12.3	486.7	61.4	104.0483701
AG4_S3_X1a	15	394.7	10.9	400.1	12.8	393.3	11	439.4	57.4	101.7289601
AG4_S3_X1b	16	400.6	13.9	448.7	19.9	399.9	13.7	707.3	89	112.2030508
AG4_S3_X1c	17	409.5	19.6	547.2	78.4	411.1	19.6	1163.7	354.3	133.1063002
AG4_S3_X2	18	200.2	70.1	3548.1	108.8	1919.4	176.2	4662.7	44.6	184.8546421
AG4_S3_X3	19	377.9	11.3	378.8	13	377.5	11.4	386.6	59.9	100.3443709
AG4_S3_X5	20	134.1	54.2	3338.2	112.6	1586	156.7	4668.3	42.4	210.4791929
AG4_S7_X1a	21	424.2	21.8	488.9	27.7	424.7	21.1	802.3	104	115.1165529
AG4_S7_X1b	22	378.5	11.5	392.4	14.5	376.6	11.5	486.7	69.3	104.1954328
AG4_S15_X1	23	379.5	16.8	386.1	19.8	377.9	16.9	435.4	90.9	102.1698862
AG4_S15_X2	24	364.6	14.2	398.4	19.7	363.5	14.1	606.2	96.4	109.6011004
AG4_S15_X3	25	385.6	14.4	408.1	17.1	382.7	14.3	555	72.3	106.6370525

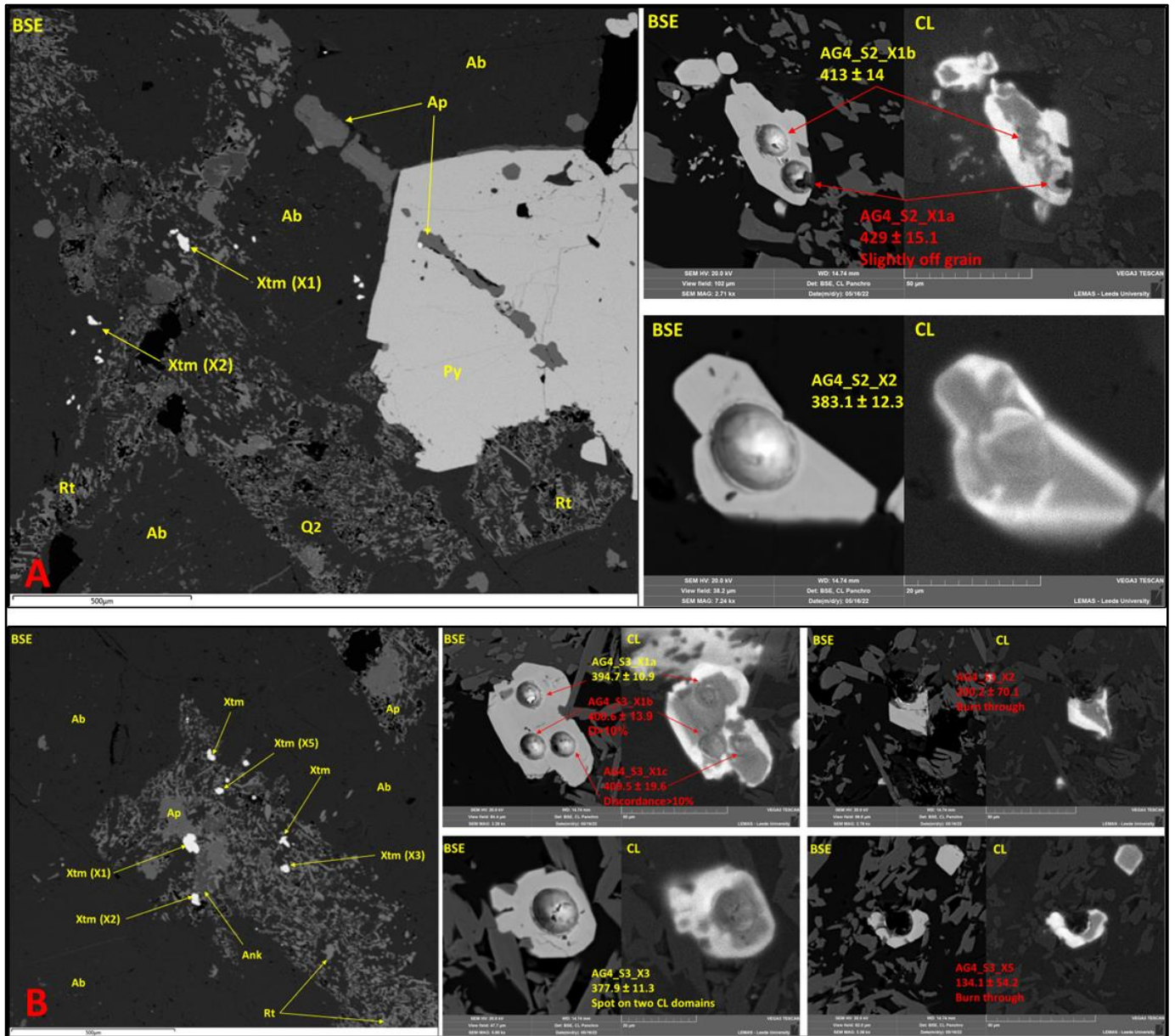


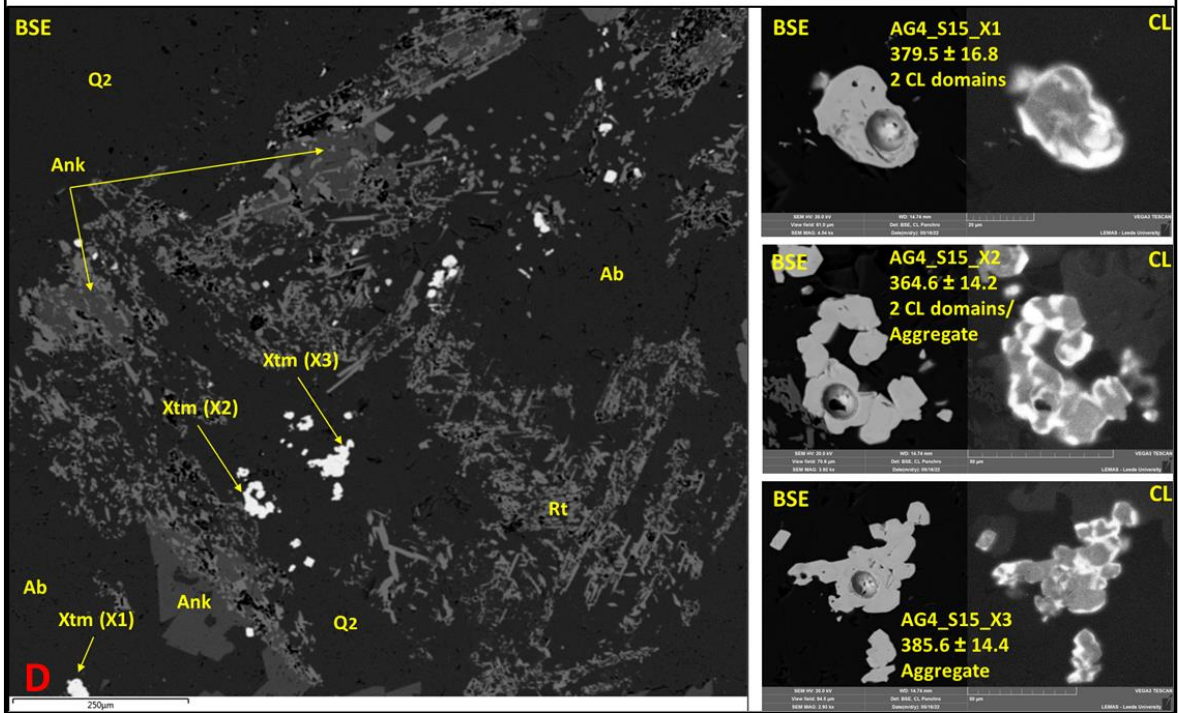
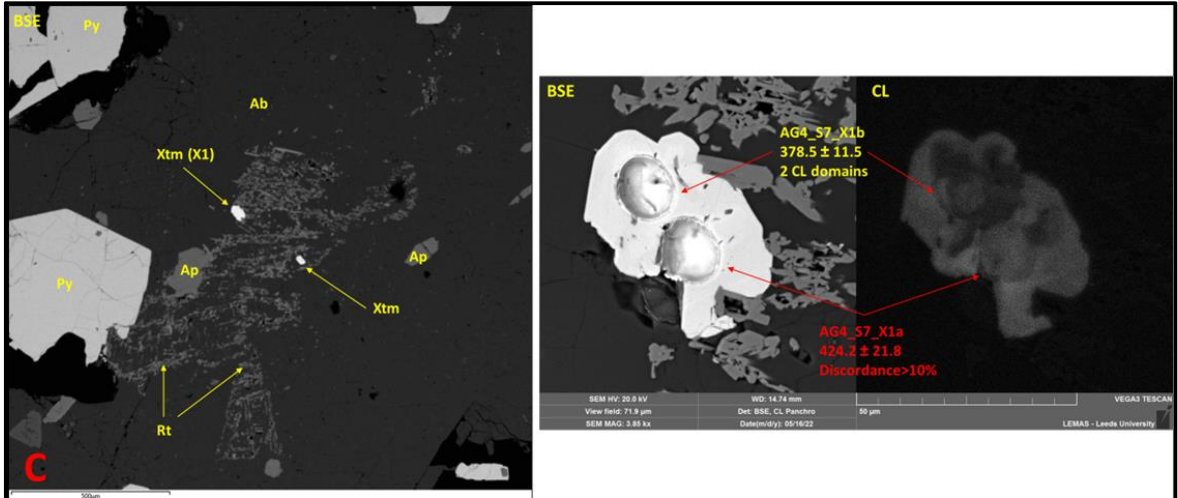
*Plate AIV.9 (next two pages) – BSE/CL images of analysed xenotime grains from sample AG3 (Argyle deposit); red annotations correspond to the rejected analysis spots, whereas the yellow ones to the accepted analysis.*





**Plate AIV.10 (next two pages) – BSE/CL images of analysed xenotime grains from sample AG4 (Argyle deposit); red annotations correspond to the rejected analysis spots, whereas the yellow ones to the accepted analysis.**





## AIV.2.3. Romeo &amp; Juliet

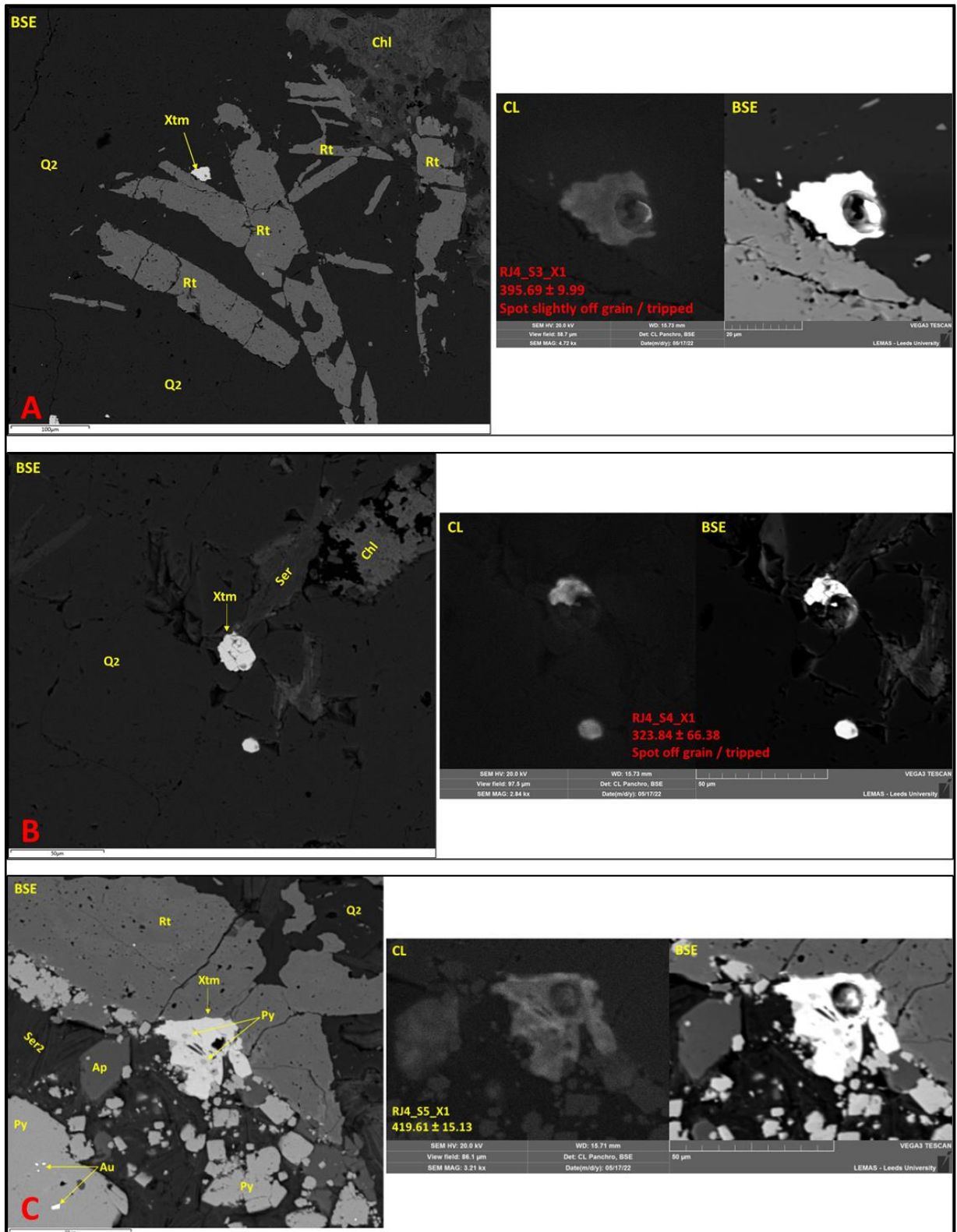
*Table A4.11 – U-Pb isotope ratios and U-Th-Pb contents recorded in the Romeo & Juliet xenotimes (red rows correspond to the rejected analysis spots)*

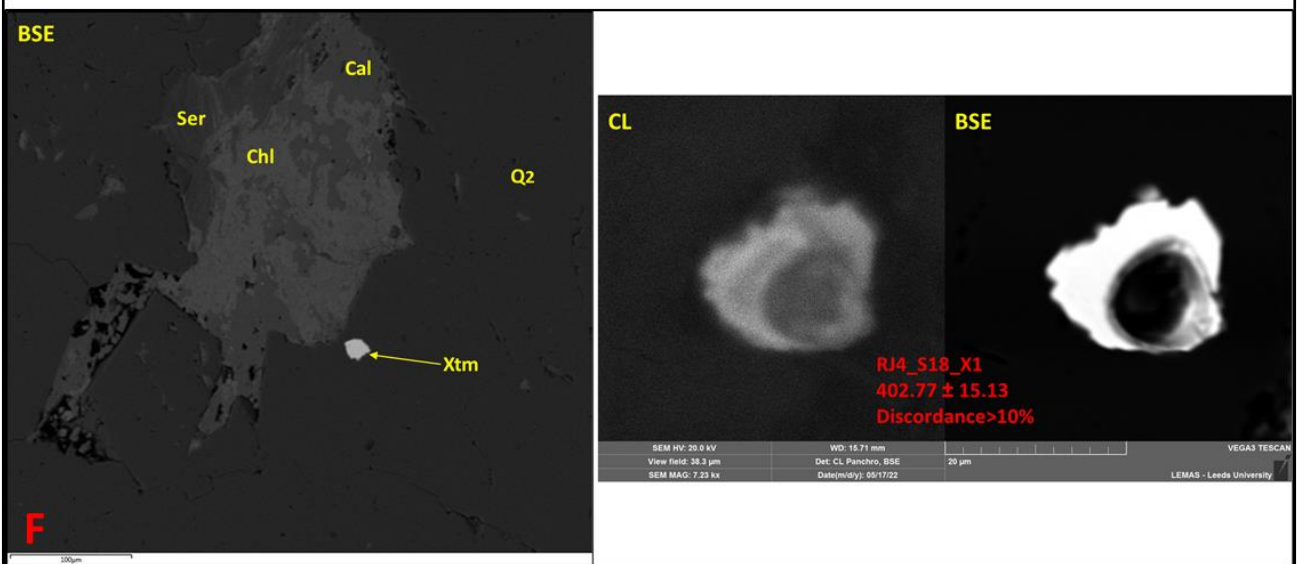
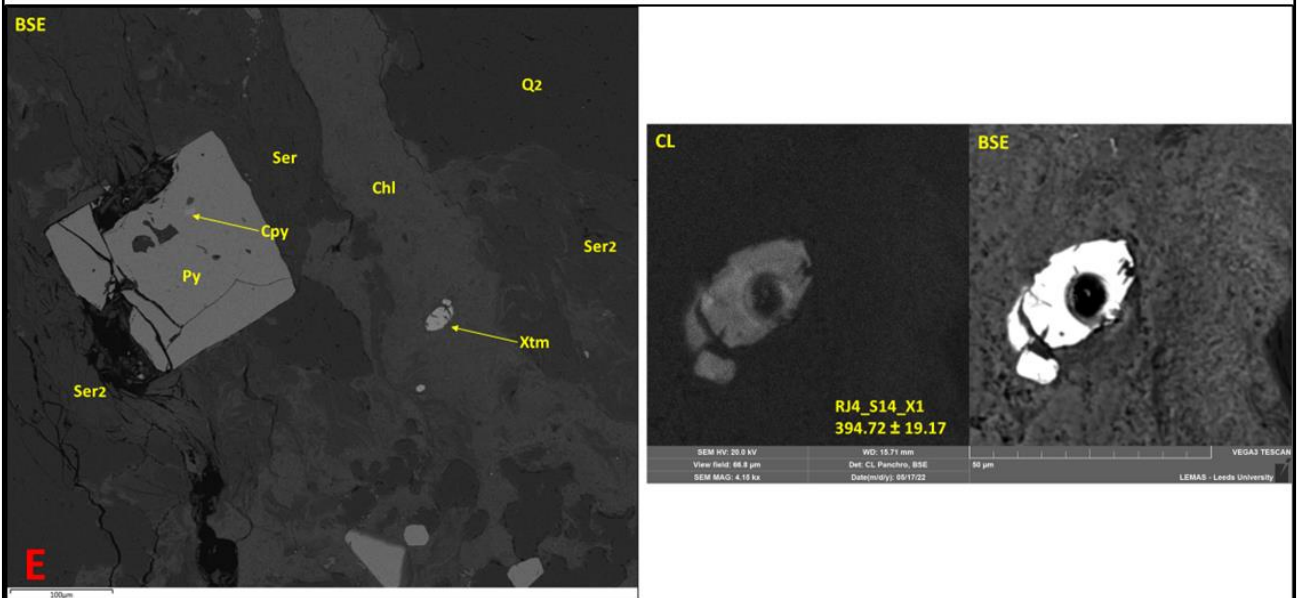
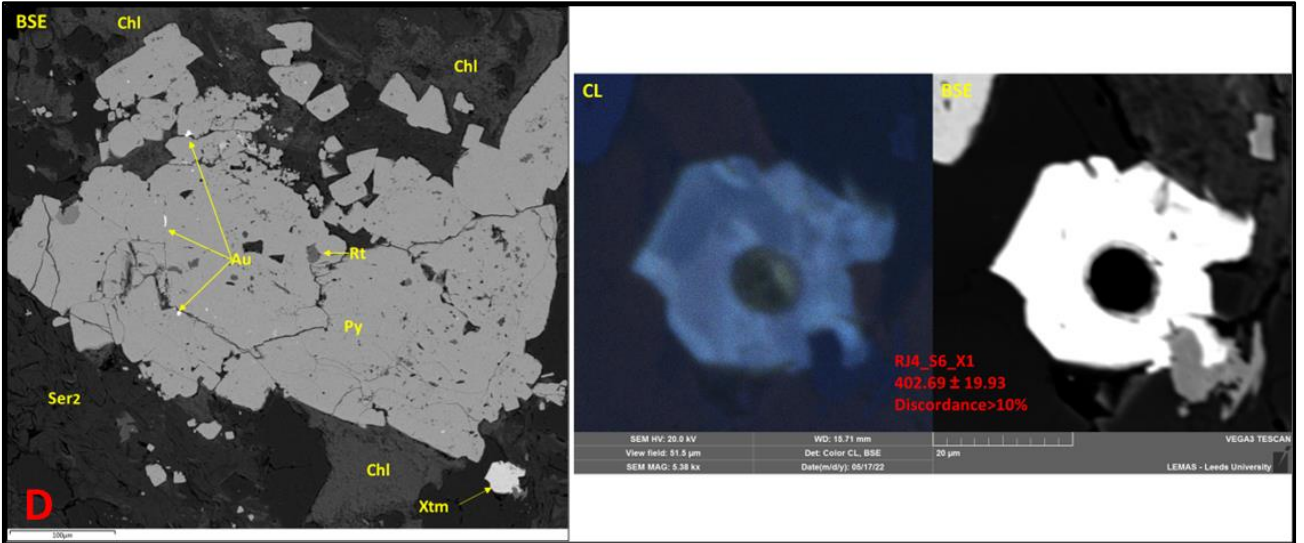
Sample code	$^{238}\text{U}/^{206}\text{Pb}$	1s %	$^{207}\text{Pb}/^{206}\text{Pb}$	1s %	Th/U (ppm)	Pb (ppm)	Th (ppm)	U (ppm)
<b>RJ4_S3_x1</b>	15.7981	1.3009	0.0590	11.2323	0.51	22.27	424.36	826.88
<b>RJ4_S4_x1</b>	18.9881	10.3912	1.0928	66.0654	0.52	0.77	12.15	23.17
RJ4_S5_x1	14.9153	1.9176	0.0557	1.3313	0.93	23.22	595.37	639.39
<b>RJ4_S6_x1</b>	15.4763	2.5222	0.0669	4.2858	1.84	2.85	119.53	64.89
RJ4_S14_x1	15.9001	2.5029	0.0583	3.1000	0.93	3.90	105.91	113.75
<b>RJ4_S18_x1</b>	15.6168	1.8899	0.0621	1.4948	0.07	4.38	12.50	186.87
RJ4_S19_x1	15.2976	1.7046	0.0562	1.9347	0.87	6.29	168.20	194.36
RJ4_S25_x1	15.4215	3.1468	0.0574	4.0800	0.04	1.52	2.44	66.58
<b>RJ4_S25_x2</b>	15.8769	2.5355	0.0621	4.8671	0.01	1.12	0.67	48.84
<b>RJ5_s2_x1a</b>	15.8306	5.0479	0.0925	13.6943	1.32	1.18	37.57	28.55
<b>RJ5_s2_x1b</b>	13.7893	3.2560	0.0957	7.1191	2.46	2.11	73.87	30.04
<b>RJ5_s2_x2</b>	3.8296	4.7867	0.6050	4.7913	2.71	1.02	8.68	3.21
<b>RJ5_s5_x1</b>	8.2789	7.8497	0.3689	8.7691	0.48	2.00	11.51	24.03
RJ5_s5_x2	14.9765	1.8728	0.0579	2.2130	0.77	5.84	130.89	169.88
RJ5_s5_x3	15.8287	1.3109	0.0598	2.2302	0.73	2.90	74.59	102.05
RJ5_s6_x1	14.7731	2.6579	0.0570	2.3568	0.69	5.14	114.69	166.64
RJ5_s7_x1	15.9641	2.0992	0.0546	1.5155	0.64	5.60	126.97	197.63

**Table A4.12** – U-Pb dates recorded in the Romeo & Juliet xenotimes (red rows correspond to the rejected analysis spots);  
 Discordance =  $(^{207}\text{Pb}/^{235}\text{U date} / ^{206}\text{Pb}/^{238}\text{U date}) * 100$

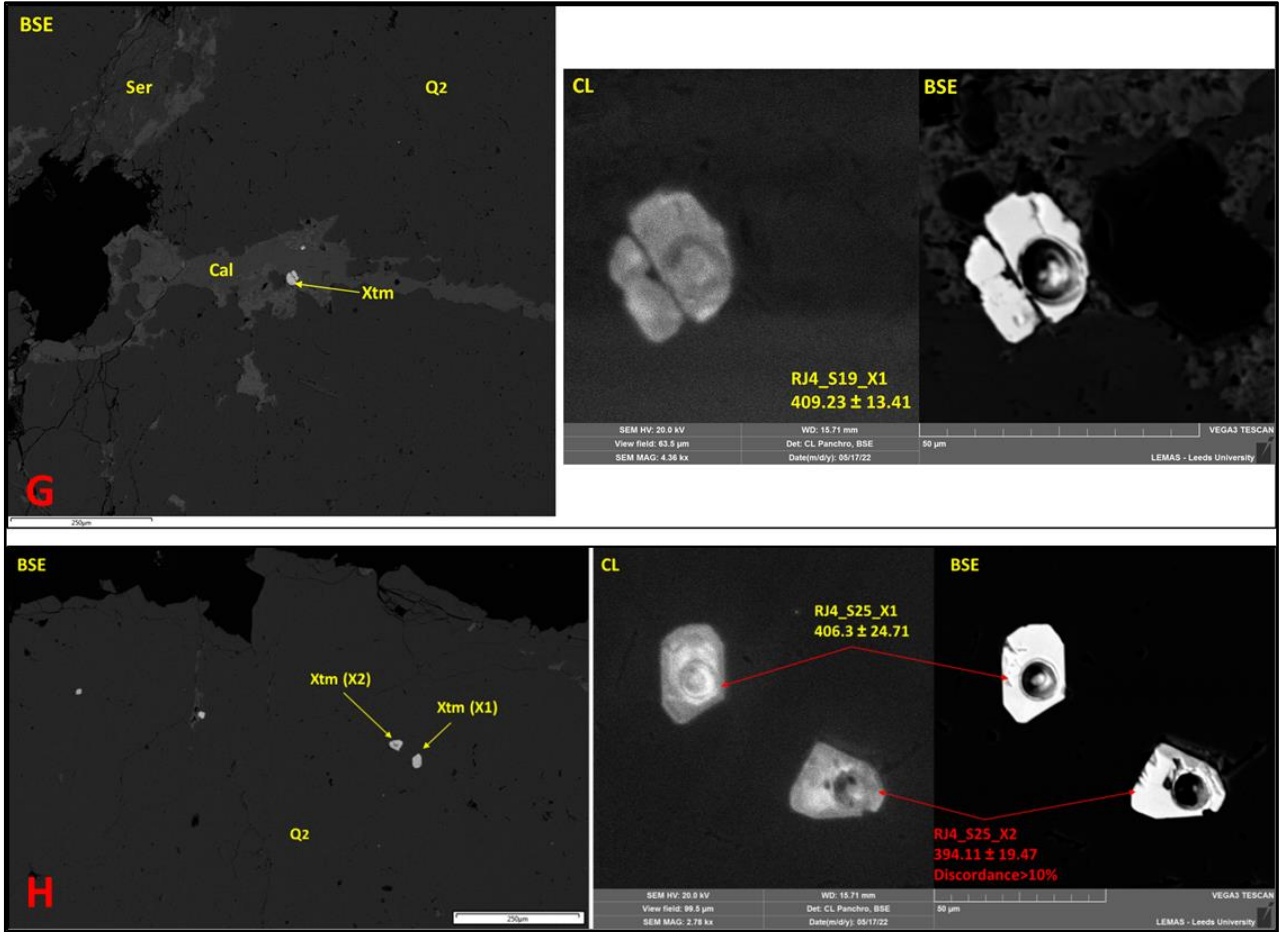
Sample code	No.	Concordia Age (Ma)	Error (2 $\sigma$ )	$^{207}\text{Pb}/^{235}\text{U}$ Age (Ma)	Error (2 $\sigma$ )	$^{206}\text{Pb}/^{238}\text{U}$ Age (Ma)	Error (2 $\sigma$ )	$^{207}\text{Pb}/^{206}\text{Pb}$ Age (Ma)	Error (2 $\sigma$ )	Discordance
RJ4_S3_x1	1	395.69	9.99	421.6	78.03	395.66	9.98	566.12	489.16	106.556134
RJ4_S4_x1	2	323.84	66.38	2223.29	1206.07	330.86	67.03	5361.13	1847.54	671.97304
RJ4_S5_x1	3	419.61	15.13	421.58	16.11	418.33	15.53	439.43	59.25	100.776899
RJ4_S6_x1	4	402.69	19.93	474.53	37.7	403.63	19.74	833.72	178.64	117.565592
RJ4_S14_x1	5	394.72	19.17	415.3	27.16	393.19	19.09	540.07	135.6	105.623236
RJ4_S18_x1	6	402.77	15.13	443.71	17.32	400.11	14.66	676.59	63.91	110.897003
RJ4_S19_x1	7	409.23	13.41	415.97	17.6	408.2	13.48	459.28	85.81	101.903479
RJ4_S25_x1	8	406.3	24.71	420.44	35.48	405.02	24.71	505.95	179.51	103.807219
RJ4_S25_x2	9	394.11	19.47	437.8	39.03	393.75	19.37	676.59	208.09	111.187302
RJ5_s2_x1a	10	388.3	38.7	599.8	132.2	394.9	38.7	1476.8	519.4	151.886554
RJ5_s2_x1b	11	439.9	28.5	681.5	77.7	451.3	28.4	1541	267.7	151.008199
RJ5_s2_x2	12	900.4	110.7	3173.6	131.5	1495.6	127.8	4519.4	139.1	212.195774
RJ5_s5_x1	13	483.3	93.2	1996.1	205.5	735.1	109.1	3786.2	265.8	271.541287
RJ5_s5_x2	14	418.4	15.1	433.7	20.5	416.7	15.1	525	97	104.079674
RJ5_s5_x3	15	395.7	10.1	425.6	18	394.9	10	595.4	96.6	107.77412
RJ5_s6_x1	16	424.5	21.6	433	25	422.2	21.7	490.5	104	102.558029
RJ5_s7_x1	17	391.8	15.5	392.1	16.8	391.7	16	394.9	68	100.102119

*Plate AIV.11 (next three pages) – BSE/CL images of analysed xenotime grains from sample RJ4 (Romeo & Juliet prospect); red annotations correspond to the rejected analysis spots, whereas the yellow ones to the accepted analysis.*

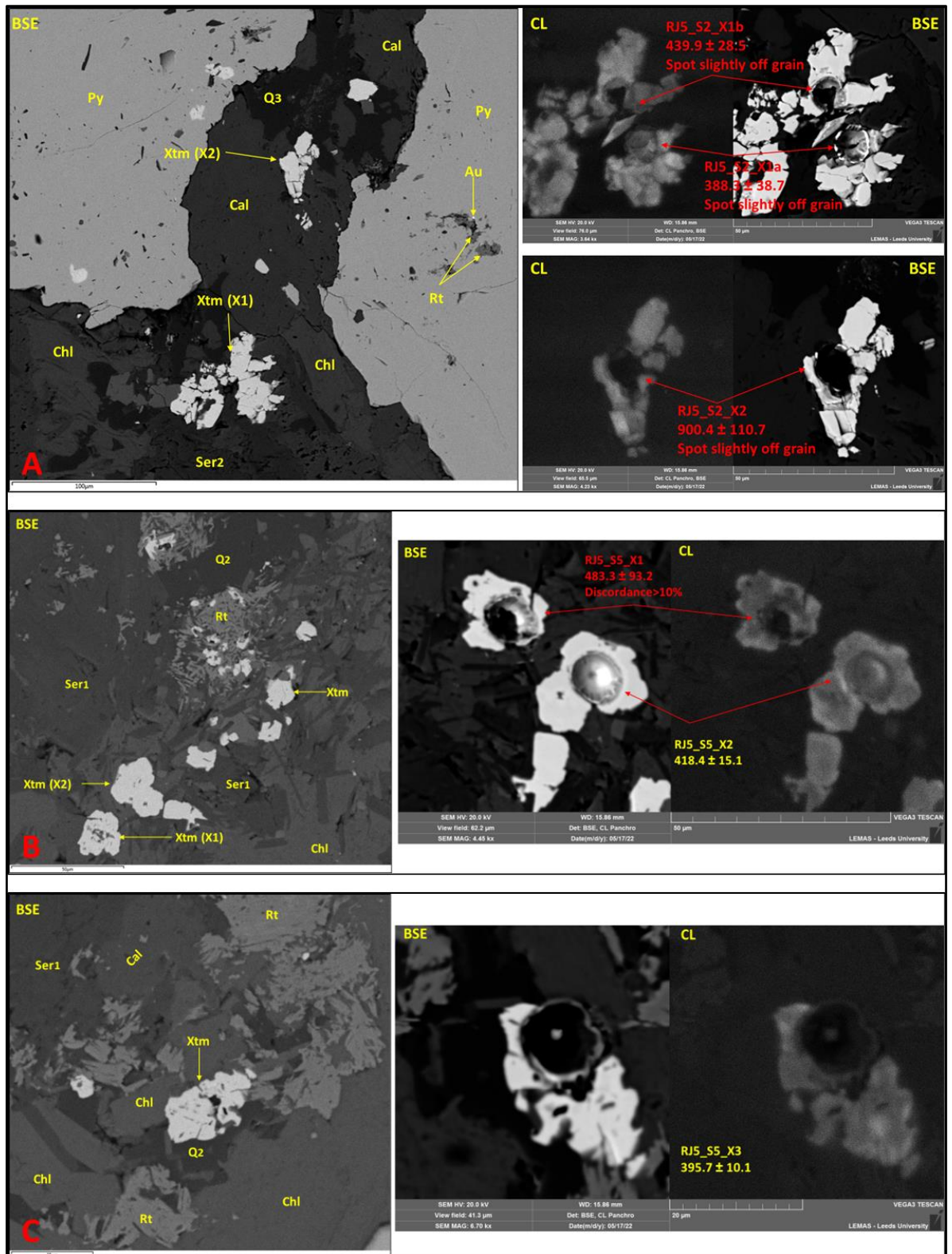


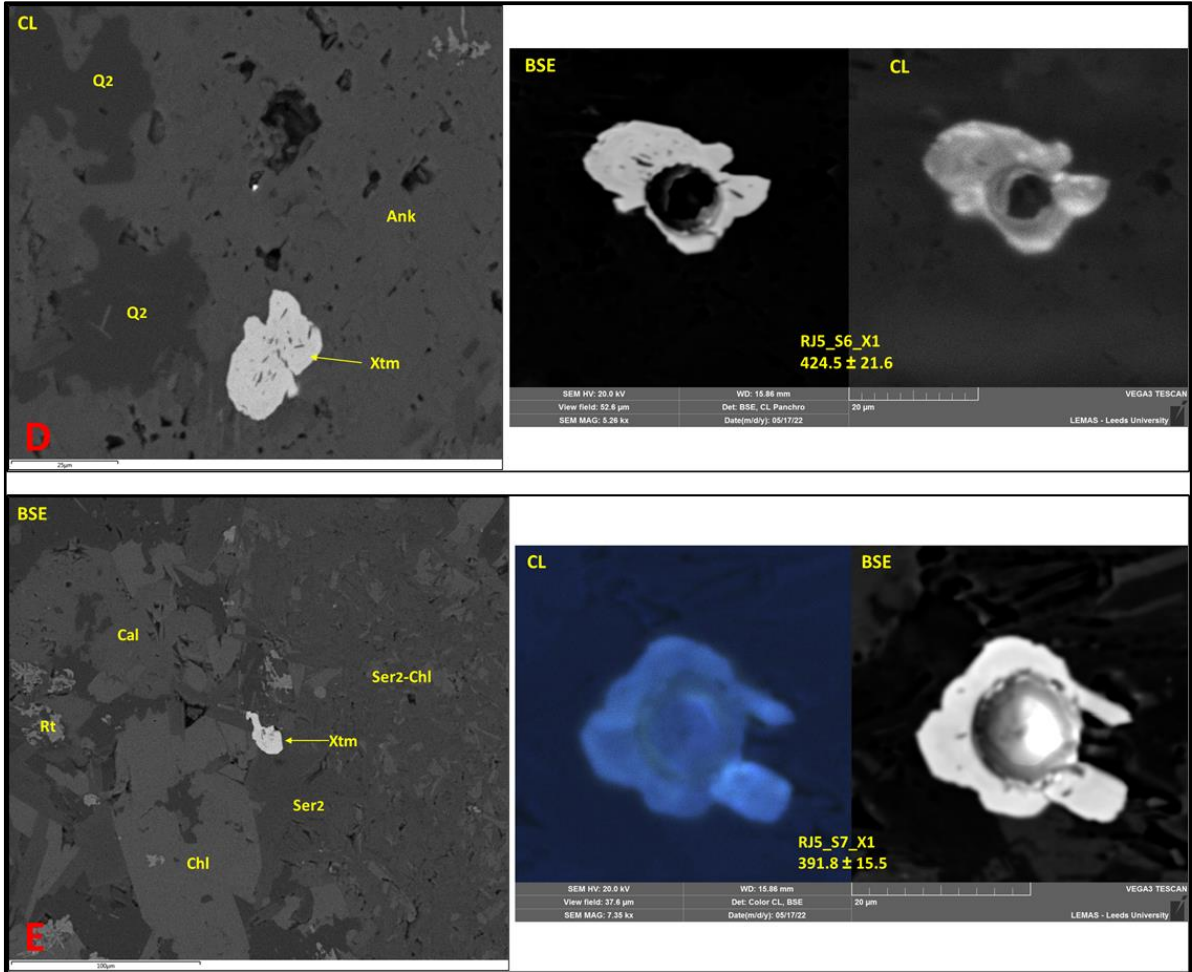






**Plate AIV.12 (next two pages)** – BSE/CL images of analysed xenotime grains from sample **RJ5** (Romeo & Juliet prospect); red annotations correspond to the rejected analysis spots, whereas the yellow ones to the accepted analysis.





**AIV.3. Titanite data****AIV.3.1. Deer Cove***Table A4.13 – U-Pb isotope ratios and U-Th-Pb contents recorded in the Deer Cove titanites*

<b>Sample code</b>	<b><math>^{238}\text{U}/^{206}\text{Pb}</math></b>	<b>1s %</b>	<b><math>^{207}\text{Pb}/^{206}\text{Pb}</math></b>	<b>1s %</b>	<b><math>^{207}\text{Pb}/^{235}\text{U}</math></b>	<b>1s %</b>	<b><math>^{206}\text{Pb}/^{238}\text{U}</math></b>	<b>1s %</b>	<b>Rho</b>
<b>DC5_ttn01</b>	6.9465	1.09	0.4586	1.17	9.0989	1.60	0.1440	1.09	0.68
<b>DC5_ttn02</b>	9.1906	2.53	0.3598	3.37	5.3957	4.22	0.1088	2.53	0.60
<b>DC5_ttn03</b>	9.3646	2.90	0.3275	2.01	4.8204	3.53	0.1068	2.90	0.82
<b>DC5_ttn04</b>	9.7108	2.28	0.3213	3.05	4.5595	3.81	0.1030	2.28	0.60
<b>DC5_ttn05</b>	5.3773	1.51	0.5354	0.92	13.7212	1.76	0.1860	1.51	0.85
<b>DC5_ttn06</b>	7.9781	1.93	0.4321	2.16	7.4650	2.90	0.1253	1.93	0.67
<b>DC5_ttn07</b>	7.9532	2.49	0.4292	2.23	7.4372	3.34	0.1257	2.49	0.74
<b>DC5_ttn08</b>	7.0884	1.18	0.4398	2.60	8.5504	2.86	0.1411	1.18	0.41
<b>DC5_ttn09</b>	10.1227	3.21	0.3239	3.76	4.4097	4.94	0.0988	3.21	0.65
<b>DC5_ttn10</b>	13.5401	5.19	0.2362	5.66	2.4045	7.68	0.0739	5.19	0.68
<b>DC5_ttn11</b>	11.8523	1.44	0.2767	1.72	3.2173	2.25	0.0844	1.44	0.64
<b>DC5_ttn12</b>	5.0526	1.95	0.5553	2.38	15.1457	3.08	0.1979	1.95	0.63
<b>DC5_ttn13</b>	8.7886	3.44	0.3966	2.90	6.2196	4.50	0.1138	3.44	0.76
<b>DC5_ttn14</b>	9.6632	3.16	0.3658	2.71	5.2172	4.16	0.1035	3.16	0.76
<b>DC5_ttn15</b>	8.6088	5.43	0.3543	4.94	5.6719	7.35	0.1162	5.43	0.74
<b>DC5_ttn16</b>	8.2463	3.20	0.3784	2.84	6.3237	4.28	0.1213	3.20	0.75
<b>DC5_ttn17</b>	9.2714	2.25	0.3819	2.54	5.6773	3.39	0.1079	2.25	0.66
<b>DC5_ttn18</b>	8.2734	1.18	0.4034	1.75	6.7195	2.11	0.1209	1.18	0.56
<b>DC5_ttn19</b>	8.3371	3.44	0.3344	2.11	5.5284	4.04	0.1199	3.44	0.85
<b>DC5_ttn20</b>	7.5446	2.80	0.4432	2.26	8.0961	3.60	0.1325	2.80	0.78
<b>DC5_ttn21</b>	10.8111	2.00	0.2879	2.44	3.6700	3.16	0.0925	2.00	0.63
<b>DC5_ttn22</b>	6.7765	2.11	0.4796	1.54	9.7547	2.62	0.1476	2.11	0.81
<b>DC5_ttn23</b>	11.1613	2.35	0.2724	3.25	3.3641	4.00	0.0896	2.35	0.59
<b>DC5_ttn24</b>	7.8074	3.90	0.4057	3.22	7.1619	5.06	0.1281	3.90	0.77

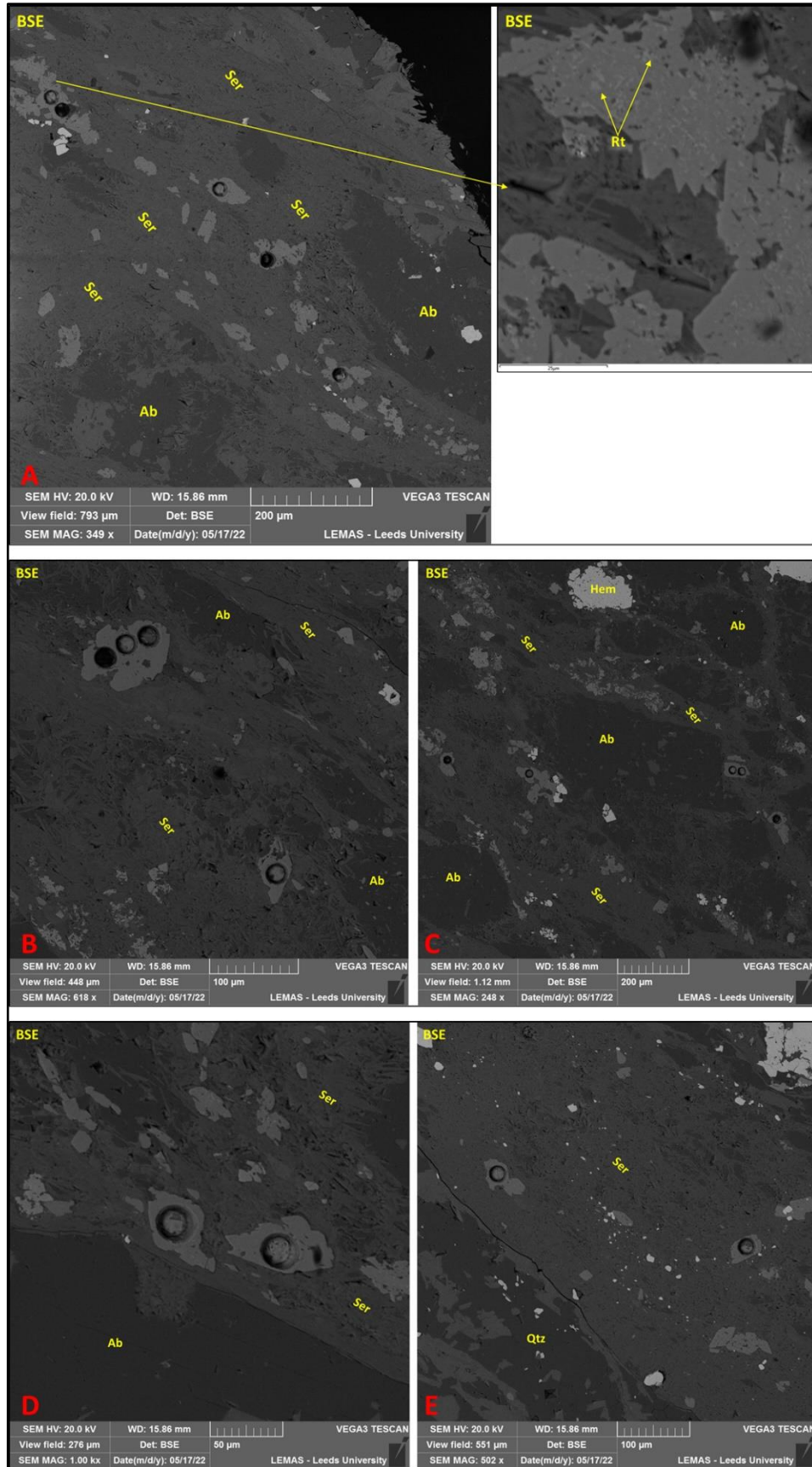
*Table A4.14 – U-Pb-Th contents recorded in the Deer Cove titanites*

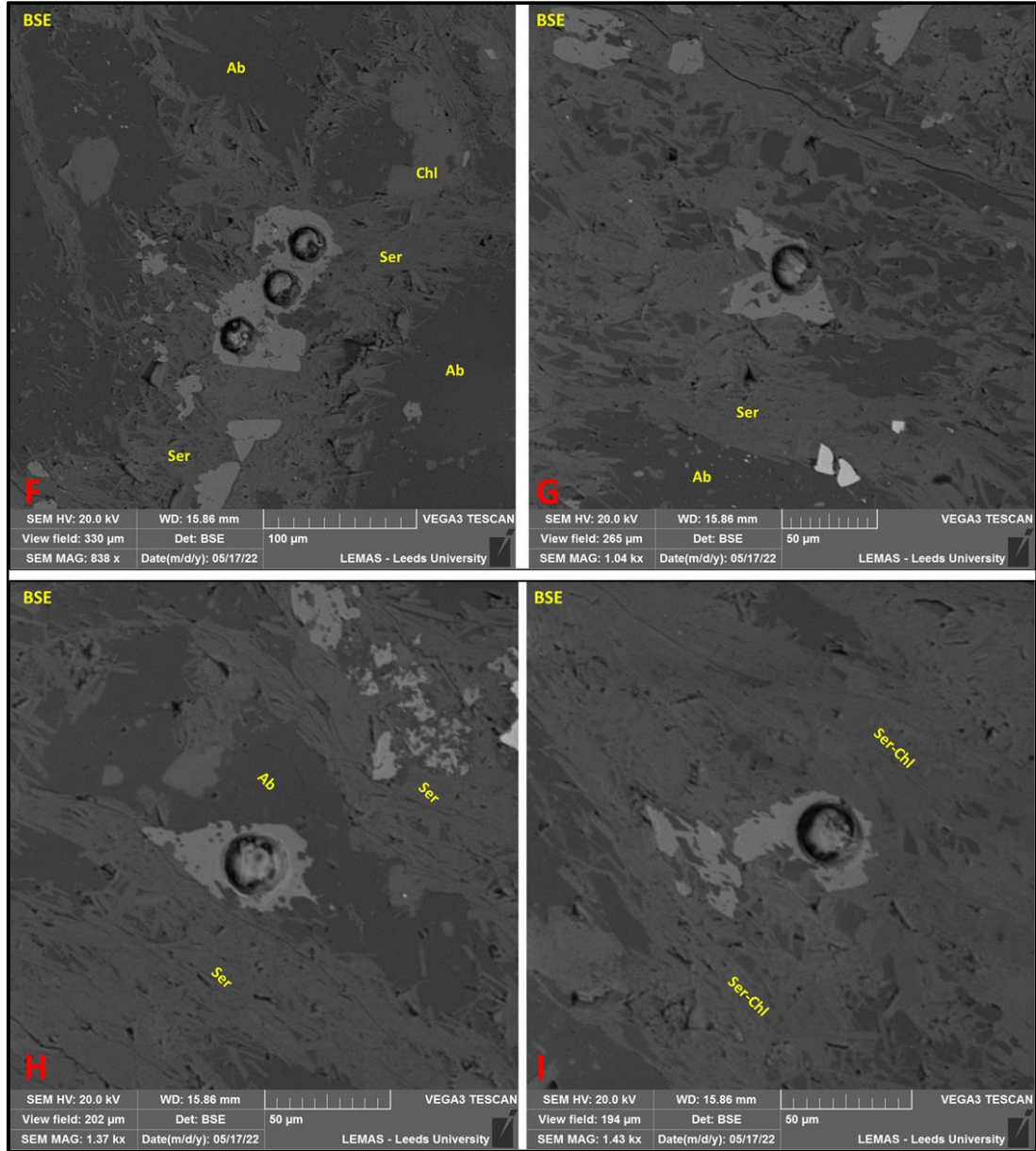
Sample code	Th/U (ppm)	Pb (ppm)	Th (ppm)	U (ppm)
DC5_ttn01	0.13	0.08	0.28	2.16
DC5_ttn02	0.03	0.02	0.02	0.73
DC5_ttn03	0.04	0.01	0.02	0.59
DC5_ttn04	0.04	0.02	0.03	0.80
DC5_ttn05	0.14	0.08	0.20	1.44
DC5_ttn06	0.03	0.02	0.02	0.59
DC5_ttn07	0.03	0.02	0.03	0.74
DC5_ttn08	0.03	0.01	0.01	0.31
DC5_ttn09	0.03	0.02	0.03	1.06
DC5_ttn10	0.04	0.03	0.10	2.48
DC5_ttn11	0.02	0.01	0.02	0.83
DC5_ttn12	0.03	0.01	0.00	0.16
DC5_ttn13	0.03	0.01	0.02	0.53
DC5_ttn14	0.03	0.01	0.02	0.56
DC5_ttn15	0.03	0.01	0.02	0.72
DC5_ttn16	0.03	0.01	0.01	0.51
DC5_ttn17	0.02	0.01	0.01	0.50
DC5_ttn18	0.02	0.02	0.01	0.65
DC5_ttn19	0.03	0.01	0.01	0.47
DC5_ttn20	0.02	0.02	0.01	0.53
DC5_ttn21	0.02	0.02	0.02	1.00
DC5_ttn22	0.04	0.04	0.04	1.05
DC5_ttn23	0.04	0.01	0.04	0.91
DC5_ttn24	0.04	0.02	0.02	0.53

*Table A4.15 – U-Pb dates recorded in the Deer Cove titanites; Discordance = ( $^{207}\text{Pb}/^{235}\text{U}$  date /  $^{206}\text{Pb}/^{238}\text{U}$  date)\*100*

Sample code	No.	Concordia Age (Ma)	Error (2 $\sigma$ )	$^{207}\text{Pb}/^{235}\text{U}$ Age (Ma)	Error (2 $\sigma$ )	$^{206}\text{Pb}/^{238}\text{U}$ Age (Ma)	Error (2 $\sigma$ )	$^{207}\text{Pb}/^{206}\text{Pb}$ Age (Ma)	Error (2 $\sigma$ )	Discordance
DC5_ttn01	1	543	14.9	2348	29.3	867	17.7	4112.7	34.7	270.8189158
DC5_ttn02	2	488.1	28.5	1884.1	72.2	665.8	32	3748.3	102.4	282.9828777
DC5_ttn03	3	275.9	25	1788.4	59.3	654.1	36.1	3604.7	61.7	273.4138511
DC5_ttn04	4	469.5	24.6	1742	63.4	631.8	27.4	3575.4	93.8	275.7201646
DC5_ttn05	5	371.1	19.7	2730.7	33.5	1099.5	30.5	4341.1	27	248.3583447
DC5_ttn06	6	491.6	23.4	2168.7	51.9	761.2	27.7	4024.1	64.5	284.9054125
DC5_ttn07	7	408.2	27.9	2165.5	59.8	763.5	35.9	4014	66.6	283.6280288
DC5_ttn08	8	751.2	18.1	2291.4	51.9	850.7	18.8	4050.4	77.5	269.3546491
DC5_ttn09	9	415.6	32.1	1714.2	81.8	607.3	37.2	3587.8	115.5	282.2657665
DC5_ttn10	10	312.2	39.4	1243.8	110.1	459.3	46	3093.8	180.5	270.8033965
DC5_ttn11	11	367.9	12.6	1461.4	34.8	522.2	14.4	3343.7	53.8	279.8544619
DC5_ttn12	12	800.8	37	2824.5	58.6	1164.1	41.5	4394.5	69.6	242.6337943
DC5_ttn13	13	351.9	34.2	2007.2	78.7	694.7	45.3	3895.6	87.3	288.9304736
DC5_ttn14	14	330	29.1	1855.4	70.9	634.8	38.2	3773.4	82.2	292.2810334
DC5_ttn15	15	395.1	57.8	1927.1	126.7	708.4	72.9	3724.9	150.3	272.0355731
DC5_ttn16	16	398.4	34.9	2021.8	75	737.8	44.6	3824.7	85.9	274.0309027
DC5_ttn17	17	432.4	23.9	1927.9	58.6	660.3	28.2	3838.6	76.7	291.9733454
DC5_ttn18	18	565.9	14.9	2075.2	37.3	735.6	16.4	3921.1	52.6	282.1098423
DC5_ttn19	19	264.6	30.8	1904.9	69.4	730.3	47.5	3636.7	64.6	260.8380118
DC5_ttn20	20	384.9	31.3	2241.8	65	802.4	42.2	4061.9	67.3	279.3868395
DC5_ttn21	21	406.3	19.2	1564.9	50.4	570.3	21.8	3405.6	76	274.3994389
DC5_ttn22	22	377.6	24.7	2411.8	48.1	887.3	35	4179	45.6	271.8133664
DC5_ttn23	23	424.4	22.6	1496	62.8	553.1	24.9	3319.2	101.8	270.4755017
DC5_ttn24	24	386.8	43.1	2131.7	90.1	776.9	57.1	3929.7	96.7	274.3853778

*Plate AIV.13 (next two pages) – BSE images of analysed titanite grains from sample DC5 (Deer Cove prospect)*







## **Appendix V – Methodology for geochronological analyses**

This appendix provides details regarding the instrumentation and the data acquisition procedure used for the in-situ LA-ICP-MS U-Th-Pb analysis of monazite, xenotime, and titanite. The full analytical conditions for each mineral are provided in Tables A5.1, A5.2, and A5.3, respectively.

Instrumentation comprised a Nu Instruments Attom single collector sector field ICP-MS coupled to a New Wave Research (now Elemental Scientific Lasers) 193UC excimer laser ablation system, fitted with a TV2 cell. A full description of the set-up is provided in Mottram et al. (2014). The ICP-MS is run in peak-hopping mode, comprising rapid measurement of Pb (206, 207, 208), Th (232) and U (235 or 238) peaks. Data are reduced using the Time Resolved Analysis function in the Attolab software, with additional normalization and uncertainty propagation completed via an Excel spreadsheet. Samples are normalized to matrix-matched standard reference materials (SRMs) using a standard-sample-standard bracketing procedure, with the addition of a two-stage normalization. This comprises normalization of Pb/Pb ratios to a NIST glass (SRM NIST 610 or NIST 612; Woodhead and Hergt, 2001), followed by normalisation to a monazite, xenotime or titanite reference material for the Pb/U and Pb/Th ratios; this approach allows for the normalisation to reference materials with variable incorporation of common lead.

Primary reference materials used were 44069 monazite ( $426 \pm 3$  Ma; Aleinikoff et al., 2006); FC1 xenotime ( $54 \pm 1$  Ma; Parrish et al., 1990) and Ontario2 titanite ( $1053.3 \pm 3.1$  Ma; Spencer et al., 2013). Secondary matrix matched reference materials are run during each session to check on accuracy and precision; these were Bananeira monazite ( $513.6 \pm 1.6$  Ma; Goncalves et al., 2016), FC1 monazite ( $55.7$  Ma; Parrish et al., 1990; Horstwood et al., 2003), 6413 xenotime ( $994 \pm 1$  Ma; Stern and Rayner, 2003), Datas xenotime ( $513.4 \pm 0.5$  Ma; Vasconcelos et al., 2018) and Fish Canyon Tuff titanite ( $28.53 \pm 0.05$  Ma; Schmitz and Bowring, 2006). Long-term data across the analytical sessions shows that accuracy is within 3% of the recommended age.

*Table A5.1 – Analytical conditions for monazite.*

<b>Laboratory &amp; Sample Preparation</b>	
Laboratory name	Geochronology and Tracers Facility (GTF) British Geological Survey
Sample type/mineral	Monazite
Sample preparation	Polished thin section
Imaging	BSE and EDS mapping of major elements
<b>Laser ablation system</b>	
Make, Model & type	ESI/New Wave Research, 193UC
Ablation cell & volume	TV2
Laser wavelength (nm)	193 nm
Pulse width (ns)	4 ns
Fluence (J.cm <sup>-2</sup> )	~2-2.5
Repetition rate (Hz)	8
Ablation duration (secs)	15
Ablation pit depth / ablation rate	ca. equivalent to 0.08µm/pulse
Spot diameter (µm) nominal/actual	~10-12
Sampling mode / pattern	Static spot ablation
Carrier gas	100% He in the cell, Ar make-up gas combined using a Y-piece along the sample transport line to the torch.
Cell carrier gas flow (l/min)	0.7 l/min
<b>ICP-MS Instrument</b>	
Make, Model & type	Nu Instruments, Attom, SC-ICP-MS
Sample introduction	Ablation aerosol
RF power (W)	1300W
Make-up gas flow (l/min)	Sourced from Nu Instruments DSN-100 desolvating nebulizer. Neb pressure 24psi (estimated at 0.7l/min) Ar.
Detection system	single Mascom Secondary Electron Multiplier

Masses measured	206, 207, 208, 232, 238
Integration time per peak/dwell times (ms); quadrupole settling time between mass jumps	400 $\mu$ s for 206; 600 $\mu$ s for 232; 800 $\mu$ s for 207 and 235; 1200 $\mu$ s for 208; 100 cycles per datapoint
Total integration time per output datapoint (secs)	0.4 secs ( <i>N.B. this should represent the time resolution of the data</i> )
‘Sensitivity’ as useful yield (%; element)	ca. 0.05% U ((#ions detected/#atoms sampled)*100; Schaltegger <i>et al.</i> 2015)
IC Dead time (ns)	11 ns
<b>Data Processing</b>	
Gas blank	100 second on-peak zero subtracted
Calibration strategy	44069 used as primary RM - standard sample bracketing
Reference Material info	44069 (Aleinikoff <i>et al.</i> , 2006) Bananeira (Gonçalves <i>et al.</i> , 2016) FC-1 (Horstwood <i>et al.</i> , 2003)
Data processing package used / Correction for LIEF	Nu Instruments Nu Attolab TRA software and in-house spreadsheet for data normalization and uncertainty propagation. IsoplotR for age calculation. LIEF correction assumes reference material and samples behave identically.
Mass discrimination	sample standard bracketing
Common-Pb correction, composition and uncertainty	Stacey & Kramers (1975) assumed common-lead composition, assuming U-Pb and Th-Pb concordance, using combined U-Th-Pb approach of Vermeesch (2020). Sample ages are quoted without common lead correction, and only sub-concordant ages are utilised.
Uncertainty level & propagation	Ages are quoted at 2s absolute, propagation is by quadratic addition. Reproducibility and age uncertainty of reference material and common-Pb composition uncertainty are propagated where appropriate.
	Bananeira - $^{208}\text{Pb}/^{232}\text{U}$ weighted mean = $510.17 \pm 3.00$ Ma (n = 110/110, MSWD = 4.6, without propagation of systematic uncertainties)

	<p>Bananeira - cmPb corrected <math>^{206}\text{Pb}/^{238}\text{U}</math> weighted mean = <math>513.59 \pm 2.08</math> Ma (n = 98/110, MSWD = 2.4, Stacey &amp; Kramers, 1075 assumed composition for common lead correction. Age uncertainty without propagation of systematic uncertainties)</p> <p>FC-1 - cmPb corrected <math>^{206}\text{Pb}/^{238}\text{U}</math> weighted mean = <math>56.45 \pm 0.21</math> Ma (n = 101/101, MSWD = 1.9, without propagation of systematic uncertainties)</p> <p>FC-1 - <math>^{208}\text{Pb}/^{232}\text{U}</math> weighted mean = <math>54.50 \pm 0.22</math> Ma (n = 101/102, MSWD = 1.8, without propagation of systematic uncertainties)</p>
<b>Other information</b>	<p>Atom measured alongside Agilent Q-ICP-MS for trace elements (Laser Ablation Split-Stream)</p>

*Table A5.2 – Analytical conditions for xenotime.*

<b>Laboratory &amp; Sample Preparation</b>	
Laboratory name	Geochronology and Tracers Facility (GTF) British Geological Survey
Sample type/mineral	Xenotime
Sample preparation	Polished thin section
Imaging	BSE and EDS mapping of major elements
<b>Laser ablation system</b>	
Make, Model & type	ESI/New Wave Research, 193UC
Ablation cell & volume	TV2
Laser wavelength (nm)	193 nm
Pulse width (ns)	4 ns
Fluence (J.cm <sup>-2</sup> )	~2-2.5
Repetition rate (Hz)	8
Ablation duration (secs)	15
Ablation pit depth / ablation rate	ca. equivalent to 0.08µm/pulse
Spot diameter (µm) nominal/actual	~10-12
Sampling mode / pattern	Static spot ablation
Carrier gas	100% He in the cell, Ar make-up gas combined using a Y-piece along the sample transport line to the torch.
Cell carrier gas flow (l/min)	0.7 l/min
<b>ICP-MS Instrument</b>	
Make, Model & type	Nu Instruments, Attom, SC-ICP-MS
Sample introduction	Ablation aerosol
RF power (W)	1300W
Make-up gas flow (l/min)	Sourced from Nu Instruments DSN-100 desolvating nebulizer. Neb pressure 24psi (estimated at 0.7l/min) Ar.

Detection system	single Mascom Secondary Electron Multiplier
Masses measured	206, 207, 208, 232, 238
Integration time per peak/dwell times (ms); quadrupole settling time between mass jumps	400 $\mu$ s for 206; 600 $\mu$ s for 232; 800 $\mu$ s for 207 and 235; 1200 $\mu$ s for 208; 100 cycles per datapoint
Total integration time per output datapoint (secs)	0.4 secs <i>(N.B. this should represent the time resolution of the data)</i>
'Sensitivity' as useful yield (% , element)	ca. 0.05% U <i>((#ions detected/#atoms sampled)*100; Schaltegger <i>et al.</i> 2015)</i>
IC Dead time (ns)	11 ns
<b>Data Processing</b>	
Gas blank	100 second on-peak zero subtracted
Calibration strategy	FC1 used as primary for U/Pb, NIST 612 used as primary for Pb/Pb
Reference Material info	FC1 (Parrish <i>et al.</i> , 1990) Datas - XN01 (Vasoncelos <i>et al.</i> , 2018) 6413 (Stern and Rayner, 2003)
Data processing package used / Correction for LIEF	Nu Instruments Nu Attolab TRA software and in-house spreadsheet for data normalization, uncertainty propagation and age calculation. LIEF correction assumes reference material and samples behave identically.
Mass discrimination	sample standard bracketing
Common-Pb correction, composition and uncertainty	Stacey & Kramers (1975) assumed common-lead composition, assuming U-Pb and Th-Pb concordance, using combined U-Th-Pb approach of Vermeesch (2020). Sample ages are quoted without common lead correction, and only sub-concordant ages are utilised.

Uncertainty level & propagation	Ages are quoted at 2σ absolute, propagation is by quadratic addition. Reproducibility and age uncertainty of reference material and common-Pb composition uncertainty are propagated where appropriate.
Quality control / Validation	XN01 - cmPb corrected 206Pb/238U weighted mean = 513.70 ± 1.68 Ma (n = 65/66, MSWD = 1.2, without propagation of systematic uncertainties)  6413 - cmPb corrected 206Pb/238U weighted mean = 1006.94 ± 15.46 Ma (n = 23/24, MSWD = 6.9, without propagation of systematic uncertainties)
<b>Other information</b>	

**Table A5.3** – Analytical conditions for titanite.

<b>Laboratory &amp; Sample Preparation</b>	
Laboratory name	Geochronology and Tracers Facility (GTF) British Geological Survey
Sample type/mineral	Titanite
Sample preparation	Polished thin section
Imaging	BSE
<b>Laser ablation system</b>	

Make, Model & type	ESI/New Wave Research, 193UC
Ablation cell & volume	TV2
Laser wavelength (nm)	193 nm
Pulse width (ns)	4 ns
Fluence ( $\text{J}\cdot\text{cm}^{-2}$ )	3.1
Repetition rate (Hz)	7
Ablation duration (secs)	20
Ablation pit depth / ablation rate	ca. equivalent to $0.08\mu\text{m}/\text{pulse}$
Spot diameter ( $\mu\text{m}$ ) nominal/actual	22
Sampling mode / pattern	Static spot ablation
Carrier gas	100% He in the cell, Ar make-up gas combined using a Y-piece along the sample transport line to the torch.
Cell carrier gas flow (l/min)	0.7 l/min
<b>ICP-MS Instrument</b>	
Make, Model & type	Nu Instruments, Attom, SC-ICP-MS
Sample introduction	Ablation aerosol
RF power (W)	1300W
Make-up gas flow (l/min)	Sourced from Nu Instruments DSN-100 desolvating nebulizer. Neb pressure 24psi (estimated at 0.7l/min) Ar.
Detection system	single Mascom Secondary Electron Multiplier
Masses measured	206, 207, 208, 232, 238
Integration time per peak/dwell times (ms); quadrupole settling time between mass jumps	300 $\mu\text{s}$ for 208 and 232; 800 $\mu\text{s}$ for 206; 1200 $\mu\text{s}$ for 207 and 238; 120 cycles per datapoint
Total integration time per output datapoint (secs)	0.5 secs ( <i>N.B. this should represent the time resolution of the data</i> )
'Sensitivity' as useful yield (% element)	ca. 0.05% U ( $(\# \text{ions detected} / \# \text{atoms sampled}) * 100$ ; Schaltegger <i>et al.</i> 2015)



IC Dead time (ns)	11 ns
<b>Data Processing</b>	
Gas blank	100 second on-peak zero subtracted
Calibration strategy	Ontario2 used as primary for U/Pb, NIST 612 used as primary for Pb/Pb
Reference Material info	Ontario2 (Spencer et al., 2013) Fish Canyon Tuff (Schmitz and Bowring, 2001)
Data processing package used / Correction for LIEF	Nu Instruments Nu Atto lab TRA software and in-house spreadsheet for data normalization, uncertainty propagation and age calculation. LIEF correction assumes reference material and samples behave identically.
Mass discrimination	sample standard bracketing
Common-Pb correction, composition and uncertainty	No common-Pb correction applied to the data. Stacey & Kramers (1975) <sup>207</sup> Pb-based correction provided for reference only.
Uncertainty level & propagation	Ages are quoted at 2σ absolute, propagation is by quadratic addition. Reproducibility and age uncertainty of reference material and common-Pb composition uncertainty are propagated where appropriate.
Quality control / Validation	Fish Canyon Tuff - FCT - Tera-Wasserburg lower intercept age = 29.73 ± 5.36 Ma (n = 13, MSWD = 2.2)
<b>Other information</b>	



*First beer in Leeds with people from the Ores and Mineralisation Research Group was a Punk IPA and the glass came with the message "To the bitter end". We all started to laugh and thought that this would be a good slogan for advertising PhD projects. My supervisor took this picture and send it to me after I passed the Transfer VIVA (1<sup>st</sup> annual evaluation) and the rest is history.*